

Theoretical Investigation of Two-dimensional (2D) Materials for Nitrogen Activation

by

Maibam Ashakiran Devi

[AcSIR Registration No. 10CC18A26016;
RMIT University Registration No. s3913967]

A thesis submitted under
AcSIR-RMIT Joint (Cotutelle) Ph.D Program
for the award of the degree of
DOCTOR OF PHILOSOPHY

In
SCIENCE

Under the supervision of



Name of the supervisor(s)
Dr. Sailaja Krishnamurty
Dr. Durba Sengupta
CSIR-NCL, Pune

Academy of Scientific and
Innovative Research
AcSIR Headquarters,
CSIR-HRDC campus
Sector 19, Kamla Nehru Nagar,
Ghaziabad, U.P. – 201 002, India



Name of the supervisor(s)
Dr. Ravichandar Babarao
Prof. Salvy Russo

RMIT University
124 La Trobe Street
Melbourne
Victoria
Australia - 3000

December 2023

Certificate

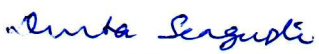
This is to certify that the work incorporated in this Ph.D. thesis entitled, “Theoretical Investigation of Two-dimensional (2D) Materials for Nitrogen Activation”, submitted by Maibam Ashakiran Devi to the Academy of Scientific and Innovative Research (AcSIR) in fulfillment of the requirements for the award of the Degree of Doctor of Philosophy In Science, embodies original research work carried-out by the student. We, further certify that this work has not been submitted to any other University or Institution in part or full for the award of any degree or diploma. Research material(s) obtained from other source(s) and used in this research work has/have been duly acknowledged in the thesis. Image(s), illustration(s), figure(s), table(s) etc., used in the thesis from other source(s), have also been duly cited and acknowledged.


(Signature of Student)

Name with date

Maibam Ashakiran Devi


Date: 18-12-2023


(Signature of Co-Supervisor)

Name with date

Dr. Durba Sengupta

Date: 18-12-2023


(Signature of Supervisor)

Name with date

Dr. Sailaja Krishnamurty

Date: 18-12-2023

STATEMENTS OF ACADEMIC INTEGRITY

I, **Maibam Ashakiran Devi**, a Ph.D. student of the Academy of Scientific and Innovative Research (AcSIR) with Registration No. **10CC18A26016** hereby undertake that, the thesis entitled “**Theoretical Investigation of Two-dimensional (2D) Materials for Nitrogen Activation**” has been prepared by me and that the document reports original work carried out by me and is free of any plagiarism in compliance with the UGC Regulations on “*Promotion of Academic Integrity and Prevention of Plagiarism in Higher Educational Institutions (2018)*” and the CSIR Guidelines for “*Ethics in Research and in Governance (2020)*”.

Maibam Ashakiran Devi
Signature of the Student

Date : 18-12-2023

Place : CSIR-NCL, Pune

It is hereby certified that the work done by the student, under my/our supervision, is plagiarism-free in accordance with the UGC Regulations on “*Promotion of Academic Integrity and Prevention of Plagiarism in Higher Educational Institutions (2018)*” and the CSIR Guidelines for “*Ethics in Research and in Governance (2020)*”.

Durba Sengupta

Signature of the Co-supervisor

Name : Dr. Durba Sengupta

Date : 18-12-2023

Place : CSIR-NCL, Pune

Sailaja

Signature of the Supervisor

Name : Dr. Sailaja Krishnamurty

Date : 18-12-2023

Place : CSIR-NCL, Pune

Dedicated to my family

Acknowledgement

As I approach the end of my PhD journey, words cannot express my heartfelt gratitude to my supervisors Dr. Sailaja Krishnamurty (CSIR-NCL), Dr. Ravichandar Babarao (RMIT), Dr. Durba Sengupta (CSIR-NCL) and Prof. Salvy Russo (RMIT) for their valuable advice, patience and feedback throughout this programme. I have been blessed with the freedom and dexterity my supervisors have given me to pursue multiple projects and plan them independently. I owe them my gratitude for making me a better person and researcher, and most importantly, imbibing the virtue of patience and resilience throughout my PhD journey in India and Australia.

I also could not have undertaken this journey without the insights and feedback from my Doctoral Advisory Committee (DAC) members Dr. Nayana Vaval, Dr. Sarika Maitra Bhattacharyya and DAC chairperson Dr. Kiran A. Kulkarni in CSIR-NCL. The feedback from the independent member Dr. Andrew Hung and Chair, Associate Professor James Tardio have helped me better my presentation skills. The suggestion and scientific advice from the defence committee has helped me a lot to the construction of my thesis.

I would like to extend my special thanks to Dr. Chepuri V. Ramana, Dr. D. Srinivasa Reddy and Dr. Kaliaperumal Selvaraj for their support in availing computational resources from CSIR-4PI. I am also grateful to the Director, Dr. Ashish Lele; Dr. B. L. V. Prashad (ex-Chair) and Dr. T. G. Ajithkumar (Chair) of Physical and Materials Chemistry Division of CSIR-NCL and Disting. Prof. Suresh Bhargava, Prof. Sujeeva Setunge and Prof. Samantha J. Richardson of RMIT University for their support. I would like to extend my gratitude to Dr. Arup Kumar Rath for the completion of the CSIR 800 project; course coordinators Dr. Kumar Vanka, Dr. Nayana Vaval, Dr. Kavita Joshi, Dr. Ram Rup Sarkar and Dr. Vinod C Prabhakaran for having taught me during my PhD. I want to further extend a warm thanks to my research collaborators Dr. Thillai Govindaraja, Dr. Jayaraj Nithyanandhan, Dr. Sukumaran Santhosh Babu, Dr. Manzoor Ahmad Dar, Dr. Manjusha V Shelke, Dr. R. Nandini Devi, Dr. Thangjam Ibomcha Singh, Dr. Seunghyun Lee and Dr. Seok-In Na.

I also acknowledge all the non-academic staff of CSIR-NCL and AcSIR, for their support and help during my PhD. I want to acknowledge Mr. Tae Kim from RMIT, STEM and RMIT connect services team for their continuous and tireless support to my enquiries and

resolving on time which is extremely beneficial to acquire my degree. I sincerely acknowledge the JRF and SRF fellowship I have received from Council of Scientific & Industrial Research (CSIR) during my tenure in India and Australian Government Research Training Program Scholarship from RMIT University for my tenure in Australia.

I am also grateful to my lab mates and cohort members - Ravi Kumar, Palak Patel, Pragnya Paramita Samal, Chandrodai Pratap Singh, Asma H. Maneri, Tushar Singh Verma, Bhavana, Nikhil Samudre, George Devasia and especially my senior Dr. Krati Joshi from CSIR-NCL; Dr. Shiva Nanadala Prasad and Ibrahim B. Orhan from RMIT for their help, late-night feedback sessions, and moral support.

It would be remiss in not mentioning my family, especially my parents and siblings for their blessings and support. Their belief in me has kept my spirits and motivation high during this process. Lastly, I am grateful to the blissful, merciful, and omnipresent GOD for providing me with the patience, courage, determination and sound health throughout my PhD journey.

Maibam Ashakiran Devi

Table of Contents

Abbreviations	i-iii
Physical Constants	iv
Synopsis	1-2
Chapter 1: A Brief Overview on two-dimensional (2D) materials for nitrogen reduction reaction (NRR)	3-42
Abstract	3
1.1 Introduction	4
1.2 Nitrogen molecule: activation and reduction to NH ₃	5
1.3 NRR in carbon-based materials	8
1.3.1 Metal single atom catalysts (SACs) on graphene for NRR	9
1.3.2 Metal diatomic atom catalysts (DACs) to single-metal cluster catalysts (SCCs) on graphene	12
1.4 NRR in metal carbides and borides (MXenes and MBenes)	15
1.4.1 MXenes for NRR	16
1.4.2 MBenes for NRR	19
1.5 NRR in transition metal dichalcogenides	21
1.5.1 Mo-based TMDs for NRR	22
1.5.2 TMDs of other transition metals for NRR	24
1.6 NRR in Metal Organic Frameworks (MOFs) and Covalent Organic Frameworks (COFs)	27
1.7 Motivation and Objectives of the Thesis	31
1.8 Organization of the thesis	33
1.9 References	34
Chapter 2: Theoretical Background and Computational Methodology	43-66
Abstract	43
2.1 Introduction	44
2.1.1 Quantum mechanics and the wave equation	44
2.1.2 Born-Oppenheimer Approximation	46
2.1.3 Hartree Approximation	46
2.1.4 Hartree-Fock Approximation	47
2.2 Density Functional Theory	48

2.2.1 The Hohenberg-Kohn Theorems	49
2.2.2 The Kohn-Sham Equations	50
2.2.3 Exchange- correlation Functional	52
2.2.3.1 Local-Density Approximation (LDA)	53
2.2.3.2 Generalized-Gradient Approximation (GGA)	54
2.2.4 Kohn-Sham Orbitals	54
2.3.1 <i>Ab initio</i> Molecular Dynamics (AIMD)	56
2.3.2 van der Waals Corrections	58
2.3.3 Implicit Solvation Model	59
2.3.4 Atomic charge analysis	61
2.4.1 Vienna <i>ab-initio</i> simulation package	63
2.4.2 deMon2K software	64
2.5 References	65
Chapter 3: Dinitrogen Activation on Graphene Anchored Single Atom Catalysts: Local Site Activity or Surface Phenomena	67-88
Abstract	67
3.1 Introduction	68
3.2 Computational Details	72
3.2.1 Nomenclature of the SACs Anchored Graphene Models	72
3.2.2 Methodology and Computational Details	74
3.3 Results and Discussions	76
3.3.1 N ₂ adsorption and N-N bond elongation	76
3.3.2 Bader charges and electronic properties	80
3.4 Conclusions	84
3.5 References	85
Chapter 4: Nitrogen activation to reduction on a recyclable V-SAC/BN-graphene heterocatalyst sifted through dual and multiphilic descriptors	89-122
Abstract	89
4.1 Introduction	90
4.2 Computational Details	94
4.2.1 Models	94
4.2.2 Computational Methodology	94
4.2.3 Reactivity descriptors and Gibbs Free Energy Calculations	96
4.3 Results and Discussions	98

4.3.1 Binding energy of metal SACs	98
4.3.2 Reactivity descriptor of metal SACs	100
4.3.3 Dinitrogen adsorption and activation on metal SACs	104
4.3.4 NRR mechanism on V-BNring-grap, W-CBN-grap and Re-CBN-grap systems	111
4.4 Conclusions	116
4.5 References	117
Chapter 5: Electrocatalytic nitrogen reduction on defective graphene modulated from single atom catalyst to aluminium clusters	123-145
Abstract	123
5.1 Introduction	124
5.2 Computational Details	126
5.3 Results and Discussions	129
5.3.1 Stability of the M@N ₄ -DVG systems	129
5.3.2 Electronic properties of M@N ₄ -DVG systems and N ₂ activation	132
5.3.3 Nitrogen reduction reaction (NRR) on M@N ₄ -DVG systems	136
5.4 Conclusions	142
5.5 References	143
Chapter 6: Electrocatalytic nitrogen reduction directed through the p-band center of boron on B_{SAC}@Mo₂C	146-164
Abstract	146
6.1 Introduction	147
6.2 Computational Details	149
6.3 Results and Discussions	151
6.3.1 N ₂ adsorption on B _{cat} Mo ₂ C	151
6.3.2 N ₂ reduction to NH ₃ on B _{cat} @Mo ₂ C catalysts	153
6.3.3 Mechanistic insights from electronic properties	158
6.4 Conclusions	160
6.5 References	160
Chapter 7: Doped 2D VX₂ (X = S, Se, Te) monolayers as electrocatalysts for ammonia production: A DFT based study	165-184
Abstract	165
7.1 Introduction	166
7.2 Computational Details	168

7.3 Results and Discussions	169
7.3.1 Formation of $VX_2@Y_{cat}$ monolayers and N_2 chemisorption	169
7.3.2 N_2 reduction on $VX_2@Y_{cat}$ monolayers	173
7.3.3 NRR mechanism on 2H- $VS_2@B$ and 1T- $VS_2@C$	176
7.4 Conclusion	180
7.5 References	181
Chapter 8: Surface electronic properties driven electrocatalytic nitrogen reduction on metal-conjugated porphyrin 2D-MOFs	185-205
Abstract	185
8.1 Introduction	186
8.2 Computational Details	188
8.3 Results and Discussions	190
8.3.1 M-TCPP surface electronics and N_2 activation	190
8.3.2 NRR mechanism	197
8.3.3 NRR electrocatalytic activity and selectivity	199
8.4 Conclusion	202
8.5 References	203
Chapter 9: Summary and Future Scope	206-212
Abstract	206
9.1 Focus of the thesis	207
9.2 Summary of results	208
9.3 Future scope	210
9.4 References	212
ABSTRACT	213
List of Publications and Abstract of Attended Conferences	214-224
Reprint of Published Research Papers	225

List of Figures

Figure 1.1: (a-b) Global ammonia demand, 1900-2020 (top), and uses (bottom); (c) Nitrogen fertiliser application by region and product as estimated in 2020.....	5
Figure 1.2: Molecular orbital diagram of N ₂ molecule.....	6
Figure 1.3: Possible mechanistic routes of nitrogen reduction reaction (NRR): distal and alternating route for N ₂ adsorbed in end-on mode, while enzymatic route is observed in side-on adsorbed N ₂	7
Figure 1.4: Schematic representation of metal-SAC embedded in N-doped graphene (a) single vacancy (SV) or M-N ₃ and (b) divalent vacancy (DV) or M-N ₄ graphene.....	10
Figure 1.5: Schematic representation of synthesizing ISAS-Fe/NC with Fe-SAC catalyst from the chemical precursors and a model representation of the Fe-SAC coordinated to N-doped carbon.....	11
Figure 1.6: Microscopic structure of diatomic PdCu catalyst anchored on N-doped carbon (PdCu/NC) obtained from (a) low-magnification and (b) magnified atomic resolution HAADF-STEM (High-angle annular dark-field scanning transmission electron microscopy) showing diatomic site as bright spots; (c) Theoretical representation of the PdCu atom pair on N-doped graphene as a schematic model of PdCu/NC.....	13
Figure 1.7: Different engineering approaches to develop graphene-based materials catalysts for nitrogen reduction reaction (NRR).....	14
Figure 1.8: Representative models of the most primarily formed two-dimensional MXene and MBene with varying stoichiometric composition.....	16
Figure 1.9: Summarization of the timeline on the MXenes reported as electrocatalysts for NRR at ambient conditions.....	19
Figure 1.10: Comprehensive picture of all possible MBenes from the transition metals of the periodic table that been reported by theoretical and experimental studies; the different stoichiometric formula and structure of the MBenes are also provided herein.....	21
Figure 1.11: A schematic overview of different transition metals that can combine with chalcogens (S, Se and Te) to form transition metal dichalcogenides (TMDs). Top and side views of 2H and 1T phases of the TMDs, with the different engineering defects that can be incorporated in TMDs to enhance the NRR catalytic efficiency.....	22
Figure 1.12: Structural images of Fe-doped ReS ₂ monolayers, Fe-ReS ₂ (a) SEM (scanning electron microscope) image, (b) HRTEM image showing the ReS ₂ monolayers, (c) atomistic	

model of Fe-ReS₂ with the two-dimensional electron localization function (ELF) mapping.....26

Figure 1.13: Atomistic presentation of (a) Fe-based 2D porphyrin MOF (Fe-TCPP) and (b) Fe incorporated in phthalocyanine-based 2D-COF (FePc-pz) framework.....29

Figure 3.1: Graphene models considered in this study as supports to SAC: (a) A periodic graphene sheet with 50 atoms in a cell; (b) 42 atom graphene nanoflake with zigzag edges (C₄₂-zz); (c) 42 atom graphene nanoflake with armchair edges (C₄₂-ac); (d) 54 atom graphene nanoflake with zigzag edges (C₅₄-zz); (e) 54 atom graphene nanoflake with armchair edges (C₅₄-ac). Elemental color codes: grey, carbon (C); teal, hydrogen (H).....71

Figure 3.2: (a) N–N bond length in graphene model–Mo–N₂ complexes for varying chemical composition, as highlighted on the x-axis. The calculated N–N bond length in free dinitrogen is 1.12 Å. (b) Average Mo–N bond length (Å) in N₂ adsorbed Mo-anchored graphene models. Solid black line represents periodic-Mo–N₂ complexes, dotted and solid lines represent graphene nanoflakes when Mo is described with DZVP and QECP basis set, respectively...76

Figure 3.3: N-N stretching frequency in graphene model-Mo-N₂ complexes (calculated ν_{N-N} in free N₂ = 2326 cm⁻¹). Solid black line represents periodic-Mo-N₂ complexes, dotted and solid lines represent graphene nanoflakes when Mo is described with DZVP and QECP basis set, respectively.....79

Figure 3.4: (a) Average of the Bader charges on the adsorbed N₂ molecule, (b) Bader charges on the Mo atom after N₂ adsorption.....80

Figure 3.5: (a) Average Löwdin charges on the adsorbed N₂ molecule, (b) Löwdin charges on the Mo atom after N₂ adsorption.....80

Figure 3.6: (a) Total charge density plots for the periodic pris-gp-sheet and finite pris-gp-C₄₂-zz models, their Mo-anchored geometries and N₂ adsorbed pris-gp-Mo geometries; (b) Charge difference density plots of the Mo-anchored periodic models with and without N₂. Density plots are made at an isosurface value of 0.06e^Å⁻³.....81

Figure 3.7: Total density of states (TDOS) and Projected density of states (PDOS) plots of (a) pris-gp-sheet-Mo-N₂ (b) BN-gp-sheet-Mo-N₂ (c) CBN-gp-sheet-Mo-N₂ (d) BNring-gp-sheet-Mo-N₂.83

Figure 3.8: HOMOs of (a) pris-gp-C₄₂-zz -Mo-N₂ (b) BN-gp-C₄₂-zz-Mo-N₂ (c) CBN-gp-C₄₂-zz-Mo-N₂ (d) BNring-gp-C₄₂-zz- Mo-N₂. LUMOs of (a1) pris-gp-C₄₂-zz-Mo-N₂ (b1) BN-gp-C₄₂-zz-Mo-N₂ (c1) CBN-gp-C₄₂-zz-Mo-N₂ (d1) BNring-gp-C₄₂-zz-Mo-N₂.....83

Figure 4.1: (a) Models of periodic C_n graphene sheet and non-periodic graphene nanoflakes $C-42_{zz}$ and $C-54_{zz}$ with their lateral widths of 8.7 Å and 12.4 Å, respectively (b) Different concentrations of BN-pair doping on graphene substrate with metal SAC represented by different colour code.....	93
Figure 4.2: Binding energies of the metal SACs on periodic and non-periodic graphene supports. Metals on the negative scale of cyan line are stable and show exothermic E_b on the graphene supports. Symbolic representations of BN-doping is provided in inset along with colour scheme of the metals.....	98
Figure 4.3: Dual descriptor, $f^{(2)}(r)$ condensed at the metal centers on periodic and non-periodic models of pristine and BN-pair doped graphene systems. Metal colour code and the notation of the support when BN-pair dopants are introduced is indicated in inset.....	100
Figure 4.4: Multiphilic descriptor, $\Delta w(r)$ around the metal center on periodic and non-periodic models of pristine and BN-pair doped graphene systems. Metal colour code and the notation of the support when BN-pair dopants are introduced is indicated in inset.....	101
Figure 4.5: $\Delta w(r)$ vs $f^{(2)}(r)$ around the metal center on periodic and non-periodic models of pristine and BN-pair doped graphene systems. Metal colour code and the notation of the support when BN-pair dopants are introduced is indicated in inset.....	103
Figure 4.6: Adsorption energy of dinitrogen on different metal SACs; inset shows the colour scheme changes from blue to red as the adsorption of N_2 becomes more feasible.....	104
Figure 4.7: Percentage increment in N-N bond lengths when N_2 is adsorbed on the M-SAC-grap systems. The gradient plot is set with a value of 1.16Å and 4.6% bond length increment observed in Ni-SAC-pris-grap as white; the intensity of the colour codes for respective metals increases as the N-N bond length increases. For each metal, the largest value of N-N bond in periodic and non-periodic models are provided along with the least value of N-N bond length.....	106
Figure 4.8: Projected Density of States of graphene supported SACs compared before and after N_2 adsorption on (a) C_n -V-BNring-grap, (b) C_n -W-CBN-grap and (c) C_n -Re-CBNgrap; the charge density difference plots of M-grap- N_2 systems, made using Vesta 3.4, are as included in inset.....	109
Figure 4.9: Enzymatic reaction mechanism of NRR on periodic and non-periodic V-BNring-grap models.....	111
Figure 4.10: Enzymatic reaction mechanism of NRR on periodic and non-periodic (a) W-CBN-grap and (b) Re-CBN-grap models.....	112

Figure 5.1: Top and side views of Ru and Mo single atom supported on N-doped double vacancy graphene considered as reference to Al atom and Al-clusters (Al _n) supported N-doped double vacancy graphene (M@N ₄ -DVG).....	128
Figure 5.2: AIMD plots of M@N ₄ -DVG catalysts at 298 K; (a) Ru@N ₄ -DVG, (b) Mo@N ₄ -DVG, (c) Al@N ₄ -DVG, (d) Al ₂ @N ₄ -DVG, (d) Al ₃ @N ₄ -DVG, (d) Al ₄ @N ₄ -DVG, (d) Al ₅ @N ₄ -DVG, (d) Al _{6a} @N ₄ -DVG, (d) Al _{6b} @N ₄ -DVG, (d) Al ₇ @N ₄ -DVG.....	129
Figure 5.3: (a) Comparative plot of work function and p-band center of all M@N ₄ -DVG systems, red and blue histograms represent the work function and p-band center respectively. (b) N ₂ adsorption energies and N-N bond elongation on the M@N ₄ -DVG systems, the histograms represent N ₂ adsorption energy while the points represent N-N bond length in Å.....	133
Figure 5.4: Projected Density of States (PDOS) with Charge Density Difference (CDD) and Electron location function (ELF) plots of side-on N ₂ adsorbed on Al ₅ @N ₄ -DVG. The CDD and ELF plots were made using VESTA software.....	133
Figure 5.5: Projected Density of States (PDOS) and Electron location function (ELF) plots of side-on N ₂ adsorbed on (a) Al@N ₄ -DVG, (b) Al ₂ @N ₄ -DVG and (c) Al ₃ @N ₄ -DVG.....	134
Figure 5.6: Possible mechanistic routes of nitrogen reduction reaction; distal and alternating route for N ₂ adsorbed in end-on mode, while enzymatic and consecutive route is observed in side-on adsorbed N ₂	136
Figure 5.7: Free energy diagram of distal and alternating routes of NRR on (a-b) Al@N ₄ -DVG, (c-d) Al ₂ @N ₄ -DVG (e-f) Al ₃ @N ₄ -DVG (g-h) enzymatic and consecutive routes of Al ₅ @N ₄ -DVG.....	136
Figure 5.8: (a) ΔG _{max} (in eV) with potential rate determining step on all active M@N ₄ -DVG catalysts. (b) Consecutive route of nitrogen reduction on Al ₅ @N ₄ -DVG catalyst computed under applied voltage of 0 V (dark-violet line) and -0.78 V (black line) respectively.....	138
Figure 5.9: Bader charge analysis on the metal centers and N atoms of the N _x H _y intermediates of enzymatic, alternating and consecutive NRR routes on (a) Ru@N ₄ -DVG, (b) Al@N ₄ -DVG, (c) Al ₅ @N ₄ -DVG, respectively (d) NRR vs HER selectivity plot of the active M@N ₄ -DVG catalysts, Ru@N ₄ -DVG and Al ₅ @N ₄ -DVG show exclusive NRR selectivity as compared to the rest of the Al-based catalysts; (e) Free energy diagram of consecutive NRR on Al ₅ @N ₄ -DVG without and with water solvent, and the corresponding ΔG _{max} reduces from 0.78 eV to 0.70 eV.....	139

Figure 6.1: Geometric structure of all the $B_{\text{cat}}@Mo_2C$ catalysts (a) $B_{\text{SAC}}@Mo_2C$, (b) $B_{\text{DAC}}@Mo_2C$, (c) $B_{\text{SAC}}@Mo_2C-Mo_{\text{vac}}$, (d) $B_{\text{SAC}}@Mo_2C-B_{\text{def}}$, (e) $B_{\text{SAC}}@Mo_2C-C_{\text{def}}$ (f) $B_{\text{SAC}}@Mo_2C-N_{\text{def}}$, (g) $B_{\text{SAC}}@Mo_2C-P_{\text{def}}$, (h) $B_{\text{SAC}}@Mo_2C-S_{\text{def}}$. Atomic colour code: C (grey), Mo (purple), B (green), N (blue), P (pink) and S (yellow).....	150
Figure 6.2: N_2 adsorption energies in different modes, and the Mo d-band center and B p-band center on different $B_{\text{cat}}@Mo_2C$ catalysts.....	151
Figure 6.3: PDOS and CDD plots of N_2 adsorbed on $B_{\text{SAC}}@Mo_2C-Mo_{\text{vac}}$ via (a) parallel/side-on mode and (b) perpendicular/end-on mode with the insets showing hybridisation of the N p-orbitals and B p-orbitals and the CDD plot generated isosurface density set to $0.003 \text{ e}\text{\AA}^{-3}$	152
Figure 6.4: Free energy diagram of distal and alternating routes of Nitrogen Reduction Reaction (NRR) on (a) $B_{\text{SAC}}@Mo_2C$ and (b) $B_{\text{DAC}}@Mo_2C$	154
Figure 6.5: Free energy diagram of distal, alternating and enzymatic routes of Nitrogen Reduction Reaction (NRR) on $B_{\text{SAC}}@Mo_2C-Mo_{\text{vac}}$ catalyst.....	155
Figure 6.6: Free energy diagram of distal, alternating and enzymatic routes of Nitrogen Reduction Reaction (NRR) on $B_{\text{SAC}}@Mo_2C-C_{\text{def}}$ catalyst.....	157
Figure 6.7: Bader charges on N and B atom catalysts for N_xH_y intermediates involved in the free energy diagram for the NRR on all the $B_{\text{cat}}@Mo_2C$ catalysts.....	158
Figure 7.1: Top and side views of 1T and 2H phases of pristine vanadium dichalcogenides, top views of VX_2 monolayer with chalcogen vacancy ($VX_2@X_{\text{vac}}$) and nonmetal dopant ($VX_2@Y_{\text{cat}}$).....	170
Figure 7.2: (a) N_2 adsorption energies on all $VX_2@Y_{\text{cat}}$ systems with the corresponding N–N bond lengths (\AA), cyan line corresponds to 0 eV of N_2 adsorption and N–N bond length in free dinitrogen molecule (1.112 \AA). (b) Average Bader charge on N-atoms of N_2 upon adsorption on $VX_2@Y_{\text{cat}}$ monolayers plotted w.r.t the d-band centers of the corresponding monolayers.....	171
Figure 7.3: (a) NRR limiting potentials (ΔG_{max}), captions indicate the potential rate determining step and preference of distal or alternating route, (b) Gibbs free energy difference plot between two crucial protonation steps and N_2 adsorption.....	173
Figure 7.4: Projected Density of States (PDOS) plots with insets showing orbital overlap and charge density difference plots of (a) 1T- $VS_2@C-N_2$ and (b) 2H- $VS_2@B-N_2$ showing favourable N_2 adsorption; the top and side views of Electron localization function (ELF) contour plots of (c) 1T- $VS_2@C-N_2$ and (d) 2H- $VS_2@B-N_2$ showing electron location on the adsorbed dinitrogen.....	176

Figure 7.5: Segmented Projected Density of States of B p-states (green line) and N p-states of all the N_xH_y intermediates from the distal route of NRR on 2H-VS ₂ @B monolayer.....	177
Figure 7.6: Gibbs free energy diagrams of distal and alternating NRR at zero and applied potentials equivalent to their respective limiting potentials on (a) 1T-VS ₂ @C (0 V and 0.42 V), (b) 2H-VS ₂ @B (0 V and 0.22 V).....	178
Figure 7.7: (a) Selectivity of NRR over HER on select active VX ₂ @Y _{cat} systems, the more positive the $\Delta G(*H) - \Delta G(*N_2H)$, the higher is the NRR selectivity, (b) Total energy and temperature of 2H-VS ₂ @B as a function of time during the AIMD simulation for 10 ps at 298 K.....	179
Figure 8.1: (a) Top view of the optimized structure of M-TCPP (M = Sc, Ti, V, Cr, Mn, Fe, Co, Ni, Cu, Zn) 2D-MOFs with the paddlewheel Zn ₂ (CO ₂) ₄ linker; elemental colour codes are as shown and unit cell marked by a dashed line. (b) The surface electronic properties of the M-TCPP MOFs recorded as work-function and d-band center for [$\epsilon_d=-5:5$]. (c) N ₂ adsorption energies and N-N bond lengths of N ₂ adsorbed in perpendicular and parallel modes in M-TCPP MOFs. (d) Linear correlation between the surface electronic properties to the N-N bond length for N ₂ adsorbed on M-TCPP MOFs, solid lines represent the side-on mode of N ₂ adsorption while the dotted lines represent the end-on mode.....	192
Figure 8.2: Linear correlation between the surface electronic properties to the (a) Gibbs free energies of N ₂ adsorption, (b) N-N bond order or bond strength of the adsorbed N ₂ , (c) Bader charge of the metal, (d) Bader charge of the N-atom attached to the transition metal center of the M-TCPP MOFs. Solid lines represent the side-on mode of N ₂ adsorption while the dotted lines represent the end-on mode.....	195
Figure 8.3: Charge density difference, Projected Density of States and Crystal Orbital Hamiltonian Population (-pCOHP) of Ti-N pair when N ₂ is adsorbed in (a) side-on or perpendicular mode and (b) end-on or parallel mode. COHP calculations are carried out with LOBSTER software.....	196
Figure 8.4: (a) ΔG_{max} (in eV) with potential rate determining steps for NRR on M-TCPP MOFs with respective colour codes for the different mechanistic routes shown by each system, (b-c) Enzymatic routes of NRR in Sc-TCPP and Ti-TCPP calculated under applied voltage of 0 V and onset limiting potentials of -0.70 V and -0.68 V respectively, (d) Consecutive route of NRR in V-TCPP calculated under applied voltage of 0 V and onset potential of -0.67 V, (e) Alternating route of NRR in Fe-TCPP calculated under applied voltage of 0 V and onset potential of -0.60 V.....	197

Figure 8.5: Linear correlation between (a) the limiting energy barrier for NRR, ΔG_{\max} to surface electronic properties – work function and d-band center, (b) Average Bader charge on adsorbed N_2 to ΔG_{\max} and N-N bond order or bond strength, (c) NRR vs HER selectivity plot of the M-TCPP MOFs with lower limiting potentials.....**199**

Figure 8.6: Free energy diagram of (a) enzymatic NRR on Ti-TCPP and (b) alternating NRR on Fe-TCPP without and with water solvent, with the corresponding ΔG_{\max} in water solvent highlighted in red. Average Bader charge on N-atoms of $*N_xH_y$ intermediates and N-N bond order for (c) enzymatic NRR on Ti-TCPP and (d) alternating NRR on Fe-TCPP MOF....**201**

List of Tables

Table 1.1: Table summarising the advantages of different 2D materials discussed in this thesis with the research gap in procuring them for commercial explorations (<i>CE</i>).....	31
Table 2.1: Table showing the differences between VASP and deMon2k packages.....	64
Table 3.1: Graphene models taken in this study along with their nomenclature.....	73
Table 3.2: N ₂ adsorption energies (E_{ad}) in eV on various Mo-anchored graphene models.....	77
Table 3.3: Mo adsorption energies in eV on various graphene models used in the study..	78
Table 4.1: Gibbs free energies, ΔG (eV) of the crucial intermediate steps involved in enzymatic Nitrogen Reduction Reaction on V-BNring-grap models. The ΔG_{max} of each model is highlighted in bold.....	113
Table 4.2: Gibbs free energies, ΔG (eV) of the crucial intermediate steps involved in enzymatic Nitrogen Reduction Reaction on W-CBN-grap models. The ΔG_{max} of each model is highlighted in bold.....	114
Table 4.3: Gibbs free energies, ΔG (eV) of the crucial intermediate steps involved in enzymatic Nitrogen Reduction Reaction on Re-CBN-grap models. The ΔG_{max} of each model is highlighted in bold.....	114
Table 5.1: Binding energies of metal single atoms and clusters, M = Ru, Mo, Al, Al _n (n=2-7) on N ₄ -DVG (N doped double vacancy graphene) to form M@N ₄ -DVG.....	131
Table 6.1: Gibbs free energies, ΔG (eV) of N ₂ adsorption, first protonation and rate determining step (ΔG_{max}) and overpotential, η for all routes of NRR on the B _{cat} @Mo ₂ C catalysts.....	157
Table 8.1: Formation energies (E_{form}) in eV and dissociation potentials (U_{diss}) in V of M-TCPP MOFs along with their surface electronic energies – work function and d-band centers.....	191
Table 8.2: Bader charges (q_M) of the transition metals in M-TCPP MOFs and the Bader charge of the N-atom (q_N) attached to the M-TCPP MOFs along with their integrated Crystal Orbital Hamiltonian Population (IpCOHP). The Bader charges and IpCOHP values indexed with ‘e’ indicate the end-on mode of N ₂ adsorption, and the rest of the values represents the side-on mode on N ₂ adsorption.....	192
Table 9.1: Summary of the research finding from different 2D material catalysts (in different chapters) considered in this thesis.....	209

Abbreviations

2D	Two-dimensional
AIMD	Ab initio Molecular Dynamics
BHT	benzenehexathiol
BSSE	Basis Set Superposition Error
C ₅₄ -ac	54-carbon armchair
C ₅₄ -zz	54-carbon zigzag
CDD	Charge Density Difference
CHE	Computational Hydrogen Electrode
COFs	Covalent Organic Frameworks
COHP	Crystal Orbital Hamiltonian Population
DAC	Di-atom Catalyst
deMon2k	density of Montréal
DFT	Density Functional Theory
DVG	Divalent vacancy graphene
DZVP	Double- ζ Valence Polarized
ECP	Effective Core Potential
ELF	Electron Localization Function
FE	Faradaic Efficiency
GGA	Generalized-Gradient Approximation
GTO	Gaussian-type-orbitals

HAB	hexaaminobenzene
HER	Hydrogen Evolution Reaction
HF	Hartree-Fock
HOMO	Highest Occupied Molecular Orbital
KS	Kohn-Sham
LANL2DZ	Los Alamos National Laboratory 2-Double- ζ
LCAOs	Linear Combination of Atomic Orbitals
LCGTO	Linear Combination of Gaussian Type Orbital
LDA	Local-Density Approximation
LUMO	Lowest Unoccupied Molecular Orbital
MOFs	Metal Organic Frameworks
NRR	Nitrogen Reduction Reaction
PBE	Perdew-Burke-Ernzerhof
PDOS	Projected Density of States
PDS	Potential rate-Determining Step
PWB	Plane-wave-basis
QECP	Quasi-relativistic Effective Core Potential
SAC	Single Atom Catalyst
SCC	Single-metal Cluster Catalyst
SCF	Self-Consistent Field
SHE	Standard Hydrogen Electrode

STO	Slater-type-orbitals
SVG	Single vacancy graphene
TCPP	tetra(4-carboxyphenyl)porphyrin
TMDs	Transition metal dichalcogenides
VASP	Vienna ab-initio simulation package
ZPE	Zero Point Energy

Physical constants

Avogadro's Constant	$(N_A) = 6.02214129 \times 10^{23} \text{mol}^{-1}$
Atomic Mass Unit	$(u) = 1.660538921 \times 10^{-27} \text{kg}$
Boltzmann's Constant	$(k) = 1.3806488 \times 10^{-23} \text{JK}^{-1}$
Elementary Charge	$(e) = 1.602176565 \times 10^{-19} \text{C}$
Gas Constant	$(R) = 8.3144621 \text{JK}^{-1} \text{mol}^{-1}$
Mass of Electron	$(m_e) = 9.10938291 \times 10^{-31} \text{kg}$
Mass of Proton	$(m_p) = 1.672621777 \times 10^{-27} \text{kg}$
Mass of Neutron	$(m_n) = 1.674927351 \times 10^{-27} \text{kg}$
Rydberg Constant	$(R) = 1.097373157 \times 10^5 \text{cm}^{-1}$
Speed of Light	$(c) = 2.99792458 \times 10^8 \text{ms}^{-1}$
Planck's Constant	$(h) = 6.62606957 \times 10^{-34} \text{Js}$

Synopsis

As the average CO₂ concentration in the air is currently at 417 ppm and rising, the commercial Bosch-Haber's process of NH₃ production being a major contributor of CO₂ emissions; it is eminent that sustainable methods of ammonia production have to be explored. While the commercial method of ammonia fixation from N₂ gas faces the bottleneck of huge energy demand and carbon footprint; a commercial substitute for Bosch-Haber process is yet to be achieved. Considering the cost and energy needed to explore new materials, computational scanning and analysis will help in reducing efforts needed to develop new materials. N₂ being a highly stable molecule, its activation at exothermic condition has always been a challenge. Given a rich electron source that can easily transfer electron to the nitrogen π^* orbitals, N-N bond activation can be achieved without supplying large amount of heat. Implementing the idea of two-dimensional (2D) surfaces that can act as electron reservoirs, the reduction of N₂ to NH₃ on different families of 2D materials have been extensively discussed. The nature of catalysis on Mo-metal single atom catalyst (Mo-SAC) anchored on heteroatom doped graphene substrate of different sizes and edge orientations has been confirmed to be a local site activity (*Chapter 3*). The scope of implementing several metal SACs has been studied for N₂ activation with the N-N bond elongation being triggered by the transfer of electrons from metal *d*-orbitals to N₂ π^* orbitals. More importantly, the quantitative catalytic efficiency of one metal over the other is highly influenced by the description of the atomic orbitals (*Chapter 4*). However, a qualitative trend in the catalytic nature of different metals can be investigated through the use of non-commercial academically licensed computational software. Further investigation on possible catalytic centers on graphene led to incorporating Al-metal clusters, the most earth abundant element, and a trade-off can be made on the catalytic center to be incorporated when graphene is to be used as the 2D support for nitrogen reduction reaction (NRR). A significant reduction in the Gibbs free energy change, ΔG_{NRR} required for NRR can be reduced to 0.78 eV in Al₅-cluster as compared to 1.24 eV in vanadium-SAC by modulating the chemical coordination around the metal centers (*Chapter 5*).

We have also studied the catalytic efficiency of two electrically conductive 2D materials – Mo₂C and vanadium dichalcogenides (VX₂). The conductive nature of these 2D substrates enhances the process of electron transfer from the catalyst the antibonding orbitals of N₂. Rather than relying on metal catalyst centers, we have used non-metal atomic centers for NRR on these conducting 2D materials. Here, boron is the atomic center of interest and when introduced as an adatom on defective Mo₂C, ΔG_{NRR} reduces to 0.57 eV (**Chapter 6**) and the same non-metallic boron atom center when introduced as a substitutional dopant on 2H-phase of VS₂ shows a further reduction in ΔG_{NRR} to 0.22 eV (**Chapter 7**). Furthermore, these catalysts can be realised as electrocatalyst due to their conducting nature, and the thesis highlights how the NRR performance can be enhanced with chemical modifications on different 2D substrates. Moving forward with the goal of obtaining commercially viable catalysts that do not involve tedious and sophisticated synthesis protocols that are mandatory for the above-mentioned materials, we have studied porous coordination compounds that can be achieved via reticular synthesis. Two-dimensional metal organic framework (MOF) comprised of porphyrin ligands and early transition metals are investigated for ammonia production at ambient aqueous condition, and Ti-based porphyrin MOF is being proposed as an active electrocatalyst for NRR with ΔG_{NRR} of 0.35 eV (**Chapter 8**).

Besides exploration on different 2D materials for N₂ reduction to NH₃, we have also put emphasis on studying the correlation between electronic properties of the catalysts and their NRR performance. The notable properties are band-centers, work function, atomic charges, density of states and free energy differences of NRR intermediates. These properties have been found to satisfactorily correspond to ΔG_{NRR} , thereby establishing them as universal parameters for developing novel catalysts.

This Ph.D. thesis focuses on the development of experimentally feasible sustainable 2D material with earth abundant and economically viable metal and non-metal active centers. The goal of this research is to develop an active, low cost, stable and efficient electrocatalyst for NRR via an exhaustive computational study.

(705)

Chapter 1

A Brief Overview on Two-dimensional (2D) Materials for Nitrogen Reduction Reaction (NRR)

This chapter summarizes the chemistry behind reduction of nitrogen (N_2) gas to ammonia in ambient conditions and the challenges associated with this chemical process. The electronic concept derived from the molecular orbitals of N_2 gas has been explained to be the driving force behind designing sustainable catalysts for N_2 activation and reduction. A detailed overview on the two-dimensional (2D) materials reported for nitrogen activation and reduction has been presented in this chapter. The bottlenecks towards implementing certain family of 2D materials have also been discussed and the layout of the thesis is described at the end of this chapter.

1.1 Introduction

Ammonia, the basic hydride of nitrogen, formed by the reaction of nitrogen (N_2) and hydrogen (H_2) gas is an essential compound to humankind and nature. With its major application as fertilizers in agriculture and global food security, ammonia is an inevitable component for our sustenance. Moreover, this compound is also inspiring diverse green energy technologies: as a fuel for electricity, heat generation, hydrogen carrier and clean-burning motors. However, the synthetic production of ammonia with the Haber-Bosch process in large plants is driven by fossil fuels at temperature of 400–500°C and pressure of 150–300 bar in the presence of an iron-based catalyst.¹ Around 96% of the hydrogen required for Haber -Bosch process is further derived from fossil fuels and with 90% of global ammonia produce derived from the combustion of non-renewable energy sources. This accounts to nearly 3–5% of the natural gas produced globally being utilized for ammonia production via the Haber-Bosch process and the carbon footprint of this industrial process surpasses 2.16 tonne of CO_2 for every tonne of NH_3 produced.² In spite of high energy consumption and CO_2 production, the global ammonia market is approximated at 122.4 billion US dollars in 2022 with a registered year-to-year growth of 4.6%.³ The global ammonia consumption as estimated by a market research carried out in 2022 showed China to be a prominent manufacturer and consumer of ammonia with the major application of ammonia being production of urea and its use in agriculture correspond to the increased demand for food with increasing population. The demand for ammonia will continue to grow with growing population and renewable ammonia production currently contributes less than 0.02 metric tonne of global ammonia produce.⁴ **Figure 1.1** shows the global ammonia demand from 1900-2020 and its usage in production of nitrogen containing compounds and the consumption of these nitrogen containing fertilizers in major regions of the world. The consumption of ammonia as urea can be seen to be relatively high for countries with large populations such as China and India.

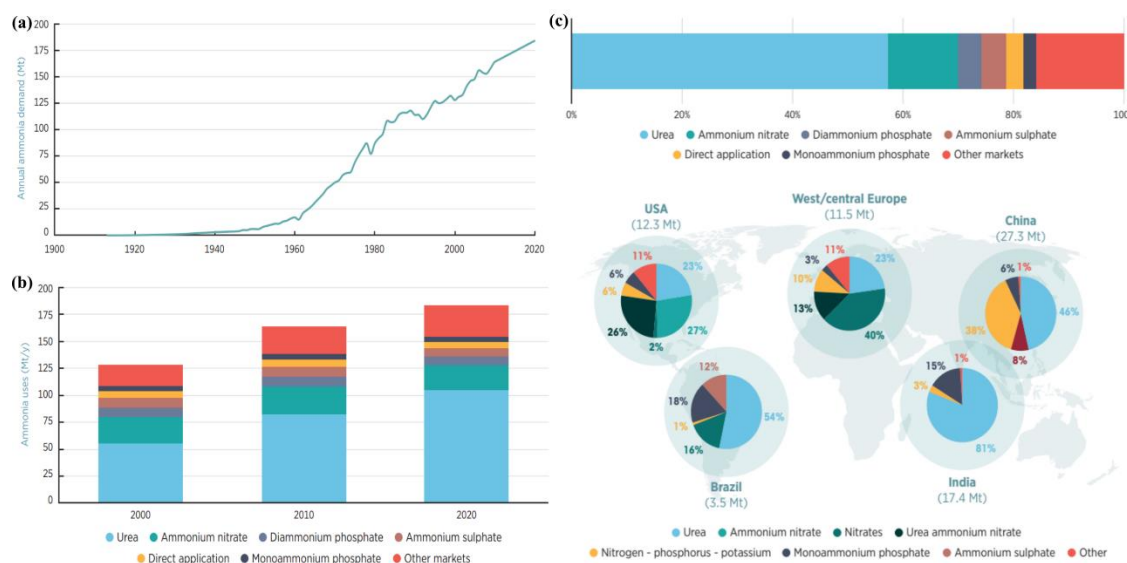


Figure 1.1: (a-b) Global ammonia demand, 1900-2020 (top), and uses (bottom); (c) Nitrogen fertiliser application by region and product as estimated in 2020.⁴

The global challenge to achieve sustainable fossil-free ammonia production has been the major focus of research for the past few decades. While several approaches to produce ammonia at ambient conditions have been attempted, the attempts ranging from mimicking the biological “nitrogen cycle” and utilizing the oxides of nitrogen as the nitrogen source; their reproducibility cannot be directed for commercial ammonia production.⁵⁻⁶ Furthermore, to efficiently screen and investigate effective materials or approaches via experimental verification is rather exhaustive and depends on the availability of capital resources. In this respect, computational and theoretical approaches to understand ammonia production from N_2 and H_2 at ambient conditions play a major role in deciphering the practicability of implementing certain materials for experimental validation and aid in the search for a utopian renewable catalyst for ammonia production.

1.2 Nitrogen molecule: activation and reduction to NH_3

N_2 gas also known as dinitrogen, is an elemental molecule formed by strong trivalent coordination of two nitrogen atoms and its dissociation requires 945 kJ/mol of energy.⁷ This high N-N bond dissociation energy justifies the need for high temperature and pressure conditions in the Haber-Bosch process. If we look into the molecular orbitals of

dinitrogen, the triple bond in N_2 has been formed by sp^3 hybridization of the $2s$ and $2p$ orbitals of nitrogen atoms as shown in **Figure 1.2**. It is important to reiterate that electron occupation in bonding molecular orbital leads to stabilization of the bonds while presence of electrons in the antibonding orbitals lead to destabilization and weakening of the bonds. The presence of paired valence electrons in the bonding π_{2px} , π_{2py} and σ_{2pz} orbitals account to the triple bond as observed in dinitrogen and the absence of electrons in the antibonding orbitals further leads to its stabilisation. When an electron is removed from the bonding orbital to form N_2^+ or an electron is added to form N_2^- , the bond order becomes 2.5 and the N-N bond is weakened in these charged species of N_2 . However, this approach to weaken the strongly bonded $N\equiv N$ bond is unfavourable due to the generation of charged species and the high ionization and electron gain enthalpies of N_2 molecule.

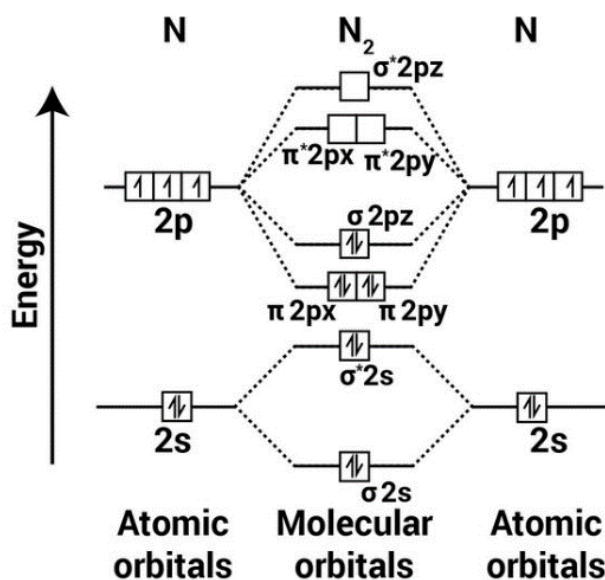


Figure 1.2: Molecular orbital diagram of N_2 molecule.⁸

As such, the importance of using a catalyst that can influence N-N bond weakening at room temperature without creating charged species becomes crucial and catalysts that act as electron reservoirs are essential to weaken the strong $N\equiv N$ bond and reduce dinitrogen to ammonia at ambient conditions. The catalyst holds on to the N_2 molecule and the charge disparity caused by electron transfer from the catalyst to the molecule

triggers the reduction process to produce ammonia. The mechanistic routes to reduce N_2 adsorbed on the catalysts are as shown in **Figure 1.3**. There are two different modes of N_2 adsorption on the catalyst – a perpendicular or end-mode mode and a parallel or side-on mode: with three possible routes of nitrogen reduction reaction (NRR). A distal and alternating route of dinitrogen reduction is anticipated for N_2 adsorbed in the perpendicular (or end-on) mode, while an enzymatic route is prominent in the parallel (or side-on) mode of N_2 adsorption. A more uncommon consecutive route on NRR has also been found and reported for the side-on mode of N_2 adsorption.

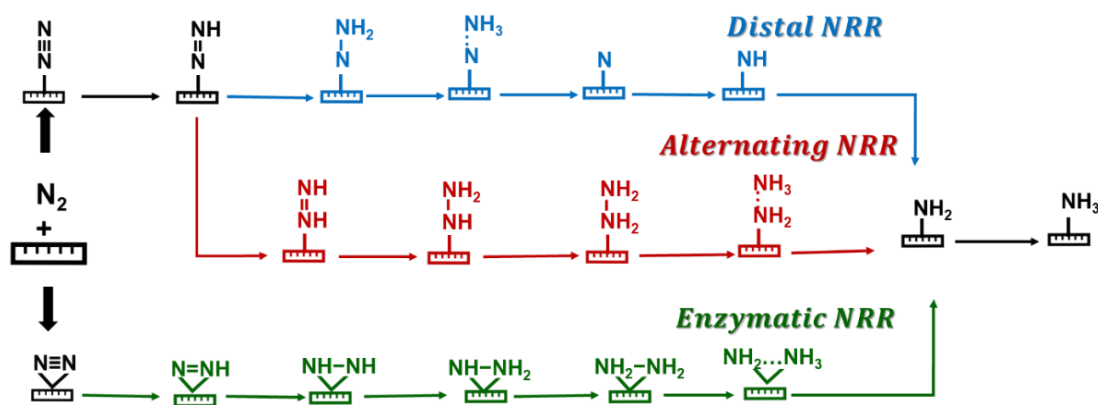


Figure 1.3: Possible mechanistic routes of nitrogen reduction reaction (NRR): distal and alternating route for N_2 adsorbed in end-on mode, while enzymatic route is observed in side-on adsorbed N_2 .

Traditional catalysts for nitrogen activation are derived from the Fe_3O_4 catalyst (Haber-Bosch process) or Fe-Mo complex of the nitrogenase enzyme. Several transition metal- N_2 complexes of Mo, Fe and Co have been reported as an approach to activate the triply bonded $N\equiv N$ at ambient condition and N_2 reduction.⁹⁻¹¹ Another transition metal catalyst reported for N_2 activation is the Mo-Ti-S cluster with a Ti center as the active site.¹² These traditional catalysts act as catalysts by donating d -electrons to the antibonding π^* -orbitals of N_2 while accepting the lone pair of electrons from N_2 , thereby the π - backdonation to cause $N\equiv N$ bond dissociation. However, there are several challenges in ensuring the stability and recyclability of these transition metal complexes; and with growing cost of metals using bulk metals as catalysts are discouraged. Materials

that act as reservoirs of electrons with a dynamic ability to give as well as donate electrons are essential. Herein, catalysts that act as electron reservoirs when coupled with an active center are attractive candidates to be implemented as catalysts for N_2 activation and reduction. Over the last few decades, two-dimensional (2D) materials have garnered attention in electrical conductivity, energy storage, catalysis, and sensors owing to their large surface area.¹³⁻¹⁵ Another advantage of these 2D materials are their flexibility to be implemented as heterocatalysts, electrocatalysts or photocatalysts. The active center incorporated in the 2D materials can be ad-atoms which can be metal or non-metal in their atomic or cluster form and surface modifications created by atom vacancy or doping. The 2D material supports reported for N_2 activation and reduction include carbon-based materials; metal carbides and borides (MXenes and MBenes); transition metal dichalcogenides; coordination network polymer materials - metal organic frameworks (MOFs) and covalent organic frameworks (COFs).

1.3 NRR in carbon-based materials

The 2D carbon-based material of interest include graphene, graphitic carbon nitride (g-C₃N₄) and reduced-graphene oxide (r-GO); with graphene being the most reported owing to its semiconducting nature, zero bandgap, mechanical strength, superior thermal conductivity, and charge mobility at room temperature. The delocalised electrons in the basal plane of graphene are weakly effective for directed catalytic N_2 activation and reduction to NH_3 . Upon manipulating the graphene surface with vacancy defects or heteroatom dopants such as B, N, P and S; the electronic and structural properties of graphene can be modulated to augment the catalytic activity.¹⁶⁻²¹ In particular, N species when present as pyridinic, pyrrolic or graphitic nitrogen and B heteroatom dopant causes polarization N-C or B-C bond, and this polarization creates an ideal condition to induce N_2 adsorption and subsequent $N\equiv N$ bond dissociation.²²⁻²⁴ However, in the absence of empty orbitals for π - backdonation, the activation of N_2 in heteroatom-doped or defective graphene is not efficient enough to lead to NH_3 production.²⁵ Consequently, introducing an active metal center to the heteroatom-doped or defective graphene is an excellent proposition to be developed as heterocatalysts or electrocatalysts for NRR. The metal

centers when incorporated as single atom catalysts (SACs), diatomic atom catalysts (DACs) and atomic nanoclusters will maximise the activity and efficiency of metals.

1.3.1 Metal single atom catalysts (SACs) on chemically modified graphene for NRR

Single atom catalysts (SACs) constructed by anchoring isolated single metal atoms on 2D materials provide high catalytic activity because of the metal low-coordination environment and significantly reduce the metal usage.²⁶ Precious metal SACs, Ru and Au, anchored on N-doped graphene have proved promising for catalysing the activation and reduction of N_2 .²⁷⁻²⁸ These single metal sites supported on N-doped carbon demonstrated a higher activity and Faradaic efficiency than their bulk nanoparticle analogues due to a much stronger interaction of N_2 with the metal SACs.²⁸ Density Functional Theory (DFT) calculations have also showed that NRR selectivity is higher in metal SACs over the bulk metal catalysts as the competing hydrogen evolution reaction (HER) is suppressed.²⁹ While the activity of the precious metals is appealing for NRR, these metals are costly, and their limited availability pose a larger challenge towards obtaining sustainable catalysts for ammonia production. In this regard, lighter transition metals being abundant and cheaper are more attractive. Fe and Mo are the preferred choice of transition metals due to their presence in nitrogenase enzyme.³⁰

Tian and co-workers reported Mo-SAC with trivalent coordination of N (MoN_3) on graphene nanoflakes, with a detailed catalytic profile of N_2 reduction on the Mo/N active site and graphene acting as an electron transportation bridge.³¹ FeN_3 -graphene catalyst with Fe SACs has been reported by Li and co-workers as a highly active catalyst for N_2 reduction. The strongly bonded $N\equiv N$ bond shows a drop in the bond order from 3 to 2.75 and 2.5 for perpendicular and parallel modes of N_2 adsorption, respectively thereby indicating inert $N\equiv N$ bond is activated.³² The N-doped graphene scaffold (N_3 -graphene) pertains to graphene with a single vacancy (SV) defect and it has been found to stabilise Mo-SAC and Cr-SAC and the M- N_3 /SV-graphene catalysts so formed showed high activity and selectivity for N_2 reduction.³³

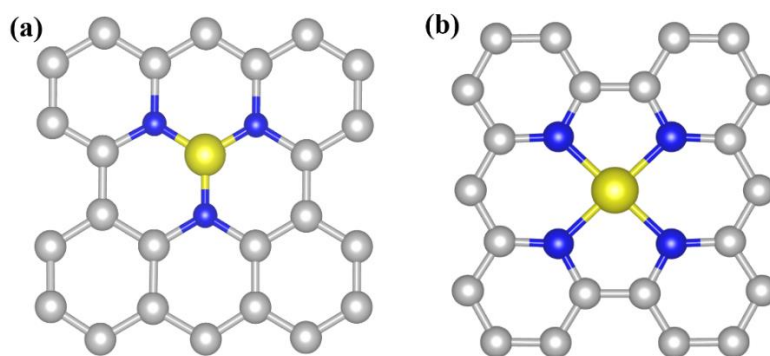


Figure 1.4: Schematic representation of metal-SAC embedded in N-doped graphene (a) single vacancy (SV) or M-N₃ and (b) divalent vacancy (DV) or M-N₄ graphene.³⁴

However, N-doped graphene with divalent vacancy (N₄/DV-graphene) defect, as represented in **Figure 1.4**, has been found to bind the Fe-SAC more strongly with a more negative binding energy and a correlation between the binding energies of metal-SACs with N₄/DV-graphene as a function of the defect, N-atom configuration and doping.³⁴ In particular, Wen and co-workers demonstrated that divalent vacancy (DV)-graphene with higher number of atom doping shows higher structural stability in Mo-SAC than single vacancy (SV)-graphene.³⁵ Mo-SAC with N₄-coordination embedded in divalent vacancy (DV)-graphene showed excellent catalytic activity towards N₂ reduction with a low energy barrier as compared to the competing Hydrogen Evolution Reaction (HER).³⁶ Another active metal SAC on N-doped graphene nanosheet reported for NRR is Fe, wherein augmenting the magnetic nature of Fe-SAC can enhance the binding efficiency and electron transfer between the catalyst and N₂ molecule.³⁷ These divalent vacancy graphene with porphyrin-like N₄-centres, when anchored with Ti-SAC and V-SAC has also been found to show higher NRR performance than the most active Ru(0001) metal surface.^{29,38} The high efficiency towards N₂ activation and reduction has been influenced by the strong electron donation from metal d-orbitals to N₂ π* orbital and back-bonding from occupied N₂ π orbital to metal d-orbitals of the single atom catalyst. Several metal SACs - Cr, Mn, Fe, and Mo embedded in divalent graphene revealed a high activity for N₂ fixation. In particular, the synergistic effect between graphene and Cr-SAC with a high spin density promoted the activation and reduction of N₂.³⁹ The activity and energy

barrier for these metal SACs to reduce N_2 were evaluated and ratified through theoretical investigations. Detailed theoretical investigations on several metal SACs placed on the edge of graphene have also been reported by Wei et. al showed a higher activity of Co-SAC due to a selective stabilization of $*N_2H$ and destabilization of $*NH_2$ intermediates which could not be seen in other metal SACs.⁴⁰

Other heteroatom dopants on graphene that have been reported for N_2 activation and reduction are B, S and Se. Co-SAC with B-doped graphene yielded a CoB_4 structure responsible for NRR attributed by the electronic nature of B-dopants, polarized C-B bonds on the graphene surface and Co showing weak adsorption for the product NH_3 , thus facilitating ammonia production.⁴¹ Sulphur coordinated Mo-SAC on graphene as reported by Wen et. al is another potential catalyst and the NRR performance can be predicted via a universal electron descriptor derived from electronegativity of metal and coordinated S-dopants.⁴² Zhou and co-workers proposed Mo-SAC anchored on Se-heteroatom doped graphene to be effective catalysts and the most favourable for NRR activity as compared to Mo catalysing NRR. Zhou et. al proposed that Mo/Se-G shows the most favourable NRR activity compared with Mo supported on graphene with other heteroatom dopants (B, N, P and S).⁴³

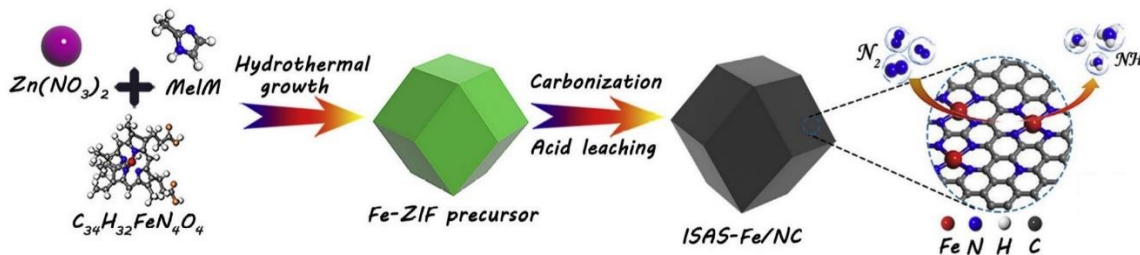


Figure 1.5: Schematic representation of synthesizing ISAS-Fe/NC with Fe-SAC catalyst from the chemical precursors and a model representation of the Fe-SAC coordinated to N-doped carbon.⁴⁵

While the high activity and selectivity of the metal SACs have been predicted and proposed from theoretical investigations, experimental research has been limited due to engineering bottlenecks and operando protocols to prove the existence of metal-SACs on graphene sheets. Nonetheless, porous carbon, which is mesostructured graphene has been

developed as electrocatalyst for NRR. Han et. al demonstrated Mo-SAC on N-doped porous carbon to give a high NH_3 yield and Faradaic efficiency (FE) of $50.0 \pm 5.3 \mu\text{gh}^{-1}\text{mgcat}^{-1}$ and $14.6 \pm 1.6\%$, respectively at 0.3 V vs. RHE.⁴⁴ Isolated single Fe atomic sites (ISAS) supported on N-doped carbon has been experimentally proven to show high durability and activity for reduction of N_2 via electrochemical process in a neutral media. This ISAS-Fe/NC electrocatalyst (**Figure 1.5**) is the first reported non-precious transition-metal-based catalyst that showed the highest NH_3 yield of $62.9 \pm 2.7 \mu\text{gh}^{-1}\text{mgcat}^{-1}$ at an onset potential of -0.4 V vs RHE and FE of $18.6 \pm 0.8\%$ in aqueous solutions.⁴⁵ Likewise, Cu-SAC on N-doped carbon electrocatalyst synthesized by Pennycook's group for NRR with NH_3 yield of $53.3 \pm 1.86 \mu\text{gh}^{-1}\text{mgcat}^{-1}$ and 13.8% FE, showed high NRR activity and selectivity. DFT investigation proved Cu- N_2 coordination in graphene to show a strong binding efficiency to N_2 , and the cleavage $\text{N}\equiv\text{N}$ triple bond following the activation of N_2 molecule.⁴⁶ In particular, modulating the coordination of the metal-SAC in N-doped porous carbon from Mn- N_4 to Mn- O_3N_1 has proven to show high NRR activity at ambient conditions. The single atom catalyst site, Mn- O_3N_1 show a synergistic adsorption of N_2 and stabilization of $^*\text{N}_2\text{H}$ intermediate, thereby enhancing NH_3 production with a high yield of $66.41 \mu\text{gh}^{-1}\text{mgcat}^{-1}$ and FE of 8.91% at -0.35 V in 0.1 M HCl solution.⁴⁷

1.3.2 Metal diatomic atom catalysts (DACs) to single-metal cluster catalysts (SCCs) on graphene

Diatomic catalysts (DACs) and single-metal cluster catalysts (SSCs) are a new development to SACs wherein a higher loading of metal atoms act as the active catalytic center to activate N_2 . While metal SACs possess a high selectivity and activity for NRR, it comes with its own limitations. The presence of only one single adsorption site for the activated reactant is unfavourable in catalytic reactions that involve the co-adsorption of reactants.⁴⁸ There is also a high possibility of metal atoms agglomeration, sintering or dispersion during a reaction when SACs are employed. Furthermore, the low metal loading of SACs on 2D materials when compared to DACs or SSCs lead to mediocre activity in long-term implementation.⁴⁹

Theoretical investigations have shown that NRR-preferred Fe and Mo metal when combined with several other transition metals form bimetallic catalysts on graphene. The Fe and Mo center are found to be responsible for nitrogen adsorption and the second transition metal showing a synergistic effect to improve the NRR catalytic efficiency by promoting electron transfer between the 2D-surface and adsorbed N_2 molecule.^{50,51} The NRR activity of homoatomic and heteroatomic DACs on graphene have been theoretically studied by Ma et. al. The stability and activity of the heteroatomic $M_1M_2@N$ -doped graphene (NG), the heteroatom combination being chemically active early transition metals, investigated via bonding/antibonding orbital population and electronic property analysis showed a synergic reactivity effect in the heteroatomic DACs as compared to the homoatomic counterparts. As such, with a lower energy barrier of 0.24 eV in VCr@NG, which shows a strong suppression of HER (hydrogen evolution reaction) – the competing reaction and the chemical space to active NRR catalysts can be expanded.⁵² The prominence of arrangement of the two metal atoms in DACs has been further explored by Qu and co-workers in their study on two metal single-atom, non-bonded double-atom and bonded double-atom centers on N-doped graphene. They reported a higher catalytic activity of NRR on the bonded double-atom catalyst; in particular, heteroatomic Mn-Fe catalyst with Mn-atom as the primary active center and Fe-atom showing a synergistic effect in stabilising the intermediates and facilitating NH_3 production.⁵³

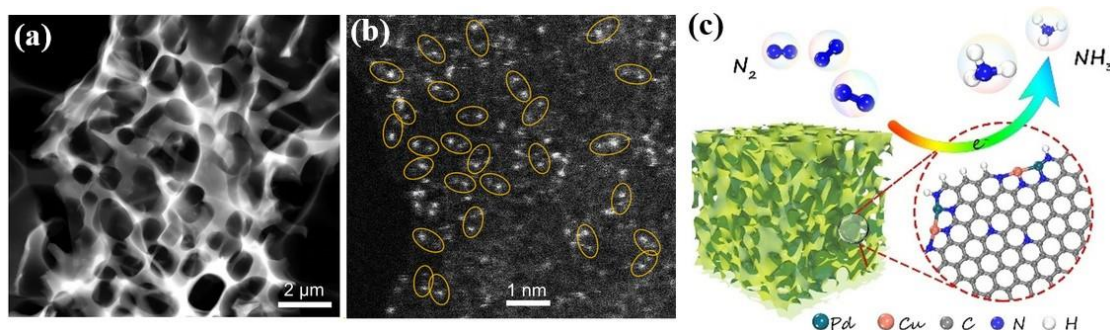


Figure 1.6: Microscopic structure of diatomic PdCu catalyst anchored on N-doped carbon (PdCu/NC) obtained from (a) low-magnification and (b) magnified atomic resolution HAADF-STEM image showing diatomic site as bright spots; (c) Theoretical

representation of the PdCu atom pair on N-doped graphene as a schematic model of PdCu/NC.⁵⁴

Experimental report on metal diatomic catalysts or dimers for NRR highlighted a higher NRR performance on combination of rare-earth and earth-abundant transition metal pair PdCu embedded in N-doped porous carbon(PdCu/NC). This modulated PdCu DAC (**Figure 1.6**) showed NH_3 yield $69.2 \pm 2.5 \mu\text{g h}^{-1} \text{mg}_{\text{cat}}^{-1}$ and a higher FE of $24.8 \pm 0.8\%$ than its single metal Pd-SAC counterpart.⁵⁴ However, Pd being a rare earth metal, a combination of NRR-preferred Fe and Mo metal as Fe-Mo dimer has been investigated by Li et. al. A higher selective NRR electroreduction in Fe-Mo anchored on N-rich carbon ($\text{FeMo@N}_x\text{C}$) is observed than the SAC-counterparts (Fe@NC and Mo@NC) owing to a combined ligand, geometric and synergistic effect of Fe-Mo dimer coordination. Albeit a lower NH_3 yield rate of $14.95 \mu\text{g h}^{-1} \text{mg}^{-1}$ at -0.4 V , the selectivity and FE of 41.7% at -0.2 V is higher than previously mention PdCu/NC catalyst.⁵⁵

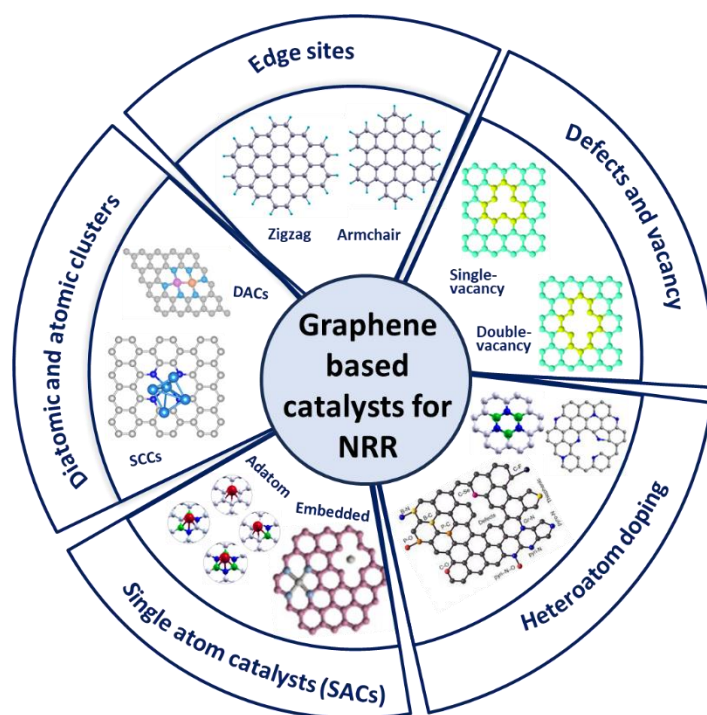


Figure 1.7: Different engineering approaches to develop graphene-based materials catalysts for nitrogen reduction reaction (NRR).

Single-metal cluster catalysts (SCCs) are relatively more stable and feasible than SACs or DACs in solvent-mediated synthesis protocols. SCCs of non-precious metals are significant in advancing towards the next generation catalysts for NRR. In particular, Fe being an NRR-preferred metal when investigated by making a comparative study for its cluster forms, Fe₃ and Fe₄ with Fe-SAC and Fe-DAC on N-doped graphene exhibited a higher NRR activity. The synergistic enhancement in charge transfer between N₂ and Fe₄ cluster along with an aided stabilization of the reactant species are crucial factors that could not be observed or pronounced in SAC and DACs.⁵⁶ Similar characteristics have been observed in trimetallic clusters of earth abundant transition metals on N-doped graphene- Mn₃@NG, Fe₃@NG, Co₃@NG, and Mo₃@NG with the SSCs inducing N₂ activation via a π -backdonation and improved charge transfer. Despite the theoretical supports proving the stability and activity of metal SCCs on graphene for NRR performance, experimental trials are yet to be reported.⁵⁷ **Figure 1.7** shows a summary of the different engineering and chemical approaches undertaken to develop graphene-based catalysts for nitrogen reduction reaction (NRR). The conventional thermal energy sources when used to cross the energy barrier of NRR are unsustainable, thereby electrical energy derived from solar or wind energy are greener routes to catalysis. Electrocatalysis is the cornerstone towards achieving a greener economy and sustainability for meeting the future energy needs. Graphene sheets and stand-alone carbon supports show limited electrical conductivity and wettability, unless incorporated with a conducting stable support. These caps the prospects of administering 2D-graphene sheets as electrocatalysts for NRR, thereby it would be important to look towards electrically conducting 2D materials.

1.4 NRR in metal carbides and borides (MXenes and MBenes)

MXenes and MBenes belong to a large family of 2D early transition metal carbides, nitrides, carbonitrides and borides with diverse stoichiometric composition and structures. These 2D materials exhibit superior stability, electrical conductivity, wettability, and surface chemistry that leads to exciting chemical, physical and electrical properties. These 2D sheets are derived from their bulk MAX or MAB (M= transition metal, A = group 13 or 14 elements, X= C or N) phases by selectively etching the group

A elements. For instance, a MXene Ti_3C_2 is obtained when Al, held by weak interaction forces with MX layer, is etched from its MAX precursor, Ti_3AlC_2 . With a hexagonal coordination of the transition metals to carbon, nitrogen or boron in MXenes and MBenes (as shown in **Figure 1.8**); the orientation and stacking can lead to formation of two prominent phases - 1T and 2H phases, both of which show contrasting magnetic and metallic properties.^{58,59}

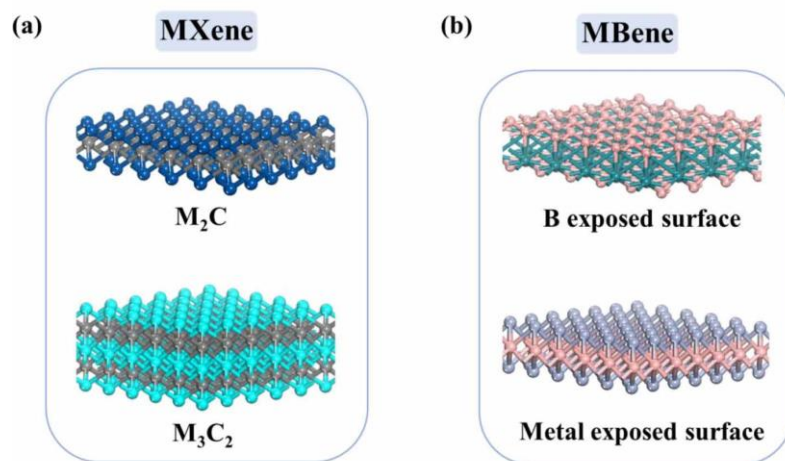


Figure 1.8: Representative models of the most primarily formed two-dimensional MXene and MBene with varying stoichiometric composition.⁵⁹

1.4.1 MXenes for NRR

The most primarily known MXenes are 2D metal carbide nanosheets, M_2C or M_3C_2 with exposed metal surfaces. They possess excellent potential as electrocatalysts owing to exposed metal surface and bonding interactions between 2s and 2p orbitals of carbon to metal d-orbitals which promote electron transfer from the 2D surface to the reactants. The layered structure and high surface area of MXenes with active sites and chemically inert surface has been influential in activating and reducing N_2 molecule in a study carried out by Azofra and co-workers. M_3C_2 MXenes of Group 4, 5 and 6 transition metals, when investigated showed promising potential for N_2 activation along with a stabilization of the protonated $^*\text{N-NH}$ and $^*\text{N-NH}_2$ intermediates. In particular, 2D monolayers of V_3C_2 and Nb_3C_2 exhibited remarkable N_2 reduction potential with overpotentials of 0.64 and

0.90 V vs. SHE, respectively.⁶⁰ Similar results are obtained when M₂C MXenes of 3d, 4d and 5d transition metals are investigated for their NRR limiting energy barriers. A lower NRR energy barrier of 0.28 eV and 0.23eV, respectively are observed in hypothetical Mn₂C and Fe₂C MXenes while the experimentally reported Mo₂C MXene show a free-energy barrier of 0.46 eV. As such, the electron arrangement of Mn and Fe with half-filled d⁵ and d⁶ electrons are desirable to influence the electron back-donation from the filled orbitals of N₂, thereby leading to weakening of the N-N bond and lowering the energy barrier. These insights from hypothetical MXenes are crucial for designing better and efficient electrocatalysts for NRR.^{61,62} However, the use of strong etching agents like hydrofluoric acid (HF) in aqueous condition used for the synthesis of MXenes from their MAX precursor leads to surface termination with F, OH or O functional groups. Pristine MXene phases without any surface termination can be achieved when synthesized via a bottom-up approach like chemical vapor deposition (CVD) which is usually more expensive than the top-down etching process. These surface termination functional groups, F and OH inactive the surface of M_{n+1}C_n leading to formation of M_{n+1}C_nT_x (T_x = O₂) MXene nanosheets leading to poor NRR performance and selectivity.

Ti₃C₂T_x (T = F, OH) nanosheet reported by Zhao's group for electrocatalytic nitrogen fixation gave an NH₃ yield of 20.4 μgh⁻¹mg⁻¹ cat with 9.3% Faraday efficiency.⁶³ However, upon introducing a metal center or dopant, an improved performance in NRR activity can be observed. Fe-SAC inserted on Ti₃C₂T_x MXene nanosheet not only act as an active center for NRR activity but also activate the surface by removing the inactive F and OH terminal groups. The reduction in the surface work function leads to a high NH₃ yield of 21.9 μgh⁻¹mg⁻¹ cat and a FE of 25.44%.⁶⁴ A relatively higher NRR yield and performance of 27.56 μg h⁻¹ mg⁻¹ and Fe (23.3 %) can be seen when Ru-SAC is anchored on Ti₃C₂O substrate. The Ru-SAC binds to the MXene layer and four terminal oxygen atoms to act as the catalytic center for NRR.⁶⁵ Wang et. al reported eight prospective metal SACs - Y, Zr, Nb, Hf, Ta, W, Re, and Os on Mo₂CT_x-MXene for NRR with Mo₂CT_x-Y_{SAC} as the optimal candidate with a low free-energy barrier of 0.08 eV for NRR.⁶⁶ However, the extremely low abundance of yttrium (Y) in earth's crust invalidates the quest for a sustainable electrocatalysts. Nevertheless, exploring other

possible dopants or MXenes yielded positive results. As such, when Ti-SAC is anchored on Mo_2CO_2 the free-energy barrier of NRR on $\text{Ti@Mo}_2\text{CO}_2$ is reported to be 0.64 eV.⁶⁷ Several transition metal SACs when anchored on $\text{Ti}_3\text{C}_2\text{O}_2$ has been reported to show high NRR activity by Gao and coworkers, the target transition metal being earth abundant Fe and Co.⁶⁸

In addition to introducing metal SACs or centers, incorporating non-metals or altering the terminal functional groups on the MXene surface can also lead to a higher NRR activity. B-doped Mo_2CO_2 and W_2CO_2 MXenes showing excellent NRR with limiting potentials of -0.20 V and -0.24 V respectively under ambient condition. The B center mimics the electronic orbital distribution of transition metals and enhance the electron backdonation from N_2 molecule and also promoting the formation of protonated $^*\text{N}_2\text{H}$ species.⁶⁹ The electron deficient nature of B in $\text{B@V}_3\text{C}_2\text{O}_{2x}$, a vanadium carbide MXene is predicted to be responsible for the adsorption of N_2 and high electrocatalytic NRR performance.⁷⁰ Besides the use of boron, another non-metal carbon when injected into MXene surfaces has been reported to interact with adjacent metal d-orbitals and the electron filling in C-2p orbitals promote N_2 adsorption with the NRR free- energy barriers ranging from 0.14 eV to 0.38 eV in $\text{C@Nb}_2\text{CO}_2$, $\text{C@Mo}_2\text{CO}_2$, and $\text{C@W}_2\text{CO}_2$.⁷¹ Modifying or altering the terminal groups in $\text{M}_{n+1}\text{C}_n\text{T}_x$ ($\text{T}_x = \text{OH}, \text{F}, \text{O}_2$) can bring about a significant reduction in the NRR limiting potential and enhance NRR selectivity.^{72,73} Various other forms of MXenes have been effectively utilized as electrocatalysts for NRR, i.e., V_3C_2 and Nb_3C_2 reported with overpotentials of 0.64 eV and 0.90 eV, respectively.⁷⁴ A considerable increase in the number of MXenes composites reported for NRR has been summarized in **Figure 1.9** and MXene composites with several other 2D materials have also been reported as electrocatalysts for NRR and the insights from these investigations are fundamental in developing a sustainable catalysts.⁷⁵

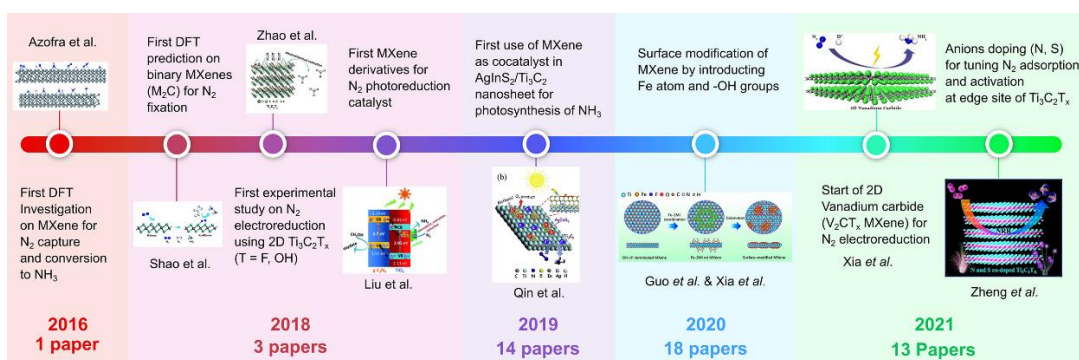


Figure 1.9: Summarization of the timeline on the MXenes reported as electrocatalysts for NRR at ambient conditions.⁷⁵

The metal nitride MXene analogues are another attractive family of conducting 2D materials with experimental and computational investigation in their infancy. While pristine 2D molybdenum nitride nanosheet is not ideal for NRR, when doped with Fe-single atom centers, rate determining potential decreases and the Fe-doped MoN_2 can be proposed as a promising electrocatalyst for NRR.⁷⁶ Cheng et. al reported metal nitride MXene Ti_2NO_2 , with single-Mo center anchored on it to exhibit a high NRR performance at a low overpotential of 0.16 V.⁷⁷ This detailed computational investigation on 2D M_2NO_2 MXene ($M = Ti, V, Cr$) anchored with several transition metal SACs- Mo, Mn, Fe, Co, Ni, or Cu highlighted the NRR performance of metal-SACs@ M_2NO_2 MXene besides their high conductivity and HER inhibition. The only known experimental report on 2D layered metal nitride is W_2N_3 MXene with N-atom vacancies and the NH_3 yield reported by Jin et. al is $11.66 \text{ mg h}^{-1} \text{ mgcat}^{-1}$ and a very low FE of 11.67%.⁷⁸

1.4.2 MBenes for NRR

MBenes or transition metal borides are counterparts of MXenes that can show either boron exposed or metal exposed surfaces, and they can be roughly classified into MB or M_2B_2 , M_3B_4 and M_4B_6 type, where M is the transition metal. Boron being more electron deficient than carbon, the combination of transition metals with boron can diversify into different geometrical arrangement and electronic properties. A high-throughput screening yielded 12 kinds of ferromagnetic MBenes (MnB , HfB , ZrB , Au_2B , Mo_2B , Nb_5B_2 , Nb_3B_4 , Ta_3B_4 , V_3B_4 , OsB_2 , FeB_2 , and RuB_2) from the MAB phases.^{79,80} The

electrocatalytic activity of these 12 MBenes when investigated showed outstanding stability in aqueous conditions and MBenes with exposed boron surfaces- OsB₂, FeB₂ and RuB₂ showed favourable NRR performance with lower limiting potentials. The coexistence of occupied B-p orbitals and unoccupied transition metal d-orbitals in these boron exposed MBenes provide even superior activity and selectivity for NRR.⁸¹ With several stoichiometric chemical composition of MBenes, identifying an ideal composition of MBene optimal for NRR is crucial. Guo et. al investigated the stability and activity of all possible defect-free, dopant-free MBenes with both boron and metal exposed surfaces. The study determined MB and M₂B (homo-atomic or heteroatomic) MBenes to show intrinsic basal activity for NRR and inhibit hydrogen evolution on the surface.⁸² Xu et. al reported a family of 2D metal monoboride, MB (M = Cr, Mn, Fe, Co, Ni and Mo) for electrocatalytic application towards NH₃ production from a detailed investigation on the adsorption energies of *N₂H and *NH₂ species. 2D-MoB nanosheet has been found to be the optimal candidate for NRR with a low limiting potential of -0.30 V.⁸³ Similar study on MB monolayers by Li and coworkers reported VB, CrB, and MoB monolayers as efficient electrocatalysts for NRR performance.⁸⁴ These MB monolayers possess similar electrocatalytic properties for NRR in their MXene forms, Mo₂B₂ and Cr₂B₂ both of which show exposed metal surfaces with reported NRR limiting potentials being -0.50 V and -0.35 V, respectively.^{85,86}

Subsequently, Qi and co-workers emphasized the importance of metallic and electron-like features in MBenes to be crucial for N₂ activation and reduction; and the promising family of MBenes with free-energy barriers < 0.7 eV are TiBene, YBene, ZrBene and WBene.⁸⁷ Furthermore, the electrocatalytic strength of the MBenes can be preliminarily gauged from the exfoliation properties of their MAB phases. A linear relationship between the exfoliation energy of element Al from M₂AlB₂ and N₂ binding energy on the corresponding MB phases can be apprehended. The highest NRR activity as predicted by Cheng et. al are in FeB and TaB, both of which show high NRR selectivity.⁸⁸ Likewise, a theoretical screening on several MBenes, shown in **Figure 1.10**, by Xiao and co-workers highlighted Ta₃B₄, Nb₃B₄, CrMnB₂, Mo₂B₂, Ti₂B₂ and W₂B₂ to show favourable stability, activity and selectivity for N₂ reduction in ambient conditions.

The lowest NRR limiting potentials -0.24, -0.43, and -0.39 V reported in their work are observed on W_2B_2 , Mo_2B_2 and Ta_3B_4 , respectively.⁸⁹ While the research in computational and experimental investigation on MXenes and MBenes are in their embryonic stage, these predictions will guide the design of next generation sustainable electrocatalysts for NRR.

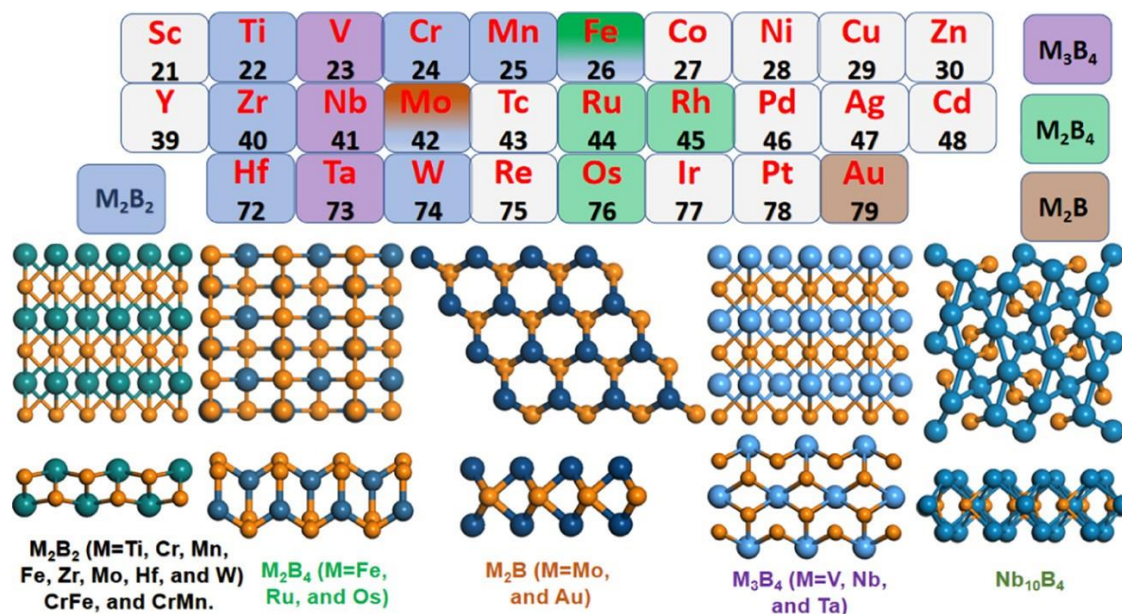


Figure 1.10: Comprehensive picture of all possible MBenes from the transition metals of the periodic table that been reported by theoretical and experimental studies; the different stoichiometric formula and structure of the MBenes are also provided herein.⁸⁹

1.5 NRR in transition metal dichalcogenides

Transition metal dichalcogenides (TMDCs) exist in MX_2 form depending on the combination of the transition metal (M) and chalcogen (X= S, Se and Te); and the 2D nanosheets of MX_2 can exist in either 1T or 2H phase based on either octahedral (1T) or trigonal prismatic (2H) coordination of metal atoms to the chalcogen. 2D-TMD monolayers possess a zero band-gap and show versatile nature ranging metallic (NbS_2 and VSe_2), semi-metallic (WTe_2 and $TiSe_2$), semiconductors (MoS_2 and WS_2), and insulators (HfS_2). Owing to the atomically thin nature of 2D-TMDs along with a high electronic conductivity, tunable and direct band-gaps, strong spin-orbit coupling and

natural abundance this family of 2D materials have attracted a lot of attention as electrocatalysts for some challenging chemical processes. Additional improvements in the catalytic properties of the 2D-TMDs can be brought about by incorporating point defects such as vacancy defect, adatoms and substitutional doping of the transition metal or chalcogen atoms, as shown in **Figure 1.11**.

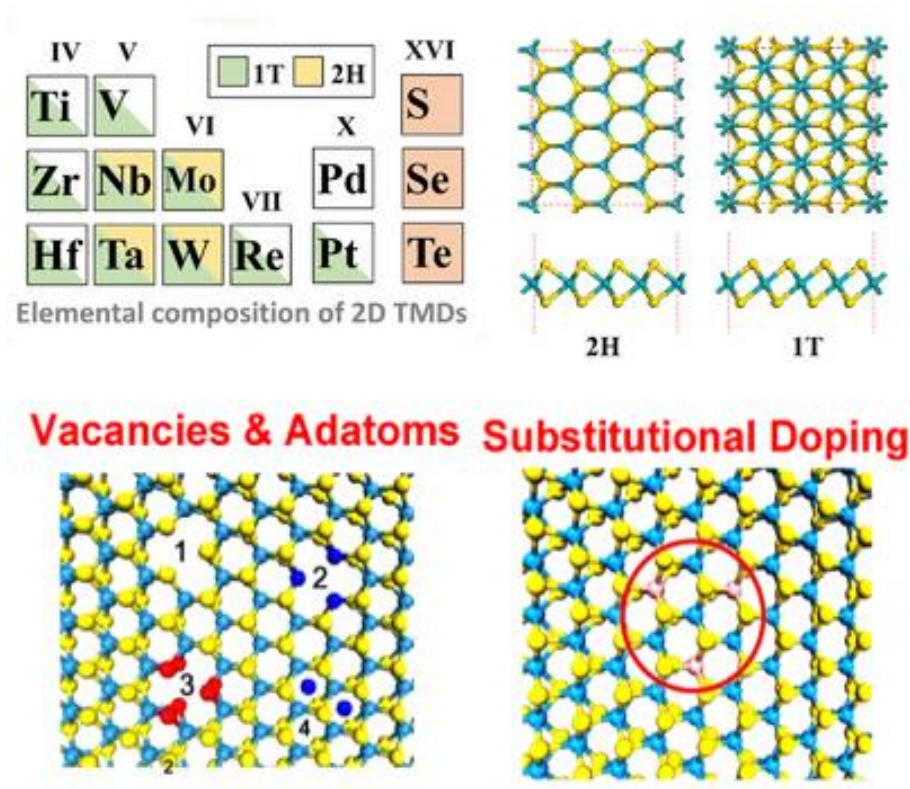


Figure 1.11: A schematic overview of different transition metals that can combine with chalcogens (S, Se and Te) to form transition metal dichalcogenides (TMDs). Top and side views of 2H and 1T phases of the TMDs, with the different engineering defects that can be incorporated in TMDs to enhance the NRR catalytic efficiency.

1.5.1 Mo-based TMDs for NRR

The first ever report on the use of TMDs for NRR is when 2D MoS₂ nanosheets has been reported by Zhang and co-workers in 2018 with NH₃ yield of 13.09 mg h⁻¹ mgcat.⁻¹ at -0.5 V vs. RHE and FE of 1.17%.⁹⁰ The prospect of utilizing 2D MoS₂ as an electrocatalyst for NRR has been derived from the computational investigation carried

out by Azofra and co-workers wherein Fe-deposited 2D MoS₂ produced NH₃ in aqueous media when an energy barrier of 1.02 eV is supplied to promote the first electron-proton transfer in NRR.⁹¹ This led to the study by Zhang et. al on Fe binuclear heterogeneous catalyst embedded in 2D-MoS₂ monolayer showed outstanding efficiency and stability for N₂ activation and reduction. The presence of two Fe-centers has been explained to be more effective than a single Fe-atom center in their study.⁹² Experimental investigations prompted by Zhao et al. found that Fe nanodots on MoS₂ exhibited superior electrocatalytic activity for NRR with average NH₃ yield of 12.5 μg·h⁻¹·cm⁻² and a relatively higher FE of 10.8% at -0.1 V vs RHE at ambient conditions.⁹³

Several other metals and non-metal catalyst have also been explored as alternatives to Fe-dopant on 2D MoS₂. The NRR performance of V-SAC anchored on 1T-MoS₂ phase has been reported to be exceptionally better than its Fe counterpart with an energy barrier of 0.66 eV.⁹⁴ Guo *et al.* carried out a theoretical screening of several transition metals and found that Ti-decorated MoS₂ is an excellent NRR electrocatalyst with a NRR limiting potential of -0.63 V in ambient condition.⁹⁵ A systematic study on 3d-transition metal SACs embedded in the vacant S-site of MoS₂ monolayer with S defect by Zhao's group highlighted Mo-SAC embedded MoS₂ (Mo@MoS₂) as an optimal electrocatalyst for NRR with the lowest energy barrier of 0.53 eV.⁹⁶ On this basis, further research showed Re-SAC embedded in MoS₂ to be another promising NRR electrocatalyst that showed high catalytic activity and selectivity with the free-energy barrier becoming as low as 0.43 eV when N₂ is reduced via the distal pathway.⁹⁷

Apart from the transition metal (TM) atom catalysts on MoS₂ for electrocatalytic NRR, diatomic boron doping in MoS₂ has also been implemented by Li and co-workers. The novel diatomic-boron-modified MoS₂ (B₂@MoS₂) is reported to show exceptionally high NRR performance at a lower overpotential of 0.02 V as compared to 0.30 V in a single-boron modified MoS₂ (B@MoS₂) analogue.⁹⁸ Experimental investigation carried out by Zhang et al. on MoS₂ nanosheets with S-vacancy when tailored with Co-dopants presented excellent NRR activity with FE of over 10% and NH₃ yield of 0.63 mmol h⁻¹g⁻¹ at -0.3 V vs RHE. The combined effect of Co-doping with defective S-vacancy on the

MoS₂ nanosheet facilitated N₂ adsorption and activation.⁹⁹ An extension to this study on defected MoS₂ nanosheet with sulphur-vacancies has been carried out by Ma and coworkers and the presence of excessive Mo-atoms in the defected MoS₂ sheet resulted in a high NH₃ yield of $46.1 \times 10^{-11} \text{ mol s}^{-1} \text{ cm}^{-2}$ and FE of 4.58%.¹⁰⁰

Besides MoS₂, the most commonly reported Mo-based TMD, the analogous molybdenum selenide, MoSe₂ that possess similar structure to MoS₂. The heterogeneous multiphasic 1T@2H-MoSe₂ has been reported as an electrocatalyst for NRR with a relatively low FE of $2.82\% \pm 0.1\%$ and NH₃ yield as high $19.91 \pm 0.89 \mu\text{g h}^{-1} \text{ mgcat}^{-1}$ at -0.6 V vs. RHE.¹⁰¹ Akin to the efficient performance of metal SACs anchored on MoS₂ for NRR, 2D MoSe₂ loaded with transition metal SACs also showed favourable NRR performance. The performance of 28 transition metal SACs on MoSe₂ studied via computational investigations highlight high N₂ adsorption and activation on Mn, Os and V anchored MoSe₂ with respective limiting potentials of -0.39 V, -0.36 V and -0.36 V.¹⁰² Similar is the case on Fe-adsorbed MoSe₂ and MoTe₂ reported by Sun et al. wherein the Fe-adatoms promote N₂ activation and N-N weakening thereby enhancing NRR performance on the Mo-based dichalcogenides.¹⁰³

1.5.2 TMDs of other transition metals for NRR

In addition to Mo-based TMDs, the dichalcogenides of other transition metals, mostly sulphides have also been used as electrocatalysts for NRR. TiS₂ nanosheet, a dichalcogenide of 3d transition metal Ti, has been shown to reduce nitrogen at ambient condition with a FE of 5.50% and NH₃ yield of $16.02 \mu\text{g h}^{-1} \text{ mgcat}^{-1}$ at -0.6 V vs RHE. The NRR performance of 2D TiS₂ nanosheet is considerably higher than that of bulk TiS₂.¹⁰⁴ The sulphides of several other transition metals have been investigated by Li and co-workers and the edges of these TMDs show efficient nitrogen fixation. The NRR electrocatalytic activity follows the order of VS₂ > NbS₂ > TiS₂ > MoS₂ > WS₂ > TaS₂ with VS₂ edges showing favourable binding of N₂ and the lowest energy barrier of 0.16 eV for N₂ reduction.¹⁰⁵ While the basal plane of VS₂ is inactive for NRR, the presence of point defects generated by sulphur atom vacancy led to a stronger binding of N₂ to V-adatom defect site in VS₂. The energy barrier to reduce N₂ to NH₃ in defective VS₂ can

be further brought down by introducing a non-metal B-dopant in S-vacant sites of VS_2 .^{106,107} Another family of transition metal sulfides reported by Wang and co-workers is the metallic NbS_2 nanosheets developed via exfoliation method. The highly cationic Nb^{4+} metal center is responsible for a high NH_3 yield of $37.58 \mu\text{g h}^{-1} \text{mgcat}^{-1}$ and FE of 10.12% at -0.5 V vs SHE.¹⁰⁸ Additionally, the defective S-vacancy sites in metal disulphides acting as the active catalytic center for NRR, the presence of adatom or anchored metal SACs is also crucial for tuning the NRR activity. Chu et al. used this strategy to develop Mo-doped SnS_2 with S-vacancy to show a high NH_3 yield of $41.3 \mu\text{g h}^{-1} \text{mgcat}^{-1}$ and a FE of 20.8 % with the higher metallic nature caused by S-vacancy influencing N_2 adsorption and reduction.¹⁰⁹

WS_2 nanosheet is another TMD that possess similar structure to MoS_2 and similar modification in WS_2 can be brought about by creating defective S-sites and introducing metal in the sulfur defect sites. Cr@WS_2 , Tc@WS_2 and Os@WS_2 SACs has been predicted to efficiently convert N_2 into NH_3 in ambient conditions with favourable limiting potentials of -0.37 V, -0.27 V and -0.33 V, respectively.¹¹⁰ The catalytic potential of Sc to Zn, Nb to Cd, W, Pt and Au SACs supported on WS_2 studied by Ma and co-workers showed the presence of Ni-SAC on WS_2 to be the most optimal transition metal for excellent NRR performance.¹¹¹ Another study by Ma and group on WS_2 led to the generation of sulphur defects on WS_2 and these WS_{2-x} nanosheets displayed NH_3 production of $16.38 \mu\text{g h}^{-1} \text{mgcat}^{-1}$ and FE of 12.1 % at -0.6 V vs RHE.¹¹² A comparison between the influence on the NRR efficiency from chalcogen vacancy defects and vacancy replaced by tungsten atom on several phases of tungsten dichalcogenides, WX_2 (X=S, Se and Te) showed a lower NRR limiting potential in the latter. The presence of tungsten atom in the chalcogen vacancy site causes a steric effect at the electrocatalyst surface and this can be utilized to develop better catalysts for NRR.¹¹³

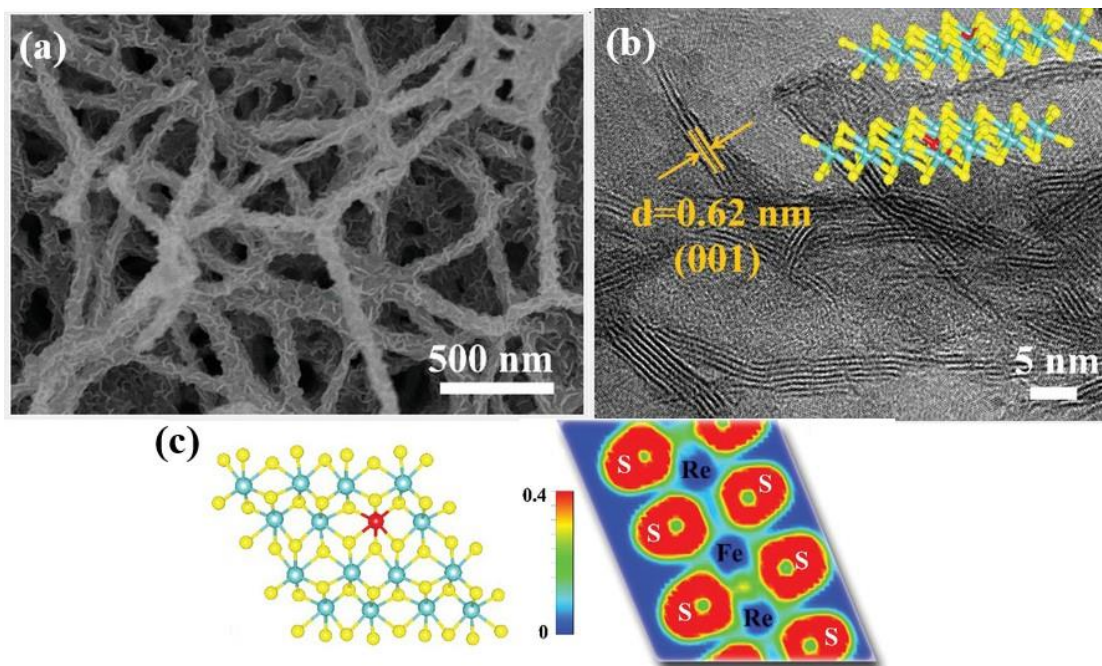


Figure 1.12: Structural images of Fe-doped ReS_2 monolayers, Fe-ReS_2 (a) SEM (scanning electron microscope) image, (b) HRTEM image showing the ReS_2 monolayers, (c) atomistic model of Fe-ReS_2 with the two-dimensional electron localization function (ELF) mapping.¹¹⁴

Rhenium disulphide (ReS_2) and platinum disulphide (PtS_2) are other 2D transition metal dichalcogenides that have been garnering the interests of several researchers for nitrogen reduction. Lai et al. proposed doping low valency transition metals (Fe, Co, Ni, Cu, Zn) in the weakly interacting Re-S layers to tune the charge density of the doped ReS_2 surfaces. A favourable modulation in the charge density can be observed on Fe-doped ReS_2 , represented in **Figure 1.12**, shows the highest NRR performance and NH_3 yield of $80.4 \mu\text{g h}^{-1} \text{mgcat}^{-1}$ (FE = 12.3 %), than the pristine ReS_2 counterpart.¹¹⁴ The same can be observed on Ru-SAC loaded PtS_2 monolayer which shows a higher NRR performance than PtS_2 or benchmark Ru (0001) surfaces.¹¹⁵ The results and findings on these conducting 2D materials depicts the impact tweaking the chemical activity in the surfaces by introducing defects or dopants or metal adatoms. These results can serve as a guide to the design of novel and cost-effective electrocatalysts for NRR.

1.6 NRR in Metal Organic Frameworks (MOFs) and Covalent Organic Frameworks (COFs)

MOFs are porous three-dimensional materials made up of metal ions/clusters as secondary building units and organic ligands as linkers whereas COFs are porous organic materials comprised of only lighter elements (i.e., H, B, C, N, O) coordinated by covalent bonds. The coordination networks of MOFs and COFs in their bulk or three-dimensional form are acknowledged for their porous nature and the large intrinsic surface area. The downsizing of MOFs and COFs into their 2D form leads to a higher electrical conductivity, decreased electron transport distance and generation of hierarchical pores with exposed active sites. The active sites in MOFs are usually the metal ions and they are responsible for adsorption and activation of N_2 . On the other hand, 2D-COFs are lacking of an active site as the lighter elements are incapable of binding N_2 ; thereby a metal center is incorporated in these 2D-COFs and implemented as catalysts for NRR. Metal single atom centers with a designated coordination environment of organic linkers when embedded in 2D-COFs are anticipated to adsorb N_2 .

Cui et. al conducted a DFT investigation on a family of $TM_3(HAB)_2$ ($HAB =$ hexaaminobenzene) 2D-MOFs for electrocatalytic NRR and a high catalytic efficacy for NRR has been reported on $Mo_3(HAB)_2$ MOF along the distal pathway at ambient conditions.¹¹⁶ An experimental investigation on hexaaminobenzene 2D-MOFs carried out by Li and co-workers reported a mixed-metal Co_3Fe -MOF with a high FE of 25.64% and NH_3 yield of $8.79 \text{ mg h}^{-1} \text{ mg}^{-1}$. The FE of NRR in the 2D MOF is much higher than the previously mentioned 2D materials.¹¹⁷ Another family of 2D MOF reported for NRR is the p-conjugated metal bis(dithiolene) MOF with the metal coordinated as MC_4S_4 ($M =$ Fe, Ru, Os, Co, Rh, Ir, Ni, Pd and Pt). The highest NRR performance has been observed on 2D-OsC₄S₄ MOF at a relatively low potential of 0.31 V. The unique coordination of the metal center with the C₄S₄-ligand is decisive in tuning the electrocatalytic performance in this family of 2D MOFs.¹¹⁸ A similar tetravalent coordination of metal in 2D- $M_3C_{12}X_{12}$ MOFs ($M =$ Cr, Mo, and W) with $X =$ NH, O, S, and Se functionalization has been reported to be accountable for the high NRR performance in $W_3C_{12}X_{12}$ ($X =$ Se,

S, and O) with limiting potentials -0.01 V, -0.14 V, and -0.59 V respectively.¹¹⁹ The reticular chemistry of MOFs and their experimental feasibility has led to the investigation on a family of nitrogen-free 2D-MOFs by Jacob's group. The metal benzenehexathiol, M-BHT MOF (M= Sc-Zn, Mo, Ru, Rh, Pd and Ag) when investigated for NRR catalysis through computational investigations showed the M-S₄ centers to act as electron reservoirs and be responsible for adsorption of N₂. Mo-BHT exhibited the highest turnover of NH₃ and a lowest energy barrier of 0.37 eV amongst all the transition metals considered in their study.¹²⁰ Dai et al. designed another family of nitrogen-free 2D MOFs, M₃(C₂O)₁₂, M = Sc-Au and the theoretical exploration on their stability, experimental feasibility and catalytic activity brought forth Mo₃(C₂O)₁₂ monolayer as a prospective electrocatalyst for NRR.¹²¹ It is also imperative to consider the sustainability and availability of these metal centers reported to be active in 2D-MOFs. As such, coronene-based 2D-MOFs (M-PTC) are more attractive electrocatalysts for NRR as a superior activity of lighter transition metals (Sc-Cu) can be achieved. V-PTC and Fe-PTC MOFs are seen to show a low overpotential of -0.60 V and -0.53 V with a high selectivity for NRR under mild conditions.¹²²

One of the major challenges in achieving excellent NRR performance is maintaining a good NH₃ yield rate and FE in aqueous reaction conditions when there is a prominence of competing hydrogen evolution reaction (HER). In an attempt to subdue HER, hydrophobic materials with the catalysts are used and a boron rich 2D COF supported on N-doped porous carbon designed by Liu et. al using this protocol delivered a maximum NRR FE of 45.4% and NH₃ yield rate of $12.53 \mu\text{gh}^{-1}\text{mg}^{-1}$ at -0.2 V.^{123,124} However, the amorphous nature of this COF and the need for a support deem it less appealing for adoption in commercial setting. As such, metal atoms embedded 2D-COFs are more appealing owing to their crystalline and free-standing nature with the metal center responsible for N₂ reduction. Stable COFs formed through the solvothermal reaction of phenylenediamine and octacarboxyphthalocyanine with transition metal SACs (M = Nb, Mo, Co, Hf, Ta, W) has been explored by Zhang et. al following the experimental evidence of Co-based COF. Three 2D-COFs (Nb, Mo, Ta) have been reported to exhibit high catalytic activity and selectivity for NRR, with Nb-COF showing the lowest NRR

limiting potential of -0.02 V.¹²⁵ A family of conductive 2D-COF constructed by the robust linkage of octaamino-metallophthalocyanine and pyrene-tetraone has been investigated with several possible transition metal SACs. Amongst the 20 metal SACs considered in the study from Su's group, Mo-based COF shows outstanding NRR catalytic activity and selectivity with excellent electrical conductivity.¹²⁶ Another family of phthalocyanine-based 2D MPC-TFPN COFs has been explored via multiple-level descriptors for NRR activity and the best NRR performance can be observed in WPc-TFPN with a low limiting potential of -0.19 V.¹²⁷ The strong binding of transition metal SACs in the N_4 -unit of phthalocyanine COFs leads to efficient adsorption of N_2 . The crucial role of N-atoms in binding the transition metals can be observed in terpyridine-based COFs and 2D Fe-terpyridine-COF shows the lowest onset potential of -0.49 V amongst the 3d-transition metals which are much more abundant and sustainable as compared to the heavier 4d and 5d metals. The Fe-SAC is involved in the charge transfer and π back-donation of electrons from N_2 , leading to optimal binding of the protonated $*N_xH_y$ species.¹²⁸ Besides metal SACs, bimetallic 3d-transition metals (Co, Fe, Mo, Ru and W) when incorporated in 2D Cu-salphen COF exhibits high NRR performance and the lowest NRR limiting potential of -0.29 V in MoRu-salphen COF is accompanied with a high theoretical FE ranging from 76–100%.¹²⁹

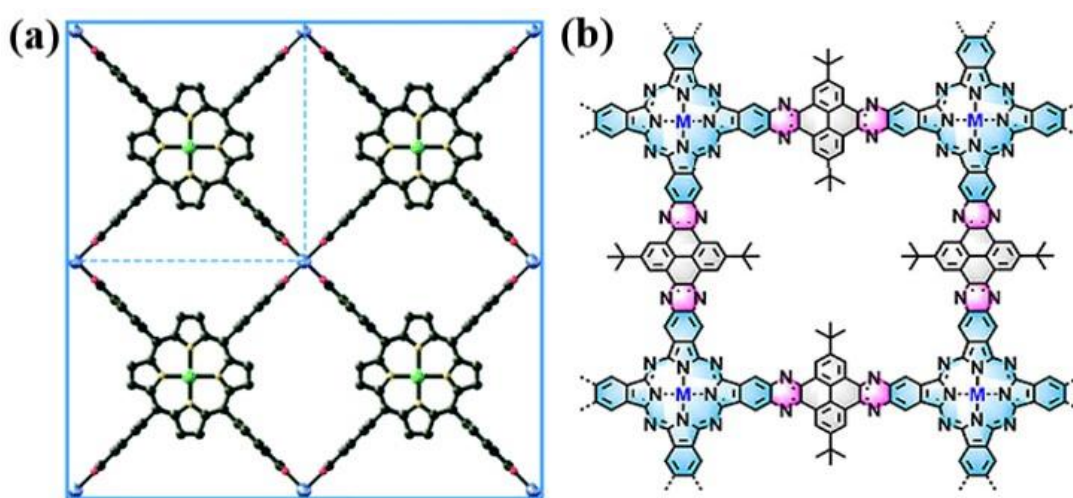


Figure 1.13: Atomistic presentation of (a) Fe-based 2D porphyrin MOF (Fe-TCPP) and (b) Fe incorporated in phthalocyanine-based 2D-COF (FePc-pz) framework.¹³¹⁻¹³²

Although the number of 2D-MOFs and COFs reported experimentally for nitrogen reduction in ambient conditions are limited, recent investigations have proven the viability and stability of 2D In-MOFs designed by Sun and co-authors with an ultra-thin thickness of 1.3 nm. The NH_3 yield has been found to increase gradually as the pH of the reaction media is increased and a maximum yield of $79.20 \mu\text{g h}^{-1}\text{mg}^{-1}$ and FE of 14.98% can be observed at an alkaline condition (pH=12).¹³⁰ The ammonia yield and FE has been found to significantly increase when naturally abundant porphyrin (M-TCPP) and phthalocyanine (MPc-pz) organic ligands are incorporated as linkers in 2D-MOFs. Fe-TCPP exhibited prominent NRR performance with a yield of $44.77 \text{ mg h}^{-1}\text{mgcat}^{-1}$ (FE = 16.23%) while the NH_3 production rate in FePc-pz is noted at $33.6 \mu\text{g h}^{-1}\text{mgcat}^{-1}$ (FE = 31.9%); the atomistic structure of these Fe-based 2D MOF and COF is as shown in **Figure 1.13**.^{131,132} The Fe-N₄ center in these MOFs present a unique electronic state and act as catalytic site thereby showing a strong N₂ binding, faster N₂ activation, NRR selectivity and kinetics. Similar NRR electrocatalytic efficiency can be observed in quasisphthalocyanine N-coordinated Ti-COF designed by Jiang et. al and the NH_3 yield of $26.89 \mu\text{g h}^{-1}\text{mgcat}^{-1}$ (FE = 34.62%) is higher than Cu-COF and Co-COF counterparts.¹³³ While 2D MOFs and COFs show the highest NRR performance to date, experimental demonstrations are limited and there is still a need for further investigation.

Although computational investigations on modelling 2D materials as catalysts for NRR is on the rise in the last few decades; the exactness and reproducibility of these reports are limited by the research methodology, atomistic model incorporated, reaction mechanism description, hypothesizing experimental feasibility and activity. Besides the need for a realistic representation of the model and methodology, it is also important to check the selectivity of the catalyst towards NRR over competing reactions such as hydrogen evolution reaction (HER) and nitric oxide reduction reaction (NO_xRR). While there is a plethora of computationally active catalysts for NRR, we are yet to attain commercial success and the search should now converge towards obtaining experimentally viable catalysts.

1.7 Motivation and Objectives of the Thesis

Ammonia production from the Bosch-Haber's process is one of the most energy expensive processes that gobbles up nearly 6% of global energy. This humongous energy consumption can be accepted owing to varied applications of ammonia in agriculture, chemicals, and industry. However, for its application as a carbon free green fuel, which is an emerging research area, the Haber's process to synthesise ammonia may pose a losing bargain as compared to the energy released from ammonia as a fuel. It is therefore time to investigate on metal and non-metal centers anchored or assimilated on two-dimensional (2D) materials at a minimal cost for effective reduction of N_2 to NH_3 . Computational explorations on the plausible design of novel 2D materials for ammonia production need to be explored and there is a need to study the catalytic activity and chemical efficacy of different metal and non-metal centers for artificial nitrogen fixation. The advantages when different 2D materials are implemented for NRR and the research gaps/challenges in reproducing the theoretical findings to experimental prototypes in each family of 2D material are being summarised in **Table 1.1**.

Table 1.1: Table summarising the advantages of different 2D materials discussed in this thesis with the research gap in procuring them for commercial explorations (*CE*).

2D material	Advantages	Research gap	<i>CE</i>
Graphene	1.Semiconducting with zero band gap. 2.Mechanical stability and flexibility. 3.Economically viable. 4.Can be used as hetero/electrocatalyst for NRR.	1.Limited wettability and low stability in aqueous environment. 2.Dopant or vacancy defect predicted by theory not engineered accurately in experiments.	1.Unfeasible bottom-up synthesis protocol.

MXenes, MBenes & TMDs	<p>1.High electrical conductivity and volumetric capacitance.</p> <p>2.Adjustable band gap and high thermal stability.</p> <p>2.Targeted use as electrocatalysts.</p>	<p>1.Restacking or agglomeration of 2D layers into dense 3D structures.</p>	<p>2.Etching technique used to procure the 2D sheets is commercially unpragmatic.</p>
2D-MOFs & COFs	<p>1.Low cost, easy synthesis and operation.</p> <p>2. Porous structures that are tailorable, high surface area and limited agglomeration of catalytic sites.</p> <p>3. Tunable band gap and can be targeted as photo/electrocatalysts.</p>	<p>1.Low conductivity and long-term stability of the frameworks.</p> <p>2.New materials and synthesis protocols other than conventional methods not being explored.</p> <p>3. Limited applications to catalysis.</p>	<p>1.Facile and commercially pragmatic bottom-up synthesis procedures.</p> <p>2.Changes can be limited to solvent used, reaction time and temperature which can be automated.</p>

The thesis provides an edge by studying different families of 2D materials, unlike most projects that focus on only one specific family, for NRR in a comprehensive fashion. The objective of this thesis is to improve NRR performance as surface modifications are implemented on different families of 2D material with a goal to move towards a sustainable and highly scalable material that can be produced in a commercial scale. This thesis has been organized in nine chapters, with an overview on the two-dimensional

(2D) materials reported for nitrogen activation and reduction, provided in this chapter. The organization of the thesis from Chapter 2 to Chapter 9 is provided in the next section.

1.8 Organization of the thesis

Chapter 2 deals with the theoretical background and provide an overview of quantum mechanical methods, the density functional theory (DFT), theories and improvements to solve the Kohn-Sham equations. A brief discussion on van der Waals correction, implicit solvation, atomic charge analysis and the software used in the thesis are detailed in this chapter.

Chapter 3 and Chapter 4, discusses the activation of N₂ molecule on metal single atomic catalysts (SACs) anchored on graphene with hetero-atom dopants. The local activity of metal SACs, upon confirmation from Chapter 3, are further explored on different transition metal SACs for N₂ activation and reduction in Chapter 4.

Chapter 5 explores the difference between aluminium (Al), the most earth abundant metal, to reported active transition metals on graphene for N₂ activation and reduction efficiency. The essential trade-off to be made on choosing an abundant metal for sustainable catalysis or high activity has been addressed in this chapter.

Chapter 6 delves into the nitrogen reduction efficiency of an electrically conductive 2D material, Mo₂C with non-metal active centers. The activation and reduction of N₂ is corroborated to the p-band centre and electron occupancy of the active boron centers, as a lead for developing metal free electrocatalysts for NRR.

Chapter 7 provides a detailed investigation on the NRR activity of chemically modified 2D vanadium dichalcogenides (VX₂) with non-metal dopants, and a pivotal role of thermodynamic favourability of NH₃ formation from the reactant N₂. An electron “donor–acceptor” mechanism between non-metal and N₂ is responsible for modulating the NRR energy barrier in VX₂ monolayers.

Chapter 8 describes the NRR activity and selectivity of metalloporphyrin metal organic frameworks (MOFs) with stable metal-N₄ complex unit. The NRR performance

of these MOFs is influenced by a linear relationship between the surface dependent electronic properties (work function, d-band center) and N-N bond strength to the energy barrier required for N₂ reduction.

Chapter 9 summarizes the important findings from all the working chapters and the future scope of this thesis.

1.9 References

- (1) Garagounis, I.; Kyriakou, V.; Skodra, A.; Vasileiou, E.; Stoukides, M. *Front. Energ. Res.* **2014**, *2*, 1–10.
- (2) Wang, L.; Xia, M.; Wang, H.; Huang, K.; Qian, C.; Maravelias, C. T. *Joule*, **2018**, *2*(6), 1-20.
- (3) <https://www.persistencemarketresearch.com/market-research/ammonia-market.asp>, accessed on July 2023.
- (4) Ammonia Energy Association. Innovative Outlook- Renewable Ammonia; *IRENA*: Masdar City, United Arab Emirates, **2022**.
- (5) Fourmond, V.; Leger, C. *Angew. Chem. Int. Ed.* **2017**, *56*, 4388–4390.
- (6) Milton, R.D.; Abdellaoui, S.; Khadka, N.; Dean, D. R.; Leech, D.; Seefeldt, L. C.; Minter, S. D. *Energy Environ. Sci.* **2016**, *9*, 2550-2554.
- (7) Tang, C.; Qiao, S.-Z. *Chem. Soc. Rev.*, **2019**, *48*, 3166–3180.
- (8) Pfennig, B. Principles of Inorganic Chemistry. Hoboken, New Jersey: John Wiley & Sons, Inc., **2015**.
- (9) Astruc, D. Organometallic chemistry and catalysis, *Springer*, **2007**.
- (10) Weare, W. W.; Dai, X.; Byrnes, M. J.; Chin, J. M.; Schrock, R. R.; Müller, P. *PNAS* **2006**, *103*, 17099–17106.
- (11) Nishibayashi, Y. *Inorg. Chem.* **2015**, *54*, 9234.
- (12) Ohki, Y.; Uchida, K.; Tada, M.; Cramer, R. E.; Ogura, T.; Ohta, T. *Nat. Commun.* **2018**, *9*, 1-6.
- (13) Geim, A. K.; Grigorieva, I. V. *Nature* **2013**, *499*, 419–425.
- (14) Tan, C.; Cao, X.; Wu, X.J.; He, Q.; Yang, J.; Zhang, X.; Chen, J.; Zhao, W.; Han, S.; Nam, G.H.; Sindoro, M; Zhang, H. *Chem. Rev.* **2017**, *117*, 6225–6331.

- (15) Yang, Q.; Su, Y.; Chi, C.; Cherian, C.T.; Huang, K.; Kravets, V.G.; Wang, F.C.; Zhang, J.C.; Pratt, A.; Grigorenko, A.N.; et al. *Nat. Mater.* **2017**, *16*, 1198–1202.
- (16) Xia, L.; Yang, J.; Wang, H.; Zhao, R.; Chen, H.; Fang, W.; Asiri, A. M.; Xie, F.; Cui, G.; Sun, X. *Chem. Commun.* **2019**, *55*, 3371–3374
- (17) Tian, Y.; Xu, D.; Chu, K.; Wei, Z.; Liu, W. *J. Mater. Sci.* **2019**, *54*, 1–10.
- (18) Song, P.; Kang, L.; Wang, H.; Guo, R.; Wang, R. *ACS Appl. Mater. Interfaces* **2019**, *11*, 12408–12414.
- (19) Yu, X.; Han, P.; Wei, Z.; Huang, L.; Gu, Z.; Peng, S.; Ma, J.; Zheng, G. *Joule* **2018**, *2*, 1610–1622.
- (20) Jia, Y.; Zhang, L.; Du, A.; Gao, G.; Chen, J.; Yan, X.; Brown, C. L.; Yao, X. *Adv. Mater.* **2016**, *28*, 9532–9538.
- (21) Haag, D.; Kung, H. H. *Top. Catal.* **2014**, *57*, 762–773.
- (22) Mukherjee, S.; Cullen, D. A.; Karakalos, S.; Liu, K.; Zhang, H.; Zhao, S.; Xu, H.; More, K. L.; Wang, G.; Wu, G. *Nano Energy* **2018**, *48*, 217.
- (23) Sreekanth, N.; Nazrulla, M. A.; Vineesh, T. V.; Sailaja, K.; Phani, K. L. *Chem. Commun.* **2015**, *51*, 16061.
- (24) Hering-Junghans, C. *Angew. Chem., Int. Ed.* **2018**, *57*, 6738.
- (25) Zhao, S.; Lu, X.; Wang, L.; Gale, J.; Amal, R. *Adv. Mater.* **2019**, *31*, 1805367.
- (26) Yang, X.-F.; Wang, A.; Qiao, B.; Li, J.; Liu, J.; Zhang, T. *Acc. Chem. Res.* **2013**, *46*, 1740–1748.
- (27) Geng, Z.; Liu, Y.; Kong, X.; Li, P.; Li, K.; Liu, Z.; Du, J.; Shu, M.; Si, R.; Zeng, J. *Adv. Mater.* **2018**, *30*, 1803498.
- (28) Qin, Q.; Heil, T.; Antonietti, M.; Oschatz, M. *Small Methods* **2018**, *2*, 1800202.
- (29) Choi, C.; Back, S.; Kim, N.-Y.; Lim, J.; Kim, Y.-H.; Jung, Y. *ACS Catal.* **2018**, *8*, 7517–7525.
- (30) Eady, R. R. *Chem. Rev.*, **1996**, *96*, 3013–3030.
- (31) Le, Y.-Q.; Gu, J.; Tian, W. Q. *Chem. Commun.* **2014**, *50*, 13319.
- (32) Li, X.-F.; Li, Q.-K.; Cheng, J.; Liu, L.; Yan, Q.; Wu, Y.; Zhang, X.-H.; Wang, Z.-Y.; Qiu, Q.; Luo, Y. *J. Am. Chem. Soc.* **2016**, *138*, 8706–8709.

- (33) Zhao, W.; Zhang, L.; Luo, Q.; Hu, Z.; Zhang, W.; Smith, S.; Yang, J. *ACS Catal.* **2019**, *9*, 3419–3425.
- (34) Kattel, S.; Atanassov P.; Kiefer, B. *J. Phys. Chem. C*, **2012**, *116*, 8161–8166.
- (35) Wen, L.; Ren, C.; Zou, Y.; Lin, W.; Ding, K. *Appl. Surf. Sci.*, **2020**, *534*, 147595.
- (36) Yang, Y.; Liu, J.; Wei, Z.; Wang, S.; Ma, J. *ChemCatChem* **2019**, *11*, 2821–2827.
- (37) Guo, X.; Huang, S. *Electrochim. Acta* **2018**, *284*, 392–399.
- (38) Ling, C.; Ouyang, Y.; Li, Q.; Bai, X.; Mao, X.; Du, A.; Wang, J. *Small Methods* **2019**, *3*, 1800376.
- (39) Riyaz, M.; Goel, N. *ChemPhysChem* **2019**, *20*, 1954–1959.
- (40) Wei, Z.; Feng, Y.; Ma, J. *J. Energy Chem.* **2020**, *48*, 322–327.
- (41) Liu, J.; Liang, T.; Wang, F.; Lai, W.; Liu, Y. *Int. J. Hydrogen Energy* **2020**, *45*, 9555–9563.
- (42) Wen, Z.; Lv, H.; Wu, D.; Zhang, W.; Wu, X.; Yang, J. *J. Phys. Chem. Lett.* **2022**, *13*, 8177–8184.
- (43) Zhou, H. Y.; Li, J. C.; Wen, Z.; Jiang, Q. *Phys. Chem. Chem. Phys.*, **2019**, *21*, 14583–14588.
- (44) Han, L.; Liu, L.; Chen, J.; Lin, R.; Liu, H.; Lue, F.; Bak, S.; Liang, Z.; Zhao, S.; Stavitski, E.; Luo, J.; Adzic, R. R.; Xin, H. L. *Angew. Chem. Int. Ed.*, **2019**, *58*, 2321–2325.
- (45) Lü, F.; Zhao, S.; Guo, R.; He, J.; Peng, X.; Bao, H.; Fu, J.; Han, L.; Qi, G.; Luo, J.; Tang, X.; Liu, X. *Nano Energy*, **2019**, *61*, 420–427.
- (46) Zang, W.; Yang, T.; Zou, H.; Xi, S.; Zhang, H.; Liu, X.; Kou, Z.; Du, Y.; Feng, Y. P.; Shen, L.; Duan, L.; Wang, J.; Pennycook, S. J. *ACS Catal.*, **2019**, *9*, 10166–10173.
- (47) Han, L.; Hou, M.; Ou, P.; Cheng, H.; Ren, Z.; Liang, Z.; Boscoboinik, J. A.; Hunt, A.; Waluyo, I.; Zhang, S.; Zhuo, L.; Song, J.; Liu, X.; Luo, J.; Xin, H. L. *ACS Catal.* **2021**, *11*, 509–516.
- (48) Chen, C.-H.; Wu, D.; Li, Z.; Zhang, R.; Kuai, C.-G.; Zhao, X.-R.; Dong, C.-K.; Qiao, S.-Z.; Liu, H.; Du, X.-W. *Advanced Energy Materials*, **2019**, *9*, 1803913.
- (49) Zhou, X.; Shen, Q.; Yuan, K.; Yang, W.; Chen, Q.; Geng, Z.; Zhang, J.; Shao, X.; Chen, W.; Xu, G.; Yang, X.; Wu, K. *J. Am. Chem. Soc.*, **2018**, *140*, 554.

- (50) Yang, W.; Huang, H.; Ding, X.; Ding, Z.; Wu, C.; Gates, I. D.; Gao, Z. *Electrochimica Acta*, **2020**, *335*, 135667.
- (51) He, T.; Santiago, A. R. P.; Du, A. *Journal of Catalysis*, **2020**, *388*, 77-83.
- (52) Ma, D.; Wang, Y.; Liu, L.; Jia, Y. *Phys. Chem. Chem. Phys.*, **2021**, *23*, 4018-4029.
- (53) Qu, M.; Qin, G.; Fan, J.; Du, A.; Sun, Q. *Applied Surface Science*, **2021**, *537*, 148012.
- (54) Han, L.; Ren, Z.; Ou, P.; Cheng, H.; Rui, N.; Lin, L.; Liu, X.; Zhuo, L.; Song, J.; Sun, J.; Luo J.; Xin, H. L. *Angew. Chem., Int. Ed. Engl.*, **2021**, *60*, 345–350.
- (55) Li, Y.; Zhang, Q.; Li, C.; Fan, H. N.; Luo, W. Bin; Liu, H. K.; Dou, S. X. *J. Mater. Chem. A*. **2019**, *7*, 22242–22247.
- (56) Cui, C.; Zhang, H.; Luo, Z. *Nano Res.* **2020**, *13*, 2280–2288.
- (57) Zheng, G.; Li, L.; Tian, Z.; Zhang, X.; Chen, L.; Zheng, G. et al. *Journal of Energy Chemistry*, **2021**, *54*, 612–619.
- (58) Gao, G.; Ding, G.; Li, J.; Yao, K.; Wu, M.; Qian, M. *Nanoscale*, **2016**, *8*, 8986–8994.
- (59) Zhou, S.; Yang, X.; Pei, W.; Jiang, Z.; Zhao, J. *Phys. Energy*, **2021**, *3*, 012002.
- (60) Azofra, L. M.; Li, N.; MacFarlane, D. R.; Sun, C. *Energy Environ. Sci.*, **2016**, *9*, 2545-2549.
- (61) Wang, S.; Li, B.; Li, L.; Tian, Z.; Zhang, Q.; Chen, L.; Zeng, X. C. *Nanoscale*, **2020**, *12*, 538.
- (62) Zhang, B.; Zhou, J.; Elliott S. R.; Sun, Z. *J. Mater. Chem. A*, **2020**, *8*, 23947–23954.
- (63) Zhao, J.; Zhang, L.; Xie X. Y. et al., *Journal of Materials Chemistry A*, **2018**, *6*, 24031–24035.
- (64) Guo, Y.; Wang, T.; Yang, Q.; Li, X.; Li, H.; Wang, H.; Jiao, T.; Huang, Z.; Dong, B.; Zhang, W.; Fan, J.; Zhi, C. *ACS Nano* **2020**, *14*, 9089–9097.
- (65) Chen, G.; Ding, M.; Zhang, K.; Shen, Z.; Wang, Y.; Ma, J.; Wang, A.; Li, Y.; Xu, H. *ChemSusChem* **2022**, *15*, e202102352.

- (66) Wang, S.; Li, L.; Hui, K. S.; Bin, F.; Zhou, W.; Fan, X.; Zalnezhad, E.; Li, J.; Hui, K. N. *Adv. Eng. Mater.* **2021**, *23*, 2100405.
- (67) Huang, B.; Li, N.; Ong, W.-J.; Zhou, N. *J. Mater. Chem. A* **2019**, *7*, 27620.
- (68) Gao, Y.; Zhuo, H.; Cao, Y.; Sun, X.; Zhuang, G.; Deng, S.; Zhong, X.; Wei, Z.; Wang, J. *Chin. J. Catal.* **2019**, *40*, 152.
- (69) Zheng, S.; Li, S.; Mei, Z.; Hu, Z.; Chu, M.; Liu, J.; Chen, X.; Pan, F. *J. Phys. Chem. Lett.* **2019**, *10*, 6984–6989
- (70) Zhang, N.; Wang, M.-Y.; Liu, J.-Y. *Mol. Catal.* **2022**, *531*, 112658.
- (71) Li, H.; Wei, S.; Wang, H.; Cai, Q.; Zhao, J. *J. Colloid Interface Sci.* **2021**, *588*, 1.
- (72) Luo, H.; Wang, X.; Wan, C.; Xie, L.; Song, M.; Qian, P. *Nanomaterials*, **2022**, *12*, 1081.
- (73) Niu, K.; Chi, L.; Rosen, J.; Bjork, J. *J. Phys. Chem. Lett.* **2022**, *13*, 2800.
- (74) Sun, J.; Kong, W.; Jin, Z.; Han, Y.; Ma, L.; Ding, X.; Niu, Y.; Xu, Y. *Chinese Chem. Lett.*, **2020**, *31*, 953–960.
- (75) Amrillah, T.; Hermawan, A.; Alviani, V. N.; Seh, Z. W.; Yin, S. *Materials Today Energy*, **2021**, *22*, 100864.
- (76) Li, Q.; He, L.; Sun, C.; Zhang, X. *J. Phys. Chem. C*, **2017**, *121*, 27563–27568.
- (77) Cheng, Y.; Dai, J.; Song, Y.; Zhang, Y. *Nanoscale* **2019**, *11*, 18132.
- (78) Jin, H.; Li, L.; Liu, X.; Tang, C.; Xu, W.; Chen, S.; Song, L. *Adv. Mater.*, **2019**, *31*, 1902709.
- (79) Jiang, Z.; Wang, P.; Jiang, X.; Zhao, J. *Nanoscale Horiz.* **2018**, *3*, 335–341.
- (80) Guo, Z.; Zhou, J.; Sun, Z. *J. Mater. Chem. A* **2017**, *5*, 23530–23535.
- (81) Yang, X.; Shang, C.; Zhou, S.; Zhao, J. *Nanoscale Horiz.* **2020**, *5*, 1106–1115.
- (82) Guo, X.; Lin, S.; Gu, J.; Zhang, S.; Chen, Z. et al., *Adv. Funct. Mater.* **2020**, *31*, 2008056.

- (83) Xu, S.; Qin, G.; Jiang, Q.; Cui, Q.; Du, A.; Zhao, C.; Sun, Q. *Int J Quantum Chem.* **2021**, *121*, e26548.
- (84) Li, Y.; Li, L.; Huang, R.; Wen, Y. *Nanoscale*, **2021**, *13*, 15002–15009.
- (85) Wang, J.; He, C.; Huo, J.; Fu, L.; Zhao, C. *Adv. Theory Simul.* **2021**, *4*, 2100003.
- (86) Lin, L.; Shi, P.; Fu, L.; He, C.; Huo, J. et al., *J. Electroanal. Chem.* **2021**, *899*, 115677.
- (87) Qi, S.; Fan, Y.; Zhao, L.; Li, W.; Zhao, M. et al., *Appl. Surf. Sci.* **2021**, *536*, 147742.
- (88) Cheng, Y.; Mo, J.; Li, Y.; Zhang, Y.; Song, Y. *Phys. Chem. Chem. Phys.*, **2021**, *23*, 6613–6622.
- (89) Xiao, Y.; Shen, C.; Long, T. *Chem. Mater.* **2021**, *33*, 4023–4034.
- (90) Zhang, L.; Ji, X.; Ren, X.; Ma, Y.; Shi, X.; Tian, Z.; Asiri, A. M.; Chen, L.; Tang, B.; Sun, X. *Adv. Mater.*, **2018**, *30*, 1800191.
- (91) Azofra, L. M.; Sun, C.; Cavallo, L.; MacFarlane, D. R. *Chemistry* **2017**, *23*, 8275–8279
- (92) Zhang, H.; Cui, C.; Luo, Z. *J. Phys. Chem. C*, **2020**, *124*, 6260–6266.
- (93) Zhao, X.; Zhang, X.; Xue, Z.; Chen, W.; Zhou, Z.; Mu, T. *J. Mater. Chem. A*, **2019**, *7*, 27417–27422.
- (94) Yang, L.; Chen, F.; Song, E.; Yuan, Z.; Xiao, B. *ChemPhysChem* **2020**, *21*, 1235–1242.
- (95) Guo, H.; Li, L.; Wang, X.; Yao, G.; Yu, H.; Tian, Z.; Li, B.; Chen, L. *ACS Appl. Mater. Interfaces* **2019**, *11*, 36506–36514
- (96) Zhao, J.; Zhao, J.; Cai, Q. *Phys. Chem. Chem. Phys.* **2018**, *20*, 9248–9255.
- (97) Zhai, X.; Li, L.; Liu, X.; Li, Y.; Yang, J.; Yang, D.; Zhang, J.; Yan, H.; Ge, G. *Nanoscale* **2020**, *12*, 10035–10043.
- (98) Li, F.; Tang, Q. *Nanoscale* **2019**, *11*, 18769–18778.
- (99) Zhang, J.; Tian, X.; Liu, M.; Guo, H.; Zhou, J.; Fang, Q.; Liu, Z.; Wu, Q.; Lou, J. *J. Am. Chem. Soc.* **2019**, *141*, 19269–19275.

- (100) Ma, C.; Zhai, N.; Liu, B.; Yan, S. *Electrochimica Acta*. **2021**, *370*, 137695.
- (101) Wu, Z.; Zhang, R.; Fei, H.; Liu, R.; Wang, D.; Liu, X. *Appl. Surf. Sci.* **2020**, *532*, 147372.
- (102) Hou, P.; Huang, Y.; Ma, F.; Zhu, G.; Du, R.; Wei, X.; Zhang, J.; Wang, M. *Molecular Catalysis* **2023**, *537*, 112967.
- (103) Sun, Y.; Ding, S.; Xia, B.; Duan, J.; Antonietti, M.; Chen, S. *Angew. Chem., Int. Ed.*, **2022**, *61*, e202115198.
- (104) Jia, K.; Wang, Y.; Qiu, L.; Gao, J.; Pan, Q.; Kong, W.; Zhang, X.; Alshehri, A. A.; Alzahrani, K. A.; Zhong, B.; Guo, X.; Yang, L. *Inorg. Chem. Front.* **2019**, *6*, 1986–1989.
- (105) Li, F.; Chen, L.; Liu, H.; Wang, D.; Shi, C.; Pan, H. *J. Phys. Chem. C* **2019**, *123*, 22221–22227.
- (106) Zhang, L.; Hu, Z. *Materials & Design* **2021**, *209*, 110006.
- (107) Li, Q.; Guo, Y.; Tian, Y.; Liu, W.; Chu, K. *J. Mater. Chem. A* **2020**, *8*, 16195–16202.
- (108) Wang, H.; Si, J.; Zhang, T.; Li, Y.; Yang, B.; Li, Z.; Chen, J.; Wen, Z.; Yuan, C.; Lei, L.; Hou, Y. *Appl. Catal. B* **2020**, *270*, 118892.
- (109) Chu, K.; Wang, J.; Liu, Y.; Li, Q.; Guo, Y. *J. Mater. Chem. A*. **2020**, *8*, 7117–7124.
- (110) Chen, Y.; Zhang, X.; Qin, J.; Liu, R. *Applied Surface Science* **2022**, *571*, 151357.
- (111) Ma, X.; Hu, J.; Zheng, M.; Li, D.; Lv, H.; He, H.; Huang, C. *Appl. Surf. Sci.* **2019**, *489*, 684–692.
- (112) Ma, L.; Kong, W.; Liu, M.; Jin, Z.; Han, Y.; Sun, J.; Liu, J.; Xu, Y.; Li, J. *Sci. China Mater.* **2021**, *64*, 1910–1918.
- (113) Tursun, M.; Wu, C. *ChemSusChem* **2022**, *15*, e202200191.
- (114) Lai, F.; Chen, N.; Ye, X.; He, G.; Zong, W.; Holt, K. B.; Pan, B.; Parkin, I. P.; Liu, T.; Chen, R. *Adv. Funct. Mater.* **2020**, *30*, 1907376.
- (115) Cai, L.; Zhang, N.; Qiu, B.; Chai, Y. *ACS Appl. Mater. Interfaces* **2020**, *12*, 20448–20455.

- (116) Cui, Q.; Qin, G.; Wang, W.; Geethalakshmi, K. R.; Du, A.; Sun, Q. *J. Mater. Chem. A*, **2019**, *7*, 14510–14518.
- (117) Li, W.; Fang, W.; Wu, C.; Dinh, K. N.; Ren, H.; Zhao, L.; Liu, C.; Yan, Q. *J. Mater. Chem. A*, **2020**, *8*, 3658–3666.
- (118) Liu, X.; Wang, Z.; Zhao, J.; Zhao, J.; Liu, Y. *Appl. Surf. Sci.*, **2019**, *487*, 833–839.
- (119) Wang, R.; He, C.; Chen, W.; Fu, L.; Zhao, C.; Huo, J.; Sun, C. *Nanoscale*, **2021**, *13*, 19247.
- (120) Lv, X.; Wei, W.; Wang, H.; Li, F.; Huang, B.; Dai, Y.; Jacob, T. *J. Mater. Chem. A*, **2020**, *8*, 20047.
- (121) Feng, Z.; Yang, Z.; Meng, X.; Li, F.; Guo, Z.; Zheng, S.; Su, G.; Ma, Y.; Tang, Y.; Dai, X. *J. Mater. Chem. A* **2022**, *10*, 4731–4738.
- (122) Li, B.; Du, W.; Wu, Q.; Dai, Y.; Huang, B.; Ma, Y. *J. Phys. Chem. C* **2021**, *125*, 20870–20876.
- (123) Lee, H. K.; Koh, C. S. L.; Lee, Y. H.; Liu, C.; Phang, I. Y.; Han, X.; Tsung, C. K.; Ling, X. Y.; *Sci. Adv.* **2018**, *4*, eaar3208.
- (124) Liu, S.; Wang, M.; Qian, T.; Ji, H.; Liu, J.; Yan, C. *Nat. Commun.* **2019**, *10*, 3898.
- (125) Zhang, N.; Wang, M.-Y.; Liu, J.-Y. *Vacuum* **2023**, *210*, 111852.
- (126) Wang, C.; Zhao, Y.-N.; Zhu, C.-Y.; Zhang, M.; Geng, Y.; Li, Y.-G.; Su, Z.-M. *J. Mater. Chem. A*, **2020**, *8*, 23599.
- (127) Wang, J.; Zhang, Z.; Li, Y.; Qu, Y.; Li, Y.; Li, W.; Zhao, M. *ACS Appl. Mater. Interfaces* **2022**, *14*, 1024–1033.
- (128) Ohashi, K.; Iwase, K.; Harada, T.; Nakanishi, S.; Kamiya, K. *J. Phys. Chem. C* **2021**, *125*, 10983–10990.
- (129) Zhang, Z.; Qi, S.; Wang, J.; Zhao, M. *Applied Surface Science* **2021**, *563*, 150352.
- (130) Sun, Y.; Xia, B.; Ding, S.; Yu, L.; Chen, S.; Duan, J. *J. Mater. Chem. A* **2021**, *9*, 20040–20047.

- (131) Cong, M.; Chen, X.; Xia, K.; Ding, X.; Zhang, L.; Jin, Y.; Gao, Y.; Zhang, Y. *J. Mater. Chem. A*, **2021**, *9*, 4673.
- (132) Zhong, H.; Wang, M.; Ghorbani-Asl, M.; Zhang, J.; Ly, K. H.; Liao, Z.; Chen, G.; Wei, Y.; Biswal, B. P.; Zschech, E.; Weidinger, I. M.; Krasheninnikov, A. V.; Dong, R.; Feng, X. *J. Am. Chem. Soc.* **2021**, *143*, 19992–20000.
- (133) Jiang, M.; Han, L.; Peng, P.; Hu, Y.; Xiong, Y.; Mi, C.; Tie, Z.; Xiang, Z.; Jin, Z. *Nano Lett.* **2022**, *22*, 372–379.
- (134) Wang, J.; Zhang, Z.; Qi, S.; Fan, Y.; Yang, Y.; Li, W.; Zhao, M. *J. Mater. Chem. A*, **2021**, *9*, 19949.
- (135) Shang, S.; Xiong, W.; Yang, C.; Johannessen, B.; Liu, R.; Hsu, H.-Y.; Gu, Q.; Leung, M. K. H.; Shang, J. *ACS Nano* **2021**, *15*, 9670–9678.
- (136) Xia, L.; Wang, Z.; Zhao, Y. *ACS Appl. Mater. Interfaces* **2022**, *14*, 5384–5394.

Chapter 2

Theoretical Background and Computational Methodology

In this chapter, the theoretical foundations of computational methodology and different quantum simulation tools implemented for obtaining the results presented in this thesis. The fundamentals of studying quantum mechanical systems as a wave function with the many-body Schrödinger equation, introductory theorems that construct density functional theory (DFT), electron correlation, ab initio functional formulation, exchange-correlation approximation, and basis-sets essential to represent the many-electron system are discussed in this chapter. DFT is a quantum mechanical modelling method used to analyse the properties of materials by using functionals of electron density. DFT is one of the most popular methods in computational chemistry and plays an increasingly important role in scientific research. This chapter introduces the theoretical aspects of computational chemistry – Schrödinger equation, Born-Oppenheimer and Hartree approximation in the first part; fundamentals of DFT – Hohenberg-Kohn theorems, Kohn-sham equation, and exchange-correlation functional in the second part; protocols beyond energy calculations- ab-initio molecular dynamics, van der Waals correction, implicit solvent model and atomic charge analysis in the third part and the introduction of deMon2K and VASP software in the final part.

2.1 Introduction

All everyday objects and the universe are comprised of matter made up of atoms and the interactions of the subatomic particles- electrons, protons and neutrons represent the properties of matter. These properties of matter can be the behaviour of macroscopic bodies whose velocity is smaller than the speed of light, or microscopic subatomic bodies. All physical phenomena of the macroscopic bodies are perceivable by human senses and are thus described with classical mechanics. The position and momentum of a macroscopic body is simultaneously known at any point of time and energy is thereby as a continuous quantity. However, microscopic particles possess velocities comparable to the speed of light and their linear momentum and position cannot be measured simultaneously. These subatomic microscopic particles possess dual nature - particle and wave nature and their energy is in the form of wave packets; thereby quantum mechanics have been implemented to describe the properties of these subatomic particles.

2.1.1 Quantum mechanics and the wave equation

Quantum mechanics was invented and fully developed in the 1920s to explain the paradoxical particle -wave nature of subatomic particles which could not be explained with classical mechanics. The fundamental backdrop of quantum mechanics is the Schrödinger equation which represents the wave-nature of the microscopic particles as a linear partial differential wave equation and the simplest form of Schrödinger equation¹ to represent the wave function of a quantum-mechanical system is,

$$\hat{H} \Psi (r, R) = E \Psi (r, R) \quad (2.1)$$

where \hat{H} is the Hamiltonian operator, $\Psi (r, R)$ is the wave function in $3n$ -space and n -spin coordinates, E is the total energy of the quantum system, respectively. The position of such a quantum system is represented as a probability density obtained from the product of the wave function, Ψ and its complex conjugate, Ψ^* . Furthermore, the observable physical properties of these quantum particles are obtained when suitable operators or functions act on the wave function Ψ .

For a many-electron quantum system where the electrostatic interactions between electrons and nuclei are Coulombic in nature, the many-particle Schrödinger equation is described as,

$$\hat{H} \Psi_i (r_1, r_2, \dots, r_N, R_1, R_2 \dots, R_N) = E_i \Psi_i (r_1, r_1, \dots, r_N, R_1, R_2 \dots, R_N) \quad (2.2)$$

where \hat{H} is the Hamiltonian operator for an N-electrons system, $\Psi_i (r_1, r_2, \dots, r_N, R_1, R_2 \dots, R_N)$ is the i^{th} state wave function of the and E_i is the energy eigenvalue of the quantum state represented by Ψ_i .

This Hamiltonian for N-electron system will involve electronic kinetic energy (T_e), electrostatic repulsion amongst electrons (V_{ee}), nuclear kinetic energy (T_N), electrostatic repulsion amongst protons in nucleus (V_{NN}) and Coulombic interaction between electrons and nucleus (V_{Ne}), which are respectively described as:

$$\hat{H} (r, R) = T_e(r_i) + V_{ee}(r_i) + T_N(R_i) + V_{NN}(R_i) + V_{Ne}(r_i, R_i) \quad (2.3)$$

$$\begin{aligned} \hat{H} (r, R) = & \sum_i^N \left(-\frac{\hbar^2}{2m_i} \nabla_i^2 \right) + \frac{1}{2} \sum_{i,j}^N \left(\frac{e^2}{|r_i - r_j|} \right) + \sum_I^M \left(-\frac{\hbar^2}{2M_I} \nabla_I^2 \right) + \frac{1}{2} \sum_{I,J}^M \left(\frac{Z_I Z_J e^2}{|R_I - R_J|} \right) + \\ & \sum_i^N \left(\sum_I^M -\frac{Z_I e^2}{|r_i - R_I|} \right) \end{aligned} \quad (2.4)$$

where T, and V are the kinetic and potential energies, m_i is the mass of the i_{th} electron, r_i the position coordinates of the i_{th} electron, M_I the mass of the I_{th} nucleus, R_I the position coordinates of the I_{th} nucleus.

However, the Schrödinger equation can be exactly solved for only very small systems like the hydrogen atom. For real life chemical problems, the analytical solution for Ψ cannot be solved accurately and therefore several approximations have been developed to solve Schrödinger equation for many body interacting systems. To reduce the dimensionality of a many-electron system, the total wavefunction must be antisymmetric to satisfy the Pauli's exclusion principle and the Hartree atomic units where $\hbar = m_e = e = 4\pi/\epsilon_0 = 1$ simplifies the problem.

2.1.2 Born-Oppenheimer Approximation

The first approximation to reduce the number of variables in the solution of the many-body Schrödinger equation is the Born-Oppenheimer approximation.² As the mass of the nucleus is much heavier, its motion is much slower and negligible as compared to that of electrons. The mass of the nucleus is thus approximated to infinity and the kinetic energy $T_N(R_i)$ can be neglected and the potential energy contribution from nucleus-nucleus repulsion $V_{NN}(R_i)$ becomes constant, thereby the Hamiltonian of the many-body system given in Eqn 2.3 can be simplified as the electronic Hamiltonian and written as,

$$\hat{H}_e = T_e + V_{ee} + V_{Ne} = \sum_i^N \left(-\frac{\hbar^2}{2m_i} \nabla_i^2 \right) + \frac{1}{2} \sum_{i,j}^N \left(\frac{e^2}{|r_i - r_j|} \right) + \sum_i^N \left(\sum_l^M -\frac{Z_l e^2}{|r_i - R_l|} \right) \quad (2.5)$$

As such, the wave function Ψ can be represented as the product of the electronic (Ψ_e) and nuclei (Ψ_N) wave function. The solution of the Schrödinger equation with the electronic Hamiltonian \hat{H}_e will give the electronic energy, E_e when operated on the electronic wave function Ψ_e , and the electronic Schrödinger equation is written as,

$$\hat{H}_e \Psi_e = E_e \Psi_e \quad (2.6)$$

and the total energy is the sum of the electronic energy, E_e and the constant nuclear repulsion term, E_N where $E_N = \frac{1}{2} \sum_{l,j}^M \left(\frac{Z_l Z_j e^2}{|R_l - R_j|} \right)$. This simplification with the Born-Oppenheimer approximation solves the hydrogen atom problem accurately, however representing all possible electron-electron interactions in a many-body problem is still a challenge and two effective approaches to solve the independent-electron approximations are the Hartree approximation and Hartree-Fock approximation.

2.1.3 Hartree Approximation

The preliminary approach to solve the many-body system is to represent it as an independent electron equation by neglecting the correlation between the electrons and the wavefunction is described by,³

$$\Psi(r_1, r_2, \dots, r_N) = \phi_1(r_1) \phi_2(r_2) \dots \phi_N(r_N) \quad (2.7)$$

where $\phi_i(r_i)$ is the i^{th} electron independent wave function of the i^{th} electron. The variational principle states that for any wavefunction ϕ with ground state energy, E_0 the total energy of the system obtained from solving the Schrödinger equation should be the minimum for the wave function $\phi_i(r_i)$, i.e.

$$\frac{\langle \phi | \hat{H} | \phi \rangle}{\langle \phi | \phi \rangle} \geq E_0 \quad (2.8)$$

Upon solving the electron independent wave function in Eqn 2.7 with the Hamiltonian in Eq. 2.5 in the Hartree approximation, the Schrödinger equation becomes,

$$\left[-\frac{1}{2} \nabla_i^2 - \sum_l \frac{Z_l}{|r_i - R_l|} + \sum_{i \neq j} \int dr_j \phi_j^*(r_j) \frac{1}{|r_i - r_j|} \phi_j(r_j) \right] \phi_i(r_i) = \epsilon_i \phi_i(r_i) \quad (2.9)$$

Under the Hartree approximation, each electron is treated with an independent wave function in an effective potential generated the integration of the wave functions of remaining electrons. The approximation reduces the difficult many-body problem into a simple mean-field potential interaction with an electron. However, this approximation accounts all electrons are indistinguishable, thereby violating Pauli's exclusion principle. A correction has been made by considering the electrons are distinguishable and many-body wave function is antisymmetric in the Hartree-Fock approximation.

2.1.4 Hartree-Fock Approximation

Hartree-Fock approximation is an improvement to the Hartree approximation when Fock implemented the fermionic character of electrons to ensure the electrons are distinguishable and Pauli's exclusion principle is valid.⁴ The overall wave function is defined by a determinant, known as Slater determinant, to incorporate the antisymmetry condition. The Slater Determinant wave-function is represented as,⁵

$$\Psi(r_1, r_2, \dots, r_N) = \frac{1}{\sqrt{N!}} \dots \begin{vmatrix} \phi_1(r_1) & \phi_2(r_1) & \dots & \phi_N(r_1) \\ \phi_1(r_2) & \phi_2(r_2) & \dots & \phi_N(r_2) \\ \vdots & \vdots & \dots & \vdots \\ \phi_1(r_N) & \phi_2(r_N) & \dots & \phi_N(r_N) \end{vmatrix} \quad (2.10)$$

Each electronic wave function is multiplied by either the + or – sign, and the argument r_i is the product of spatial coordinate and spin coordinate, thus it appears for each orbital

ϕ_i only once.⁶ Adding this constraint to the independent electron wave function to the Hartree equation in Eqn 2.9, the Hartree-Fock equation is defined as,

$$\left[-\frac{1}{2}\nabla_i^2 - \sum_l \frac{Z_l}{|r_i - R_l|} + \sum_j \int dr_j \phi_j^*(r_j) \frac{1}{|r_i - r_j|} \phi_j(r_j) \right] \phi_i(r_i) - \sum_j \int dr_j \phi_j^*(r_j) \frac{1}{|r_i - r_j|} \phi_i(r_j) \phi_j(r_i) = \epsilon_i \phi_i(r_i) \quad (2.11)$$

where, the first three terms are the kinetic energy of electron, potential energy of the electron in the external field of nuclei, and Coulombic potential energy of all electronic charges acting on the i^{th} electron wave function. The last term is the exchange term between two distinguishable electrons, which arises from the incorporation of the Pauli exclusion principle.⁷

2.2 Density Functional Theory

With the Hartree-Fock approximation, electron correlations are calculated in an average way which lead to higher computational costs.⁸⁻⁹ The density functional theory (DFT) redefines the many-electron Schrödinger equation as the electron density $\rho(r)$ to give a reliable balance between the description of electronic structure and computational efficiency. The electron density $\rho(r)$, also known as the probability density of an N electron system is defined as the integral over the spin coordinates of all N electrons within a volume element of d^3r ,

$$\rho(r) = N \int d^3r_1 \dots \int d^3r_N \Psi^*(r_1, r_2, \dots, r_N) \Psi(r_1, r_2, \dots, r_N) \quad (2.12)$$

This probability density $\rho(r)$ is a non-negative function of the position variables of N electrons which integrates to the total number of electrons N present in the system and $\rho(r) \rightarrow 0$ when $r \rightarrow \infty$. Further, this electron density $\rho(r)$ can be used to calculate various properties of the material that are related to the ground-state energy, E_0 and electron density of the system. The Hohenberg-Kohn theorem,¹⁰ was proposed in 1964 by Hohenberg and Kohn and the theorem led to the formulation of Density Functional Theory (DFT) and the theorem was described in two parts.

2.2.1 The Hohenberg-Kohn Theorems

Theorem I: The ground state electron density $\rho(r)$ of an interacting system of particles uniquely determines the external potential $V_{\text{ext}}(r)$, except for an additive constant.

Proof: Considering that the opposite of the theorem was true, thereby for a given electron density $\rho(r)$, there can be two different external potentials $V_{\text{ext}}(r)$ and $V'_{\text{ext}}(r)$ which differ by more than an additive constant. For these two different external potentials, there will be two different Hamiltonians, \hat{H} and \hat{H}' for ground state wave functions Ψ and Ψ' with ground state energies E and E' respectively. On applying the variational principle, it gives us the following,

$$\begin{aligned} E &= \langle \Psi | \hat{H} | \Psi \rangle < \langle \Psi' | \hat{H} | \Psi' \rangle \\ E &< \langle \Psi' | \hat{H}' - V'_{\text{ext}}(r) + V_{\text{ext}}(r) | \Psi' \rangle \\ E &< E' + \int (V_{\text{ext}}(r) - V'_{\text{ext}}(r)) \rho(r) dr \end{aligned} \quad (2.13)$$

Similarly, $E' < \langle \Psi | \hat{H}' | \Psi \rangle$ will give

$$E' < E + \int (V'_{\text{ext}}(r) - V_{\text{ext}}(r)) \rho(r) dr \quad (2.14)$$

Upon combining Eqns 2.13 and 2.14, we get $E + E' < E' + E$, which is a contradiction. Thus, we can conclude that for a ground state electron density $\rho(r)$, there cannot be two different external potentials. This theorem establishes a one-to-one correspondence between the ground electronic ground state density and the external potential, $V_{\text{ext}}(r)$. The integral of the electron density $\rho(r)$ will give the total number electrons (N), i.e. $\int \rho(r) dr = N$.

Theorem II: A universal functional for the energy $E[\rho(r)]$ in terms of the density $\rho(r)$ can be defined for all electron systems, and the exact ground state is the global minimum of a given external potential $V_{\text{ext}}(r)$. Simultaneously, the exact ground state density is the electron density $\rho(r)$ that minimizes the functional $E[\rho(r)]$.

Proof: As the external potential is uniquely determined by the electron density, $\rho(r)$ and this also determines the ground state wavefunction, all other observables of the system like kinetic energy are uniquely determined. Therefore, for a given external potential $V_{\text{ext}}(r)$, the total energy can be written as a functional of electron density $\rho(r)$.

$$\begin{aligned} E[\rho(r)] &= T[\rho(r)] + V_{ee}[\rho(r)] + \int V_{ext}(r) \rho(r) dr \\ &= F_{HK}[\rho(r)] + \int V_{ext}(r) \rho(r) dr \end{aligned} \quad (2.15)$$

where, $F_{HK}[\rho(r)] = T[\rho(r)] + V_{ee}[\rho(r)]$ is known as the Hohenberg-Kohn functional and is a universal functional of $\rho(r)$ independent of the external potential.

In the ground state the energy is defined by the unique ground state density, $\rho(r)$

$$E[\rho(r)] = \langle \Psi | \hat{H} | \Psi \rangle \quad (2.16)$$

By the variational principle, a different density, $\rho'(r)$ will necessarily give a higher energy, $E[\rho'(r)]$

$$E[\rho(r)] = \langle \Psi | \hat{H} | \Psi \rangle < \langle \Psi' | \hat{H} | \Psi' \rangle = E[\rho'(r)] \quad (2.17)$$

It can be observed that minimizing the total energy with respect to $\rho(r)$ will give the the ground state energy and any other electron density $\rho'(r)$ energy will correspond to a higher energy state.

2.2.2 The Kohn-Sham Equations

The Hohenberg-Kohn theorems prove that the ground state properties can be calculated using the ground state energy density, however the theorems do not provide any computational techniques to calculate this $\rho(r)$ as the universal functional F_{HK} is unknown. The second seminal contribution to the development of DFT came in the year 1965 by Kohn and Sham with the development of Kohn-Sham formalism.¹¹ The concept of a non-interacting system built from a set of orbitals was introduced in such a way that the kinetic energy part of the universal F_{HK} functional could be solved with sufficient accuracy.

For a given system with N -interacting electrons, the Kohn-Sham invoked a non-interacting reference system with the Hamiltonian,

$$\hat{H} = \sum_{i=1}^N \left(-\frac{1}{2} \nabla_i^2 \right) + \sum_{i=1}^N V_s(r_i) \quad (2.18)$$

where $V_s(r_i)$ is the single electron potential which is unknown and there are no electron repulsion terms in the Hamiltonian, and the only constraint set is that this reference non-interacting system has the same ground state density as the interacting system of interest. Therefore, the ground state wave function Ψ_s can be represented as a Slater determinant of

single electron wavefunctions ψ_i 's for which the kinetic energy of this non-interacting system can be calculated as

$$\begin{aligned} T_s[\rho] &= \left\langle \Psi_s \left| \sum_{i=1}^N \left(-\frac{1}{2} \nabla_i^2 \right) \right| \Psi_s \right\rangle \\ &= \sum_{i=1}^N \left\langle \psi_i \left| -\frac{1}{2} \nabla^2 \right| \psi_i \right\rangle \end{aligned} \quad (2.19)$$

We must note that the kinetic energy functional of the original interacting system is not equal to $T_s[\rho]$. The total energy functional $E[\rho]$ as expressed by Kohn and Sham is,

$$E[\rho] = T[\rho] + J[\rho] + E_{xc}[\rho] + \int V_{ext}(r) \rho(r) dr \quad (2.20)$$

where $J[\rho] = \frac{1}{2} \int \int \frac{\rho(r_1)\rho(r_2)}{|r_1 - r_2|} dr_1 dr_2$ is the classical electron-electron repulsion energy,

$E_{xc} = T[\rho] - T_s[\rho] + V_{ee}$ is called the exchange-correlation energy which contains the difference between $T[\rho]$ and $T_s[\rho]$ and the non-classical electron-electron interaction (V_{ee}).

When comparing this with the non-interacting reference system, we have the expression,

$$\begin{aligned} V_s(r) &= V_{ext}(r) + \frac{\delta J[\rho]}{\delta \rho(r)} + \frac{\delta E_{xc}[\rho]}{\delta \rho(r)} \\ &= V_{ext}(r) + \int \frac{\rho(r_1)}{|r_1 - r_2|} dr_2 + V_{xc} \end{aligned} \quad (2.21)$$

where the exchange correlation potential V_{xc} is defined as $V_{xc} = \frac{\delta E_{xc}[\rho]}{\delta \rho(r)}$.

In this fashion, the problem of interacting N-electron system is mapped into a problem of N non-interacting electrons moving in an effective external potential of $V_{eff}(r) = V_s(r)$ with the Kohn-Sham formalism. This gives us a set of N single electron Schrodinger equations called Kohn-Sham equations with Kohn-Sham orbitals, ψ .

$$\left[-\frac{1}{2} \nabla_i^2 + V_{eff}(r) \right] \psi_i = \epsilon_i \psi_i \quad (2.22)$$

Eqn. 2.22 can now be written as

$$\hat{H}_{KS} |\psi_i\rangle = \epsilon_i |\psi_i\rangle \quad (2.23)$$

where $\hat{H}_{KS} = \left[-\frac{1}{2} \nabla_i^2 + V_{eff}(r) \right]$ is the Kohn-Sham Hamiltonian.

The ground state electron density $\rho(r)$ is then obtained from the summation of the single electron wave functions as follows.

$$\rho(r) = \sum_{i=1}^N |\langle \psi_i(r) \rangle|^2 \quad (2.24)$$

The solution to Eqn 2.22 can be obtained self consistently from Eqns. 2.21 and 2.24 upon knowing V_{eff} . Hence, within the Kohn-Sham formalism, the total energy can be determined from the resultant density as follows,

$$\begin{aligned} E[\rho] &= \sum_{i=1}^N \left\langle \Psi_i \left| -\frac{1}{2} \nabla^2 \right| \Psi_i \right\rangle + \frac{1}{2} \int \int \frac{\rho(r_1)\rho(r_2)}{|r_1 - r_2|} dr_1 dr_2 + E_{xc}[\rho] + \int V_{\text{ext}}(r) \rho(r) dr \\ &= \sum_{i=1}^N \epsilon_i - \frac{1}{2} \int \int \frac{\rho(r_1)\rho(r_2)}{|r_1 - r_2|} dr_1 dr_2 + E_{xc}[\rho] - \int V_{xc}(r) \rho(r) dr \end{aligned} \quad (2.25)$$

$$\text{where } \sum_{i=1}^N \epsilon_i = \sum_{i=1}^N \left\langle \Psi_i \left| -\frac{1}{2} \nabla_i^2 + V_{\text{eff}}(r) \right| \Psi_i \right\rangle$$

When the exact form of the exchange-correlation energy, E_{xc} are known, the exact ground state energy could be obtained from the Kohn-Sham equations. While the Kohn-Sham formalism is in principle exact, approximations are to be made to find an explicit form of the exchange-correlation functional which is described in the following section and is also the central goal of improving DFT calculations.

2.2.3 Exchange- correlation Functional

The difference in the kinetic and potential energies of the real interacting many-electron system and the reference system of non-interacting many-electron system in the Kohn-Sham Formalism is known as exchange and correlation energy, E_{xc} . The functional to calculate the exchange and correlation energy, E_{xc} is comprised of two sections:

Exchange energy: As per Pauli's exclusion principle, two electrons cannot have the same quantum numbers and on introducing spatial separation between the electrons of the same spin, there is a reduction in Coulomb energy as electrons with same spin repel each other. The energy difference between Hartree and the Hartree-Fock energy is the mathematical equivalent of Exchange energy,

$$E_{\text{exch}} = E_H - E_{\text{HF}} \quad (2.26)$$

Correlation energy: When the electrons are allowed to avoid each other completely, there is a further reduction in the Coulomb energy and this energy is equivalent to the energy difference between Hartree-Fock limit and exact non-relativistic energy, which can be written as

$$E_{corr} = E_{exact} - E_{HF} \quad (2.27)$$

Both the exchange and correlation component of the total-energy functional needs to be approximated to an accurate limit. The approaches to obtain an approximate exchange-correlation functional are: (1) local and semi-local approximation, i.e., local density approximation (LDA), generalized gradient approximation (GGA), meta-GGA and (2) non-local approximation such as hybrid functional (hyper-GGA), random phase approximation (RPA) etc. In this thesis, the local and semi-local local approaches of exchange-correlation functional are discussed.

2.2.3.1 Local-Density Approximation (LDA)

The local density approximation (LDA) for approximate exchange-correlation functionals is the general basis of all density functional theory-based approximations. The LDA model is based on the notion of a uniform electron gas where the electron moves in a positive background charge distribution, and the total charge distribution of the ensemble is neutralised. The exchange correlation energy at any given point for the particle remains the same in an ideal homogeneous electron gas with electron density $\rho(\mathbf{r})$, thereby the exchange-correlation approximation functional $E_{xc}[\rho(\mathbf{r})]$ can be split into two parts, the exchange $E_x^{LDA}[\rho(\mathbf{r})]$ and correlation $E_c^{LDA}[\rho(\mathbf{r})]$ contribution as,

$$E_{xc}^{LDA}[\rho(\mathbf{r})] = \int \rho(\mathbf{r}) \epsilon_{xc}^{hom} \rho(\mathbf{r}) d\mathbf{r} \quad (2.28)$$

$$= \int \rho(\mathbf{r}) \left[\left(\epsilon_x^{hom} \rho(\mathbf{r}) \right) + \left(\epsilon_c^{hom} \rho(\mathbf{r}) \right) \right] d\mathbf{r} \quad (2.29)$$

$$= E_x^{LDA}[\rho(\mathbf{r})] + E_c^{LDA}[\rho(\mathbf{r})] \quad (2.30)$$

The exchange part $E_x^{LDA}[\rho(\mathbf{r})]$ for an electron in a uniform electron gas system is given as,¹²

$$E_x^{LDA}[\rho(\mathbf{r})] = -\frac{3}{4} \left(\frac{3\rho(\mathbf{r})}{\pi} \right)^{\frac{3}{2}} \quad (2.31)$$

The correlation part $E_c^{LDA}[\rho(\mathbf{r})]$, on the other hand, does not have an analytical solution and is determined using quantum Monte-Carlo simulations.¹³ The LDA model based on homogenous electron gas works very well for metals, however it fails in the cases of atoms

and molecules and is insufficient to accurately describe most materials. Within the LDA approximation structural properties such as bond lengths, vibrational energies, phonon spectra can be predicted correctly.

2.2.3.2 Generalized-Gradient Approximation (GGA)

For real systems, the electron density is not homogenous and it varies in entire space, LDA formalism will not give an accurate description of the non-local electron density. An improvement to LDA approximation is made by including information about the varying change of density functional, $\rho(r)$ with the addition of gradient terms, $\nabla\rho(r)$ and the approach is called the generalized gradient approximation (GGA). GGA is a semi-local approximation method where the exchange correlation energy is a functional of the electron density and its gradient as,

$$E_{xc}^{GGA}[\rho(r)] = \int \rho(r) \epsilon_{xc}^{GGA}(\rho(r), |\nabla\rho(r)|) dr \quad (2.32)$$

GGA is found to be an improvement over LDA in predicting the properties of the materials where the electron density varies gradually and slowly. The gradient corrected density approach to calculate the exchange-correlation energy has proved successful for semiconducting systems to get the cohesive energy, dielectric function, bandgap and elastic constants within 3% accuracy to the experimental data. The most prominently used GGA functionals are Perdew-Wang (PW91), Perdew-Burke-Ernzerhof (PBE) and Lee-Yang-Parr (LYP). In this thesis and most of our work the Perdew-Burke-Ernzerhof (PBE) approach of generalized gradient approximation has been used.¹⁴

2.2.4 Kohn-Sham Orbitals

The Schrodinger equation solved with the Kohn-Sham formalism required the existed of single electron wave functions called Kohn-Sham orbitals, ψ . The concept of Kohn-Sham orbitals, although they are auxiliary entities that do not have any physical significance, in DFT has been introduced to calculate the total energy and charge density. These orbitals are an approximate representation of the electron density and are defined as a linear combination of basis functions, such that

$$|\psi_i\rangle = \sum_{\mu} c_{\mu i} |\mu\rangle, \quad (2.33)$$

where $c_{\mu i}$ are the expansion coefficients and this linear combination of basis functions are known as basis sets. The basis sets can be largely distinguished into the localized basis sets and plane-wave basis sets. The localized basis sets include the Slater type orbitals (STO) and Gaussian type orbitals (GTO) to represent the orbitals of electrons making up atoms and molecules. The plane-wave basis sets, on the other hand, are used to represent the electrons of three-dimensional materials in periodic boundary conditions.

Slater-type-orbitals (STO): The STO basis functions are optimal for describing the wave functions of atomic and diatomic systems. One feature of the STOs is their exponential nature with a cusp in short range and gradual decay at long range, thereby they look similar to the wavefunctions of hydrogen-like atom. The typical representation of STO is,¹⁵

$$\eta^{STO} = N r^{n-1} \exp[-\beta r] Y_{lm}(\theta, \varphi) \quad (2.34)$$

where, η is the principal quantum number with the orbital exponent denoted by β and the spherical harmonics Y_{lm} . However, it is difficult to solve the many electron-systems and their integrals; therefore, the use of STO basis sets is mostly discouraged.

Gaussian-type-orbitals (GTO): GTO basis sets are represented with a gaussian functional and is the usual choice of basis functions in describing atoms, molecules and materials in computational chemistry. The Gaussian type electron orbitals for atomic and molecular structures are expressed as,¹⁶

$$\eta^{GTO} = N x^l y^m z^n \exp[-\alpha r^2] \quad (2.35)$$

where, η is the principal quantum number, N is normalization factor ensuring $\langle \eta_{\mu} | \eta_{\mu} \rangle = 1$, and α is the orbital exponent. The secondary quantum number, L which is the sum of l , m and n is used to classify the GTO functions as s , p , d or f -functions. The GTO functions decay rapidly at long range of r and it does not show a cusp around the nuclei. To predict and calculate the electronic and molecular properties of many-electron systems, a large number of basis functions are needed.

Plane-wave-basis (PWB): The plane wave basis sets are mostly used for periodic solids, and the Kohn-Sham orbitals for periodic solids are Bloch states. Using Fourier analysis and Bloch theorem, the Kohn-Sham eigenfunction with wave vector k is expressed as,¹⁷

$$\Psi_k(r) = e^{ik \cdot r} u_k(r) \quad (2.36)$$

where $u_k(r)$ is the periodic function which can be expressed as a Fourier series,

$$u_k(r) = \frac{1}{\sqrt{\Omega}} \sum_G c_k(G) e^{iG \cdot r} \quad (2.37)$$

where G is the reciprocal lattice vector, known as plane waves, for a unit cell of volume Ω , $c_k(G)$ and $e^{iG \cdot r}$ is the expansion coefficient and exponent phase G , respectively. Thereby, the Kohn-Sham eigenfunction, $\Psi_k(r)$ can be expressed with the Fourier series representing the plane -wave basis set as,

$$\Psi_k(r) = \frac{1}{\sqrt{\Omega}} \sum_G c_k(G) e^{i(k+G) \cdot r} \quad (2.38)$$

An exact solution to the Kohn-Sham equations in principle requires an infinite number of plane waves, G and as the contribution from the Fourier coefficients decreases for increasing $|k+G|$. Thereby, the plane wave basis sets need to be truncated at some finite value of $|k+G|$, which can be set as the kinetic energy cutoff.

In most of the materials, only the valence electrons are prominently involved in the orbital interactions and the pseudopotential concept has been used to represent the electronic interactions between valence electrons with an effective ionic core. As the ionic core is usually frozen, the pseudopotential wavefunctions are built as orthogonal and complete functions of valence electrons.

2.3.1 *Ab initio* Molecular Dynamics (AIMD)

One of the fundamental properties of many-body system is the dynamics or the physical movement of the atoms constituting the system. In classical approach, the molecular dynamics of the system is determined by solving Newton's second law of motions for the atoms or molecules and their trajectories, forces and potential energies are

deduced. For quantum particles that can be represented in terms of the nuclear and electron coordinates, when the Born-Oppenheimer approximation is invoked, the nuclear position is fixed for an instantaneous position of the atom. The time-independent Schrödinger equation can then be solved for the many-body wave function of the electrons. When this Schrödinger equation is assigned into the time-dependent equation, the energy of the system for that instant of time can be solved. This energy is now a function of time and nuclear coordinates and it can be used as the interatomic potential needed to compute the forces in Newton's equation of motion. After gradients of this energy are calculated for this fixed position to all nuclear coordinates and the forces are calculated, the nuclei are moved to get to the next time step accordingly. This process is repeated with new nuclear coordinates for the desired time scale, usually a few picoseconds. To surmise, ab-initio Molecular Dynamics (AIMD) involves solving Newton's equation of motion with the interatomic forces or potential calculated instantaneously from Density Functional Theory,

The integration of equations of motion to DFT has been used to explain the progression of the system with time. The equations of motion are as follows,¹⁸⁻¹⁹

$$F_i = m_i a_i = m_i \ddot{r}_i, i = 1, 2, \dots N \quad (2.39)$$

$$F_i(r_1, r_2, \dots r_N) = -\nabla_i V(r_1, r_2, \dots r_N) \quad (2.40)$$

where, F_i is the force acting on the i^{th} particle; m_i , r_i , a_i are the mass, position and acceleration of particle I and N is the total number of particles in the system. Following the first law of motion, the total energy of the system is conserved,

$$E = \sum_{i=1}^N \frac{m_i \dot{r}_i^2}{2} + V(r_1, r_2, \dots r_N) \quad (2.41)$$

where the first and second components of E are the kinetic energy and potential energy terms. For a quantum system, the total energy E is also equal to the Hamiltonian, thereby $\hat{H} = \sum_{i=1}^N \frac{m_i \dot{r}_i^2}{2} + V(r_1, r_2, \dots r_N)$. Using the Hamiltonian, the equations of motions are solved analytically using an integrating method, the most common one being Velocity-Verlet algorithm. Following this algorithm, the positions of the particles are updated after

every Δt step, the velocities of the particles are updated after every $(\Delta t + \Delta t/2)$ step and the acceleration and velocity are calculated in the $(t + \Delta t)$ step.

$$r_i(t + \Delta t) = r_i(t) + \dot{r}_i(t)\Delta t + \frac{1}{2} a_i(t)\Delta t^2 \quad (2.42)$$

$$\dot{r}_i(t + \Delta t/2) = \dot{r}_i(t) + \frac{1}{2} a_i(t)\Delta t \quad (2.43)$$

$$a_i(t + \Delta t) = -\frac{1}{m_i} \nabla U(r_i(t + \Delta t)) \quad (2.44)$$

$$\dot{r}_i(t + \Delta t) = \dot{r}_i(t + \Delta t/2) + \frac{1}{2} a_i(t + \Delta t)\Delta t \quad (2.45)$$

2.3.2 van der Waals Corrections

As the size of the system increases, other than the described electron-electron interactions, there are long range dispersion interactions which cannot be accounted with the LDA and GGA exchange-correlation functionals of DFT. A dynamical correlation between the fluctuating charge distributions needs to be accounted for long range forces and one of the dispersion corrected DFT approaches has been proposed by Grimme, popularly known as DFT-D2 or D3 method. In this approach, the total electronic energy is written as,

$$E_{tot} = E_{KS-DFT} + E_{disp} = E_{vdW} \quad (2.46)$$

where, E_{KS-DFT} is the self-consistent Kohn-Sham DFT energy in Eqn. 2.25 and E_{disp} is the empirical dispersion correction.²⁰

$$E_{disp} = -\frac{S_6}{2} \sum_i^{N_{atom}} \sum_{j=i+1}^{N_{atom}} \frac{C_{ij}^6}{R_{ij}^6} f_{damp}(R_{ij}, R_{ij}^0) \quad (2.47)$$

$$\text{and, } f_{damp} = \frac{1}{1 + \exp\left(-d\left(\frac{R_{ij}}{R_{ij}^0 - 1}\right)\right)} \quad (2.48)$$

here S_6 is the global scaling factor optimized for different functionals; C_{ij}^6 , R_{ij} , R_{ij}^0 are the dispersion coefficient, interatomic distances and cutoff distance which is equivalent to sum of vdW radii for the atom pair ij respectively; f_{damp} is the damping function to

determine the range of dispersion interaction and it is defined in such a way that the dispersion contribution is minimized within default van der Waals distances.

2.3.3 Implicit Solvation Model

Most of the chemical processes in nature occur in the presence of a solvent and the electronic energy is susceptible to the nature of the solvent surrounding the many-electron system. The solvent model is necessary to present a realistic description of such chemical process, in particular, electrochemical processes. To treat each solvent molecule and represent their influence to the solute or our system of interest is quite expensive as all electronic and ionic degrees of freedom of the solute-solvent complex need to be relaxed. The alternative is to represent the solvent as a bath of continuum dielectric material and the influence of the solvent is implicit. Depending on the nature of the solvent, the solvation effects can vary; for polar solvents the electronic interaction between the solute and the solvent will make a significant contribution to the solvation and electronic energy. The opposite is seen in non-polar solvents where the van der Waals interaction dominates the electronic forces. There is also a possibility of solvent cavity formation around the system. Therefore, the dielectric response of the solvent is represented as a functional of the solute electronic charge density, dispersion effect and cavitation.

The theoretical framework for implicit solvation model in DFT is to represent the solvent as a perturbation to the solute Hamiltonian as an external potential,

$$\hat{H}_{tot}(r) = \hat{H}_{solute}(r) + \hat{V}_{solute+solvent}(r) \quad (2.49)$$

The external potential term, $\hat{V}_{solute+solvent}(r)$ is composed of the interaction operators that include the electrostatic, dispersion, cavitation and repulsion. A mathematical approach to implement the implicit solvent model is representing the solute/solvent functional as electron density of the solute and external potential of the solute and then calculating and minimizing the free energy of the same solute/solvent complex. The free energy of the solute/solvent system can be described as,²¹

$$A = F[n_{tot}(r), N_i(r)] + \int d^3r V_{ext}(r) (\sum_i (Z_i N_i(r) - n(r))) \quad (2.50)$$

where, $n_{tot}(r)$ is the total electron density and is equal to $n_{solute}(r) + n_{solvent}(r)$, F is the universal functional that represents the total electronic charge density $n_{tot}(r)$ and $N_i(r)$ is thermodynamically averaged atomic densities of the chemical species i in the solvent, $V_{ext}(r)$ is the external potential due to solute nuclei.

Using the variational principle, the minimum ground state free energy of the combined solute-solvent system in a fixed external potential $V_{ext}(r)$ can be solved as,

$$A_0 = \min_{n_{tot}, N_i(r)} \left\{ F[n_{tot}(r), N_i(r)] + \int d^3r V_{ext}(r) (\sum_i (Z_i N_i(r) - n(r))) \right\} \quad (2.51)$$

When minimized over $n_{solvent}$ the free energy in Eqn 2.50 becomes,

$$\tilde{A} = G[n_{solute}(r), N_i(r), V_{ext}(r)] - \int d^3r V_{ext}(r) n_{solute}(r) \quad (2.52)$$

$$\text{where, } G[n_{solute}(r), N_i(r), V_{ext}(r)] = \min_{n_{solvent}} \left\{ F[n_{tot}(r), N_i(r)] + \int d^3r V_{ext}(r) (\sum_i (Z_i N_i(r) - n_{solvent}(r))) \right\} \quad (2.53)$$

and G is the universal functional of $n_{solute}(r)$, $N_i(r)$ and $V_{ext}(r)$, and the universal functional can be separated into the DFT Kohn-Sham functional, A_{KS} and a dielectric response term, A_{diel} of the solute that include all solvent-solute interaction and internal energy of solvent as,

$$G[n_{solute}(r), N_i(r), V_{ext}(r)] = A_{KS}[n_{solute}(r), N_i(r), V_{ext}(r)] + A_{diel}[n_{solute}(r), N_i(r), V_{ext}(r)] \quad (2.54)$$

The dielectric functional, A_{diel} can be minimized with respect to the average atomic densities $N_i(r)$ in the solvent,

$$\tilde{A}_{diel}[n_{solute}(r), V_{ext}(r)] = \min_{N_i(r)} A_{diel}[n_{solute}(r), N_i(r), V_{ext}(r)] \quad (2.55)$$

Introducing the terms from Eqns 2.52 -2.55 in Eqn 2.44, the ground state free energy of the composite solute/solvent system can be written as,

$$A_0 = \min_{n_{solute}(r)} \left\{ A_{KS}[n_{solute}(r), V_{ext}(r)] + \int d^3r V_{ext}(r) n_{solute}(r) \right\} + \tilde{A}_{diel}[n_{solute}(r), V_{ext}(r)] \quad (2.56)$$

This minimization procedure in terms of the solute electron density function, $n_{solute}(r)$ and external potential of the solute nuclei $V_{ext}(r)$ yields the free energy of solute/solvent system. The solvent effect is represented in a continuum model to \tilde{A}_{diel} , a functional minimized in terms of solvent electron density and thermodynamically averaged densities of the solvent.

2.3.4 Atomic charge analysis

As all materials are made up of nuclei and electrons, with the electron density determining most of the crucial properties of the material. Furthermore, all processes in nature are inherently driven by electron/charge transfer from one state of form to another and it is important to materialise the charge density distribution of a system over space. This has been represented as a measurable parameter in term so of the atomic charges calculated via population analysis. Some of the commonly known protocols to calculate atomic charges are Mulliken, Löwdin, Hirshfield and Bader charges. The following section will describe the theoretical framework to calculate Löwdin and Bader charge analysis that has been used in this thesis.

Löwdin charge analysis:

For a system with N electrons and the electrons are represented by atomic orbital basis sets, the number of electrons N can be written as the trace of the product PS,

$$N = \sum_{\mu} (PS)_{\mu} = Tr PS \quad (2.57)$$

where, P is the density matrix, S is the atomic orbitals overlap matrix which is the sum over all basis functions. Considering the electron population on an atom, A as the non-intersecting subsets of all the basis sets on that atom we can denote the electron population $\mu \in A$ and the Löwdin charge can be defined as,²²

$$q_A^{Löwdin} = Z_A - \sum_{\mu \in A} (\mathbf{S}^{-1} \mathbf{P} \mathbf{S}^{-1})_{\mu\mu} \quad (2.58)$$

where Z_A is the nuclear charge of atom A. This derivation of Löwdin charge is obtained upon modification of the Mulliken charge equation which is,

$$q_A^{Mulliken} = Z_A - \sum_{\mu \in A} (PS)_{\mu\mu} \quad (2.59)$$

Bader charge analysis:

The Bader charge analysis method defines an atom purely on the electronic charge density and a zero-flux surface has been used to divide different atoms comprising a system. A zero-flux surface is a two-dimensional surface on which the charge density is minimum for a point perpendicular to the surface. This holds true as in molecular systems, the electron charge density is a minimum between atoms and can be used to separate atoms from each other. For the system with electronic charge density $\rho(\mathbf{r})$, critical points (CP) such as maxima, minima or saddle points are generated for every point r_s on the system such that the zero-flux surfaces are obtained by,²³

$$\nabla\rho(r_s) \cdot n(r_s) = 0 \quad (2.60)$$

where $n(r_s)$ is the unit vector normal to the surface at r_s , and at the critical points the gradient of $\rho(\mathbf{r})$ vanish, i.e., $\nabla\rho(r_{CP}) = 0$ and the Hessian matrix of $\rho(\mathbf{r})$ at the critical points when diagonalized give the eigenvalues and eigenvectors that will correspond to the principal curvatures of $\rho(\mathbf{r})$ at r_{CP} and the respective axes. There are four possible signatures of the CP's and they are labelled by (ω, σ) where ω is the number of all non-zero curvatures and σ is the sum of the signs of the curvatures.

(3, -3) or the Nuclear Attractor CP when all three curvatures are negative, and therefore $\rho(\mathbf{r})$ is a local maximum at r_{CP} .

(3, -1) or the Bond Critical Point (BCP) where two curvatures are negative and $\rho(\mathbf{r})$ is a local maximum at r_{CP} in the plane obtained by the two axes associated with these two curvatures. The third curvature which is positive for minimum $\rho(\mathbf{r})$ at r_{CP} along the axis perpendicular to the plane formed by the former two axes.

(3, +1) or Ring Critical Point (RCP) when two curvatures are positive and $\rho(\mathbf{r})$ is a local minimum at r_{CP} in the plane obtained by the two axes associated with these two curvatures. The third curvature is negative with maximum $\rho(\mathbf{r})$ at r_{CP} along the axis perpendicular to the plane formed by the former two axes.

(3, +3) or Cage Critical Point (CCP) when all three curvatures are positive, indicating the local minima of $\rho(\mathbf{r})$.

2.4.1 Vienna *ab-initio* simulation package

Vienna Ab-initio Simulation Package (VASP)²⁴ is one of the software used to carry out the computational calculation in this thesis. VASP has been developed at the university of Vienna by Hafner' group to calculate electronic structure studies with density functional theory. The Kohn-Sham equations are solved by using a plane-wave basis set implemented within this code with the interaction of the ions and electrons defined by a projector-augmented wave (PAW) pseudopotential method. The total electronic energy is calculated by optimizing the wave functions via iterative matrix diagonalization schemes and the convergence in total energy is controlled the kinetic energy cut off and k-mesh sampling. Several electronic smearing methods, e.g., Fermi, Gaussian, and tetrahedron smearing are used to describe the partial occupancies for faster convergence of energy. To run a VASP calculation, four input files INCAR, POSCAR, POTCAR, and KPOINTS are needed. The INCAR file contains the input tags and parameters to calculate the desired properties of a material. The POSCAR file contains the coordinates of the elements constituting the materials in real space lattice and the POTCAR file contain the individual pseudopotential file of the elements and this file will describe the valence and core electron information. The KPOINTS file contains the reciprocal lattice or wave vector coordinates in a weighted k-mesh form. Upon optimization of the geometry of the material, the optimized lattice coordinates are stored in the CONTCAR file and the minimized total energy, Hellmann-Feynman forces on individual atomic species are printed in the OUTCAR file. The desired electronic properties of the material can be extracted from the WAVECAR and CHGCAR files that contain the wave function of the Kohn-Sham equation and ground state charge density of a material, respectively. VASP is one of the most popular computational software for periodic systems and materials. It can carry out surface system optimization and molecular dynamics simulation; and details of structure parameters, electronic structures properties, optical properties, magnetic properties, mechanical and lattice dynamic properties of different materials can be easily extracted.

2.4.2 deMon2K software

deMon2k²⁵ is developed at the Université de Montréal as deMon program which stands for “density of Montréal” for density functional theory (DFT) calculations of atoms, molecules, and clusters. The software defines electron wave functions as a linear combination of Gaussian type orbital (LCGTO) with the help of auxiliary functions to improve the efficiency of solving the electron-electron interaction terms which include the Coulomb potential and exchange-correlation potential. To achieve a good self-consistent field (SCF) convergence of the electronic energy, adaptive grid techniques have been implemented to integrate the exchange-correlation and developed as auxiliary density functional theory (ADFT) that enables calculations of large systems with modest computational resources. ADFT is now accepted as an efficient and stable alternative to solve the conventional Kohn-Sham DFT equations. Other than standard DFT optimization protocol to calculate electronic energy and structural properties, the software also contains internal modules for time-dependent density functional theory (TD-DFT), Born-Oppenheimer molecular dynamics (BOMD), hybrid DFT and quantum mechanical-molecular mechanical (QM/MM) calculations. To carry out DFT calculations with deMon2k software, only a ‘deMon.inp’ file is needed, this file contains all essential tags and parameters to calculate the desired properties followed by a GEOMETRY block that contains the coordinates of the atoms in the system. All output information is printed in the ‘deMon.out’ file and the electron density information can be extracted from the ‘deMon.mol’ file. A table highlighting the differences in VASP and deMon2k packages has been drawn out in **Table 2.1**.

Table 2.1: Table showing the differences between VASP and deMon2k packages.

	VASP	deMon2k
Chemical model	Atomic clusters, periodic 2D and 3D systems	Atoms, molecules and clusters

Wave functions or orbitals	Plane wave basis set	Localized basis sets (linear combination of atomic orbitals)
Handling of atomic orbitals	Valence orbital only	Implicit and explicit orbitals
Electronic ground state calculation	Projector Augmented Wave method	Auxiliary Function Density method
Maximum number of atoms/ions	256	1000
Licensing	License fee dependent on license type and number of users.	Free academic license

2.5 References

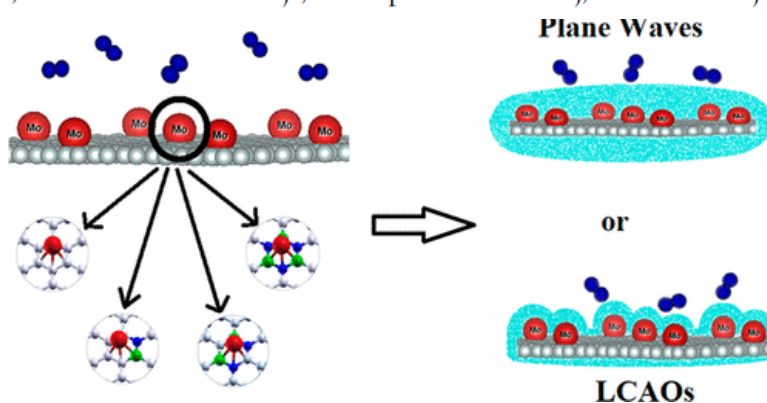
- (1) Schrödinger, E. *Phys. Rev.* **1926**, 28, 1049–1070.
- (2) Born, M.; Oppenheimer, J. R. *Annalen der Physik* **1927**, 389, 457–484.
- (3) Hartree, D. R. *Proc. Cambridge Phil. Soc.* **1927**, 84, 457.
- (4) Fock, V. A. *Z. Phys.* **1930**, 61, 126.
- (5) Slater, J. C. *Phys. Rev.* **1929**, 34, 1293.
- (6) Dawydow, A. S. (1978) *Quantenmechanik*, Deutscher Verlag der Wissenschaften, Berlin.
- (7) Levine, I. N. *Quantum Chemistry (4th ed.)*, Englewood Cliffs, New Jersey, **1991**.
- (8) Dreizler, R. M.; Gross, E. K. V. *Density Functional Theory*, Springer, Berlin, **1990**.
- (9) Ziegler, T. *Chem. Rev.* **1991**, 91, 651.
- (10) Hohenberg, P.; Kohn, W. *Phys. Rev.* **1964**, 136, 864.

- (11) Kohn, W.; Sham, L. J. *Phys. Rev.* **1965**, *140*, A1133–A1138.
- (12) Ashcroft, N. W.; Mermin, N. D.; *Solid state physics*, Thomson Learning: Toronto, 1976.
- (13) Ceperley, D. M.; Alder, B. *Phys. Rev. Lett.* **1980**, *45*, 566.
- (14) Perdew, J. P.; Burke, K.; Ernzerhof, M. *Phys. Rev. Lett.* **1996**, *77*, 3865.
- (15) Slater, J. C. *Physical Review*. **1930**, *36*, 57.
- (16) Szabo, A.; Ostlund, N. *Modern Quantum Chemistry*, Dover, New York, 1989.
- (17) Blochl, P. E. *Phys. Rev. B: Condens. Matter Mater. Phys.* **1994**, *50*, 17953–17979.
- (18) Alder, B.J.; Wainwright, T.E. *Journal of Chemical Physics*, **1959**, *31*, 459-466.
- (19) Marx, D.; Hutter, J. *Ab Initio Molecular Dynamics: Theory and Implementation* published in *Modern Methods and Algorithms of Quantum Chemistry*, J. Grotendorst, NIC series 3, **2000**.
- (20) Grimme, S.; Ehrlich, S.; Goerigk, L. *J. Comput. Chem.*, **2011**, *32*, 1456-1465.
- (21) Mathew, K.; Sundararaman, R.; Letchworth-Weaver, K.; Arias, T. A.; Hennig, R. G.; *J. Chem. Phys.* **2014**, *140*, 084106.
- (22) Löwdin, P.O. *J. Chem. Phys.* **1950**, *18*, 365.
- (23) Bader, R. F. W. *Atoms in Molecules - A quantum theory*, Oxford University Press, New York, **1990**.
- (24) Kresse, G.; Furthmüller, J. *Comput. Mater. Sci.* **1996**, *6*, 15–50.
- (25) Koster, A. M.; Calaminici, P.; Casida, M. E.; Moreno, R. F.; Geudtner, G.; Goursot, A.; Heine, T.; Ipatov, A.; Janetzko, F.; del Campo, J. M.; et al. deMon 5.0; deMon Developers, **2006**.

Chapter 3

Dinitrogen Activation on Graphene Anchored Single Atom Catalysts: Local Site Activity or Surface Phenomena

Ashakiran Maibam,^{†,§} Thillai Govindaraja,[‡] Kaliaperumal Selvaraj,^{‡,§} and Sailaja Krishnamurthy^{*,†,§}



Maibam, A. et. al, *J. Phys. Chem. C*, 2019, 123, 27492–27500.

This chapter explores the nature of catalysis on two-dimensional (2D) materials anchored with a single atom catalyst (SAC). When single atom catalysts (SACs) are anchored on such materials with delocalized electron density, for instance graphene, the stimulant for catalysis may be either the *d*-electrons on the metal or the system altogether. To understand the contributing factors of catalysis on such systems, a case study of dinitrogen (N₂) activation on Mo anchored graphene has been made by employing periodic and finite models of graphene. Besides the physical aspects, such as size/finiteness of graphene, the influence of varying B and N dopant concentrations in graphene on the activity is evaluated. N₂ activation is highlighted through an analysis of red shift in the N–N stretching frequency, charge transfer to N₂ from the catalytic system, and electronic characteristics of the catalytic system. The projected density of states plots, and frontier molecular orbital analysis depict a strong chemisorption of N₂ with the metal–graphene supports on account of direct hybridization between the *d* orbitals of the supported metal atom and the *p*-orbitals of N₂. The Bader and Löwdin charge distribution on the adsorbed dinitrogen in periodic and finite models shows the preeminence of local site over the surface activity.

3.1 Introduction

N_2 fixation and activation is essential for the sustenance of life. Although N_2 is the most abundant constituent in air, its fixation and activation is a highly endothermic process on account of its triple bond, thus making it a nearly inert gas. Up to this date, the most efficient chemical reduction of N_2 is through the well-known Haber-Bosch process which involves chemical transformation of N_2 to NH_3 using an iron oxide, Fe_3O_4 , catalyst in the presence of hydrogen under extremely harsh conditions of about 400 °C and 200 atm.¹ On the other hand, naturally occurring nitrogenase enzyme secreted by prokaryotic organisms found in the root nodules of plants complete this task under mild conditions without utilizing gaseous hydrogen.²⁻⁴ Research has shown that biological N_2 fixation occurs under ambient conditions and that the active sites are rich in Fe and S and, additionally, contain Mo or V atoms.^{5,6} However, the detailed mechanism of N_2 reduction by these enzymes remains elusive.⁶ As a consequence, finding an ambient catalyst for the N_2 reduction is a challenge for the organometallic chemists. Intuitively, N_2 fixation and its dissociation require an efficient catalytic center coupled to an electron reservoir.

Metal clusters in the nano regime offer promise in this context on account of their quantum confinement of electrons. Few research works have explored the potential of simple inorganic metal clusters for N_2 activation using experimental and theoretical approaches.⁷⁻¹¹ Notable among them is a work by Fielicke and co-workers,⁷ where N_2 activation on neutral Ru clusters is evaluated using infrared-multiphoton dissociation (IR-MPD). Other transition metal catalysts have also been reported, Ohki et al. in an experimental work showed Mo-Ti-S cluster elongates the N-N bond up to 1.294 Å, and the active site for the catalyst is titanium (Ti).⁸ In another work, Roy et al.⁹ have demonstrated dinitrogen activation on solid Li_n ($2 < n < 8$) clusters, with the N-N bond stretching frequency red-shifted up to 810 cm^{-1} . The work also demonstrated that even a small metal cluster, such as Li^8 , has the potential to split the N-N bond completely in an exothermic process. Among the metal clusters, Al clusters are the most notable ones that have been studied for N_2 activation. Jarrold and co-workers,¹⁰ using concerted experimental and theoretical methods, reported for the first time that Al clusters with 44

and 100 atoms lower the activation energy of the N_2 molecule by nearly 1 eV at high temperatures. In another work, the same group has demonstrated that the structure and size of the cluster have implications on the N_2 activation potential.¹¹ Studies on the reaction trajectories have demonstrated that high energy conformations of the Al clusters show a lower activation barrier toward dinitrogen.¹² However, the potential of the high energy conformations to be present at ambient conditions is relatively low. Thus, doping a ground state cluster is a more practical design of catalyst for N_2 activation. Along these lines, theoretical studies have shown that silicon- and phosphorus-doped aluminum clusters demonstrate increased activation as compared to their pristine ground-state counterparts.¹³

With the growing cost of the metals, exploring alternative catalysts such as metal-free or single-atom catalysts (SACs) is the need of the hour. Metal-free catalysts include frustrated Lewis pairs¹⁴ that form iminium complexes upon reaction with N_2 , polymeric carbon nitride electrocatalyst,¹⁵ and edges of 2D boron nitride (BN)¹⁶ surfaces. SACs anchored on suitable supports, on the other hand, considerably bring down the usage of metals by making each site available for the reaction while not compromising with the activity. In this context, there are several 2D materials that can be exploited as electron reservoirs when embedded with metal active centers. A well-crafted 2D material support with an active metal center has an enormous potential to adsorb the N_2 molecule and activate it. 2D material supports reported so far with a high N_2 fixation potential include graphene, Mo-doped BN nanosheet materials, BiOBr nanosheets, and boron anti-sites on BN nanotubes.^{17–20} Among them, graphene is an attractive one and has always been tapped as a support in reactions such as water splitting,²¹ hydrogen evolution reaction,²² and so on. Experimentally, few research groups have applied graphene based materials as catalysts toward N_2 fixation.^{23,24}

In comparison to the experimental explorations, there are more theoretical works toward exploring the potential of graphene-based nanomaterials as catalysts/support materials for N_2 fixation. Using Density Functional Theory (DFT)-based methodologies, Le and co-workers demonstrated that doping graphene with Mo/N can lead to the

successful dissociation of the N_2 molecule.²⁵ In another work, Li and co-workers reported an activation of the N_2 molecule up to nearly 2.5 Å on FeN_3 -embedded graphene, wherein nitrogen atoms act as anchors, while iron is the active center.²⁶ Kumar et al. more recently have demonstrated the catalytic role of the BN-doped graphene substrate for N_2 activation on aluminum clusters.²⁷

Another interesting property of graphene is a higher reactivity when scissored to smaller sizes of the order of tens of nanometers (90 nm).^{28,29} On scissoring, the electronic as well as magnetic properties are seen to differ with respect to size and edge effect.^{30,31} Depending on the orientation of the edges, graphene nanoflakes can have two types of edges, namely, armchair and zigzag. A DFT study carried out by Nazrulla et al. on different graphene nanoflake sizes reported that, given a spin state and nanoflake size, the armchair isomer is more reactive than the zigzag isomer.³² An intensive study carried out by Yu et al. on graphene sheets to explore the reactive carbon edge responsible for oxygen reduction reaction (ORR) predicted the armchair edge to more active than the zigzag edge.³³ Another work by Owens showed a gradual decrease in the band gap with the increase in chain length of both armchair and zigzag graphene isomers.³⁴ Inherently, the zigzag isomers demonstrated a higher gap between HOMO (highest occupied molecular orbital) and LUMO (lowest unoccupied molecular orbital) in the case of nanoflakes with odd electrons with respect to the ones with an even number of electrons. In short, the band gap and, henceforth, reactivity would change upon tweaking the edge orientation, chain length, and number of electrons in these graphene nanoflakes. Further changes in the reactivity can be brought about by introducing defect sites and dopant atoms such as boron, nitrogen, sulfur, silicon, and so on.

In this chapter, the activity of a SAC, namely, Mo, anchored on pristine and doped (boron and nitrogen) graphene sheets as well as model nanoflakes toward dinitrogen. Graphene sheets are periodic models defined using plane wave basis sets to incorporate the periodic nature. The use of plane wave (PW) basis sets offers a set of advantages, such as quicker convergence and avoiding basis set superposition error (BSSE); however, it comes with an approximation of treating core electrons implicitly. The plane wave basis

sets also incorporate the concept of pseudopotentials toward the description of the atomic orbitals. The query is whether the periodic model that represents a delocalized electron density on the metal-anchored systems gives the correct picture of catalytic activity of the single (metals) atom catalyst. On the other hand, graphene nanoflakes are represented by finite models of 42 and 54 carbon atoms, are defined using linear combination of atomic orbitals (LCAOs). These nanoflakes can be synthesized by cutting” extended sheets of graphene using lithography³⁵ and chemical etching³⁶ techniques. Two different edge orientations are possible in finite models, namely, zigzag and armchair. In the finite model, factors such as (a) edge effects, (b) size, and (c) dopant atoms (B and N) are taken into account; while in the periodic models, only the influence of boron and nitrogen dopants are considered as edge and size effects are irrelevant in the context of a periodic system (see **Figure 3.1**). The choice of B and N as dopant atoms stems from the fact that although several dopants in graphene have been reported and explored, boron and nitrogen remain the most attractive as they have similar atomic radii to carbon. Also, a B–N unit is isoelectronic to C–C unit and the planarity is conserved, leaving the delocalized electron cloud intact. Apart from that, methods to dope boron and nitrogen are diverse, ranging from solid phase³⁷ and chemical vapor deposition^{37,38} synthesis to plasma doping,³⁹ and are synthetically cost-effective.

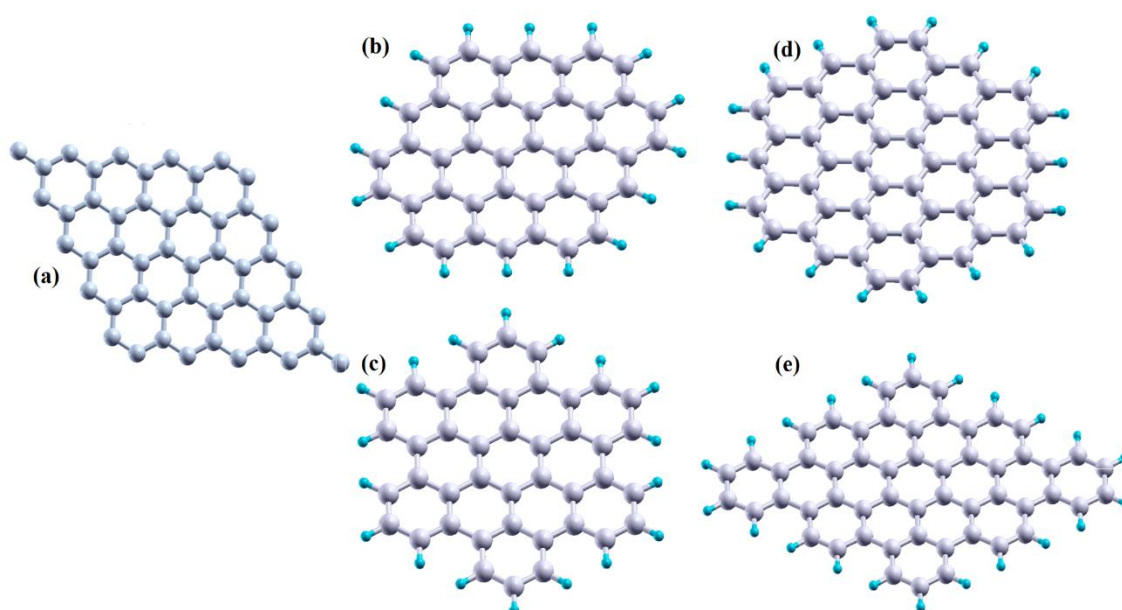


Figure 3.1. Graphene models considered in this study as supports to SAC: (a) A periodic graphene sheet with 50 atoms in a cell; (b) 42 atom graphene nanoflake with zigzag edges (C_{42} -zz); (c) 42 atom graphene nanoflake with armchair edges (C_{42} -ac); (d) 54 atom graphene nanoflake with zigzag edges (C_{54} -zz); (e) 54 atom graphene nanoflake with armchair edges (C_{54} -ac). Elemental color codes: grey, carbon (C); teal, hydrogen (H).

3.2 Computational Details

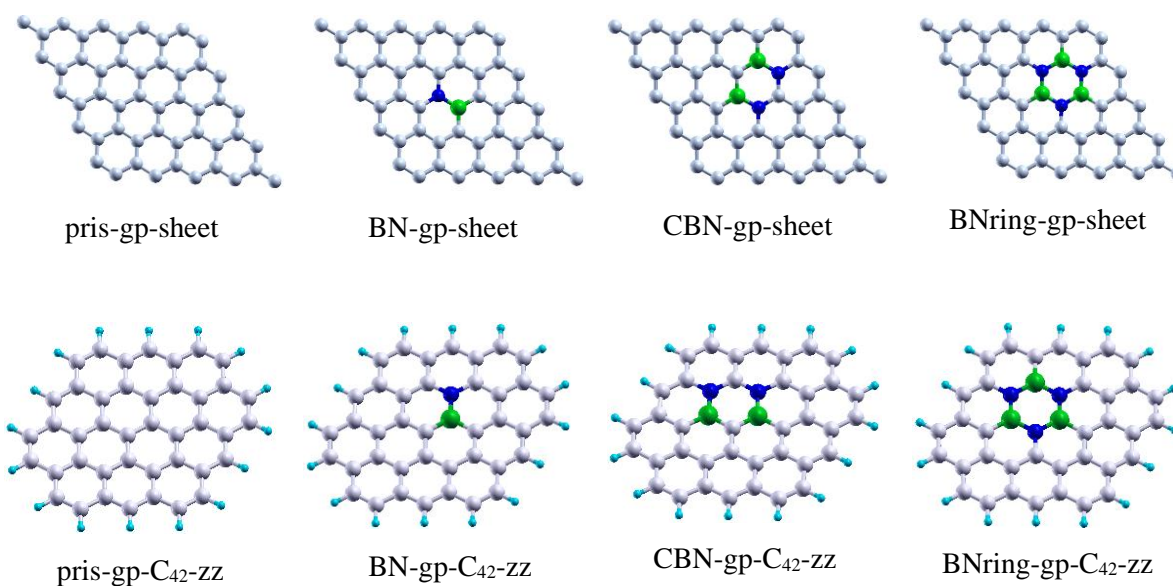
3.2.1 Nomenclature of the SACs Anchored Graphene Models

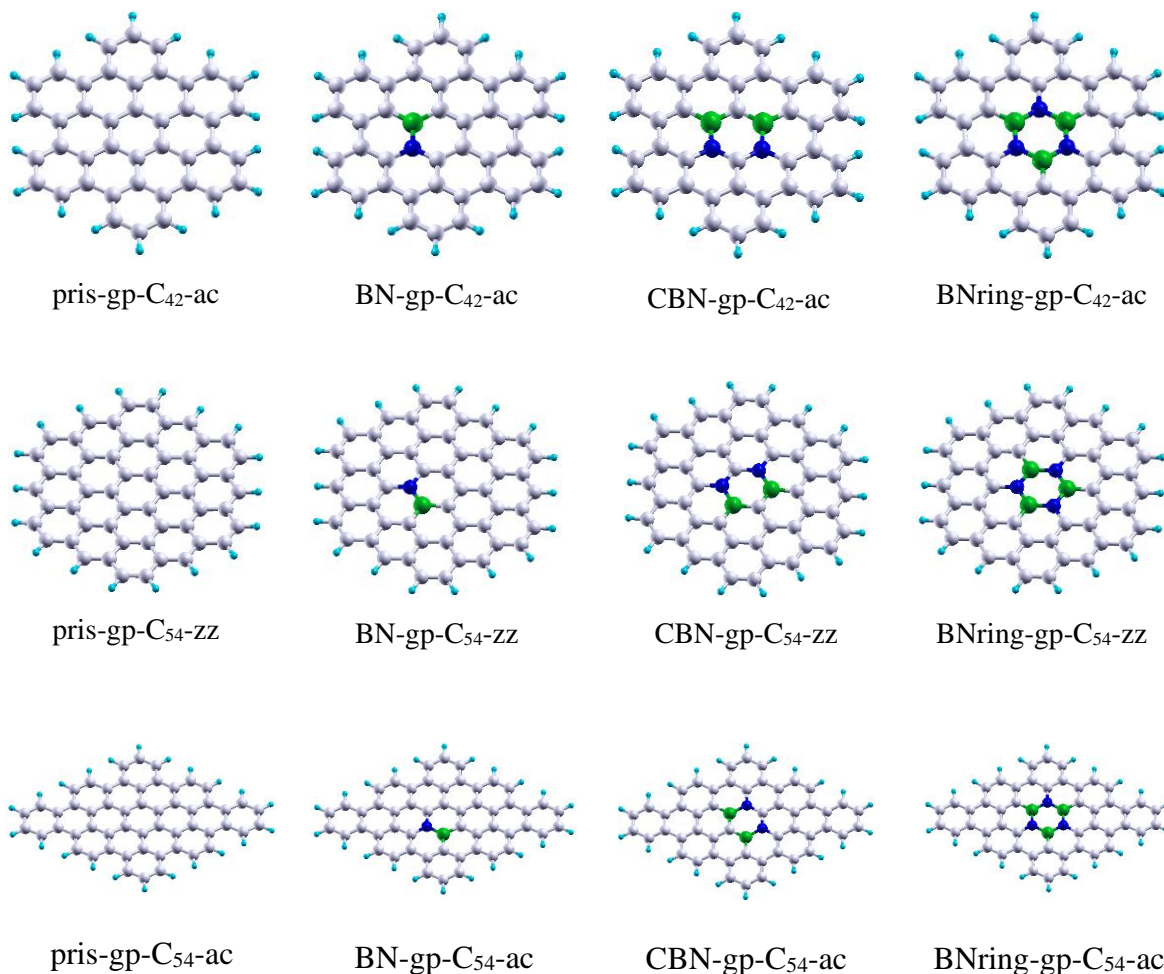
All the graphene models implemented in this study are shown in **Figure 3.1**. The chemical composition of the graphene substrate is varied by doping it with different number of B and N atoms. Single atom catalyst, namely, Mo, is anchored on the pristine and doped counterparts of all graphene models. We would like to highlight that the Mo metal center used in this study is inspired on account of its presence in the nitrogenase enzyme. A periodic graphene sheet is as represented in **Figure 3.1 (a)**. The smaller-sized graphene model we have considered in this chapter is a graphene nanoflake with 42 carbon atoms, with two possible edge effects – zigzag and armchair edges, as seen in **Figure 3.1 (b, c)**. This model is extended by incorporating 12 additional carbon atoms leading to a 54-atom graphene nanoflake, as shown in **Figure 3.1(d, e)** with similar edge orientations. The pictorial representation for all the models and the nomenclature applied to these models are shown in **Table 3.1**. The finite and periodic graphene models made up of all carbons atoms is referred to as pristine graphene (pris-gp) by definition. The graphene sheet/nanoflakes with dopants are generated by replacing the carbon atoms with boron and nitrogen in such a way that a C–C bond is replaced by B–N bond. When one such replacement is made on the model it is referred to as BN-gp; two C–C bonds are replaced by B–N bonds (leading to a C–B–N–C–B–N structure in a ring) it is referred to as CBN-gp, (c)) and when all C–C bonds in a ring are replaced by B–N bonds so as to form a borazine ring it is referred to as BNring-gp model. The model name is suffixed after each system. For example, for periodic models, the names of pristine and doped substrates are referred to as pris-gp-sheet, BN-gp-sheet, CBN-gp-sheet, and BNring-gp-sheet. The SAC-anchored complexes of periodic models are referred to as pris-gp-sheet-Mo, BN-gp-sheet-

Mo, CBN-gp-sheet-Mo and BNring-gp-sheet-Mo, respectively. Finally, the N_2 adsorbed complexes of the same are referred to as pris-gp-sheet-Mo- N_2 , BN-gp-sheet-Mo- N_2 , CBN-gp-sheet-Mo- N_2 , and BNring-gp-sheet-Mo- N_2 respectively. Along the same lines, the chemically distinct graphene nanoflake models for C_{42} with zigzag edges are referred to as pris-gp- C_{42} -zz, BN-gp- C_{42} -zz, CBN-gp- C_{42} -zz, BNring-gp- C_{42} -zz, and so on. Their corresponding metal SAC anchored models are called as pris-gp- C_{42} -zz-Mo, BN-gp- C_{42} -zz-Mo, CBN-gp- C_{42} -zz-Mo, and BNring-gp- C_{42} -zz-Mo, respectively. Their N_2 adsorbed complexes are called as pris-gp- C_{42} -zz-Mo- N_2 , BN-gp- C_{42} -zz-Mo- N_2 , CBN-gp- C_{42} -zz-Mo- N_2 , and BNring-gp- C_{42} -zz-Mo- N_2 respectively. Nomenclature of C_{42} graphene nanoflakes with armchair edges and C_{54} graphene nanoflakes with zigzag and armchair edges follow the same way.

Table 3.1: Graphene models taken in this study along with their nomenclature.

Elemental color codes - ● carbon (C) ● hydrogen (H) ● boron (B) ● nitrogen (N)





3.2.2 Methodology and Computational Details

Previous investigations have shown that the parallel or side-on mode of adsorption shows stronger N–N bond elongation as compared to the perpendicular or end-on mode of N₂ adsorption.^{40,41} Hence, in this study we exclusively focus on the parallel mode/side-on mode of N₂ adsorption on Mo and their corresponding N₂ adsorption energies are calculated as follows:

$$E_{\text{ad}} = E(\text{system-Mo-N}_2) - E(\text{system-Mo}) - E(\text{N}_2) \quad (3.1)$$

where, $E(\text{system-Mo-N}_2)$ represents the energy of the N₂ molecule adsorbed on the catalytic systems. The $E(\text{N}_2)$ and $E(\text{system-Mo})$ represent the energies of the N₂ molecule and SAC-anchored graphene models, respectively.

The adsorption of Mo atom on the graphene models is also calculated to ensure that the proposed catalytic systems are energetically/thermodynamically stable. The adsorption energies of Mo on the various graphene models are calculated as follows:

$$E_{\text{Mo}} = E(\text{system-Mo}) - E(\text{system}) \quad (3.2)$$

where $E(\text{system-Mo})$ represents the energy of the SAC anchored graphene models and $E(\text{system})$ represent the energy of the graphene models.

The periodic model, its SAC-anchored, BN-doped, and N_2 adsorbed counterparts are studied using Vienna Ab initio Simulation Package (VASP)⁴² software with PBE functional.⁴³ A projected augmented wave (PAW)⁴⁴ method is used to describe plane wave basis set with an energy cutoff of 520 eV to. The 2D graphene sheets are simulated using periodic DFT and to avoid agglomeration or interaction of neighbouring layers, a vacuum space of 20 Å is created along the Z-direction. The 5×5 super cell with 50 atoms is used as graphene surface model, as shown in **Figure 3.1(a)** and the optimized C–C bond length in graphene sheet is 1.42 Å. The structural optimization of all geometries is carried out using the conjugate gradient method.⁴⁵ Brillouin zone is sampled by a $(2 \times 2 \times 1)$ kpoint grid using the Monkhorst–Pack scheme.⁴⁶ For Density of State (DOS) calculation, the Monkhorst–Pack generated $(9 \times 9 \times 1)$ set of k-point grid is used.

All the calculations on finite models (graphene nanoflake models with 42 atoms and 54 atoms) are performed using a linear combination of Gaussian-type orbitals within an auxiliary framework of DFT,⁴⁷ as implemented in the deMon 5.0. program.⁴⁸ All structures are optimized using the Perdew-Burke-Ernzerhof (PBE) exchange and correlation functional.⁴³ Two different basis sets are used for describing the atomic orbitals of Mo in finite-sized models: (a) first case where its atomic orbitals are described with DZVP basis set (as was the case for H, C, B, and N) and (b) second case where Los Alamos National Laboratory 2-double- ζ quasi-relativistic effective core potential (QECP)^{49,50} basis is used for Mo, while all other atoms were treated with a DZVP basis set. The charge density for all the cases is calculated by fitting the GEN-A2 auxiliary functions.⁵¹ Gradient and displacement criteria used for geometrical convergence is 5×10^{-4} a.u., while the SCF convergence criterion is set at 10^{-8} a.u.

All the atoms in periodic and finite graphene models considered in this chapter are relaxed at the lowest spin state (spin multiplicity = 1). It can also be noted that the singlet spin state of all the graphene nanoflakes correspond to the lowest electronic energy, thereby conforming to the ground state. On these relaxed graphene models, Mo atom is anchored and the entire geometry is relaxed. This is followed by the adsorption of N_2 and relaxing the dinitrogen adsorbed geometries at the lowest spin state. A restricted Kohn-Sham formalism is adopted for the optimization of all the above geometries. Following the optimization of all the structures discussed above, frequencies are calculated to ensure these optimized conformations correspond to local minima.

3.3 Results and Discussions

3.3.1 N_2 adsorption and N-N bond elongation

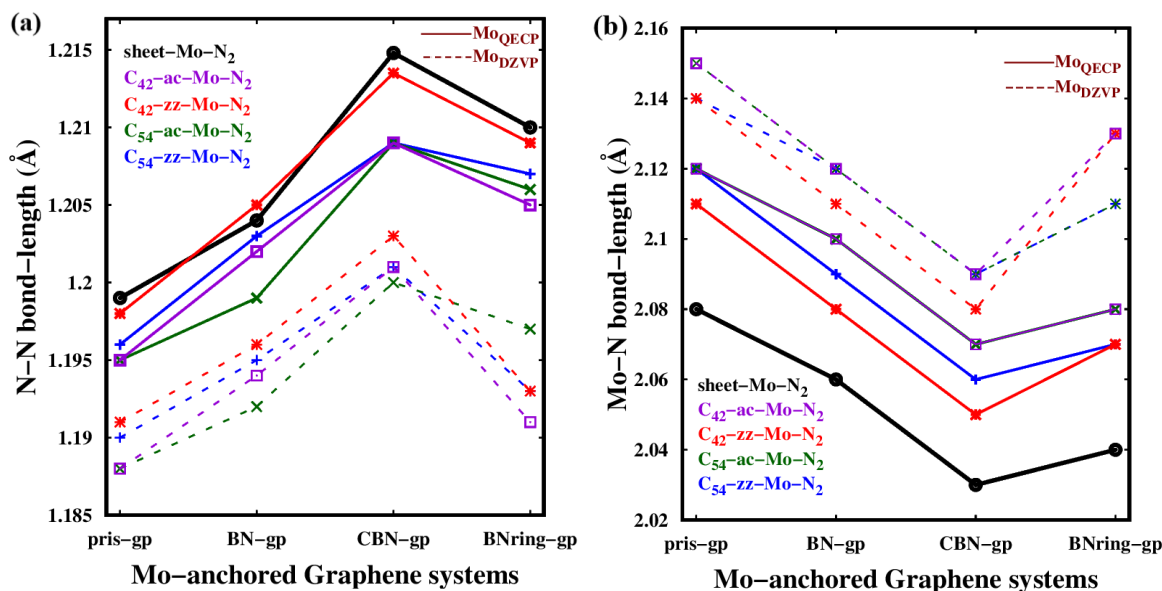


Figure 3.2: (a) N–N bond length in graphene model–Mo–N₂ complexes for varying chemical composition, as highlighted on the x-axis. The calculated N–N bond length in free dinitrogen is 1.12 Å. (b) Average Mo–N bond length (Å) in N₂ adsorbed Mo-anchored graphene models. Solid black line represents periodic–Mo–N₂ complexes, dotted and solid lines represent graphene nanoflakes when Mo is described with DZVP and QECP basis set, respectively.

The adsorption of dinitrogen molecule on all the periodic models is exothermic with the adsorption energies ranging between -1.70 and -1.87 eV, as shown in **Table 3.2**. The adsorption energies obtained when we use DZVP basis set for Mo range between -1.4 and -1.6 eV and somewhat higher than those obtained with QECP basis set for Mo. The adsorption of Mo on the graphene models is also exothermic with the adsorption energies ranging between -3 and -4 eV, as shown in **Table 3.3**. The negative adsorption energies are indicative of the stability of the catalytic systems energetically. All the studied SAC-anchored graphene models have been found to be effective catalysts toward the activation of dinitrogen. This is understood from the fact that the N–N bond is elongated to 1.19 – 1.21 Å from its value of 1.12 Å in the free state on various systems. The N–N bond elongation on various SAC anchored graphene models is plotted in **Figure 3.2(a)**, with CBN-gp-Mo models showing the maximum N–N bond activation. Most interestingly, both periodic and finite-sized models show the same trend of N–N bond activation with respect to varying chemical composition. The second salient observation is that the difference in absolute numbers between the periodic and finite-sized models is negligible (amounting to only 1%) when Mo is treated using the QECP basis set. N–N bond elongation is also seen to be associated with interatomic distance between one of the N atoms (of dinitrogen) and the Mo metal anchored on the graphene model, as seen in **Figure 3.2(b)**. Longer N–N bond elongation is correlated with the shorter Mo–N interatomic distance.

Table 3.2: N₂ adsorption energies (E_{ad}) in eV on various Mo-anchored graphene models.

Models	N ₂ adsorption energies (E_{ad}) in eV				
	C ₅₄ -zz	C ₅₄ -ac	C ₄₂ -zz	C ₄₂ -ac	Periodic
pris-gp-Mo-N ₂	-1.42	-1.40	-1.42	-1.41	-1.74
pris-gp-Mo _{QECP} -N ₂	-1.70	-1.70	-1.71	-1.71	
BN-gp-Mo-N ₂	-1.55	-1.50	-1.57	-1.53	

BN-gp-Mo _{QECP} -N ₂	-1.77	-1.74	-1.85	-1.77	-1.84
CBN-gp-Mo-N ₂	-1.55	-1.55	-1.57	-1.56	-1.87
CBN-gp-Mo _{QECP} -N ₂	-1.79	-1.78	-1.80	-1.81	
BNring-gp-Mo-N ₂	-1.52	-1.49	-1.55	-1.51	-1.86
BNring-gp-Mo _{QECP} -N ₂	-1.75	-1.74	-1.78	-1.74	

Table 3.3: Mo adsorption energies in eV on various graphene models used in the study.

Models	Mo adsorption energies (E_{Mo}) in eV				
	C ₅₄ -zz	C ₅₄ -ac	C ₄₂ -zz	C ₄₂ -ac	Periodic
pris-gp-Mo	-4.05	-4.33	-3.97	-4.39	-4.09
pris-gp-Mo _{QECP}	-4.22	-4.48	-4.08	-4.52	
BN-gp-Mo	-3.93	-4.19	-3.90	-4.23	-3.93
BN-gp-Mo _{QECP}	-4.24	-4.48	-4.07	-4.52	
CBN-gp-Mo	-3.89	-4.11	-3.90	-4.14	-3.86
CBN-gp-Mo _{QECP}	-4.24	-4.46	-4.20	-4.47	
BNring-gp-Mo	-3.21	-3.37	-3.18	-3.41	-3.02
BNring-gp-Mo _{QECP}	-3.33	-3.5	-3.28	-3.54	

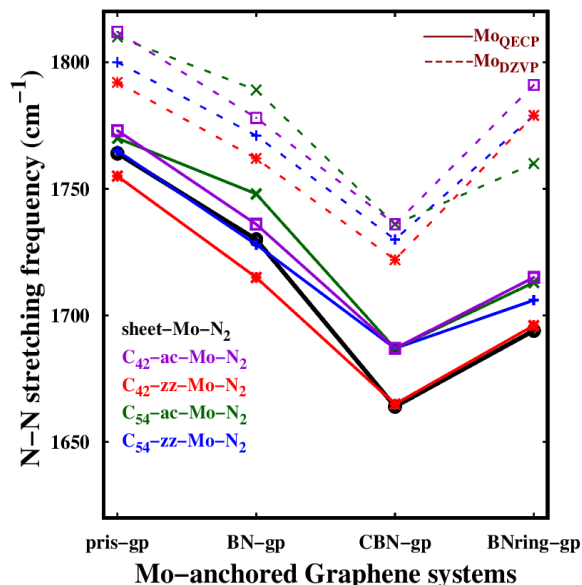


Figure 3.3: N-N stretching frequency in graphene model-Mo-N₂ complexes (calculated ν_{N-N} in free N₂ = 2326 cm⁻¹). Solid black line represents periodic-Mo-N₂ complexes, dotted and solid lines represent graphene nanoflakes when Mo is described with DZVP and QECP basis set, respectively.

The increase in the N-N bond length is validated by both red shift in the N-N stretching frequency and the total amount of charge transferred to the dinitrogen. N-N stretching frequencies in various N₂ adsorbed SAC-anchored graphene models is given in **Figure 3.3**. Inherently, the bond stretching frequencies of the all the models is consistent with the trend of bond elongation and CBN-gp-Mo models show a red shift up to 1636 cm⁻¹, as compared to 2359 cm⁻¹ in free N₂. It is once again noted that the finite model calculation carried out with Mo-QECP basis set falls in trend to the periodic model, while the “all-electron” calculation using DZVP basis shows a slightly lower red shift. Change in the size of finite graphene nanoflakes and edge orientations does not show any significant impact on N-N bond elongation when compared to the periodic graphene model.

3.3.2 Bader charges and electronic properties

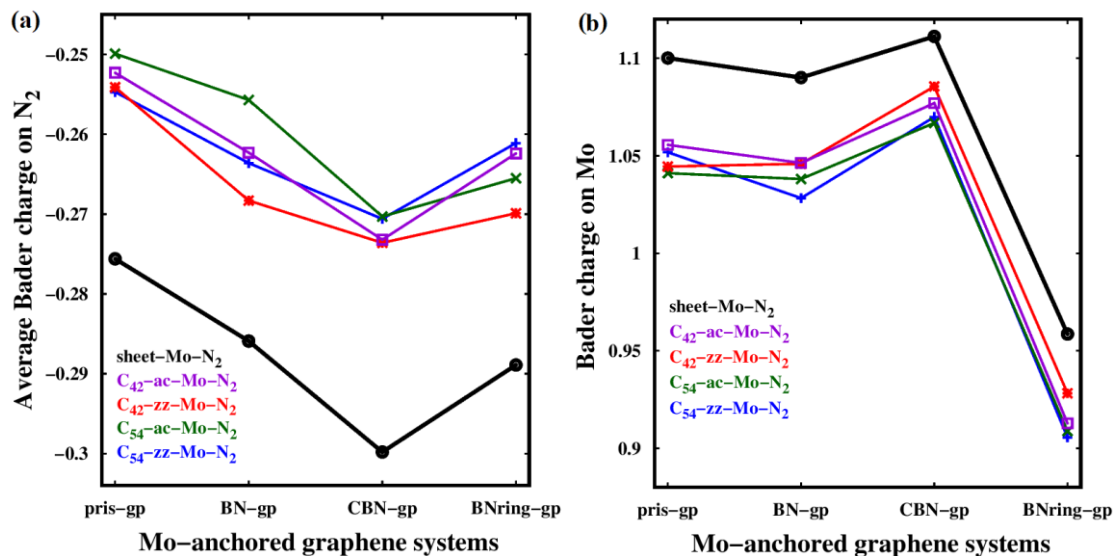


Figure 3.4: (a) Average of the Bader charges on the adsorbed N₂ molecule, (b) Bader charges on the Mo atom after N₂ adsorption.

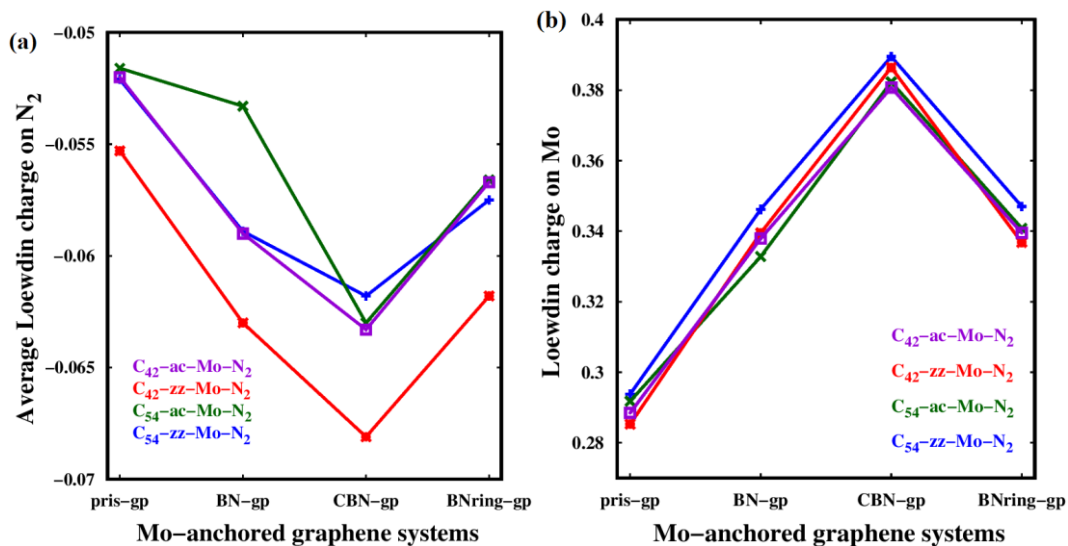
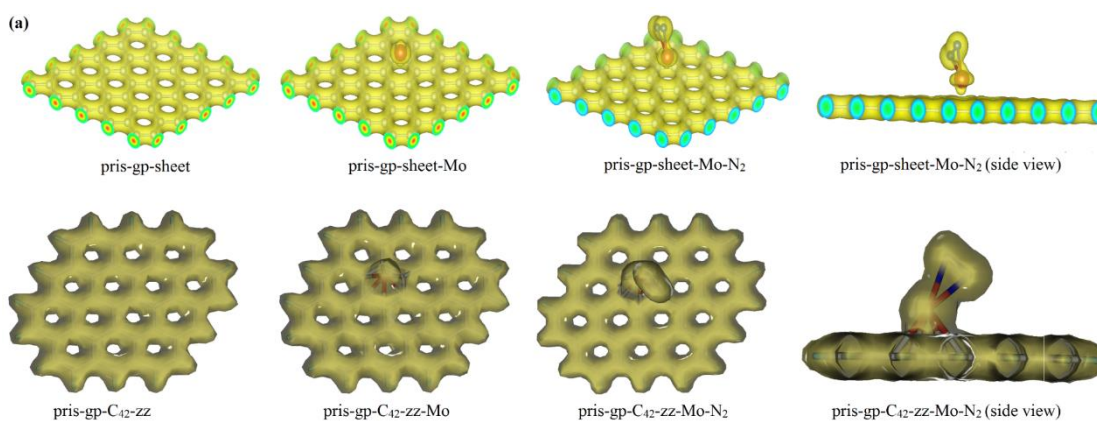


Figure 3.5: (a) Average Löwdin charges on the adsorbed N₂ molecule, (b) Löwdin charges on the Mo atom after N₂ adsorption.

Charges on the Mo-anchored graphene models after N₂ adsorption are calculated, and a significant change in charge could be observed only on the adsorbed N₂ molecule and

Mo atom. Thus, the charge redistribution is completely localized. Bader charges are calculated for all the periodic models and finite models, where Mo is treated with a DZVP basis set. Since Bader charges are not well-defined with metal Electron Core Potentials, for the finite models where Mo has been treated with QECP basis set, Löwdin⁵² charges are calculated. The average Bader charges on N₂ and Bader charges on Mo after dinitrogen adsorption is plotted in **Figure 3.4 (a-b)**. The Bader charges on CBN-gp-Mo models are most negative and reflect a higher charge transfer from the catalyst to dinitrogen in both periodic as well as finite models. The elongation of N–N bond is favored when electrons are transferred to the N– π^* orbital, in short, a larger electron gain on N atom is essential for bond dissociation. The charges accumulated on the N atoms, as shown in **Figure 3.4(a)**, correspond to the extent of N–N bond elongation in various studied systems. The charge on Mo metal follows reverse trend of the charges gained by the N₂, indicative of the fact that the charge transfer is primarily from Mo. The same pattern could be seen from the Löwdin charges on N₂ and Mo, plotted in **Figure 3.5 (a-b)**. This is further validated in the electronic structure analysis discussed in the next paragraph.



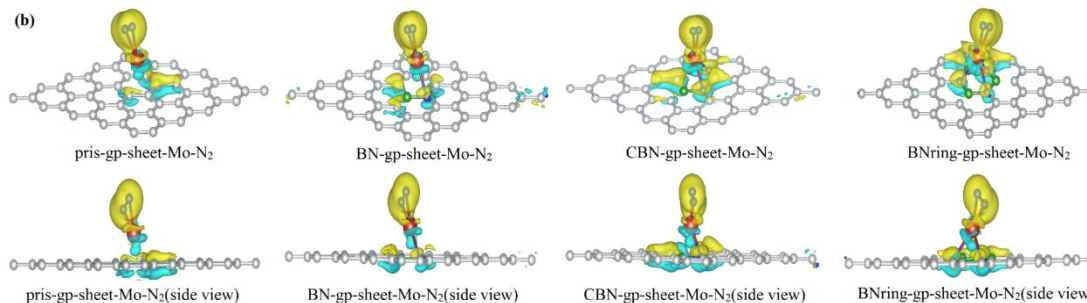


Figure 3.6: (a) Total charge density plots for the periodic pris-gp-sheet and finite pris-gp-C₄₂-zz models, their Mo-anchored geometries and N₂ adsorbed pris-gp-Mo geometries; (b) Charge difference density plots of the Mo-anchored periodic models with and without N₂. Density plots are made at an isosurface value of $0.06\text{e}\text{\AA}^{-3}$.

We next come to the underlying electronic factors that are responsible for the activation of dinitrogen on various SAC anchored graphene models. The total charge density plots of periodic and finite models made at an isosurface value of $0.06\text{e}\text{\AA}^{-3}$ show a delocalized electron density over the dinitrogen adsorbed SAC anchored graphene models, as seen in **Figure 3.6(a)**. The electron density plot with Mo-QECP basis set is not shown as it is similar to the all-electron calculation from DZVP basis set. The charge density difference plots of the Mo-anchored periodic models with and without N₂ show an exclusive overlap of the electron density on Mo with that of N₂, as shown in **Figure 3.6(b)**. However, the electron density from the graphene substrate, in particular, the C, B, and N atoms in the local environment around Mo could not interact with the electron density of N₂. Rather, these surrounding atoms interact with Mo metal and indirectly influence the interaction of Mo with N₂. Since the catalytic activity of these SAC anchored graphene models is governed by the metal atom and the local environment of the catalytic metal center, it is a local site activity and not a surface phenomenon. To understand the mechanism of catalysis, the electronic nature around the Fermi level in the periodic models and the Frontier Molecular Orbitals of the finite models are investigated.

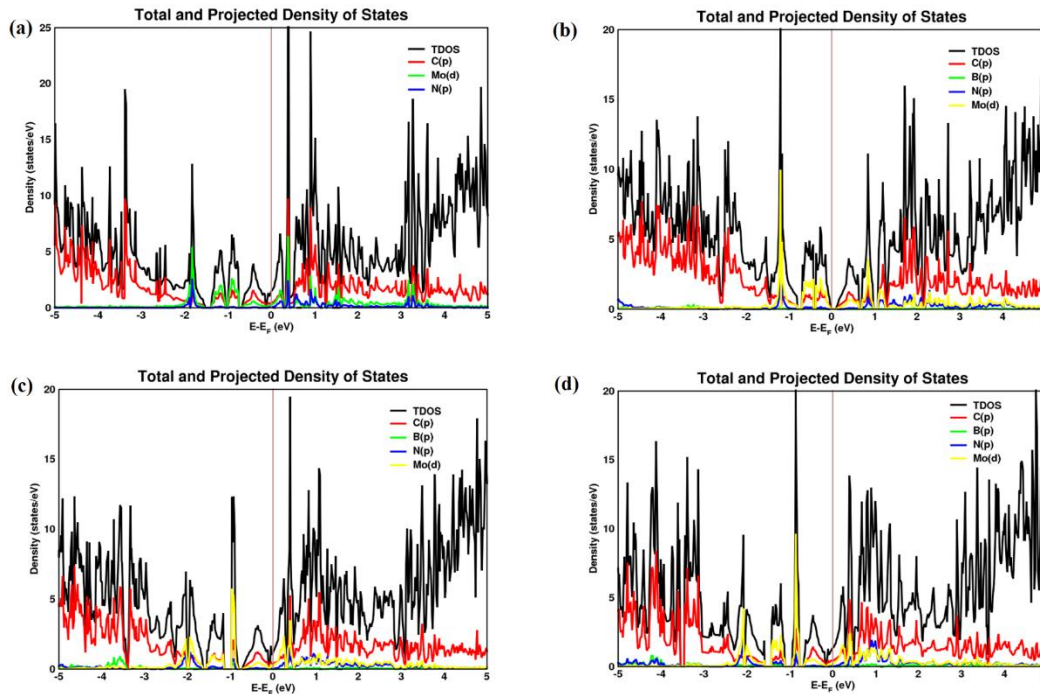


Figure 3.7: Total density of states (TDOS) and Projected density of states (PDOS) plots of (a) pris-gp-sheet-Mo-N₂ (b) BN-gp-sheet-Mo-N₂ (c) CBN-gp-sheet-Mo-N₂ (d) BNring-gp-sheet-Mo-N₂.

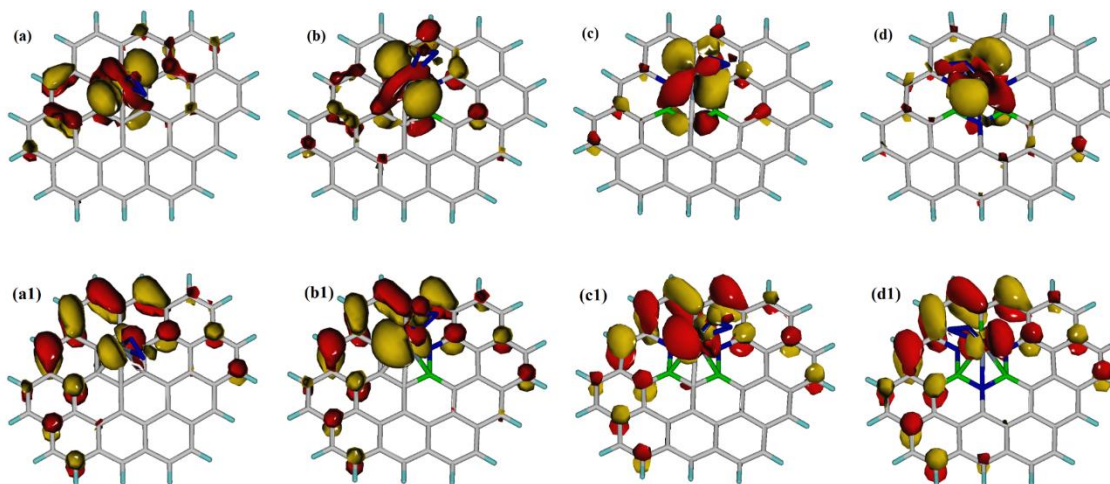


Figure 3.8: HOMOs of (a) pris-gp-C₄₂-zz-Mo-N₂ (b) BN-gp-C₄₂-zz-Mo-N₂ (c) CBN-gp-C₄₂-zz-Mo-N₂ (d) BNring-gp-C₄₂-zz-Mo-N₂. LUMOs of (a1) pris-gp-C₄₂-zz-Mo-N₂ (b1) BN-gp-C₄₂-zz-Mo-N₂ (c1) CBN-gp-C₄₂-zz-Mo-N₂ (d1) BNring-gp-C₄₂-zz-Mo-N₂.

The total density of states (TDOS) and projected density of states (PDOS) of N₂ adsorbed graphene systems, as shown in **Figure 3.7**, shows nearly zero density at the Fermi level (E_F) and a nonzero density around E_F inferring the semi-metallic nature of pristine graphene. The conduction band near E_F has a larger density of Mo d-orbital, this region would correspond to the Highest Occupied Molecular Orbital (HOMO); while a d-p hybridized orbital in the valence band will correspond to the Lowest Unoccupied Molecular Orbital (LUMO). The Frontier Molecular Orbital (FMO) picture of the finite C₄₂-zz-Mo-N₂ models (**Figure 3.8**) corresponds to the orbital composition of HOMO and LUMO as interpreted from the PDOS plot. The FMO pictures of the finite models remain the same even when Mo-QECP basis has been used. Also, the HOMO–LUMO energy gap of the finite gp-Mo-N₂ systems (MODZVP and MOQECP basis set) lies within 1.0 and 2.0 eV; this also happens to be the $E-E_F$ value of the closest conduction-valence gap in the PDOS plot.

3.4 Conclusions

In this chapter, single atom catalysts (SACs) on graphene supports have been explored as a catalytic system for dinitrogen activation. While metal clusters of 4–20 atoms have been reported to show excellent N–N bond dissociation, the challenge has always been to synthesize the metal cluster. It is easier to absorb a single atom on a stable framework and this idea has been exploited in this chapter by utilizing graphene as the framework to hold the metal atom which will act as the catalytic centers. Also, size and edge orientation of graphene have been reported to affect its activity, therefore the size and edge orientations are taken into account by taking graphene nanoflakes of two different sizes and the periodic model which inherently assumes the graphene nanoflake is repeated infinitely in all directions. The critical findings obtained from this extensive study of investigating periodic and finite graphene models as catalyst for dinitrogen activation are the following:

(a) This study shows that all Mo-anchored graphene models are good catalysts for dinitrogen activation with a potential for designing them experimentally. In particular, a better catalytic activity is seen in the case of CBN-gp- Mo models.

(b) It has also been observed that the role of dopants is far more influential in dinitrogen activation as compared to graphene surface orientation in both periodic and finite models.

(c) Interestingly, the extent of bond elongation in the periodic model has also been found to be nearly similar to that in finite models where Mo is treated with QECP basis set. In spite of different molecular orbital treatments in periodic and finite models, the similar activity trend that we have obtained is because of the local activity of the catalytic centers.

The finite models can give factual details of clusters and highlight which atoms are the catalytic centers. The periodic models give a better understanding of the surface phenomena and the influence of delocalized electron density for catalysis; however, it comes with its own complexity of implementing several approximations and intensive calculation. This chapter proposes that, for SAC-anchored graphene, since the catalytic center is the metal atom and the catalysis is driven by the local environment around the metal center, finite model calculations are as reliable as periodic model calculations.

3.5 References

- (1) Fryzuk, M. D.; Johnson, S. A. *Coord. Chem. Rev.* **2000**, *200*, 379–409.
- (2) Kim, J.; Rees, D. C. *Science* **1992**, *257*, 1677–1682.
- (3) Einsle, O.; Tezcan, F. A.; Andrade, S. L. A.; Schmid, B.; Yoshida, M.; Howard, J. B.; Rees, D. C. *Science* **2002**, *297*, 1696–1700.
- (4) Sellmann, D.; Sutter, *J. Acc. Chem. Res.* **1997**, *30*, 460–469.
- (5) Dance, I. G. *Dalton Transactions* **2008**, *43*, 5977–5991.
- (6) Boyd, E. S.; Hamilton, T. L.; Peters, J. W. *Front. Microbiol.* **2011**, *2*, 1–15.
- (7) Kerpál, C.; Harding, D. J.; Lyon, J. T.; Meijer, G.; Fiellicke, A. *J. Phys. Chem. C* **2013**, *117*, 12153–12158.

- (8) Ohki, Y.; Uchida, K.; Tada, M.; Cramer, R. E.; Ogura, T.; Ohta, T. *Nat. Commun.* **2018**, *9*, 1–6.
- (9) Roy, D.; Navarro-Vazquez, A.; Schleyer, P. V. R. *J. Am. Chem. Soc.* **2009**, *131*, 13045–13053.
- (10) Cao, B.; Starace, A. K.; Judd, O. H.; Bhattacharyya, I.; Jarrold, M. F.; Lopez, J. M.; Aguado, A. *J. Am. Chem. Soc.* **2010**, *132*, 12906–12918.
- (11) Cao, B.; Starace, A. K.; Judd, O. H.; Bhattacharyya, I.; Jarrold, M. F. *J. Chem. Phys.* **2009**, *131*, 1–6.
- (12) Kulkarni, B. S.; Krishnamurty, S.; Pal, S. *J. Phys. Chem. C* **2011**, *115*, 14615–14623.
- (13) Das, S.; Pal, S.; Krishnamurty, S. *J. Phys. Chem. C* **2014**, *118*, 19869–19878.
- (14) Melen, R. L. *Angew. Chem., Int. Ed.* **2018**, *57*, 880–882.
- (15) Lv, C.; Qian, Y.; Yan, C.; Ding, Y.; Liu, Y.; Chen, Y.; Yu, G. *Angew. Chem., Int. Ed.* **2018**, *57*, 10246–10250.
- (16) Mao, X.; Zhou, S.; Yan, C.; Zhu, Z.; Du, A. *Phys. Chem. Chem. Phys.* **2019**, *21*, 1110–1116.
- (17) Zhao, J.; Chen, Z. *J. Am. Chem. Soc.* **2017**, *139*, 12480–12487.
- (18) Li, H.; Shang, J.; Ai, Z.; Zhang, L. *J. Am. Chem. Soc.* **2015**, *137*, 6393–6399.
- (19) Kumar, C. V. S.; Subramanian, V. *Phys. Chem. Chem. Phys.* **2017**, *19*, 15377–15387.
- (20) Legare, M.-A.; Belanger-Chabot, G.; Dewhurst, R. D.; Welz, E.; Krummenacher, I.; Engels, B.; Braunschweig, H. *Science* **2018**, *359*, 896–900.
- (21) Guo, X.; Liu, S.; Huang, S. *Int. J. Hydrogen Energy* **2018**, *43*, 4880–4892.
- (22) Ouyang, Y.; Li, Q.; Shi, S.; Ling, C.; Wang, J. *J. Mater. Chem. A* **2018**, *6*, 2289–2294.

- (23) Jeon, I. Y.; Choi, H. J.; Ju, M. J.; Choi, I. T.; Lim, K.; Ko, J.; Kim, H. K.; Kim, J. C.; Lee, J.-J.; Shin, D.; et al. *Sci. Rep.* **2013**, *3*, 1–7.
- (24) Lu, Y.; Yang, Y.; Zhang, T.; Ge, Z.; Chang, H.; Xiao, P.; Xie, Y.; Hua, L.; Li, Q.; Li, H.; et al. *ACS Nano* **2016**, *10*, 10507–10515.
- (25) Le, NY-Q.; Gu, J.; Tian, W. Q. *Chem. Commun.* **2014**, *50*, 13319–13322.
- (26) Li, X.-F.; Li, Q.-K.; Cheng, J.; Liu, L.; Yan, Q.; Wu, Y.; Zhang, X.-H.; Wang, Z.-Y.; Qiu, Q.; Luo, Y. *J. Am. Chem. Soc.* **2016**, *138*, 8706–8709.
- (27) Kumar, D.; Pal, S.; Krishnamurty, S. *Phys. Chem. Chem. Phys.* **2016**, *18*, 27721–27727.
- (28) Sharma, R.; Baik, J. H.; Perera, C. J.; Strano, M. S. *Nano Lett.* **2010**, *10*, 398–405.
- (29) Son, Y. W.; Cohen, M. L.; Louie, S. G. *Nature* **2006**, *444*, 347–349.
- (30) Son, Y. W.; Cohen, M. L.; Louie, S. G. *Phys. Rev. Lett.* **2006**, *97*, 1–4.
- (31) Hu, W.; Lin, L.; Yang, C.; Yang, J. *J. Chem. Phys.* **2014**, *141*, 1–10.
- (32) Nazrulla, M. A.; Krishnamurty, S.; Phani, K. L. N. *J. Phys. Chem. C* **2014**, *118*, 23058–23069.
- (33) Ly, Q.; Merinov, B. V.; Xiao, H.; Goddard, W. A.; Yu, T. H. *J. Phys. Chem. C* **2017**, *121*, 24408–24417.
- (34) Owens, F. J. *J. Chem. Phys.* **2008**, *128*, 1–4.
- (35) Berger, C.; Song, Z.; Li, X.; Wu, X.; Brown, N.; Naud, C.; Mayou, D.; Li, T.; Hass, J.; Marchenkov, A. N.; et al. *Science* **2006**, *312*, 1191–1196.
- (36) Li, X.; Wang, X.; Zhang, L.; Lee, S.; Dai, H. *Science* **2008**, *319*, 1229–1232.
- (37) Agnoli, S.; Favaro, M. *J. Mater. Chem. A* **2016**, *4*, 5002–5025.
- (38) Bepete, G.; Voiry, D.; Chhowalla, M.; Chiguvare, Z.; Coville, N. J. *Nanoscale* **2013**, *5*, 6552–6557.

- (39) Xu, J.; Jang, S. K.; Lee, J.; Song, Y. J.; Lee, S. *J. Phys. Chem. C* **2014**, *118*, 22268–22273.
- (40) Kumar, D.; Krishnamurty, S.; Pal, S. *J. Phys. Chem. C* **2017**, *121*, 26493–26498.
- (41) Kumar, D.; Govindaraja, T.; Krishnamurty, S.; Kaliaperumal, S.; Pal, S. *Phys. Chem. Chem. Phys.* **2018**, *20*, 26506–26512.
- (42) Kresse, G.; Furthmuller, J. *Comput. Mater. Sci.* **1996**, *6*, 15–50.
- (43) Perdew, J. P.; Burke, K.; Ernzerhof, M. *Phys. Rev. Lett.* **1996**, *77*, 3865–3868.
- (44) Blochl, P. E. *Phys. Rev. B: Condens. Matter Mater. Phys.* **1994**, *50*, 17953–17979.
- (45) Payne, M. C.; Teter, M. P.; Allan, D. C.; Arias, T. A.; Joannopoulos, J. D. *Rev. Mod. Phys.* **1992**, *64*, 1045–1097.
- (46) Monkhorst, H. J.; Pack, J. D. *Phys. Rev. B* **1976**, *13*, 5188–5192.
- (47) Koster, A. M.; Reveles, J. U.; del Campo, J. M. *J. Chem. Phys.* **2004**, *121*, 3417–3424.
- (48) Koster, A. M.; Calaminici, P.; Casida, M. E.; Moreno, R. F.; Geudtner, G.; Goursot, A.; Heine, T.; Ipatov, A.; Janetzko, F.; del Campo, J. M.; et al. deMon 5.0; deMon Developers, 2006.
- (49) Feller, D. J. *J. Comput. Chem.* **1996**, *17*, 1571–1586.
- (50) Schuchardt, K. L.; Didier, B. T.; Elsethagen, T.; Sun, L.; Gurumoorthi, V.; Chase, J.; Li, J.; Windus, T. L. *J. Chem. Inf. Model.* **2007**, *47*, 1045–1052.
- (51) Calaminici, P.; Janetzko, F.; Koster, A. M.; Mejia-Olvera, R.; Zuniga-Gutierrez, B. *J. Chem. Phys.* **2007**, *126*, 1–10.
- (52) Löwdin, P. O. *J. Chem. Phys.* **1950**, *18*, 365–375.

Chapter 4

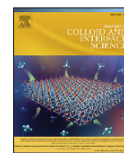
Journal of Colloid and Interface Science 600 (2021) 480–491



Contents lists available at ScienceDirect

Journal of Colloid and Interface Science

journal homepage: www.elsevier.com/locate/jcis

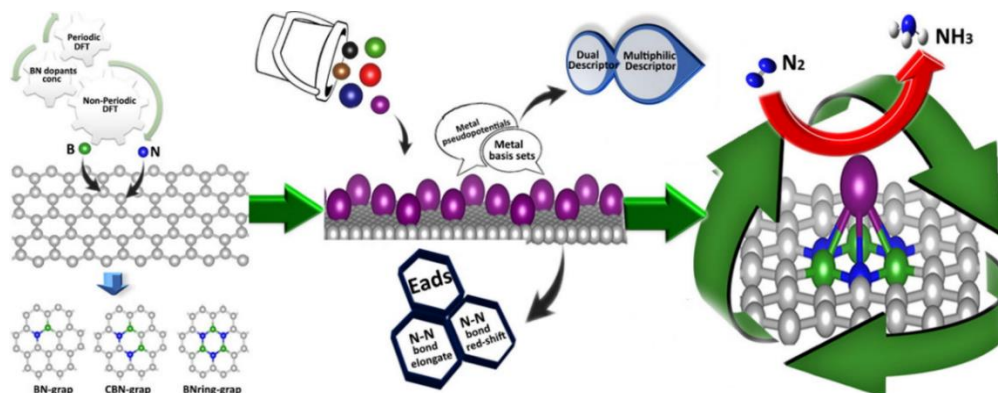


Regular Article

Nitrogen activation to reduction on a recyclable V-SAC/BN-graphene heterocatalyst sifted through dual and multiphilic descriptors



Ashakiran Maibam, Sailaja Krishnamurthy*



Maibam, A. et. al, *J. Colloid Interface Sci.*, 2021, 600, 480-491.

This chapter explores which metal single atom catalyst on graphene substrate will be an optimal candidate for N_2 activation and reduction. Efficient reduction of nitrogen to ammonia at a minimal cost would require a recherche catalyst tailored by assimilating the inherent electronic and reactive nature of Single Atom Catalysts (SACs) on heteroatom doped graphene. A full-scale DFT study accounting for disparate descriptions of atomic orbitals and representation of support, has been carried out to identify the most active and recyclable SAC/B-graphene composite as catalyst for Nitrogen Reduction Reaction (NRR). Dual and Multiphilic descriptors derived reactivity pattern of six different metal SACs V, Fe, Ni, Ru, W and Re on periodic and non-periodic paradigms of pristine and BN-pair doped graphene supports, align with the calculated chemisorption efficacy and activation of N_2 . The enzymatic route of nitrogen reduction on three most ideal metal SACs (V, W and Re) culminates vanadium SAC, a relatively cheaper metal, anchored on BNring-graphene with an energy barrier of ≤ 1.24 eV as a highly active and recyclable catalyst for NRR.

4.1 Introduction

Ammonia (NH_3), the most stable basic hydride formed by Hydrogen and nitrogen is not only an essential precursor to fertilizers and modern chemicals,^{1,2} but also a molecule with tremendous potential towards green energy due to its high energy density with zero carbon footprint.^{3,4} Large scale industrial NH_3 production is carried out with the conventional Haber–Bosch⁵ process using H_2 and N_2 gases as raw materials at high temperature and pressure that gobbles up approximately 1–2% of global energy and generates an alarming carbon footprint amounting to 6% of global CO_2 emissions.⁶ Thereby, alternative greener technology of converting N_2 to NH_3 via simple and cost effective technologies will provide a holistic approach for sustainable ammonia production.⁷ However, the advancement of sustainable technology will rely on the development and procurement of highly stable and efficient catalysts.

Several experimental studies in the past few decades have been focused on Transition Metal (TMs) such as Mo ^{8,9}, Cr ^{10,11}, Fe ^{12–14} and their heteromultimetallic clusters as NRR catalysts at ambient conditions. While these transition metals and their heteromultimetallic clusters form stable metal-dinitrogen complexes and show catalytic features for N_2 activation there is a heavy loss of metals which are unrecoverable in the following catalytic cycle.¹⁵ This led to an impetus of tangential studies on employing metal nanoclusters as catalysts to reduce dinitrogen under experimental and theoretical approaches.^{16,17} While metal nanoclusters are intriguing due to electronic quantum confinement, thereby leading to higher catalytic activity as compared to bulk catalyst; not all the metal atom centers are exploited.

Metal Single Atom Catalysts (SACs)^{18,19}, in this regard, not only offer a higher catalytic activity and selectivity; but curbs metal loss during the catalytic cycle by exploiting every metal centre as an active catalyst and also provides vacant coordination sites for electron transfer or electron gain from the dinitrogen molecule.^{20–22} However, isolated metal SACs owing to strong metal d-d orbital interactions²³ require a support that secures it without compromising the catalytic activity. In this respect, electron-rich two-dimensional (2D) materials such as graphene^{24–26}, graphitic carbon nitride ($\text{g-C}_3\text{N}_4$)^{27–29}, boron nanosheet^{30–32}, MBenes³³, MXenes^{34,35}, phosphorene^{36,37}, hexagonal boron nitride (h-BN)^{38–40}, MoS_2 ^{41–43},

etc. not only act as a support to secure the metal SACs but also assist in their catalytic performance.

Interestingly, compared to pristine 2D substrates, heteroatom doped 2D substrates such as N-doped carbon^{44,45}, (g-C₃N₄)²⁷⁻²⁹ or (h-BN)³⁸⁻⁴⁰ with isolated boron sites have been reported to be remarkably efficient towards NRR in several experimental as well as theoretical investigations. The N-atoms in the substrate increase metal coordination to the substrate and tune the selectivity of metals toward N₂ molecule^{46,47}, while the B-atoms can inherently induce charge redistribution on the substrate and favour adsorption of N₂.^{48,49} Moreover, the presence of B hetero-dopants on B and N dual-doped carbon nanospheres has been reported to inhibit the competing Hydrogen Evolution Reaction (HER) and enhance adsorption of N₂ in electrocatalytic NRR.⁵⁰ From the previous study on BN-pair dual doped graphene support that showed a better anchoring of Mo SAC on the CBN-doped graphene support⁵¹ and as well as higher activation of dinitrogen when compared to pristine graphene.^{51,52} It is evident that boron and nitrogen doped graphene can act as an effective 2D substrate for anchoring various metal SACs. Furthermore, with plasma doping and chemical vapour deposition atomically precise BN-doped graphene supports become highly feasible in certain experimental conditions.⁵³⁻⁵⁵

This brings us to the computational studies that have brought an insight on the underlying chemical morphology and composition to which the catalytic activity is susceptible. Density Functional Theory (DFT) based studies, attempted over the last two decades, to identify an ideal SAC/support combination leading an efficient NRR are worth mentioning at this juncture.⁵⁶⁻⁵⁹ These studies focus on either scanning several transition metal SACs on a particular substrate^{56,57} or propositions of a particular SAC as an electrocatalyst with a lower overpotential than earlier reported catalysts.^{58,59} The notable among these works is the study by Liu et al. with an objective to bridge the chemical understanding behind the activity of different transition metal SACs from an electrochemical viewpoint by examining the activity trends and electronic nature of the SACs through the Gibbs free energies of limiting steps in electrocatalytic NRR.⁶⁰

However, an insightful and penetrating study highlighting the electronic nature and reactivity of SACs on graphene and the implications of doped support in augmenting the

catalytic activity of metal SAC in question is still amiss. In short, we are missing out on the innate feature of metal atoms that distinguishes the catalytic reactivity of one metal from the other and are bereft in principle. Further, the trend of scanning several SACs, based on the Gibbs free energy of the limiting step of NRR is extremely erratic, with sensitivity to the methodology used. Reported prognosis of efficient electrocatalysts for NRR from DFT calculations are deduced based on the method applied and description of the metal with a given set of atomic orbitals and given model.

Considering all the above-mentioned key points, this chapter presents a consolidated study to address the so far unaccounted aspects of theoretical studies in identifying a graphene based 2D supported SAC for NRR. The purpose of the study is to identify a low cost, active, stable and reusable metal SAC on graphene support that is unvarying with respect to the method applied, description of the metal atom and model implemented in the computational study. For this, we carry out one of the most extensive study on six different transition metal SACs, i.e. V, Fe, Ni, Ru, W and Re anchored at distinct modes of BN-doping on periodic model (Cn sheet) and non-periodic models (C-42zz and C-54zz nanoflakes) of graphene. These metal SACs (V, Fe, Ni, Ru, W and Re) are chosen looking into their high NRR activity as per previous experimental reports on SAC^{44,61-63} and to account for a correlation between the magnetic property and catalytic nature.⁶⁴ The implication of atomic/orbital representation of metals has been critically analysed through different pseudopotentials, implemented as Plane Wave (PW) basis, in periodic calculations and basis sets defined by Linear Combination of Atomic Orbitals (LCAOs) in nonperiodic calculations. While the periodic DFT methodology provides a closer-to-real system electronic description of metal SACs anchored on graphene; the non-periodic calculations have been employed to provide a more pronounced electronic description of atomic orbitals. Thereby, a more accurate description of the electronic structure and the activity of the metals can be achieved from non-periodic calculations. This becomes essential when there is a need to identify the optimal substrate for metal SACs. Thus, the robustness of different concentrations of BN dopants on graphene models such as nanoflakes of different sizes and nanosheet, DFT methodologies and orbital definition of different metals to their chemical nature has been gauged. Reactivity descriptors such as

Dual descriptor^{65,66} and Multiphilic descriptor⁶⁷ are applied as leads while we explore the exhaustive aspects of methodology, model and description of the metal center. This investigation provides a detailed examination of metal SACs through their reactivity descriptors and is an absolute bridge to correlate the activity of metal SACs and their implementation as catalysts for NRR.

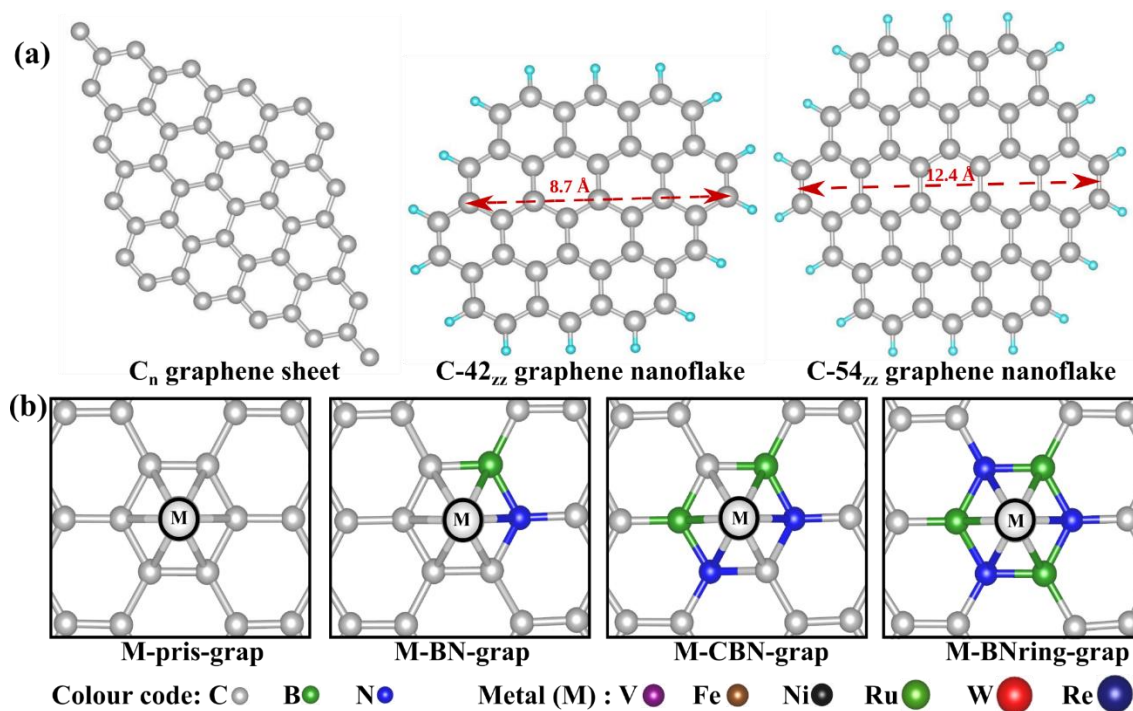


Figure 4.1: (a) Models of periodic C_n graphene sheet and non-periodic graphene nanoflakes C-42_{zz} and C-54_{zz} with their lateral widths of 8.7 Å and 12.4 Å, respectively (b) Different concentrations of BN-pair doping on graphene substrate with metal SAC represented by different colour code.

4.2 Computational Details

4.2.1 Models

The 2D graphene models of varying size and lateral width: a periodic model and two non-periodic models considered in this study are as shown in **Figure 4.1(a)**. The periodic C_n graphene sheet has been modeled by considering that the sp^2 hybridised carbon atoms are repeated infinitesimally along the xy-plane. Coming to the two non-periodic models, graphene nanoflakes with hydrogen termination on 42 carbon atoms with a lateral width of

8.7 Å and 54 carbon atoms with a lateral width of 12.4 Å, are respectively modeled as C-42_{zz} and C-54_{zz}. BN-pair dopants are introduced on the basal plane of the graphene models and the concentration of doping varies from zero, one, two and three BN-pair dopants in pris-grap, BN-grap, CBN-grap and BNring-grap systems, respectively. The periodic graphene models with varying concentration of BN-pair dopants are referred as C_n-pris-grap, C_n-BN-grap, C_n-BNring-grap, C_n-BNring-grap, respectively. Similar nomenclature of the nonperiodic graphene models with different BN-pair dopants are referred to C-42_{zz}-pris-grap and C-54_{zz}-pris-grap, and so on. When metal SACs are anchored on the graphene supports, it is ensured that the metal SAC is coordinated to the basal plane of graphene with BN-dopants and the same is referred to as M-pris-grap, M-BN-grap, M-grap-CBN and M-BNring-grap systems, respectively as shown in **Figure 4.1(b)**. When molecular dinitrogen is adsorbed on the SAC anchored graphene models, the associated systems are explicitly referred as M-pris-grap-N₂, MBN-grap-N₂, M-grap-CBN-N₂ and M-BNring-grap-N₂, respectively of periodic C_n model or non-periodic C-42_{zz} and C-54_{zz} models.

4.2.2 Computational Methodology

All periodic calculations on C_n graphene sheet and its BN-pair doped analogues are carried out using the Vienna ab initio Simulation Package (VASP) software based on plane wave (PW) basis.⁶⁸ The projected augmented wave (PAW) method⁶⁹ has been employed to describe the electron core-interactions. The nonmetallic atoms: C, B and N are described by PAW potentials that treat 2s and 2p as valence states while the metal SACs are described by two different PAW potentials: the conventional PBE pseudopotential with ns(n-1)d valence states and PBE_{pv} pseudopotential with ns(n-1)p(n-1)d valence states. A generalized gradient approximation (GGA) implemented in the Perdew- Burke-Ernzerhof (PBE)⁷⁰ functional has been used for geometry optimization with the cutoff energy set at 520 eV. The geometries are allowed to relax till the energy and forces of each atom reach a convergence criterion of 10⁻⁶ eV and 0.005 eV/atom respectively. All the geometries are sampled by a (2 × 2 × 1) Monkhorst–Pack kpoint grid with a vacuum space of 20 Å along the Z-direction to avoid inter-layer interactions. Spin polarized calculation has been carried

out for geometries with Fe, Ni and Ru metal atoms; while non-spin polarized calculation has been carried out for V, W and Re counterparts. For electronic structure calculations, the relaxed geometries are sampled at $(11 \times 11 \times 1)$ Monkhorst–Pack kpoint grid.

The non-periodic calculations are carried out with a linear combination of Gaussian-type orbitals and an auxiliary framework of DFT implemented in the deMon.5.0. program.⁷¹ A Perdew- Burke-Ernzerhof (PBE) exchange and correlation functional⁷⁰ has been considered to optimize pristine and BN-pair doped geometries of C-42_{zz} and C-54_{zz} nanoflakes to their corresponding lowest spin state with a restricted or restricted-open Kohn Sham formalism. The GEN-A2 auxiliary functions have been used to fit the charge density⁷² of all the geometries and their N₂ adsorbed geometries with their geometrical and SCF convergence criteria set at 5×10^{-4} a.u. and 10^{-8} a.u. respectively. Several basis sets shipped with the program have been considered for representing the atomic orbitals of the metal SACs, while a DZVP⁷³ (double ζ valence polarized) basis set has been employed for C, B, N and H atoms. The lighter 3-d transition metal: V, Fe and Ni are described by the DZVP, DZVP-GGA⁷⁴ and WACHTERS⁷⁵ basis sets that treat both core and valence electrons explicitly; as well with the Stuttgart-Dresden effective core potential (ECP)⁷⁶ and Los Alamos National Laboratory 2-double- ζ effective core potential (LANL2DZ)⁷⁷ basis that provide an implicit treatment to core electrons with an explicit treatment of valence electrons. The heavier 4-d and 5-d metals (Ru, W and Re) have been represented with an implicit treatment of core and explicit treatment of valence electrons defined by Stuttgart-Dresden ECP and quasi-relativistic effective core potential (QECP), and LANL2DZ basis sets. The QECP basis has been considered only for heavier 4-d and 5-d metals to account for their relativistic effect. Non-periodic calculations portray a definite electronic description, therefore an ideal electronic description of 2D materials and the metals can be achieved. To bring forth the factual electronic nature and the chemical activity of these 2D material supported SACs, non-periodic calculations have been carried out in this study.

The stability of metal SACs on the 2D graphene based supports has been measured through their binding energy, E_b . The binding energy of the metal on the pristine and BN-pair doped graphene supports is calculated by the equation,

$$E_b = E(\text{SAC-grap}) - E(\text{grap}) - E(\text{SAC}) \quad (4.1)$$

where, $E(\text{SAC-grap})$ and $E(\text{grap})$ are the total electronic energies of the various graphene supports with and without metal SAC and $E(\text{SAC})$ is the electronic energy of the single metal atom. The efficacy of these SAC-grap systems to capture free dinitrogen molecule has been computed in terms of the adsorption energy, E_{ads} of dinitrogen and it has been calculated by the equation,

$$E_{\text{ads}} = E(\text{SAC-grap-N}_2) - E(\text{grap-SAC}) - E(\text{N}_2) \quad (4.2)$$

where, $E(\text{SAC-grap-N}_2)$ is the total electronic energy of N_2 adsorbed SAC-grap systems, $E(\text{grap-SAC})$ and $E(\text{N}_2)$ are the electronic energies of graphene support with metal atom and free nitrogen molecule respectively. Earlier reports on metal SACs have highlighted the parallel or side-on mode of adsorption to show a larger N-N bond elongation as compared to the perpendicular or end-on mode of adsorption⁷⁸, therefore, only the parallel mode of N_2 adsorption has been considered in this chapter.

4.2.3 Reactivity descriptors and Gibbs Free Energy Calculations

The Dual Descriptor and Multiphilic descriptor are derived respectively, from the Fukui indices and group philicity of the metal centers. For periodic DFT calculations, the Fukui function or local philicity is calculated by the finite difference method as reported by Ceñón et al.⁷⁹ where electrons are added or removed by using the NELECT keyword to/from the neutral system. The Fukui indices, $f^-(r)$ and $f^+(r)$ of the metal SACs and coordinating atoms are computed by using the Henkelman's program⁸⁰ that integrate charges of the systems from their Voronoi volumes. The expressions for computing Fukui indices from their condensed charges are represented by,

$$f^-(r) = q^N - q^{N-1} \quad \text{and} \quad f^+(r) = q^{N+1} - q^N \quad (4.3)$$

where, q^N , q^{N-1} and q^{N+1} are charges on the atoms with N, N-1 and N+1 electrons, respectively. For non-periodic DFT calculations, the Fukui indices of metal centers and coordinating atoms on C-42_{zz} and C-54_{zz} nanoflakes are computed analytically as reported by Flores-Moreno et al.⁸¹ and implemented in the deMon.5.0 program. The electrophilic and nucleophilic Fukui functions are evaluated by removing or adding electrons to the frontier orbitals and thereby corresponds to $f^-(r)$ and $f^+(r)$, respectively. The group

philicity w_g^α , on the other hand, corresponds to the condensed local philicity over the metal center and atoms coordinated to it and is thereby expressed as,

$$w_g^\alpha = \sum_{k=1}^n w_k^\alpha \quad (4.4)$$

where $\alpha = +$ for nucleophilicity or $-$ for electrophilicity, k is the metal SAC and n is the number of atoms coordinated to the metal center, w_k^α is the local philicity. Accordingly, the Dual descriptor $f^{(2)}(r)$ and Multiphilic descriptor $\Delta w(r)$ are defined as the difference between nucleophilic and electrophilic Fukui indices and group nucleophilicity and electrophilicity, respectively. They are evaluated by using the equations,

$$f^{(2)}(r) = f^+(r) - f^-(r) \quad \text{and} \quad \Delta w(r) = w_g^+ - w_g^- \quad (4.5)$$

These reactivity descriptors have been reported to be more accurate descriptors^{82,67} than the Fukui function as it can reveal the nucleophilic ($f^{(2)}(r)$ and $\Delta w(r) < 0$) and electrophilic ($f^{(2)}(r)$ and $\Delta w(r) > 0$) centres simultaneously.

Although the reactivity descriptors provide a description to the electrophilicity or nucleophilicity of the metals, the feasibility of these metals to adsorb dinitrogen and reduce it to ammonia will rest on their free energy change. The Gibbs free energy change for periodic calculations on dinitrogen adsorption and elementary reaction steps of NRR has been calculated by the equation, $\Delta G = \Delta E + \Delta ZPE - T\Delta S$, where ΔE is the change in electronic energy, ΔZPE is the change in Zero Point Energy, T ($=298.15$ K) is the room temperature in Kelvin scale and ΔS is the change in vibrational entropy between the final and initial geometries. The zero-point energy and entropy terms are evaluated from the vibrational frequency calculations. The free energy of N_2 adsorption and the elementary reaction steps of NRR for non-periodic calculations of SACs on C-42_{zz} and C-54_{zz} systems are computed with the thermodynamic quantities derived from frequency calculations at room temperature. The relation for free energy change in non-periodic calculations is $\Delta G = \Delta E + \Delta H_{\text{corr}} - T\Delta S_{\text{corr}}$, where ΔE is the change in electronic energy, ΔH_{corr} is the change in enthalpy correction and ΔS_{corr} is the change in entropy correction at room temperature.

4.3 Results and Discussions

4.3.1 Binding energy of metal SACs

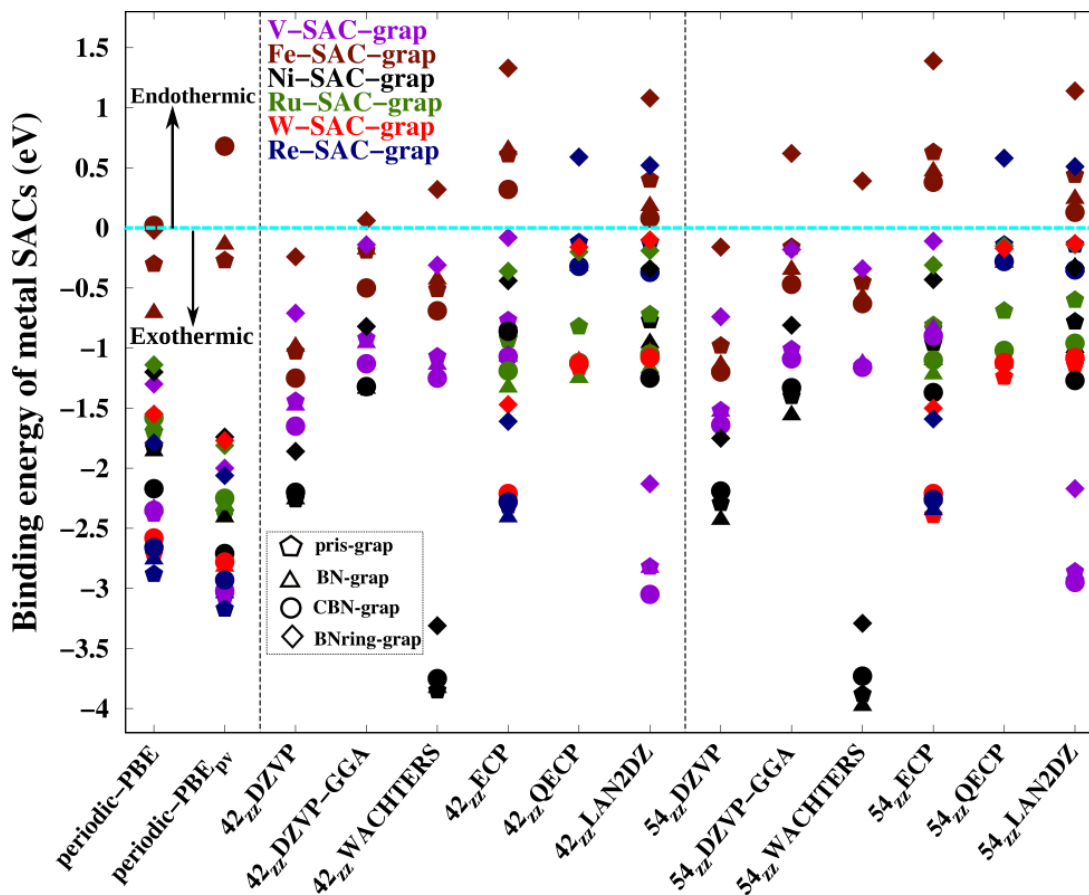


Figure 4.2: Binding energies of the metal SACs on periodic and non-periodic graphene supports. Metals on the negative scale of cyan line are stable and show exothermic E_b on the graphene supports. Symbolic representations of BN-doping is provided in inset along with colour scheme of the metals.

The binding energies, E_b of single metal atoms on periodic and non-periodic models of graphene with different modes of BN-pair doping is provided in **Figure 4.2**. It is observed that most of the metals considered in our study show a stable anchoring on the graphene supports with their exothermic binding energies varying with respect to the change in graphene model, DFT methodology and description of the metal atom. Coming to the observations of binding energies from periodic calculations, the metals are found to

anchor strongly, with higher negative binding energies, on the graphene support when PBE_{pv} pseudopotentials are used for defining the metals as compared to PBE pseudopotentials in all metals, except Fe metal. From **Figure 4.2** the heavier 5-d transition metals, W and Re are found to show higher binding energies than the lighter 3-d and 4-d metals, with the exception of V. It can be noted that most metal single atoms show higher binding energies on the pristine graphene support and it decreases as the concentration of B and N dopants increases with all the metal single atoms being the least stable on their corresponding BNring-grap support. On the other hand, the binding energies obtained from non-periodic calculations are found to be insensitive to the size of the graphene nanoflakes; however as anticipated, the binding energy of metals are sensitive to the basis set describing the metal orbitals. The binding energies of 3-d metals, except V-SAC, tend to be higher as the basis sets become more exhaustive and all electrons are treated exclusively i.e., DZVP, DZVP-GGA and WACHTERS when compared to basis sets with implicit core electrons. Amongst the metals described with implicit core electrons, the 4-d metal Ru shows a consistent binding energy on all supports irrespective of the change in metal basis. It is also to be noted that the heavier 5-d metals are extremely sensitive to the metal basis set and their stability on the graphene support decreases when QECP and LANL2DZ basis are implemented instead of the ECP basis; in particular, Re on BNring-grap support shifts from an exothermic binding energy of 1.5 eV (with ECP basis) to an endothermic binding energy of - 0.5 eV when computed with QECP and LANL2DZ basis sets. Coming to the role of dopants, the influence of B and N dopants on the substrate and their efficacy to stabilise the metal atom becomes more prominent with a definite electronic description of the metal as different metals show optimal binding conditions on different substrates. For instance, V and Fe metals are found to prefer CBN-grap substrates; Ni, Ru and Re prefer BN-grap substrates and W prefers pris-grap substrate. While a conclusive comment cannot be made on which metal shows the highest stability than the rest due to diverse treatment of core and valence electrons; it is interesting to note that in all basis set considerations, Fe metal shows a lower stability on graphene and its BN-pair doped substrates in periodic as well as non-periodic calculations.

4.3.2 Reactivity descriptor of metal SACs

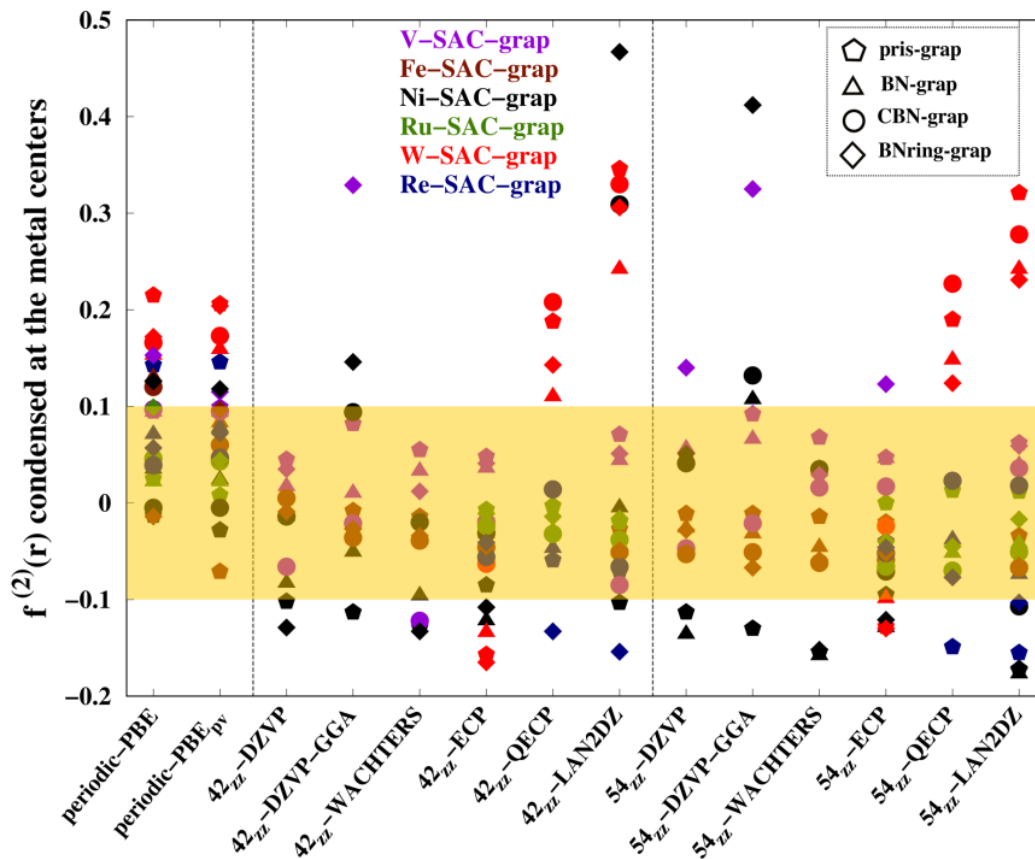


Figure 4.3: Dual descriptor, $f^{(2)}(r)$ condensed at the metal centers on periodic as well as non-periodic models of pristine and BN-heteroatom doped graphene systems. Metal colour code and the notation of the support when BN-pair dopants are introduced is indicated in inset.

While it is important to account for the stability of the metals on the graphene substrates, the activity of the metal defined by the reactivity descriptor is a more crucial factor to be accounted for the SAC-grap system to be employed as a catalyst for NRR. The reactivity of carbon atoms in basal plane of graphene nanoflakes has been discussed by Azeez et. al⁸³ to be lower than those of peripheral atoms. It was observed that as boron and nitrogen dopants are introduced on the basal plane of the C-42_{zz} graphene model, there is a significant change in the reactivity pattern as B-atoms become nucleophilic centres and N-atoms become electrophilic centres in BN-grap and CBN-grap support; while in BNring-

grap support both B and N atoms behave as electrophilic and nucleophilic centres and the overall reactivity of the support increases as such. It can be observed that the charge disparity created by boron and nitrogen atoms when doped on graphene plays a major role in influencing the reactivity pattern of the graphene supports. Thereby, when SACs are anchored on the basal plane of these graphene supports, the metal d-orbitals form hybridized d-p orbitals upon conjugation with the p-orbitals of B and N atoms bonded to it. The nature of dopant atoms on the support influences the reactivity pattern of the metals and the same has been computed in terms of Dual and Multiphilic descriptors.

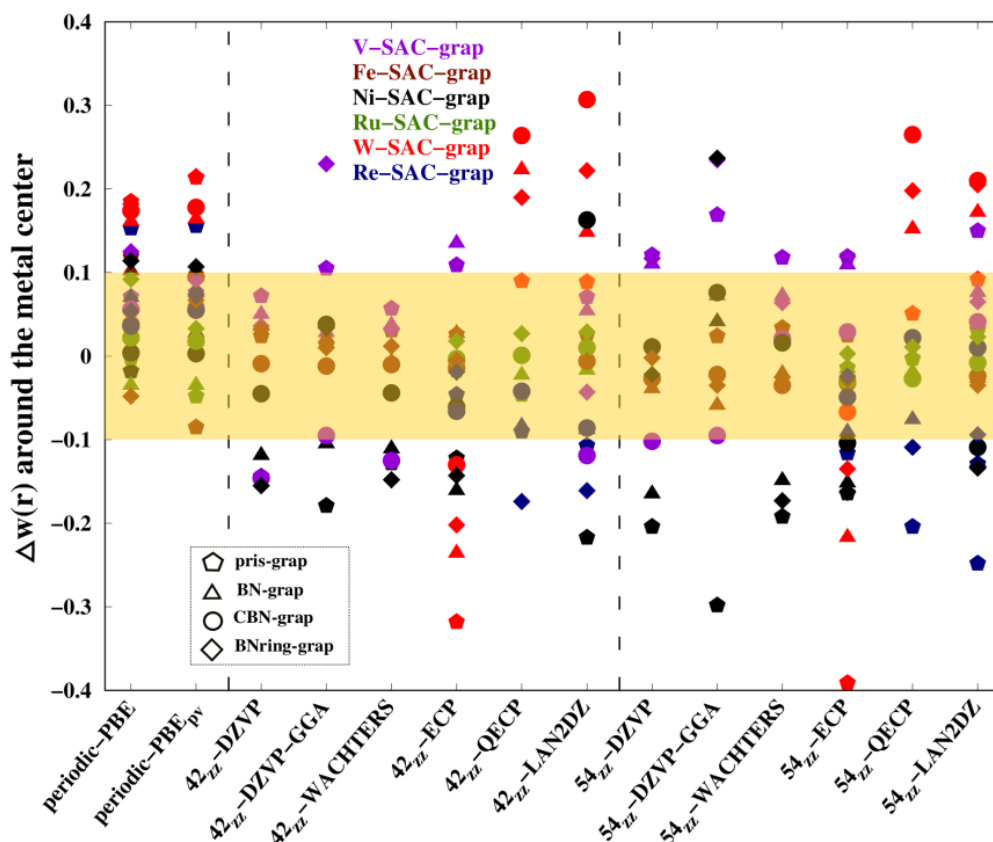


Figure 4.4: Multiphilic descriptor, $\Delta w(r)$ around the metal center on periodic periodic as well as non-periodic models of pristine and BN-heteroatom doped graphene systems. Metal colour code and the notation of the support when BN-pair dopants are introduced is indicated in inset.

The Dual descriptor, $f^{(2)}(r)$ and Multiphilic descriptor $\Delta w(r)$ on different BN-pair doped metal SAC-graphene supports as obtained from periodic and non-periodic calculations carried out by considering several metal pseudopotentials and basis sets are as shown **Figures 4.3** and **4.4**. SAC-graphene systems with $f^{(2)}(r)$ and $\Delta w(r) \approx 0$ are neither strong electrophilic or nucleophilic centers, thereby we will focus on the systems with higher electrophilicity ($f^{(2)}(r)$ and $\Delta w(r) > 0.1$) and nucleophilicity ($f^{(2)}(r)$ and $\Delta w(r) < 0.1$). It can be seen from **Figures 4.3** and **4.4** that W and Ni followed by Re systems show higher nucleophilicity, whereas W shows the highest electrophilicity on all graphene supports followed by V-BNring-grap, Re-pris-grap, Ni-BNring-grap and Fe on pris-grap and BN-grap supports. While periodic calculations show an inclination towards an electrophilic nature of the metal SAC/graphene systems, there is no significant change in the reactivity pattern, both $f^{(2)}(r)$ and $\Delta w(r)$, when different metal pseudopotentials are employed. Coming to the non-periodic calculations, the Multiphilic descriptor which incorporates the philicity of atoms coordinated to metal centers, gives an overall understanding of the reactivity of SAC-graphene supports and it becomes more pronounced. The nucleophilicity of SAC-graphene systems are more pronounced when the local environment of the metal and group philicity are considered, as seen in **Figure 4.4**. Additionally, the reactivity pattern of the SACs and SAC-graphene systems is predictably sensitive to the metal basis but it also becomes sensitive to the change in size of the nanoflakes. For instance, the reactivity of V-SAC and V-grap systems become more pronounced in larger C-54_{zz} graphene nanoflake, while that of Ni and W gets masked. The Dual Descriptor analysis reveals a consensus on the higher activity pattern of W, V, Re and Ni metals from periodic as well as non-periodic calculations. The same pattern can be seen from Multiphilic descriptor analysis which highlights the role of B and N dopants in accentuating the reactivity of the SAC-graphene systems.

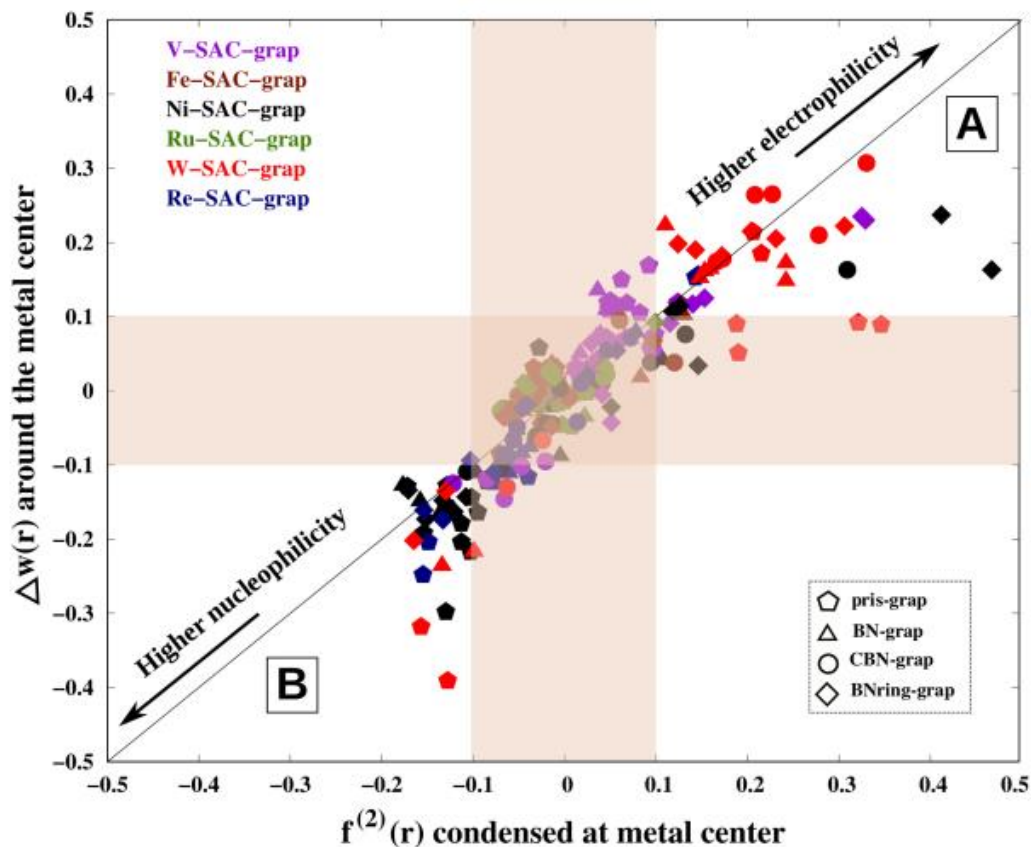


Figure 4.5: $\Delta w(r)$ vs $f^{(2)}(r)$ around the metal center on periodic periodic as well as non-periodic models of pristine and BN-heteroatom doped graphene systems. Metal colour code and the notation of the support when BN-pair dopants are introduced is indicated in inset.

One fascinating aspect is the linear relationship observed between the Dual descriptor and Multiphilic descriptor as seen in **Figure 4.5**. It can be noted from $f^{(2)}(r)$ and $\Delta w(r)$ values of SACs and SAC-graphene systems that the metal centers show a major contribution in directing the reactivity of the system and these two descriptors can be used synonymously for SACs anchored graphene systems. Another interesting aspect from the linear plot in **Figure 4.5** is the two designated regions of higher electrophilicity, A and higher nucleophilicity, B. In region A, aside from the information that W, V, Ni and Re metals show higher electrophilicity, the graphene supports are mostly BN-grap, CBN-grap and BNring-grap. On the other hand, region B of higher nucleophilicity with W, Re and Ni metals are mostly coupled with pris-grap and a few BN-grap supports. In general, the

reactivity of the SAC/graphene systems is higher when B and N dopants are introduced in the support and the overall system tends to be electrophilic in nature. It is also notable that V, Ni, W and Re SACs are found to be stable on the pristine and BN-pair doped supports from our earlier section on metal binding energy. Thereby, it becomes interesting as these metals with a higher reactivity are also stable on the graphene support and their synthesis is feasible from experimental point-of-view.

4.3.3 Dinitrogen adsorption and activation on metal SACs

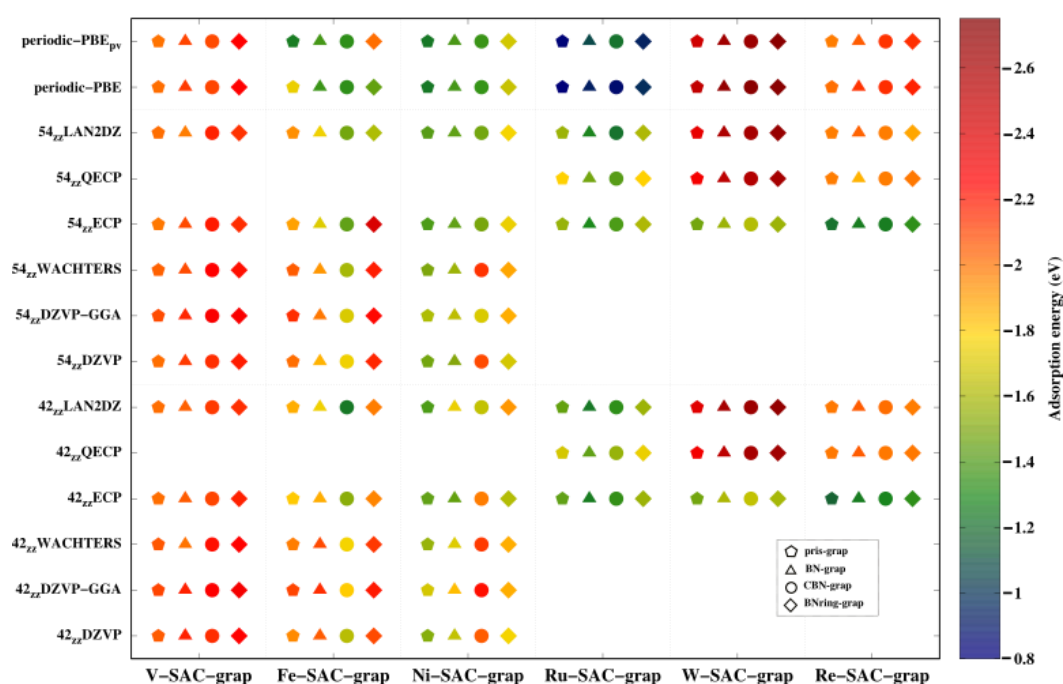


Figure 4.6: Adsorption energy of dinitrogen on different metal SACs; inset shows the colour scheme changes from blue to red as the adsorption of N_2 becomes more feasible.

The activity pattern of metal SACs on different graphene supports, as observed from the analysis of reactivity descriptors, has been further corroborated to the efficacy of the metals to adsorb and activate dinitrogen molecule. The adsorption energies of free dinitrogen molecule on the SAC-grap systems are calculated and plotted in **Figure 4.6**. The adsorption of N_2 on all SACs anchored graphene supports are found to be feasible and exothermic (-0.82 eV to -2.80 eV) in periodic as well as non-periodic calculations. The

exothermic chemisorption energies of dinitrogen on all metal- SAC-grap systems validate the potential of these metals to be employed as catalysts for dinitrogen activation and NRR. It is particularly notable that Ru metal SAC with a milder activity as compared to the rest of the metals also shows a lower chemisorption of N₂, -0.82 to -1.80 eV on periodic and non-periodic systems of graphene and BN-pair doped analogues. It can be observed from **Figure 4.6** that the efficacy of the SAC-grap systems to adsorb N₂ has been influenced by different modes of BN-pair doping, metal pseudopotentials and basis sets and size of the nanoflakes considered in periodic and non-periodic calculations. In periodic calculations with the introduction of B and N dopants and as the system changes from SAC-pris-grap to SAC-BNring-grap, the chemisorption of N₂ tends to become more exothermic. However, a significant change brought about by the addition of valence (n-1)p-states in PBE_{pv} pseudopotentials of metals is seen in the case of Fe-SAC and Ru-SAC anchored graphene systems, while the rest of the metals remain insensitive to the change in metal pseudopotentials. Amongst the metal-graphene systems considered in this chapter; V, W and Re systems are found to show higher chemisorption of N₂ with adsorption energies of -2.3 eV, -2.8 eV and -2.2 eV respectively on their respective BNring-grap systems.

Likewise, the adsorption of dinitrogen on all metal anchored non-periodic graphene models are found to be enhanced as the concentration of BN-pair dopants increases around the metal in the basal plane of graphene. The implication of considering several metal basis sets cannot be prominently seen in the case of V-SAC-grap systems as the N₂ adsorption energies remain nearly consistent despite the implicit treatment of core electrons in ECP and LANL2DZ basis sets. Fe-SAC-grap and Ni-SAC-grap systems tend to show a more exothermic adsorption of dinitrogen when described with explicit core and valence electrons in DZVP, DZVP-GGA and WACHTERS basis sets as compared to ECP and LANL2DZ basis. The heavier metals (Ru, W and Re) described with implicit core electrons tend to show a higher chemisorption when quasi-relativistic metal basis sets, QECP and LANL2DZ are employed over the metal ECP basis set. Thereby, the 3-d metals show a pronounced chemisorption of dinitrogen with metal basis that define both core and valence electrons explicitly while the heavier 4-d and 5-d metals are highly affected with the inclusion of quasi-relativistic factors in the metal basis. In addition, the adsorption energies

of N₂ on V-SAC-grap, W-SAC-grap and Re-SAC-grap systems are found to be insensitive to the size of graphene nanoflakes, while the same cannot be seen for Fe, Ni and Ru systems.

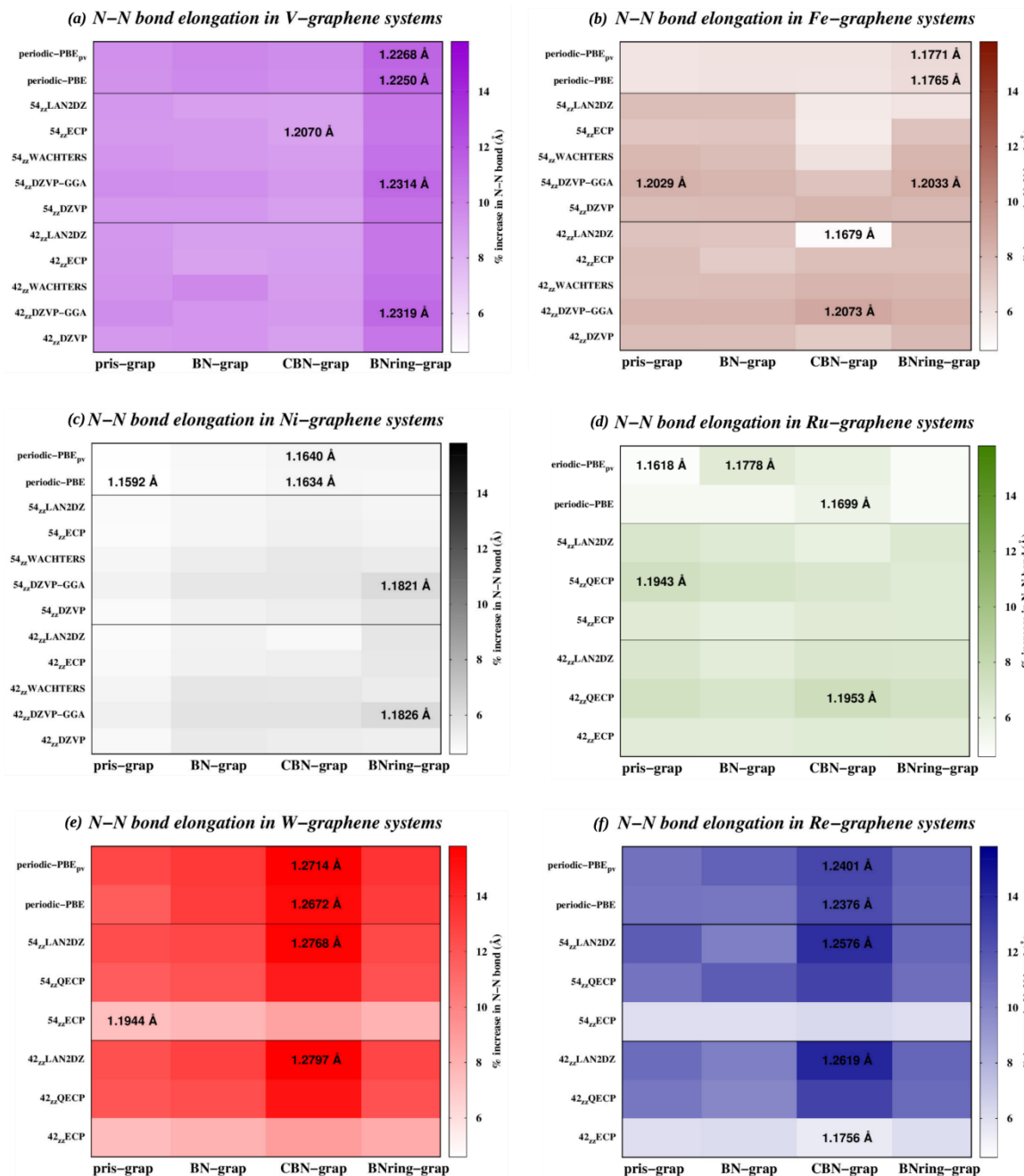


Figure 4.7: Percentage increment in N-N bond lengths when N₂ is adsorbed on the M-SAC-grap systems. The gradient plot is set with a value of 1.16 Å and 4.6% bond length increment observed in Ni-SAC-pris-grap as white; the intensity of the colour codes for respective

metals increases as the N-N bond length increases. For each metal, the largest value of N-N bond in periodic and non-periodic models are provided along with the least value of N-N bond length.

Most significantly, it can be noted that V, W and Re metals show a consistently higher and similar affinity towards chemisorption of N₂ molecule in periodic as well as non-periodic calculations, albeit the difference in the DFT methodologies implemented. In particular, adsorption energies computed with the V metal defined by the DZVP-GGA basis set is found to show similar results to the periodic calculations on V-SAC-grap systems. A similar case can be observed on W-SAC-grap and Re-SAC-grap systems when metal atomic orbitals described by LANL2DZ basis set has been found to show nearly similar N₂ adsorption energies to the periodic calculations. The same cannot be seen in the case of Fe-SAC-grap, Ni-SAC-grap and Ru-SAC-grap systems where the adsorption energies in nonperiodic models tend to be overestimated as compared to the adsorption energies in the periodic models. This consistent and similar pattern of adsorption energy observed in the case of V, W and Re metal SACs, in spite of different DFT methodologies and atomic orbital representation, validates the prepotency of local reactivity of these metals which is in direct correspondence to the reactivity pattern achieved from their reactivity descriptors.

The chemisorption energies of N₂ on different metal SACs can be correlated to the activation of dinitrogen which is measured in terms of the elongated N-N bond of dinitrogen molecule when adsorbed on the M-SAC-grap systems. A percentage increase in the N-N bond length is made with reference to the N-N bond length in free N₂ molecule, i.e. 1.11 Å and 1.12 Å for periodic and non-periodic calculations respectively. A gradient plot on the percentage increment in N-N bond length on periodic and nonperiodic V-SAC-grap-N₂ systems with different modes of BN-pair doping is as provided in **Figure 4.7(a)**. A consistent pattern of N-N bond activation on V-SAC-grap-N₂ can be observed where the BNringgrap substrates show the largest bond elongation in spite of the difference in DFT methodologies, basis sets and pseudopotentials to define the metal and nanoflake size in the periodic and nonperiodic models. The N-N bond in V-BNring-grap-N₂ systems is elongated by 11%, i.e., 1.23 Å in the periodic model and nonperiodic nanoflakes when V metal is defined by DZVP-

GGA basis set. The higher bond activation observed in V-BNring-grap-N₂ systems is in direct correlation to the adsorption energy of dinitrogen molecule and the higher reactivity of V metal as discussed earlier in the adsorption and reactivity descriptor section. While the extent of bond activation in Fe, Ni and Ru systems, **Figures 4.7(b-d)** range from 4.6–8.7 % owing to their less exothermic adsorption of dinitrogen molecule, which correlates to their lower reactivity pattern, these metals fail to show a consistent pattern in N-N bond activation with the change in concentration of BN-pair dopants, different basis sets or pseudopotentials to define the metal and size of graphene models in the periodic and nonperiodic calculations. Coming to the W-SAC-grap-N₂ and Re-SACgrap-N₂ systems in **Figures 4.7(e-f)**, these metals show a consistent pattern where a larger N-N bond elongation is found on their respective CBN-grap substrates in periodic and non-periodic calculations. The extent of N-N bond activation on W-CBN-grap-N₂ and Re-CBN-grap-N₂ systems range from 15.4% (1.27 Å) and 13% (1.24 Å) respectively in periodic models to approximately 16% (or 1.28 Å) and 14% (or 1.26Å) respectively in their non-periodic counterparts when the metal is represented by the LANL2DZ basis set. Therefore, W and Re metals anchored on CBN-grap substrate possess a higher potential to chemisorp and activate dinitrogen molecule followed by V on a BNring-grap substrate. It is notable that periodic calculations carried out with metal PBEpv pseudopotentials generated geometries with higher N-N bond activation as compared to those carried out with PBE pseudopotentials in V, W and Re metals.

To also account for the experimental analogy of N-N bond activation on the adsorbed N₂ molecule; IR-stretching frequency which is a fingerprint to represent the strength of a chemical bond has been evaluated for the M-SAC-grap-N₂ systems and a redshift is observed in N-N stretching frequency. The red-shift in N-N bond is consistently higher on the V-BNring-grap, W-CBN-grap and Re-CBN-grap systems despite the change in DFT methodology, size of the graphene models, metal pseudopotentials and basis sets. This consistent pattern of red-shift in V, W and Re corresponds to the N-N bond activation observed earlier; with W-CBN-grap showing the highest red-shift of 1026 cm⁻¹ in periodic calculations and 950 cm⁻¹ in non-periodic calculations. This is followed by Re-CBN-grap systems with a N-N bond red-shift of 894 cm⁻¹ and 876 cm⁻¹ from its corresponding periodic and non-periodic systems, respectively. Finally, the V-BNring-grap systems with an 11 %

N-N activation shows a red-shift of around 810 cm^{-1} in its periodic system and 740 cm^{-1} in the non-periodic system. It has been also found that Fe, Ni and Ru metal SACs with a relatively lower bond activation of 4.6–8.7 % shows a correspondingly lower red-shift ranging from 373 cm^{-1} to 612 cm^{-1} , respectively. This trend on N-N bond redshift corroborates to the earlier section on N-N bond activation and dinitrogen chemisorption energies on different metal SACs. Our observation on N-N bond red-shift and activation by V, W and Re SACs corroborate the N_2 adsorption energies and reactivity of the metals described via their reactivity descriptors earlier. Therefore, the qualitative reactivity description of metal SACs discussed earlier can be implemented as an important descriptor in the probe for a highly active metal SAC and a suitable 2D substrate that amplifies its activity.

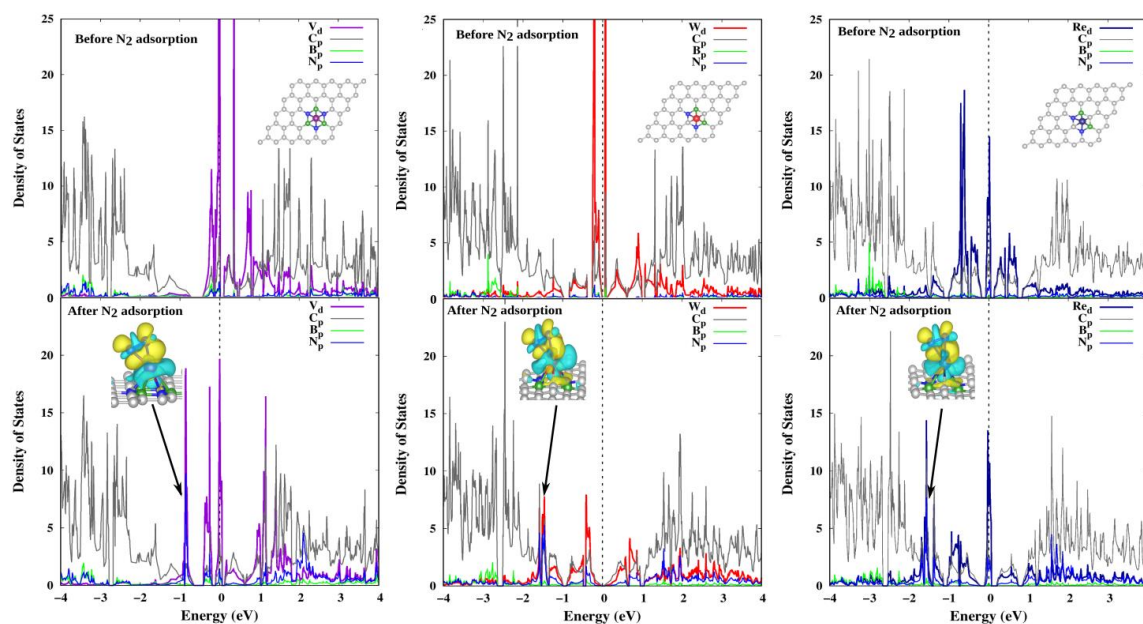


Figure 4.8: Projected Density of States of graphene supported SACs compared before and after N_2 adsorption on (a) $\text{C}_n\text{-V-BNring-grap}$, (b) $\text{C}_n\text{-W-CBN-grap}$ and (c) $\text{C}_n\text{-Re-CBN-grap}$; the charge density difference plots of M-grap- N_2 systems, made using Vesta 3.4⁸⁴, are as included in inset.

Following the investigation on N-N bond activation, the later part of the study is now restricted to the more active metals, i.e V, W and Re. While the activity of V, W and Re metals have been affirmed through their reactivity descriptor, higher N₂ chemisorption energies and N-N bond activation; a detailed understanding on the electronic properties before and after dinitrogen adsorption has to be accounted. Thus, an electronic analysis of V-BNring-grap-N₂, W-CBN-grap-N₂ and Re-CBN-grap-N₂ systems through the Projected Density of States (PDOS) examined before and after dinitrogen adsorption of the periodic models has been shown in **Figure 4.8**. The electron transfer from the metals to the dinitrogen molecule can be emphasized by the decrease in electron densities of the metal d-orbitals in the valence band. W and Re metals decrease significantly owing to charge transfer from metal to N₂. However, V-CBN-grap shows an exception as the decrease in electron densities in the valence band leads to generation of vacant d-orbitals in its conduction band. The reactivity of V-SAC on CBN-grap substrate can be thereby accounted to its electrophilic nature. While the heavier W and Re metals have electron rich d-orbitals and coordinate with dinitrogen via transfer of electrons to the π^* - π^* orbitals of N₂ molecule, V metal with its vacant d-orbitals coordinate to the N₂ molecule via π - π back donation. The charge density difference plots generated after the adsorption of dinitrogen in all three systems displays the hybridisation of metal d-orbitals with the π^* - π^* orbital of N₂ to form a stable M-SAC-grap-N₂ complex. Similarly, a metal-nitrogen d-p hybridized Highest Occupied Molecular Orbital (HOMO) can be observed when the Frontier Molecular Orbitals (FMO) of non-periodic models of V-BNring-grap-N₂, W-CBN-grap-N₂ and Re-CBN-grap-N₂ systems on the C-42_{zz} and C-54_{zz} nanoflakes. This hybridization of metal-nitrogen d-p orbital validates the analogy we had speculated to correlate catalytic activity with descriptors rather than hard-hard interactions controlled by charges.⁸⁵ With the consistent results obtained from periodic and non-periodic calculations on V, W and Re SACs described with specific metal basis sets in non-periodic calculations. The NRR process on V-BNring-grap is then subsequently investigated with DZVPGGA basis set while W-CBN-grap and Re-CBN-grap are investigated with LANL2DZ basis set.

4.3.4 NRR mechanism on V-BNring-grap, W-CBN-grap and Re-CBN-grap systems

Reduction of dinitrogen to ammonia on V-BNring-grap, W-CBN-grap and Re-CBN-grap systems has been evaluated on their corresponding periodic and non-periodic models. Periodic calculations on the above systems have been continued with metal PBE_{pv} and PBE pseudopotentials to account for the larger N-N bond activation in-spite of similar energetics. on-periodic calculations with DZVP-GGA basis set for V and LANL2DZ basis set for W and Re metals, has been carried out on the C-42_{zz} and C-54_{zz} nanoflakes. The NRR process, for N₂ adsorbed in parallel mode on these M-SAC-grap systems, follow the enzymatic route

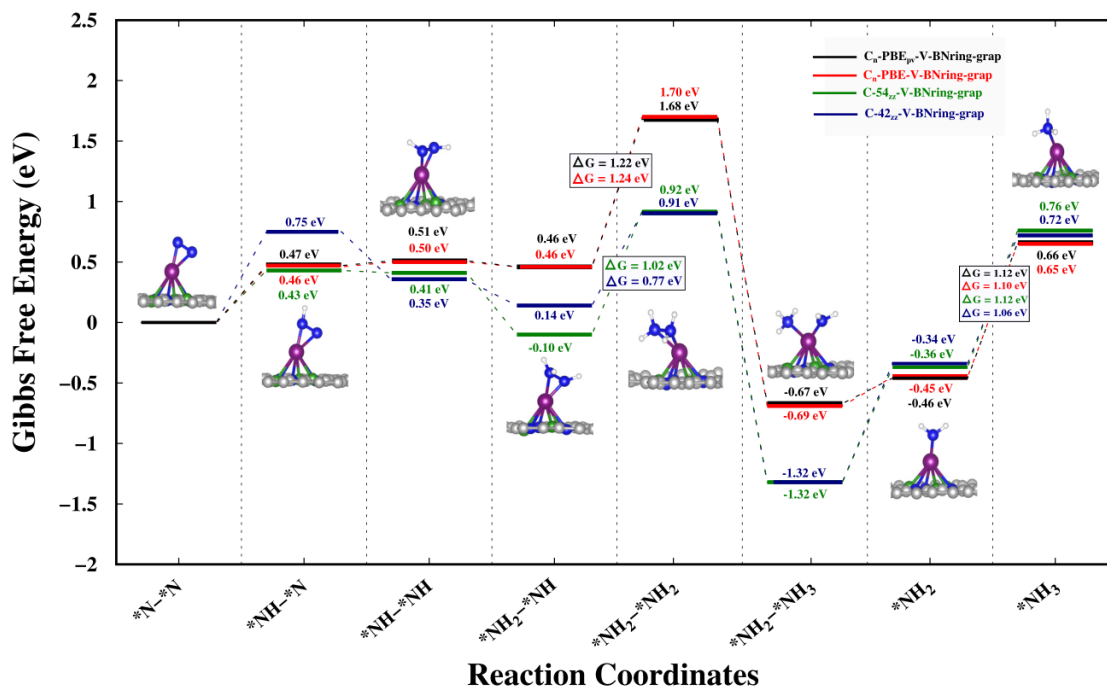


Figure 4.9: Enzymatic reaction mechanism of NRR on periodic and non-periodic V-BNring-grap models.

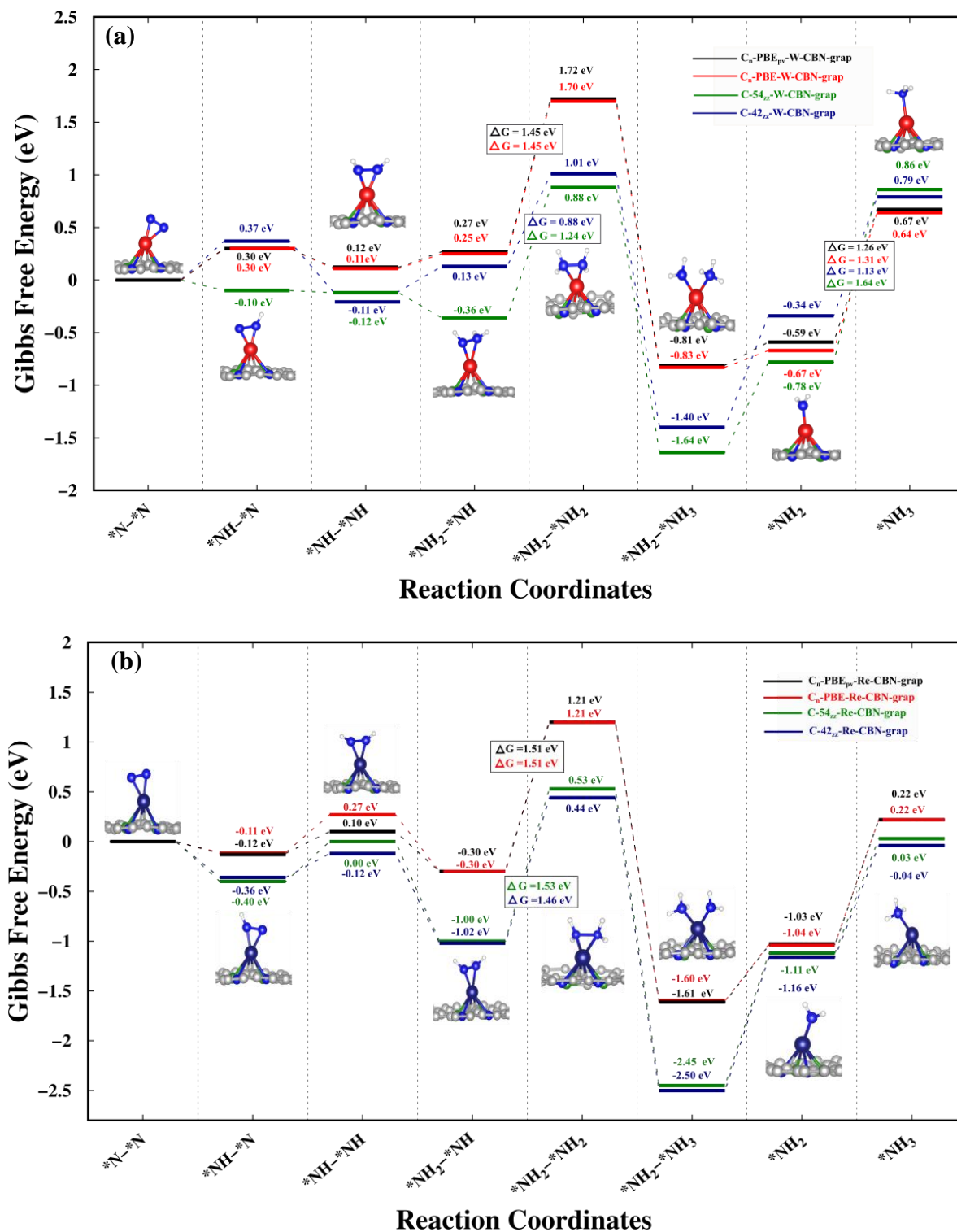


Figure 4.10: Enzymatic reaction mechanism of NRR on periodic and non-periodic (a) W-CBN-grap and (b) Re-CBN-grap models.

where atomic hydrogen atoms attack the N-atoms in an alternating fashion. The structures of N_xH_y intermediates and the change in Gibbs free energy for each hydrogenation step on periodic and non-periodic models of V-BNring-grap system are as shown in **Figure 4.9**, while those of W-CBN-grap and Re-CBN-grap systems are provided in **Figure 4.10**. It can be observed from the free energy diagram of V-BNring-grap system that the energies of intermediate reaction steps are more negative (i.e., exergonic) in non-periodic calculations as compared to periodic calculations. The orbital descriptions are more pronounced in non-periodic calculations with basis sets, thereby the electronic energy of the system becomes more negative leading to the lowering of free energy. Other than this overall lowering of free energy in non-periodic calculations, the energetics of each step is seen to follow the same pattern as in periodic calculations; for instance, the energy uphill steps, $*N_2 \rightarrow *N_2H$, $*NH_2-*NH \rightarrow *NH_2-*NH_2$ and $*NH_2 \rightarrow *NH_3$ are endergonic in both periodic and non-periodic calculations on V-BNring-grap. This pattern of free energy lowering along with similar energetics can be observed in the free energy diagram of W-CBN-grap and Re-CBN-grap systems provided in **Figure 4.10**. While the energy uphill steps in W-CBN-grap system is similar to that observed in V-BNring-grap system, Re-CBN-grap shows an exception with an exergonic (or energy downhill) $*N_2 \rightarrow *N_2H$ step but an endergonic $*N_2H \rightarrow *NH-*NH$ step.

Table 4.1: Gibbs free energies, ΔG (eV) of the crucial intermediate steps involved in enzymatic Nitrogen Reduction Reaction on V-BNring-grap models. The ΔG_{\max} of each model is highlighted in bold.

ΔG	C_nPBE_{pv}	C_nPBE	$C-42_{zz}$	$C-54_{zz}$
$* \rightarrow *N_2$	-1.62	-1.62	-2.23	-2.28
$*N_2 \rightarrow *N_2H$	0.47	0.46	0.75	0.43
$*NH_2-*NH \rightarrow *NH_2-*NH_2$	1.22	1.24	0.77	1.02

$*\text{NH}_2 \rightarrow *\text{NH}_3$	1.12	1.10	1.06	1.12
$*\text{NH}_3 \rightarrow *\text{N}_2$	-0.66	-0.65	-0.72	-0.76

Table 4.2: Gibbs free energies, ΔG (eV) of the crucial intermediate steps involved in enzymatic Nitrogen Reduction Reaction on W-CBN-grap models. The ΔG_{max} of each model is highlighted in bold.

ΔG	$\text{C}_n\text{PBE}_{\text{pv}}$	C_nPBE	C-42_{zz}	C-54_{zz}
$* \rightarrow *\text{N}_2$	-2.09	-2.04	-2.62	-2.52
$*\text{N}_2 \rightarrow *\text{N}_2\text{H}$	0.30	0.30	0.37	-0.10
$*\text{NH}_2\text{-}*\text{NH} \rightarrow *\text{NH}_2\text{-}*\text{NH}_2$	1.45	1.45	0.88	1.24
$*\text{NH}_2 \rightarrow *\text{NH}_3$	1.26	1.31	1.13	1.64
$*\text{NH}_3 \rightarrow *\text{N}_2$	-0.67	-0.79	-0.79	-0.86

Table 4.3: Gibbs free energies, ΔG (eV) of the crucial intermediate steps involved in enzymatic Nitrogen Reduction Reaction on Re-CBN-grap models. The ΔG_{max} of each model is highlighted in bold.

ΔG	$\text{C}_n\text{PBE}_{\text{pv}}$	C_nPBE	C-42_{zz}	C-54_{zz}
$* \rightarrow *\text{N}_2$	-1.52	-1.53	-1.98	-1.99
$*\text{N}_2 \rightarrow *\text{N}_2\text{H}$	-0.12	-0.11	-0.36	-0.40

$*\text{NH}_2\text{-*NH} \rightarrow *\text{NH}_2\text{-*NH}_2$	1.51	1.51	1.46	1.53
$*\text{NH}_2 \rightarrow *\text{NH}_3$	1.25	1.26	1.12	1.14
$*\text{NH}_3 \rightarrow *\text{N}_2$	-0.22	-0.22	0.04	-0.03

Tables 4.1-4.3 summarizes the crucial intermediate steps involved in NRR process on the above-mentioned SAC-graphene systems. These include N_2 adsorption, first hydrogenation step ($*\text{N}_2 \rightarrow *\text{N}_2\text{H}$), fourth hydrogenation step ($*\text{NH}_2\text{-*NH} \rightarrow *\text{NH}_2\text{-*NH}_2$) that generates a highly strained intermediate, final hydrogenation step ($*\text{NH}_2 \rightarrow *\text{NH}_3$) and the last NH_3 desorption step. The Gibbs free energy of N_2 adsorption on non-periodic systems is seen to be more exoergic, i.e. more negative than the periodic counterparts for all three SAC-graphene systems. The Potential-Determining Step (PDS) in V-BNring-grap and W-CBN-grap systems is seen to change from the fourth hydrogenation step ($*\text{NH}_2\text{-*NH} \rightarrow *\text{NH}_2\text{-*NH}_2$) in periodic calculations to the final hydrogenation step ($*\text{NH}_2 \rightarrow *\text{NH}_3$) in non-periodic calculations. It is notable that these two steps are the most energy uphill reaction steps ($\Delta G > 1.0$ eV), thereby both the steps limit the feasibility of N_2 reduction to NH_3 . The limiting potential, ΔG_{max} in periodic V-BNring-grap systems is found to be 1.22 eV to 1.24 eV, while the non-periodic counterparts show a limiting potential of 1.06 eV and 1.12 eV in C-42_{zz} and C-54_{zz} graphene nanoflakes, respectively. For W-CBN-grap systems, the limiting potential is found to be 1.45 eV in periodic systems, 1.13 eV in C-42_{zz} and 1.64 eV in C-54_{zz} graphene nanoflakes respectively. However, for periodic and non-periodic Re-CBN-grap systems, the PDS is the fourth hydrogenation step ($*\text{NH}_2\text{-*NH} \rightarrow *\text{NH}_2\text{-*NH}_2$) which involves formation of a torsionally bulk intermediate and the limiting potential ranges from 1.51 eV in periodic system to 1.46 eV in C-42_{zz}-Re-CBN-grap and 1.53 eV in C-54_{zz}-Re-CBN-grap system. From this investigation on N_2 reduction to NH_3 in SAC-graphene systems, it can be noted that the free energy of intermediate hydrogenation steps are more pronounced in non-periodic calculations as electronic descriptions are more accurate when basis sets are implemented. While all three metal-graphene systems can be seen to reduce dinitrogen to ammonia effectively, a lower

energy barrier is observed on V-BNring-grap where $1.06 \text{ eV} < \Delta G_{\text{max}} > 1.24 \text{ eV}$. Although the ΔG_{max} of V-BNring-grap is higher than previously reported V-SAC catalyst⁸⁶, the interesting aspect of our SAC-graphene system is the NH_3 desorption step. Most SAC/2Dsupport reported with lower ΔG_{max} would require the assistance of solution, heating, electropotential or etching to desorb NH_3 from the catalyst.⁸⁶⁻⁸⁸ The recyclability/reclaimability of the catalyst is another looming question that needs to be answered beyond an effective NRR process. From this computational study, we observed that NH_3 desorption can be easily carried out by N_2 as the $^*\text{NH}_3 \rightarrow ^*\text{N}_2$ step is exergonic and feasible by $\approx -0.66 \text{ eV}$ in $\text{C}_n\text{-V-BNring-grap}$, -0.72 eV in $\text{C-42}_{zz}\text{-V-BNring-grap}$ and -0.76 eV in $\text{C-54}_{zz}\text{-V-BNring-grap}$ systems. Thereby, this reclaimable V-BNring-grap catalyst with a low-cost metal has an advantage over several other 2D catalysts.

4.4 Conclusions

In summary, a comprehensive periodic and non-periodic DFT calculation has been carried out on six transition metal SACs anchored on pristine and BN-pair doped 2D graphene models with an objective to tailor a pragmatic heterocatalyst for NRR. This consolidated study highlights the susceptibility of metal reactivity with respect to the change in DFT methodology, size of the model, coordination of B and N dopants with the metal and most importantly, the orbital description provided by several basis sets and pseudopotentials. Dual and Multiphilic descriptors are found to bridge the inherent local activity and innate electronic nature of SACs. These descriptors yield consistently similar trends to the chemisorption efficacy and activation of N_2 and can be employed as leads to design efficient SAC/support couple for dinitrogen reduction. The mechanistic studies on the enzymatic mode of N_2 reduction to NH_3 on three select SAC/graphene system highlights similar free energy diagram in periodic as well as non-periodic calculations. This exhaustive analysis emphasizes that a qualitative idea of energetics and NRR limiting potential can be achieved from computational studies made on a less complex non-periodic model. Additionally, this study focuses on most convenient way to desorb NH_3 with N_2 and reclaimability of the catalyst which is usually ignored in most studies. Our computational investigation proposes V-BNring-grap catalyst as a low cost, highly active,

stable and reclaimable catalyst for NRR that can be developed with the currently available synthesis technology, thereby enabling efficient large scale and eco-friendly NH_3 production in future.

4.5 References

- (1) Schlögl, R.; *Angew Chem. Int. Ed.* **2003**, *42*, 2004–2008.
- (2) Erisman, J.W.; Sutton, M.A.; Galloway, J.; Klimont, Z.; Winiwarter, W.; *Nat. Geosci.* **2008**, *1*, 636–639.
- (3) Afif, A.; Radenahmad, N.; Cheok, Q.; Shams, S.; Kim, J. H.; Azad, A.K.; *Renewable Sustainable Energy Rev.* **2016**, *60*, 822–835.
- (4) Lan, R.; Tao, S.; *Electrochem. Solid-State Lett.* **2010**, *13*, B83–B86.
- (5) Haber, F.; *Naturwissenschaften* **1923**, *9*, 753–756.
- (6) Cherkasov, N.; Ibadon, O.; Fitzpatrick, P.; *Chem. Eng. Process.* **2015**, *90*, 24–33.
- (7) Zheng, G.; Yan, J. M.; Yu, G; *Small Methods* **2019**, *3*, 1900070.
- (8) Flöser, B. M.; Tuzek, F.; *Coord. Chem. Rev.* **2017**, *345*, 263–280.
- (9) Miyazaki, T.; Tanaka, H.; Tanabe, H.; Yuki, M.; Nakajima, K.; Yoshizawa, K.; Nishibayashi, Y.; *Angew. Chem. Int. Ed.* **2014**, *53*, 11488–11492.
- (10) Turner, J. J.; Simpson, M.B.; Poliakoff, M.; Maier, W.B.; Graham, M.A.; *Inorg. Chem.* **1983**, *22*, 911–920.
- (11) Kendall, A. J.; Mock, M. T.; *Eur. J. Inorg. Chem.* **2020**, *15*, 1358–1375.
- (12) Burford, R. J.; Yeo, A.; Fryzuk, M. D.; *Coord. Chem. Rev.* **2017**, *334*, 84–99.
- (13) Ostermann, N.; Siewert, I.; *Curr. Opin. Electrochem.* **2019**, *15*, 97–101.
- (14) Gu, N. X.; Ung, G.; Peters, J. C.; *Chem. Commun.* **2019**, *55*, 5363–5366.

- (15) Foster, S. L.; Perez Bakovic, S. I.; Duda, R. D.; Maheshwari, S.; Milton, R. D.; Minter, S. D.; Janik, M. J.; Renner, J. N.; Greenlee, L. F.; *Nat. Catal.* **2018**, 490–500.
- (16) Ohki, Y.; Uchida, K.; Tada, M.; Cramer, R. E.; Ogura, T.; Ohta, T.; *Nat. Commun.* **2018**, 9, 1–6.
- (17) Cao, B.; Starace, A. K.; Judd, O. H.; Bhattacharyya, I.; Jarrold, M. F.; López, J. M.; Aguado, A.; *J. Am. Chem. Soc.* **2010**, 132, 12906–12918.
- (18) Gates, B. C.; Flytzani-Stephanopoulos, M.; Dixon, D. A.; Katz, A.; *Catal. Sci. Technol.* **2017**, 7, 4259–4275.
- (19) Zhang, L.; Ren, Y.; Liu, W.; Wang, A.; Zhang, T.; *Natl. Sci. Rev.* **2018**, 5, 653–672.
- (20) Liu, L.; Corma, A.; *Chem. Rev.* **2018**, 118, 4981–5079.
- (21) Samantaray, M. K.; D’Elia, V.; Pump, E.; Falivene, L.; Harb, M.; Chikh, S. O.; Cavallo, L.; Basset, J.-M.; *Chem. Rev.* **2020**, 120, 734–813.
- (22) Alarawi, A.; Ramalingam, V.; He, J.-H.; *Mater. Today Energy.* **2019**, 11, 1–23.
- (23) Zhou, J.; Sun, Q.; *J. Am. Chem. Soc.* **2011**, 113, 15113–15119.
- (24) Lu, Y.; Yang, Y.; Zhang, T.; Ge, Z.; Chang, H.; Xiao, P.; Xie, Y.; Hua, L.; Li, Q.; Li, H.; et al., *ACS Nano* **2016**, 10, 10507–10515.
- (25) Wang, F.; Liu, Y.; Zhang, H.; Chu, K.; *ChemCatChem* **2019**, 11, 1441–1447.
- (26) Chu, K.; Liu, Y.; Li, Y.-B.; Wang, J.; Zhang, H.; *ACS Appl. Mater. Interfaces* **2019**, 11, 31806–31815.
- (27) Yin, H.; Li, S.-L.; Gan, L.-Y.; Wang, P.; *J. Mater. Chem. A* **2019**, 7, 11908–11914.
- (28) Chen, Z.; Zhao, J.; Cabrera, C. R.; Chen, Z.; *Small Methods* **2019**, 3, 1800368.
- (29) Ren, C.; Jiang, Q.; Lin, W.; Zhang, Y.; Huang, S.; Ding, K.; *ACS Appl. Nano Mater.* **2020**, 3, 5149–5159.

- (30) Zhang, X.; Wu, T.; Wang, H.; Zhao, R.; Chen, H.; Wang, T.; Wei, P.; Luo, Y.; Zhang, Y.; Sun, X.; *ACS Catal.* **2019**, *9*, 4609–4615.
- (31) Liu, C.; Li, Q.; Zhang, J.; Jin, Y.; MacFarlane, D. R.; Sun, C.; *J. Mater. Chem. A* **2019**, *7*, 4771–4776.
- (32) Zhu, H.-R.; Hu, Y.-L.; Wei, S.-H.; Hua, D.-Y.; *J. Phys. Chem. C* **2019**, *123*, 4274–4281.
- (33) Yang, X.; Shang, C.; Zhou, S.; Zhao, J.; *Nanoscale Horiz.* **2020**, *5*, 1106–1115.
- (34) Azofra, L. M.; Li, N.; MacFarlane, D. R.; Sun, C.; *Energy Environ. Sci.* **2016**, *9*, 2545.
- (35) Li, L.; Wang, X.; Guo, H.; Yao, G.; Yu, H.; Tian, Z.; Li, B.; Chen, L.; *Small Methods* **2019**, *3*, 1900337.
- (36) Zhang, L.; Ding, L.-X.; Chen, G.-F.; Yang, X.; Wang, H.; *Angewandte Chemie Int. Ed.* **2019**, *58*, 2612–2616.
- (37) Liang, X.; Deng, X.; Guo, C.; Wu, C.-M. L.; *Nano Res.* **2020**, *13*, 2925–2932.
- (38) Zhang, Y.; Du, H.; Ma, Y.; Ji, L.; Guo, H.; Tian, Z.; Chen, H.; Huang, H.; Cui, G.; Asiri, A. M.; Qu, F.; Chen, L.; Sun, X.; *Nano Res.* **2019**, *12*, 919–924.
- (39) Ma, Z.; Cui, Z.; Xiao, C.; Dai, W.; Lv, Y.; Li, Q.; Sa, R.; *Nanoscale* **2020**, *12*, 1541–1550.
- (40) Zhao, J.; Chen, Z.; *J. Am. Chem. Soc.* **2017**, *139*, 12480–12487.
- (41) Yang, T.; Song, T. T.; Zhou, J.; Wang, S.; Chi, D.; Shen, L.; Yang, M.; Feng, Y. P.; *Nano Energy* **2020**, *68*, 104304.
- (42) Zhang, H.; Cui, C.; Luo, Z.; *J. Phys. Chem. C* **2020**, *124*, 6260–6266.
- (43) Zhai, X.; Li, L.; Liu, X.; Li, Y.; Yang, J.; Yang, D.; Zhang, J.; Yan, H.; Ge, G.; *Nanoscale* **2020**, *12*, 10035–10043.

- (44) Han, L.; Liu, X.; Chen, J.; Lin, R.; Liu, H.; Lü, S.; Bak, Z.; Liang, S.; Zhao, E.; Stavitski, J.; Luo, R. R.; Xin Adzic, H. L.; *Angew. Chem. Int. Ed.* **2019**, *58*, 2321.
- (45) Tao, H.; Choi, C.; Ding, L.-X.; Jiang, Z.; Han, Z.; Jia, M.; Fan, Q.; Gao, Y.; Wang, H.; Robertson, A. W.; Hong, S.; Jung, Y.; Liu, S.; Sun, Z.; *Chem.* **2019**, *5*, 204–214.
- (46) Ling, C.; Ouyang, Y.; Li, Q.; Bai, X.; Mao, X.; Du, A.; Wang, J.; *Small Methods* **2019**, *3*, 1800376.
- (47) Jiao, D.; Liu, Y.; Cai, Q.; *J. Mater. Chem. A* **2021**, *9*, 1240-1251.
- (48) Liu, X.; Jiao, X.; Zheng, Y.; Qiao, S.-Z.; *ACS Catal.* **2020**, *10*, 1847–1854.
- (49) Liu, C.; Li, Q.; Wu, C.; Zhang, J.; Jin, Y.; MacFarlane, D. R.; Sun, C.; *J. Am. Chem. Soc.* **2019**, *141*, 2884–2888.
- (50) Xiao, S.; Luo, F.; Hua, H.; Yang, Z.; *Chem. Commun.* **2020**, *56*, 446–449.
- (51) Maibam, A.; Govindaraja, T.; Selvaraj, K.; Krishnamurty, S.; *J. Phys. Chem. C* **2019**, *123*, 27492–27500.
- (52) Huang, Y.; Yang, T.; Yang, L.; Liu, R.; Zhang, G.; Jiang, J.; Luo, Y.; Lian, P.; Tang, S.; *J. Mater. Chem. A* **2019**, *7*, 15173–15180.
- (53) Zhu, T.; Li, S.; Ren, B.; Zhang, L.; Dong, L.; Tan, L.; *J. Mater. Sci.* **2019**, *54*, 9632–9642.
- (54) Wu, T.; Shen, H.; Sun, L.; Cheng, B.; Liua, B.; Shen, J.; *New J. Chem.* **2012**, *36*, 1385–1391.
- (55) Boas, C. R. S. V.; Focassio, B.; Marinho Jr., E.; Larrude, D. G.; Salvadori, M. C.; Rocha Leão, C.; dos Santos, D. J.; *Scientific Reports* **2019**, *9*, 13715.
- (56) Xie, J.; Dong, H.; Cao, X.; Li, Y.; *Mater. Chem. Phys.* **2020**, *243*, 122622.
- (57) Yang, Y.; Liu, J.; Wei, Z.; Wang, S.; Ma, J.; *ChemCatChem* **2019**, *11*, 2821–2827.
- (58) Li, X.-F.; Li, Q.-K.; Cheng, J.; Liu, L.; Yan, Q.; Wu, Y.; Zhang, X.-H.; Wang, Z.-Y.; Qiu, Q.; Luo, Y.; *J. Am. Chem. Soc.* **2016**, *138*, 8706–8709.

- (59) Zhao, W.; Zhang, L.; Luo, Q.; Hu, Z.; Zhang, W.; Smith, S.; Yang, J.; *ACS Catal.* **2019**, *9*, 3419–3425.
- (60) Liu, X.; Jiao, Y.; Zheng, Y.; Jaroniec, M.; Qiao, S.-Z.; *J. Am. Chem. Soc.* **2019**, *141*, 9664–9672.
- (61) He, T.; Matta, S.; Du, A.; *Phys. Chem. Chem. Phys.* **2019**, *21*, 1546.
- (62) Otake, K.; Cui, Y.; Buru, C. T.; Li, Z.; Hupp, J. T.; Farha, O. K.; *J. Am. Chem. Soc.* **2018**, *140*, 8652–8656.
- (63) Liu, X.; Jiao, Y.; Zheng, Y.; Jaroniec, M.; Qiao, S.-Z.; *ACS Appl. Energy Mater.* **2020**, *3*, 8739–8745.
- (64) Guo, X.; Huang, S.; *Electrochim. Acta* **2018**, *284*, 392–399.
- (65) Morell, C.; Grand, A.; Toro-Labbé, A.; *J. Phys. Chem. A* **2005**, *109*, 205–212.
- (66) Morell, C.; Grand, A.; Toro-Labbé, A.; *Chem. Phys. Lett.* **2006**, *425*, 342–346.
- (67) Padmanabhan, J.; Parthasarathi, R.; Elango, M.; Subramanian, V.; Krishnamoorthy, B. S.; Gutierrez-Oliva, S.; Toro-Labbé, A.; Roy, D. R.; Chattaraj, P. K.; *J. Phys. Chem. A* **2007**, *37*, 9130–9138.
- (68) Kresse, G.; Furthmüller, J.; *Comput. Mater. Sci.* **1996**, *6*, 15–50.
- (69) Blochl, P. E.; *Phys. Rev. B: Condens. Matter Mater. Phys.* **1994**, *50*, 17953–17979.
- (70) Perdew, J. P.; Burke, K.; Ernzerhof, M.; *Phys. Rev. Lett.* **1996**, *77*, 3865–3868.
- (71) Koster, A. M.; Calaminici, P.; Casida, M. E.; Moreno, R. F.; Geudtner, G.; Goursot, A.; Heine, T.; Ipatov, A.; Janetzko, F.; del Campo, J. M.; et al., *deMon 5.0* **2006** deMon Developers.
- (72) Calaminici, P.; Janetzko, F.; Köster, A. M.; Mejia-Olvera, R.; Zuniga-Gutierrez, B.; *J. Chem. Phys.* **2007**, *126*, 1–10.
- (73) Godbout, N.; Salahub, D. R.; Andzelm, J.; Wimmer, E.; *Can. J. Phys.* **1992**, *70*, 560.

- (74) Calaminici, P.; Janetzko, F.; Köster, A. M.; Mejia-Olvera, R.; Zúñiga Gutiérrez, B.; *J. Chem. Phys.* **2007**, *126*, 044108.
- (75) Wachters, A. J. H.; *J. Chem. Phys.* **1970**, *52*, 1033.
- (76) <http://www.theochem.uni-stuttgart.de>, **2020**. Accessed: 2020-07-01.
- (77) Schuchardt, K. L.; Didier, B. T.; Elsethagen, T.; Sun, L.; Gurumoorthi, V.; Chase, J.; Li, J.; Windus, T. L.; *J. Chem. Inf. Model.* **2007**, *47*, 1045–1052.
- (78) Kumar, D. Krishnamurty, S.; Pal, S.; *J. Phys. Chem. C* **2017**, *121*, 26493–26498.
- (79) Cerón, M. L.; Gomez, T.; Calatayud, M.; Cárdenas, C.; *J. Phys. Chem. A* **2020**, *124*, 2826–2833.
- (80) Tang, W.; Sanville, E.; Henkelman, G.; *J. Phys.: Condens. Matter* **2009**, *21*, 084204.
- (81) Flores-Moreno, R.; Melin, J.; Ortiz, J.V.; Merino, G.; *J. Chem. Phys.* **2008**, *129*, 224105.
- (82) Martínez Araya, J. I.; *J Math Chem* **2015**, *53*, 451–465.
- (83) Nazrulla, M. A.; Krishnamurty, S.; Phani, K. L. N.; *J. Phys. Chem. C* **2014**, *118*, 23058–23069.
- (84) Momma, K.; Izumi, F.; *J. Appl. Crystallogr.* **2011**, *44*, 1272–1276.
- (85) Chattaraj, P. K.; *J. Phys. Chem. A* **2001**, *105*, 511–513.
- (86) Xiao, B. B.; Yang, L.; Song, E. H.; Jiang, Q.; *Appl. Surf. Sci.* **2020**, *513*, 145855.
- (87) Choi, C.; Back, S.; Kim, N.-Y.; Lim, J.; Kim, Y.-H.; Jung, Y.; *ACS Catal.* **2018**, *8*, 7517–7525.
- (88) Qiu, W.; Xie, X.-Y.; Qiu, J.; Fang, W.-H.; Liang, R.; Ren, X.; Ji, X.; Cui, G.; Asiri, A. M.; Cui, G.; Tang, B.; Sun, X.; *Nat. Commun.* **2018**, *9*, 3485.

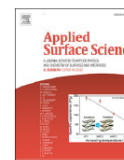
Chapter 5

Applied Surface Science 623 (2023) 157024



Contents lists available at ScienceDirect

Applied Surface Science

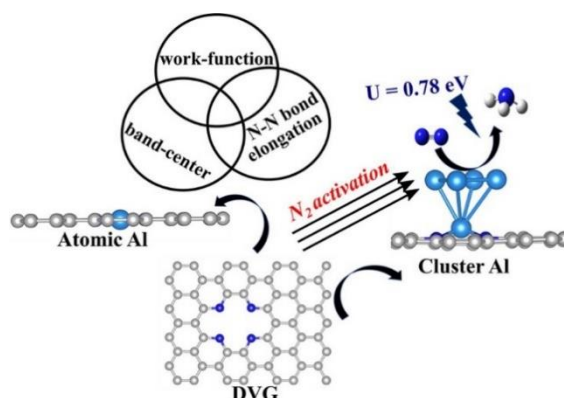
journal homepage: www.elsevier.com/locate/apsusc

Full Length Article

Electrocatalytic nitrogen reduction on defective graphene modulated from single atom catalyst to aluminium clusters



Ashakiran Maibam^{a,b,c}, Sailaja Krishnamurthy^{a,c,*}, Ravichandar Babarao^{b,d,*}



Maibam, A. et. al, *Applied Surface Science.*, 2023, 623, 157024.

The most earth-abundant element, Aluminium has been studied with Density Functional Theory (DFT) and investigations are conducted to detail its electronic properties and catalytic efficacy for nitrogen reduction at ambient condition. The Al-based catalysts have been modulated to perform as par a highly performing, but rare, Ru-single atom catalytic center by varying number of Al atoms, shape, and size. The coalesce of band-center, work function and electronic properties in metal atom catalysts along with N-N bond activation has been demonstrated to be responsible for an efficient nitrogen reduction reaction (NRR) with ΔG_{max} of 0.78 eV in Al_5 supported on N-doped double vacancy graphene ($Al_5@N_4$ -DVG) catalyst. Electron localization function analysis has shown a weak physisorption of N_2 in the Al-based catalysts. Projected Density of States illustrates the enhancement of aluminium electron density in $Al_5@N_4$ -DVG led to enhanced orbital densities overlap of Al_p and N_p electrons. The Bader charge analysis and electronic analysis of the intermediates show efficient electron gain on the N atoms, leading to formation of NH_3 from the N_xH_y intermediates in $Al_5@N_4$ -DVG catalyst.

5.1 Introduction

With increasing demands for fuel and deteriorating fossil fuel reserves, the primary concern over the last five decades have been exploring sustainable fuels and revamping energy efficient technologies. However, the research to achieve ambient temperature reduction of nitrogen to ammonia is far from perceivable. The N_2 molecule being non-polarizable, highly inert and a strong triple bond, its dissociation energy of 940 kJ/mol is attainable only under high temperature and pressure.¹ This also lays forth the constant reliance on the highly energy intensive Haber-Bosch process of ammonia synthesis. Therefore, a scalable and viable synthetic route of N_2 reduction at ambient conditions is an absolute necessity. The electrocatalytic nitrogen reduction reaction (eNRR) is a green alternative to substitute Haber–Bosch process, as this process can be actuated from renewable sources of energy and ammonia synthesis can be regulated at ambient conditions.² However, electrochemical N_2 reduction is laced with two major challenges: a large NRR overpotential and low NH_3 faradaic efficiency (FE) caused by its competing hydrogen evolution reaction (HER).^{3,4}

An extensive research in the recent years have been made to improve the Faradaic efficiency of NRR by implementing noble-earth metal electrocatalysts (Pd, Au, Ru, *etc.*), transition metal electrocatalysts (Mo, Fe, Co, V, *etc.*), and metal-free electrocatalysts (B-doped graphene, black phosphorus, *etc.*).⁵⁻¹² Efficient NRR performance at lower overpotentials have been reported mostly on metal based electrocatalysts; in particular, NRR with FE > 20% till date has been reported on Ru single atom catalysts anchored on N-doped porous carbon (21% FE) and active Mo/MoO₂ species anchored on carbon cloth (FE = 22.3% FE).^{13,14} A major advantage of such metal centers@porous carbon electrocatalyst is the synergistic utilization of buffer electrons from the two-dimensional (2D) substrates and the catalytic metal center. These metal centers route the delocalised electrons from the 2D surfaces into the antibonding orbitals of N_2 molecule leading to an activation of the N-N bond, which in turn is an essential determinant to the reduction of N_2 . Consequently, this has prompted computationally driven studies on several noble and earth abundant transition metal centers@2D electrocatalysts for nitrogen reduction.^{15,16}

In this respect, the main group metals owing to their electronic arrangement show only specific oxidation number and restricted orbital states fail to exhibit purported N_2 reduction, except for Li and Al clusters. Li has been reported to be used directly as a catalyst for NRR or via a lithium-mediated route as metallic Li forms the only stable nitride, Li_3N in ambient conditions. The Li-mediated NRR electrocatalysts are known to exhibit high NRR FE closely approaching 100% in a high-concentration imide-based lithium salt interface.¹⁷ However, the implementation of Li for NRR becomes unsustainable due to its limited presence in the earth's crust which correspond to only 0.002–0.006 wt%. On the other hand, Al being the most abundant metal in earth's crust, has been less explored for ambient nitrogen reduction. Notable reports have been made on Al-based electrocatalyst for ammonia fixation include Li-aided Al doped graphene, aluminium (III) coordination complex, Al- Co_3O_4/NF , MoAlB single crystals, and Al- N_2 battery with an Al - ionic liquid electrolyte. Huang et al implemented Al metal as a dopant on graphene as a ligating center to the N_xH_y intermediates generated by Li^+ ion aided reduction of N_2 to NH_3 at ambient conditions.¹⁸ A substantial advancement in NRR performance of Al-electrocatalysts had been realized by Berben and co-workers when an aluminium (III) complex with 0.3 M Bu_4NPF_6 THF and DMAPH⁺ electrolyte exhibited ammonia production at -1.16 V (vs. SCE) with 21% FE in ambient condition.¹⁹ However, Al as a catalytic metal center for nitrogen reduction was reported in urchin like Al-doped Co_2O_3 nanospheres (Al- Co_3O_4/NF) with a FE of 6.25% at -0.2 V vs RHE by Yuan et. al, and in a multicomponent boride, MoAlB wherein the layered electrocatalyst reported by Ma and co-workers showed ammonia production with a FE of 30.1% at -0.05 V vs RHE.^{20,21} The highest FE of 51.2% at -0.1 V for Al-based electrocatalyst in ammonia production has been reported by Zhi and co-workers in a rechargeable Al- N_2 battery composed of a graphene-supported Pd (graphene/Pd) cathode and Al anode with an ionic liquid electrolyte (AlCl/1-butyl-3-methylimidazolium chloride).²² The study reveals a higher feasibility of AlN ($\Delta G=-287$ kJ/mol) formation as compared to Li_3N ($\Delta G=-154$ kJ/mol), thereby revealing a more spontaneous nitriding reaction in Al over Li. However, AlN is extremely susceptible to

air unlike its lithium counterpart, and it gets easily oxidised, thereby the catalytic activity of Al gets thwarted.

Fundamentally, Al being an element of boron family possess similar electronic distribution and certain similarities in electronic properties can be expected. Boron has been reported in several metal-free electrocatalyst as a dopant or catalytic center that can hold N_2 and influence ammonia production via an electron “donation-acceptor” mechanism.^{23,24} While the “donation-acceptor” mechanism is unlikely to occur in Al atom catalyst due to a lower electronegativity of Al (1.61) as compared to B (2.01), Al clusters have been reported to chemisorb N_2 and activate the N-N bond effectively. Aguado et al. reported the chemisorption of N_2 and N-N bond activation upto 1.65 Å on Al_{44} nanoclusters with an energy barrier of 3.4 eV.²⁵ The N-N bond activation barrier becomes as low as 0.65 eV in smaller Al-clusters, in particular, Al_5 cluster on BN-graphene, as observed by Kumar and co-workers.²⁶ Henceforth, it is important to probe into these smaller Al clusters and explore the plausibility of implementing them as NRR electrocatalyst. Furthermore, the experimental realization of Al-based catalysts on graphene is not far-fetched research as synthesis of pristine Al-clusters with pulsed laser vaporization can be dated back to 2007 by Neal et. al.²⁷ With experimental improvements brought about by electron-beam irradiation, single atom substitution on graphene has been reported by Zagler and co-workers.²⁸ However, the evidence of graphene-Al clusters/nanoparticle composites is as well-known as other graphene-metal composites and the synthesis route follows the conventional chemical exfoliation or powder metallurgy technique.²⁹⁻³¹ In this chapter, we make a radical comparison of the electronic properties of NRR active Ru and Mo single atom to Al atom and Al-clusters (Al_n) supported on N-doped double vacancy graphene (N_4 -DVG). The study focuses on modulating the electronic and catalytic properties of atomic Al catalysts by inducing changes in their shape and size.

5.2 Computational Details

All metal atoms and clusters supported N-doped double vacancy graphene ($M@N_4$ -DVG) systems, as shown in **Figure 5.1**, are optimized using Density Functional Theory

(DFT) calculations with Vienna ab-initio Simulation Package (VASP.5.4).³² The ionic-electronic interactions on all systems are sampled with a $2 \times 2 \times 1$ Monkhorst-Pack kpoint grid and 520 eV energy cut-off with a generalized gradient approximation Perdew-Burke-Ernzerhof (PBE) functional.³³ All $M@N_4$ -DVG systems have been relaxed with DFT-D3 corrections to incorporate long range forces till the atomic forces and energies converge to 0.005 eV/\AA and 10^{-5} eV/atom , respectively.³⁴ Electronic property analysis has been carried out to evaluate the density of states and Bader charges of the $M@N_4$ -DVG systems by considering a higher kpoint grid of $(9 \times 9 \times 1)$ Monkhorst-Pack grid.³⁵ The thermal stability of the $M@N_4$ -DVG systems analysed through Ab initio molecular dynamics (AIMD) simulations carried out in an NVT ensemble at 298 K described with a Nose-Hoover thermostat at 3 ps time step for 10 ps.³⁶ Furthermore, the feasibility of achieving chemically stable $M@N_4$ -DVG systems is realized via the binding energies (E_b) of atomic metal catalysts and clusters on the N_4 -DVG system computed using the equation,

$$E_b = (E_{M@N_4-DVG}) - (E_{N_4-DVG}) - E_M \quad (5.1)$$

where, $E_{M@N_4-DVG}$ is the total electronic energy of Ru, Mo, Al metal atom catalysts or Al_n ($n=2-7$) clusters supported N_4 -DVG systems, E_{N_4-DVG} is the total electronic energy of N_4 -DVG systems and E_M is the electronic energy of Ru, Mo, Al single atom catalysts or Al_n clusters. Following this, the N_2 chemisorption efficacy on the $M@N_4$ -DVG catalysts is investigated via the end-on and side-on modes of N_2 adsorption; and the adsorption energy, E_{ads} is computed using the equation,

$$E_{ads} = (E_{M@N_4-DVG-N_2}) - (E_{M@N_4-DVG}) - E_{N_2} \quad (5.2)$$

where, $E_{M@N_4-DVG-N_2}$ is the total electronic energy of $M@N_4$ -DVG system after N_2 adsorption, $E_{M@N_4-DVG}$ and E_{N_2} are the total electronic energy of $M@N_4$ -DVG systems and free N_2 molecule, respectively.

The free energy of the N_xH_y intermediates involved in the Nitrogen Reduction Reaction (NRR) is represented by the Gibbs free energy change, ΔG and the

computational Standard Hydrogen Electrode model of Nørskov et al. has been implemented to calculate ΔG using the following equation,³⁷

$$\Delta G = \Delta E + \Delta ZPE - T \Delta S \quad (5.3)$$

where, ΔE and ΔZPE is the change in electronic energy and zero-point energy

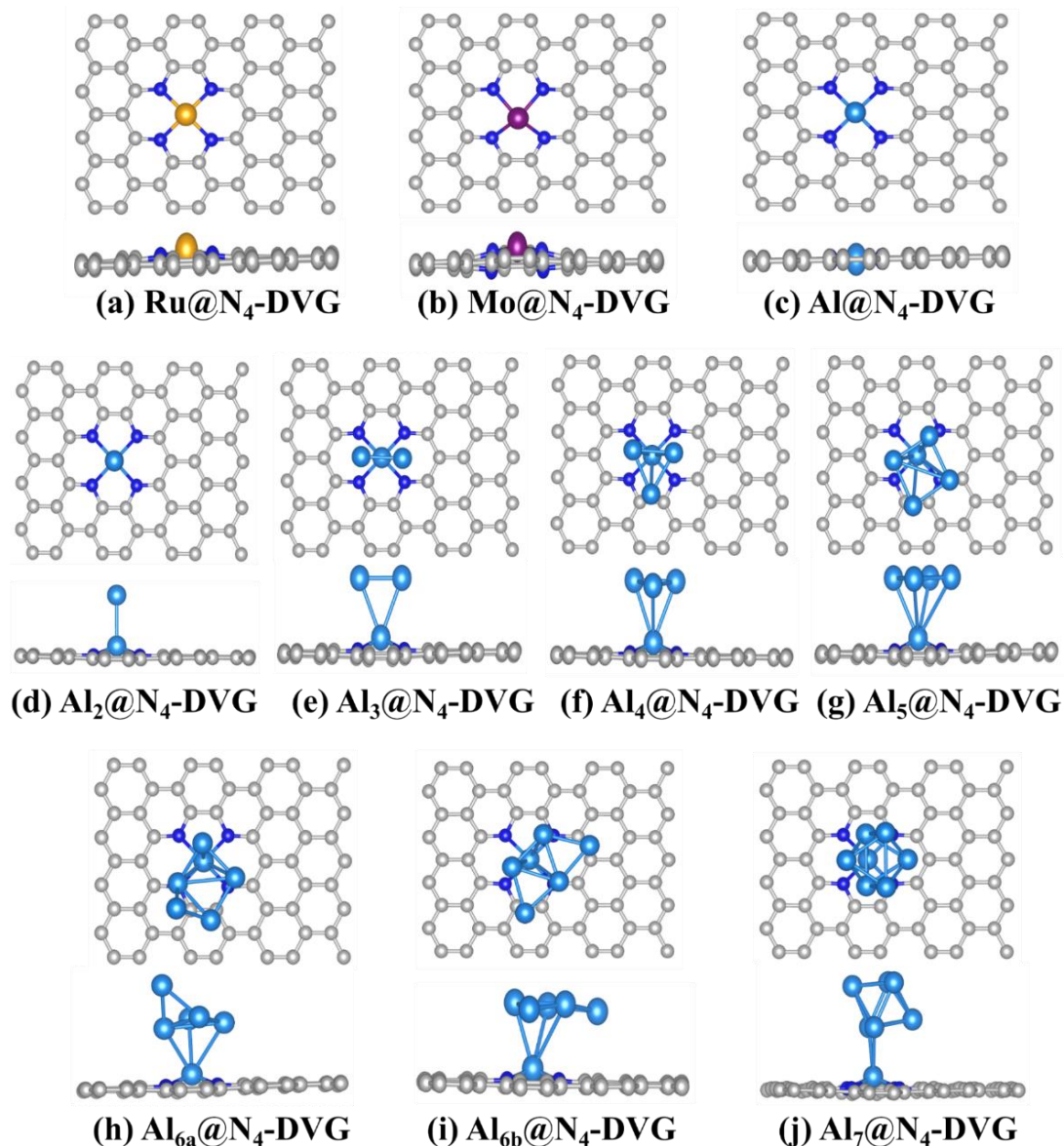
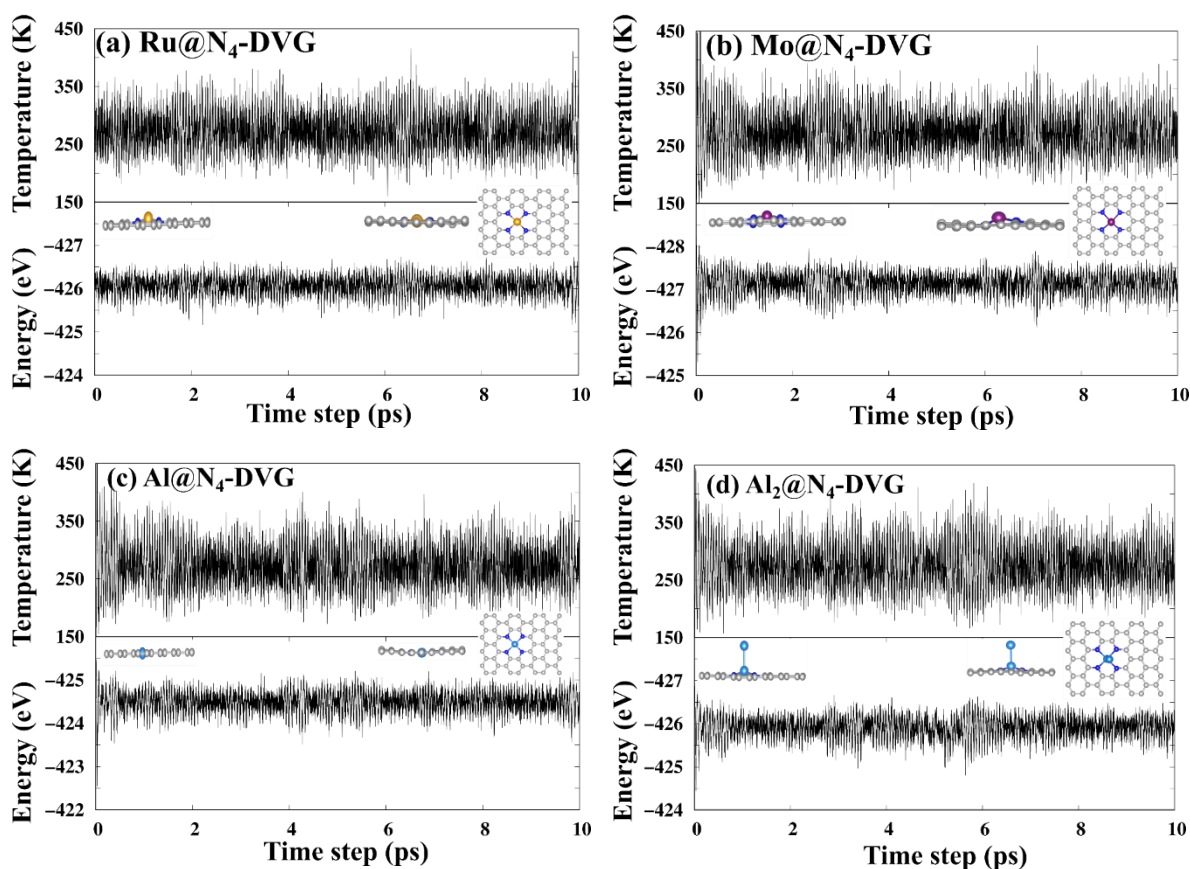


Figure 5.1: Top and side views of Ru and Mo single atom supported on N-doped double vacancy graphene considered as reference to Al atom and Al-clusters (Al_n) supported N-doped double vacancy graphene (M@N₄-DVG).

respectively, ΔS is the change in entropy at room temperature, T is room temperature (298.15 K). The zero-point energy and entropy corrections are computed from the non-negative vibrational frequencies of the gas phase species in each intermediate. The potential rate-determining step (PDS) for the reaction is intermediate step with the highest free energy change (ΔG_{\max}) and the limiting potential, U_L is equal to $-(\Delta G_{\max})/e$. For an electrocatalyst under applied potential, the free energy is calculated as, $\Delta G_{NRR} = \Delta E + \Delta ZPE - T\Delta S + neU + \Delta G_{pH}$, where n is the number of electrons, U is the applied electrode potential equivalent to the limiting potential, U_L and ΔG_{pH} is the free energy correction to pH of the solvent. The pH correction to free energy is represented by $\Delta G_{pH} = 2.303 \times k_B T \times \text{pH}$, where k_B is the Boltzmann constant. The pH value is assumed to be zero as the overpotential of NRR is unaffected by the change in pH.^{38,39}

5.3 Results and Discussions

5.3.1 Stability of the M@N₄-DVG systems



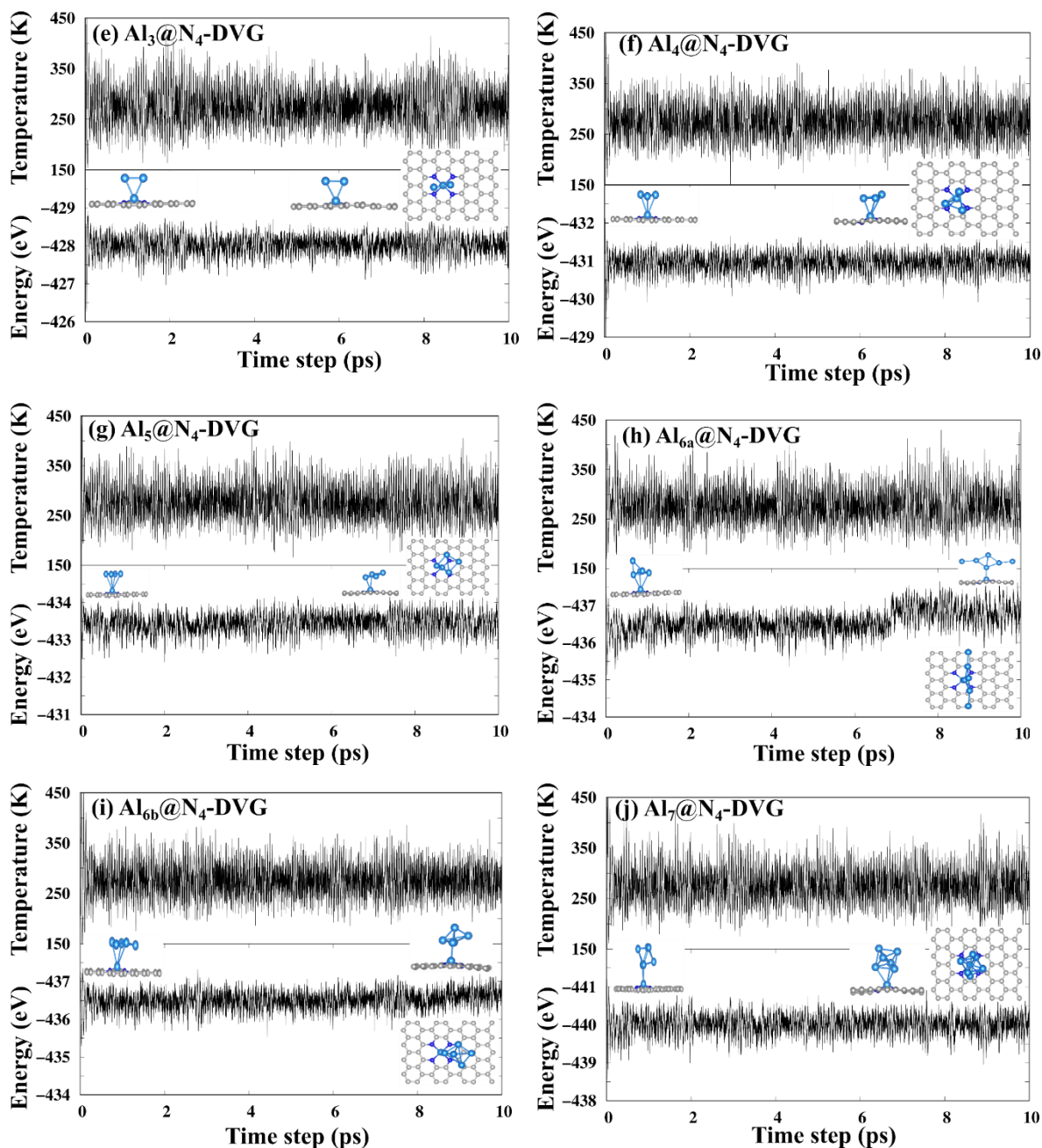


Figure 5.2: AIMD plots of M@N₄-DVG catalysts at 298 K; (a) Ru@N₄-DVG, (b) Mo@N₄-DVG, (c) Al@N₄-DVG, (d) Al₂@N₄-DVG, (d) Al₃@N₄-DVG, (d) Al₄@N₄-DVG, (d) Al₅@N₄-DVG, (d) Al_{6a}@N₄-DVG, (d) Al_{6b}@N₄-DVG, (d) Al₇@N₄-DVG.

Table 5.1: Binding energies of metal single atoms and clusters, M = Ru, Mo, Al, Al_n (n=2-7) on N₄-DVG (N doped double vacancy graphene) to form M@N₄-DVG.

Catalyst System	Binding energy (eV)
Ru@N ₄ -DVG	-8.19
Mo@N ₄ -DVG	-9.78
Al@N ₄ -DVG	-7.81
Al ₂ @N ₄ -DVG	-7.54
Al ₃ @N ₄ -DVG	-6.60
Al ₄ @N ₄ -DVG	-7.27
Al ₅ @N ₄ -DVG	-7.10
Al _{6a} @N ₄ -DVG	-7.11
Al _{6b} @N ₄ -DVG	-7.45
Al ₇ @N ₄ -DVG	-5.82

The electronic stability of the M@N₄-DVG systems as evaluated from the binding energy calculations show the metal single atoms (Ru, Mo and Al) to be positioned in the N tetra-coordinated vacancy in the graphene plane, while the Al_n clusters are anchored with one Al atom occupying the double vacant site in graphene plane (i.e., in-plane) and the remaining Al atoms bound to the in-plane Al-atom. Mo single atom (Mo@N₄-DVG) has been found to possess the highest binding energy of -9.78 eV followed by Ru@N₄-DVG with -8.19 eV and Al@N₄-DVG with -7.81 eV. The Al_n clusters supported N₄-DVG systems show a gradual decrease in their binding energies as the size of the clusters increase. The Al_n clusters with a planar geometry and higher coordination with the in-plane Al are more stable with binding energies ranging from -7.1 to -7.5 eV as provided in **Table 5.1**. On the other hand, Al₇@N₄-DVG system with a nearly spherical structure and two coordinated Al atoms to the in-plane Al atom show the least binding energy of -5.82 eV. Larger clusters are thus, not considered in this study as they tend to form spherical and symmetric structures. For ambient nitrogen fixation, the thermal stability of all M@N₄-DVG systems are further analysed through AIMD simulations at 298 K and small structural distortions are observed in Al₄@N₄-

DVG, $\text{Al}_5@N_4\text{-DVG}$ and $\text{Al}_7@N_4\text{-DVG}$ while both Al_6 clusters showed large distortions after 10 ps, as seen in **Figure 5.2**. Henceforth, all the $M@N_4\text{-DVG}$ systems, except $\text{Al}_{6a}@N_4\text{-DVG}$ and $\text{Al}_{6b}@N_4\text{-DVG}$ are eligible candidates to be implemented as stable catalysts at room temperature and further electrocatalytic studies will be carried out on the stable catalysts.

5.3.2 Electronic properties of $M@N_4\text{-DVG}$ systems and N_2 activation

The catalytic activity of a system, being an inflection of electronic properties and charge distribution or transfer efficiency, can be primitively assessed from its work function (Φ) and p-band center. While catalysts with a lower work-function will require a smaller energy to activate the N_2 molecule, a more positive p-band center will ascertain the p-orbitals of the active centers are closer to the Fermi level and possess higher carrier density. A comparative plot of work function and p-band centers of Ru, Mo, Al metal atoms and Al_n clusters in **Figure 5.3(a)** shows the Ru single atom with most positive p-band center of -5.25 eV and work function of 4.29 eV. The p-band centers of Ru and Mo has been computed in place of d-band center to have a consistent comparison with Al which possess only p-orbitals. Ru, being the best performing metal single atom catalyst on N-doped graphene, is used as a reference for another active transition metal, Mo and our metal atom of interest Al and its clusters, Al_n . $\text{Al}@N_4\text{-DVG}$ system with Al single atom shows a much lower (i.e., negative) work function than the Ru or Mo counterparts, however its p-band center is relatively more negative (-5.74 eV) thereby inferring a lower charge carrier density. Although the work function gradually increases with the increase in size of Al_n clusters and a decrease in catalytic activity is expected, the p-band centers show an interesting trend with the $\text{Al}_5@N_4\text{-DVG}$ system has its p-band center at -5.69 eV and more positive than $\text{Al}@N_4\text{-DVG}$. This primitive screening of catalytic activity is ratified through the N_2 adsorption strengths of the $M@N_4\text{-DVG}$ catalysts.

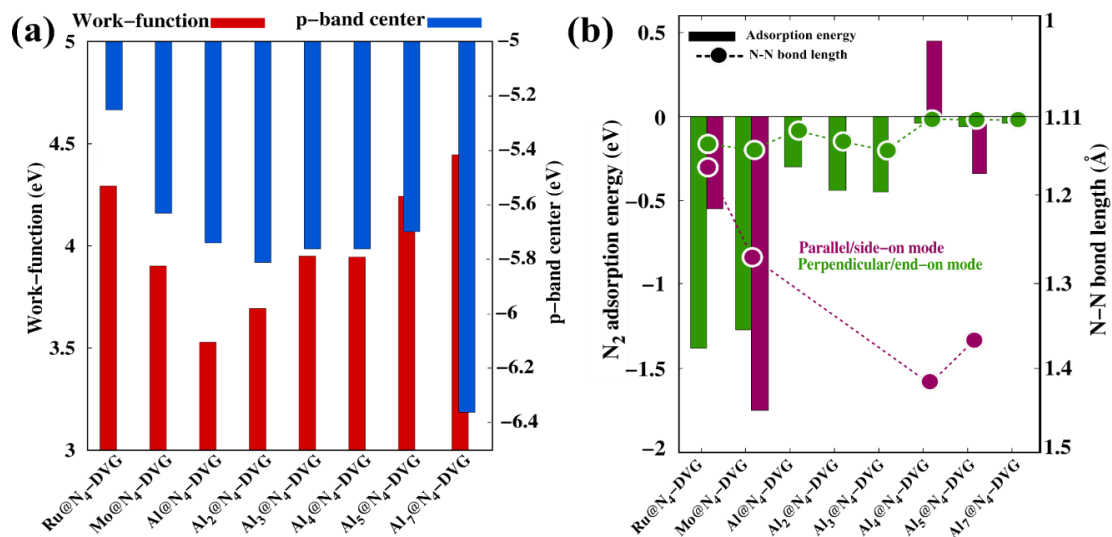


Figure 5.3: (a) Comparative plot of work function and p-band center of all M@N₄-DVG systems, red and blue histograms represent the work function and p-band center respectively. (b) N₂ adsorption energies and N-N bond elongation on the M@N₄-DVG systems, the histograms represent N₂ adsorption energy while the points represent N-N bond length in Å.

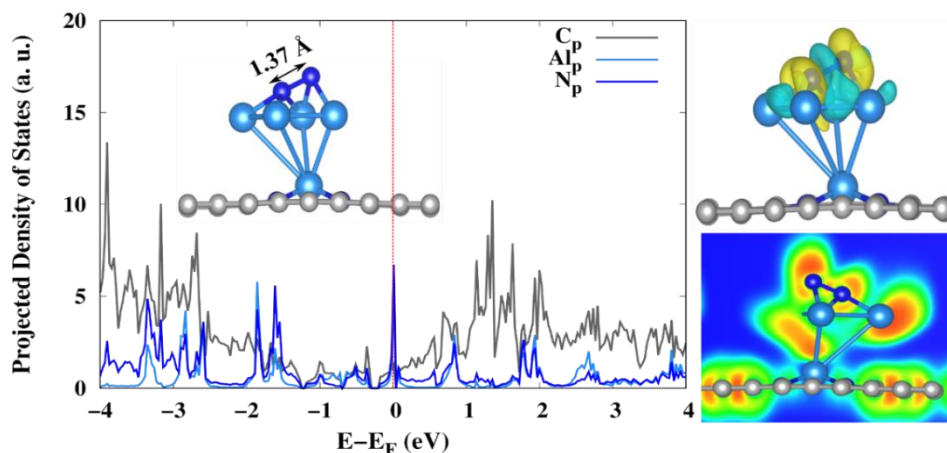


Figure 5.4: Projected Density of States (PDOS) with Charge Density Difference (CDD) and Electron location function (ELF) plots of side-on N₂ adsorbed on Al₅@N₄-DVG. The CDD and ELF plots were made using VESTA software.⁴⁰

While the presence of d-orbitals in Ru and Mo single atom catalyst allows both parallel and perpendicular modes of N₂ adsorption on Ru@N₄-DVG and Mo@N₄-DVG, the most optimal adsorption mode and site of N₂ on the Al_n@N₄-DVG catalysts are

found to vary with the change in shape and size of the Al cluster. From **Figure 5.3(b)**, it is evident that lower (or positive) p-band center in Ru@N₄-DVG influences the exothermic adsorption of N₂, while a lower work function is responsible for the same in Mo@N₄-DVG. The higher activity and exothermic adsorption of N₂ on Al₅ cluster can also be ratified due to the shape and orientation of the Al atoms that are available for interaction with the incoming N₂ molecule. As the Al_n cluster size increases, one Al atom lies in-plane to the N-doped graphene sheet while the remaining Al atoms orient themselves with 3 or 4 as its coordination number. While most Al_n clusters prefer to form 3- or 4- coordination leading to triangular facets, the stable Al₅@N₄-DVG catalyst prefers to form a rectangular facet with four Al-atoms exposed as catalytic sites. Furthermore, these exposed Al atoms are found to be electron rich while the Al-atom ingrained to the graphene plane is positively charged or electron deficient. This further corroborates to the lower N-N activation of Al single atom as compared to electron rich Al-atoms lying above the graphene plane which can easily render electrons to N₂ molecule.

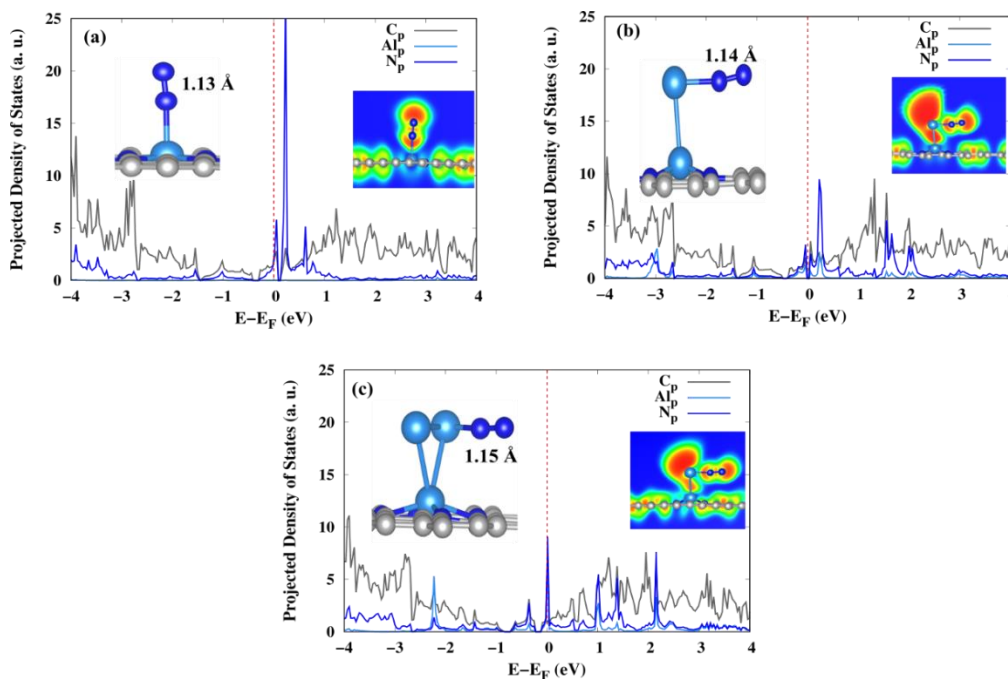


Figure 5.5: Projected Density of States (PDOS) and Electron location function (ELF) plots of side-on N₂ adsorbed on (a) Al@N₄-DVG, (b) Al₂@N₄-DVG and (c) Al₃@N₄-DVG.

The N_2 adsorption energies on Al single atom and its clusters are relatively lower than the transition metal counterparts; however, a similar trend of work-function influencing adsorption can be observed in $Al@N_4$ -DVG, $Al_2@N_4$ -DVG and $Al_3@N_4$ -DVG while the p-band center becomes accountable for $Al_5@N_4$ -DVG. More interestingly, $Al_5@N_4$ -DVG is the only Al_n based catalyst that shows exothermic side-on N_2 adsorption (-0.34 eV) and N-N bond activation (1.37 Å) brought about with the nitrogen atoms attached to different Al centers. **Figure 5.4** shows the overlap of Al p-orbitals ($Al_5@N_4$ -DVG) and N p-orbitals (N_2) in the Fermi region of Projected Density of States plot and electron localization function (ELF) plot with localized electrons on the N_2 . Besides $Al_5@N_4$ -DVG, the systems of interest that show exothermic N_2 adsorption and N-N bond activation are $Ru@N_4$ -DVG, $Mo@N_4$ -DVG, $Al@N_4$ -DVG, $Al_2@N_4$ -DVG and $Al_3@N_4$ -DVG. ELF plots with higher electron density concentration on the atoms will correspond to ionic bonding while contribution from covalent bonding can be accounted when the electron density is concentrated on the respective bond between two atoms. A prominent electron localization on N_2 can be observed in $Ru@N_4$ -DVG and $Mo@N_4$ -DVG systems inferring an ionic bonding or stronger binding which can be interpreted as chemisorption led by electron transfer, whereas a more covalent bonding between Al atoms and N_2 molecule can be observed in the Al-based catalysts inferring towards physisorption of N_2 . The presence of higher electron density in Al_n clusters as compared to Al single atom can be a major contributor in enhancing the catalytic activity of Al metal for NRR. This is supported by the PDOS and ELF plots of N_2 adsorbed $Al@N_4$ -DVG catalyst in **Figure 5.5(a)** that shows minimal contribution from the Al p-orbitals. However, in aluminium cluster catalysts the contribution of Al p-orbitals is found to increase gradually, **Figure 5.5 (b-c)** along with a shift towards the Fermi level due to the conducting nature of Al. The distribution of electron density as seen from ELF plots and smaller orbital overlap between Al and N_2 can be inferred as N_2 physisorption on the Al-based catalysts and the N_2 adsorption energies corroborate to this finding.

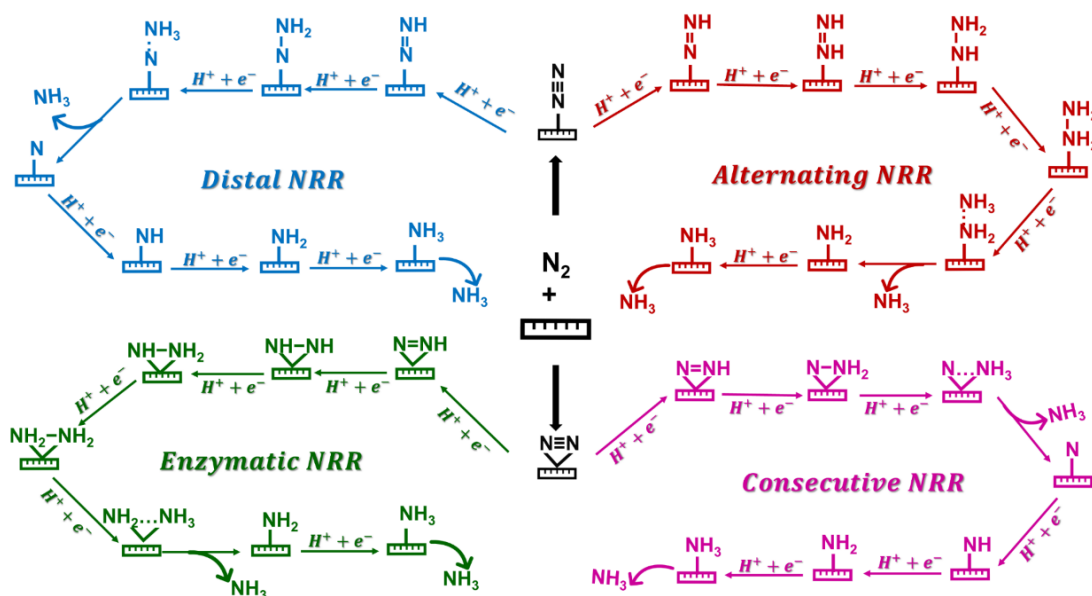
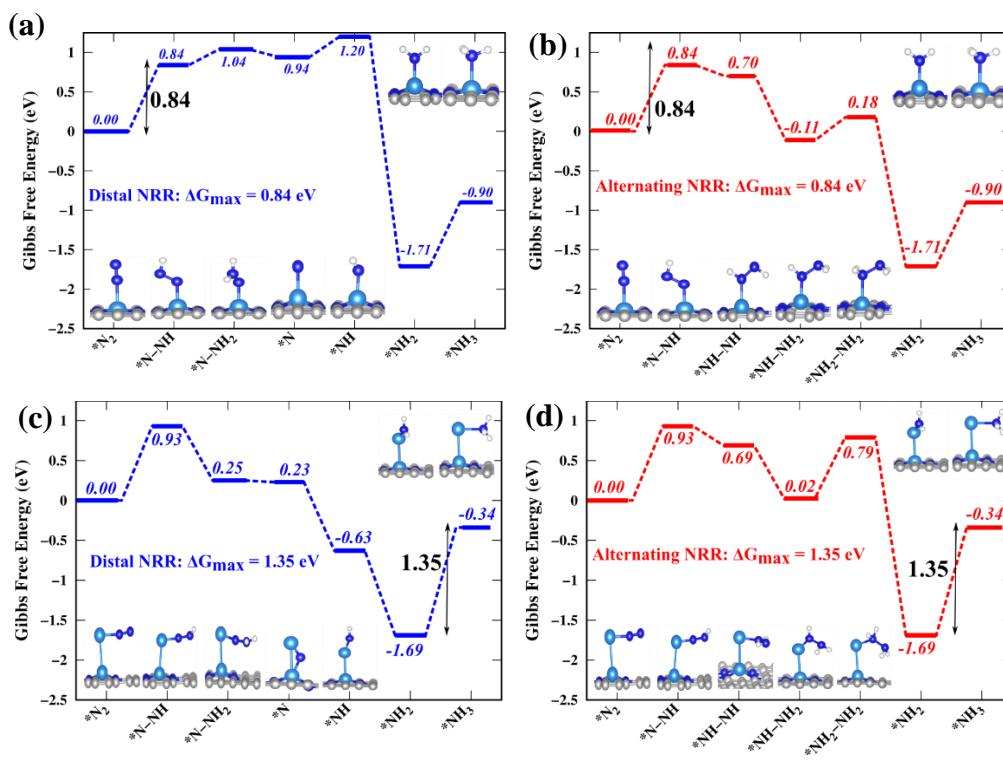


Figure 5.6: Possible mechanistic routes of nitrogen reduction reaction; distal and alternating route for N_2 adsorbed in end-on mode, while enzymatic and consecutive route is observed in side-on adsorbed N_2 .

5.3.3 Nitrogen reduction reaction (NRR) on $M@N_4$ -DVG systems



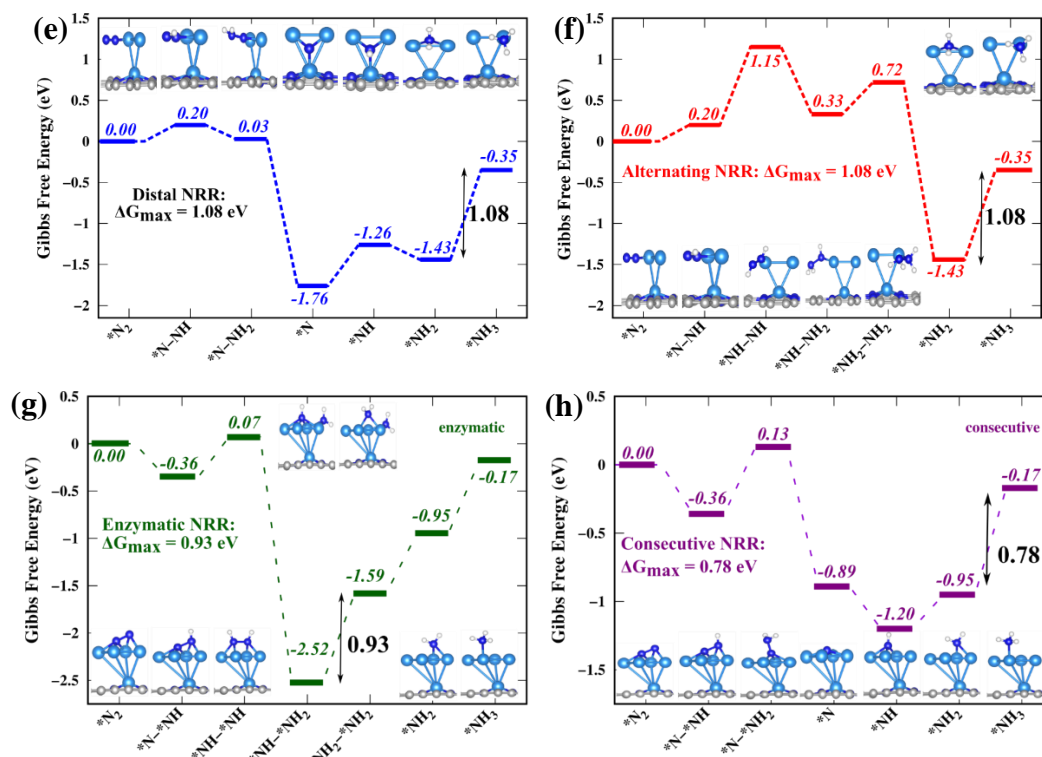


Figure 5.7: Free energy diagram of distal and alternating routes of NRR on (a-b) $Al@N_4$ -DVG, (c-d) $Al_2@N_4$ -DVG (e-f) $Al_3@N_4$ -DVG (g-h) enzymatic and consecutive routes of $Al_5@N_4$ -DVG.

Following this screening of N_2 activation, the mechanisms of nitrogen reduction reaction (NRR) on all possible routes, **Figure 5.6**, are explored on the select $M@N_4$ -DVG catalysts that show exothermic N_2 adsorption. Nitrogen reduction on $Ru@N_4$ -DVG and $Mo@N_4$ -DVG catalysts with Ru and Mo single atom center have been investigated via the distal, alternating and enzymatic route. The consecutive route has been found unfeasible as the $*N$ - $*NH_2$ intermediate could not be realized on the single atoms. Computational calculations on $Al@N_4$ -DVG, $Al_2@N_4$ -DVG and $Al_3@N_4$ -DVG catalysts that show end-on N_2 adsorption have been restricted only for the distal and alternating route. Finally, $Al_5@N_4$ -DVG catalyst which showed exothermic side-on N_2 adsorption have been investigated for enzymatic and consecutive route of NRR, with multiple Al atoms being involved in N_2 adsorption, the consecutive route becomes feasible in this catalyst. The free energy diagrams of the above-mentioned routes of NRR

reaction coordinates on stable Al@N₄-DVG, Al₂@N₄-DVG, Al₃@N₄-DVG and Al₅@N₄-DVG catalysts are provided in **Figure 5.7(a-h)**.

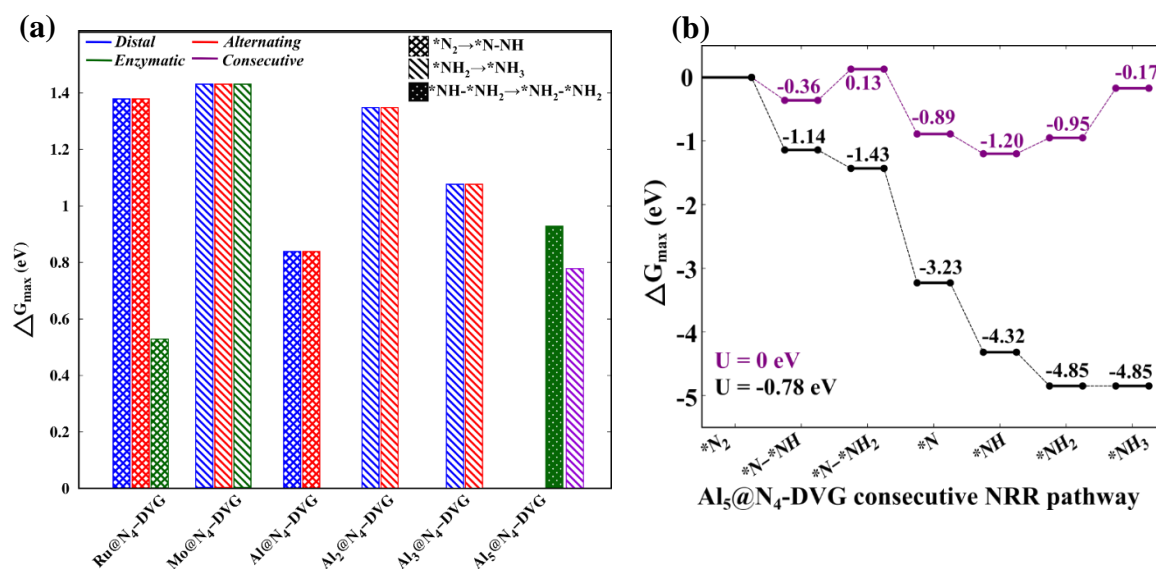
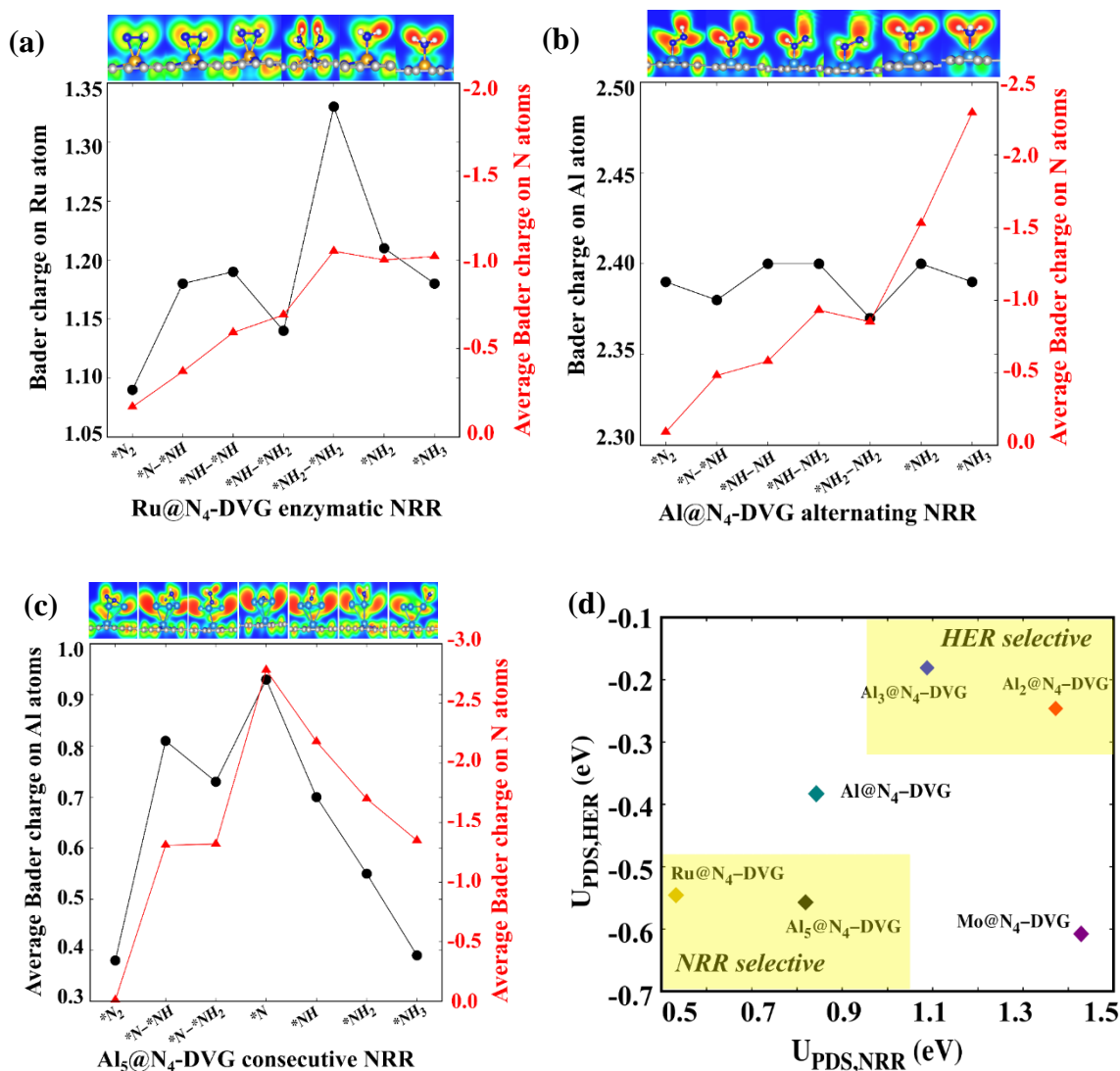


Figure 5.8: (a) ΔG_{\max} (in eV) with potential rate determining step on all active M@N₄-DVG catalysts. (b) Consecutive route of nitrogen reduction on Al₅@N₄-DVG catalyst computed under applied voltage of 0 V (dark-violet line) and -0.78 V (black line) respectively.

The reduction of N₂ to NH₃ is a multistep reaction with six elementary protonation steps and release of two NH₃ molecules, the usual uphill reaction steps are the first (*N₂→*N₂H) and last protonation (*NH₂→*NH₃) steps in all routes along with the fourth protonation (*N₂H₃→*N₂H₄) step in alternating route. The uphill elementary step with the highest energy barrier becomes the potential rate determining step (PDS) of NRR and a summary of all possible routes and the PDS with ΔG_{\max} values on all M@N₄-DVG catalysts as shown in **Figure 5.8(a)**. The ΔG_{\max} value on Ru single atom, reported as the best catalyst, has been found to be 0.53 eV in the first protonation step. However, Mo single atom which has been reported as an active NRR catalyst shows a relatively high energy barrier of 1.43 eV in the last protonation step. The ΔG_{\max} values on the Al-based catalysts are 0.84 eV (*N₂→*N₂H), 1.35 eV (*NH₂→*NH₃) and 1.08 eV (*NH₂→*NH₃) in Al@N₄-DVG, Al₂@N₄-DVG and Al₃@N₄-DVG respectively. While Al single atom

and smaller Al-clusters show a relatively higher NRR performance than Mo single atom, the NRR performance improves to 0.78 eV in $\text{Al}_5\text{@N}_4\text{-DVG}$ catalyst that showed exothermic side-on N_2 adsorption. Furthermore, upon application of an external potential 0.78 eV as shown in **Figure 5.8(b)**, the elementary ($\text{*NH}_2 \rightarrow \text{*NH}_3$) protonation steps become exothermic, thereby inferring this catalyst can also be implemented as an electrocatalyst.



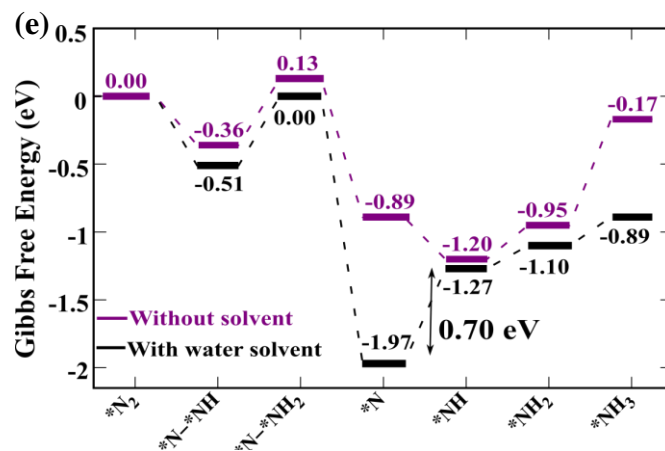


Figure 5.9: Bader charge analysis on the metal centers and N atoms of the N_xH_y intermediates of enzymatic, alternating and consecutive NRR routes on (a) Ru@N₄-DVG, (b) Al@N₄-DVG, (c) Al₅@N₄-DVG, respectively (d) NRR vs HER selectivity plot of the active M@N₄-DVG catalysts, Ru@N₄-DVG and Al₅@N₄-DVG show exclusive NRR selectivity as compared to the rest of the Al-based catalysts; (e) Free energy diagram of consecutive NRR on Al₅@N₄-DVG without and with water solvent, and the corresponding ΔG_{\max} reduces from 0.78 eV to 0.70 eV.

A detailed electronic analysis of the Bader charges as shown in **Figure 5.9(a)** of Ru@N₄-DVG shows a correlation between the charge transfer from Ru to the N atoms. Most importantly, the PDS fourth protonation step, $*NH-*NH_2 \rightarrow *NH_2-*NH_2$ step has been found to show a large difference between Ru charge and N charges, thus signifying that the electronic barrier essential to bring about ammonia production. Al@N₄-DVG catalyst that show a preference of the alternating route with better stabilized $*N_xH_y$ intermediates exhibit contrastingly higher Bader charge difference in the last protonation step although the PDS is the first protonation step, $*N_2 \rightarrow *N-NH$. Furthermore, in the ELF plot shown in **Figure 5.9(b)** inset for $*NH_3$ intermediate, a relatively higher electron density can be observed in the N atoms from the Al single atom along with Al-N covalent bond further stabilising the system. This possess a major challenge in the functionality and applicability of Al@N₄-DVG catalyst, as the active Al metal site gets deactivated due to strong adsorption efficacy of NH₃, which is -0.90 eV exergonic from N₂ adsorption. Interestingly, Al₅@N₄-DVG catalyst behaves similar to Ru@N₄-DVG catalyst and shows

a large variation in Bader charge of Al and N only in its PDS step, i.e., $*\text{NH}_2 \rightarrow *\text{NH}_3$ step, **Figure 5.9(c)**. Additionally, the dissemination of electron density in the constituting Al atoms in Al_5 center leads to efficient electron transfer to N atoms, leading to formation of NH_3 without the manifestation of any covalent bond between Al center and N atoms of N_xH_y intermediates. The corresponding NH_3 adsorption on $\text{Al}_5@N_4\text{-DVG}$ is exoergic by -0.41 eV as compared to N_2 adsorption and the possibility of catalytic center deactivation or poisoning can be reduced as 5-Al metal centers are involved. Another similarity of the $\text{Al}_5@N_4\text{-DVG}$ catalyst to the $\text{Ru}@N_4\text{-DVG}$ catalyst is an exclusive NRR selectivity over HER, **Figure 5.9(d)**. An interesting outlook can be accounted on the NRR performance of $\text{Al}_5@N_4\text{-DVG}$ catalyst in the presence of water solvent, details of implementing solvent model and calculations are discussed in Supplementary Information. N_2 molecule being non-polar, its adsorption energy in water should be endothermic as compared to its value in vacuum; while the protonated N_xH_y intermediates possess dipoles and water as a solvent enhances the formation of N_xH_y intermediates. Thereby, a lower adsorption energy of N_2 and higher free energies of N_xH_y intermediates on $\text{Al}_5@N_4\text{-DVG}$ system can be expected with solvent effects and the same has been compared with the energetics in vacuum for the consecutive route of NRR on $\text{Al}_5@N_4\text{-DVG}$, as seen in **Figure 5.9(e)**. In the presence of water, the adsorption energy of N_2 on $\text{Al}_5@N_4\text{-DVG}$ system reduces from -0.06 eV to -0.05 eV in perpendicular mode and -0.37 eV to -0.27 eV in parallel mode. As anticipated, the following protonation steps leading to formation of N_xH_y intermediates are energetically favourable with more negative ΔG values when compared to vacuum state. The corresponding ΔG_{max} reduces from 0.78 eV to 0.70 eV for the consecutive route and PDS shift from the last protonation step, $*\text{NH}_2 \rightarrow *\text{NH}_3$ in vacuum to fourth protonation step, $*\text{N} \rightarrow *\text{NH}$ in water solvent. This can be attributed to the solvation of the $*\text{N}$ intermediate with open coordination sites and the water pockets hindering the transport of H^+ to form the $*\text{NH}$ intermediate. SContrastingly, the protonation of $*\text{NH}_2$ intermediate to $*\text{NH}_3$ intermediate which was less feasible in vacuum becomes more facile as water can enhance the transport of protons and formation of $*\text{NH}_3$. This also substantiates that $\text{Al}_5@N_4\text{-DVG}$ catalyst can be rendered for lab-scale experimentations in aqueous conditions.

The ΔG_{\max} of NRR on $\text{Al}_5@N_4\text{-DVG}$ catalyst has been observed to be higher than several homoatomic or heteroatomic bimetallic transition metal catalysts, however in several cases of homoatomic catalysts, i.e., $\text{Ru}_2@PC_6$, $\text{Cu}_2@NG$, $\text{Ni}_4@Gr$ catalysts the NRR performance is on-par and higher in some cases. It can also be noted that Al_5 cluster anchored on BN-doped graphene showed the lowest barrier for N-N bond activation in the study carried out by Kumar et al. and our studies concur to their findings.²⁶ Aluminium clusters on N-doped double vacancy graphene, despite a less attractive NRR performance than transition metal single atoms, perform as par the Ru single atom catalyst with a high selectivity for NRR and a trade-off can be achieved when researchers aim for scalable and sustainable catalyst for ammonia production.

5.4 Conclusions

In this study, DFT investigation has been made to conform an earth-abundant metal Al to conform and exhibit similar catalytic properties to another rare earth transition metal, Ru for nitrogen reduction. Al-based catalysts have been modulated into a Ru-single atom like catalytic center by varying number of Al centers. A detailed study on the electronic and thermal stability of the model catalysts have been made via AIMD studies and the catalytic properties are primitively scoured through their inherent electronic properties. An analysis of the electron localization function and projected density of states plots shows a strong chemisorption in the transition metal, while a weak physisorption is observed in the Al-based catalysts. The change in shape and size of the atomic Al clusters reflects to a change in their corresponding catalytic properties, and Al_5 supported on N-doped double vacancy graphene ($N_4\text{-DVG}$) conform to Ru-single atom like catalyst. Bader charge analysis of the NRR reaction intermediates show a similarity in the large charge transfer to N atoms from Ru single atom and Al_5 center, with respective ΔG_{\max} of 0.53 eV and 0.78 eV in $\text{Ru}@N_4\text{-DVG}$ and $\text{Al}_5@N_4\text{-DVG}$ catalysts. Despite a higher free energy change in the potential rate determining step, the high NRR selectivity of $\text{Al}_5@N_4\text{-DVG}$ catalyst makes it a highly attractive catalyst for electrocatalytic ammonia production. The understanding from this chapter can be used to further the research on developing Al-

based catalysts for nitrogen fixation and feasible ambient ammonia production with the most abundant metal, aluminium.

5.5 References

- (1) Cherkasov, N.; Ibadon, A. O.; Fitzpatrick, P.; *Chem. Eng. Process. Process Intensif.* **2015**, *90*, 24–33.
- (2) Van Der Ham, C. J. M.; Koper, M. T. M.; Hettterscheid, D. G. H.; *Chem. Soc. Rev.* **2014**, *43* (15), 5183–5191.
- (3) Liu, D.; Chen, M.; Du, X.; Ai, H.; Lo, K. H.; Wang, S.; Chen, S.; Xing, G.; Wang, X.; Pan, H.; *Adv. Funct. Mater.* **2021**, *31* (11), 1–36.
- (4) Chanda, D.; Xing, R.; Xu, T.; Liu, Q.; Luo, Y.; Liu, S.; Tufa, R. A.; Dolla, T. H.; Montini, T.; Sun, X.; *Chem. Commun.* **2021**, *57* (60), 7335–7349.
- (5) Wang, J.; Yu, L.; Hu, L.; Chen, G.; Xin, H.; Feng, X.; *Nat. Commun.* **2018**, *9* (1).
- (6) Nazemi, M.; El-Sayed, M. A.; *J. Phys. Chem. Lett.* **2018**, *9* (17), 5160–5166.
- (7) Geng, Z.; Liu, Y.; Kong, X.; Li, P.; Li, K.; Liu, Z.; Du, J.; Shu, M.; Si, R.; Zeng, J.; *Adv. Mater.* **2018**, *30* (40), 2–7.
- (8) Han, J.; Ji, X.; Ren, X.; Cui, G.; Li, L.; Xie, F.; Wang, H.; Li, B.; Sun, X.; *J. Mater. Chem. A* **2018**, *6* (27), 12974–12977.
- (9) Wang, M.; Liu, S.; Qian, T.; Liu, J.; Zhou, J.; Ji, H.; Xiong, J.; Zhong, J.; Yan, C.; *Nat. Commun.* **2019**, *10* (1), 1–8.
- (10) Guo, W.; Liang, Z.; Zhao, J.; Zhu, B.; Cai, K.; Zou, R.; Xu, Q.; *Small Methods* **2018**, *2* (12), 1–6.
- (11) Yu, X.; Han, P.; Wei, Z.; Huang, L.; Gu, Z.; Peng, S.; Ma, J.; Zheng, G.; *Joule* **2018**, *2* (8), 1610–1622.
- (12) Zhang, L.; Ding, L. X.; Chen, G. F.; Yang, X.; Wang, H.; *Angew. Chemie - Int. Ed.* **2019**, *58* (9), 2612–2616.

- (13) Tao, H.; Choi, C.; Ding, L. X.; Jiang, Z.; Han, Z.; Jia, M.; Fan, Q.; Gao, Y.; Wang, H.; Robertson, A. W.; Hong, S.; Jung, Y.; Liu, S.; Sun, Z.; *Chem* **2019**, *5* (1), 204–214.
- (14) Chen, J.; Wang, H.; Wang, Z.; Mao, S.; Yu, J.; Wang, Y.; *ACS Catal.* **2019**, 5302–5307.
- (15) Maibam, A.; Govindaraja, T.; Selvaraj, K.; Krishnamurty, S.; *J. Phys. Chem. C* **2019**, *123*, 27492–27500.
- (16) Maibam, A.; Krishnamurty, S.; *J. Colloid Interface Sci.* **2021**, *600*, 480–491.
- (17) Du, H.-L.; Chatti, M.; Hodgetts, R. Y.; Cherepanov, P. V.; Nguyen, C. K.; Matuszek, K.; MacFarlane, D. R.; Simonov, A. N.; *Nature* **2022**, *609* (September).
- (18) Tian, Y. H.; Hu, S.; Sheng, X.; Duan, Y.; Jakowski, J.; Sumpter, B. G.; Huang, J.; *J. Phys. Chem. Lett.* **2018**, *9* (3), 570–576.
- (19) Sherbow, T. J.; Thompson, E. J.; Arnold, A.; Sayler, R. I.; Britt, R. D.; Berben, L. A.; *Chem. - A Eur. J.* **2019**, *25* (2), 454–458.
- (20) Lv, X. W.; Liu, Y.; Hao, R.; Tian, W.; Yuan, Z. Y.; *ACS Appl. Mater. Interfaces* **2020**, *12* (15), 17502–17508.
- (21) Fu, Y.; Richardson, P.; Li, K.; Yu, H.; Yu, B.; Donne, S.; Kisi, E.; Ma, T.; *Nano-Micro Lett.* **2020**, *12* (1), 1–13.
- (22) Guo, Y.; Yang, Q.; Wang, D.; Li, H.; Huang, Z.; Li, X.; Zhao, Y.; Dong, B.; Zhi, C.; *Energy Environ. Sci.* **2020**, *13* (9), 2888–2895.
- (23) Maibam, A.; Krishnamurty, S.; Ahmad Dar, M.; *Mater. Adv.* **2022**, *3* (1), 592–598.
- (24) Maibam, A.; Babarao, R.; Krishnamurty, S.; *Appl. Surf. Sci.* **2022**, *602*, 154401.
- (25) Cao, B.; Starace, A. K.; Judd, O. H.; Bhattacharyya, I.; Jarrold, M. F.; López, J. M.; Aguado, A.; *J. Am. Chem. Soc.* **2010**, *132* (37), 12906–12918.
- (26) Kumar, D.; Pal, S.; Krishnamurty, S.; *Phys. Chem. Chem. Phys.* **2016**, *18* (40), 27721–27727.

- (27) Neal, C. M.; Breaux, G. A.; Cao, B.; Starace, A. K.; Jarrold, M. F.; *Rev. Sci. Instrum.* **2007**, *78*.
- (28) Zagler, G.; Stecher, M.; Trentino, A.; Kraft, F.; Su, C.; Postl, A.; Längle, M.; Pesenhofer, C.; Mangler, C.; Harriet Åhlgren, E.; Markevich, A.; Zettl, A.; Kotakoski, J.; Susi, T.; Mustonen, K.; *2D Mater.* **2022**, *9*
- (29) Somasekaran, B.; Thirunarayanaswamy, A.; Palanivel, I.; *Mater. Today Proc.* **2021**, *50*, 2436–2442.
- (30) Khanna, V.; Kumar, V.; Bansal, S. A.; *Mater. Res. Bull.* **2021**, *138*, 111224.
- (31) Brodova, I. G.; Petrova, A. N.; Shirinkina, I. G.; Rasposienko, D. Y.; Yolshina, L. A.; Muradymov, R. V.; Razorenov, S. V.; Shorokhov, E. V.; *J. Alloys Compd.* **2021**, *859*, 158387.
- (32) Kresse, G.; Furthmüller, J.; *Comput. Mater. Sci.* **1996**, *6* (1), 15–50.
- (33) Perdew, J. P.; Burke, K.; Ernzerhof, M.; *Phys. Rev. Lett.* **1996**, *77* (18), 3865–3868.
- (34) Grimme, S.; Antony, J.; Ehrlich, S.; Krieg, H.; *J. Chem. Phys.* **2010**, *132* (15).
- (35) Tang, W.; Sanville, E.; Henkelman, G.; *J. Phys. Condens. Matter* **2009**, *21* (8).
- (36) Nosé, S.; *J. Chem. Phys.* **1984**, *81* (1), 511–519.
- (37) Nørskov, J. K.; Rossmeisl, J.; Logadottir, A.; Lindqvist, L.; Kitchin, J. R.; Bligaard, T.; Jónsson, H.; *J. Phys. Chem. B* **2004**, *108* (46), 17886–17892.
- (38) Zhao, J.; Chen, Z.; *J. Am. Chem. Soc.* **2017**, *139*, 12480–12487.
- (39) Ling, C.; Niu, X.; Li, Q.; Du, A.; Wang, J.; *J. Am. Chem. Soc.* **2018**, *140*, 14161–14168.
- (40) Momma, K.; Izumi, F.; *J. Appl. Cryst.* **2008**, *41*, 653–658.

Chapter 6

Materials
Advances



PAPER

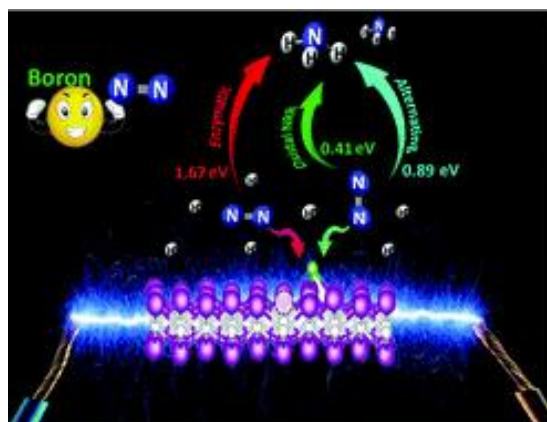
View Article Online
View Journal



Cite this: DOI: 10.1039/d1ma00953b

Electrocatalytic nitrogen reduction directed through the p-band center of boron on $B_{SAC}@Mo_2C\ddagger$

Ashakiran Maibam, ^{ab} Sailaja Krishnamurthy ^{*ab} and Manzoor Ahmad Dar ^{*c}



Maibam, A. et. al, *Mater. Adv.*, 2022, 3, 592-598.

In this chapter, greener modes of ammonia synthesis via the electrocatalytic route have been investigated on pristine and defective Mo_2C based monolayers anchored with metal-free boron atom catalysts. Boron single atom catalysts (SACs) on the defective Mo_2C monolayer has been found to activate N_2 strongly with an adsorption energy of 1.92 eV and reduce it to NH_3 efficiently with a significantly low overpotential of 0.41 eV. The exothermic adsorption of N_2 and low overpotential for the nitrogen reduction reaction (NRR) appertain to the p-band center of the boron atom catalyst and charge transfer between the adsorbed N_2 and the catalyst, respectively. This chapter brings forth the correlation between electron occupancy on the boron center and NRR catalytic efficiency on a metal-free SACs@ Mo_2C monolayer couple, thereby serving as a lead in designing metal free electrocatalysts for the NRR.

6.1 Introduction

With the rise in global temperature and greenhouse gas emissions, most industrial processes aim to achieve carbon neutrality. However, one process with an extremely high carbon footprint accounting for 6% of global CO₂ emissions and the consumption of approximately 1–2% of global energy¹ is the Haber–Bosch² ammonia synthesis process. With ammonia being an irreplaceable precursor in agriculture, various industries and energy applications,^{3,4} there is an urgent need to develop greener techniques for NH₃ synthesis through photocatalytic, electrocatalytic or photo-electrocatalytic routes to meet the current demands.^{5,6} The optimal goal towards achieving ammonia economy is to develop a catalyst that reduces N₂ to NH₃ under ambient conditions like the nitrogenase enzyme. The electrocatalytic route of nitrogen fixation is an attractive alternative owing to its efficiency and environment-friendly nature.^{7,8} However, with N₂ being a highly stable molecule with a N–N triple bond energy of 940 kJ mol⁻¹, the kinetics associated with the electrocatalytic nitrogen reduction reaction (NRR) are sluggish and the faradaic efficiency is low.⁷ As a result, the competing hydrogen evolution reaction (HER) is usually preferred over the sluggish NRR. Therefore, it is essential to design new and smart materials with high electrical conductivity that have the capability to subjugate the HER and enhance the NRR. Several scarce metals such as Ru,^{9,10} Au^{11,12} and Pd^{13,14} have been known to be highly effective NRR electrocatalysts with faradaic efficiencies of up to 36.6%,¹³ their cost and availability are issues that cannot be overcome. Hence, identifying cost effective electrocatalysts based on earth abundant metals such as Mo, Fe, and Co, etc. as potential alternatives for the NRR is the need of the hour.¹⁵

Notably, Mo metal is present as an active centre in nitrogenase enzymes, and possesses the requisite electronic structure to capture N₂ molecules and has been extensively studied for the NRR.¹⁶ Several other Mo-based two-dimensional (2D) materials, nanoparticles and nanoclusters, single atom catalysts (SACs) and organometallic complexes have been reported as efficient catalysts for the NRR.^{17–26} While Mo-containing organic and inorganic complexes efficiently adsorb and form stable dinitrogen complexes, their application as electrocatalysts or electrodes are not warranted.¹⁸ Mo clusters and SACs, on the other hand, require a conducting/semi-conducting support for further usage as electrocatalysts.^{19,20,22,27}

In this regard, Mo-based 2D materials such as MoS₂,^{24,28–31} MXenes (Mo₂C)^{32–34} and MBenes (Mo₂B₂)^{35,36} are appealing electrocatalysts owing to their high electrical conductivity and the presence of active Mo metal centres. These 2D materials not only show high hydrophilicity, stability and conductivity but are interesting from the catalytic aspect of nitrogen reduction as the Mo metal is accessible to the nitrogen molecule. Compared to MBenes, MXenes have been extensively investigated experimentally for the electrocatalytic NRR.^{32,37–39}

While computational studies on the electrochemical applications of Mo₂C based 2D materials have been extensively carried out, they have rarely been explored for the electrocatalytic NRR. One notable study on the electrocatalytic application of Mo₂C for the NRR was made recently by Zhang et al. wherein Mo₂C monolayers were investigated for the NRR through density functional theory (DFT) calculations.³⁴ It would be imperative to recollect that effective strategies to fine tune and improve the N₂ binding efficacy on a 2D monolayer are structural modifications and incorporating active atomic centers on it.⁴⁰ Thereby, pristine and defective Mo₂C monolayers coupled with a metal free single atom catalyst, in particular boron, are expected to enhance the N₂ adsorption and inherently improve the NRR process. Several experimental and computational studies have reported boron-based metal free catalysts on 2D materials to remarkably augment the electrocatalytic NRR by promoting N₂ adsorption and inhibiting the HER.^{41–43} The boron center behaves as a Lewis acid with empty p-orbitals, thereby resulting in a strong π - π^* interaction with N₂ and less energy demanding subsequent protonation steps for the NRR.^{44,45}

The correlation between charge transfer from the catalytic center and nitrogen reduction efficacy is one aspect of paramount importance that has not been explored to date. Thus, in the present chapter, we conducted a comprehensive investigation to provide a complete picture concerning the fundamental understanding of nitrogen activation and reduction on active boron atoms anchored on a pristine Mo₂C monolayer. Specifically, the coupling effect of boron single atom catalysts with defects on the Mo₂C monolayer and its influence on nitrogen activation and reduction was thoroughly investigated. The p-band center and electronic structure of 2D Mo₂C monolayers upon the anchoring of non-metallic boron atoms directly influences their NRR catalytic efficiency. Based on our results, we found that

a single boron atom catalyst anchored on a defective Mo₂C monolayer can effectively produce NH₃ at an overpotential as low as 0.41 eV.

6.2 Computational Details

All DFT calculations were carried out with the Vienna ab initio Simulation Package (VASP).⁴⁶ The generalized gradient approximation (GGA) and the Perdew–Burke–Ernzerhof (PBE)⁴⁷ functional has been employed with an energy cutoff of 532 eV to describe all electron core–interactions. A DFT-D3 correction method has been incorporated to account for the long-range van der Waals (vdW) interactions.⁴⁸ All the catalyst systems sampled with a (5 × 5 × 1) Monkhorst–Pack k-point grid and a vacuum space of 20 Å along the Z-direction are relaxed until the atomic energy and forces converge to 105 eV per atom and 0.005 eV Å⁻¹, respectively. For the density of states and electronic structure calculations, a higher (11 × 11 × 1) Monkhorst–Pack k-point grid has been employed. The stability of atomic boron catalysts on Mo₂C and its analogues is evaluated in terms of binding energy, E_b which is calculated by using the equation,

$$E_b = E(\text{B}_{\text{cat}}@\text{Mo}_2\text{C}) - E(\text{Mo}_2\text{C}) - E(\text{B}_{\text{cat}}) \quad (6.1)$$

where, E(B_{cat}@Mo₂C) and E(Mo₂C) are the total electronic energies of the 2D Mo₂C monolayer with and without atomic boron catalysts and E(B_{cat}) is the electronic energy of atomic boron. The adsorption of N₂ on the 2D Mo₂C monolayer has been computed for the parallel and perpendicular modes and the efficiency of these materials to chemisorp N₂ molecule has been calculated in terms of the N₂ adsorption energy, (E_{ads}) as given below,

$$E_{\text{ads}} = E(\text{B}_{\text{cat}}@\text{Mo}_2\text{C}-\text{N}_2) - E(\text{B}_{\text{cat}}@\text{Mo}_2\text{C}) - E(\text{N}_2) \quad (6.2)$$

where, E(B_{cat}@Mo₂C–N₂), E(B_{cat}@Mo₂C) and E(N₂) are the total electronic energies of N₂ adsorbed systems, B_{cat}@Mo₂C and free N₂ molecules, respectively. The Gibbs free energy change, ΔG in every protonation step of the NRR has been calculated by employing the computational SHE (standard hydrogen electrode) model proposed by Nørskov et al.⁴⁹ using the equation, ΔG = ΔE + ΔZPE - TΔS

where, ΔE is the change in electronic energy, ΔZPE is the change in zero-point energy, T is the room temperature (298.15 K) and ΔS is the change in entropy. The zero-point energies and entropy contributions are calculated by considering the vibrational

frequencies of the adsorbed gas phase species. Furthermore, the overpotential for the electrocatalytic NRR on the Mo₂C monolayer and its analogues has been calculated as $\eta = U_{\text{SHE}} - U_{\text{PDS}}$, where $U_{\text{SHE}} = -0.16$ eV, is the standard reduction potential of N₂ to NH₃ and $U_{\text{PDS}} = -\Delta G_{\text{max}}/e$ for the NRR pathway.

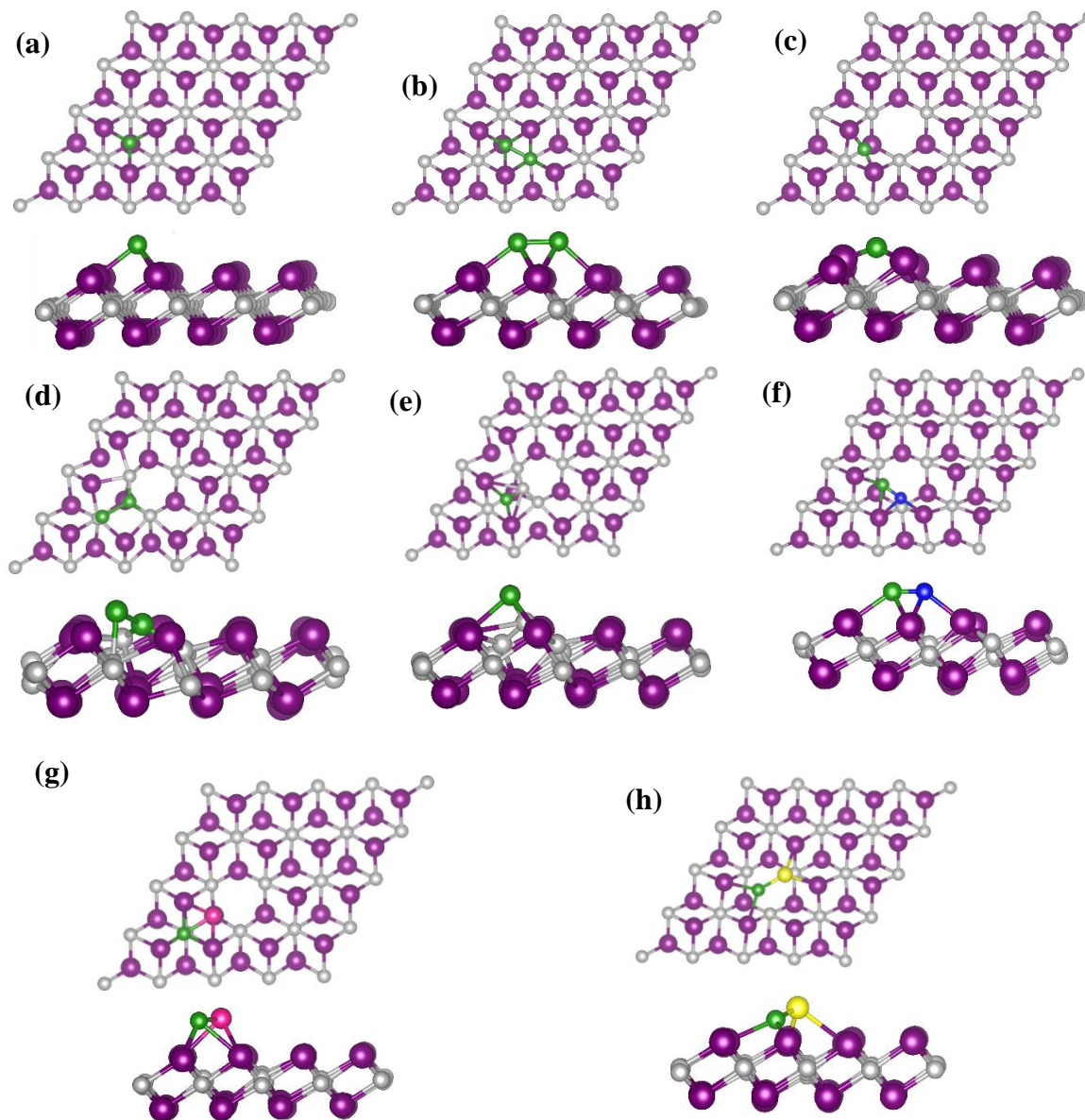


Figure 6.1: Geometric structure of all the $B_{\text{cat}}@Mo_2C$ catalysts (a) $B_{\text{SAC}}@Mo_2C$, (b) $B_{\text{DAC}}@Mo_2C$, (c) $B_{\text{SAC}}@Mo_2C-MO_{\text{vac}}$, (d) $B_{\text{SAC}}@Mo_2C-B_{\text{def}}$, (e) $B_{\text{SAC}}@Mo_2C-C_{\text{def}}$ (f) $B_{\text{SAC}}@Mo_2C-N_{\text{def}}$, (g) $B_{\text{SAC}}@Mo_2C-P_{\text{def}}$, (h) $B_{\text{SAC}}@Mo_2C-S_{\text{def}}$. Atomic colour code: C (grey), Mo (purple), B (green), N (blue), P (pink) and S (yellow).

6.3 Results and Discussions

6.3.1 N₂ adsorption on B_{cat}Mo₂C

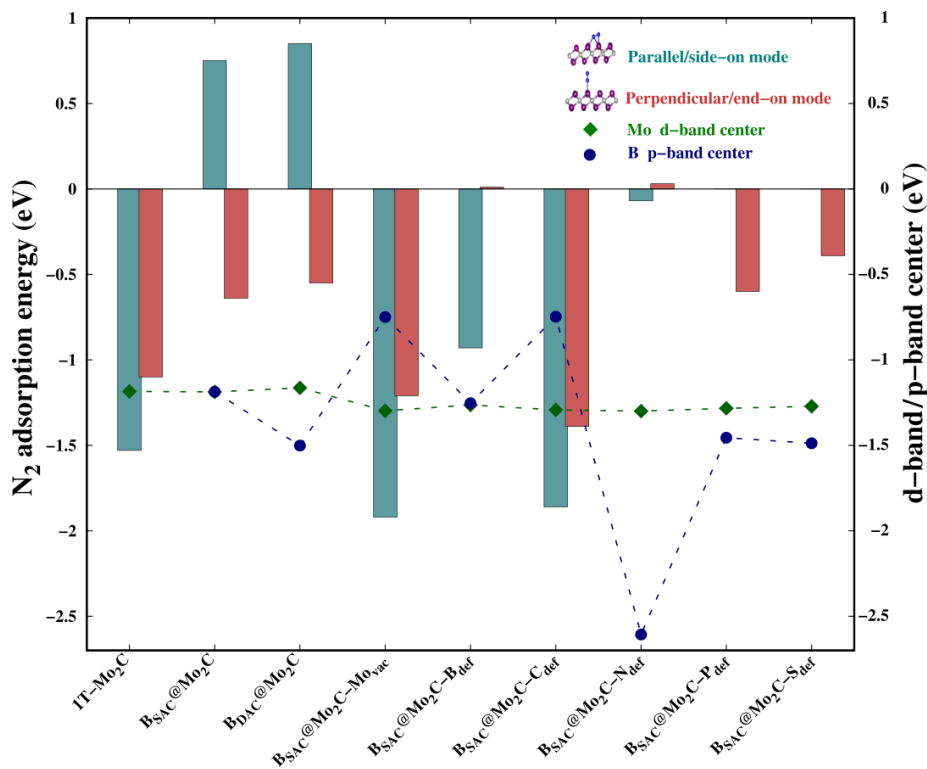


Figure 6.2: N₂ adsorption energies in different modes, and the Mo d-band center and B p-band center on different B_{cat}@Mo₂C catalysts.

The stability of atomic boron catalysts on Mo₂C is one of the fundamental prerequisites for their implementation as electrocatalysts for the NRR. Boron has been anchored on conventional pristine 1T-Mo₂C as a single atom catalyst (SAC) or a diatom catalyst (DAC), respectively referred to as B_{SAC}@Mo₂C and B_{DAC}@Mo₂C from now onwards. The geometric structures of the B_{SAC}@Mo₂C and B_{DAC}@Mo₂C catalysts are presented in **Figure 6.1(a-b)**. Anchoring B_{DAC} on Mo₂C was found to be more feasible with a binding energy of -7.07 eV as compared to B_{SAC} (-6.90 eV). The 2D Mo₂C monolayer was then subjected to two major surface modifications: a Mo-vacancy and defective Mo₂C with non-metal dopants as shown in **Figure 6.1(c-h)** Mo₂C with a vacant Mo-site is referred to as Mo₂C-Mo_{vac} and defective Mo₂C obtained by replacing one Mo atom from the surface with metal-free dopants is designated as Mo₂C-X_{def}, where X = B, C, N, P and S. On these

Mo-vacant and defective analogues of Mo_2C , we next adsorbed B single atoms to create a metal-free catalyst couple for nitrogen activation and reduction. The binding energy of B_{SAC} ranges from -5.35 eV on the $\text{Mo}_2\text{C}-\text{Mo}_{\text{vac}}$ catalyst to -6.25 eV, -5.37 eV, -7.92 eV, -5.81 eV and -4.77 eV respectively, on the $\text{Mo}_2\text{C}-\text{B}_{\text{def}}$, $\text{Mo}_2\text{C}-\text{C}_{\text{def}}$, $\text{Mo}_2\text{C}-\text{N}_{\text{def}}$, $\text{Mo}_2\text{C}-\text{P}_{\text{def}}$ and $\text{Mo}_2\text{C}-\text{S}_{\text{def}}$ catalysts. The exothermic binding energies of the boron atom catalysts on all Mo_2C analogues illustrates the stability of the boron SAC integrated on the defective Mo_2C monolayers.

We next investigated the N_2 adsorption efficacy and electronic properties of the $\text{B}_{\text{cat}}@ \text{Mo}_2\text{C}$ catalysts through the d-band centre of Mo, the p-band centre of B and the projected density of states (PDOS) with reference to pristine 1T- Mo_2C . **Figure 6.2** highlights the N_2 adsorption energies of the $\text{B}_{\text{cat}}@ \text{Mo}_2\text{C}$ catalysts with reference to 1T- Mo_2C and the correlation between N_2 adsorption with the d-band center of Mo and the p-band center of B. $\text{B}_{\text{SAC}}@ \text{Mo}_2\text{C}$ and $\text{B}_{\text{DAC}}@ \text{Mo}_2\text{C}$ exhibit a lower exothermic end-on mode of dinitrogen adsorption with E_{ads} values of -0.64 eV and -0.55 eV, respectively with respect to -1.10 eV on 1T- Mo_2C . It can also be noted that there are no significant changes in the Mo d-band center when B_{SAC} and B_{DAC} are anchored on Mo_2C , however the B p-center on $\text{B}_{\text{SAC}}@ \text{Mo}_2\text{C}$ is more positive than that of $\text{B}_{\text{DAC}}@ \text{Mo}_2\text{C}$. A more positive B p-band center infers that the B p-orbitals are closer to the Fermi level ($E_{\text{F}} = 0$ eV), which in turn leads to the feasible adsorption of N_2 .

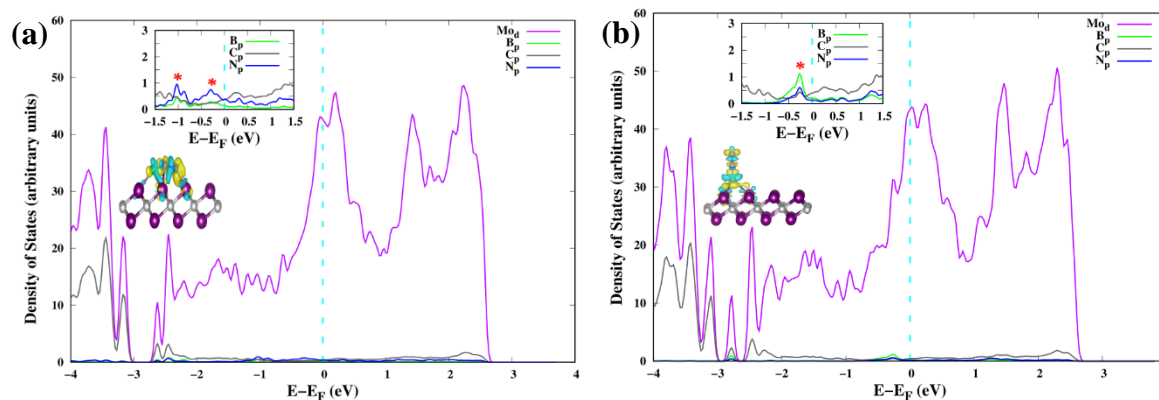


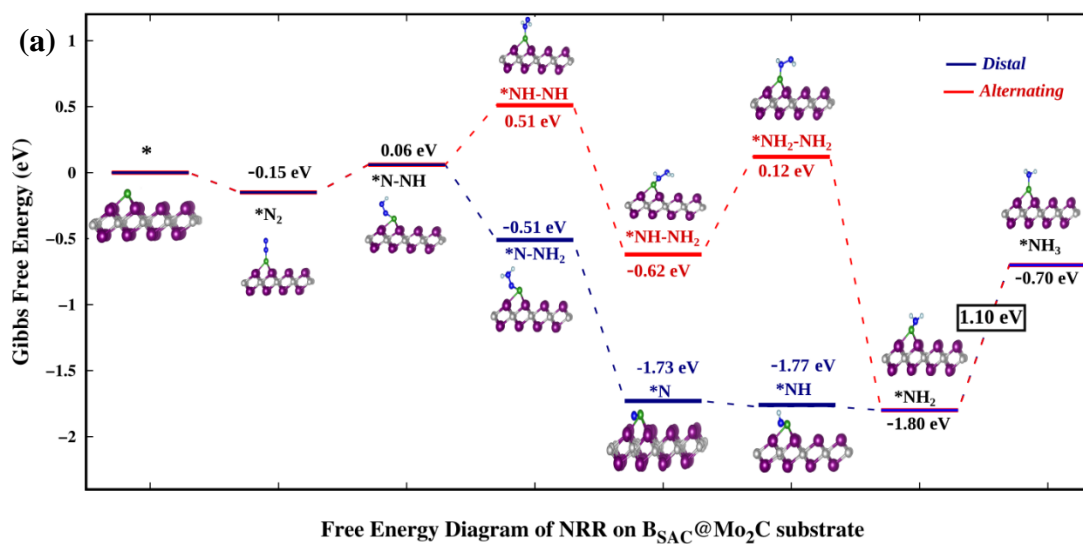
Figure 6.3: PDOS and CDD plots of N_2 adsorbed on $\text{B}_{\text{SAC}}@ \text{Mo}_2\text{C}-\text{Mo}_{\text{vac}}$ via (a) parallel/side-on mode and (b) perpendicular/end-on mode with the insets showing hybridisation of the N p-orbitals and B p-orbitals and the CDD plot generated isosurface density set to $0.003 \text{ e}\text{\AA}^{-3}$.

Generating a Mo-vacancy on the Mo₂C monolayer leads to a less positive Mo d-band center, but in contrast, the B p-band becomes more positive, which in turns leads to higher chemisorption (-1.92 eV) of N₂ on B_{SAC}@Mo₂C–Mo_{vac}. Moreover, on analysing the Bader charges on the B_{cat} centers, all the B_{cat} centers are found to be negatively charged, thereby implying that there is a charge transfer from the Mo₂C monolayer to B. The only exception being the B_{SAC}@Mo₂C–N_{def} and B_{SAC}@Mo₂C–S_{def} systems with positively charged or nearly neutral B_{cat} centers, respectively. Interestingly, these two systems possess a more negative B p-band center as compared to the rest of the systems, and thereby show lower exothermic N₂ adsorption. It is also important to note that a higher exothermic N₂ adsorption is not only influenced by the B p-band center but also by a more pronounced overlap between the p orbitals of the B and N atoms. The parallel/side-on mode of N₂ adsorption involves two B–N bonds, and results in two peaks in the PDOS plot as shown in **Figure 6.3**, with a greater electron density overlap when compared to a single B–N bond for the perpendicular/ end-on mode of N₂ adsorption on B_{SAC}@Mo₂C–Mo_{vac}. The B_{SAC}@Mo₂C–X_{def} catalysts follow a similar pattern of N₂ adsorption. For instance, B_{SAC}@Mo₂C–C_{def} with a more positive B p-band center exhibits better chemisorption of N₂ when compared to B_{SAC}@Mo₂C–N_{def} with a highly negative p-band center of B. It can be established that the activation of N₂ is influenced by the p-band center of B_{cat} on the B-anchored Mo₂C catalysts. Interestingly, it was noticed that the N₂ chemisorption efficacy of B_{SAC} with a Mo-vacancy is on a par with that of B_{SAC} with C-defective Mo₂C, while the rest of the non-metals, i.e. B, P, S and N show moderate to minimal adsorption of N₂. The PDOS plots also show the very interesting phenomenon of a synergistic effect between the C from the Mo₂C and B_{cat} centers. The systems that show a higher exothermic N₂ adsorption, in turn show a more pronounced overlap between the C p-orbitals and B p-orbitals, thus the synergistic effect of C and B enhances the N₂ adsorption efficiency in the B_{cat}@Mo₂C catalysts.

6.3.2 N₂ reduction to NH₃ on B_{cat}@Mo₂C catalysts

Finally, we explored the thermodynamics for the reduction of N₂ to NH₃ on the B_{cat}@Mo₂C catalysts that showed strong exothermic N₂ chemisorption. Also, the NRR pathways on B_{SAC}@Mo₂C and B_{DAC}@Mo₂C were analysed to deduce whether the role of a second B

atom enhances or inhibits the reduction process. Among the defective monolayers with surface modification $B_{SAC}@Mo_2C-Mo_{vac}$ and $B_{SAC}@Mo_2C-C_{def}$ were considered as both showed highly exothermic chemisorption of dinitrogen in both the parallel as well as the perpendicular mode. Previous studies have revealed that the reduction of N_2 can proceed via three pathways, viz. distal or alternating and enzymatic, respectively, for N_2 adsorbed in the perpendicular and parallel modes. On the $B_{SAC}@Mo_2C$ and $B_{DAC}@Mo_2C$ catalysts with N_2 adsorbed preferentially in an end-on mode, the NRR pathway was explored through the distal and alternating routes as shown in **Figure 6.4 (a-b)**, respectively. The last protonation step, i.e., $*NH_2 \rightarrow *NH_3$ has been found to be the potential determining step (PDS) for nitrogen reduction on $B_{SAC}@Mo_2C$ and $B_{DAC}@Mo_2C$ for both the distal and alternating route with a ΔG_{max} of 1.10 eV and 0.90 eV, respectively. The corresponding overpotentials, η for reducing nitrogen to ammonia on the two catalysts are therefore, 0.94 eV and 0.74 eV, respectively.



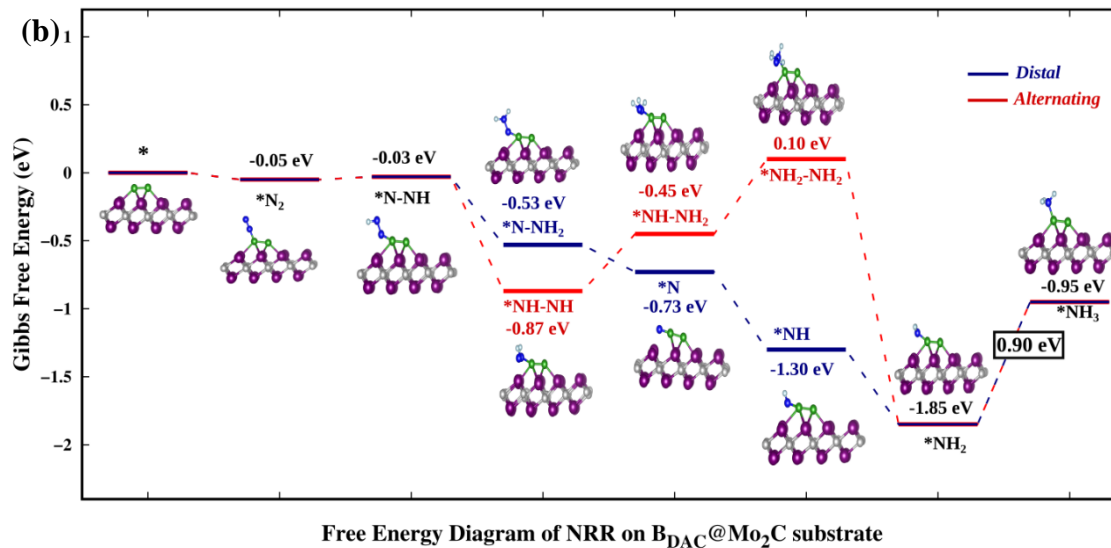


Figure 6.4: Free energy diagram of distal and alternating routes of Nitrogen Reduction Reaction (NRR) on (a) $B_{SAC}@Mo_2C$ and (b) $B_{DAC}@Mo_2C$.

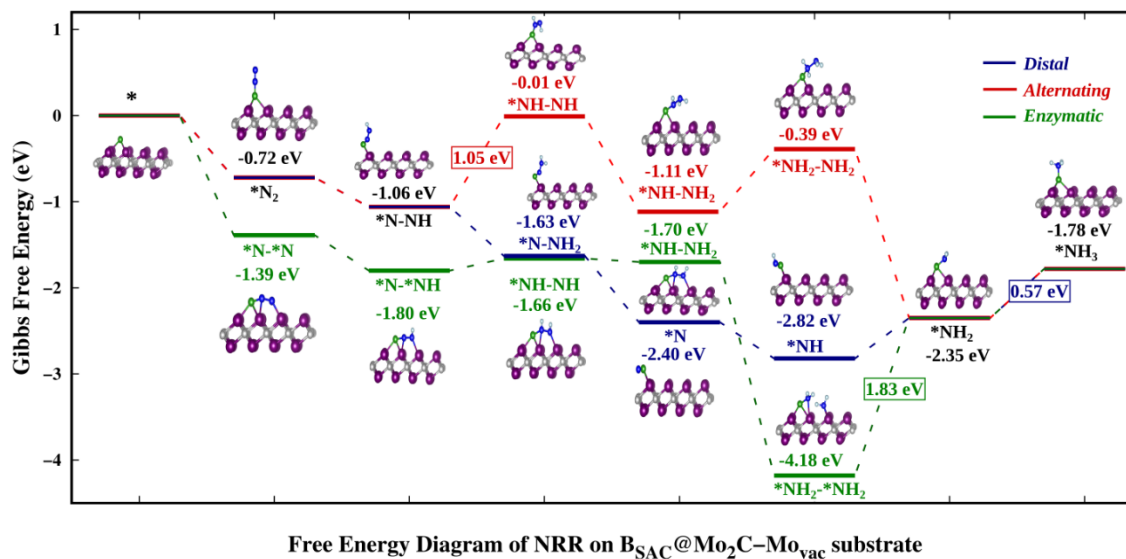


Figure 6.5: Free energy diagram of distal, alternating and enzymatic routes of Nitrogen Reduction Reaction (NRR) on $B_{SAC}@Mo_2C-Mo_{vac}$ catalyst.

It would be interesting to note that $B_{SAC}@Mo_2C$, which is more exergonic towards N_2 (0.15 eV) as compared to $B_{SAC}@Mo_2C$ (0.05 eV) follows a more uphill first protonation step (0.21 eV) and a complementary more uphill PDS. For the $B_{SAC}@Mo_2C-Mo_{vac}$

monolayer with one Mo-atom vacancy that shows exothermic N₂ adsorption in the side-on as well as end-on modes, the NRR mechanisms for all three possible routes were computed and are presented in **Figure 6.5**. Although, the parallel mode of N₂ adsorption is more exergonic than the perpendicular mode, and we expect the enzymatic route to be favoured over the distal or alternating route, the limiting potential for the NRR on the B_{SAC}@Mo₂C–Mo_{vac} catalyst was found to be 0.57 eV (*NH₂ → *NH₃) for the distal, 1.05 eV (*N–NH → *NH–NH) for the alternating and 1.83 eV (*NH₂–*NH₂ → *NH₂) for the enzymatic route. The distal route, which involves the protonation of only one nitrogen atom to form the first ammonia molecule, can be seen to show downhill reaction steps until the fourth protonation step. The preference for the distal mode could be accounted for by less steric hindrance caused by subsequent protonation on the nitrogen atoms. It is interesting to note that the B_{SAC}@Mo₂C–Mo_{vac} catalyst shows a high affinity for capturing the *NH₂ moiety as it can be found from the enzymatic route. The *NH₂–*NH₂ intermediate shows a highly exergonic adsorption with dissociation of the N–N bond and the adsorption of one *NH₂ on the Mo atom of the monolayer. Dissociating the N–N bond would be the ultimate goal of the NRR, however, if the catalyst holds onto the ammonia molecule strongly, the effectiveness and applicability of the catalyst is restricted. As a result, the enzymatic route would be a highly unlikely and unfavoured route for reducing N₂ molecules. A similar case of the high exergonic adsorption of the *NH₂–*NH₂ intermediate can be seen for the B_{SAC}@Mo₂C–Cd_{ef} catalyst (**Figure 6.6**), wherein the limiting potentials for nitrogen reduction were found to be 1.42 eV for the distal and alternating routes (*NH₂ → *NH₃) and 2.26 eV for the enzymatic route (*NH₂–*NH₂ → *NH₂). The limiting potentials and the corresponding potential determining steps on the above mentioned B_{cat}@Mo₂C catalysts are summarised in **Table 6.1**.

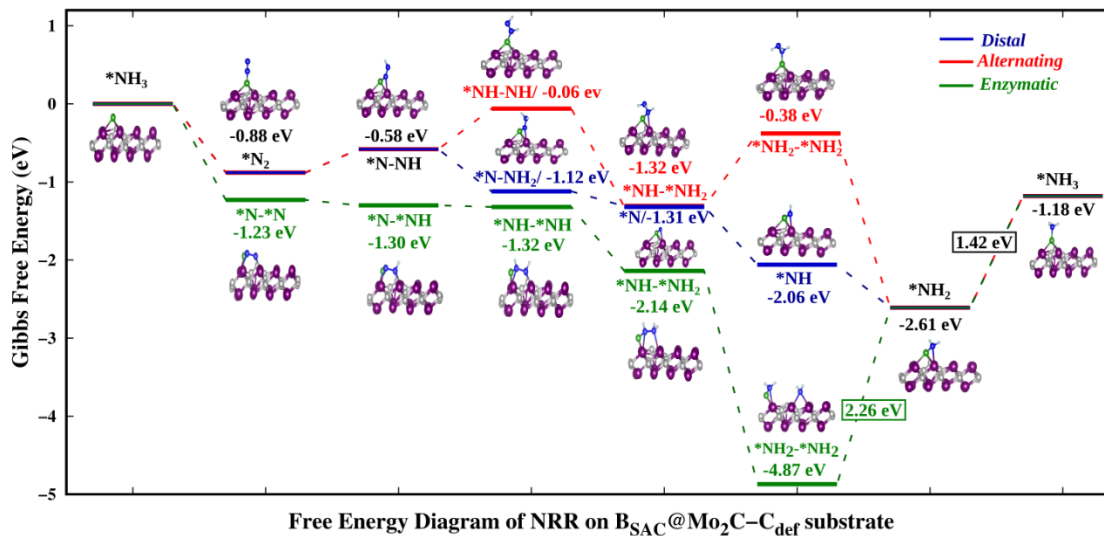


Figure 6.6: Free energy diagram of distal, alternating and enzymatic routes of Nitrogen Reduction Reaction (NRR) on $B_{SAC}@Mo_2C-C_{def}$ catalyst.

Table 6.1: Gibbs free energies, ΔG (eV) of N_2 adsorption, first protonation and rate determining step (ΔG_{max}) and overpotential, η for all routes of NRR on the $B_{cat}@Mo_2C$ catalysts.

$B_{cat}@Mo_2C$ catalysts	NRR route	ΔG in eV (* $N_2 \rightarrow *N_2H$)	Rate determining step	ΔG_{max} (eV)	η (eV)
$B_{SAC}@Mo_2C$	Distal	0.21	* $NH_2 \rightarrow *NH_3$	1.10	0.94
	Alternating	0.21	* $NH_2 \rightarrow *NH_3$	1.10	0.94
$B_{DAC}@Mo_2C$	Distal	0.02	* $NH_2 \rightarrow *NH_3$	0.90	0.74
	Alternating	0.02	* $NH_2 \rightarrow *NH_3$	0.90	0.74
$B_{SAC}@Mo_2C-Mo_{vac}$	Distal	-0.34	* $NH_2 \rightarrow *NH_3$	0.57	0.41
	Alternating	-0.34	* $N-NH \rightarrow *NH-NH$	1.05	0.89
	Enzymatic	-0.42	* $NH_2-*NH_2 \rightarrow *NH_2$	1.83	1.67
$B_{SAC}@Mo_2C-C_{def}$	Distal	0.30	* $NH_2 \rightarrow *NH_3$	1.42	1.26
	Alternating	0.30	* $NH_2 \rightarrow *NH_3$	1.42	1.26
	Enzymatic	-0.07	* $NH_2-*NH_2 \rightarrow *NH_2$	2.26	2.10

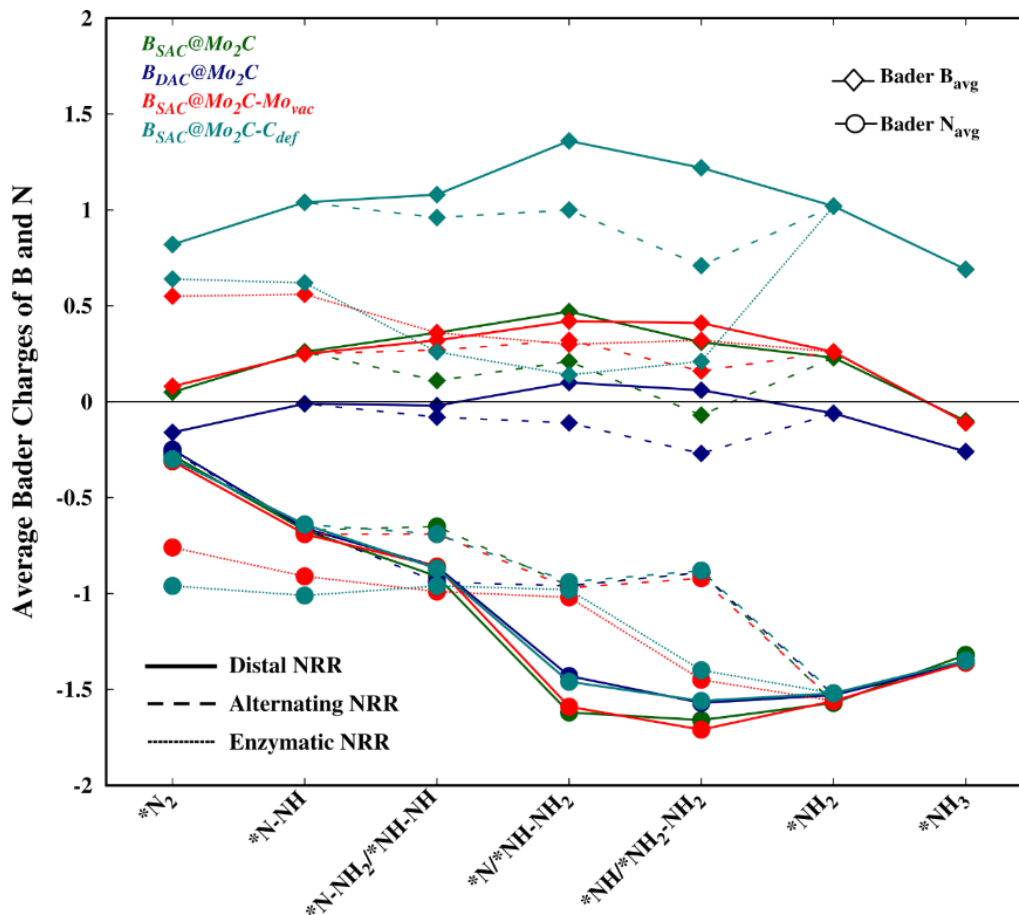


Figure 6.7: Bader charges on N and B atom catalysts for N_xH_y intermediates involved in the free energy diagram for the NRR on all the $B_{cat}@Mo_2C$ catalysts.

6.3.3 Mechanistic insights from electronic properties

While an exergonic adsorption of N_2 is essential for the feasible capture of N_2 , it is not the only deciding factor for successful nitrogen reduction. There have been no accounts correlating dinitrogen adsorption to the efficacy of nitrogen reduction and the corresponding limiting potential. The exergonic free energy of N_2 follows the order $B_{SAC}@Mo_2C-Mo_{vac} > B_{SAC}@Mo_2C-C_{def} > B_{SAC}@Mo_2C > B_{DAC}@Mo_2C$, however the limiting potential of nitrogen reduction follows the order $B_{SAC}@Mo_2C-C_{def} > B_{SAC}@Mo_2C > B_{DAC}@Mo_2C > B_{SAC}@Mo_2C-Mo_{vac}$. In order to correlate the N_2 adsorption and the limiting potential, we probe into the electronic properties of the adsorbed N_2 and N_xH_y species via the Bader charges on the B atom and N atoms for all the $B_{cat}@Mo_2C$ catalysts

as shown in **Figure 6.7**. The N-atoms are seen to be negatively charged on all the N_xH_y intermediates and tend to be more electron rich for subsequent reaction steps thereby making the protonation facile. While the differences in Bader charge on the N-atoms are minute for different catalysts, the charges on the B-atoms are prominent with less positive B-atoms on the $B_{DAC}@Mo_2C$, $B_{SAC}@Mo_2C-Mo_{vac}$ and $B_{SAC}@Mo_2C$ catalysts, followed by the $B_{SAC}@Mo_2C-C_{def}$ catalyst. A highly positive B-atom on the corresponding N_xH_y intermediates would deplete the negative charge on the N-atom, thereby restricting the protonation steps as seen in the case of $B_{SAC}@Mo_2C-C_{def}$. Therefore, the $B_{SAC}@Mo_2C-Mo_{vac}$ catalyst with strong N_2 chemisorption captures the dinitrogen molecule effectively and the electron deficient B-atom aids the protonation steps in the NRR, thus making it an attractive electrocatalyst when 0.57 eV is supplied as limiting potential and the corresponding overpotential observed is 0.41 eV. In contrast, the relatively high limiting potential of 1.10 eV for $B_{SAC}@Mo_2C$ in spite of the similar charges on the B-atoms can be accounted for by a less exergonic N_2 adsorption as compared to $B_{SAC}@Mo_2C-Mo_{vac}$. Additionally, $B_{DAC}@Mo_2C$ with electron rich B-atoms shows a relatively higher limiting potential of 0.90 eV owing to its less exergonic N_2 adsorption. We further correlate our analogy to the first protonation step of the NRR, which is usually considered a crucial step in the NRR. It has been reported that a less endergonic or exergonic $*N_2 \rightarrow *N_2H$ step leads to a lower limiting potential for nitrogen reduction. Upon comparison of the free energies of the first protonation steps, the $B_{cat}@Mo_2C$ catalysts with less endergonic free energies, i.e., $B_{SAC}@Mo_2C-Mo_{vac}$ (-0.34 eV) and $B_{DAC}@Mo_2C$ (0.02 eV) exhibit lower limiting potentials as compared to $B_{SAC}@Mo_2C$ and $B_{SAC}@Mo_2C-C_{def}$. This analogy holds true only for the distal and alternating routes wherein N_2 has been adsorbed in the end-on mode. Our previous argument correlating N_2 adsorption free energies and Bader charges is in agreement with the analogy of first protonation energies, and therefore can give insightful information on the mutual correlation between the free energies of the adsorption and electronic properties that directly govern the limiting potentials of the NRR on $B_{cat}@Mo_2C$ catalysts. Furthermore, the $B_{SAC}@Mo_2C-Mo_{vac}$ catalyst with one Mo -vacancy is found to efficiently capture and accentuate the catalytic activity of the boron SAC with a very low overpotential of 0.41 eV for the NRR. This study provides an indepth

analysis of the electronic factors crucial for efficient N₂ adsorption and reduction, and proposes the B_{SAC}@Mo₂C–Mo_{vac} catalyst as a potential candidate for the NRR.

6.4 Conclusions

In summary, a detailed and systematic DFT investigation has been carried out to analyse the efficacy of N₂ adsorption and reduction on B_{cat}@Mo₂C monolayers. Our study identifies a metal-free boron anchored defective Mo₂C monolayer with superior electrocatalytic activity for the NRR at 0.41 eV on account of a more positive p-band center and the negative charge of boron SACs that implicitly stabilizes the intermediates along the energy profile of the NRR. The insights gained from this chapter can be implemented for further research towards the design of efficient B-atom based electrocatalysts for the nitrogen reduction reaction.

6.5 References

- (1) Cherkasov, N.; Ibadon, O.; Fitzpatrick, P.; *Chem. Eng. Process.* **2015**, *90*, 24-33.
- (2) Ham, C. J. M.; Koper, M. T. M.; Hetterscheid, D. G. H.; *Chem. Soc. Rev.* **2014**, *43*, 5183-5191.
- (3) Erisman, J. W.; Sutton, M. A.; Galloway, J.; Klimont, Z.; Winiwarter, W.; *Nat. Geosci.* **2008**, *1*, 636-639.
- (4) Afif, A.; Radenahmad, N.; Cheok, Q.; Shams, S.; Kim, J. H.; Azad, A. K.; *Renewable Sustainable Energy Rev.* **2016**, *60*, 822-835.
- (5) Zheng, G.; Yan, J. M.; Yu, G.; *Small Methods* **2019**, *3*, 1900070.
- (6) Xue, X.; Chen, R.; Yan, C.; Zhao, P.; Hu, Y.; Zhang, W.; Yang, S.; Jin, Z.; *Nano Res.* **2019**, *12*, 1229-1249.
- (7) Tang, C.; Qiao, S.-Z.; *Chem. Soc. Rev.* **2019**, *48*, 3166-3180.

- (8) Qing, G.; Ghazfar, R.; Jackowski, S. T.; Habibzadeh, F.; Ashtiani, M. M.; Chen, C.-P.; Smith III, M. R.; Hamann, T. W.; *Chem. Rev.* **2020**, *120*, 5437-5516.
- (9) Tao, H.; Choi, C.; Ding, L.-X.; Jiang, Z.; Han, Z.; Jia, M.; Fan, Q.; Gao, Y.; Wang, H.; Robertson, A. W.; Hong, S.; Jung, Y.; Liu, S.; Sun, Z.; *Chem* **2019**, *5*, 204-214.
- (10) Yao, Y.; Wang, H.; Yuan, X.-Z.; Li, H.; Shao, M.; *ACS Energy Lett.* **2019**, *4*, 1336-1341.
- (11) Qin, Q.; Heil, T.; Antonietti, M.; Oschatz, M.; *Small Methods* **2018**, *2*, 1800202.
- (12) Zhang, K.; Guo, R.; Pang, F.; He, J.; Zhang, W.; *ACS Sustainable Chem. Eng.* **2019**, *7*, 10214-10220.
- (13) Zhao, H.; Zhang, D.; Li, H.; Qi, W.; Wu, X.; Han, Y.; Cai, W.; Wang, Z.; Lai, J.; Wang, L.; *Adv. Energy Mater.* **2020**, *10*, 2002131.
- (14) Deng, G.; Wang, T.; Alshehri, A. A.; Alzahrani, K. A.; Wang, Y.; Ye, H.; Luo, Y.; Sun, X.; *J. Mater. Chem. A* **2019**, *7*, 21674-21677.
- (15) Foster, S. L.; Perez Bakovic, S. I.; Duda, R. D.; Maheshwari, S.; Milton, R. D.; Minter, S. D.; Janik, M. J.; Renner, J. N.; Greenlee, L. F.; *Nat. Catal.* **2018**, 490-500.
- (16) Hoffman, B. M.; Lukoyanov, D.; Yang, Z.-Y.; Dean, D. R.; Seefeldt, L. C.; *Chem. Rev.* **2014**, *114*, 4041-4062.
- (17) Guo, X.; Wan, X.; Shui, J.; *Cell Reports Physical Science* 2021, *2*, 100447.
- (18) MacLeod, K. C.; Holland, P. L.; *Nat. Chem.* **2013**, *5*, 559-565.
- (19) Yesudoss, D. K.; Lee, G.; Shanmugam, S.; *Applied Catalysis B: Environmental* **2021**, *287*, 119952.
- (20) Han, L.; Liu, X.; Chen, J.; Lin, R.; Liu, H.; Lü, F.; Bak, S.; Liang, Z.; Zhao, S.; Stavitski, E.; Luo, J.; Adzic, R. R.; Xin, H. L.; *Angew. Chem. Int. Ed.* **2019**, *58*, 2321-2325.

- (21) Li, Q.; Qiu, S.; Liu, C.; Liu, M.; He, L.; Zhang, X.; Sun, C.; *J. Phys. Chem. C* **2019**, *123*, 2347-2352.
- (22) Maibam, A.; Govindaraja, T.; Selvaraj, K.; Krishnamurty, S.; *J. Phys. Chem. C* **2019**, *123*, 27492-27500.
- (23) Johnson, L. R.; Sridhar, S.; Zhang, L.; Fredrickson, K. D.; Raman, A. S.; Jang, J.; Leach, C.; Padmanabhan, A.; Price, C. C.; Frey, N. C.; Raizada, A.; Rajaraman, V.; Saiprasad, S. A.; Tang, X.; Vojvodic, A.; *ACS Catal.* **2020**, *10*, 253-264.
- (24) Suryanto, B. H. R.; Wang, D.; Azofra, L. M.; Harb, M.; Cavallo, L.; Jalili, R.; Mitchell, D. R. G.; Chatti, M.; MacFarlane, D. R.; *ACS Energy Lett.* **2019**, *4*, 430-435.
- (25) Zhang, B.; Zhou, J.; Elliott, S. R.; Sun, Z.; *J. Mater. Chem. A* **2020**, *8*, 23947-23954.
- (26) Li, Q.; He, L.; Sun, C.; Zhang, X.; *J. Phys. Chem. C* **2017**, *121*, 27563-27568.
- (27) Ou, P.; Zhou, X.; Meng, F.; Chen, C.; Chen, Y.; Song, J.; *Nanoscale* **2019**, *11*, 13600-13611.
- (28) Yang, T.; Song, T. T.; Zhou, J.; Wang, S.; Chi, D.; Shen, L.; Yang, M.; Feng, Y. P.; *Nano Energy* **2020**, *68*, 104304.
- (29) Zhang, L.; Ji, X.; Ren, X.; Ma, Y.; Shi, X.; Tian, Z.; Asiri, A. M.; Chen, L.; Tang, B.; Sun, X.; *Adv. Mater.* **2018**, *30*, 1800191.
- (30) Zhai, X.; Li, L.; Liu, X.; Li, Y.; Yang, J.; Yang, D.; Zhang, J.; Yan, H.; Ge, G.; *Nanoscale* **2020**, *12*, 10035-10043.
- (31) Ma, C.; Yan, X.; He, H.; Liu, B.; Yan, S.; *Sustainable Energy Fuels* **2021**, *5*, 2415-2418.
- (32) Ba, K.; Wang, G.; Ye, T.; Wang, X.; Sun, Y.; Liu, H.; Hu, A.; Li, Z.; Sun, Z.; *ACS Catal.* **2020**, *10*, 7864-7870.

- (33) Ramaiyan, K. P.; Ozden, S.; Maurya, S.; Kelly, D.; Babu, S. K.; Benavidez, A.; Garzon, F. G.; Kim, Y. S.; Kreller, C. R.; Mukundan, R.; *J. Electrochem. Soc.* **2020**, *167*, 044506.
- (34) Zhang, B.; Zhou, J.; Elliott, S. R.; Sun, Z.; *J. Mater. Chem. A* **2020**, *8*, 23947-23954.
- (35) Qi, S.; Fan, Y.; Zhao, L.; Li, W.; Zhao, M.; *Appl. Surf. Sci.* **2021**, *536*, 147742.
- (36) Yang, X.; Shang, C.; Zhou, S.; Zhao, J.; *Nanoscale Horiz.*, **2020**, *5*, 1106-1115.
- (37) Liu, Y.; Gu, L.; Zhu, X.; Zhang, Q.; Tang, T.; Zhang, Y.; Li, Y.; Bao, J.; Dai, Z.; Hu, J. S.; *J. Mater. Chem. A* **2020**, *8*, 8920-8926.
- (38) Ren, X.; Zhao, J.; Wei, Q.; Ma, Y.; Guo, H.; Liu, Q.; Wang, Y.; Cui, G.; Asiri, A. M.; Li, B.; Tang, B.; Sun, X.; *ACS Cent. Sci.* **2019**, *5*, 116-121.
- (39) Ma, Y.; Yang, T.; Zou, H.; Zang, W.; Kou, Z.; Mao, L.; Feng, Y.; Shen, L.; Pennycook, S. J.; Duan, L.; Li, X.; Wang, J.; *Adv. Mater.* **2020**, *32*, 2002177.
- (40) Maibam, A.; Krishnamurty, S.; *Journal of Colloid and Interface Science* **2021**, *600*, 480-491.
- (41) Liu, X.; Jiao, X.; Zheng, Y.; Qiao, S.-Z.; *ACS Catal.* **2020**, *10*, 1847-1854.
- (42) Liu, C.; Li, Q.; Wu, C.; Zhang, J.; Jin, Y.; MacFarlane, D. R.; Sun, C.; *J. Am. Chem. Soc.* **2019**, *141*, 2884-2888.
- (43) Xiao, S.; Luo, F.; Hua, H.; Yang, Z.; *Chem. Commun.* **2020**, *56*, 446-449.
- (44) Shi, L.; Li, Q.; Ling, C.; Zhang, Y.; Ouyang, Y.; Baia, X.; Wang, J.; *J. Mater. Chem. A* **2019**, *7*, 4865-4871.
- (45) Ling, C.; Niu, X.; Li, Q.; Du, A.; Wang, J.; *J. Am. Chem. Soc.* **2018**, *140*, 14161-14168.
- (46) Kresse, G.; Furthmuller, J.; *Comput. Mater. Sci.* **1996**, *6*, 15-50.

- (47) Perdew, J. P.; Burke, K.; Ernzerhof, M.; *Phys. Rev. Lett.* **1996**, *77*, 3865-3868.
- (48) Grimme, S.; Antony, J.; Ehrlich, S.; Krieg, H.; *J. Chem. Phys.* **2010**, *132*, 154104.
- (49) Nørskov, J. K.; Rossmeisl, J.; Logadottir, A.; Lindqvist, L.; Kitchin, J. R.; Bligaard, T.; Jónsson, H.; *J. Phys. Chem. B* **2004**, *108*, 17886-17892.

Chapter 7

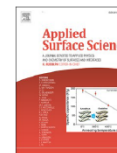
Applied Surface Science 602 (2022) 154401



Contents lists available at ScienceDirect

Applied Surface Science

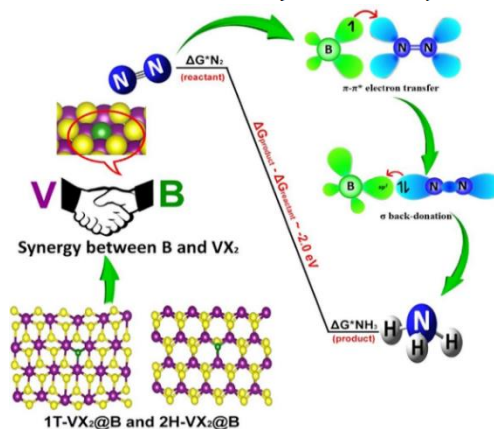
journal homepage: www.elsevier.com/locate/apsusc



Full Length Article

Doped 2D VX_2 ($X = S, Se, Te$) monolayers as electrocatalysts for ammonia production: A DFT based study

Ashakiran Maibam^{a,b,c}, Ravichandar Babarao^{b,d,*}, Sailaja Krishnamurthy^{a,c,*}



Maibam, A. et. al, *Applied Surface Science*, 2022, 602, 154401

In this chapter, electrocatalytic nitrogen fixation under ambient conditions on vanadium dichalcogenides (VX_2) with non-metal dopants has been explored herein. Understanding the interface chemistry, inherent electronic and acute synergistic nature of non-metal dopants on two unique phases of VX_2 has been meticulously explored through a scrutiny of several non-metal atoms as catalytic centers. The efficacy of N_2 chemisorption and $N-N$ bond activation has been implemented as crucial parameters to realize boron and carbon doped VX_2 monolayers to be electrocatalytically active for nitrogen reduction reaction (NRR). Detailed investigation on the NRR mechanism brings out the pivotal role of thermodynamic favourability for product formation obtained from Gibbs free energy differences. The charge transfer on N and $\pi-\pi^*$ orbital hybridization and electron “donor–acceptor” mechanism between the non-metal and N_2 has been found to modulate the electrocatalytic barrier for NRR on VX_2 monolayers. This study proposes boron doped VS_2 as an efficient chemically feasible, earth abundant sustainable electrocatalyst for NRR with an overpotential as low as 0.06 eV.

7.1 Introduction

With the average CO₂ concentration in the air hitting a maximum of 419 ppm in 2021, global warming and climate change are looming over the earth. To meet the 2030 sustainable goals, there is a need to halt the release of greenhouse gases in the atmosphere and curb processes that have a high carbon footprint.¹ One industrial process associated with 6% of global CO₂ emissions is artificial nitrogen fixation via the Haber-Bosch process.^{2,3} Ammonia is one of the most influential chemicals driving the economy of several countries and its latent energy density, when tapped properly will open up avenues for new generation fuels. Consequently, there is a need to develop carbon free technologies for artificial nitrogen fixation through electrocatalytic, photocatalytic, or photoelectrocatalytic routes to cater to the ever-increasing demand for ammonia.⁴ The crux of achieving ammonia economy via an electrocatalytic route for artificial nitrogen fixation is one of the most sought after green modes of ammonia synthesis and several materials have been explored for efficient nitrogen fixation.^{5,6} However, the major setback in the advancement of electrocatalytic nitrogen reduction reaction (eNRR) is the slothful kinetics of N-N triple bond dissociation in addition to a low yield and Faradaic efficiency.⁷ Henceforth, it is imperative to develop state-of-the-art highly conducting smart chemically affordable materials for prospective applications in eNRR.

A remarkably inexpensive material of high electrical conductivity and prospects for application as electrocatalysts is transition metal dichalcogenides (TMDs).^{8,9} These two-dimensional (2D) materials possess exceptional properties as compared to their bulk counterparts and have piqued the interest of several researchers since the last decade.^{10,11} Interestingly, TMDs have been reported to exhibit metallic or semiconducting properties upon varying the combination of chalcogens (S, Se, Te) with different transition metals. Most intriguingly, the change in crystal phases can also influence the electronic as well as magnetic properties. This ambidexterity in the electronic and magnetic properties of TMDs further makes them attractive candidates for novel applications. Notably, vanadium dichalcogenides, VX₂ (X = S, Se, Te) which shows intrinsic ferromagnetism is one such TMD with versatile attributes that exhibits different electronic and magnetic properties in different phases, i.e., 1T and 2H phases or with different dichalcogens.¹²⁻¹⁴

Recent studies on vanadium dichalcogenides have prompted the 1T phase of VX_2 to be metallic, while the 2H phase is semimetallic in VS_2 and VSe_2 and metallic in VTe_2 monolayers. Several experimental and computational studies have also reported the 2H phase to show higher stability and magnetic moment than the 1T phase for VS_2 monolayers, while most studies of VSe_2 and VTe_2 monolayers are focused on the metallic 1T-phase.¹⁵⁻²⁰ Besides showing conformable properties, the presence of vanadium metal in nitrogenase enzyme, its high catalytic activity for nitrogen reduction along with natural abundance and durability is an added advantage of these vanadium based materials for application in eNRR.^{21,22} Furthermore, the electronic, magnetic, and optical properties of the VX_2 monolayers can be altered either by inducing physical constraints like mechanical strain, modulating temperature, tuning the material width and thickness, or chemical influence such as metal or non-metal doping and charge doping.²³⁻²⁸

In this aspect, it would be imperative to look into introducing dopants on vanadium dichalcogenides as this approach has been pursued widely on several 2D materials as a non-destructive, chemically feasible method to activate the dormant basal planes and calibrate the electrocatalytic activity of VX_2 monolayers. The debate would then be to critically choose the dopants that will enhance the electrocatalytic properties of these monolayers for nitrogen fixation. While metal atom dopants and non-metals have been explored simultaneously, it is important that research on developing efficient electrocatalysts for nitrogen fixation also accounts for the sustainability of developing these novel materials and the dopants to be employed. Non-metal dopants offer an advantage of non-toxicity and abundance when compared to metals, and one such non-metal dopant that has been extensively employed as a dopant on several 2D materials for promoting nitrogen fixation is boron.²⁹⁻³²

In this chapter, we have investigated the role of several non-metals dopants for activating the electrocatalytic activity of vanadium dichalcogenides. It would be essential to probe for a non-metal dopant that would lead to synergistic activation of the different phases of vanadium dichalcogenide monolayers. This chapter delves into the criticality of considering the N–N bond elongation as another parameter to be considered alongside the Gibbs Free energy of N_2 adsorption and the first protonation step as we have discussed

in the previous chapter.³³ Furthermore, we believe a linear relationship between Gibbs Free energy differences of the intermediate steps in NRR plays an integral role in determining the limiting potential of nitrogen reduction. From our results, we found boron and carbon atoms when doped on 2H and 1T phases, respectively, of VS₂ monolayers to synergistically enhance their electrocatalytic properties and produce ammonia at limiting potentials as low as 0.22 eV and 0.42 eV, respectively.

7.2 Computational Details

Spin-polarized DFT calculations to optimize all vanadium dichalcogenide monolayers were carried out with Vienna ab-initio Simulation Package (VASP.5.4).³⁴ An energy cut-off of 400 eV has been employed to describe all electron interactions in the framework of a generalized gradient approximation Perdew-Burke-Ernzerhof (PBE) functional.³⁵ The long- range van der Waals (vdW) interactions between TMD monolayers have been incorporated in the electronic calculations with a DFT-D3 correction.³⁶ All the VX₂ monolayer has been sampled with a vacuum space of 20 Å along the Z-direction and a (5 × 5 × 1) Monkhorst- Pack kpoint grid. The vanadium dichalcogenide monolayer systems are allowed to relax till the atomic energy and forces reach a cutoff of 10⁻⁶ eV/atom and 0.001 eV/Å respectively. The electronic property analysis has been carried out by considering a higher kpoint grid of (11 × 11 × 1) Monkhorst-Pack grid. Ab initio molecular dynamics simulations (AIMD) simulations have been performed with a Noé–Hoover thermostat of 298 K in an NVT ensemble for 10 ps, with a time step of 3 fs to evaluate the thermodynamic stability of VX₂ systems.³⁷⁻³⁹ The feasibility of formation of 1 T and 2H monolayer phases of pristine and non-metal doped vanadium dichalcogenides has been computed in terms of formation energy per atom, E_{form} by using the equation,

$$E_{\text{form}} = 1/n \{ E(\text{VX}_2 @ \text{Y}_{\text{cat}}) - N_{\text{V}}E_{\text{V}} - N_{\text{X}}E_{\text{X}} - N_{\text{Y}}E(\text{Y}_{\text{cat}}) \} \quad (7.1)$$

where, n is the number of atoms in a TMD monolayer, E(VX₂@Y_{cat}) is the total electronic energy of the pristine or non-metal doped vanadium dichalcogenide monolayer, N_a and E_a are the number of atoms and corresponding electronic energies of each isolated atom respectively, X is the chalcogen (S, Se or Te) and Y is the non-metal dopant.

N₂ adsorption on the basal plane of pristine and non-metal doped VX₂ monolayers could proceed either through the end-on or side mode modes. The end-on or perpendicular mode of N₂ adsorption has been observed to be more prominent over the side-on or parallel mode on all VX₂ systems, thereby only the end-on mode of nitrogen adsorption will be presented in this study. The N₂ chemisorption efficacy of all pristine and doped VX₂ monolayers is calculated as adsorption energy, E_{ads} with the equation below,

$$E_{\text{ads}} = E(\text{VX}_2@Y_{\text{cat}}-\text{N}_2) - E(\text{VX}_2@Y_{\text{cat}}) - E(\text{N}_2) \quad (7.2)$$

where, E(VX₂@Y_{cat}-N₂), E(VX₂@Y_{cat}) and E(N₂) are the total electronic energies of N₂ adsorbed VX₂ systems, pristine and doped VX₂@Y_{cat} and free N₂ molecule, respectively.

The energetics of each intermediate protonation step in the Nitrogen Reduction Reaction is represented by the Gibbs free energy change, ΔG. The computational Standard Hydrogen Electrode model of Nørskov et al.⁴⁰ has been implemented to calculate ΔG using the following equation,

$$\Delta G = \Delta E + \Delta ZPE - T\Delta S \quad (7.3)$$

where, ΔE and ΔZPE are the change in electronic energy and zero-point energy respectively, ΔS is the change in entropy at room temperature, T is room temperature (298.15 K). All zero-point energy and entropy corrections are computed from the non-negative vibrational frequencies of the gas phase species in each intermediate. Finally, the overpotential for electrocatalytic NRR has been calculated as η = U_{SHE} - U_{PDS}, where U_{SHE} = -0.16 eV, is the standard reduction potential of N₂ to NH₃ and U_{PDS} = -ΔG_{max}/e for the NRR pathway.

7.3 Results and Discussions

7.3.1 Formation of VX₂@Y_{cat} monolayers and N₂ chemisorption

The formation energies of pristine and non-metal doped vanadium dichalcogenide monolayers, VX₂@Y_{cat} have been computed to be approximately -4.9 eV/atom, -4.4 eV/atom and -3.8 eV/atom respectively for the sulphides, selenides and tellurides systems. The highly negative formation energies confirm the experimental feasibility of synthesizing the vanadium dichalcogenide monolayers, and the vanadium disulphides to be more stable than the other dichalcogenides. Two different phases of vanadium

dichalcogenides have been considered owing to earlier reports that 2H-VS₂ phase shows higher stability and magnetic moment over its 1T phase. The 2H phase of pristine VS₂ shows a slightly higher formation energy (-4.94 eV/atom) and magnetic moment of 0.98 μ B as compared to 0.47 μ B of 1T-VS₂. Contrastingly, pristine VSe₂ showed higher formation energies (-4.44 eV/atom) in its metallic 1T-phase with a higher magnetic moment of 0.90 μ B in the semimetallic 2H-phase. VTe₂, on the other hand, demonstrated higher stability with a formation energy of -3.81 eV/atom and a magnetic moment of 0.15 μ B in its 1T-phase exclusively.

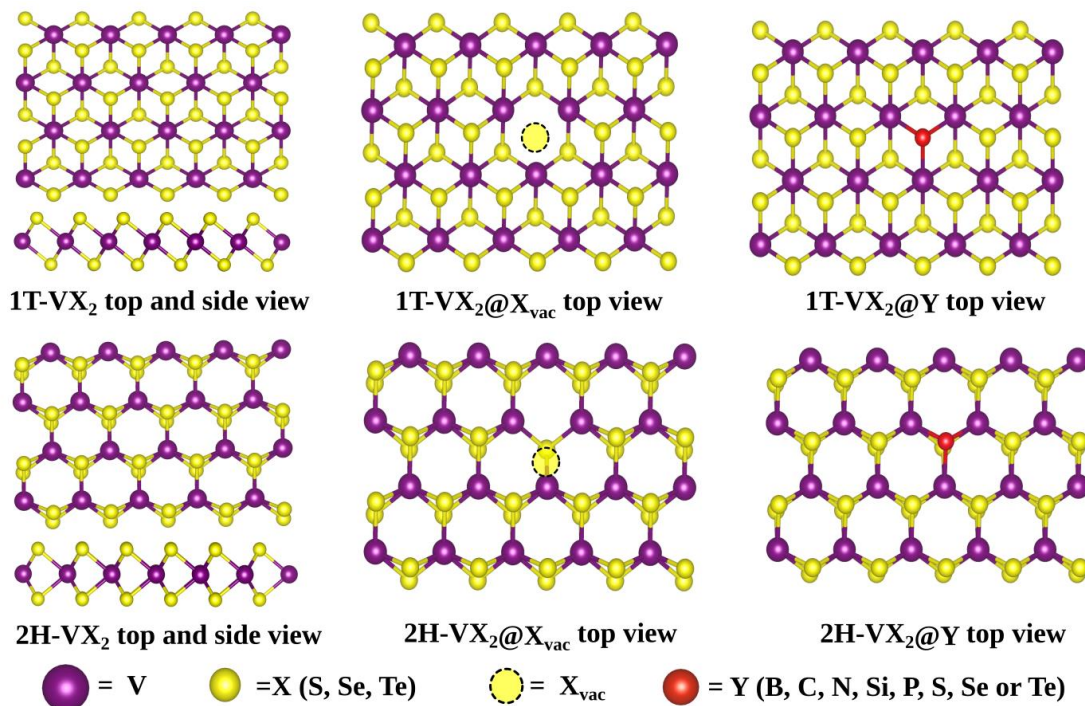


Figure 7.1: Top and side views of 1T and 2H phases of pristine vanadium dichalcogenides, top views of VX₂ monolayer with chalcogen vacancy (VX₂@X_{vac}) and nonmetal dopant (VX₂@Y_{cat}).

The VX₂@Y_{cat} systems are further modeled with a chalcogen vacancy (VX₂@X_{vac}) and substitutional doping of non-metals on the chalcogen vacancy to generate VX₂@Y_{cat}, as seen in **Figure 7.1**. The formation energies of VX₂@Y_{cat} systems are found to be higher than their corresponding pristine counterparts with a few exceptions in VS₂ and VSe₂ when the non-metal dopant is heavier than the parent chalcogen, e.g., VS₂@Se,

VS₂@Te and VSe₂@Te. The magnetic properties, on the other hand, show a gradual decrease as non-metal dopants are introduced in the VX₂@Y_{cat} systems except for 2H-VTe₂@B and 2H-VTe₂@C systems. The highly exothermic formation energies of VX₂@Y_{cat} systems demonstrate the stability of both 1T and 2H phase of vanadium dichalcogenides and their magnetic moments further exemplifies the incidence of ferromagnetic nature of these systems.

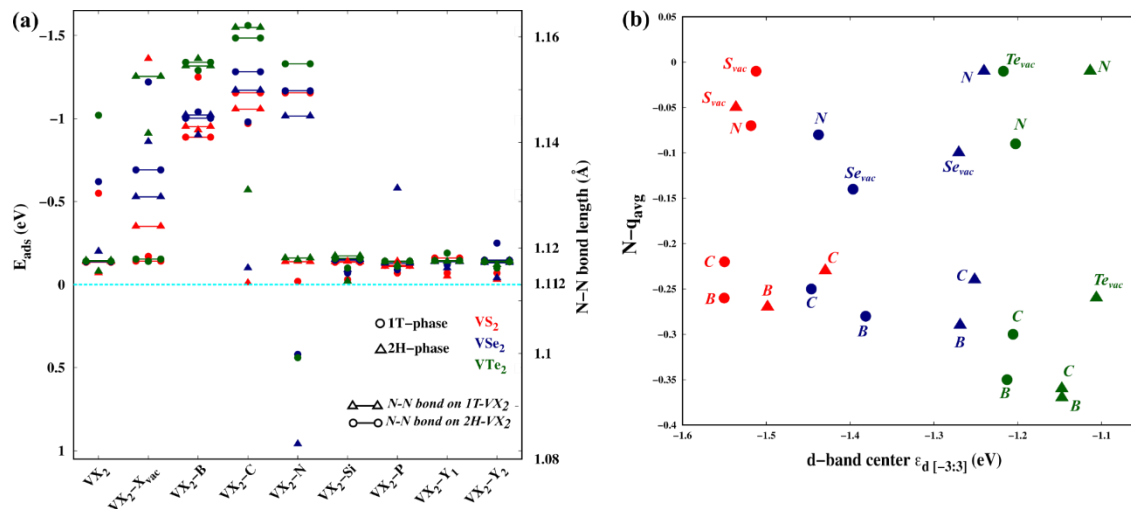


Figure 7.2: (a) N₂ adsorption energies on all VX₂@Y_{cat} systems with the corresponding N–N bond lengths (Å), cyan line corresponds to 0 eV of N₂ adsorption and N–N bond length in free dinitrogen molecule (1.112 Å). (b) Average Bader charge on N-atoms of N₂ upon adsorption on VX₂@Y_{cat} monolayers plotted w.r.t the d-band centers of the corresponding monolayers.

The N₂ chemisorption efficacy and the extent of N–N bond activation on 1T and 2H phases of all VX₂@Y_{cat} systems are then investigated to determine the synergistically favourable non-metal dopant for a family of VX₂. The adsorption energies and N–N bond lengths of the dinitrogen molecule adsorbed in end-on or perpendicular mode on all VX₂@Y_{cat} systems are shown in **Figure 7.2(a)**. It can be observed that pristine VX₂ systems show minimal to moderately exothermic N₂ adsorption without activating or elongating the N–N bond. Such systems would imperatively require a large potential when employed for nitrogen fixation as the nitrogen atoms remain strongly bonded. VX₂@X_{vac} systems except 1T-VS₂ and 1T-VTe₂, boron and carbon doped VX₂@B and

$VX_2@C$ systems show favourable N_2 adsorption as well as N–N bond activation up to 1.16 Å. Interestingly, for boron and carbon doped VS_2 and VSe_2 systems, the non-metals play a major role in tuning the catalytic property of the monolayer. Although both boron and carbon dopant showed higher N_2 adsorption on 1T phases of VS_2 and VSe_2 ; boron induces a higher N–N bond activation on 2H phase while carbon doping leads to a more pronounced N–N bond elongation on 1T phase. However, on VTe_2 systems, the impact of B or C doping is not very prominent as N_2 adsorption and N–N bond activation remain nearly similar in both 1T and 2H phases. Eventually, it can be deduced that boron and carbon dopants synergistically enhance the catalytic properties of 2H and 1T phases respectively, of VS_2 and VSe_2 ; whilst VTe_2 monolayers prefer both boron and carbon dopants. The $VX_2@N$ systems show a unique aspect of high N–N bond activation under endothermic conditions, thereby excess energy is needed to ensure N_2 adsorption and this condition is the most unfavourable scenario for electrocatalysis. It would be imperative to recapitulate that the N_2 adsorption energies and activated N–N bond lengths of $VX_2@B$ and $VX_2@C$ systems are comparable to earlier reports made by Wu et. al on W-doped BP monolayer and Mo-doped Fe_3P monolayer.^{41,42} It can also be noted that the N_2 adsorption energies of $VX_2@Si$ systems range from -0.02 eV to -0.14 eV and is comparable to those observed by Gholizadeh et. al on Si-doped graphene systems.⁴³ The rest of nonmetal dopants: Si, P, S, Se and Te show weak N_2 chemisorption as well as bond elongation, thereby employing these heavier non-metal dopants will be unfavourable.

A Bader charge⁴⁴ analysis of adsorbed N_2 molecule highlights an extensive charge gain mostly on the $VX_2@B$ and $VX_2@C$ systems followed by $VX_2@X_{vac}$ and 1T-phases of $VX_2@N$. These systems with higher charge transfer on N_2 correspond to the systems showing N–N bond activation or elongation, thereby justifying our reasoning behind consideration of N–N bond length elongation as a crucial parameter. The plot of average Bader charge on N-atoms upon adsorption on $VX_2@Y_{cat}$ monolayers with respect to the d-band centers of the corresponding monolayers in **Figure 7.2(b)** shows the charge transfer on the $VX_2@X_{vac}$, $VX_2@B$ and $VX_2@C$ systems are facilitated by a more positive d-band center, which in turn corroborates to higher exothermicity of N_2

adsorption. In particular, $\text{VTe}_2@B$ and $\text{VTe}_2@C$ systems with a more positive d-band center has been found to show higher charge transfer and N_2 chemisorption as compared to its VS_2 or VSe_2 counterparts. Taking the efficacy of N_2 chemisorption, N–N bond elongation, Bader charge on N-atoms and d-band center of the monolayers into account; the non-metal doped VX_2 systems of interest which show exothermic N_2 adsorption, N–N bond elongation and charge gain on N_2 are the $\text{VX}_2@B$ and $\text{VX}_2@C$ systems in both phases along with $1T\text{-VS}_2@N$, $2H\text{-phases of } \text{VX}_2@X_{\text{vac}}$ and $1T\text{-VSe}_2@Se_{\text{vac}}$. Moving forward, we will focus on the energy profile and NRR mechanism of these active $\text{VX}_2@Y_{\text{cat}}$ monolayers to determine the limiting potential for NRR and decipher the critical factors that affect the limiting potential.

7.3.2 N_2 reduction on $\text{VX}_2@Y_{\text{cat}}$ monolayers

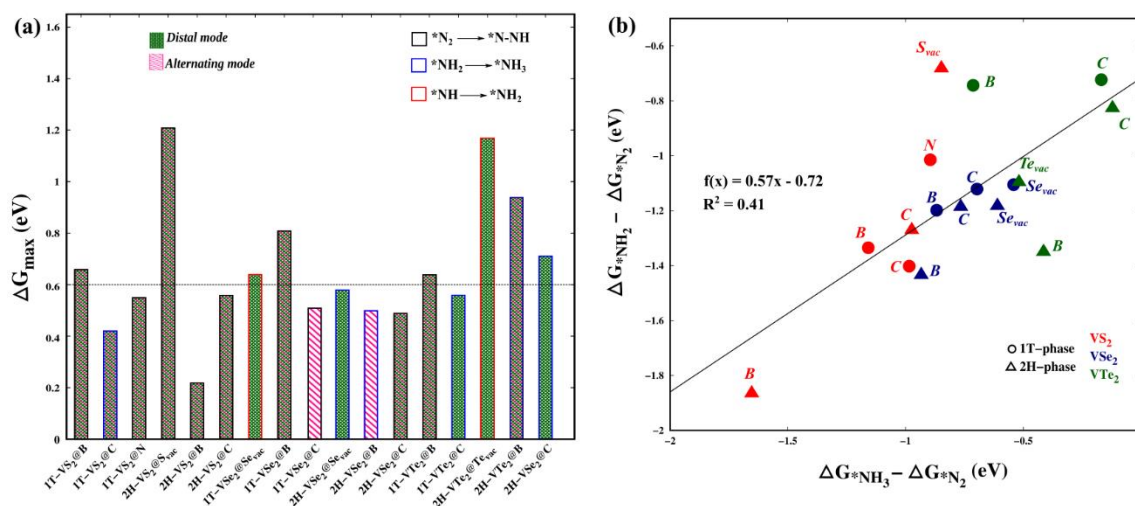


Figure 7.3: (a) NRR limiting potentials (ΔG_{max}), captions indicate the potential rate determining step and preference of distal or alternating route, (b) Gibbs free energy difference plot between two crucial protonation steps and N_2 adsorption.

Following the chemisorption of N_2 and electronic analysis on catalytically active $\text{VX}_2@Y_{\text{cat}}$, $\text{VX}_2@B$ and $\text{VX}_2@C$ monolayers, we investigated the thermodynamics of ammonia synthesis from dinitrogen via the associative pathway. Taking into account that only the perpendicular or end-on mode of N_2 adsorption is more prominent, the two possible routes of associative NRR pathway are the distal and alternating routes.⁴⁵ The

distal route involves protonation of end N to release NH_3 , followed by subsequent protonation of the next N; whereas the alternating route shows alternate protonation of N atoms to form ammonia. The most probable route of N_2 reduction has been deliberated by accounting the lowest energy barrier on the free energy profiles of each $\text{VX}_2@Y_{\text{cat}}$ system and plotted in **Figure 7.3(a)**.

The chemically modified vanadium disulphide, VS_2 monolayers are found to show equivalent preference of distal and alternating route with the first protonation step, $*\text{N}_2 \rightarrow *\text{N-NH}$ as the potential rate determining step (PDS), except on $1\text{T-VS}_2@\text{C}$ system with PDS in its last protonation step, i.e., $*\text{NH}_2 \rightarrow *\text{NH}_3$. Intriguingly, the lowest NRR limiting potential on the two different phases of VS_2 has been found to be 0.42 eV and 0.22 eV on $1\text{T-VS}_2@\text{C}$ and $2\text{H-VS}_2@\text{B}$, respectively. It would be important to recollect that the synergistic doping of carbon and boron on 1T-VS_2 and 2H-VS_2 also led to strong chemisorption of N_2 and N–N bond activation. Coming to $\text{VSe}_2@Y_{\text{cat}}$ monolayers, $\text{VSe}_2@\text{Sevac}$ systems are found to show a preference for the distal route on both 1T and 2H-phases, while $1\text{T-VSe}_2@\text{C}$ and $2\text{H-VSe}_2@\text{B}$ systems advance through the alternating route with an equal prevalence of distal and alternating route of NRR on $1\text{T-VSe}_2@\text{B}$ and $2\text{H-VSe}_2@\text{C}$ systems. Nonetheless, a lower barrier for nitrogen reduction on VSe_2 has been observed on $1\text{T-VSe}_2@\text{C}$, $2\text{H-VSe}_2@\text{B}$ and $2\text{H-VSe}_2@\text{C}$ with limiting potentials of 0.51 eV, 0.50 eV and 0.49 eV, respectively. In both phases of VTe_2 monolayers, the boron-doped systems show an identical affinity for distal or alternating route, while the remaining show a prevalence of the distal route over the alternating path with a lower energy barrier on $1\text{T-VTe}_2@\text{C}$ and $2\text{H-VTe}_2@\text{C}$. In retrospect, the lowest energy barrier for 1 T as well as 2H phases of VTe_2 , which has been reported to be metallic, is observed on the carbon doped systems. Similarly, the prevalence of carbon doping can be found to lower the NRR limiting potential on the metallic 1 T phases of VS_2 and VSe_2 , while boron doping does the same on the semi-metallic 2H phases. The energetics of the active $\text{VX}_2@Y_{\text{cat}}$ monolayers are further investigated to elucidate the critical aspects of each intermediate step in factors that affect the limiting potential of NRR. Two crucial intermediate steps of NRR are the first ($*\text{N}_2 \rightarrow *\text{N-NH}$) and last ($*\text{NH}_2 \rightarrow *\text{NH}_3$) protonation steps, with both processes being endergonic. As such, these two steps are the

most prominent rate limiting steps in all of the systems we have considered, except for 1T-VSe₂@Se_{vac} and 2H-VTe₂@Te_{vac} where the *NH → *NH₂ is the energy uphill step. Also, conceptually for a multistep reaction, the *NH₂ and *NH₃ intermediates can be considered as systems belonging to the product side wherein the reactant is the *N₂ intermediate, and the feasibility of such a reaction increases as the exoergicity between the product and reactant increases. This analogy can be implemented as a rationale for achieving a lower energy barrier in the NRR process by mapping a Gibbs Free energy difference plot. In **Figure 7.3(b)**, a nearly linear relationship can be observed between the Gibbs free energy differences of products to reactant, i.e., *NH₃–*N₂ w.r.t. *NH₂–*N₂. The 2H-VS₂@B system with the lowest limiting potential of 0.22 eV is found to show a larger energy difference (~2.0 eV) between *NH₂ to *N₂ and *NH₃ to *N₂, thereby emphasizing that systems with a higher potential to form the products, i.e., NH₃ or alike intermediates are prone to show a lower limiting potential for NRR.^{46,47} The remaining VX₂@B and VX₂@C systems with energy barriers 0.49 eV to 0.58 eV show Gibbs free energy differences of 1.2 to 1.4 eV and a lower tenacity of product formation as compared to 2H-VS₂@B. Except for VSe₂@Se_{vac} systems which show a lower limiting NRR potential, the VS₂@S_{vac} and VTe₂@Te_{vac} systems show a much lower energy difference or lower exoergicity of *NH₃ intermediate and the energy differences are found to be around 0.5 eV to 1.0 eV. Amongst all the active VX₂@Y_{cat} monolayers, the systems of significance will be systems with a lower NRR limiting potential wherein a lower electrode potential would be needed for implementing them as electrocatalysts for NRR. Therefore, 2H-VS₂@B and 1T-VS₂@C systems with ΔG_{max} of 0.22 eV and 0.42 eV, respectively are of interest and their electronic properties are investigated further for their application as electrocatalysts for NRR.

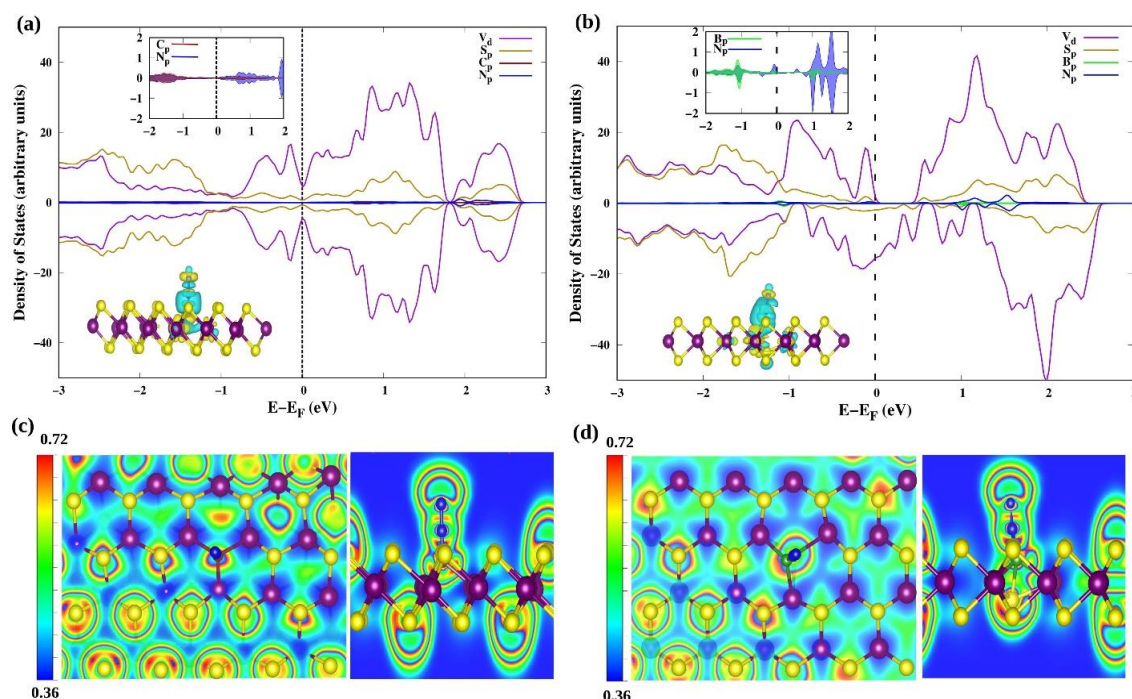


Figure 7.4: Projected Density of States (PDOS) plots with insets showing orbital overlap and charge density difference plots of (a) 1T-VS₂@C-N₂ and (b) 2H-VS₂@B-N₂ showing favourable N₂ adsorption; the top and side views of Electron localization function (ELF) contour plots of (c) 1T-VS₂@C-N₂ and (d) 2H-VS₂@B-N₂ showing electron location on the adsorbed dinitrogen.

7.3.3 NRR mechanism on 2H-VS₂@B and 1T-VS₂@C

A detailed electronic analysis through Projected Density of States (PDOS) and charge density plots of these systems reveal that the p-orbitals of non-metal dopants hybridize with the empty π^* orbitals of N₂, this orbital overlap coupled with charge transfer inherently leads to electron occupation in the antibonding π orbitals of N₂ leading to activation of the N–N bond. The PDOS, charge density difference plots and Electron Localization Function (ELF) contour plots of 1T-VS₂@C and 2H-VS₂@B monolayers, as shown in **Figure 7.4**, demonstrate the overlap of carbon and nitrogen p-orbitals to hybridize with the π^* orbitals on N₂, respectively and the localization of electron density around the N₂ molecule, thereby affirming the electron transfer on the adsorbed N₂. The electronic properties of each intermediate nitrogen reduction step on 2H-VS₂@B systems

has been further investigated to root out the essential parameter behind the energy barrier for NRR. The segmented p-states of B and N alone for the $*N_xH_y$ intermediates observed via the distal route of NRR has been plotted in **Figure 7.5**. The chemisorption of N_2 on $2H-VS_2@B$ has been found to be associated with a $\pi-\pi^*$ hybridization between the B p-states and N p-states. These electronic orbitals hybridization or overlap gets more enhanced as the adsorbed N_2 gets reduced and the N p-states turn into electron rich states. Prior to the first ammonia desorption in the $*N-NH_2$ intermediate, a charge back-transfer from the filled N p-states to the empty p-states of B can be observed. The σ -back donation augments the activity of the boron center and assists in following protonation steps to form the second NH_3 molecule. Such electron back-donation could not be observed on our next best system, $1T-VS_2@C$ and we believe the thermodynamic favourability of NH_3 formation from N_2 along with the electron “donor–acceptor” mechanism between boron and nitrogen is responsible for high NRR performance.

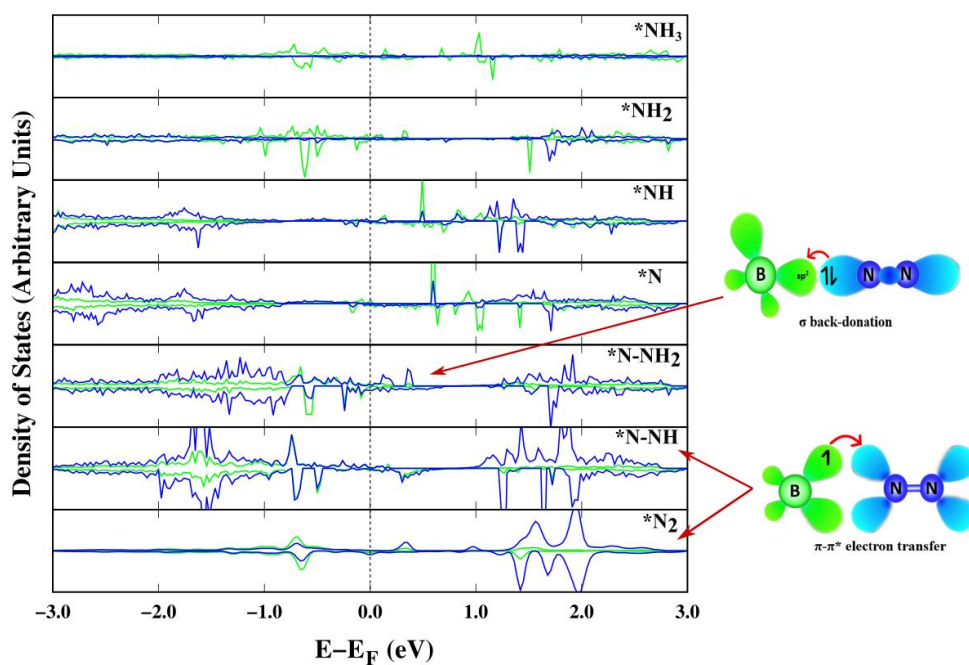


Figure 7.5: Segmented Projected Density of States of B p-states (green line) and N p-states of all the N_xH_y intermediates from the distal route of NRR on $2H-VS_2@B$ monolayer.

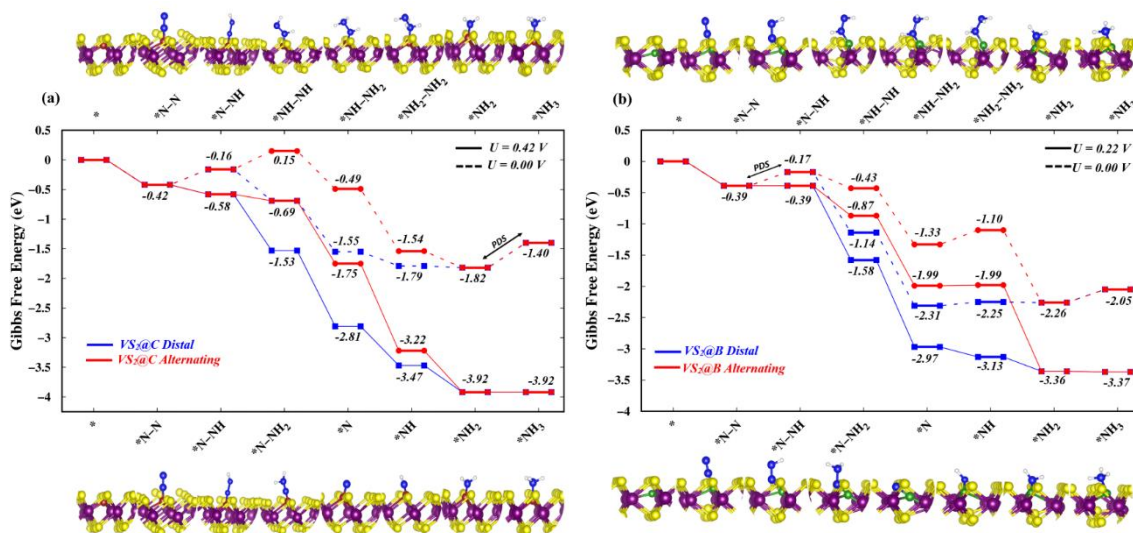


Figure 7.6: Gibbs free energy diagrams of distal and alternating NRR at zero and applied potentials equivalent to their respective limiting potentials on (a) 1T-VS₂@C (0 V and 0.42 V), (b) 2H-VS₂@B (0 V and 0.22 V).

In terms of electrocatalytic application for NRR, the distal and alternating routes of dinitrogen reduction on 1T-VS₂@C and 2H-VS₂@B has been investigated at applied potentials of 0.42 V and 0.22 V respectively and is shown in **Figure 7.6**. The Gibbs free energies of each intermediate protonation steps are computed with the CHE model (computational hydrogen electrode) developed by Nørskov et al.⁴⁰, $\Delta G_{\text{eNRR}} = \Delta E + \Delta \text{ZPE} - \text{TAS} - neU$, where ΔG is the free energy change of each intermediate step (as calculated in equation 7.3, n is the number of electrons and U is the applied potential. The endergonic intermediate steps in both systems are the first ($*\text{N}_2 \rightarrow *\text{N}_2\text{H}$) and last ($*\text{NH}_2 \rightarrow *\text{NH}_3$) protonation steps with the PDS being either of the two steps. The initially energy uphill step of $*\text{N}_2\text{H}$ formation in 1T-VS₂@C becomes exergonic under the application of an applied potential of 0.42 V. Similarly, the endoergic sixth protonation step to form 1T-VS₂@C-NH₃ intermediate is also found to flip into an exergonic process as shown in **Figure 7.6(a)**. The analogous endoergic intermediate steps of 2H-VS₂@B are also found to revert into energy downhill processes in **Figure 7.6(b)** upon application of 0.22 V. It can be observed that with the application of an external potential equivalent to their respective limiting potentials in 1T-VS₂@C and 2H-VS₂@B, all the intermediate protonation steps of NRR become feasible and thereby employed for electrocatalytic

nitrogen reduction. Furthermore, our analogy of synergic non-metal doping on vanadium dichalcogenides has shown that 1T-VS₂@C and 2H-VS₂@B are the best electrocatalysts so far with NRR limiting potentials of 0.42 eV and 0.22 eV, respectively. The corresponding overpotentials, η of 0.26 eV and 0.06 eV respectively on boron or carbon doped VX₂ systems are the lowest reported so far on vanadium dichalcogenides.^{48,49}

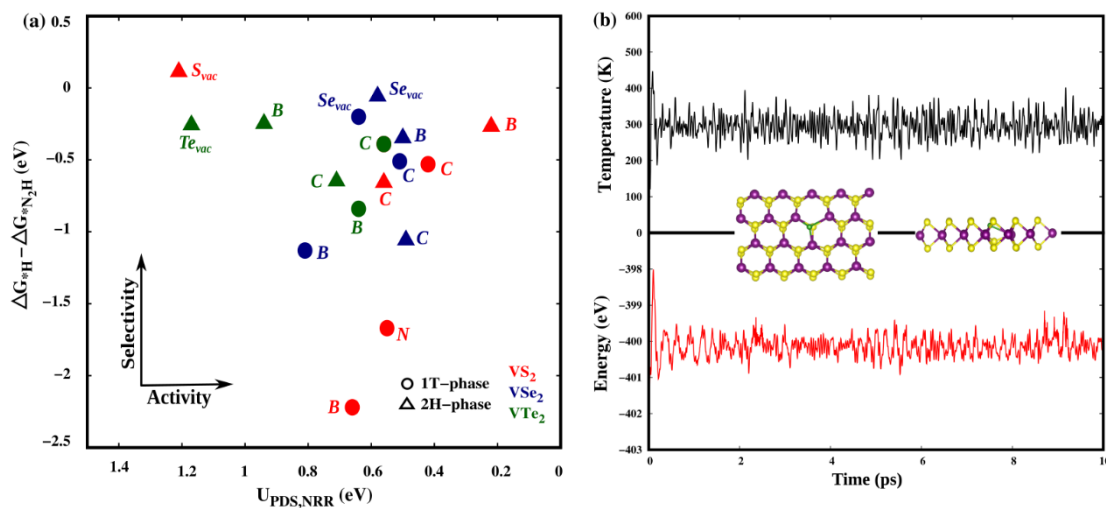


Figure 7.7: (a) Selectivity of NRR over HER on select active VX₂@Y_{cat} systems, the more positive the $\Delta G(*\text{H}) - \Delta G(*\text{N}_2\text{H})$, the higher is the NRR selectivity, (b) Total energy and temperature of 2H-VS₂@B as a function of time during the AIMD simulation for 10 ps at 298 K.

Consequently, the NRR selectivity of 1T-VS₂@C and 2H-VS₂@B systems have also been investigated and it has been found that both systems can selectively suppress the competing hydrogen evolution reaction (HER). Although the adsorption of H is usually more negative than N₂ adsorption, former involves proton and electron transfer, thereby it is easily influenced by electrode potential. N₂ adsorption, on the other hand, does not involve proton transfer and the more appropriate step to be considered is the first protonation step of NRR, i.e., *N₂H adsorption. Therefore, the selectivity of NRR over HER can be evaluated from the free energy difference of *H and *N₂H adsorption, $\Delta G(*\text{H}) - \Delta G(*\text{N}_2\text{H})$. **Figure 7.7(a)** shows the $\Delta G(*\text{H}) - \Delta G(*\text{N}_2\text{H})$ vs NRR limiting potential plot of all active VX₂@Y_{cat} systems and it can be seen that 2H-VS₂@B shows a relatively higher selectivity as well as activity for NRR. With the exception of 1 T-VS₂@B

and 1T-VS₂@N, all the catalytically active VX₂@Y_{cat} systems possess enhance NH₃ production as supported as exothermic *NH₃ formation on all VX₂@Y_{cat} systems. The, the thermal stability of the best performing catalyst, 2H-VS₂@B has been investigated at room temperature, 298 K. It can be seen from **Figure 7.7(b)** that the structure of 2H-VS₂@B is retained and there are no structural distortions after 10 ps, this is also supported by the total electronic energy of the systems which remains nearly constant throughout the simulation. This elucidates the possibility of experimental realization of B-doped vanadium disulphide in 2H-phase as a thermally stable, highly active and selective electrocatalyst for NRR at room temperature. This study presents a detailed analysis of synergistically introducing a non-metal dopant on vanadium dichalcogenides monolayer for developing efficient electrocatalysts for NRR and delves into energy difference and electronic factors as crucial parameters for N₂ adsorption, activation and reduction. We propose vanadium dichalcogenide monolayers with substitutionally doped boron as potential electrocatalyst for NRR.

7.4 Conclusion

In summary, a detailed study has been made on the synergistic doping of several non-metal dopants on vanadium dichalcogenide monolayers to enhance its electrocatalytic activity. An analysis of the electronic properties on VX₂@Y_{cat} catalysts with high N₂ chemisorption efficacy demonstrates an overlap between the p-orbitals of non-metal dopants with the empty antibonding π^* orbitals of N₂. This π - π^* orbital hybridization coupled with high charge transfer on N₂ inherently leads to N–N activation and reduction of dinitrogen to ammonia. Further investigation on the energetics of the intermediate steps of NRR brings forth a correlation between the limiting potential and thermodynamic favourability of NH₃ (i.e., product) formation from N₂ (i.e., reactant) along with the electron “donor–acceptor” mechanism between boron and nitrogen. Our findings propose 1T-VS₂@C and 2H-VS₂@B as efficient electrocatalysts with high NRR performance at overpotentials of 0.26 eV and 0.06 eV, respectively. The understanding from this chapter can be implemented for further research on introducing earth abundant,

non-toxic non-metal doped transition metal dichalcogenides electrocatalysts for nitrogen reduction reaction.

7.5 References

- (1) United Nations, *UN General Assembly*, **2015**, 16301, 1–35.
- (2) Cherkasov, N.; Ibhaddon, A. O.; Fitzpatrick, P.; *Chem. Eng. Process. Process Intensif.* **2015**, *90*, 24–33.
- (3) Van Der Ham, C. J. M.; Koper, M. T. M.; Hetterscheid, D. G. H.; *Chem. Soc. Rev.* **2014**, *43*, 5183–5191.
- (4) Xue, X.; Chen, R.; Yan, C.; Zhao, P.; Hu, Y.; Zhang, W.; Yang, S.; Jin, Z.; *Nano Res.* **2019**, *12*, 1229–1249.
- (5) Sun, H.; Yin, H.-Q.; Shi, W.; Yang, L.-L.; Guo, X.-W.; Lin, H.; Zhang, J.; Lu T.-B.; Zhang, Z.-M.; *Nano Research* **2022**, *15*, 3026–3033.
- (6) Yin, H.; Yang, L.; Sun, H.; Wang, H.; Wang, Y.; Zhang, M.; Lu, T.; Zhang, Z.; *Chinese Chemical Letters* **2022**, *17*.
- (7) Tang, C.; Qiao, S. Z.; *Chem. Soc. Rev.* **2019**, *48*, 3166–3180.
- (8) Wang, P.; Huan, Y.; Yang, P.; Cheng, M.; Shi, J.; Zhang, Y.; *Accounts Mater. Res.* **2021**, *2*, 751–763.
- (9) Zhao, B.; Shen, D.; Zhang, Z.; Lu, P.; Hossain, M.; Li, J.; Li, B.; Duan, X.; *Adv. Funct. Mater.* **2021**, *31*, 1–36.
- (10) Pan, H.; *J. Phys. Chem. C.* **2014**, *118*, 13248–13253.
- (11) Abdulsalam, M.; Joubert, D.; *Comput. Mater. Sci.* **2016**, *115*, 177–183.
- (12) Fuh, H. R.; Chang, C. R.; Wang, Y. K.; Evans, R. F. L.; Chantrell, R. W.; Jeng, H. T.; *Sci. Rep.* **2016**, *6*, 1–11.

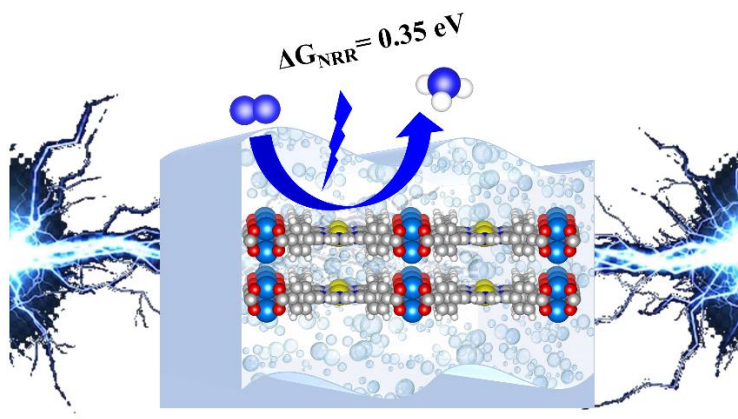
- (13) Guo, N.; Fan, X.; Chen, Z.; Luo, Z.; Hu, Y.; An, Y.; Yang, D.; Ma, S.; *Comput. Mater. Sci.* **2020**, *176*, 109540.
- (14) Samal, R.; Rout, C. S.; *Adv. Mater. Interfaces.* **2020**, *7*, 1–24.
- (15) Wasey, A. H. M. A.; Chakrabarty, S.; Das, G. P.; *J. Appl. Phys.* **2015**, *117*, 064313.
- (16) Arnold, F.; Stan, R. M.; Mahatha, S. K.; Lund, H. E.; Curcio, D.; Dendzik, M.; Bana, H.; Travaglia, E.; Bignardi, L.; Lacovig, P.; Lizzit, D.; Li, Z.; Bianchi, M.; Miwa, J. A.; Bremholm, M.; Lizzit, S.; Hofmann, P.; Sanders, C. E.; *2D Mater.* **2018**, *5*, 0455009.
- (17) Zhang, Z.; Niu, J.; Yang, P.; Gong, Y.; Ji, Q.; Shi, J.; Fang, Q.; Jiang, S.; Li, H.; Zhou, X.; Gu, L.; Wu, X.; Zhang, Y.; *Adv. Mater.* **2017**, *29*, 1–9.
- (18) Li, F.; Tu, K.; Chen, Z.; *J. Phys. Chem. C.* **2014**, *118*, 21264–21274.
- (19) Wong, P. K. J.; Zhang, W.; Zhou, J.; Bussolotti, F.; Yin, X.; Zhang, L.; N'Diaye, A. T.; Morton, S. A.; Chen, W.; Goh, J.; De Jong, M. P.; Feng, Y. P.; Wee, A. T. S.; *ACS Nano* **2019**, *13*, 12894–12900.
- (20) Sugawara, K.; Nakata, Y.; Fujii, K.; Nakayama, K.; Souma, S.; Takahashi, T.; Sato, T.; *Phys. Rev. B.* **2019**, *99*, 1–6.
- (21) Rehder, D.; *J. Inorg. Biochem.* **2000**, *80*, 133–136
- (22) Maibam, A.; Krishnamurty, S.; *J. Colloid Interface Sci.* **2021**, *600*, 480–491.
- (23) Duvjir, G.; Choi, B. K.; Jang, I.; Ulstrup, S.; Kang, S.; Thi Ly, T.; Kim, S.; Choi, Y. H.; Jozwiak, C.; Bostwick, A.; Rotenberg, E.; Park, J. G.; Sankar, R.; Kim, K. S.; Kim, J.; Chang, Y. J.; *Nano Lett.* **2018**, *18*, 5432–5438.
- (24) Memarzadeh, S.; Roknabadi, M. R.; Modarresi, M.; Mogulkoc, A.; Rudenko, A. N.; *2D Mater.* **2021**, *8*, 035022.

- (25) Coelho, P. M.; Lasek, K.; Nguyen Cong, K.; Li, J.; Niu, W.; Liu, W.; Oleynik, I. I.; Batzill, M.; *J. Phys. Chem. Lett.* **2019**, *10*, 4987–4993.
- (26) Wang, T.; Li, Y.; Xia, C.; Zhao, X.; An, Y.; Dai, X.; *J. Mater. Chem. C* **2016**, *4*, 8111–8120.
- (27) Luo, N.; Si, C.; Duan, W.; *Phys. Rev. B* **2017**, *95*, 1–7.
- (28) Cui, Y.; Fan, W.; Liu, X.; Ren, J.; Gao, Y.; *Comput. Mater. Sci.* **2021**, *200*, 110767.
- (29) Liu, X.; Jiao, Y.; Zheng, Y.; Qiao, S. Z.; *ACS Catal.* **2020**, *10*, 1847–1854.
- (30) Liu, C.; Li, Q.; Wu, C.; Zhang, J.; Jin, Y.; Macfarlane, D. R.; Sun, C.; *J. Am. Chem. Soc.* **2019**, *141*, 2884–2888.
- (31) Maibam, A.; Govindaraja, T.; Selvaraj, K.; Krishnamurty, S.; *J. Phys. Chem. C* **2019**, *123*, 27492–27500.
- (32) Wu, J.; Yu, Y.-X.; *J. Phys. Chem. C* **2021**, *125*, 23699–23708.
- (33) Maibam, A.; Krishnamurty, S.; Ahmad Dar, M.; *Mater. Adv.* **2022**, *3*, 592–598.
- (34) Kresse, G.; Furthmüller, J.; *Comput. Mater. Sci.* **1996**, *6*, 15–50.
- (35) Perdew, J. P.; Burke, K.; Ernzerhof, M.; *Phys. Rev. Lett.* **1996**, *77*, 3865–3868.
- (36) Grimme, S.; Antony, J.; Ehrlich, S.; Krieg, H.; *J. Chem. Phys.* **2010**, *132*, 154104.
- (37) Nosé, S.; *J. Chem. Phys.* **1984**, *81*, 511.
- (38) Hoover, W. G.; *Phys. Rev. A* **1985**, *31*, 1695.
- (39) Kresse, G.; Hafner, J.; *Phys. Rev. B* **1993**, *47*, 558.
- (40) Nørskov, J. K.; Rossmeisl, J.; Logadottir, A.; Lindqvist, L.; Kitchin, J. R.; Bligaard, T.; Jónsson, H.; *J. Phys. Chem. B* **2004**, *108*, 17886–17892.
- (41) Wu, J.; Li, J.-H.; Yu, Y.-X.; *ACS Appl. Mater. Interfaces* **2013**, *13*, 10026–10036.
- (42) Wu, J.; Li, J.-H.; Yu, Y.-X. *Catal. Sci. Technol.* **2021**, *11*, 1419–1429.

- (43) Gholizadeh, R.; Yu, Y.-X.; *Applied Surface Science* **2015**, *357*, 1187-1195.
- (44) Tang, W.; Sanville, E.; Henkelman, G.; *J. Phys. Condens. Matter.* **2009**, *21*, 084204.
- (45) Foster, S. L.; Bakovic, S. I. P.; Duda, R. D.; Maheshwari, S.; Milton, R. D.; Minteer, S. D.; Janik, M. J.; Renner, J. N.; Greenlee, L. F.; *Nat. Catal.* **2018**, *1*, 490–500.
- (46) Bar-Even, A.; Flamholz, A.; Noor, E.; Milo, R.; *Biochimica et Biophysica Acta (BBA) - Bioenergetics* **2012**, *1817*, 1646-1659.
- (47) Halling, P. J.; *ACS Omega* **2020**, *5*, 15843–15849.
- (48) Li, Q.; Guo, Y.; Tian, Y.; Liu, W.; Chu, K.; *J. Mater. Chem. A.* **2020**, *8*, 16195–16202.
- (49) Zhang, L.; Hu, Z.; *Mater. Des.* **2021**, *209*, 110006.

Chapter 8

Surface electronic properties driven electrocatalytic nitrogen reduction on metal-conjugated porphyrin 2D-MOFs



In this chapter two-dimensional (2D) metal organic framework (MOF) or metalloporphyrin nanosheets with stable metal-N₄ complex unit presents the metal as single atom catalyst dispersed in the 2D porphyrin framework. First-principles calculations on the 3d-transition metals in M-TCPP are investigated for their surface dependent electronic properties-work function and d-band center. Crystal Orbital Hamiltonian Population (-pCOHP) analysis highlights a higher contribution of bonding state in M-N bond and antibonding state in N-N bond to be essential for N-N bond activation. A linear relationship between ΔG_{max} and surface electronic properties, N-N bond strength and Bader charge has been found to influence the rate determining potential for Nitrogen Reduction Reaction (NRR) in M-TCPP MOFs. Ti-TCPP with an excellent NRR selectivity and limiting potential of -0.35 V in water solvent is proposed as an attractive candidate for electrocatalytic NRR.

8.1 Introduction

Ammonia (NH_3), formed by the thermal combustion of N_2 and H_2 in a highly energy intensive Haber-Bosch reaction¹, is of immense importance to agriculture and energy storage. With increasing population and demands for energy, the sustainability of a century old industrial for ammonia production possess a jarring strain to the future of earth. While questions are raised on mimicking the biological “nitrogen cycle” with nitrogenase enzyme to convert nitrogen to ammonia, the efficiency of such biological approaches are nowhere close to meeting the commercial demands.^{2,3} Influenced by the biological nitrogen cycle operating at ambient temperature and pressure conditions, electrocatalytic Nitrogen Reduction Reaction (eNRR) in aqueous solvent is an emerging alternative to substantiable ammonia production.^{4,5} To achieve commercially acceptable scale of ammonia; low cost, high durability and activity, high nitrogen reduction selectivity over hydrogen evolution, and high Faradaic efficiency are crucial attributed of the electrocatalysts to be purported.

Over the last few decades, the research on two-dimensional (2D) materials as electrocatalysts for room-temperature activation and reduction of N_2 have been on the rise.^{6,7} The objective of this research is to conceive a sustainable electrocatalyst that can offer near-commercial levels of NH_3 production. Thereby, the greenness of the raw materials comprising these electrocatalysts is an important aspect to be a noted. In particular, coordination polymer frameworks or organic frameworks of porphyrin, a ligand found in almost every biological system, when assembled with an active transition metal to form 2D-metal organic framework (MOF) or metalloporphyrin nanosheets are a fascinating family of electrocatalysts and photocatalysts.⁸ The porous architecture of this family of MOFs driven by the reticular chemistry of the metal centers and the organic linkers creates conducting channels and the π - π electron conjugation in the porphyrin ligands brings forth excellent electronic conductivity in these 2D materials.⁹⁻¹¹ Additional structural features of the 2D MOFs include larger surface area, conducive diffusion of gases in the framework and mechanical stability. The metalloporphyrin MOFs have been reported as active electrocatalysts and photocatalysts for HER (hydrogen evolution reaction) and CO_2RR (CO_2 reduction reaction), C-H

activation and nitrous oxide decomposition.¹²⁻¹⁹ The extraordinary performance of metalloporphyrin MOFs in CO₂RR, a multistep CO₂ reduction to CO and CH₄ as end products prompted their application into electrocatalysts for nitrogen reduction reaction which is a six-electron-reduction process.

An added advantage is the reducing nature of porphyrin ligand which has been highlighted in the study by Hegg et. al. wherein the porphyrin ligands induce the reduction of N₂ to NH₃.²⁰ It is also important to note that the metal center in the metalloporphyrin MOFs also serves as a single atom catalyst (SAC) as the four nitrogen atoms in the porphyrin network form a highly stable M-N₄ complex thereby avoiding metal aggregation or migration.^{21,22} The single atom nature of Fe center in metalloporphyrin MOFs have been affirmed from the work by Zhang et.al when PCN-222(Fe) MOF comprised of (iron(III)meso-tetra(4-carboxyphenyl)porphyrin chloride) and H₂-TCPP (tetra(4-carboxyphenyl)porphyrin), showed excellent electrocatalytic NRR yield of 1.56×10^{-11} mol cm⁻² s⁻¹ with a Faradaic Efficiency (FE) of 4.51% at -0.05 V vs. RHE. The nitrogen reduction has been guided by the atomically dispersed Fe site and the porous nature of the MOF thereby providing accessible active sites.²³ A remarkable improvement in the electrocatalytic NRR performance was reported in 2021 by Cong and co-workers with Fe-TCPP MOF showing NH₃ yield of 44.77 μg h⁻¹ mg_{cat.}⁻¹ and FE of 16.23 % at -0.3 V vs RHE.²⁴ Further adjustments in the electronic and catalytic properties of the metalloporphyrin can be brought about by swapping the metal center, in particular, transition metals that show a variation in their outermost valence or *d*-electrons. The design of metalloporphyrin is relatively facile and low cost via hydro-/solvothetical methods at low temperature with a high yield and tuning the transition metal center can be brought about by using different metal salts.²⁵ This makes the metalloporphyrin MOFs, in particular M-TCPP (metal- tetrakis (4-carboxyphenyl) porphyrin MOFs, one of the most attractive candidates for electrocatalytic NRR. However, the development and research on M-TCPP MOFs are limited and sporadic owing to their low stability in aqueous media.

In this chapter, we explore a series of M-TCPP MOFs formed by the coordination of metal-porphyrin complex with Zn(II)-paddlewheel linker. The metals of interest are the lighter 3d-transition metals which are earth abundant and economically viable for commercial exploration. The surface electronics of the M-TCPP MOFs have been found to drive the chemisorption and back-bonding of N₂ to the metal centers. A stronger correlation has been found between the surface electronics of the M-TCPP MOFs to the NRR limiting potential, thereby exemplifying the role of the porphyrin ligand and the metal linker nodes. Furthermore, a stabilisation of the M-N₂ interaction and destabilisation of the N-N bond in the lighter 3d-transition metals has been affirmed to prompt the reduction of N₂. We propose Ti-TCPP MOF that shows an alleviated NRR performance at lower onset potential (-0.35 V) from experimentally reported Fe-TCPP MOF (-0.45 V) in water solvent as an attractive NRR selective electrocatalyst for ammonia production.

8.2 Computational Details

All Density Functional Theory (DFT) calculations on the M-TCPP (M= Sc, Ti, V, Cr, Mn, Fe, Co, Ni, Cu, Zn) MOFs, the unit structure of which is shown in **Figure 8.1(a)**, are carried out using Vienna ab-initio Simulation Package (VASP.5.4).²⁶ The structures are optimized with a $5 \times 5 \times 1$ Monkhorst-Pack kpoint grid and 300 eV energy cut-off and all interactions of the ions and electrons are calculated with a generalized gradient approximation Perdew-Burke-Ernzerhof (PBE) functional.²⁷ A DFT-D3 correction has been incorporated to include long range van der Waals interaction and the structures are relaxed till the atomic forces and energies converge to 0.005 eV/Å and 10⁻⁵ eV/atom, respectively.²⁸ The electronic properties – Density of States, Work Function and Bader charges of the M-TCPP MOFs and their N₂ adsorbed structures are analysed at a higher kpoint grid of (11 × 11 × 1) Monkhorst-Pack grid.²⁹ To analyse the thermal stability of the M-TCPP MOFs, ab-initio molecular dynamics (AIMD) simulations in an NVT ensemble at 298 K described with a Nose-Hoover thermostat at 1 ps time step have been carried out for 10 ps.³⁰ Additionally, the thermodynamical and electrochemical stability of the M-TCPP MOFs have been verified with the formation energy, E_{form} of the single

transition metal attaching to the porphyrin framework and the metal dissolution potential, U_{diss} using the equation,³¹

$$E_{form} = (E_{M-TCPP}) - E_{TCPP} - E_M \quad \text{and}, \quad (8.1)$$

$$U_{diss} = U_{diss}^0 (metal, bulk) - (E_{form}/n_e) \quad (8.2)$$

where, E_{M-TCPP} , E_{TCPP} and E_M are the total electronic energies of M-TCPP MOF unit cell, TCPP structure and single atom transition metal, respectively; $U_{diss}^0 (metal, bulk)$ and n_e are the standard dissolution potential of bulk metal and number of electrons involved in their dissolution at pH=0. Following this, the adsorption of N₂ on the M-TCPP MOFs via end-on and side-on modes are investigated and N₂ adsorption energy, E_{ads} is computed using the equation,

$$E_{ads} = (E_{M-TCPP-N_2}) - (E_{M-TCPP}) - E_{N_2} \quad (8.3)$$

where, $E_{M-TCPP-N_2}$ is the total electronic energy of M-TCPP system after N₂ adsorption, E_{M-TCPP} and E_{N_2} are the total electronic energy of M-TCPP MOF and free N₂ molecule, respectively. The Gibbs free energy of N₂ adsorption and their protonated counterparts, N_xH_y intermediates involved in the Nitrogen Reduction Reaction (NRR) is calculated from the electronic energy with zero-point energy, ZPE and entropy contributions, S at room temperature using the equation,

$$G = E + ZPE - T S \quad (8.4)$$

and, the Gibbs free energy change of each protonation step in NRR are also calculated using the above equation with the correction terms computed from the non-negative vibrational frequencies of the gas phase species in each intermediate. The potential rate-determining step (PDS) for the multistep NRR reaction is the single step with the highest free energy change (ΔG_{max}) and the limiting potential, U_L is equal to $-(\Delta G_{max})/e$. The corresponding theoretical NRR overpotential, $\eta_{NRR} = U_L - U_{SHE}$, where $U_{SHE} = -0.16$ V is the standard N₂/NH₃ reduction potential. For an electrocatalyst under applied potential, the free energy is calculated as, $\Delta G_{NRR} = \Delta E + \Delta ZPE - T\Delta S + neU + \Delta G_{pH}$, where n is the number of electrons, U is the applied electrode potential equivalent to the

limiting potential, U_L and ΔG_{pH} is the free energy correction to pH of the solvent.³² The pH correction to free energy is represented by $\Delta G_{pH} = 2.303 \times k_B T \times \text{pH}$, where k_B is the Boltzmann constant. The pH value is assumed to be zero as the overpotential of NRR is unaffected by the change in pH.^{33,34} Calculations with implicit solvation have been carried out using a self-consistent continuum model as implemented in VASPsol, a software package that incorporates solvation into VASP.³⁵ The default parameters of water solvent, i.e. bulk dielectric constant $\epsilon_b = 78.4$, width of dielectric cavity $\sigma = 0.6$, the cutoff charge density $\rho_{\text{cut}} = 0.0025 \text{ \AA}^{-3}$ and a surface tension parameter of 0.525 meV/\AA^2 are fitted from its empirical parameters of neutral water molecule.

8.3 Results and Discussions

8.3.1 M-TCPP surface electronics and N_2 activation

The formation energies and dissolution potentials of the 10 M-TCPP MOFs with 3d transition metals are provided in **Table 8.1**. The thermodynamic and electrochemical stability of the M-TCPP MOFs can be affirmed when the formation energies, E_{form} are exothermic and their corresponding dissociation potential, U_{diss} is greater than $E_{\text{N}_2/\text{NH}_3}^0$ reduction potential, 0.16 V.³⁶ An exothermic E_{form} demonstrates a strong binding of the transition metal to the porphyrin framework and all the M-TCPP MOFs show negative E_{form} ranging from -3.02 eV to -8.10 eV. Furthermore, all M-TCPP MOFs possess a dissolution potential ranging from 0.56 V to 3.18 V, thereby the metals will not undergo dissolution under electrochemical conditions. The thermal stability of the 10 M-TCPP MOFs are further investigated with AIMD simulations at 298 K and minute structural distortions are observed in all the M-TCPP MOFs after 10 ps. Hence, all 10 M-TCPP MOFs are thermodynamically, electrochemically and thermally stable at room temperature and are thus eligible candidates for electrocatalytic nitrogen reduction reaction (eNRR).

Table 8.1: Formation energies (E_{form}) in eV and dissociation potentials (U_{diss}) in V of M-TCPP MOFs along with their surface electronic energies – work function and d-band centers.

M-TCPP MOFs	E_{form} (eV)	U_{diss}^0 (V)	n_e	U_{diss} (V)	Work-function (eV)	d-band center (eV) [$\epsilon_d = -5:5$]
Sc-TCPP	-7.92	-2.08	3	0.56	3.57	-0.92
Ti-TCPP	-7.41	-1.63	2	2.08	3.79	1.34
V-TCPP	-8.10	-1.18	2	2.87	3.48	-0.40
Cr-TCPP	-7.72	-0.91	2	2.95	4.55	-2.19
Mn-TCPP	-5.83	-1.19	2	1.72	3.78	-0.24
Fe-TCPP	-6.55	-0.45	2	2.83	4.07	-0.18
Co-TCPP	-6.93	-0.28	2	3.18	4.7	-2.07
Ni-TCPP	-6.47	-0.26	2	2.98	5.02	-3.70
Cu-TCPP	-4.32	0.34	2	2.50	4.77	-2.87
Zn-TCPP	-3.03	-0.76	2	0.75	5.05	-3.93

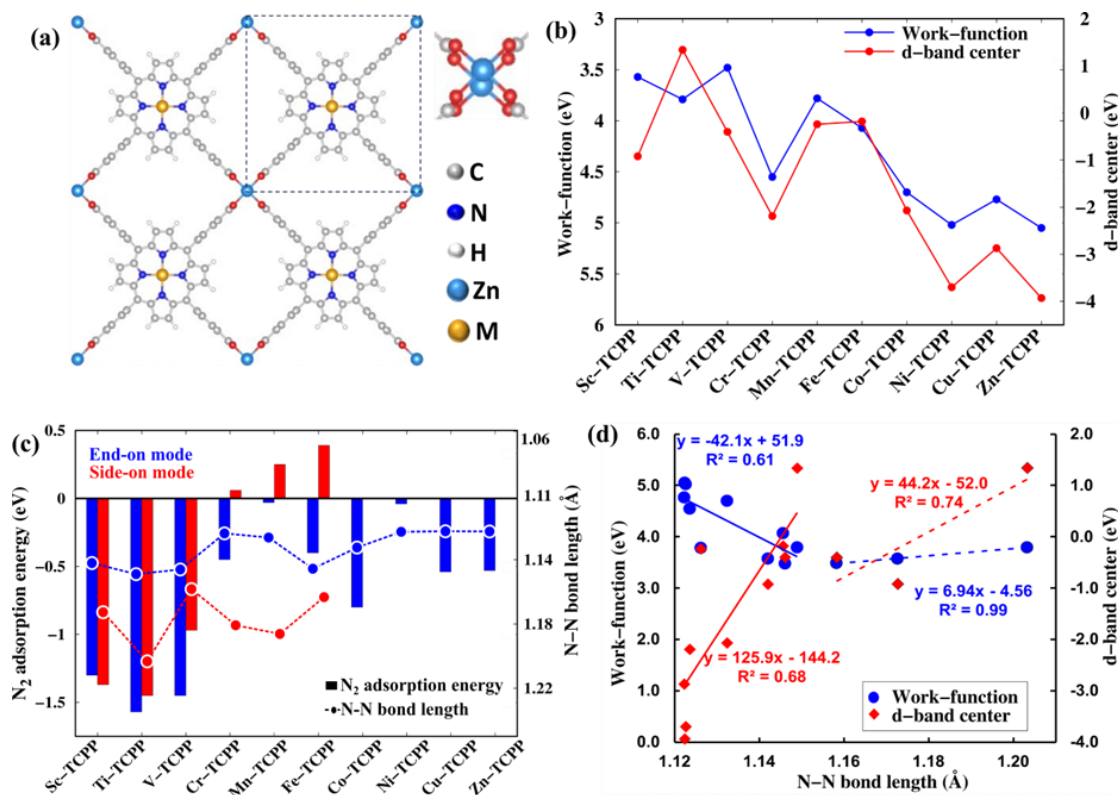


Figure 8.1: (a) Top view of the optimized structure of M-TCPP (M = Sc, Ti, V, Cr, Mn, Fe, Co, Ni, Cu, Zn) 2D-MOFs with the paddlewheel Zn₂(CO₂)₄ linker; elemental colour codes are as shown and unit cell marked by a dashed line. (b) The surface electronic properties of the M-TCPP MOFs recorded as work-function and d-band center for [ε_d = 5:5]. (c) N₂ adsorption energies and N-N bond lengths of N₂ adsorbed in perpendicular and parallel modes in M-TCPP MOFs. (d) Linear correlation between the surface electronic properties to the N-N bond length for N₂ adsorbed on M-TCPP MOFs, solid lines represent the side-on mode of N₂ adsorption while the dotted lines represent the end-on mode.

Table 8.2: Bader charges (q_M) of the transition metals in M-TCPP MOFs and the Bader charge of the N-atom (q_N) attached to the M-TCPP MOFs along with their integrated Crystal Orbital Hamiltonian Population (IpCOHP). The Bader charges and IpCOHP values indexed with ‘e’ indicate the end-on mode of N₂ adsorption, and the rest of the values represents the side-on mode on N₂ adsorption.

M-TCPP MOFs	q_M	q_N	M-N IpCOHP		N-N IpCOHP	
			Spin-up	Spin-down	Spin-up	Spin-down
Sc-TCPP	1.74	-0.25	-1.28	-1.11	-10.71	-11.39
		-0.21 ^e	-0.98 ^e	-0.72 ^e	-9.57 ^e	-10.68 ^e
Ti-TCPP	1.51	-0.47	-1.94	-1.44	-10.19	-11.05
		-0.27 ^e	-1.31 ^e	-1.31 ^e	-9.22 ^e	-9.22 ^e
V-TCPP	1.38	-0.26	-1.99	-1.45	-10.30	-11.11
		-0.14 ^e	-0.90 ^e	-0.62 ^e	-10.17 ^e	-10.97 ^e
Cr-TCPP	1.29	-0.08	-0.09	-0.11	-11.48	-11.60
Mn-TCPP	1.29	-0.12	-0.30	-0.53	-11.53	-11.53
Fe-TCPP	1.16	-0.33	-2.15	-2.15	-10.56	-10.56
Co-TCPP	1.08	-0.13	-0.61	-1.33	-11.12	-11.11
Ni-TCPP	0.91	-0.05	-0.06	-0.06	-11.63	-11.63
Cu-TCPP	0.94	-0.03	-0.06	-0.06	-11.60	-11.60
Zn-TCPP	1.16	-0.03	-0.06	-0.06	-11.61	-11.61

The M-TCPP MOFs exist as 2D nanosheets due to the planar π -electron conjugation of the metal-porphyrin with the paddlewheel $Zn_2(CO_2)_4$ linker. The electronic properties of the M-TCPP MOFs are thus driven by the exposed surface, and one anisotropic electronic property is the work function(Φ) which is direction and surface dependent.³⁷ While all M-TCPP MOFs are planar and oriented in the same direction, the difference in their electronic properties is caused by the transition metal coordinating with porphyrin framework and the corresponding work-function is surface dependent. Another intrinsic electronic property is the d-band center (ϵ_d) of a material which determines the charge distribution and in turn the electrocatalytic activity. A system with lower work-function will require a smaller energy to activate the N_2 molecule, and a correspondingly less negative d-band center will conform to possessing higher carrier density and availability of d-orbitals near the Fermi level. As such, systems with a lower work-function are optimal for stronger adsorption of N_2 and less negative d-band center will enhance charge transfer to the N_2 molecule which will further activate and weaken the strongly bonded $N\equiv N$ bond. It can be seen from **Figure 8.1(b)** that the surface electronic properties of Sc-TCPP, Ti-TCPP, V-TCPP, Mn-TCPP and Fe-TCPP MOFs show these optimal conditions while the rest of the M-TCPP MOFs show a more negative d-band center and higher work-function. The anticipated trend in N_2 adsorption and N-N bond activation from the surface electronic properties can be documented in the lighter transition metals Sc-TCPP, Ti-TCPP and V-TCPP MOFs as seen in **Figure 8.1(c)**. The same cannot be inferred for Mn-TCPP and Fe-TCPP and their lower activity chemisorption efficiency can be correlated to the Bader charge transfer from the metal center to the adsorbed N_2 , provided in **Table 8.2**. Furthermore, when a correlation of the surface electronic properties is investigated to the N_2 adsorption efficacy in terms of their free energy and the activated N-N bond lengths or the N-N bond strength; a stronger correlation could be observed to the order of N-N bond activation as seen in **Figure 8.1(d)** as compared to **Figure 8.2(a-b)**. The linear relationship is much more pronounced in the side-on modes of N_2 adsorption which is exothermic and feasible only in Sc-TCPP, Ti-TCPP and V-TCPP MOFs. In addition, the R^2 values of linear fits for the work-function is higher than the d-band center for all response properties observed: N_2 Gibbs free energy of adsorption, N-

N bond activation, N-N bond strength or bond order, charge transferred to the N atom adsorbed on M-TCPP MOFs (**Figure 8.2**). Thus, the work function which is only surface-dependent can be expected to give a more reliable correlation to the catalytic properties of the M-TCPP MOFs as compared to the d-band center which is dependent to the range of band energy considered to calculate the average band center.

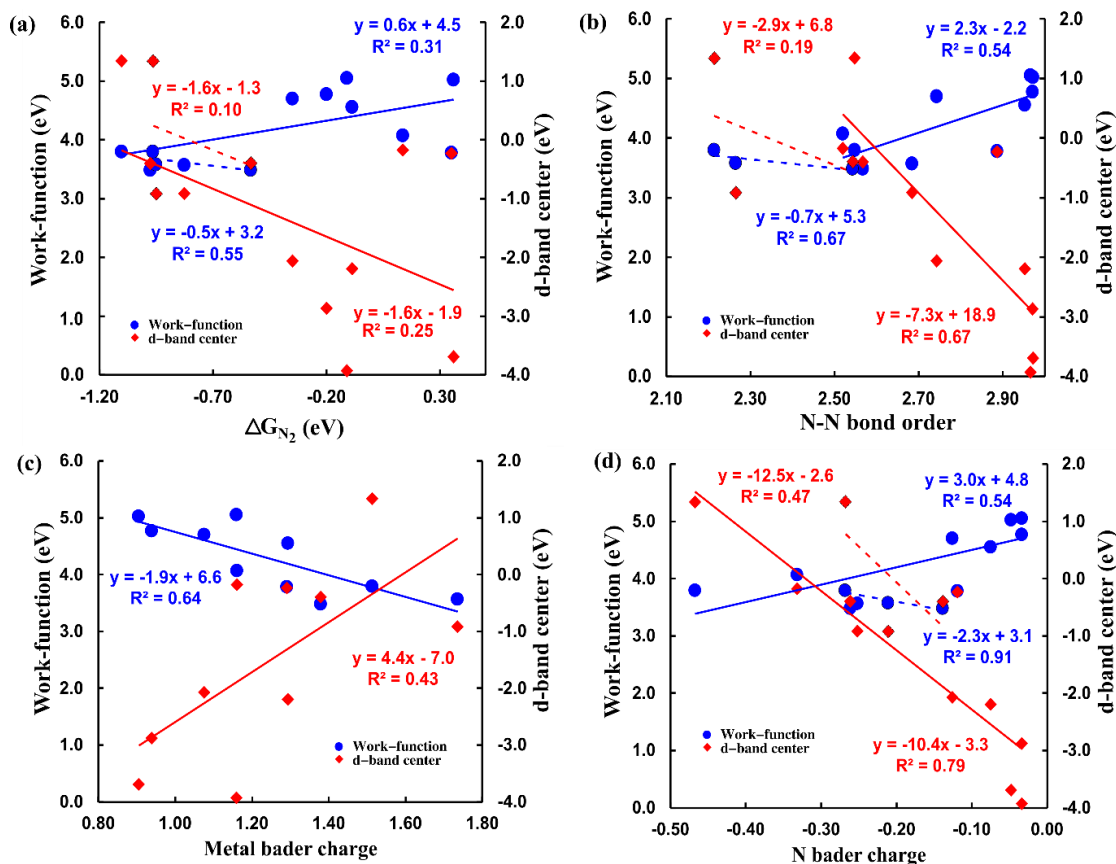


Figure 8.2: Linear correlation between the surface electronic properties to the (a) Gibbs free energies of N₂ adsorption, (b) N-N bond order or bond strength of the adsorbed N₂, (c) Bader charge of the metal, (d) Bader charge of the N-atom attached to the transition metal center of the M-TCPP MOFs. Solid lines represent the side-on mode of N₂ adsorption while the dotted lines represent the end-on mode.

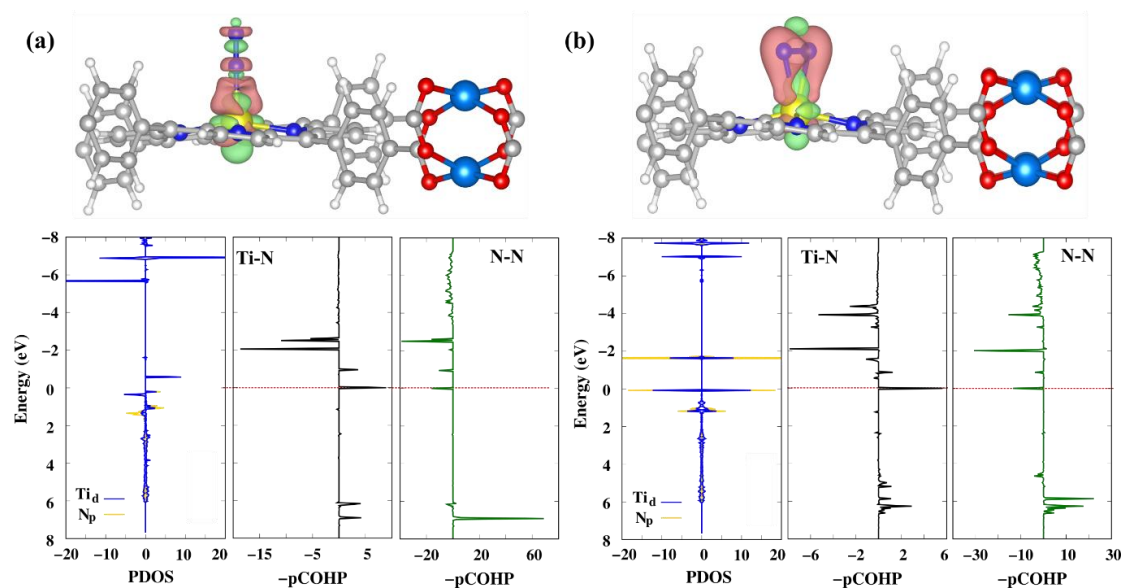


Figure 8.3: Charge density difference, Projected Density of States and Crystal Orbital Hamiltonian Population (-pCOHP) of Ti-N pair when N_2 is adsorbed in (a) side-on or perpendicular mode and (b) end-on or parallel mode. COHP calculations are carried out with LOBSTER software.³⁸

While the activation of N-N bond is subsequently brought about by charge transfer on the adsorbed N_2 molecule, the side-on mode of N_2 adsorption in spite of showing a larger N-N bond activation show a relatively lower charge transfer to the N-atoms, the values of which are provided in **Table 8.2**. Further investigations into the nature of M-N and N-N interaction are explored with the Crystal Orbital Hamiltonian Population (-pCOHP) of the M-N atom pair for the perpendicular/end-on and parallel/side-on modes of N_2 adsorption. The covalent bonding and antibonding states are characterized by the positive and negative overlap population of the -pCOHP plots respectively. The positive or bonding contribution for the M-N atom pair is higher in Sc-TCPP, Ti-TCPP, V-TCPP and Fe-TCPP as compared to the rest of M-TCPP MOFs for the end-on mode of N_2 adsorption shown in **Figure 8.3(a)**. The corresponding integral of the -pCOHP (I_{pCOHP}) up to the Fermi level are provided in **Table 8.2** with a more negative I_{pCOHP} corresponding to stronger bonding in the atom pair considered. The I_{pCOHP} values for the spin-up or spin-down states in the above mentioned four MOFs have been found to be more negative than the rest. Upon comparing the -pCOHP contributions and I_{pCOHP}

values of the M-N pair for the side-on mode of N₂ adsorption shown in **Figure 8.3(b)** to their side-on interaction mode, the covalent bonding contribution has been found to be lower and this explicates the lower charge in the end-on modes of N₂ adsorption. Interestingly, the orbital contributions of the N-N bond pair, **Figures 8.3(c-d)** show a higher contribution of the negative or antibonding state, thus affirming the presence of electrons in the N₂ antibonding states that influences N-N bond activation. As such, a positive or bonding orbital contribution in M-N atom pair and negative or antibonding contribution in N-N atom pair favours the activation of N≡N bond.

8.3.2 NRR mechanism

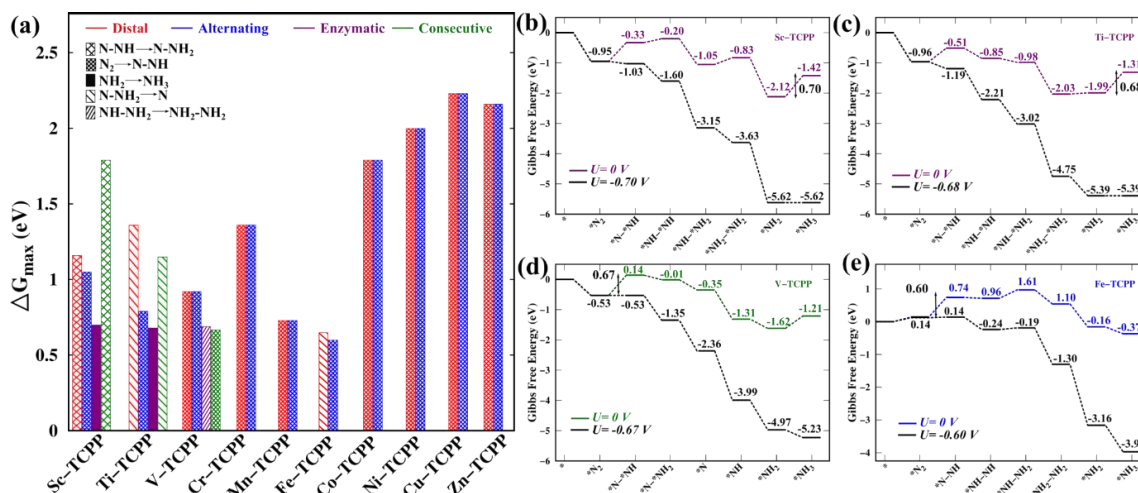


Figure 8.4: (a) ΔG_{\max} (in eV) with potential rate determining steps for NRR on M-TCPP MOFs with respective colour codes for the different mechanistic routes shown by each system, (b-c) Enzymatic routes of NRR in Sc-TCPP and Ti-TCPP calculated under applied voltage of 0 V and onset limiting potentials of -0.70 V and -0.68 V respectively, (d) Consecutive route of NRR in V-TCPP calculated under applied voltage of 0 V and onset potential of -0.67 V, (e) Alternating route of NRR in Fe-TCPP calculated under applied voltage of 0 V and onset potential of -0.60 V.

Subsequent investigations into mechanism of nitrogen reduction on the M-TCPP MOFs show the incidence of distal and alternating routes of NRR for end-on mode of N₂

adsorption and enzymatic and consecutive routes for side-on mode of N_2 adsorption. The enzymatic route predominates the free energy profile of Sc-TCPP and Ti-TCPP with the last protonation step, $*NH_2 \rightarrow *NH_3$ as the potential rate determining step (PDS) and the energy barrier of 0.70 eV and 0.68 eV, respectively. The preference of the enzymatic route in these two MOFs can be speculated from the higher stability of the $*N_xH_y$ intermediates that are more exoergic as compared to its analogues in the distal, alternating or consecutive routes. Contrastingly, V-TCPP MOFs show an inclination towards a consecutive route for NRR with the first protonation step, $*N_2 \rightarrow *N-*NH$ being the PDS with ΔG_{max} of 0.67 eV; despite the $*N_xH_y$ intermediates in the distal route being more exoergic. The first protonation step in distal mode being highly endoergic (0.92 eV) becomes unfavourable and the energy barrier for NRR is lowered when the reduction proceeds via enzymatic or consecutive route. The rest of M-TCPP MOFs had earlier shown feasible side-on mode on N_2 adsorption and the nitrogen reduction show an inclination towards following distal or alternating route of NRR. The first protonation step, $*N_2 \rightarrow *N-NH$ is the rate determining step in the remaining M-TCPP MOFs with the precedence of the distal route of NRR in Cr-TCPP (1.36 eV) and Mn-TCPP (0.73 eV) while the alternating route predominates in Fe-TCPP (0.60 eV), Co-TCPP (1.70 eV), Ni-TCPP (2.0 eV), Cu-TCPP (2.23 eV) and Zn-TCPP (2.16 eV). A summary of all mechanistic NRR routes and the potential rate determining step with ΔG_{max} values on all M-TCPP MOFs are shown in **Figure 8.4(a)**. The candidate of interest with lower $\Delta G_{max} \leq 0.70$ eV values are Sc-TCPP, Ti-TCPP, V-TCPP and Fe-TCPP MOFs with corresponding limiting potentials of -0.70 V, -0.68 V, -0.67 V and -0.60 V, respectively. **Figures 8.4(b-e)** show the free energy profiles of nitrogen reduction in Sc-TCPP, Ti-TCPP, V-TCPP and Fe-TCPP via the most efficient routes and the reaction becomes feasible with each protonation steps being exoergic under an applied onset potential equivalent to the respective limiting potentials, thereby inferring these MOFs can be implemented as electrocatalysts for NRR.

8.3.3 NRR electrocatalytic activity and selectivity

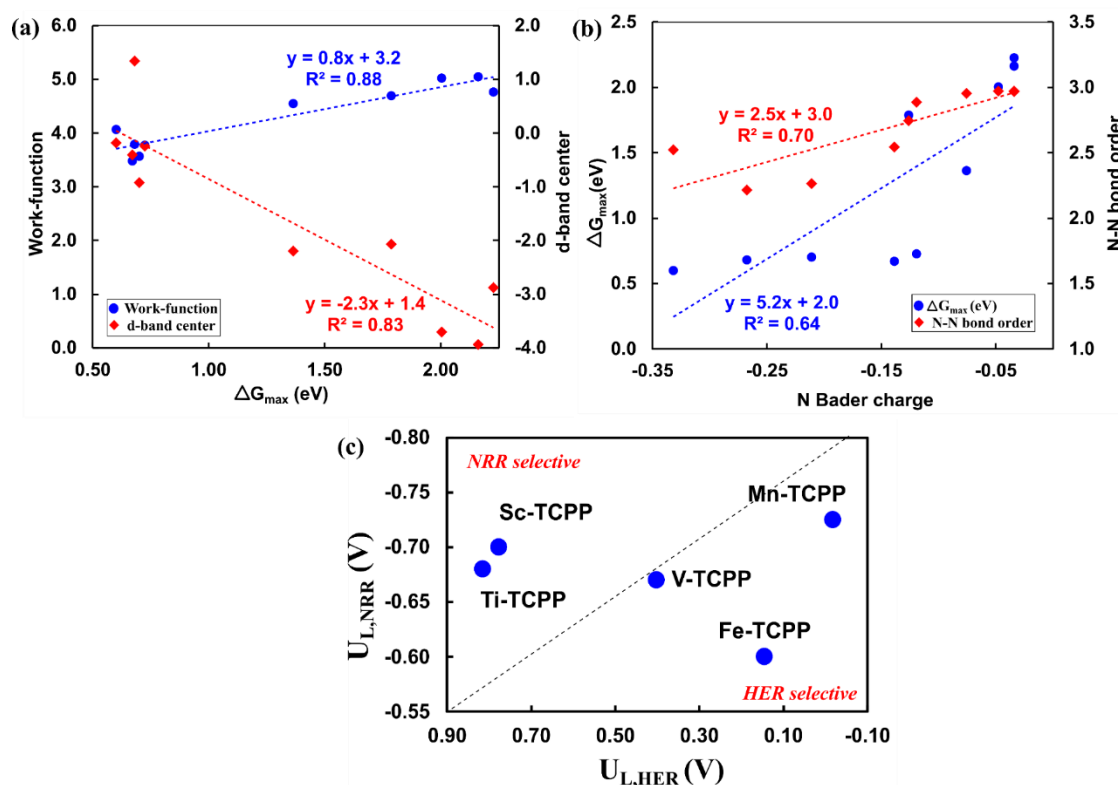


Figure 8.5: Linear correlation between (a) the limiting energy barrier for NRR, ΔG_{\max} to surface electronic properties – work function and d-band center, (b) Average Bader charge on adsorbed N_2 to ΔG_{\max} and N-N bond order or bond strength, (c) NRR vs HER selectivity plot of the M-TCPP MOFs with lower limiting potentials.

Following the investigations on the NRR reaction mechanism and the potential rate determining energy barrier on the M-TCPP MOFs, a correlation between the energy barrier for nitrogen reduction is probed to the electronic and response properties of the MOFs. A linear relationship has been observed between ΔG_{\max} and the surface electronic properties as seen in **Figure 8.5(a)**. The R^2 value of the work-function is higher than that of the d-band center, thereby signifying a stronger correlation of the energy barrier to the work function and the positive slope infers to a proportional relationship between the two, as such the MOFs with a lower value of work function also show a lower energy barrier. As the optimal mechanistic NRR routes for Sc-TCPP, Ti-TCPP and V-TCPP MOFs emanate from the side-on mode of N_2 adsorption, while for the remaining M-TCPP MOFs

is derived from the end-on mode of N₂ adsorption. Thereby, a correlation of the charge transferred on the adsorbed N₂ is then accounted to the ΔG_{\max} attributed from the optimal N₂ adsorption that leads to lower energy barrier for nitrogen reduction and N-N bond order, which accounts for the strength of the N-N bond, in **Figure 8.5(b)**. A better fit can be observed when the bond order on N₂ is considered as a determining response property and the positive slope further ratifies that a larger charge gain on the adsorbed N₂ corresponds to smaller N-N bond order or activated N-N bond. The same can be seen wherein ΔG_{\max} shows a linear relationship to the average Bader charge on the N-atoms. This linear relationship facilitates the surface electronic properties, N-N bond strength and Bader charge as fundamental parameters in determining the rate determining potential for metalloporphyrin MOFs with 3d-transition metals. The theoretical NRR Faraday efficiency of the M-TCPP MOFs with lower limiting potentials as evaluated using the Boltzmann distribution function,³⁹ $f_{NRR} = \frac{1}{1 + \exp\left(-\frac{\Delta G_{NRR} - \Delta G_{HER}}{k_B T}\right)}$ $\times 100\%$ at room temperature have been found to be 100%, thereby inferring high selectivity of NRR over the competing HER. However, Fe-TCPP MOF tends to show an increasing occurrence of HER under onset-potential of -0.3 V to -0.5 V in 0.1 M HCl (aqueous) electrolyte, as confirmed by Cong and co-workers. This corroborates to our finding of Fe-TCPP MOF with NRR limiting potential of -0.60 V and overpotential of -0.44 V showing a higher selectivity towards HER in **Figure 8.5(c)**. However, Sc-TCPP and Ti-TCPP MOFs despite showing slightly higher NRR limiting potentials, -0.70 V and -0.68 V, respectively show a higher NRR selectivity and 100% theoretical Faradaic efficiency.

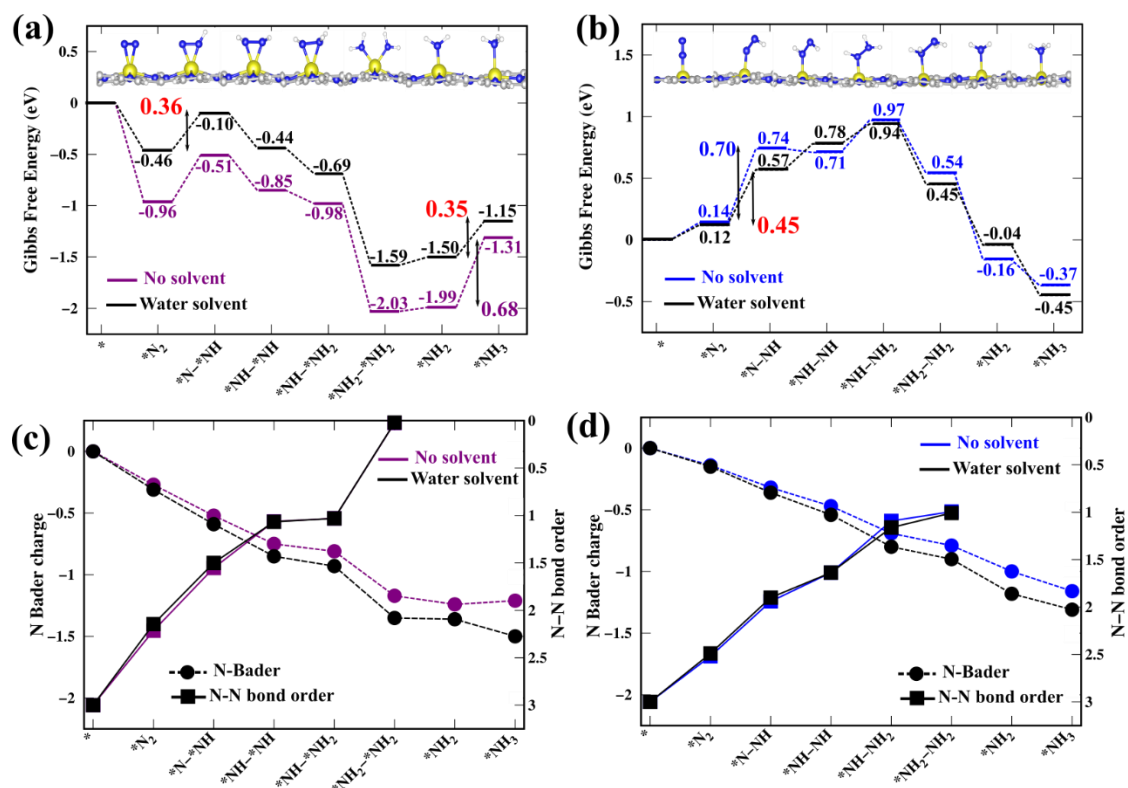


Figure 8.6: Free energy diagram of (a) enzymatic NRR on Ti-TCPP and (b) alternating NRR on Fe-TCPP without and with water solvent, with the corresponding ΔG_{max} in water solvent highlighted in red. Average Bader charge on N-atoms of $*\text{N}_x\text{H}_y$ intermediates and N-N bond order for (c) enzymatic NRR on Ti-TCPP and (d) alternating NRR on Fe-TCPP MOF.

An interesting outlook can be accounted on the NRR performance of Sc-TCPP, Ti-TCPP, V-TCPP and Fe-TCPP MOFs in the presence of water solvent. The adsorption of N_2 in a polar solvent is expected to be endoergic as the molecule is non-polar, and the same is established with a less negative free energy of its adsorption energy in water for all four MOF systems as seen in **Figures 8.6(a-b)**. Nonetheless, the protonated $*\text{N}_x\text{H}_y$ intermediates possess dipole moments and their formation should be exoergic in water solvent as compared to their free energy of formation in vacuum. However, the hydrophobic nature of the porphyrin components in the metalloporphyrin MOFs masks the hydrophilic contribution of the $*\text{N}_x\text{H}_y$ intermediates. This limited stabilisation of the $*\text{N}_x\text{H}_y$ intermediates aids in lowering the energy barrier of the rate determining first and

last protonation steps, $*N_2 \rightarrow *N_2H$ and $*NH_2 \rightarrow *NH_3$, as shown in **Figure 8.6(a)** and **8.6(b)** for Ti-TCPP and Fe-TCPP MOFs respectively. As such, the NRR limiting potential on Sc-TCPP, Ti-TCPP, V-TCPP and Fe-TCPP MOFs are seen to reduce to -0.50 V, -0.35 V, -0.51 V and -0.45 V, respectively. Furthermore, an analysis of the average Bader charge on the N-atoms of the $*N_xH_y$ intermediates in water solvent exhibited an increase in the charge gained on the N-atoms as compared to the vacuum state, as seen in **Figure 8.6(c-d)** for Ti-TCPP and Fe-TCPP MOF. This enhanced charge transfer on the N-atoms explains the lowering of NRR limiting potential in water solvent. While a significant increase in the N-N bond order cannot be observed in water solvent, the presence of solvent leads to the stabilisation of the more dissociated N-N bond can be observed in **Figure 8.6(c)** on Ti-TCPP MOF as the N-N bond order gradually decreases to zero in the $*NH_2-*NH_2$ species. Henceforth, with a higher NRR performance in water solvent and exclusive selectivity for NRR, Ti-TCPP MOF can be recommended as a highly efficient electrocatalyst for nitrogen reduction reaction.

8.4 Conclusion

In summary, DFT investigation has been carried out to understand the surface electronic properties of two-dimensional M-TCPP MOFs with the change in transition metal center in the metalloporphyrin unit. Economically viable and earth abundant 3d-transition metals are influential in enhancing the stability and catalytic properties of M-TCPP MOFs. The surface-dependent work function can be implemented as a reliable correlation to the catalytic properties of the M-TCPP MOFs as compared to the electronic properties. Orbital population (-pCOHP) analysis emphasizes the higher contribution of the positive or bonding state in M-N bond and negative or antibonding state in N-N bond are essential for N-N bond activation. Furthermore, a linear relationship between ΔG_{max} and surface electronic properties, N-N bond strength and Bader charge is fundamental in determining the rate determining potential for NRR in M-TCPP MOFs. Upon employing the fundamental parameter, NRR selective Ti-TCPP MOF with a limiting potential of -0.35 V in water solvent has been proposed as an attractive candidate for eNRR. Overall, this study offers insights on the stability, catalytic activity and selectivity of 2D M-TCPP

MOFs with approaches to incorporate parameters influential in determining energy barrier to inspire further research on sustainable electrocatalysts for feasible ambient ammonia production.

8.5 References

- (1) Haber, F. *Naturwissenschaften* **1923**, *9*, 753–756.
- (2) Cherkasov, N.; Ibhaddon, A.O.; Fitzpatrick, P. *Chem. Eng. Process. Process Intensif.* **2015**, *90*, 24–33.
- (3) Van Der Ham, C. J. M.; Koper, M. T. M.; Hetterscheid, D. G. H. *Chem. Soc. Rev.* **2014**, *43*, 5183–5191.
- (4) Liu, D.; Chen, M.; Du, X.; Ai, H.; Lo, K.H.; Wang, S.; Chen, S.; Xing, G.; Wang, X.; Pan, H. *Adv. Funct. Mater.* **2021**, *31*, 1–36.
- (5) Chanda, D.; Xing, R.; Xu, T.; Liu, Q.; Luo, Y.; Liu, S.; Tufa, R. A.; Dolla, T. H.; Montini, T.; Sun, X. *Chem. Commun.* **2021**, *57*, 7335–7349.
- (6) Wang, Y.; Mao, J.; Meng, X.; Yu, L.; Deng, D.; Bao, X. *Chem. Rev.* **2019**, *119*, 1806–1854.
- (7) Jin, H.; Guo, C.; Liu, X.; Liu, J.; Vasileff, A.; Jiao, Y.; Zheng, Y.; Qiao, S.-Z. *Chem. Rev.* **2018**, *118*, 6337–6408.
- (8) Asselin, P.; Harvey, P. D. *ACS Appl. Nano Mater.* **2022**, *5*, 6055–6082.
- (9) Cui, Q.; Qin, G.; Wang, W.; Geethalakshmi, K. G.; Du, A.; Sun, Q. *J. Mater. Chem. A* **2019**, *7*, 14510–14518.
- (10) Liu, S.; Liu, Y.; Gao, X.; Tan, Y.; Shen, Z.; Fan, M. *Appl. Surf. Sci.* **2020**, *500*, 144032.
- (11) Sun, Q.; Dai, Y.; Ma, Y.; Li, X.; Wei, W.; Huang, B. *J. Mater. Chem. C* **2015**, *3*, 6901–6907.

- (12) Maitarad, P.; Namuangruk, S.; Zhang, D.; Shi, L.; Li, H.; Huang, L.; Boekfa, B.; Ehara, M. *Environ. Sci. Technol.* **2014**, *48*, 7101–1710.
- (13) Liu, J.-H.; Yang, L.-M.; Ganz, E. *J. Mater. Chem. A* **2019**, *7*, 11944–11952.
- (14) Shen, J.; Kortlever, R.; Kas, R.; Birdja, Y. Y.; Diaz-Morales, O.; Kwon, Y.; Ledezma-Yanez, I.; Schouten, K. J. P.; Mul, G.; Koper, M. T. M. *Nat. Commun.* **2015**, *6*, 8177.
- (15) Chen, X.; Cong, M.; Tang, M.; Liu, J.; Chen, S.; Gao, Y. *Inorg. Chem. Front.*, **2022**, *9*, 4369.
- (16) Xie, M.-H.; Yang, X.-L.; He, Y.; Zhang, J.; Chen, B.; Wu, C.-D. *Chem. - Eur. J.* **2013**, *19*, 14316–14321.
- (17) Shen, H.-M.; Wang, X.; Huang, H.; Liu, Q.-P.; Lv, D.; She, Y.-B. *Chemical Engineering Journal*, **2022**, *443*, 136126.
- (18) Micheroni, D.; Lan, G.; Lin, W. *J. Am. Chem. Soc.* **2018**, *140*, 15591.
- (19) Kornienko, N.; Zhao, Y.; Kley, C. S.; Zhu, C.; Kim, D.; Lin, S.; Chang, C. J.; Yaghi, O. M.; Yang, P. *J. Am. Chem. Soc.* **2015**, *137*, 14129.
- (20) Hegg, A. S.; Mercado, B. Q.; Miller, A. J. M.; Holland, P. L. *Faraday Discuss.*, **2023**, *Advance Article*, <https://doi.org/10.1039/D2FD00166G>.
- (21) Zhou, J.; Sun, Q. *J. Am. Chem. Soc.* **2011**, *133*, 15113–15119.
- (22) Baranowski, D.; Cojocariu, I.; Sala, A.; Africh, C.; Comelli, G.; Schio, L.; Tormen, M.; Floreano, L.; Feyer, V.; Schneider, C. M. *Angew. Chem.* **2022**, *134*, e202210326.
- (23) Zhang, R.; Jiao, L.; Yang, W.; Wan, G.; Jiang, H.-L. *J. Mater. Chem. A*, **2019**, *7*, 26371.
- (24) Cong, M.; Chen, X.; Xia, K.; Ding, X.; Zhang, L.; Jin, Y.; Gao, Y.; Zhang, L. *J. Mater. Chem. A*, **2021**, *9*, 4673.

- (25) Zhao, M.; Wang, Y.; Ma, Q.; Huang, Y.; Zhang, X.; Ping, J.; Zhang, Z.; Lu, Q.; Yu, Y.; Xu, H.; Zhao, Y.; Zhang, H., *Adv Mater* **2015**, *27*, 7372-7378.
- (26) Kresse, G.; Furthmüller, *J. Comput. Mater. Sci.* **1996**, *6*, 15–50.
- (27) Perdew, J. P.; Burke, K.; Ernzerhof, M.; *Phys. Rev. Lett.* **1996**, *77*, 3865–3868.
- (28) Grimme, S.; Antony, J.; Ehrlich, S.; Krieg, H.; *J. Chem. Phys.* **2010**, *132*, 154104.
- (29) Tang, W.; Sanville, E.; Henkelman, G.; *J. Phys. Condens. Matter.* **2009**, *21*, 084204.
- (30) Nosé, S.; *J. Chem. Phys.* **1984**, *81*, 511.
- (31) Greeley, J.; Norskov, J. K. *Electrochim. Acta* **2007**, *52*, 5829–5836.
- (32) Nørskov, J. K.; Rossmeisl, J.; Logadottir, A.; Lindqvist, L.; Kitchin, J. R.; Bligaard, T.; Jónsson, H.; *J. Phys. Chem. B* **2004**, *108*, 17886–17892.
- (33) Zhao, J.; Chen, Z. *J. Am. Chem. Soc.* **2017**, *139*, 12480–12487.
- (34) Ling, C.; Niu, X.; Li, Q.; Du, A.; Wang, J. *J. Am. Chem. Soc.* **2018**, *140*, 14161–14168.
- (35) Mathew, K.; Sundararaman, R.; Letchworth-Weaver, K.; Arias, T. A.; Henning, R. G. *J. Chem. Phys.* **2014**, *140*, 084106.
- (36) Guo, X.; Lin, S.; Gu, J.; Zhang, S.; Chen, Z.; Huang, S. *ACS Catal.* **2019**, *9* (12), 11042–11054.
- (37) Hu, G.; Fung, F.; Huang, J.; Ganesh, P. *J. Phys. Chem. Lett.* **2021**, *12*, 2320–2326.
- (38) Nelson, R.; Ertural, C.; George, J.; Deringer, V. L.; Hautier, G.; Dronskowski, R. *J Comput Chem.* **2020**, *41*, 1931-1940.
- (39) Chittibabu, D. K. D.; Sathishkumar, N.; Wu, S.-Y.; Chen, H.-T. *ACS Appl. Energy Mater.* **2023**, *6* (12), 6636–6645.

Chapter 9

Summary and Future Scope

This chapter discusses the outcomes and findings of the computational studies performed from Chapters 3 to 8 on different 2D materials in the thesis. An additional perspective on the future of this research is also presented in this chapter.

9.1 Focus of the thesis

The present-day ammonia synthesis is carried out through the Bosch-Haber's process or steam reforming process, both of which requires a high amount of energy. Ammonia synthesis sucks upto 6% of the world's total energy and releasing 451 million metric tonnes of CO₂ during the process. Its carbon footprint goes well above the energy demand and is certainly a cause of concern. While industries face the bottleneck of huge energy demand and carbon footprint; nature, interestingly, produces ammonia very efficiently with the help of enzymes at ambient condition. Few research groups work on experimental studies to develop new organometallic compounds and metal catalysts that are efficient catalyst for nitrogen reduction. One way to reduce the depleting metal reserves is to make each and every atom active and this idea has been implemented by introducing them as atomic catalyst centers with cheaper and efficient substrates, one such being 2D materials, to hold the single atom sites is the focus of this thesis. Implementing the idea of 2D surfaces, which has a large delocalised electron density to act as an electron reservoir to the active single atom sites, this electron rich system has been explored to study N₂ activation. However, considering the cost of developing these compounds experimentally, computational scanning and analysis will help in reducing the cost of materials and metal loss. A thermochemical model of the proposed catalysts has been implemented using Density Functional Theory (DFT) with benchmarked electronic representation. The thermochemical calculations adopted in this thesis include calculating the enthalpic parameters and incorporating the computational hydrogen electrode (CHE) method for prospective 2D materials that can be explored as electrocatalysts. The CHE model developed based the one-electron hydrogen revolution reaction (HER), despite its simplicity and undermining reaction kinetics and applied potential that are crucial for multistep reactions, is successful in identifying electrocatalysts and rate limiting step. The instance where CHE model has been found to predict the same NRR pathway and rate determining step when compared to electrochemical solid-liquid interface model that incorporated reaction intermediates in solvent and applied potential validates the methodology adopted in the thesis.¹

An inherent modulation in the electronic nature of 2D materials can be brought about when atomic metal and non-metal centers when anchored or embedded on it. The catalytic activity of the materials can be augmented via this practice and the atomic dopants/defects that can work selectively on almost all 2D materials need to be investigated. The most commonly and actively implemented atomic catalysts that can be integrated into 2D materials are the transition metal single atom catalysts (SACs). However, the use of non-metal atomic centers is much more attractive considering the future of ammonia economy and obtaining sustainable goals. A stark improvement in the NRR performance can be investigated theoretically by investigating the Gibbs free energy of the limiting step of NRR. Additionally, a correlation between charge transfer from the catalytic centre and nitrogen reduction efficacy is one aspect of paramount importance that can be explored. This opens a new window for understanding the origin of the electrocatalytic properties of non-metals atoms, in particular, on the 2D materials and their role in nitrogen fixation, which can help experimentalists to a great extent in the design and fabrication of doped 2D materials for sustainable ammonia production. Moving towards a sustainable goal, the research has been framed on exploring experimentally procurable, earth-abundant, low cost, stable and efficient NRR electrocatalysts by tuning the properties through synergistic enhancement on different phases and active to bring down the NRR overpotential.

9.2 Summary of results

The activity of metal single atom catalyst (SAC), Mo anchored on pristine and BN-doped graphene sheets and nanoflakes have been studied for dinitrogen activation. This study carried out with the use of two different methodologies and electronic description is further extended on several metal SACs that possess enormous potential for nitrogen activation. The association between the electronic nature and activity of the metal SACs are made via Fukui and Multiphilic descriptors and a reusable V-BNring-grap catalyst had been found to reduce nitrogen to ammonia. This study has been extended on the most earth abundant element aluminium anchored as single atom catalysts or clusters and a trade-off can be achieved when researchers aim for scalable and sustainable catalyst for ammonia production with smaller clusters of Al on nitrogen-doped graphene. The results from the above studies highlights the

need to shift towards electrocatalysis and explore the challenges of electrocatalytic nitrogen reduction reaction (eNRR) on a highly conducting 2D material, MXenes with a very high efficiency to reduce nitrogen to ammonia with an overpotential of 0.41 eV. It then brings us to an inexpensive material of high electrical conductivity with prospects for application in eNRR, vanadium dichalcogenides, VX_2 . This most recent work on two different phases of VX_2 that exhibits different electronic and magnetic properties and the synergistic nature of non-metal dopants on these two phases which govern the reduction of nitrogen. It has been found that boron and carbon atoms when doped on 2H and 1T phases, respectively, of VS_2 monolayer to synergistically enhance their electrocatalytic properties and produce ammonia at limiting potentials as low as 0.22 eV and 0.42 eV, respectively. The final aspect of this thesis investigates the ammonia production efficacy of a family of porous material which are relatively easier to synthesize, 2D paddle-wheel MOFs studied with different earth-abundant metal centers. Fe-based 2D-MOF in non-aqueous condition and Ti-based MOF has been predicted as excellent electrocatalysts for NRR at ambient aqueous condition. The outcomes on different 2D materials from this thesis has been summarised in **Table 9.1** below,

Table 9.1: Summary of the research finding from different 2D material catalysts (in different chapters) considered in this thesis.

Chapter	2D-catalyst	Key findings
3	Mo-CBN-grap	<ol style="list-style-type: none"> 1. N-N bond activation in N_2 is a local site activity. 2. Size and edge orientation of graphene does not influence N_2 activation. 3. N_2 bond elongation by 9% (1.21 Å) on the catalyst. <i>Maibam, A. et. al, J. Phys. Chem. C, 2019, 123, 27492–27500.</i>
4	V-BNring-grap	<ol style="list-style-type: none"> 1. Description of atomic orbitals is critical for metal single atom centers. 2. Role of electronic descriptors in deciphering the catalytic activity. 3. Recyclable catalyst that shows N-N bond elongation by 11% (1.23Å) with $\Delta G_{NRR} \leq 1.24$ eV. <i>Maibam, A. et. al, J. Colloid Interface Sci., 2021, 600, 480-491.</i>

5	Al ₅ @N ₄ -DVG	<ol style="list-style-type: none"> 1. Comparison of single atom catalyst to metal cluster catalyst. 2. Stabilization of atomic clusters and $\Delta G_{\text{NRR}} = 0.78 \text{ eV}$. 3. Trade-off between NRR performance and cost of metal catalysts. <p><i>Maibam, A. et. al, Applied Surface Science., 2023, 623, 157024.</i></p>
6	B _{SAC} @Mo ₂ C-Mo _{vac}	<ol style="list-style-type: none"> 1. Incorporation of boron atomic catalyst on defective 2D material. 2. $\Delta G_{\text{NRR}} = 0.57 \text{ eV}$ and role of p-band center in deciphering catalytic activity. <p><i>Maibam, A. et. al, Mater. Adv., 2022, 3, 592-598.</i></p>
7	2H-VS ₂ @B	<ol style="list-style-type: none"> 1. Mon-metallic dopants on 1T and 2H dichalcogenides of vanadium. 2. $\Delta G_{\text{NRR}} = 0.22 \text{ eV}$ and electron “donation–acceptor” between B-dopant and N₂. 3. Thermodynamai favourability of product, NH₃ formation is decisive in directing NRR. <p><i>Maibam, A. et. al, Applied Surface Science, 2022, 602, 154401</i></p>
8	Ti-TCPP	<ol style="list-style-type: none"> 1. Biocompatible porphyrin-based catalyst with stabilised metal centers. 2. Ti-TCPP showing $\Delta G_{\text{NRR}} = 0.35 \text{ eV}$ in aqueous solvent and an attractive NRR electrocatalyst.

9.3 Future scope

Academically, this research would open a new door towards 2D-materials as catalysts for one of the most energy intensive chemical process and understanding the factors involved in ammonia production. The electronic properties can be designated as parameters crucial for N₂ activation and reduction. Other parameters include the surface electronic properties of the 2D materials that can be pre-screened before the material is subjected to N₂ reduction. NRR being a six-electron transfer process, the electronic state of the intermediates is crucial for

driving the reduction process. While all these parameters can be incorporated into machine learning modules to predict the optimal next generation catalysts for NRR; the same approach can be implemented in other multi-electron transfer processes such as CO₂ reduction reaction and NO_x reduction reaction. It is important to note that this approach of employing the thermodynamic parameter - enthalpy is a conventional method to describe the NRR activity of the chemically modified 2D materials in their most stable state for an ideal scenario with an implicit solvent media taken into account. In an experimental setting, the reaction is not static and the kinetics of reactants, intermediates and products in the reaction media play a crucial role in driving the rate limiting potentials discussed in the thesis. This limitation has not been addressed in the thesis and the kinetic factors need to be addressed as prospects as we move forward with NRR. As such, microkinetic modelling of the reaction intermediates can be adopted for nitrogen reduction reaction to inculcate the kinetic parameters and the equilibrium rate constant of the reaction via the transition state theory.^{2,3} As we move ahead to mimic experimental conditions, there is also a need to incorporate the solvent media and applied potential in understanding the mechanism and kinetics of NRR; therefore, a combination of density functional theory with statistical model, i.e., grand canonical ensemble (GCE) can be implemented to incorporate the kinetic factors incited by the solvent media or reaction intermediates. under a constant potential.⁴⁻⁶ The GCE model with DFT which give a comprehensive NRR mechanism inclusive of thermodynamic, kinetic and electrochemical factors will be the prospective advancement from the work done in this thesis.

The experimental relevance of the proposed 2D materials and computational results in this thesis is yet to be validated and the electrochemical parameters presented in this thesis being atomic or micro-properties cannot be transferred in an experimental setting. Furthermore, the 2D models discussed in this thesis are of one-atom layer thickness or monolayer sheets; in experimental conditions these 2D sheets will need a scaffold for support and the dynamic experimental conditions, such as – electrolyte, pH, solvent and applied potential, are ignored or approximated as implicit addendums. This raises a disparity in the quantitative values of the rate limiting potentials between the experiments and computational results as observed in several recent research works.⁷⁻⁹ Rather, a qualitative trend of the computational results and the experimental data are usually used to verify the higher activity

of any catalyst explored by experimentalists; therefore, further theoretical exploration is required to obtain a more accurate description of the experimental conditions.

On an industrial scale, insights from this thesis plan will help in designing energy efficient materials oriented for ammonia production and storage. Considering the importance of commercially pragmatic materials, a trade-off or choice can be made for selecting a material that shows moderate NRR performance, but shows scalability and recyclability in term of their usage. Ammonia is more competitive than H₂ due to its high volumetric energy density; when this stored ammonia is released and employed in ammonia-based fuel cells, it can serve as an approach to solve the demanding problems on energy shortage.

9.4 References

- (1) Höskuldsson, Á. B.; Tayyebi, E.; Skúlason, E.; *Journal of Catalysis*, **2021**, *404*, 362-370.
- (2) Sathishkumar, N.; Chen, H.-T.; *ACS Appl. Mater. Interfaces*, **2023**, *15*, 15545–15560.
- (3) Choi, C.; Gu, G. H.; Noh, J.; Park, H. S.; Jung, Y.; *Nat Commun*, **2021**, *12*, 4353.
- (4) Wu, T.; Melander, M. M.; Honkala, K.; *ACS Catal.* **2022**, *12*, 2505–2512.
- (5) Rehman, F.; Kwon, S.; Hossain, Md. D.; Musgrave III, C. B.; Goddard III, W. A.; Luo, Z.; *J. Mater. Chem. A*, **2022**, *10*, 23323-23331.
- (6) Tezak, C. R.; Singstock, N. R.; Alherz, A. W.; Vigil-Fowler, D.; Sutton, C. A.; Sundararaman, R.; Musgrave, C. B.; *ACS Catal.* **2023**, *13*, 12894–12903.
- (7) Zhang, J.; Zheng, J.; Wang, Z.; *Chemical Engineering Science*, **2023**, *280*, 119076.
- (8) Ma, C.; Zhang, Y.; Yan, S.; Liu, B.; *Applied Catalysis B: Environmental*, **2022**, *315*, 121574.
- (9) Wu, S.; Zhang, M.; Huang, S.; Cai, L.; He, D.; Liu, Y.; *Chinese Chemical Letters*, **2023**, *34*, 107282.

List of publications emanating from the thesis work

1. **Ashakiran Maibam**, Thillai Govindaraja, Kaliaperumal Selvaraj, Sailaja Krishnamurty, Dinitrogen Activation on Graphene Anchored Single Atom Catalysts: Local Site Activity or Surface Phenomena, *J. Phys. Chem. C*, **2019**, 123, 27492–27500.
2. **Ashakiran Maibam** and Sailaja Krishnamurty, Nitrogen activation to reduction on a recyclable V-SAC/BN-graphene heterocatalyst sifted through Dual and Multiphilic descriptors, *Journal of Colloid and Interface Science*, **2021**, 600, 480-491.
3. **Ashakiran Maibam**, Sailaja Krishnamurty and Manzoor Ahmad Dar, Electrocatalytic nitrogen reduction directed through the p-band center of boron on B_{SAC}@Mo₂C, *Mater. Adv.*, **2022**, 3, 592-598.
4. **Ashakiran Maibam**, Ravichandar Babarao and Sailaja Krishnamurty, Doped 2D VX₂ (X = S, Se, Te) monolayers as electrocatalysts for ammonia production: A DFT based study, *Applied Surface Science*, **2022**, 602, 154401.
5. **Ashakiran Maibam**, Sailaja Krishnamurty, Ravichandar Babarao, Electrocatalytic nitrogen reduction on defective graphene modulated from single atom catalyst to aluminium clusters, *Applied Surface Science*, **2023**, 623, 157024.

Other publications and manuscripts in preparation

6. Ambarish Singh, **Ashakiran Maibam**, Bharathkumar Javaregowda, Rajesh Bisht, Ashwath Kudlu, Sailaja Krishnamurthy, Kothandam Krishnamoorthy, Jayaraj Nithyanandhan, Unsymmetrical Squaraine Dyes for Dye-Sensitized Solar Cells: Position of Anchoring Group Controls the Orientation and Self-Assembly of Sensitizers on TiO₂ Surface and Modulate Its Flat Band Potential, *J. Phys. Chem. C*, **2020**, 124, 18436–18451.
7. **Ashakiran Maibam**, Sawan Kumar Das, Pragnya Paramita Samal and Sailaja Krishnamurthy, Enhanced photocatalytic properties of a chemically modified blue phosphorene, *RSC Advances*, **2021**, 11, 13348-13358.
8. **Ashakiran Maibam**, Debalina Chakraborty, Krati Joshi and Sailaja Krishnamurthy, Exploring edge functionalised blue phosphorene nanoribbons as novel photocatalysts for water splitting, *New J. Chem.*, **2021**, 45, 3570-3580.
9. Kayaramkodath Chandran Ranjeesh, Leena George, **Ashakiran Maibam**, Sailaja Krishnamurthy and Santhosh Babu Sukumaran, A Durable Metalloporphyrin 2D-Polymer for Photocatalytic Hydrogen and Oxygen Evolution from River and Sea Waters, *ChemCatChem*, **2021**, 7, 1717-1721.
10. Krati Joshi, **Ashakiran Maibam** and Sailaja Krishnamurthy, Finite Temperature Behavior of Carbon Atom Doped Silicon Clusters: Depressed Thermal Stabilities, Co-existing isomers, Reversible Dynamical Pathways and Fragmentation Channels, *New J. Chem.*, **2021**, 45, 8217-8227.
11. Anjumun Rasool, Insha Anis, Mudit Dixit, **Ashakiran Maibam**, Afshana Hassan, Sailaja Krishnamurthy and Manzoor Ahmad Dar, Tantalum based single, double, and triple atom catalysts supported on g-C₂N monolayer for effective nitrogen reduction reaction: a comparative DFT investigation, *Catal. Sci. Technol.*, **2022**, 12, 310-319.

12. Asma H. Maneri, Chandrodai Pratap Singh, Ravi Kumar, **Ashakiran Maibam** and Sailaja Krishnamurty, Mapping the Finite-Temperature Behavior of Conformations to Their Potential Energy Barriers: Case Studies on Si₆B and Si₅B Clusters, *ACS Omega* **2022**, 7, 7, 6167–6173.
13. Avinash P Jadhav, Ambarish Kumar Singh, **Ashakiran Maibam**, Sailaja Krishnamurty, Kothandam Krishnamoorthy, Jayaraj Nithyanandhan, D-A-D-based Unsymmetrical Thiosquaraine Dye for the Dye-Sensitized Solar Cells, *Photochemistry and Photobiology*, **2023**, 99, 529-537.
14. Thangjam Ibomcha Singh, **Ashakiran Maibam**, Dun Chan Cha, Sunghoon Yoo, Ravichandar Babarao, Sang Uck Lee and Seunghyun Lee, High-Alkaline Water-Splitting Activity of Mesoporous 3D Heterostructures: An Amorphous-Shell@Crystalline-Core Nano-Assembly of Co-Ni-Phosphate Ultrathin-Nanosheets and V-Doped Cobalt-Nitride Nanowires, *Advanced Science*, **2022**, 9, 2201311.
15. Apurva Patrike, Indrapal Karbhala, Kundan Wasnika, Arun Torris, **Ashakiran Maibam**, Sailaja Krishnamurty, Manjusha V. Shelke, High Rate, High Temperature, Dendrite Free Plating/Stripping of Li in 3-Dimensional Honeycomb Boron Carbon Nitride to Realize an Ultrastable Lithium Metal Anode, *Journal of Energy Storage*, **2023**, 68, 107547.
16. Dun Chan Cha, Thangjam Ibomcha Singh, **Ashakiran Maibam**, Tae Hyeong Kim, Dong Hwan Nam, Ravichandar Babarao, Seunghyun Lee, Metal-Organic Framework-Derived Mesoporous B-Doped CoO/Co@N-Doped Carbon Hybrid 3-D Heterostructured Interfaces with Modulated Cobalt Oxidation States for Alkaline Water Splitting, *Small*, **2023**, 2301405.
17. Pramila Patil, **Ashakiran Maibam**, Sushil S Sangale, Dilpreet Singh Mann, Hyun-Jung Lee, Sailaja Krishnamurty, Sung-Nam Kwon, Seok-In Na, Chemical Bridge-Mediated Heterojunction Electron Transport Layers Enable Efficient and Stable Perovskite Solar Cells, *ACS Appl. Mater. Interfaces*, **2023**, 15, 29597-29608.

18. Indrajeet Nawghare, Ambarish Kumar Singh, **Ashakiran Maibam**, Shivdeep Suresh Deshmukh, Sailaja Krishnamurty, Kothandam Krishnamoorthy and Jayaraj Nithyanandhan, Halogen Functionalized D-A-D Type Unsymmetrical Squaraine Dyes for Dye-Sensitized Solar Cells, *Mater. Adv.*, **2023**, 4, 3270-3284.
19. Asma Maneri, Shruti Suhas Varode, **Ashakiran Maibam**, Priyatosh Ranjan, Sailaja Krishnamurty, Krati Joshi, Quantum Dot (Au_n/Ag_n , $n= 3-8$) Capped Single Lipids: Interactions and Physicochemical Properties, *Phys. Chem. Chem. Phys.*, **2023**, 25, 22294-2230.
20. Manjinder Singh, Dun Chan Cha, Thangjam Ibomcha Singh, **Ashakiran Maibam**, Dasu Ram Paudel, Dong Hwan Nam, Tae Hyeong Kim, Sunghoon Yoo, Seunghyun Lee, A critical review on amorphous–crystalline heterostructured electrocatalysts for efficient water splitting, *Mater. Chem. Front.*, **2023**, 7, 6254-6280.
21. Indrajeet S. Nawghare, Ambarish Kumar Singh, **Ashakiran Maibam**, Sailaja Krishnamurty, Kothandam Krishnamoorthy, Jayaraj Nithyanandhan, Steric and Electronic Effect in Unsymmetrical Squaraine Dyes for Dye-Sensitized Solar Cells, *J. Phys. Chem. C* **2023**, 127, 46, 22473–22488.
22. Shafeeq Sarfudeen, Sruthi Vadamkall, **Ashakiran Maibam**, Sellappan Senthilkumar, Premchand Panda, Ravichandar Babarao, Tamas Panda, Robust Zeolitic Tetrazole Framework for Electrocatalytic Dopamine Detection with High Selectivity, *Inorg. Chem.* **2023**, Accepted manuscript.
<https://doi.org/10.1021/acs.inorgchem.3c03189>
23. **Ashakiran Maibam**, Ibrahim B. Orhan, Sailaja Krishnamurty, Salvy P Russo and Ravichandar Babarao, Surface electronic properties driven electrocatalytic nitrogen reduction on metal-conjugated porphyrin 2D-MOFs, (Submitted)

24. Ratul Paul, **Ashakiran Maibam**, Rupak Chatterjee, Triya Mukherjee, Nitumani Das, Masapogu Yellappa, Tanmay Banerjee, Asim Bhaumik, Ravichandar Babarao, S. Venkata Mohan, John Mondal, Two-Dimensional Covalent Organic Framework for Selective CO₂ Adsorption and Purification Biogas Mixture, (**Submitted**)

Abstract of Papers Presented at Conferences

1. **CSIR-National Chemical Laboratory Science Day** (Poster presentation)
(Receiver of Best Poster Award in Physical & Materials Chemistry Division)

Place: CSIR-National Chemical Laboratory, Pune, India - 411008

Date: 26-02-2020 to 28-02-2020

Dinitrogen Activation on Graphene Anchored Single Atom

Catalysts: A DFT study

Ashakiran Maibam,^{a,c} Thillai Govindaraja,^b Kaliaperumal Selvaraj,^{b,c} and Sailaja Krishnamurthy^{a,c*}

^aPhysical Chemistry Division, CSIR-National Chemical Laboratory, Pune 411008, India.

^bNano and Computational Materials Lab, Catalysis Division, CSIR-National Chemical Laboratory, Pune 411008, India.

^cAcademy of Scientific and Innovative Research, CSIR-Human Resource Development Centre (CSIR-HRDC) Campus, Postal Staff College area, Ghaziabad, 201 002, Uttar Pradesh, India.

Abstract

Research in catalysis has shifted towards Single Atom Catalysts (SACs) to overcome the growing cost of metals, by making each site available for the reaction while not compromising with the activity. Also, the issue of self-agglomeration in SACs can be easily avoided if the metal SACs are anchored on suitable two-dimensional (2D) materials. When metal Single Atom Catalysts (SACs) are anchored on a 2D material with delocalized electron density; the debate is whether the catalysis is driven by the metal, the surface or the system altogether. All the while, catalysis on a 2D material has generally been treated as a surface phenomenon under the conjecture that the

delocalized electron density is the driving force. To understand the contributing factors of catalysis on such systems, a case study of dinitrogen (N_2) activation on metal SACs anchored graphene has been made by employing periodic and finite models of graphene. The study highlights that different metal centres when coupled with 2D materials show varying catalytic nature, i.e., local activity or surface activity.

2. DAE Symposium on Current Trends in Theoretical Chemistry (Poster presentation - online)

(Receiver of Best Poster Presentation Award)

Place: Chemistry Division, Bhabha Atomic Research Center, Mumbai, India - 400085

Date: 23-09-2021 to 25-09-2021

Sustainable reduction of N_2 on metal SACs@graphene directed through computational studies

Ashakiran Maibam,^{a,b} and Sailaja Krishnamurty^{a,b*}

^aPhysical Chemistry Division, CSIR-National Chemical Laboratory, Pune 411008, India.

^bAcademy of Scientific and Innovative Research, CSIR-Human Resource Development Centre (CSIR-HRDC) Campus, Postal Staff College area, Ghaziabad, 201 002, Uttar Pradesh, India.

Abstract

Sustainable reduction of nitrogen to ammonia with minimal energy feed is achieved by assimilating the inherent electronic and reactive nature of Single Atom Catalysts (SACs) on heteroatom doped-graphene and tailoring SAC@graphene for N_2 reduction. A full-scale DFT study accounting for disparate descriptions of atomic orbitals and representation of support, has been carried out to identify the most active and recyclable SAC/B-graphene composite as catalyst for Nitrogen Reduction Reaction (NRR). Non-periodic DFT have been implemented to give the factual details of metal SACs and highlight their catalytic activity. The periodic paradigm gives a better understanding of the surface phenomena and the influence of delocalized electron density for catalysis. Accounting the pros and cons of both methodologies,

along with the implementation of Dual and Multiphilic descriptors, the reactivity pattern of six different metal SACs V, Fe, Ni, Ru, W and Re are derived on pristine and BN-pair doped graphene supports. Vanadium SAC, a relatively cheaper metal, anchored on BNring-graphene with an energy barrier of < 1.24 eV as a highly active and recyclable catalyst for NRR.

3. Theoretical Chemistry Symposium, TCS-2021 (Poster presentation - online)

(Receiver of PCCP Poster Prize)

Place: IISER Kolkata, West Bengal, India - 741246

Date: 11-12-2021 to 14-12-2021

Electrocatalytic nitrogen reduction reaction on active B@Mo₂C interface

Ashakiran Maibam,^{a,b} Manzoor Ahmad Dar,^c and Sailaja Krishnamurthy^{a,b,*}

^aPhysical Chemistry Division, CSIR-National Chemical Laboratory, Pune 411008, India.

^bAcademy of Scientific and Innovative Research, CSIR-Human Resource Development Centre (CSIR-HRDC) Campus, Postal Staff College area, Ghaziabad, 201 002, Uttar Pradesh, India.

^cDepartment of Chemistry, Islamic University of Science and Technology, Awantipora, Jammu and Kashmir 192122, India

Abstract

The electrocatalytic mode of nitrogen fixation is an attractive route to its efficiency and environment friendly nature. Abundant and metal-free boron atom catalysts anchored on pristine and defective Mo₂C based monolayers have been explored as electrocatalysts for nitrogen reduction reaction (NRR) through first principles simulations. Single boron atom catalysts on the defective Mo₂C monolayer with a Mo-atom vacancy (referred as B_{SAC}@Mo₂C-Mo_{vac}) was found to show a very high N₂ adsorption energy of -1.92 eV and significantly low overpotential of 0.41 eV for nitrogen reduction to NH₃ along the distal pathway. The low NRR overpotential on B_{SAC}@Mo₂C-Mo_{vac} can be accounted to less positively charged B-atom along with an exergonic adsorption of N₂. Further, for the first time a correlation between the B p-

band center in the $B_{SAC}@Mo_2C$ catalysts and the NRR catalytic efficiency is revealed by our calculations. This understanding provides new insights into the rational design of transition metal free centers like boron as future electrocatalysts for efficient ammonia production.

4. 3rd Commonwealth Chemistry Posters (Poster presentation - online)

Date: 28-09-2022 to 29-09-2022

Theoretical Investigation on 2D Materials for Ambient Nitrogen Fixation

Ashakiran Maibam,^{a,b,c} Ravichandar Babarao,^{b,d} and Sailaja Krishnamurthy^{a,c*}

^aPhysical Chemistry Division, CSIR-National Chemical Laboratory, Pune 411008, India.

^bSchool of Science, RMIT University, Melbourne 3001, Victoria, Australia

^cAcademy of Scientific and Innovative Research, CSIR-Human Resource Development Centre (CSIR-HRDC) Campus, Postal Staff College area, Ghaziabad, 201 002, Uttar Pradesh, India.

^dCSIRO, Normanby Road, Clayton 3168, Victoria, Australia

Abstract

Commercial ammonia production with the Bosch-Haber's process is highly energy-intensive with a carbon footprint. It is eminent that sustainable methods and materials for ammonia production need to be explored and computational tools can be implemented for catalyst design and establishing large scale ammonia synthesis from N_2 under mild conditions. Chemical insights from molecular orbitals of N_2 molecule has been adopted to design its activation and N-N bond can be activated by introducing electrons into the empty anti-bonding orbitals. In this context, two-dimensional (2D) materials can be exploited as electron reservoirs and the electrons can be tapped and directed to the anti-bonding orbital of N_2 through metallic or non-metallic single atom catalyst (SAC) or catalytic centres introduced as surface modifications on the 2D surface. DFT driven analysis on metal anchored graphene successfully showed N_2 activation and reduction with the utilization of each metal site, thereby reducing the

stress on depleting metal reserves. N-N bond activation and efficacy of N₂ chemisorption have been implemented as two crucial factors to scour the catalytic nature of the materials for nitrogen reduction. With a limiting potential of 1.24 eV for nitrogen reduction, the metal SAC anchored graphene has been found to be a recyclable catalyst capable of ammonia fixation under mild temperature and pressure. Electrocatalytic nitrogen reduction reaction (eNRR), being an environment friendly approach to ammonia fixation, the investigations on electrically conducting 2D materials coupled with non-metal catalytic centers or dopants led to efficient nitrogen reduction. These materials brought about ammonia fixation through an augmented electron transfer (i.e., donation) from the non-metal@2D material to N₂ molecule, which is then followed by back-donation from N₂. DFT study on non-metals anchored Mo₂C (MXenes) showed higher NRR performance when the non-metals are more electron rich. In particular, a lower limiting potential of 0.57 eV was found on boron anchored Mo₂C with surface modification on the 2D surface. Another computational study on vanadium dichalcogenides, an inexpensive material of high electrical conductivity with tunable magnetic properties, demonstrated high performance for electrocatalytic nitrogen fixation. Doping non-metals on the basal plane of vanadium dichalcogenides led to synergistic enhancement of nitrogen activation and reduction. 2H-VS₂@B has been reported with a record low overpotential of 0.06 eV with higher selectivity from reported vanadium dichalcogenides.

5. International Conference on Emerging Advanced Nanomaterials (Poster presentation)

Place: Newcastle Exhibition & Conference Center, Newcastle Australia, 2302

Date: 17-10-2022 to 21-10-2022

Synergic non-metal doping on vanadium dichalcogenides for dinitrogen fixation

Ashakiran Maibam,^{a,b,c} Ravichandar Babarao,^{b,d} and Sailaja Krishnamurty^{a,c*}

^aPhysical Chemistry Division, CSIR-National Chemical Laboratory, Pune 411008, India.

^bSchool of Science, RMIT University, Melbourne 3001, Victoria, Australia

^cAcademy of Scientific and Innovative Research, CSIR-Human Resource Development Centre (CSIR-HRDC) Campus, Postal Staff College area, Ghaziabad, 201 002, Uttar Pradesh, India.

^dCSIRO, Normanby Road, Clayton 3168, Victoria, Australia

Abstract

The prospect of nitrogen fixation under ambient conditions mandates the materialization of active, low cost, stable, earth-abundant and efficient hetero- and electro-catalysts. for artificial ammonia fixation. Computational study on vanadium dichalcogenides, an inexpensive material of high electrical conductivity with tunable magnetic properties, demonstrated high performance for electrocatalytic nitrogen fixation. Doping non-metals on the basal plane of vanadium dichalcogenides led to synergistic enhancement of nitrogen activation and reduction. The study highlights the cruciality of N-N bond activation and efficacy of N₂ chemisorption in tuning the electronic and catalytic nature of the materials. Detailed investigation on the nitrogen reduction mechanism brings out the pivotal role of thermodynamic favourability for product formation obtained from Gibbs free energy differences. The charge transfer on adsorbed N₂ and electron “donor–acceptor” mechanism between the catalytic center and N₂ has been found to modulate the electrocatalytic barrier for nitrogen fixation. 2H-VS₂@B has been reported with a record low overpotential of 0.06 eV with higher selectivity from reported vanadium dichalcogenides.

6. 19th Biennial Conference of the Australian and New Zealand Associations of von Humboldt Fellows (Oral presentation)

Place: Deakin University, Waterfront Campus, Geelong, Australia, 3220

Date: 18-11-2022 to 20-11-2022

7. R&D Topics 2022 (Oral presentation)

Place: RMIT University, Melbourne, Australia, 3000

Date: 4-12-2022 to 7-12-2022

Sustainable ammonia production on single site catalyst anchored 2D materials

Ashakiran Maibam,^{a,b,c} Ravichandar Babarao,^{b,d} and Sailaja Krishnamurty^{a,c*}

^aPhysical Chemistry Division, CSIR-National Chemical Laboratory, Pune 411008, India.

^bSchool of Science, RMIT University, Melbourne 3001, Victoria, Australia

^cAcademy of Scientific and Innovative Research, CSIR-HRDC Campus, Postal Staff College area, Ghaziabad, 201 002, Uttar Pradesh, India.

^dCSIRO, Normanby Road, Clayton 3168, Victoria, Australia

Abstract

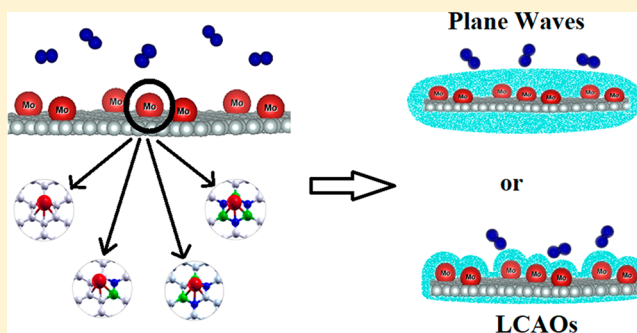
Sustainable large scale ammonia production from N₂ under mild conditions has been explored through catalyst design with computational tools. Two-dimensional (2D) materials are exploited as electron reservoirs which are directed to the anti-bonding orbital of N₂ through metallic or non-metallic single atom catalyst (SAC) or catalytic centres introduced as surface modifications. Density Functional Theory (DFT) study implemented with N-N bond activation and N₂ chemisorption as two crucial factors showed metal SAC anchored graphene to be a recyclable heterocatalyst capable of ammonia fixation under mild temperature and pressure with an energy barrier of 1.2 eV. Another environment friendly approach to ammonia fixation is the electrocatalytic nitrogen reduction reaction (eNRR), and investigations on electrically conducting 2D materials (Mo₂C and VX₂) coupled with non-metal catalytic centers or dopants has led to efficient nitrogen reduction. These materials brought about ammonia fixation through an augmented electron transfer (i.e., donation) from the non-metal@2D material, which is then followed by back-donation from N₂. Boron anchored Mo₂C (MXenes) showed high NRR performance with a lower limiting potential of 0.57 eV, while boron doped VX₂ demonstrated higher performance with a record low overpotential of 0.06 eV and selectivity from reported vanadium dichalcogenides. This research highlights the aspect of implementing earth abundant metals and non-metals on several 2D materials to develop an active, low cost, stable and efficient electrocatalyst for NRR via an exhaustive DFT study.

Dinitrogen Activation on Graphene Anchored Single Atom Catalysts: Local Site Activity or Surface Phenomena

Ashakiran Maibam,^{†,§} Thillai Govindaraja,[‡] Kaliaperumal Selvaraj,^{‡,§} and Sailaja Krishnamurty^{*,†,§}[†]Physical Chemistry Division, CSIR-National Chemical Laboratory, Pune 411 008, India[‡]Nano and Computational Materials Lab, Catalysis Division, CSIR-National Chemical Laboratory, Pune 411 008, India[§]Academy of Scientific and Innovative Research, CSIR-Human Resource Development Centre (CSIR-HRDC) Campus, Postal Staff College area, Gaziabad, 201 002 Uttar Pradesh, India

S Supporting Information

ABSTRACT: Catalysis on two-dimensional (2D) substrates with metal clusters or centers is generally dealt with as a surface phenomenon under the conjecture that the delocalized electron density is the driving force. When single atom catalysts (SACs) are anchored on such materials with delocalized electron density, for instance graphene, the stimulant for catalysis may be either the *d*-electrons on the metal or the system altogether. To understand the contributing factors of catalysis on such systems, a case study of dinitrogen (N_2) activation on Mo anchored graphene has been made by employing periodic and finite models of graphene. The periodic model represents a continuum of SACs anchored periodically on graphene, while the finite models are graphene nanoflakes of varying sizes and edge orientations. In addition to the physical aspects, such as size/finiteness of graphene, the influence of varying chemical compositions of the substrate on the activity is also evaluated by doping graphene with different B and N concentrations. This study, while clearly bringing out the connotation of regulating atomic composition of graphene substrate for dinitrogen activation, also surprisingly unveils the relative insignificance of varying the size and edge effects of the substrate. These features are highlighted through an analysis of red shift in the N–N stretching frequency, charge transfer to dinitrogen from the catalytic system, and structural and electronic characteristics of the catalytic system. The total and projected density of states plots reveal hybridization between the metal *d* orbitals and the *p* orbitals of carbon and nitrogen in the valence band. On the other hand, the frontier molecular orbital analysis also depicts a strong chemisorption of dinitrogen with the metal–graphene supports on account of direct hybridization between the *d* orbitals of the supported metal atom and the *p* orbitals of dinitrogen. The Bader and Löwdin charge distribution on the adsorbed dinitrogen in periodic and finite models shows the preeminence of local site over the surface activity.



INTRODUCTION

N_2 fixation and activation is essential for the sustenance of life. Although N_2 is the most abundant constituent in air, its fixation and activation is a highly endothermic process on account of its triple bond, thus making it a nearly inert gas. Up to this date, the most efficient chemical reduction of N_2 is through the well-known Haber-Bosch process which involves chemical transformation of N_2 to NH_3 using an iron oxide, Fe_3O_4 , catalyst in the presence of hydrogen under extremely harsh conditions of about 400 °C and 200 atm.¹ On the other hand, naturally occurring nitrogenase enzyme secreted by prokaryotic organisms found in the root nodules of plants complete this task under mild conditions without utilizing gaseous hydrogen.^{2–4} Research has shown that biological N_2 fixation occurs under ambient conditions and that the active sites are rich in Fe and S and, additionally, contain Mo or V atoms.^{5,6} However, the detailed mechanism of N_2 reduction by these enzymes remains elusive.⁶ As a consequence, finding an ambient catalyst for the N_2 reduction is a challenge for the

organometallic chemists. Intuitively, N_2 fixation and its dissociation require an efficient catalytic center coupled to an electron reservoir.

Metal clusters in the nano regime offer promise in this context on account of their quantum confinement of electrons. Few research works have explored the potential of simple inorganic metal clusters for N_2 activation using experimental and theoretical approaches.^{7–11} Notable among them is a work by Fielicke and co-workers,⁷ where N_2 activation on neutral Ru clusters is evaluated using infrared-multiphoton dissociation (IR-MPD). Other transition metal catalysts have also been reported, Ohki et al. in an experimental work showed Mo–Ti–S cluster elongates the N–N bond up to 1.294 Å, and the active site for the catalyst is titanium (Ti).⁸ In another work, Roy et al.⁹ have demonstrated dinitrogen activation on solid

Received: July 16, 2019

Revised: October 21, 2019

Published: October 28, 2019

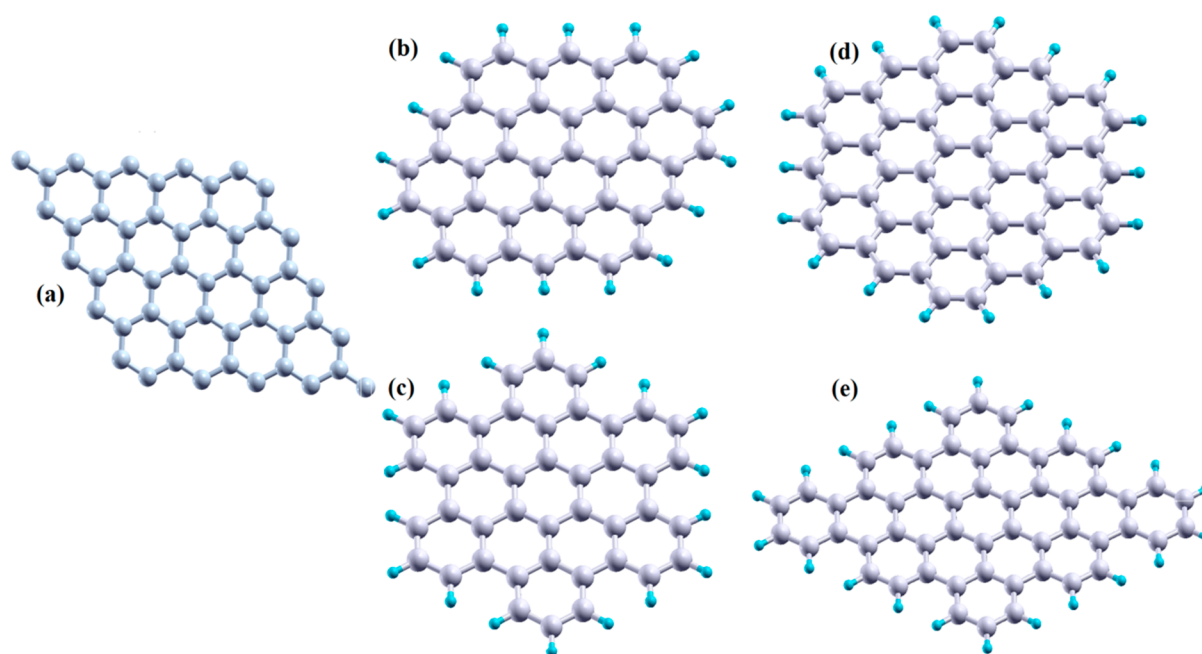


Figure 1. Graphene models considered in this study as supports to SAC: (a) A periodic graphene sheet with 50 atoms in a cell; (b) 42 atom graphene nanoflake with zigzag edges ($C_{42}\text{-zz}$); (c) 42 atom graphene nanoflake with armchair edges ($C_{42}\text{-ac}$); (d) 54 atom graphene nanoflake with zigzag edges ($C_{54}\text{-zz}$); (e) 54 atom graphene nanoflake with armchair edges ($C_{54}\text{-ac}$). Elemental color codes: gray, carbon (C); teal, hydrogen (H).

Li_n ($2 < n < 8$) clusters, with the N–N bond stretching frequency red-shifted up to 810 cm^{-1} . The work also demonstrated that even a small metal cluster, such as Li_8 , has the potential to split the N–N bond completely in an exothermic process. Among the metal clusters, Al clusters are the most notable ones that have been studied for N_2 activation. Jarrold and co-workers,¹⁰ using concerted experimental and theoretical methods, reported for the first time that Al clusters with 44 and 100 atoms lower the activation energy of the N_2 molecule by nearly 1 eV at high temperatures. In another work, the same group has demonstrated that the structure and size of the cluster have implications on the N_2 activation potential.¹¹ Studies on the reaction trajectories have demonstrated that high energy conformations of the Al clusters show a lower activation barrier toward dinitrogen.¹² However, the potential of the high energy conformations to be present at ambient conditions is relatively low. Thus, doping a ground state cluster is a more practical design of catalyst for N_2 activation. Along these lines, theoretical studies have shown that silicon- and phosphorus-doped aluminum clusters demonstrate increased activation as compared to their pristine ground-state counterparts.¹³

With the growing cost of the metals, exploring alternative catalysts such as metal-free or single-atom catalysts (SACs) is the need of the hour. Metal-free catalysts include frustrated Lewis pairs¹⁴ that form iminium complexes upon reaction with N_2 , polymeric carbon nitride electrocatalyst,¹⁵ and edges of 2D boron nitride (BN)¹⁶ surfaces. SACs anchored on suitable supports, on the other hand, considerably bring down the usage of metals by making each site available for the reaction while not compromising with the activity. In this context, there are several 2D materials that can be exploited as electron reservoirs when embedded with metal active centers. A well-crafted 2D material support with an active metal center has an enormous potential to adsorb the N_2 molecule and activate it.

2D material supports reported so far with a high N_2 fixation potential include graphene, Mo-doped BN nanosheet materials, BiOBr nanosheets, and boron anti-sites on BN nanotubes.^{17–20} Among them, graphene is an attractive one and has always been tapped as a support in reactions such as water splitting,²¹ hydrogen evolution reaction,²² and so on. Experimentally, few research groups have applied graphene-based materials as catalysts toward N_2 fixation.^{23,24}

In comparison to the experimental explorations, there are more theoretical works toward exploring the potential of graphene-based nanomaterials as catalysts/support materials for N_2 fixation. Using Density Functional Theory (DFT)-based methodologies, Le and co-workers demonstrated that doping graphene with Mo/N can lead to the successful dissociation of the N_2 molecule.²⁵ In another work, Li and co-workers reported an activation of the N_2 molecule up to nearly 2.5 \AA on FeN_3 -embedded graphene, wherein nitrogen atoms act as anchors, while iron is the active center.²⁶ Kumar et al. more recently have demonstrated the catalytic role of the BN-doped graphene substrate for N_2 activation on aluminum clusters.²⁷

Another interesting property of graphene is a higher reactivity when scissored to smaller sizes of the order of tens of nanometers (90 nm).^{28,29} On scissoring, the electronic as well as magnetic properties are seen to differ with respect to size and edge effect.^{30,31} Depending on the orientation of the edges, graphene nanoflakes can have two types of edges, namely, armchair and zigzag. A DFT study carried out by Nazrulla et al. on different graphene nanoflake sizes reported that, given a spin state and nanoflake size, the armchair isomer is more reactive than the zigzag isomer.³² An intensive study carried out by Yu et al. on graphene sheets to explore the reactive carbon edge responsible for oxygen reduction reaction (ORR) predicted the armchair edge to be more active than the zigzag edge.³³ Another work by Owens showed a gradual decrease in the band gap with the increase in chain length of

both armchair and zigzag graphene isomers.³⁴ Inherently, the zigzag isomers demonstrated a higher gap between the highest occupied molecular orbital (HOMO) and the lowest unoccupied molecular orbital (LUMO) in the case of nanoflakes with odd electrons with respect to the ones with an even number of electrons. In short, the band gap and, henceforth, reactivity would change upon tweaking the edge orientation, chain length, and number of electrons in these graphene nanoflakes. Further changes in the reactivity can be brought about by introducing defect sites and dopant atoms such as boron, nitrogen, sulfur, silicon, and so on.

In the above context, the present work explores the activity of a SAC, namely, Mo, anchored on pristine and doped (boron and nitrogen) graphene sheets as well as model nanoflakes toward dinitrogen (see Figure 1). Graphene sheets are periodic models defined using plane wave basis sets to incorporate the periodic nature. The use of plane wave (PW) basis sets offer a set of advantages, such as quicker convergence and avoiding basis set superposition error (BSSE); however, it comes with an approximation of treating core electrons implicitly. The plane wave basis sets also incorporate the concept of pseudopotentials toward the description of the atomic orbitals. The query is whether the periodic model that represents a delocalized electron density on the metal-anchored systems gives the correct picture of catalytic activity of the single (metals) atom catalyst. On the other hand, graphene nanoflakes are represented by finite models of 42 and 54 carbon atoms, as shown in Figure 1, and defined using linear combination of atomic orbitals (LCAOs). These nanoflakes can be synthesized by “cutting” extended sheets of graphene using lithography³⁵ and chemical etching³⁶ techniques. Two different edge orientations are possible in finite models, namely, zigzag and armchair. In the finite model, factors such as (a) edge effects, (b) size, and (c) dopant atoms (B and N) are taken into account; while in the periodic models, only the influence of boron and nitrogen dopants are considered as edge and size effects are irrelevant in the context of a periodic system (see Figure 1). The choice of B and N as dopant atoms stems from the fact that although several dopants in graphene have been reported and explored, boron and nitrogen remain the most attractive as they have similar atomic radii to carbon. Also, a B–N unit is isoelectronic to C–C unit and the planarity is conserved, leaving the delocalized electron cloud intact. Apart from that, methods to dope boron and nitrogen are diverse, ranging from solid phase³⁷ and chemical vapor deposition^{37,38} synthesis to plasma doping,³⁹ and are synthetically cost-effective.

■ NOMENCLATURE, METHODOLOGY, AND COMPUTATIONAL DETAILS

a. Nomenclature of the SACs Anchored Graphene Models. All the graphene models implemented in this study are shown in Figure 1. The periodic model is shown in Figure 1a. The chemical composition of this graphene substrate is varied by doping it with different number of B and N atoms (see Supporting Information, Figures S1–S5). Single atom catalyst, namely, Mo, is anchored on the pristine and doped counterparts of periodic graphene (see Supporting Information, Figure S1, for graphical representation of the structures and the nomenclature used for the periodic models). We would like to highlight that the metal center used in this study is inspired on account of its presence in the nitrogenase enzymes, namely, Mo. The dinitrogen molecule is adsorbed on

the SAC-anchored periodic graphene models discussed above, that is, the catalyst (see Supporting Information, Figures S1 and a2–d2).

The finite-sized graphene models are shown in Figure 1b–e. The smaller-sized graphene model we have considered in the present work is a graphene nanoflake with 42 carbon atoms. The two possible edge effects accounted for in this model are as seen in Figure 1b,c. This model is extended by incorporating 12 additional carbon atoms leading to a 54 atom graphene nanoflake, as shown in Figure 1d,e. Similar to the case of periodic system, the chemical composition of the nanoflakes with both the sizes and edges is modified using varying concentrations of B and N atoms. Mo is anchored on graphene nanoflakes followed by N₂ adsorption on these chemically and physically distinct models. The pictorial representation for the same and the nomenclature applied to these models are shown in Supporting Information, Figures S2–S5.

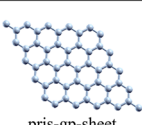
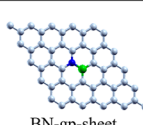
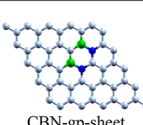
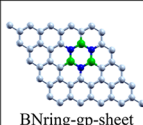
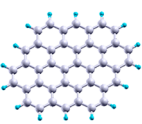
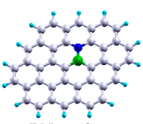
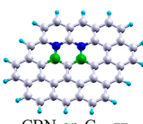
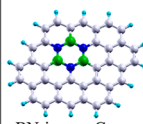
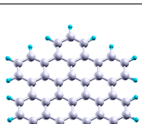
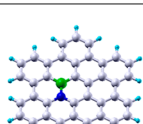
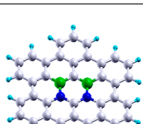
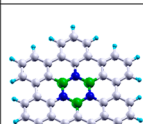
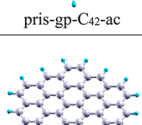
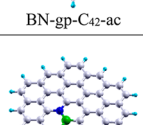
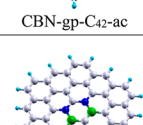
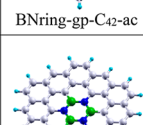
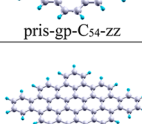
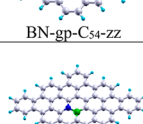
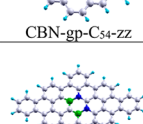
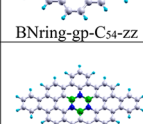
The finite and periodic graphene models made up of all carbons atoms is referred to as pristine graphene (**pris-gp**) by definition. The graphene sheet/nanoflakes with dopants are generated by replacing the carbon atoms with boron and nitrogen in such a way that a C–C bond is replaced by B–N bond. When one such replacement is made on the model it is referred to as **BN-gp** (see Supporting Information, Figures S1–S5, (b)); two C–C bonds are replaced by B–N bonds (leading to a C–B–N–C–B–N structure in a ring) it is referred to as **CBN-gp** (see Supporting Information, Figures S1–S5, (c)) and when all C–C bonds in a ring are replaced by B–N bonds so as to form a borazine ring it is referred to as **BNring-gp** model (see Supporting Information, Figures S1–S5, (d)).

The model name is suffixed after each system. For example, for periodic models, the names of pristine and doped substrates are referred to as pris-gp-sheet, BN-gp-sheet, CBN-gp-sheet, and BNring-gp-sheet. The SAC-anchored complexes of periodic models are referred to as pris-gp-sheet-Mo, BN-gp-sheet-Mo, CBN-gp-sheet-Mo and BNring-gp-sheet-Mo, respectively. Finally, the N₂ adsorbed complexes of the same are referred to as pris-gp-sheet–Mo–N₂, BN-gp-sheet–Mo–N₂, CBN-gp-sheet–Mo–N₂, and BNring-gp-sheet–Mo–N₂ respectively. The nomenclature is also highlighted in Supporting Information, Figure S1.

Along the same lines, the chemically distinct graphene nanoflake models for C₄₂ with zigzag edges are referred to as pris-gp-C₄₂-zz, BN-gp-C₄₂-zz, CBN-gp-C₄₂-zz, BNring-gp-C₄₂-zz, and so on (refer to Supporting Information, Figure S2). Their corresponding SAC anchored models are called as pris-gp-C₄₂-zz-Mo, BN-gp-C₄₂-zz-Mo, CBN-gp-C₄₂-zz-Mo, and BNring-gp-C₄₂-zz-Mo, respectively. Their N₂ adsorbed complexes are called as pris-gp-C₄₂-zz–Mo–N₂, BN-gp-C₄₂-zz–Mo–N₂, CBN-gp-C₄₂-zz–Mo–N₂, and BNring-gp-C₄₂-zz–Mo–N₂ respectively. Nomenclature of C₄₂ graphene nanoflakes with armchair edges and C₅₄ graphene nanoflakes with zigzag and armchair edges follow the same way and are given in the Supporting Information, Figures S2–S5. A brief description of model structures (scaled-down) along their nomenclature is as given in Table 1. They are named system-Mo (e.g., pris-gp-sheet-Mo) upon anchoring Mo and system–Mo–N₂ (e.g., pris-gp-sheet–Mo–N₂) when a particular system-Mo adsorbs dinitrogen.

b. Methodology and Computational Details. Earlier studies have demonstrated that the parallel mode shows higher N–N bond dissociation as compared to the vertical mode of

Table 1. Graphene Models Taken in This Study along with Their Nomenclature^a

 pris-gp-sheet	 BN-gp-sheet	 CBN-gp-sheet	 BNring-gp-sheet
 pris-gp-C42-zz	 BN-gp-C42-zz	 CBN-gp-C42-zz	 BNring-gp-C42-zz
 pris-gp-C42-ac	 BN-gp-C42-ac	 CBN-gp-C42-ac	 BNring-gp-C42-ac
 pris-gp-C54-zz	 BN-gp-C54-zz	 CBN-gp-C54-zz	 BNring-gp-C54-zz
 pris-gp-C54-ac	 BN-gp-C54-ac	 CBN-gp-C54-ac	 BNring-gp-C54-ac

^aElemental color codes: gray, carbon (C); teal, hydrogen (H); green, boron (B); blue, nitrogen (N).

dissociation.^{40,41} Hence, in this study we restrict to the parallel mode of N₂ adsorption on Mo. The adsorption energies of the N₂ molecule, adsorbed in a parallel mode on a Mo-anchored graphene system are calculated as follows:

$$E_{\text{ad}} = E(\text{system-Mo-N}_2) - E(\text{system-Mo}) - E(\text{N}_2)$$

where, $E(\text{system-Mo-N}_2)$ represents the energy of the N₂ molecule adsorbed on the catalytic systems. The $E(\text{N}_2)$ and $E(\text{system-Mo})$ represent the energies of the N₂ molecule and SAC-anchored graphene models, respectively.

The adsorption of Mo atom on the graphene models is also calculated to ensure that the proposed catalytic systems are energetically/thermodynamically stable. The adsorption energies of Mo on the various graphene models are calculated as follows:

$$E_{\text{ad}} = E(\text{system-Mo}) - E(\text{system})$$

where $E(\text{system-Mo})$ represents the energy of the SAC-anchored graphene models and $E(\text{system})$ represent the energy of the graphene models.

The periodic model, its SAC-anchored, BN-doped, and N₂-adsorbed counterparts are studied using Vienna Ab initio Simulation Package (VASP)⁴² software with PBE functional.⁴³ The projected augmented wave (PAW)⁴⁴ method is employed using an energy cutoff of 520 eV to describe plane wave basis set. The two-dimensional graphene sheets are simulated using periodic boundary conditions. To avoid the interactions between the different nearest neighboring layers, a vacuum space of 20 Å is created along the Z-direction. The 5 × 5 super cell with 50 atoms is used as graphene surface model, as shown in Figure 1a and the optimized C–C bond length in graphene sheet is 1.42 Å. The structural optimization of all geometries is carried out using the conjugate gradient method.⁴⁵ Brillouin zone is sampled by a (2 × 2 × 1) kpoint grid using the Monkhorst–Pack scheme.⁴⁶ For Density of State (DOS) calculation, the Monkhorst–Pack generated (9 × 9 × 1) set of k-point grid is used.

All the calculations on finite models (graphene nanoflake models with 42 atoms and 54 atoms) are performed using a linear combination of Gaussian-type orbitals within an auxiliary framework of DFT,⁴⁷ as implemented in the *deMon 5.0* program.⁴⁸ All structures are optimized using the Perdew–Burke–Ernzerhof (PBE) exchange and correlation functional.⁴³ Two different basis sets are used for describing the atomic orbitals of Mo in finite-sized models: (a) first case

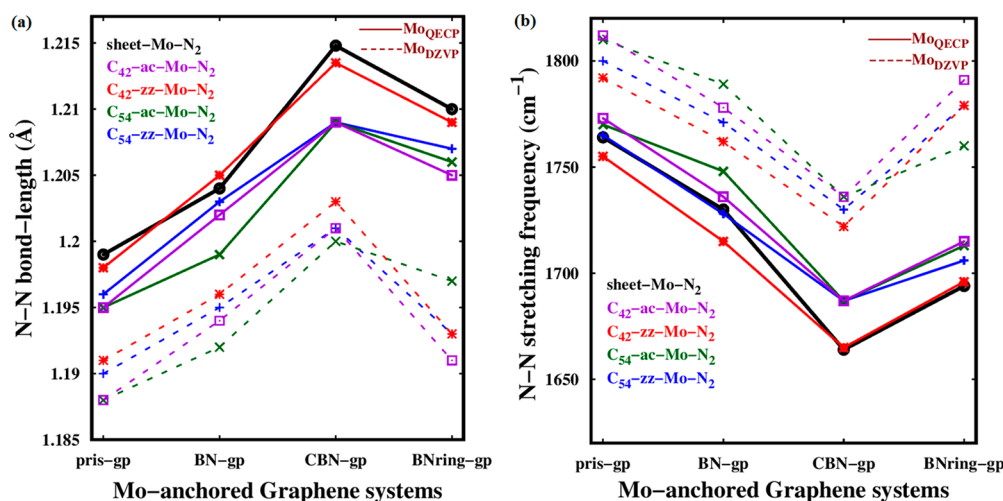


Figure 2. (a) N–N bond length in graphene model–Mo–N₂ complexes for varying chemical composition, as highlighted on the x-axis. The calculated N–N bond length in free dinitrogen is 1.12 Å. The solid black line refers to the N–N bond length noted for various chemically distinct periodic–Mo–N₂ complexes. The dotted lines refer to the case when Mo is treated using DZVP basis set in finite models (graphene nanoflakes) and solid lines refer to the case when Mo is treated with QECP basis set in finite models (graphene nanoflakes). (b) N–N stretching frequency in graphene model–Mo–N₂ complexes (calculated $\nu_{\text{N-N}}$ in free N₂ = 2326 cm⁻¹).

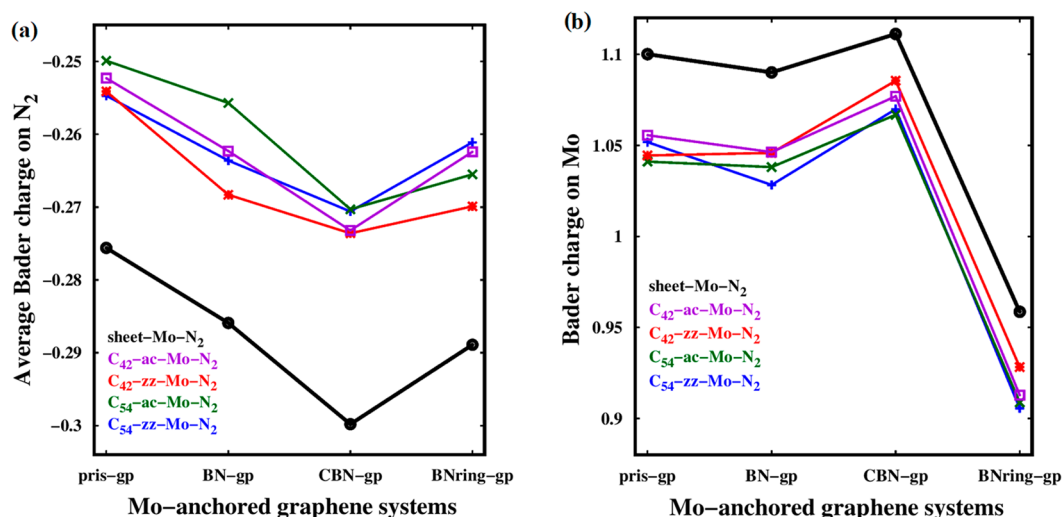


Figure 3. (a) Average of the Bader charges on the adsorbed N₂ molecule. (b) Bader charges on the Mo atom after N₂ adsorption.

where its atomic orbitals are described with DZVP basis set (as was the case for H, C, B, and N) and (b) second case where Los Alamos National Laboratory 2-double- ζ quasi-relativistic effective core potential (QECP)^{49,50} basis is used for Mo, while all other atoms were treated with a DZVP basis set. The charge density for all the cases is calculated by fitting the GEN-A2 auxiliary functions.⁵¹ Gradient and displacement criteria used for geometrical convergence is 5×10^{-4} a.u., while the SCF convergence criterion is set at 10^{-8} a.u.

All the atoms in periodic and finite graphene models considered in this work are relaxed at the lowest spin state (spin multiplicity = 1). It can also be noted that the singlet spin state of all the graphene nanoflakes correspond to the lowest electronic energy, thereby conforming to the ground state. On these relaxed graphene models, Mo atom is anchored and the entire geometry is relaxed. This is followed by the adsorption of N₂ and relaxing the dinitrogen adsorbed geometries at the lowest spin state. A restricted Kohn–Sham formalism is adopted for the optimization of all the above geometries. Following the optimization of all the structures discussed above, frequencies are calculated to ensure these optimized conformations correspond to local minima.

RESULTS AND DISCUSSIONS

The adsorption of dinitrogen molecule on all the periodic models is exothermic with the adsorption energies ranging between -1.70 and -1.87 eV (see Table S1 and Figure S6). The adsorption energies obtained when we use DZVP basis set for Mo range between -1.4 and -1.6 eV and somewhat higher than those obtained with QECP basis set for Mo. The adsorption of Mo on the graphene models is also exothermic with the adsorption energies ranging between -3 and -4 eV (see Table S2). The negative adsorption energies are indicative of the stability of the catalytic systems energetically. All the studied SAC-anchored graphene models have been found to be effective catalysts toward the activation of dinitrogen. This is understood from the fact that the N–N bond is elongated to 1.19 – 1.21 Å from its value of 1.12 Å in the free state on various systems. The N–N bond elongation on various SAC-anchored graphene models is plotted in Figure 2a, with CBN-gp-Mo models showing the maximum N–N bond activation. Most interestingly, both periodic and finite-sized models show

the same trend of N–N bond activation with respect to varying chemical composition. The second salient observation is that the difference in absolute numbers between the periodic and finite-sized models is negligible (amounting to only 1%) when Mo is treated using the QECP basis set. N–N bond elongation is also seen to be associated with interatomic distance between one of the N atoms (of dinitrogen) and the Mo metal anchored on the graphene model, as seen from the Supporting Information, Figure S7. Longer N–N bond elongation is correlated with the shorter Mo–N interatomic distance.

The increase in the N–N bond length is validated by both red shift in the N–N stretching frequency and the total amount of charge transferred to the dinitrogen. N–N stretching frequencies in various N₂-adsorbed SAC-anchored graphene models is given in Figure 2b. Inherently, the bond stretching frequencies of all the models is consistent with the trend of bond elongation and CBN-gp-Mo models show a red shift up to 1636 cm⁻¹, as compared to 2359 cm⁻¹ in free N₂. It is once again noted that the finite model calculation carried out with Mo-QECP basis set falls in trend to the periodic model, while the “all-electron” calculation using DZVP basis shows a slightly lower red shift. Change in the size of finite graphene nanoflakes and edge orientations does not show any significant impact on N–N bond elongation when compared to the periodic graphene model.

Charges on the Mo-anchored graphene models after N₂ adsorption are calculated, and a significant change in charge could be observed only on the adsorbed N₂ molecule and Mo atom. Thus, the charge redistribution is completely localized. Bader charges are calculated for all the periodic models and finite models, where Mo is treated with a DZVP basis set. Since Bader charges are not well-defined with metal Electron Core Potentials, for the finite models where Mo has been treated with QECP basis set, Löwdin⁵² charges are calculated. The average Bader charges on N₂ and Bader charges on Mo after dinitrogen adsorption is plotted in Figure 3a,b; the corresponding plots of the Löwdin charges are provided in the Supporting Information, Figures S8a,b. The Bader charges on CBN-gp-Mo models are most negative and reflect a higher charge transfer from the catalyst to dinitrogen in both periodic as well as finite models. The elongation of N–N bond is favored when electrons are transferred to the N– π^* orbital, in short, a larger electron gain on N atom is essential for bond

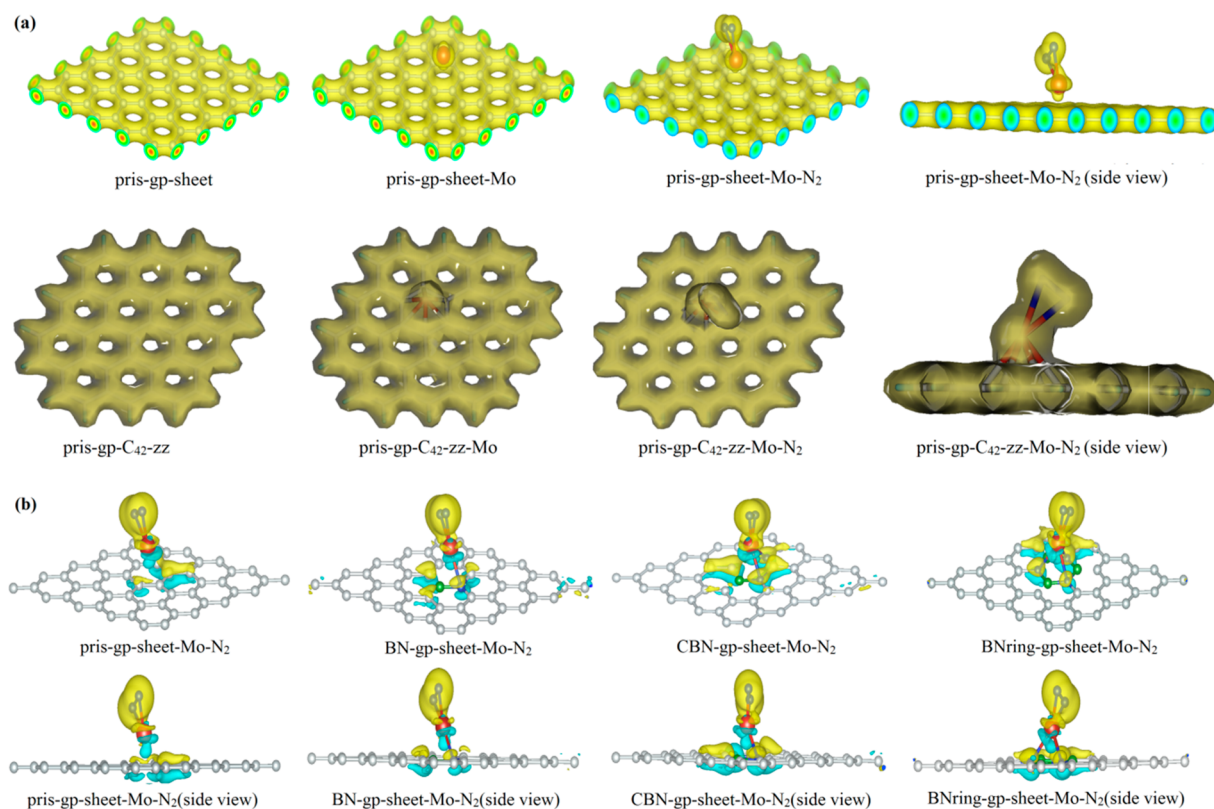


Figure 4. (a) Total charge density plots for the periodic pris-gp-sheet and finite pris-gp-C₄₂-zz models, their Mo-anchored geometries and N₂ adsorbed pris-gp-Mo geometries. (b) Charge difference density plots of the Mo-anchored periodic models with and without N₂. Density plots are made at an isosurface value of 0.06eÅ⁻³.

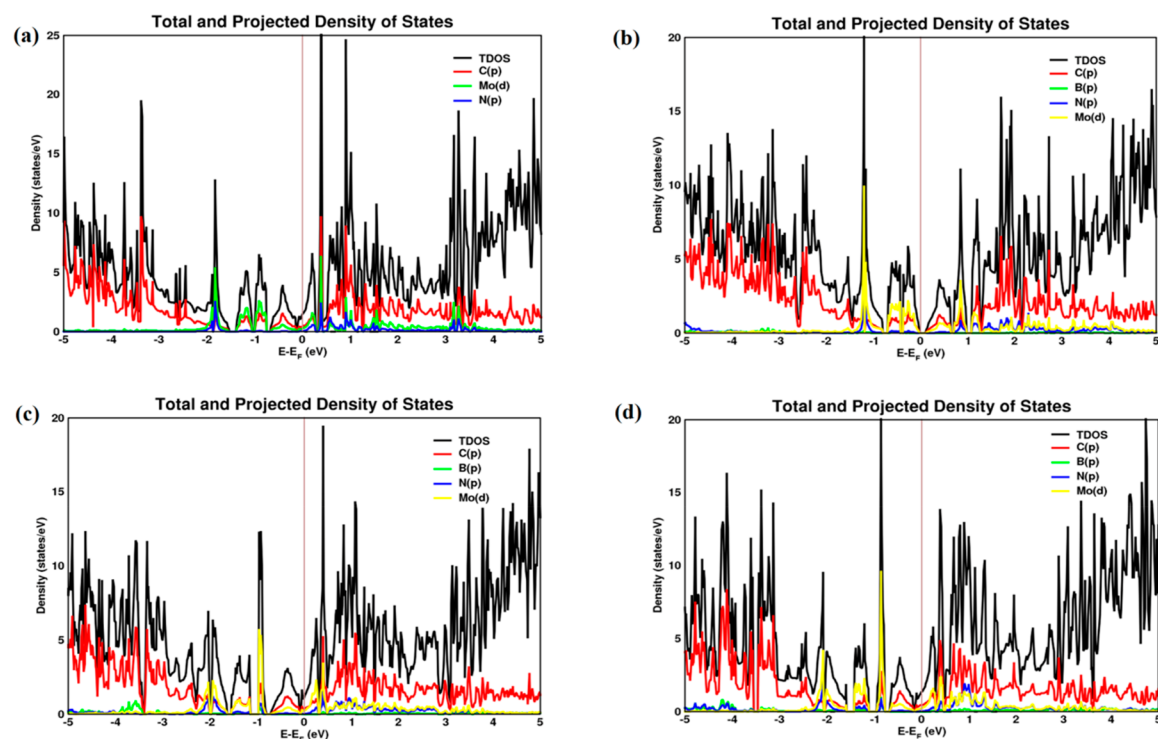


Figure 5. Total density of states (TDOS) and projected density of states (PDOS) plots of (a) pris-gp-sheet-Mo-N₂, (b) BN-gp-sheet-Mo-N₂, (c) CBN-gp-sheet-Mo-N₂, and (d) BNring-gp-sheet-Mo-N₂.

dissociation. The charges accumulated on the N atoms, as shown in Figure 3a, correspond to the extent of N–N bond

elongation in various studied systems. The charge on Mo metal follow reverse trend of the charges gained by the N₂, indicative

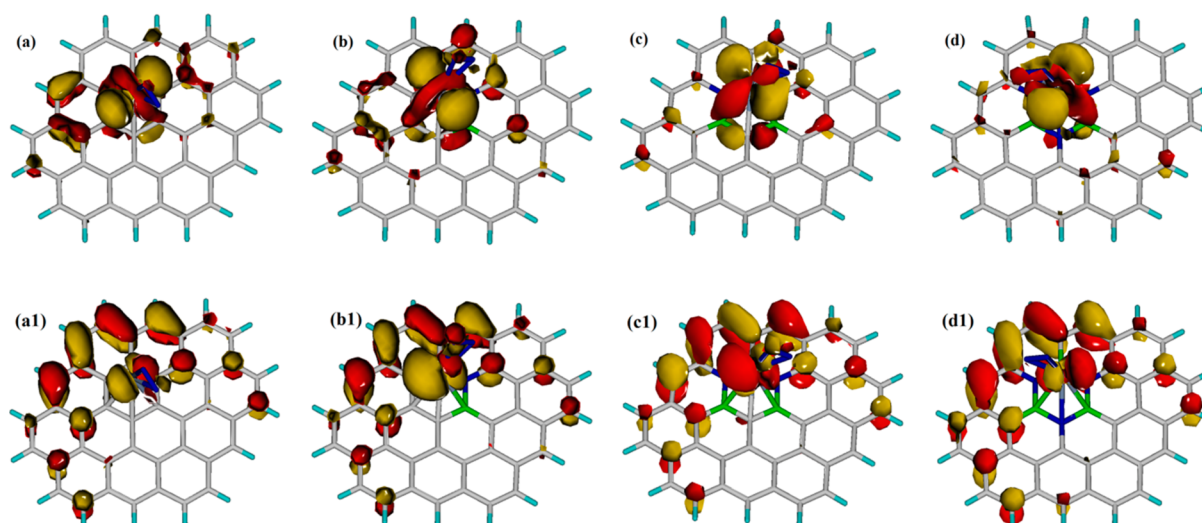


Figure 6. HOMOs of (a) pris-gp- C_{42} -zz-Mo- N_2 , (b) BN-gp- C_{42} -zz-Mo- N_2 , (c) CBN-gp- C_{42} -zz-Mo- N_2 , (d) BNring-gp- C_{42} -zz-Mo- N_2 . LUMOs of (a1) pris-gp- C_{42} -zz-Mo- N_2 , (b1) BN-gp- C_{42} -zz-Mo- N_2 , (c1) CBN-gp- C_{42} -zz-Mo- N_2 , and (d1) BNring-gp- C_{42} -zz-Mo- N_2 .

of the fact that the charge transfer is primarily from Mo. The same pattern could be seen from the Löwdin charges on N_2 and Mo. This is further validated in the electronic structure analysis discussed in the next paragraph.

We next come to the underlying electronic factors that are responsible for the activation of dinitrogen on various SAC anchored graphene models. The total charge density plots of periodic and finite models made at an isosurface value of $0.06 \text{ e}\text{\AA}^{-3}$ show a delocalized electron density over the dinitrogen adsorbed SAC anchored graphene models (Figure 4a). The electron density plot with Mo-QECP basis set is not shown as it is similar to the all electron calculation from DZVP basis set. The charge density difference plots of the Mo-anchored periodic models with and without N_2 show an exclusive overlap of the electron density on Mo with that of N_2 , as shown in Figure 4b. However, the electron density from the graphene substrate, in particular, the C, B, and N atoms in the local environment around Mo could not interact with the electron density of N_2 . Rather, these surrounding atoms interact with Mo metal and indirectly influence the interaction of Mo with N_2 . Since the catalytic activity of these SAC-anchored graphene models is governed by the metal atom and the local environment of the catalytic metal center, it is a local site activity and not a surface phenomenon. To understand the mechanism of catalysis, the electronic nature around the Fermi level in the periodic models and the Frontier Molecular Orbitals of the finite models are investigated.

The total density of states (TDOS) and projected density of states (PDOS) of N_2 adsorbed graphene systems, as shown in Figure 5, shows nearly zero density at the Fermi level (E_F) and a nonzero density around E_F inferring the semimetallic nature of pristine graphene. The conduction band near E_F has a larger density of Mo d -orbital, this region would correspond to the Highest Occupied Molecular Orbital (HOMO); while a d - p hybridized orbital in the valence band will correspond to the Lowest Unoccupied Molecular Orbital (LUMO). The Frontier Molecular Orbital (FMO) picture of the finite C_{42} -zz-Mo- N_2 models (Figure 6) corresponds to the orbital composition of HOMO and LUMO as interpreted from the PDOS plot. The FMO pictures of the finite models remain the same even when Mo-QECP basis has been used. Also, the HOMO-LUMO

energy gap of the finite gp-Mo- N_2 systems (Mo_{DZVP} and Mo_{QECP} basis set) lies within 1.0 and 2.0 eV; this also happens to be the $E-E_F$ value of the closest conduction-valence gap in the PDOS plot. The HOMO-LUMO gaps of the finite gp-Mo- N_2 models, in eV, are given in Supporting Information, Figure S9.

CONCLUSIONS

In this work, single atom catalysts (SACs) on graphene supports have been explored as a catalytic system for dinitrogen activation. While metal clusters of 4–20 atoms have been reported to show excellent N–N bond dissociation, the challenge has always been to synthesize the metal cluster. It is easier to absorb a single atom on a stable framework and this idea has been exploited in this work by utilizing graphene as the framework to hold the metal atom which will act as the catalytic centers. Also, size and edge orientation of graphene have been reported to affect its activity, therefore the size and edge orientations are taken into account by taking graphene nanoflakes of two different sizes and the periodic model which inherently assumes the graphene nanoflake is repeated infinitely in all directions.

The critical findings obtained from this extensive study of investigating periodic and finite graphene models as catalyst for dinitrogen activation are the following:

- This study shows that all Mo-anchored graphene models are good catalysts for dinitrogen activation with a potential for designing them experimentally. In particular, a better catalytic activity is seen in the case of CBN-gp-Mo models.
- It has also been observed that the role of dopants is far more influential in dinitrogen activation as compared to graphene surface orientation in both periodic and finite models.
- Interestingly, the extent of bond elongation in the periodic model has also been found to be nearly similar to that in finite models where Mo is treated with QECP basis set. In spite of different molecular orbital treatments in periodic and finite models, the similar activity trend that we have obtained is because of the local activity of the catalytic centers.

The finite models can give factual details of clusters and highlight which atoms are the catalytic centers. The periodic models give a better understanding of the surface phenomena and the influence of delocalized electron density for catalysis; however, it comes with its own complexity of implementing several approximations and intensive calculation. This work proposes that, for SAC-anchored graphene, since the catalytic center is the metal atom and the catalysis is driven by the local environment around the metal center, finite model calculations are as reliable as periodic model calculations.

■ ASSOCIATED CONTENT

Supporting Information

The Supporting Information is available free of charge on the ACS Publications website at DOI: 10.1021/acs.jpcc.9b06757.

Demonstration of all graphene models (periodic sheets and finite nanoflakes of different sizes and edges) with various chemical compositions, their Mo-anchored structures and N₂-adsorbed orientations, adsorption energies of N₂ and Mo in eV, Löwdin charges on adsorbed N₂ and Mo metal, HOMO–LUMO gap of finite graphene models, and Cartesian coordinates of periodic and C₄₂-zz models (PDF)

■ AUTHOR INFORMATION

Corresponding Author

*E-mail: k.sailaja@ncl.res.in; sailaja.raaj@gmail.com.

ORCID

Ashakiran Maibam: 0000-0003-0168-5374

Kaliaperumal Selvaraj: 0000-0002-9996-8112

Sailaja Krishnamurty: 0000-0001-5090-1892

Notes

The authors declare no competing financial interest.

■ ACKNOWLEDGMENTS

A.M. acknowledges CSIR for funding of the JRF (Junior Research Fellowship). T.G. acknowledges DST-SERB for funding of the NPDF (National Post-Doctoral Fellowship). K.S. acknowledges the funding from CSIR-FTT Project, MLP034026. S.K. acknowledges the Centre of Excellence in Scientific Computing (CoESC) at CSIR-NCL Pune and CSIR fourth Paradigm Institute, Bangalore, for providing access to their High-Performance Computing Facility.

■ REFERENCES

- (1) Fryzuk, M. D.; Johnson, S. A. The continuing story of dinitrogen activation. *Coord. Chem. Rev.* **2000**, *200*, 379–409.
- (2) Kim, J.; Rees, D. C. Structural models for the metal centers in the nitrogenase molybdenum iron protein. *Science* **1992**, *257*, 1677–1682.
- (3) Einsle, O.; Tezcan, F. A.; Andrade, S. L. A.; Schmid, B.; Yoshida, M.; Howard, J. B.; Rees, D. C. Nitrogenase MoFe-protein at 1.16 Å resolution: A central ligand in the FeMo-cofactor. *Science* **2002**, *297*, 1696–1700.
- (4) Sellmann, D.; Sutter, J. In quest of competitive catalysts for nitrogenases and other metal sulfur enzymes. *Acc. Chem. Res.* **1997**, *30*, 460–469.
- (5) Dance, I. G. The chemical mechanism of nitrogenase: calculated details of the intramolecular mechanism for hydrogenation of η_2 -N₂ on FeMo-Co to NH₃. *Dalton Transactions* **2008**, No. 43, S977–S991.
- (6) Boyd, E. S.; Hamilton, T. L.; Peters, J. W. An alternative path for the evolution of biological nitrogen fixation. *Front. Microbiol.* **2011**, *2*, 1–15.
- (7) Kerpel, C.; Harding, D. J.; Lyon, J. T.; Meijer, G.; Fielicke, A. N₂ activation by neutral ruthenium clusters. *J. Phys. Chem. C* **2013**, *117*, 12153–12158.
- (8) Ohki, Y.; Uchida, K.; Tada, M.; Cramer, R. E.; Ogura, T.; Ohta, T. N₂ activation on molybdenum-titanium-sulfur cluster. *Nat. Commun.* **2018**, *9*, 1–6.
- (9) Roy, D.; Navarro-Vazquez, A.; Schleyer, P. V. R. Modeling dinitrogen activation by lithium: A mechanistic investigation of the cleavage of N₂ by stepwise insertion into small lithium clusters. *J. Am. Chem. Soc.* **2009**, *131*, 13045–13053.
- (10) Cao, B.; Starace, A. K.; Judd, O. H.; Bhattacharyya, I.; Jarrold, M. F.; Lopez, J. M.; Aguado, A. Activation of dinitrogen by solid and liquid aluminium nanoclusters: A combined experimental and theoretical study. *J. Am. Chem. Soc.* **2010**, *132*, 12906–12918.
- (11) Cao, B.; Starace, A. K.; Judd, O. H.; Bhattacharyya, I.; Jarrold, M. F. J. Metal clusters with hidden ground states: melting and structural transitions in Al₁₁⁵⁺, Al₁₁⁶⁺, and Al₁₁⁷⁺. *J. Chem. Phys.* **2009**, *131*, 1–6.
- (12) Kulkarni, B. S.; Krishnamurty, S.; Pal, S. Size and shape sensitivity behaviour of Al_n (n = 2–5, 13, 30, and 100) clusters toward the N₂ molecule: a first-principle investigation. *J. Phys. Chem. C* **2011**, *115*, 14615–14623.
- (13) Das, S.; Pal, S.; Krishnamurty, S. Dinitrogen activation by silicon and phosphorus doped aluminum clusters. *J. Phys. Chem. C* **2014**, *118*, 19869–19878.
- (14) Melen, R. L. A step closer to metal-free dinitrogen activation: A new chapter in the chemistry of frustrated lewis pairs. *Angew. Chem., Int. Ed.* **2018**, *57*, 880–882.
- (15) Lv, C.; Qian, Y.; Yan, C.; Ding, Y.; Liu, Y.; Chen, Y.; Yu, G. Defect engineering metal-free polymeric carbon nitride electrocatalyst for effective nitrogen fixation under ambient conditions. *Angew. Chem., Int. Ed.* **2018**, *57*, 10246–10250.
- (16) Mao, X.; Zhou, S.; Yan, C.; Zhu, Z.; Du, A. A single boron atom doped boron nitride edge as a metal-free catalyst for N₂ fixation. *Phys. Chem. Chem. Phys.* **2019**, *21*, 1110–1116.
- (17) Zhao, J.; Chen, Z. Single Mo atom supported on defective boron nitride monolayer as an efficient electrocatalyst for nitrogen fixation: a computational study. *J. Am. Chem. Soc.* **2017**, *139*, 12480–12487.
- (18) Li, H.; Shang, J.; Ai, Z.; Zhang, L. Efficient visible light nitrogen fixation with BiOBr nanosheets of oxygen vacancies on the exposed {001} facets. *J. Am. Chem. Soc.* **2015**, *137*, 6393–6399.
- (19) Kumar, C. V. S.; Subramanian, V. Can boron antisites of BBTs be an efficient metal-free catalyst for nitrogen fixation? - a DFT investigation. *Phys. Chem. Chem. Phys.* **2017**, *19*, 15377–15387.
- (20) Legare, M.-A.; Belanger-Chabot, G.; Dewhurst, R. D.; Welz, E.; Krummenacher, I.; Engels, B.; Braunschweig, H. Nitrogen fixation and reduction at boron. *Science* **2018**, *359*, 896–900.
- (21) Guo, X.; Liu, S.; Huang, S. Single Ru atom supported on defective graphene for water splitting: DFT and microkinetic investigation. *Int. J. Hydrogen Energy* **2018**, *43*, 4880–4892.
- (22) Ouyang, Y.; Li, Q.; Shi, S.; Ling, C.; Wang, J. Molybdenum sulfide clusters immobilized on defective graphene: a stable catalyst for the hydrogen evolution reaction. *J. Mater. Chem. A* **2018**, *6*, 2289–2294.
- (23) Jeon, I. Y.; Choi, H. J.; Ju, M. J.; Choi, I. T.; Lim, K.; Ko, J.; Kim, H. K.; Kim, J. C.; Lee, J.-J.; Shin, D.; et al. Direct nitrogen fixation at the edges of graphene nanoplatelets as efficient electrocatalysts for energy conversion. *Sci. Rep.* **2013**, *3*, 1–7.
- (24) Lu, Y.; Yang, Y.; Zhang, T.; Ge, Z.; Chang, H.; Xiao, P.; Xie, Y.; Hua, L.; Li, Q.; Li, H.; et al. Photoprompted hot electrons from bulk cross-linked graphene materials and their efficient catalysis for atmospheric ammonia synthesis. *ACS Nano* **2016**, *10*, 10507–10515.
- (25) Le, N.Y.-Q.; Gu, J.; Tian, W. Q. Nitrogen fixation catalyst based on graphene: every part counts. *Chem. Commun.* **2014**, *50*, 13319–13322.
- (26) Li, X.-F.; Li, Q.-K.; Cheng, J.; Liu, L.; Yan, Q.; Wu, Y.; Zhang, X.-H.; Wang, Z.-Y.; Qiu, Q.; Luo, Y. Conversion of dinitrogen to

ammonia by FeN₃-embedded graphene. *J. Am. Chem. Soc.* **2016**, *138*, 8706–8709.

(27) Kumar, D.; Pal, S.; Krishnamurty, S. N₂ activation on Al metal clusters: catalyzing role of BN-doped graphene support. *Phys. Chem. Chem. Phys.* **2016**, *18*, 27721–27727.

(28) Sharma, R.; Baik, J. H.; Perera, C. J.; Strano, M. S. Anomalous large reactivity of single graphene layers and edges towards electron transfer chemistries. *Nano Lett.* **2010**, *10*, 398–405.

(29) Son, Y. W.; Cohen, M. L.; Louie, S. G. Half-metallic graphene nanoribbons. *Nature* **2006**, *444*, 347–349.

(30) Son, Y. W.; Cohen, M. L.; Louie, S. G. Energy gaps in graphene nanoribbons. *Phys. Rev. Lett.* **2006**, *97*, 1–4.

(31) Hu, W.; Lin, L.; Yang, C.; Yang, J. Electronic structure and aromaticity of large-scale hexagonal graphene nanoflakes. *J. Chem. Phys.* **2014**, *141*, 1–10.

(32) Nazrulla, M. A.; Krishnamurty, S.; Phani, K. L. N. Discerning site selectivity on graphene nanoflakes using conceptual density functional theory based reactivity descriptors. *J. Phys. Chem. C* **2014**, *118*, 23058–23069.

(33) Ly, Q.; Merinov, B. V.; Xiao, H.; Goddard, W. A.; Yu, T. H. The oxygen reduction reaction on graphene from quantum mechanics: comparing armchair and zigzag carbon edges. *J. Phys. Chem. C* **2017**, *121*, 24408–24417.

(34) Owens, F. J. Electronic and magnetic properties of armchair and zigzag graphene nanoribbons. *J. Chem. Phys.* **2008**, *128*, 1–4.

(35) Berger, C.; Song, Z.; Li, X.; Wu, X.; Brown, N.; Naud, C.; Mayou, D.; Li, T.; Hass, J.; Marchenkov, A. N.; et al. Electronic confinement and coherence in patterned epitaxial graphene. *Science* **2006**, *312*, 1191–1196.

(36) Li, X.; Wang, X.; Zhang, L.; Lee, S.; Dai, H. Chemically derived, ultrasmooth graphene nanoribbon semiconductors. *Science* **2008**, *319*, 1229–1232.

(37) Agnoli, S.; Favaro, M. Doping graphene with boron: a review of synthesis methods, physicochemical characterization, and emerging applications. *J. Mater. Chem. A* **2016**, *4*, 5002–5025.

(38) Bepete, G.; Voiry, D.; Chhowalla, M.; Chiguvare, Z.; Coville, N. J. Incorporation of small BN domains in graphene during CVD using methane, boric acid and nitrogen gas. *Nanoscale* **2013**, *5*, 6552–6557.

(39) Xu, J.; Jang, S. K.; Lee, J.; Song, Y. J.; Lee, S. The preparation of BN-doped atomic layer graphene via plasma treatment and thermal annealing. *J. Phys. Chem. C* **2014**, *118*, 22268–22273.

(40) Kumar, D.; Krishnamurty, S.; Pal, S. Dissociative adsorption of molecular hydrogen on BN-doped graphene-supported aluminum clusters. *J. Phys. Chem. C* **2017**, *121*, 26493–26498.

(41) Kumar, D.; Govindaraja, T.; Krishnamurty, S.; Kaliaperumal, S.; Pal, S. Dissociative chemisorption of hydrogen molecules on defective graphene-supported aluminium clusters: A computational study. *Phys. Chem. Chem. Phys.* **2018**, *20*, 26506–26512.

(42) Kresse, G.; Furthmüller, J. Efficiency of *ab-initio* total energy calculations for metals and semiconductors using a plane-wave basis set. *Comput. Mater. Sci.* **1996**, *6*, 15–50.

(43) Perdew, J. P.; Burke, K.; Ernzerhof, M. Generalized gradient approximation made simple. *Phys. Rev. Lett.* **1996**, *77*, 3865–3868.

(44) Blochl, P. E. Projector augmented-wave method. *Phys. Rev. B: Condens. Matter Mater. Phys.* **1994**, *50*, 17953–17979.

(45) Payne, M. C.; Teter, M. P.; Allan, D. C.; Arias, T. A.; Joannopoulos, J. D. Iterative minimization techniques for *ab initio* total-energy calculations: molecular dynamics and conjugate gradients. *Rev. Mod. Phys.* **1992**, *64*, 1045–1097.

(46) Monkhorst, H. J.; Pack, J. D. Special points for Brillouin-zone integrations. *Phys. Rev. B* **1976**, *13*, 5188–5192.

(47) Koster, A. M.; Reveles, J. U.; del Campo, J. M. Calculation of exchange-correlation potentials with auxiliary function densities. *J. Chem. Phys.* **2004**, *121*, 3417–3424.

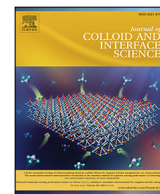
(48) Koster, A. M.; Calaminici, P.; Casida, M. E.; Moreno, R. F.; Geudtner, G.; Goursot, A.; Heine, T.; Ipatov, A.; Janetzko, F.; del Campo, J. M.; et al. *deMon 5.0*; deMon Developers, 2006.

(49) Feller, D. J. The role of databases in support of computational chemistry calculations. *J. Comput. Chem.* **1996**, *17*, 1571–1586.

(50) Schuchardt, K. L.; Didier, B. T.; Elsethagen, T.; Sun, L.; Gurumoorhi, V.; Chase, J.; Li, J.; Windus, T. L. Basis set exchange: a community database for computational sciences. *J. Chem. Inf. Model.* **2007**, *47*, 1045–1052.

(51) Calaminici, P.; Janetzko, F.; Koster, A. M.; Mejia-Olvera, R.; Zuniga-Gutierrez, B. Assessment of density functional theory optimized basis sets for gradient corrected functionals to transition metal systems: the case of small Ni_n (n ≤ 5) clusters. *J. Chem. Phys.* **2007**, *126*, 1–10.

(52) Löwdin, P. O. On the non-orthogonality problem connected with the use of atomic wave functions in the theory of molecules and crystals. *J. Chem. Phys.* **1950**, *18*, 365–375.



Regular Article

Nitrogen activation to reduction on a recyclable V-SAC/BN-graphene heterocatalyst sifted through dual and multiphilic descriptors

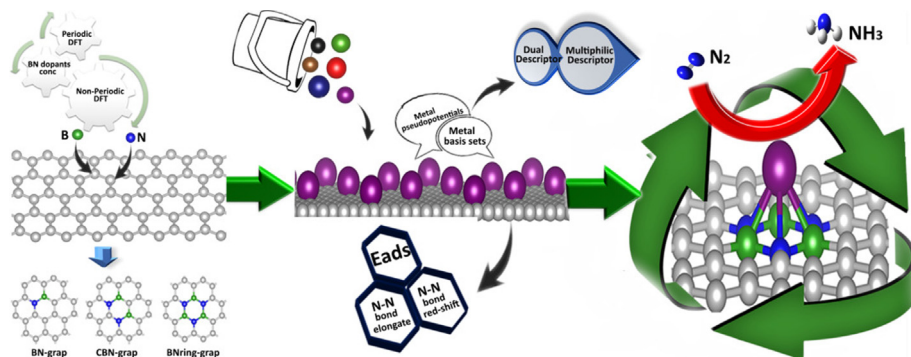
Ashakiran Maibam, Sailaja Krishnamurthy*



Physical and Materials Division, CSIR-National Chemical Laboratory, Pune 411 008, India

Academy of Scientific and Innovative Research, CSIR-Human Resource Development Centre (CSIR-HRDC) Campus, Postal Staff College area, Gaziabad 201 002, Uttar Pradesh, India

GRAPHICAL ABSTRACT



ARTICLE INFO

Article history:

Received 9 March 2021

Revised 6 May 2021

Accepted 6 May 2021

Available online 11 May 2021

Keywords:

SACs
Dual descriptor
Multiphilic descriptor
Dinitrogen activation
Frequency red-shift
PDOS
Reaction mechanism

ABSTRACT

Efficient reduction of nitrogen to ammonia at a minimal cost would require a rechner catalyst tailored by assimilating the inherent electronic and reactive nature of Single Atom Catalysts (SACs) on heteroatom doped-graphene. A full-scale DFT study accounting for disparate descriptions of atomic orbitals and representation of support, has been carried out to identify the most active and recyclable SAC/BN-graphene composite as catalyst for Nitrogen Reduction Reaction (NRR). Dual and Multiphilic descriptors derived reactivity pattern of six different metal SACs V, Fe, Ni, Ru, W and Re on periodic and non-periodic paradigms of pristine and BN-pair doped graphene supports, align with the calculated chemisorption efficacy and activation of N_2 . The enzymatic route of nitrogen reduction on three most ideal metal SACs (V, W and Re) culminates Vanadium SAC, a relatively cheaper metal, anchored on BNring-graphene with an energy barrier of ≤ 1.24 eV as a highly active and recyclable catalyst for NRR.

© 2021 Elsevier Inc. All rights reserved.

1. Introduction

Ammonia (NH_3), the most stable basic hydride formed by hydrogen and nitrogen is not only an essential precursor to fertil-

izers and modern chemicals,[1,2] but also a molecule with tremendous potential towards green energy due to its high energy density with zero carbon footprint.[3,4] Large scale industrial NH_3 production is carried out with the conventional Haber-Bosch[5] process using H_2 and N_2 gases as raw materials at high temperature and pressure that gobbles up approximately 1–2% of global energy and generates an alarming carbon footprint amounting to 6% of global CO_2 emissions.[6] Accordingly, alternative technology of

* Corresponding author at: Physical and Materials Division, CSIR-National Chemical Laboratory, Pune 411 008, India.

E-mail address: k.sailaja@ncl.res.in (S. Krishnamurthy).

converting N_2 to NH_3 via simple, eco-friendly and cost effective technologies such as direct photocatalytic, electrocatalytic or enzymatic Nitrogen Reduction Reaction (NRR) provides a holistic approach for a clean NH_3 production.[7] The advancement of such technology, however, relies greatly on the development of highly efficient catalysts that exhibit high activity, stability and recyclability.

Over the years, various experimental studies were devoted to Transition Metal (TMs) such as Mo[8,9], Cr[10,11], Fe[12–14], etc. and their bimetallic heteromultimetallic complexes as catalysts for NRR at ambient conditions. Although, these transition metal and heteromultimetallic complexes form stable metal-dinitrogen complexes with N_2 and show features similar to the nitrogenase enzyme, there is a heavy loss of metals and their recovery for the next catalytic cycle is unfeasible[15]. This led to an impetus of tangential studies on employing metal nanoclusters as catalysts to reduce dinitrogen under experimental and theoretical approaches.[16,17] While metal nanoclusters are intriguing due to electronic quantum confinement, thereby leading to higher catalytic activity as compared to bulk catalyst; not all the metal atom centres are exploited.

Metal Single Atom Catalysts (SACs)[18,19], in this regard, not only offer a higher catalytic activity and selectivity; but curbs metal loss during the catalytic cycle by exploiting every metal centre as an active catalyst and also provides vacant coordination sites for electron transfer or electron gain from the dinitrogen molecule.[20–22] However, isolated metal SACs owing to strong metal d-d orbital interactions[23] require a support that secures it without compromising the catalytic activity. In this respect, electron-rich two-dimensional (2D) materials such as graphene[24–26], graphitic carbon nitride ($g-C_3N_4$)[27–29], boron nanosheet [30–32], MBenes[33], MXenes[34,35], phosphorene [36,37], hexagonal boron nitride (h-BN)[38–40], MoS_2 [41–43], etc. not only act as a support to secure the metal SACs but also assist in their catalytic performance.

Interestingly, compared to pristine 2D substrates, heteroatom doped 2D substrates such as N-doped carbon [44,45], $g-C_3N_4$ [27–29] or h-BN[38–40] with isolated boron sites have been reported to be remarkably efficient towards NRR in several experimental as well as theoretical investigations. The N-atoms in the substrate increase metal coordination to the substrate and tune the selectivity of metals toward N_2 molecule,[46,47] while the B-atoms can inherently induce charge redistribution on the substrate and favour adsorption of N_2 .[48,49] Moreover, the presence of B hetero-dopants on B and N dual-doped carbon nanospheres has been reported to inhibit the competing Hydrogen Evolution Reaction (HER) and enhance adsorption of N_2 in electrocatalytic NRR.[50] Our previous study on one such BN-pair dual doped graphene support showed a better anchoring of Mo SAC on the CBN-doped graphene support[51] and as well as higher activation of dinitrogen when compared to pristine graphene.[51,52] It is evident that boron and nitrogen doped graphene can act as an effective 2D substrate for anchoring various metal SACs. Besides, the practical development of such BN-doped graphene supports is highly feasible with atomic precision via plasma doping and chemical vapour deposition under appropriate experimental conditions.[53–55] In short, a meticulously designed transition metal SAC supported on BN-pair doped graphene is one such material that can be achieved experimentally in the coming years for large scale NRR.

This brings us to the computational studies that have brought an insight on the underlying chemical morphology and composition to which the catalytic activity is susceptible. Density Functional Theory (DFT) based studies, attempted over the last two decades, to identify an ideal SAC/support combination leading an efficient NRR are worth mentioning at this juncture.[56–59] These

studies focus on either scanning several transition metal SACs on a particular substrate[56,57] or propositions of a particular SAC as an electrocatalyst with a lower overpotential than earlier reported catalysts.[58,59] The notable among these works is the study by Liu et al. with an objective to bridge the chemical understanding behind the activity of different transition metal SACs from an electrochemical viewpoint by examining the activity trends and electronic nature of the SACs through the Gibbs free energies of limiting steps in electrocatalytic NRR.[60].

However, an insightful and penetrating study highlighting the inherent electronic and reactive nature of SACs on graphene and the implications of doped support in augmenting the catalytic activity of metal SAC in question is still amiss. In short, we are missing out on the innate feature of metal atoms that distinguishes the catalytic activity of one metal from the other and are bereft in principle. Further, the trend of scanning several SACs, based on the Gibbs free energy of the limiting step of NRR is extremely erratic, with sensitivity to the methodology used. Reported prognosis of efficient electrocatalysts for NRR from DFT calculations are deduced based on the method applied and description of the metal with a given set of atomic orbitals and given model.

Considering all the above mentioned key points, this work presents a consolidated study to address the so far unaccounted aspects of theoretical studies in identifying a graphene based 2D supported SAC for NRR. The purpose of the study is to identify a low cost, active, stable and reusable metal SAC on graphene support that is unvarying with respect to the method applied, description of the metal atom and model implemented in the computational study. For this, we carry out one of the most extensive study on six different metal SACs, i.e. V, Fe, Ni, Ru, W and Re anchored at distinct modes of BN-doping on periodic model (C_n sheet) and non-periodic models ($C-42_{zz}$ and $C-54_{zz}$ nanoflakes) of graphene. These metal SACs (V, Fe, Ni, Ru, W and Re) are chosen looking into their high NRR activity as per previous experimental reports on SAC[44,61–63] and to account for a correlation between the magnetic property and catalytic nature.[64] The implication of atomic/orbital representation of metals has been critically analysed through different pseudopotentials, implemented as Plane Wave (PW) basis, in periodic calculations and basis sets defined by Linear Combination of Atomic Orbitals (LCAOs) in non-periodic calculations. While the periodic DFT methodology provides a closer-to-real system electronic description of metal SACs anchored on graphene; the non-periodic calculations have been employed to provide a more pronounced electronic description of atomic orbitals. Thereby, a more accurate description of the electronic structure and the activity of the metals can be achieved from non-periodic calculations. This becomes essential when there is a need to identify the optimal substrate for metal SACs. Thus, the robustness of different concentrations of BN dopants on graphene models such as nanoflakes of different sizes and nanosheet, DFT methodologies and orbital definition of different metals to their chemical nature has been gauged. Reactivity descriptors such as Dual descriptor [65,66] and Multiphilic descriptor [67] are applied as leads while we explore the exhaustive aspects of methodology, model and description of the metal centre. This investigation provides a detailed examination of metal SACs through their reactivity descriptors and is an absolute bridge to correlate the activity of metal SACs and their implementation as catalysts for NRR.

2. Computational models and methods

2.1. Models

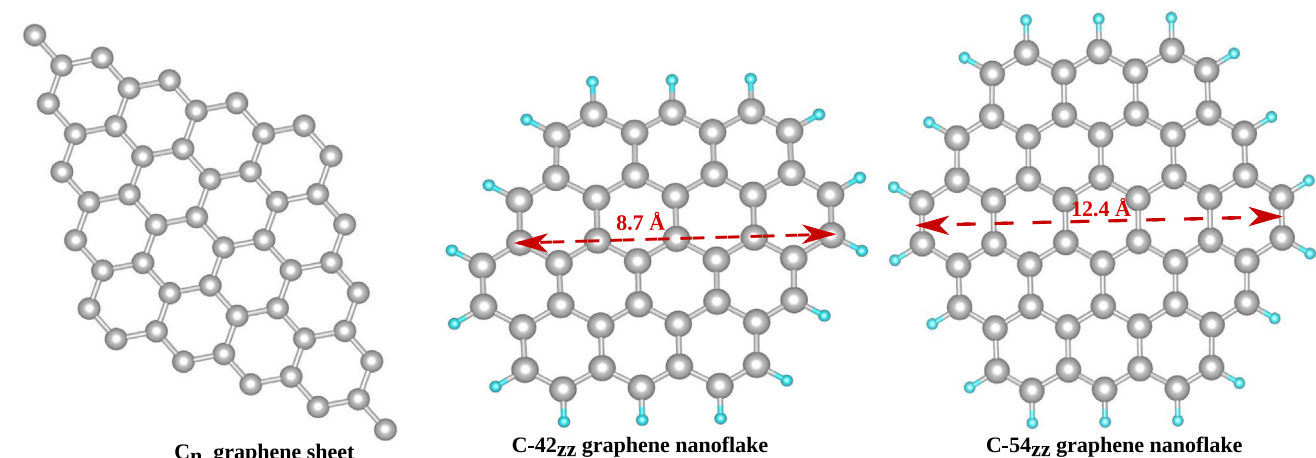
The 2D graphene models of varying size and lateral width: a periodic model and two non-periodic models considered in this

study are as shown in Fig. 1(a). The periodic C_n graphene sheet has been modeled by considering that the sp^2 hybridised carbon atoms are repeated infinitesimally along the xy plane. Coming to the two non-periodic models, graphene nanoflakes with hydrogen termination on 42 carbon atoms with a lateral width of 8.7 Å and 54 carbon atoms with a lateral width of 12.4 Å, are respectively modeled as $C-42_{zz}$ and $C-54_{zz}$. BN-pair dopants are introduced on the basal plane of the graphene models and the concentration of doping varies from zero, one, two and three BN-pair dopants in pris-grap, BN-grap, CBN-grap and BNring-grap systems, respectively. The periodic graphene models with varying concentration of BN-pair dopants are referred as C_n -pris-grap, C_n -BN-grap, C_n -CBN-grap, C_n -BNring-grap, respectively. The nomenclature of the non-periodic graphene models with different BN-pair dopants are as provided in Table S1 of Supplementary Information. When metal SACs are anchored on the graphene supports, it is ensured that the metal SAC is coordinated to the basal plane of graphene with BN-dopants and the same is referred to as M-pris-grap, M-BN-grap, M-grap-CBN and M-BNring-grap systems, respectively as shown in Fig. 1(b). The corresponding nomenclature of SAC anchored periodic and non-periodic graphene models are as provided in Table S1 of Supplementary Information along with specifications of the graphene model. Furthermore, it can be seen from Table S1 of Supplementary Information that when molecular dinitrogen is adsorbed on the SAC anchored graphene models, the associated systems are explicitly referred as M-pris-grap- N_2 , M-BN-grap- N_2 , M-grap-CBN- N_2 and M-BNring-grap- N_2 , respectively of periodic C_n model or non-periodic $C-42_{zz}$ and $C-54_{zz}$ models.

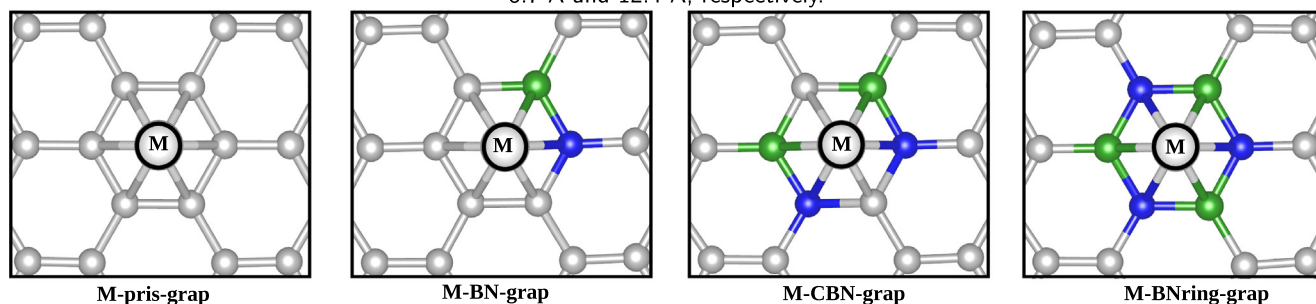
2.2. Computational Details

All periodic calculations on C_n graphene sheet and its BN-pair doped analogues are carried out using the Vienna *ab-initio* Simulation Package (VASP) software based on plane wave (PW) basis. [68] The projected augmented wave (PAW) method [69] has been employed to describe the electron core-interactions. The non-metallic atoms: C, B and N are described by PAW potentials that treat 2s and 2p as valence states while the metal SACs are described by two different PAW potentials: the conventional PBE pseudopotential with $ns(n-1)d$ valence states and PBE_{pv} pseudopotential with $ns(n-1)p(n-1)d$ valence states. A generalized gradient approximation (GGA) implemented in the Perdew-Burke-Ernzerhof (PBE) [70] functional has been used for geometry optimization with the cutoff energy set at 520 eV. The geometries are allowed to relax till the energy and forces of each atom reach a convergence criteria of 10^{-6} eV and 0.005 eV/atom respectively. All the geometries are sampled by a $(2 \times 2 \times 1)$ Monkhorst-Pack kpoint grid with a vacuum space of 20 Å along the Z-direction to avoid inter-layer interactions. Spin polarized calculation has been carried out for geometries with Fe, Ni and Ru metal atoms; while non-spin polarized calculation has been carried out for V, W and Re counterparts. For electronic structure calculations, the relaxed geometries are sampled at $(11 \times 11 \times 1)$ Monkhorst-Pack kpoint grid.

The non-periodic calculations are carried out with a linear combination of Gaussian-type orbitals and an auxiliary framework of DFT implemented in the *deMon.5.0* program. [71] A Perdew-Burke-Ernzerhof (PBE) exchange and correlation functional [70]



(a) Models of periodic C_n graphene sheet and non-periodic graphene nanoflakes $C-42_{zz}$ and $C-54_{zz}$ with their lateral widths of 8.7 Å and 12.4 Å, respectively.



Elemental colour code: C = ●, B = ●, N = ●; Metal (M) colour code: V = ●, Fe = ●, Ni = ●, Ru = ●, W = ●, Re = ●

(b) Different concentrations of BN-pair doing on graphene substrate with metal SAC represented by different colour code.

Fig. 1. Graphene models with different concentrations of BN-pair doping.

has been considered to optimize pristine and BN-pair doped geometries of C – 42_{zz} and C – 54_{zz} nanoflakes to their corresponding lowest spin state with a restricted or restricted-open Kohn Sham formalism. The GEN-A2 auxiliary functions have been used to fit the charge density [72] of all the geometries and their N₂ adsorbed geometries with their geometrical and SCF convergence criteria set at 5×10^{-4} a.u. and 10^{-8} a.u. respectively. Several basis sets shipped with the program have been considered for representing the atomic orbitals of the metal SACs, while a DZVP [73] (double ζ valence polarized) basis set has been employed for C, B, N and H atoms. The lighter 3-d transition metal: V, Fe and Ni are described by the DZVP, DZVP-GGA [74] and WACHTERS [75] basis sets that treat both core and valence electrons explicitly; as well with the Stuttgart-Dresden effective core potential (ECP) [76] and Los Alamos National Laboratory 2-double- ζ effective core potential (LANL2DZ) [77] basis that provide an implicit treatment to core electrons with an explicit treatment of valence electrons. The heavier 4-d and 5-d metals (Ru, W and Re) have been represented with an implicit treatment of core and explicit treatment of valence electrons defined by Stuttgart-Dresden ECP and quasi-relativistic effective core potential (QECP), and LANL2DZ basis sets. The QECP basis has been considered only for heavier 4-d and 5-d metals to account for their relativistic effect. Non-periodic calculations portray a definite electronic description, therefore an ideal electronic description of 2D materials and the metals can be achieved. To bring forth the factual electronic nature and the chemical activity of these 2D material supported SACs, non-periodic calculations have been carried out in this study.

The stability of metal SACs on the 2D graphene based supports has been measured through their binding energy, E_b . The binding energy of the metal on the pristine and BN-pair doped graphene supports is calculated by the equation,

$$E_b = E_{SAC-grap} - E_{grap} - E_{SAC} \quad (1)$$

where, $E_{SAC-grap}$ and E_{grap} are the total electronic energies of the various graphene supports with and without metal SAC and E_{SAC} is the electronic energy of the single metal atom. The efficacy of these SAC-grap systems to capture free dinitrogen molecule has been computed in terms of the adsorption energy, E_{ads} of dinitrogen and it has been calculated by the equation,

$$E_{ads} = E_{SAC-grap-N_2} - E_{grap-SAC} - E_{N_2} \quad (2)$$

where, $E_{SAC-grap-N_2}$ is the total electronic energy of N₂ adsorbed SAC-grap systems, $E_{grap-SAC}$ and E_{N_2} are the electronic energies of graphene support with metal atom and free nitrogen molecule respectively. Earlier reports on metal SACs have highlighted the parallel or side-on mode of adsorption to show a higher N-N bond dissociation as compared to the vertical or end-on mode of adsorption, [78] therefore, only the parallel mode of N₂ adsorption has been considered in this work.

2.3. Reactivity descriptors and Gibbs Free Energy Calculations

The Dual Descriptor and Multiphilic descriptor are derived respectively, from the Fukui indices and group philicity of the metal centers. For periodic DFT calculations, the Fukui function or local philicity is calculated by the finite difference method as reported by Cefon et al. [79] where electrons are added or removed by using the NELECT keyword to/from the neutral system. The Fukui indices, $f^-(r)$ and $f^+(r)$ of the metal SACs and coordinating atoms are computed by using the Henkelman's program [80] that integrate charges of the systems from their Voronoi volumes. The expressions for computing Fukui indices from their condensed charges are represented by,

$$f^-(r) = q^N - q^{N-1} \quad (3)$$

$$f^+(r) = q^{N+1} - q^N \quad (4)$$

where, q^N , q^{N-1} and q^{N+1} are charges on the atoms with N, N-1 and N + 1 electrons, respectively. For non-periodic DFT calculations, the Fukui indices of metal centers and coordinating atoms on C – 42_{zz} and C – 54_{zz} nanoflakes are computed analytically as reported by Flores-Moreno et al. [81] and implemented in the deMon.5.0 program. The electrophilic and nucleophilic Fukui functions are evaluated by removing or adding electrons to the frontier orbitals and thereby corresponds to $f^-(r)$ and $f^+(r)$, respectively. The group philicity w_g^α , on the other hand, corresponds to the condensed local philicity over the metal center and atoms coordinated to it and is thereby expressed as,

$$w_g^\alpha = \sum_{k=1}^n w_k^\alpha \quad (5)$$

where $\alpha = +$ for nucleophilicity or $-$ for electrophilicity, k is the metal SAC and n is the number of atoms coordinated to the metal center, w_k^α is the local philicity. Accordingly, the Dual descriptor $f^{(2)}(r)$ and Multiphilic descriptor $\Delta w(r)$ are defined as the difference between nucleophilic and electrophilic Fukui indices and group nucleophilicity and electrophilicity, respectively. They are evaluated by using the equations,

$$f^{(2)}(r) = f^+(r) - f^-(r) \quad (6)$$

$$\Delta w(r) = w_g^+ - w_g^- \quad (7)$$

These reactivity descriptors have been reported to be more accurate descriptors [82,67] than the Fukui function as it can reveal the nucleophilic ($f^{(2)}(r)$ and $\Delta w(r) < 0$) and electrophilic ($f^{(2)}(r)$ and $\Delta w(r) > 0$) centres simultaneously.

Although the reactivity descriptors provide a description to the electrophilicity or nucleophilicity of the metals, the feasibility of these metals to adsorb dinitrogen and reduce it to ammonia will rest on their free energy change. The Gibbs free energy change for periodic calculations on dinitrogen adsorption and elementary reaction steps of NRR has been calculated by the equation, $\Delta G = \Delta E + \Delta ZPE - T\Delta S$, where ΔE is the change in electronic energy, ΔZPE is the change in Zero Point Energy, T (=298.15 K) is the room temperature in Kelvin scale and ΔS is the change in vibrational entropy between the final and initial geometries. The zero point energy and entropy terms are evaluated from the vibrational frequency calculations. The free energy of N₂ adsorption and the elementary reaction steps of NRR for non-periodic calculations of SACs on C – 42_{zz} and C – 54_{zz} systems are computed with the thermodynamic quantities derived from frequency calculations at room temperature. The relation for free energy change in non-periodic calculations is $\Delta G = \Delta E + \Delta H_{corr} - T\Delta S_{corr}$, where ΔE is the change in electronic energy, ΔH_{corr} is the change in enthalpy correction and ΔS_{corr} is the change in entropy correction at room temperature.

3. Results and discussion

3.1. Binding energy of metal SACs

The binding energies, E_b of single metal atoms on periodic and non-periodic models of graphene with different modes of BN-pair doping is provided in Fig. 2. It is observed that most of the metals considered in our study show a stable anchoring on the graphene supports with their exothermic binding energies varying with respect to the change in graphene model, DFT methodology and description of the metal atom. Coming to the observations of

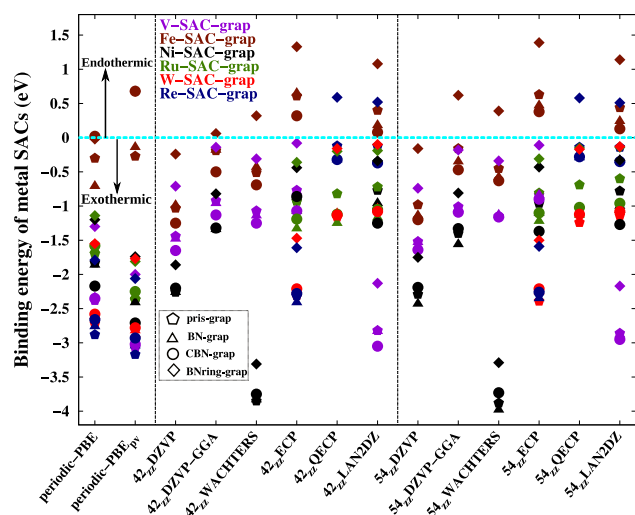


Fig. 2. Binding energies of the metal SACs on periodic and non-periodic graphene supports. Metals on the negative scale of cyan line are stable and show exothermic E_b on the graphene supports. Symbolic representations of BN-doping is provided in inset along with colour scheme of the metals as mentioned in Fig. 1(b). (For interpretation of the references to colour in this figure legend, the reader is referred to the web version of this article.)

binding energies from periodic calculations, the metals are found to anchor strongly, with higher negative binding energies, on the graphene support when PBE_{pv} pseudopotentials are used for defining the metals as compared to PBE pseudopotentials in all metals, except Fe metal. From Fig. 2 and values of E_b provided in Supplementary Information Table S2, the heavier 5-d transition metals, W and Re are found to show higher binding energies than the lighter 3-d and 4-d metals, with the exception of V. It can be noted that most metal single atoms show higher binding energies on the pristine graphene support and it decreases as the concentration of B and N dopants increases with all the metal single atoms being the least stable on their corresponding BNring-grap support. On the other hand, the binding energies obtained from non-periodic calculations are found to be insensitive to the size of the graphene nanoflakes; however as anticipated, the binding energy of metals are sensitive to the basis set describing the metal orbitals. The binding energies of 3-d metals, except V-SAC, tend to be higher as the basis sets become more exhaustive and all electrons are treated exclusively i.e. DZVP, DZVP-GGA and WACHTERS when compared to basis sets with implicit core electrons. Amongst the metals described with implicit core electrons, the 4-d metal Ru shows a consistent binding energy on all supports irrespective of the change in metal basis. It is also to be noted that the heavier 5-d metals are extremely sensitive to the metal basis set and their stability on the graphene support decreases when QECP and LANL2DZ basis are implemented instead of the ECP basis; in particular, Re on BNring-grap support shifts from an exothermic binding energy of -1.5 eV (with ECP basis) to an endothermic binding energy of ≈ 0.5 eV when computed with QECP and LANL2DZ basis sets. Coming to the role of dopants, the influence of B and N dopants on the substrate and their efficacy to stabilise the metal atom becomes more prominent with a definite electronic description of the metal as different metals show optimal binding conditions on different substrates. For instance, V and Fe metals are found to prefer CBN-grap substrates; Ni, Ru and Re prefer BN-grap substrates and W prefers pris-grap substrate. While a conclusive comment cannot be made on which metal shows the highest stability than the rest due to diverse treatment of core and valence electrons; it is interesting to note that in all basis set considerations, Fe metal shows a lower stability on graphene and its BN-

pair doped substrates in periodic as well as non-periodic calculations.

3.2. Reactivity descriptor of metal SACs

While it is important to account for the stability of the metals on the graphene substrates, the activity of the metal defined by the reactivity descriptor is a more crucial factor to be accounted for the SAC-grap system to be employed as a catalyst for NRR. The reactivity of carbon atoms in basal plane of graphene nanoflakes has been discussed by Azeez et al. [83] to be lower than those of peripheral atoms. From Figure S1 in Supplementary Information, it can be seen that as boron and nitrogen dopants are introduced on the basal plane of the C – 42_{zz} graphene model, there is a significant change in the reactivity pattern as B-atoms become nucleophilic centres and N-atoms become electrophilic centres in BN-grap and CBN-grap support; while in BNring-grap support both B and N atoms behave as electrophilic and nucleophilic centres and the overall reactivity of the support increases as such. It can be observed that the charge disparity created by boron and nitrogen atoms when doped on graphene plays a major role in influencing the reactivity pattern of the graphene supports. Thereby, when SACs are anchored on the basal plane of these graphene supports, the metal d-orbitals form hybridized d-p orbitals upon conjugation with the p-orbitals of B and N atoms bonded to it. The nature of dopant atoms on the support influences the reactivity pattern of the metals and the same has been computed in terms of Dual and Multiphlic descriptors. The Dual descriptor, $f^{(2)}(r)$ and Multiphlic descriptor, $\Delta w(r)$ on different BN-pair doped metal SAC/graphene supports as obtained from periodic and non-periodic calculations carried out by considering several metal pseudopotentials and basis sets are as shown in Supplementary Information, Figures, S2 and S3. SAC/graphene systems with $f^{(2)}(r)$ or $\Delta w(r) \approx 0$ are neither strong electrophilic or nucleophilic centers, thereby we will focus on the systems with higher electrophilicity ($f^{(2)}(r)$ or $\Delta w(r) > 0.1$) and nucleophilicity ($f^{(2)}(r)$ or $\Delta w(r) < -0.1$). It can be seen from Figures S2 and S3 that W and Ni followed by Re systems show higher nucleophilicity, whereas W shows the highest electrophilicity on all graphene supports followed by V-BNring-grap, Re-pris-grap, Ni-BNring-grap and Fe on pris-grap and BN-grap supports. While periodic calculations show an inclination towards an electrophilic nature of the metal SAC/graphene systems, there is no significant change in the reactivity pattern, both $f^{(2)}(r)$ and $\Delta w(r)$, when different metal pseudopotentials are employed. Coming to the non-periodic calculations, the Multiphlic descriptor which incorporates the philicity of atoms coordinated to metal centers, gives an overall understanding of the reactivity of SAC-graphene supports and it becomes more pronounced. The nucleophilicity of SAC/graphene systems are more pronounced when the local environment of the metal and group philicity are considered, as seen in Figure S3. Additionally, the reactivity pattern of the SACs and SAC/graphene systems is predictably sensitive to the metal basis but it also becomes sensitive to the change in size of the nanoflakes. For instance, the reactivity of V-SAC and V-grap systems become more pronounced in larger C – 54_{zz} graphene nanoflake, while that of Ni and W gets masked. The Dual Descriptor analysis reveals a consensus on the higher activity pattern of W, V, Re and Ni metals from periodic as well as non-periodic calculations. The same pattern can be seen from Multiphlic descriptor analysis which highlights the role of B and N dopants in accentuating the reactivity of the SAC/graphene systems.

One fascinating aspect is the linear relationship observed between the Dual descriptor and Multiphlic descriptor as seen in Fig. 3. It can be noted from $f^{(2)}(r)$ and $\Delta w(r)$ values of SACs and

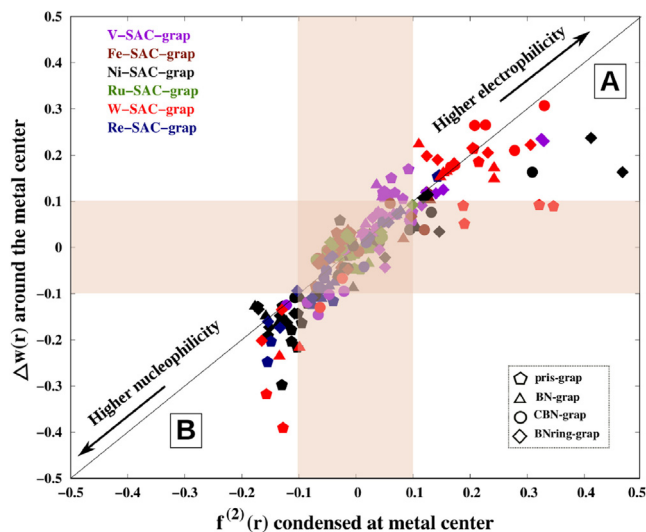


Fig. 3. $\Delta w(r)$ vs $f^{(2)}(r)$ plot of the SAC/graphene systems, the symbolic representations of BN-doping is provided in inset. Less active metals on their corresponding graphene supports are indicated in the shaded region. Colour scheme of the metals is as mentioned in Fig.1(b). (For interpretation of the references to colour in this figure legend, the reader is referred to the web version of this article.)

SAC/graphene systems that the metal centers show a major contribution in directing the reactivity of the system and these two descriptors can be used synonymously for SACs anchored graphene systems. Another interesting aspect from the linear plot in Fig. 3 is the two designated regions of higher electrophilicity, A and higher nucleophilicity, B. In region A, aside from the information that W, V, Ni and Re metals show higher electrophilicity, the graphene supports are mostly BN-grap, CBN-grap and BNring-grap. On the other hand, region B of higher nucleophilicity with W, Re and Ni metals are mostly coupled with pris-grap and a few BN-grap supports. In general, the reactivity of the SAC/graphene systems is higher when B and N dopants are introduced in the support and the overall system tends to be electrophilic in nature. It is also notable that V, Ni, W and Re SACs are found to be stable on the pristine and BN-pair doped supports from our earlier section on metal binding energy. Thereby, it becomes interesting as these metals with a higher reactivity are also stable on the graphene support and their synthesis is feasible from experimental point-of-view.

3.3. Dinitrogen adsorption and activation on metal SACs

The activity pattern of metal SACs on different graphene supports, as observed from the analysis of reactivity descriptors, has been further corroborated to the efficacy of the metals to adsorb and activate dinitrogen molecule. The adsorption energies of free dinitrogen molecule on the SAC-grap systems are calculated and plotted in Fig. 4. The adsorption of N_2 on all SACs anchored graphene supports are found to be feasible and exothermic (-0.82 eV to -2.80 eV) in periodic as well as non-periodic calculations. The exothermic chemisorption energies of dinitrogen on all metal-SAC-grap systems validates the potential of these metals to be employed as catalysts for dinitrogen activation and NRR. It is particularly notable that Ru metal SAC with a milder activity as compared to the rest of the metals also shows a lower chemisorption of N_2 , -0.82 to -1.80 eV on periodic and non-periodic models of pristine and BN-pair doped graphene supports. It can be observed from Fig. 4 that the efficacy of the SAC-grap systems to adsorb N_2 has been influenced by different modes of BN-pair doping, metal pseudopotentials and basis sets and size of the nanoflakes considered in periodic and non-periodic calculations. In periodic calculations,

with the introduction of B and N dopants and as the system changes from SAC-pris-grap to SAC-BNring-grap, the chemisorption of N_2 tends to become more exothermic. However, a significant change brought about by the addition of valence ($n-1$)p-states in PBE_{pv} pseudopotentials of metals is seen in the case of Fe-SAC and Ru-SAC anchored graphene systems, while the rest of the metals remain insensitive to the change in metal pseudopotentials. Amongst the metal-graphene systems considered in this work; V, W and Re systems are found to show higher chemisorption of N_2 with adsorption energies of -2.3 eV, -2.8 eV and -2.2 eV respectively on their respective BNring-grap systems.

Likewise, the adsorption of dinitrogen on all metal anchored non-periodic graphene models are found to be enhanced as the concentration of BN-pair dopants increases around the metal in the basal plane of graphene. The implication of considering several metal basis sets cannot be prominently seen in the case of V-SAC-grap systems as the N_2 adsorption energies remain nearly consistent despite the implicit treatment of core electrons in ECP and LANL2DZ basis sets. Fe-SAC-grap and Ni-SAC-grap systems tend to show a more exothermic adsorption of dinitrogen when described with explicit core and valence electrons in DZVP, DZVP-GGA and WACHTERS basis sets as compared to ECP and LANL2DZ basis. The heavier metals (Ru, W and Re) described with implicit core electrons tend to show a higher chemisorption when quasi-relativistic metal basis sets, QECP and LANL2DZ are employed over the metal ECP basis set. Thereby, the 3-d metals show a pronounced chemisorption of dinitrogen with metal basis that define both core and valence electrons explicitly while the heavier 4-d and 5-d metals are highly affected with the inclusion of quasi-relativistic factors in the metal basis. In addition, the adsorption energies of N_2 on V-SAC-grap, W-SAC-grap and Re-SAC-grap systems are found to be insensitive to the size of graphene nanoflakes, while the same cannot be seen for Fe, Ni and Ru systems.

Most significantly, it can be noted that V,W and Re metals show a consistently higher and similar affinity towards chemisorption of N_2 molecule in periodic as well as non-periodic calculations, albeit the difference in the DFT methodologies implemented. In particular, adsorption energies computed with the V metal defined by the DZVP-GGA basis set is found to show similar results to the periodic calculations on V-SAC-grap systems. A similar case can be observed on W-SAC-grap and Re-SAC-grap systems when metal atomic orbitals described by LANL2DZ basis set has been found to show nearly similar N_2 adsorption energies to the periodic calculations. The same cannot be seen in the case of Fe-SAC-grap, Ni-SAC-grap and Ru-SAC-grap systems where the adsorption energies in non-periodic models tend to be overestimated as compared to the adsorption energies in the periodic models. This consistent and similar pattern of adsorption energy observed in the case of V, W and Re metal SACs, in-spite of different DFT methodologies and atomic orbital representation, validates the prepotency of local reactivity of these metals which is in direct correspondence to the reactivity pattern achieved from their reactivity descriptors.

The chemisorption energies of N_2 on different metal SACs can be correlated to the activation of dinitrogen which is measured in terms of the elongated N-N bond of dinitrogen molecule when adsorbed on the M-SAC-grap systems. A percentage increase in the N-N bond length is made with reference to the N-N bond length in free N_2 molecule, i.e. 1.11 Å and 1.12 Å for periodic and non-periodic calculations respectively. A gradient plot on the percentage increment in N-N bond length on periodic and non-periodic V-SAC-grap- N_2 systems with different modes of BN-pair doping is as provided in Fig. 5(a). A consistent pattern of N-N bond activation on V-SAC-grap- N_2 can be observed where the BNring-grap substrates show the largest bond elongation in-spite of the

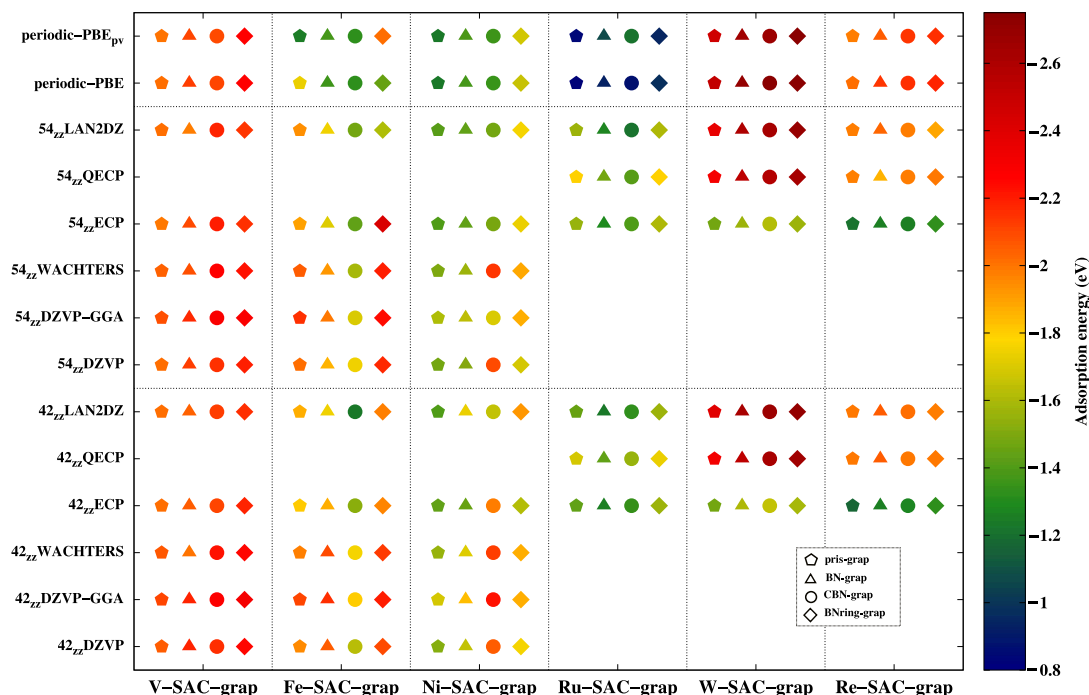


Fig. 4. Adsorption energy of dinitrogen on different metal SACs; inset shows the colour scheme changes from blue to red as the adsorption of N_2 becomes more feasible.

difference in DFT methodologies, basis sets and pseudopotentials to define the metal and nanoflake size in the periodic and non-periodic models. The N-N bond in V-BNring-grap- N_2 systems is elongated by 11%, i.e. 1.23 Å in the periodic model and non-periodic nanoflakes when V metal is defined by DZVP-GGA basis set. The higher bond activation observed in V-BNring-grap- N_2 systems is in direct correlation to the adsorption energy of dinitrogen molecule and the higher reactivity of V metal as discussed earlier in the adsorption and reactivity descriptor section. While the extent of bond activation in Fe, Ni and Ru systems, Figs. 5(b), 5(c) and 5(d), range from 4.6–8.7 % owing to their less exothermic adsorption of dinitrogen molecule, which correlates to their lower reactivity pattern, these metals fail to show a consistent pattern in N-N bond activation with the change in concentration of BN-pair dopants, different basis sets or pseudopotentials to define the metal and size of graphene models in the periodic and non-periodic calculations. Coming to the W-SAC-grap- N_2 and Re-SAC-grap- N_2 systems in Figs. 5(e) and 5(f), these metals show a consistent pattern where a larger N-N bond elongation is found on their respective CBN-grap substrates in periodic and non-periodic calculations. The extent of N-N bond activation on W-CBN-grap- N_2 and Re-CBN-grap- N_2 systems range from 15.4% (1.27 Å) and 13% (1.24 Å) respectively in periodic models to approximately 16% (or 1.28 Å) and 14% (or 1.26 Å) respectively in their non-periodic counterparts when the metal is represented by the LANL2DZ basis set. Therefore, W and Re metals anchored on CBN-grap substrate possess a higher potential to chemisorp and activate dinitrogen molecule followed by V on a BNring-grap substrate. It is notable that periodic calculations carried out with metal PBE_{pv} pseudopotentials generated geometries with higher N-N bond activation as compared to those carried out with PBE pseudopotentials in V, W and Re metals.

To also account for the experimental analogy of N-N bond activation on the adsorbed N_2 molecule; IR-stretching frequency which is a fingerprint to represent the strength of a chemical bond has been evaluated for the M-SAC-grap- N_2 systems and the red-shift observed in N-N stretching frequency has been provided in Supplementary Information, Figure S4. It can be noted from Fig-

ure S4(a), S4(e) and S4(f) that the red-shift in N-N bond is consistently higher on the V-BNring-grap, W-CBN-grap and Re-CBN-grap systems despite the change in DFT methodology, size of the graphene models, metal pseudopotentials and basis sets. This consistent pattern of red-shift in V, W and Re corresponds to the N-N bond activation observed earlier; with W-CBN-grap showing the highest red-shift of 1026 cm^{-1} in periodic calculations and 950 cm^{-1} in non-periodic calculations. This is followed by Re-CBN-grap systems with a N-N bond red-shift of 894 cm^{-1} and 876 cm^{-1} from its corresponding periodic and non-periodic systems, respectively. Finally, the V-BNring-grap systems with an 11 % N-N activation shows a red-shift of around 810 cm^{-1} in its periodic system and 740 cm^{-1} in the non-periodic system. It can be further noted from Figure S4(b)–S4(d) of Supplementary Information that Fe, Ni and Ru metal SACs with a relatively lower bond activation of 4.6–8.7 % shows a correspondingly lower red-shift ranging from 373 cm^{-1} to 612 cm^{-1} , respectively. This trend on N-N bond red-shift corroborates to the earlier section on N-N bond activation and dinitrogen chemisorption energies on different metal SACs. Our observation on N-N bond red-shift and activation by V, W and Re SACs corroborate the N_2 adsorption energies and reactivity of the metals described via their reactivity descriptors earlier. Therefore, the qualitative reactivity description of metal SACs discussed earlier can be implemented as an important descriptor in the probe for a highly active metal SAC and a suitable 2D substrate that amplifies its activity.

Following the investigation on N-N bond activation, the later part of the study is now restricted to the more active metals, i.e. V, W and Re. While the activity of V, W and Re metals have been affirmed through their reactivity descriptor, higher N_2 chemisorption energies and N-N bond activation; a detailed understanding on the electronic properties before and after dinitrogen adsorption has to be accounted. Thus, an electronic analysis of V-BNring-grap- N_2 , W-CBN-grap- N_2 and Re-CBN-grap- N_2 systems through the Projected Density of States (PDOS) examined before and after dinitrogen adsorption of the periodic models has been shown in Fig. 6. The electron transfer from the metals to the dinitrogen

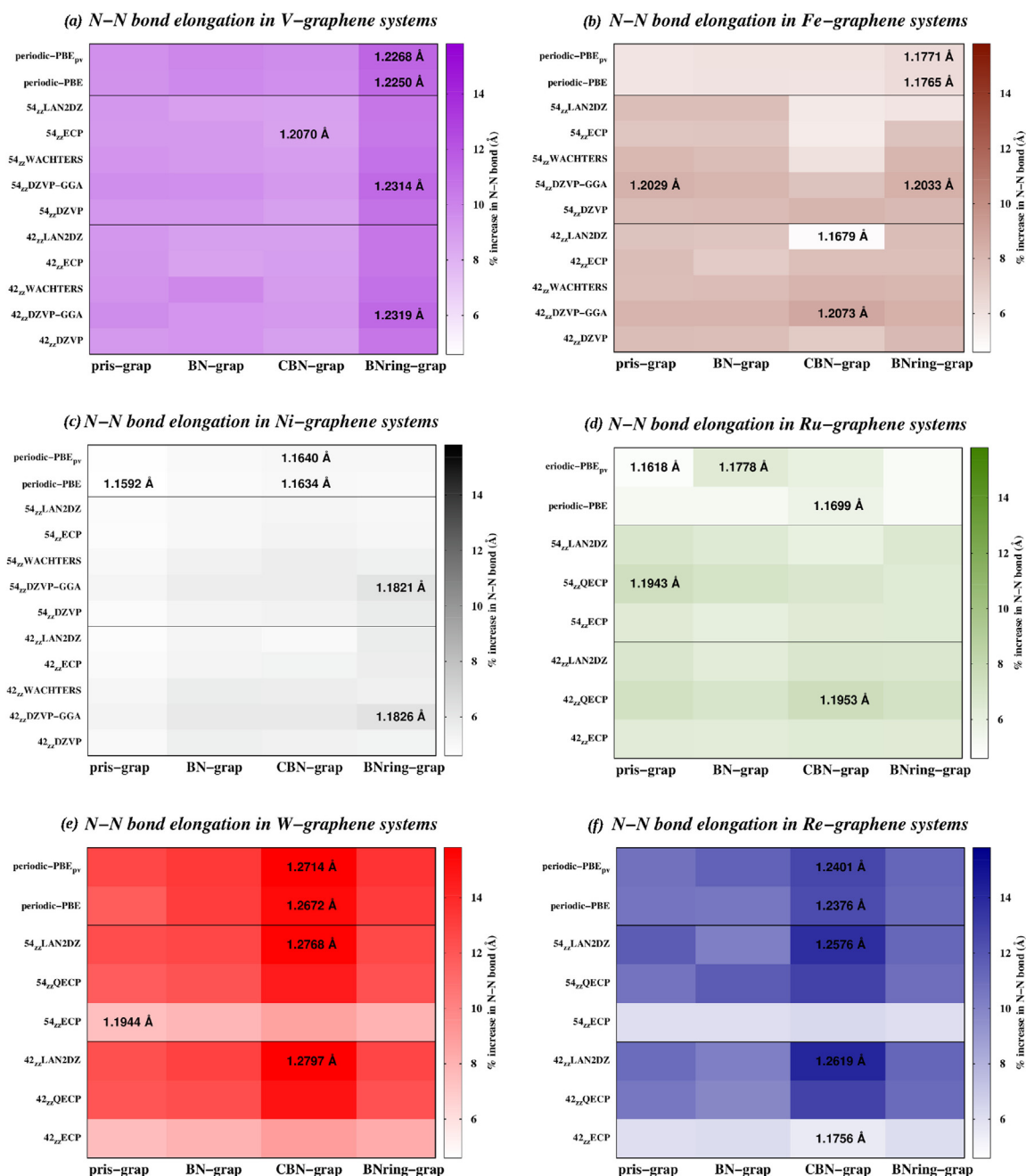


Fig. 5. Percentage increment in N-N bond lengths when N₂ is adsorbed on the M-SAC-grap systems. The gradient plot is set with a value of 1.16 Å and 4.6% bond length increment observed in Ni-SAC-pris-grap as white; the intensity of the colour codes for respective metals increases as the N-N bond length increases. For each metal, the largest value of N-N bond in periodic and non-periodic models are provided along with the least value of N-N bond as observed from our calculations.

molecule can be emphasized by the decrease in electron densities of the metal d-orbitals in the valence band. W and Re metals decreases significantly owing to charge transfer from metal to N₂. However, V-CBN-grap shows an exception as the decrease in electron densities in the valence band leads to generation of vacant d-orbitals in its conduction band. The reactivity of V-SAC on CBN-grap substrate can be thereby accounted to its electrophilic nature. While the heavier W and Re metals have electron rich d-orbitals and coordinate with dinitrogen via transfer of electrons to the $\pi^*-\pi^*$ orbitals of N₂ molecule, V metal with its vacant d-orbitals coordinate to the N₂ molecule via $\pi-\pi$ back donation. The charge density difference plots generated after the adsorption of dinitrogen in all three systems displays the hybridisation of metal d-

orbitals with the $\pi^*-\pi^*$ orbital of N₂ to form a stable M-SAC-grap-N₂ complex. Similarly, a metal-nitrogen d-p hybridized Highest Occupied Molecular Orbital (HOMO) can be observed when the Frontier Molecular Orbitals (FMO) of non-periodic models of V-BNring-grap-N₂, W-CBN-grap-N₂ and Re-CBN-grap-N₂ systems on the C – 42_{zz} and C – 54_{zz} nanoflakes are plotted in Supplementary Information Figure S5. This hybridization of metal-nitrogen d-p orbitals verifies our analogy to correlate activity with descriptors and not as charge controlled hard-hard interaction.[85] The PDOS and FMO analysis further solidifies the prevalence of metal d-orbitals and its reactivity in directing the catalytic activity of V, W and Re SACs supported on graphene towards dinitrogen activation. As we observed consistent results in periodic and non-

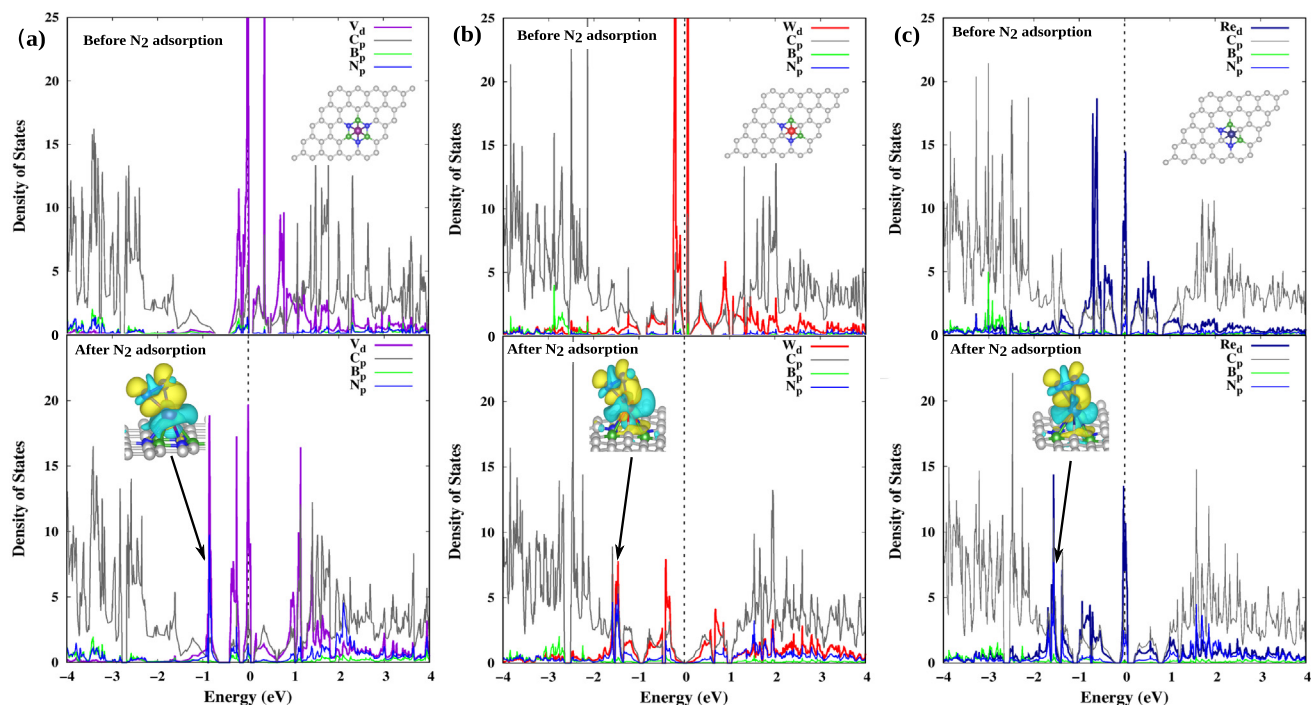


Fig. 6. Projected Density of States of graphene supported SACs compared before and after N_2 adsorption on (a) C_n -V-BNring-grap, (b) C_n -W-CBN-grap and (c) C_n -Re-CBN-grap; the charge density difference plots of M-grap- N_2 systems, made using Vesta 3.4 [84], are as included in inset.

periodic calculations on V, W and Re SACs described with specific metal basis sets, the NRR process on V-BNring-grap, W-CBN-grap and Re-CBN-grap systems have been subsequently investigated on their respective periodic and non-periodic models with DZVP-GGA basis set for V and LANL2DZ basis set for W and Re.

3.4. NRR mechanism on V-BNring-grap, W-CBN-grap and Re-CBN-grap systems

Reduction of dinitrogen to ammonia on V-BNring-grap, W-CBN-grap and Re-CBN-grap systems has been evaluated on their corresponding periodic and non-periodic models. Periodic calculations on the above systems has been continued with metal PBE_{pv} and PBE pseudopotentials to account for the larger N-N bond activation in-spite of similar energetics. Non-periodic calculations with DZVP-GGA basis set for V and LANL2DZ basis set for W and Re metals, has been carried out on the C-42_{zz} and C-54_{zz} nanoflakes. The NRR process, for N_2 adsorbed in parallel mode on these M-SAC-grap systems, follow the enzymatic route where atomic hydrogen atoms attack the N-atoms in an alternating fashion. The structures of N_xH_y intermediates and the change in Gibbs free energy for each hydrogenation step on periodic and non-periodic models of V-BNring-grap system are as shown in Fig. 7, while those of W-CBN-grap and Re-CBN-grap systems are provided in Supplementary Information, Figures S6 and S7. It can be observed from the free energy diagram of V-BNring-grap system that the energies of intermediate reaction steps are more negative (i.e. exergonic) in non-periodic calculations as compared to periodic calculations. The orbital descriptions are more pronounced in non-periodic calculations with basis sets, thereby the electronic energy of the system becomes more negative leading to the lowering of free energy. Other than this overall lowering of free energy in non-periodic calculations, the energetics of each step is seen to follow the same pattern as in periodic calculations; for instance the energy uphill steps, $*N_2 \rightarrow *N_2H$, $*NH_2-*NH \rightarrow *NH_2-*NH_2$ and $*NH_2 \rightarrow *NH_3$ are endergonic in both periodic and non-periodic calculations on V-

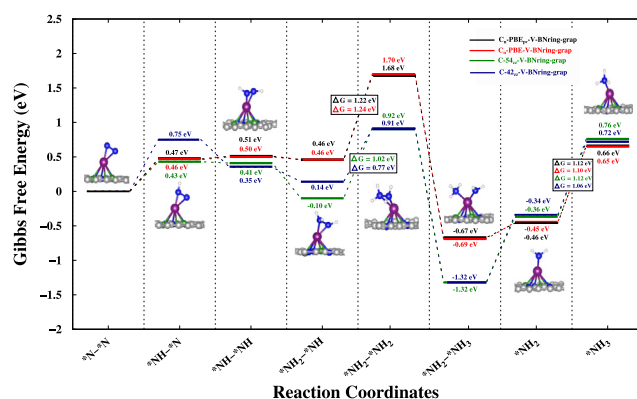


Fig. 7. Enzymatic reaction mechanism of NRR on periodic and non-periodic V-BNring-grap models.

BNring-grap. This pattern of free energy lowering along with similar energetics can be observed in the free energy diagram of W-CBN-grap and Re-CBN-grap systems provided in Supplementary Information. While the energy uphill steps in W-CBN-grap system is similar to that observed in V-BNring-grap system, Re-CBN-grap shows an exception with an exergonic (or energy downhill) $*N_2 \rightarrow *N_2H$ step but an endergonic $*N_2H \rightarrow *NH-*NH$ step.

Table 1 summarizes the crucial intermediate steps involved in NRR process on the above mentioned SAC/graphene systems. These include N_2 adsorption, first hydrogenation step ($*N_2 \rightarrow *N_2H$), fourth hydrogenation step ($*NH_2-*NH \rightarrow *NH_2-*NH_2$) that generates a highly strained intermediate, final hydrogenation step ($*NH_2 \rightarrow *NH_3$) and the last NH_3 desorption step. The Gibbs free energy of N_2 adsorption on non-periodic systems is seen to be more exoergic, i.e. more negative than the periodic counterparts for all three SAC/graphene systems. The Potential-Determining Step (PDS) in V-BNring-grap and W-CBN-grap systems is seen to change from the fourth hydrogenation step ($*NH_2-*NH \rightarrow *NH_2-*$

Table 1

Gibbs free energies, ΔG (eV) of the crucial intermediate steps involved in enzymatic Nitrogen Reduction Reaction on V-BNring-grap, W-CBN-grap and Re-CBN-grap models. The ΔG_{max} of each model is highlighted in bold.

SAC/graphene system	V-BNring-grap					W-CBN-grap				Re-CBN-grap			
ΔG	C_n PBE _{pv}	C_n PBE	C_{42ZZ}	C_{54ZZ}	C_n PBE _{pv}	C_n PBE	C_{42ZZ}	C_{54ZZ}	C_n PBE _{pv}	C_n PBE	C_{42ZZ}	C_{54ZZ}	
$* \rightarrow *N_2$	-1.62	-1.62	-2.23	-2.28	-2.09	-2.04	-2.62	-2.52	-1.52	-1.53	-1.98	-1.99	
$*N_2 \rightarrow *N_2H$	0.47	0.46	0.75	0.43	0.30	0.30	0.37	-0.10	-0.12	-0.11	-0.36	-0.40	
$*NH_2 \rightarrow *NH \rightarrow *NH_2 \rightarrow *NH_2$	1.22	1.24	0.77	1.02	1.45	1.45	0.88	1.24	1.51	1.51	1.46	1.53	
$*NH_2 \rightarrow *NH_3$	1.12	1.10	1.06	1.12	1.26	1.31	1.13	1.64	1.25	1.26	1.12	1.14	
$*NH_3 \rightarrow *N_2$	-0.66	-0.65	-0.72	-0.76	-0.67	-0.64	-0.79	-0.86	-0.22	-0.22	0.04	-0.03	

NH_2) in periodic calculations to the final hydrogenation step ($*NH_2 \rightarrow *NH_3$) in non-periodic calculations. It is notable that these two steps are the most energy uphill reaction steps ($\Delta G > 1.0$ eV), thereby both the steps limit the feasibility of N_2 reduction to NH_3 . The limiting potential, ΔG_{max} in periodic V-BNring-grap systems is found to be 1.22 eV to 1.24 eV, while the non-periodic counterparts show a limiting potential of 1.06 eV and 1.12 eV in C-42_{zz} and C-54_{zz} graphene nanoflakes, respectively. For W-CBN-grap systems, the limiting potential is found to be 1.45 eV in periodic systems, 1.13 eV in C-42_{zz} and 1.64 eV in C-54_{zz} graphene nanoflakes respectively. However, for periodic and non-periodic Re-CBN-grap systems, the PDS is the fourth hydrogenation step ($*NH_2 \rightarrow *NH \rightarrow *NH_2 \rightarrow *NH_2$) which involves formation of a torsionally bulk intermediate and the limiting potential ranges from 1.51 eV in periodic system to 1.46 eV in C-42_{zz}-Re-CBN-grap and 1.53 eV in C-54_{zz}-Re-CBN-grap system. From this investigation on N_2 reduction to NH_3 in SAC/graphene systems, it can be noted that the free energy of intermediate hydrogenation steps are more pronounced in non-periodic calculations as electronic descriptions are more accurate when basis sets are implemented. While all three metal-graphene systems can be seen to reduce dinitrogen to ammonia effectively, a lower energy barrier is observed on V-BNring-grap where $1.06 \text{ eV} < \Delta G_{max} > 1.24 \text{ eV}$. Although the ΔG_{max} of V-BNring-grap is higher than previously reported V-SAC catalyst [86], the interesting aspect of our SAC/graphene system is the NH_3 desorption step. Most SAC/2D-support reported with lower ΔG_{max} would require the assistance of solution, heating, electropotential or etching to desorb NH_3 from the catalyst.[86–88] The recyclability/reclaimability of the catalyst is another looming question that needs to be answered beyond an effective NRR process. From this computational study, we observed that NH_3 desorption can be easily carried out by N_2 as the $*NH_3 \rightarrow *N_2$ step is exergonic and feasible by ≈ -0.66 eV in C_n -V-BNring-grap, -0.72 eV in C-42_{zz}-V-BNring-grap and -0.76 eV in C-54_{zz}-V-BNring-grap systems. Thereby, this reclaimable V-BNring-grap catalyst with a low-cost metal has an advantage over several other 2D catalysts.

4. Conclusions

In summary, a comprehensive periodic and non-periodic DFT calculation has been carried out on six transition metal SACs anchored on pristine and BN-pair doped 2D graphene models with an objective to tailor a pragmatic heterocatalyst for NRR. This consolidated study highlight the susceptibility of metal reactivity with respect to the change in DFT methodology, size of the model, coordination of B and N dopants with the metal and most importantly, the orbital description provided by several basis sets and pseudopotentials. Dual and Multiphilic descriptors are found to bridge the inherent local activity and innate electronic nature of SACs. These descriptors yield consistently similar trends to the chemisorption efficacy and activation of N_2 and can be employed

as leads to design efficient SAC/support couple for dinitrogen reduction. The mechanistic studies on the enzymatic mode of N_2 reduction to NH_3 on three select SAC/graphene system highlights similar free energy diagram in periodic as well as non-periodic calculations. This exhaustive analysis emphasizes that a qualitative idea of energetics and NRR limiting potential can be achieved from computational studies made on a less complex non-periodic model. Additionally, this study focuses on most convenient way to desorb NH_3 with N_2 and reclaimability of the catalyst which is usually ignored in most studies. Our computational investigation proposes V-BNring-grap catalyst as a low cost, highly active, stable and reclaimable catalyst for NRR that can be developed with the currently available synthesis technology, thereby enabling efficient large scale and eco-friendly NH_3 production in future.

Declaration of Competing Interest

The authors declare that they have no known competing financial interests or personal relationships that could have appeared to influence the work reported in this paper.

Acknowledgement

A.M. acknowledges CSIR for funding of the SRF (Senior Research Fellowship). A.M. acknowledges Dr. Ibomcha Thangjam and Dr. Thillai Govindaraja for their valuable insights. S.K. acknowledges the CSIR fourth Paradigm Institute, Bangalore, for providing access to their High-Performance Computing Facility. The authors gratefully acknowledge the support and the resources provided by 'PARAM Brahma Facility' under the National Supercomputing Mission, Government of India at the Indian Institute of Science Education and Research (IISER) Pune.

Appendix A. Supplementary material

Supplementary data associated with this article can be found, in the online version, at <https://doi.org/10.1016/j.jcis.2021.05.027>.

References

- [1] R. Schlögl, Catalytic synthesis of ammonia - a never-ending story?, *Angew Chem. Int. Ed.* 42 (2003) 2004–2008.
- [2] J.W. Erisman, M.A. Sutton, J. Galloway, Z. Klimont, W. Winiwarter, How a century of ammonia synthesis changed the world, *Nat. Geosci.* 1 (2008) 636–639.
- [3] A. Afif, N. Radenahmad, Q. Cheok, S. Shams, J.H. Kim, A.K. Azad, Ammonia-fed fuel cells: a comprehensive review, *Renewable Sustainable Energy Rev.* 60 (2016) 822–835.
- [4] R. Lan, S. Tao, Direct ammonia alkaline anion-exchange membrane fuel cells, *Electrochem. Solid-State Lett.* 13 (2010) B83–B86.
- [5] F. Haber, Neue arbeitsweisen - wissenschaft und wirtschaft nach dem kriege, *Naturwissenschaften* 9 (1923) 753–756.
- [6] N. Cherkasov, O. Ibhaddon, P. Fitzpatrick, A review of the existing and alternative methods for greener nitrogen fixation, *Chem. Eng. Process.* 90 (2015) 24–33.
- [7] G. Zheng, J.M. Yan, G. Yu, Nitrogen reduction reaction, *Small Methods* 3 (2019) 1900070.

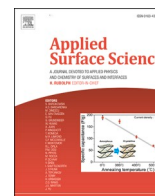
- [8] B.M. Flöser, F. Tuczek, Synthetic nitrogen fixation with mononuclear molybdenum complexes: electronic-structural and mechanistic insights from dft, *Coord. Chem. Rev.* 345 (2017) 263–280.
- [9] T. Miyazaki, H. Tanaka, H. Tanabe, M. Yuki, K. Nakajima, K. Yoshizawa, Y. Nishibayashi, Cleavage and formation of molecular dinitrogen in a single system assisted by molybdenum complexes bearing ferrocenyldiphosphine, *Angew. Chem. Int. Ed.* 53 (2014) 11488–11492.
- [10] J.J. Turner, M.B. Simpson, M. Poliakoff, W.B. Maier, M.A. Graham, Mixed carbonyl-dinitrogen compounds: synthesis and thermal stability of $\text{Cr}(\text{CO})_6 \cdot x(\text{N}_2)_x$ in liquid xenon solution and low-temperature matrixes, *Inorg. Chem.* 22 (1983) 911–920.
- [11] A.J. Kendall, M.T. Mock, Dinitrogen activation and functionalization with chromium, *Eur. J. Inorg. Chem.* (2020) 1358–1375.
- [12] R.J. Burford, A. Yeo, M.D. Fryzuk, Dinitrogen activation by group 4 and group 5 metal complexes supported by phosphine-amido containing ligand manifolds, *Coord. Chem. Rev.* 334 (2017) 84–99.
- [13] N. Ostermann, I. Siewert, Electrochemical N_2 splitting at well-defined metal complexes, *Curr. Opin. Electrochem.* 15 (2019) 97–101.
- [14] N.X. Gu, G. Ung, J.C. Peters, Catalytic hydrazine disproportionation mediated by a thiolate-bridged VFe complex, *Chem. Commun.* 55 (2019) 5363–5366.
- [15] S.L. Foster, S.I. Perez Bakovic, R.D. Duda, S. Maheshwari, R.D. Milton, S.D. Minter, M.J. Janik, J.N. Renner, L.F. Greenlee, Catalysts for nitrogen reduction to ammonia, *Nat. Catal.* (2018) 490–500.
- [16] Y. Ohki, K. Uchida, M. Tada, R.E. Cramer, T. Ogura, T. Ohta, N_2 activation on molybdenum-titanium-sulfur cluster, *Nat. Commun.* 9 (2018) 1–6.
- [17] B. Cao, A.K. Starace, O.H. Judd, I. Bhattacharyya, M.F. Jarrold, J.M. López, A. Aguado, Activation of dinitrogen by solid and liquid aluminum nanoclusters: a combined experimental and theoretical study, *J. Am. Chem. Soc.* 132 (2010) 12906–12918.
- [18] B.C. Gates, M. Flytzani-Stephanopoulos, D.A. Dixon, A. Katz, Atomically dispersed supported metal catalysts: perspectives and suggestions for future research, *Catal. Sci. Technol.* 7 (2017) 4259–4275.
- [19] L. Zhang, Y. Ren, W. Liu, A. Wang, T. Zhang, Single-atom catalyst: a rising star for green synthesis of fine chemicals, *Natl. Sci. Rev.* 5 (2018) 653–672.
- [20] L. Liu, A. Corma, Metal catalysts for heterogeneous catalysis: from single atoms to nanoclusters and nanoparticles, *Chem. Rev.* 118 (2018) 4981–5079.
- [21] M.K. Samantaray, V. D’Elia, E. Pump, L. Falivene, M. Harb, S.O. Chikh, L. Cavallo, J.-M. Basset, The comparison between single atom catalysis and surface organometallic catalysis, *Chem. Rev.* 120 (2020) 734–813.
- [22] A. Alarawi, V. Ramalingam, J.-H. He, Recent advances in emerging single atom confined two-dimensional materials for water splitting applications, *Mater. Today Energy.* 11 (2019) 1–23.
- [23] J. Zhou, Q. Sun, Magnetism of phthalocyanine-based organometallic single porous sheet, *J. Am. Chem. Soc.* 113 (2011) 15113–15119.
- [24] Y. Lu, Y. Yang, T. Zhang, Z. Ge, H. Chang, P. Xiao, Y. Xie, L. Hua, Q. Li, H. Li, et al., Photoprompted hot electrons from bulk cross-linked graphene materials and their efficient catalysis for atmospheric ammonia synthesis, *ACS Nano* 10 (2016) 10507–10515.
- [25] F. Wang, Y. Liu, H. Zhang, K. Chu, CuO/graphene nanocomposite for nitrogen reduction reaction, *ChemCatChem* 11 (2019) 1441–1447.
- [26] K. Chu, Y. Liu, Y.-B. Li, J. Wang, H. Zhang, Electronically coupled SnO_2 quantum dots and graphene for efficient nitrogen reduction reaction, *ACS Appl. Mater. Interfaces* 11 (2019) 31806–31815.
- [27] H. Yin, S.-L. Li, L.-Y. Gan, P. Wang, Pt-embedded in monolayer (gC_3N_4) as a promising single-atom electrocatalyst for ammonia synthesis, *J. Mater. Chem. A* 7 (2019) 11908–11914.
- [28] Z. Chen, J. Zhao, C.R. Cabrera, Z. Chen, Computational screening of efficient single-atom catalysts based on graphitic carbon nitride (gC_3N_4) for nitrogen electroreduction, *Small Methods* 3 (2019) 1800368.
- [29] C. Ren, Q. Jiang, W. Lin, Y. Zhang, S. Huang, K. Ding, Density functional theory study of single-atom v, nb, and ta catalysts on graphene and carbon nitride for selective nitrogen reduction, *ACS Appl. Nano Mater.* 3 (2020) 5149–5159.
- [30] X. Zhang, T. Wu, H. Wang, R. Zhao, H. Chen, T. Wang, P. Wei, Y. Luo, Y. Zhang, X. Sun, Boron nanosheet: an elemental two-dimensional (2D) material for ambient electrocatalytic N_2 -to- NH_3 fixation in neutral media, *ACS Catal.* 9 (2019) 4609–4615.
- [31] C. Liu, Q. Li, J. Zhang, Y. Jin, D.R. MacFarlane, C. Sun, Conversion of dinitrogen to ammonia on ru atoms supported on boron sheets: a dft study, *J. Mater. Chem. A* 7 (2019) 4771–4776.
- [32] H.-R. Zhu, Y.-L. Hu, S.-H. Wei, D.-Y. Hua, Single-metal atom anchored on boron monolayer ($\beta 12$) as an electrocatalyst for nitrogen reduction into ammonia at ambient conditions: a first-principles study, *J. Phys. Chem. C* 123 (2019) 4274–4281.
- [33] X. Yang, C. Shang, S. Zhou, J. Zhao, Mbenes: emerging 2d materials as efficient electrocatalysts for the nitrogen reduction reaction, *Nanoscale Horiz.* 5 (2020) 1106–1115.
- [34] L.M. Afzofra, N. Li, D.R. MacFarlane, C. Sun, Promising prospects for 2D d $_{2-d}$ M $_{3C_2}$ transition metal carbides (MXenes) in N_2 capture and conversion into ammonia, *Energy Environ. Sci.* 9 (2016) 2545.
- [35] L. Li, X. Wang, H. Guo, G. Yao, H. Yu, Z. Tian, B. Li, L. Chen, Theoretical screening of single transition metal atoms embedded in mxene defects as superior electrocatalyst of nitrogen reduction reaction, *Small Methods* 3 (2019) 1900337.
- [36] L. Zhang, L.-X. Ding, G.-F. Chen, X. Yang, H. Wang, Ammonia synthesis under ambient conditions: selective electroreduction of dinitrogen to ammonia on black phosphorus nanosheets, *Angewandte Chemie Int. Ed.* 58 (2019) 2612–2616.
- [37] X. Liang, X. Deng, C. Guo, C.-M.L. Wu, Activity origin and design principles for atomic vanadium anchoring on phosphorene monolayer for nitrogen reduction reaction, *Nano Res.* 13 (2020) 2925–2932.
- [38] Y. Zhang, H. Du, Y. Ma, L. Ji, H. Guo, Z. Tian, H. Chen, H. Huang, G. Cui, A.M. Asiri, F. Qu, L. Chen, X. Sun, Hexagonal boron nitride nanosheet for effective ambient N_2 fixation to NH_3 , *Nano Res.* 12 (2019) 919–924.
- [39] Z. Ma, Z. Cui, C. Xiao, W. Dai, Y. Lv, Q. Li, R. Sa, Theoretical screening of efficient single-atom catalysts for nitrogen fixation based on a defective bn monolayer, *Nanoscale* 12 (2020) 1541–1550.
- [40] J. Zhao, Z. Chen, Single mo atom supported on defective boron nitride monolayer as an efficient electrocatalyst for nitrogen fixation: a computational study, *J. Am. Chem. Soc.* 139 (2017) 12480–12487.
- [41] T. Yang, T.T. Song, J. Zhou, S. Wang, D. Chi, L. Shen, M. Yang, Y.P. Feng, High-throughput screening of transition metal single atom catalysts anchored on molybdenum disulfide for nitrogen fixation, *Nano Energy* 68 (2020) 104304.
- [42] H. Zhang, C. Cui, Z. Luo, MoS $_2$ -supported Fe $_2$ clusters catalyzing nitrogen reduction reaction to produce ammonia, *J. Phys. Chem. C* 124 (2020) 6260–6266.
- [43] X. Zhai, L. Li, X. Liu, Y. Li, J. Yang, D. Yang, J. Zhang, H. Yan, G. Ge, A DFT screening of single transition atoms supported on MoS $_2$ as highly efficient electrocatalysts for the nitrogen reduction reaction, *Nanoscale* 12 (2020) 10035–10043.
- [44] L. Han, X. Liu, J. Chen, R. Lin, H. Liu, S. Lü, Z. Bak, S. Liang, E. Zhao, J. Stavitski, R. Luo, H.L. Xin Adzic, Atomically dispersed molybdenum catalysts for efficient ambient nitrogen fixation, *Angew. Chem. Int. Ed.* 58 (2019) 2321.
- [45] H. Tao, C. Choi, L.-X. Ding, Z. Jiang, Z. Han, M. Jia, Q. Fan, Y. Gao, H. Wang, A.W. Robertson, S. Hong, Y. Jung, S. Liu, Z. Sun, Nitrogen fixation by Ru single-atom electrocatalytic reduction, *Chem.* 5 (2019) 204–214.
- [46] C. Ling, Y. Ouyang, Q. Li, X. Bai, X. Mao, A. Du, J. Wang, A general two-step strategy-based high-throughput screening of single atom catalysts for nitrogen fixation, *Small Methods* 3 (2019) 1800376.
- [47] D. Jiao, Y. Liu, Q. Cai, Coordination tunes the activity and selectivity of the nitrogen reduction reaction on single-atom iron catalysts: a computational study, *J. Mater. Chem. A* (2021).
- [48] X. Liu, X. Jiao, Y. Zheng, S.-Z. Qiao, Isolated boron sites for electroreduction of dinitrogen to ammonia, *ACS Catal.* 10 (2020) 1847–1854.
- [49] C. Liu, Q. Li, C. Wu, J. Zhang, Y. Jin, D.R. MacFarlane, C. Sun, Single-boron catalysts for nitrogen reduction reaction, *J. Am. Chem. Soc.* 141 (2019) 2884–2888.
- [50] S. Xiao, F. Luo, H. Hua, Z. Yang, Boron and nitrogen dual-doped carbon nanospheres for efficient electrochemical reduction of N_2 to NH_3 , *Chem. Commun.* 56 (2020) 446–449.
- [51] A. Maibam, T. Govindaraja, K. Selvaraj, S. Krishnamurty, Dinitrogen activation on graphene anchored single atom catalysts: local site activity or surface phenomena, *J. Phys. Chem. C* 123 (2019) 27492–27500.
- [52] Y. Huang, T. Yang, L. Yang, R. Liu, G. Zhang, J. Jiang, Y. Luo, P. Lian, S. Tang, Graphene-boron nitride hybrid-supported single mo atom electrocatalysts for efficient nitrogen reduction reaction, *J. Mater. Chem. A* 7 (2019) 15173–15180.
- [53] T. Zhu, S. Li, B. Ren, L. Zhang, L. Dong, L. Tan, Plasma-induced synthesis of boron and nitrogen co-doped reduced graphene oxide for super-capacitors, *J. Mater. Sci.* 54 (2019) 9632–9642.
- [54] T. Wu, H. Shen, L. Sun, B. Cheng, B. Liao, J. Shen, Nitrogen and boron doped monolayer graphene by chemical vapor deposition using polystyrene, urea and boric acid, *New J. Chem.* 36 (2012) 1385–1391.
- [55] C.R.S.V. Boas, B. Focassio, E. Marinho Jr., D.G. Larrude, M.C. Salvadori, C. Rocha Leão, D.J. dos Santos, Characterization of nitrogen doped graphene bilayers synthesized by fast, low temperature microwave plasma-enhanced chemical vapour deposition, *Scientific Reports* 9 (2019) 13715.
- [56] J. Xie, H. Dong, X. Cao, Y. Li, Computational insights into nitrogen reduction reaction catalyzed by transition metal doped graphene: comparative investigations, *Mater. Chem. Phys.* 243 (2020) 122622.
- [57] Y. Yang, J. Liu, Z. Wei, S. Wang, J. Ma, Transition metal-dinitrogen complex embedded graphene for nitrogen reduction reaction, *ChemCatChem* 11 (2019) 2821–2827.
- [58] X.-F. Li, Q.-K. Li, J. Cheng, L. Liu, Q. Yan, Y. Wu, X.-H. Zhang, Z.-Y. Wang, Q. Qiu, Y. Luo, Conversion of dinitrogen to ammonia by FeN $_3$ -embedded graphene, *J. Am. Chem. Soc.* 138 (2016) 8706–8709.
- [59] W. Zhao, L. Zhang, Q. Luo, Z. Hu, W. Zhang, S. Smith, J. Yang, Single mo1(cr1) atom on nitrogen-doped graphene enables highly selective electroreduction of nitrogen into ammonia, *ACS Catal.* 9 (2019) 3419–3425.
- [60] X. Liu, Y. Jiao, Y. Zheng, M. Jaroniec, S.-Z. Qiao, Building up a picture of the electrocatalytic nitrogen reduction activity of transition metal single-atom catalysts, *J. Am. Chem. Soc.* 141 (2019) 9664–9672.
- [61] T. He, S. Matta, A. Du, Single tungsten atom supported on n-doped graphyne as a high-performance electrocatalyst for nitrogen fixation under ambient conditions, *Phys. Chem. Phys.* 21 (2019) 1546.
- [62] K. Otake, Y. Cui, C.T. Buru, Z. Li, J.T. Hupp, O.K. Farha, Single-atom-based vanadium oxide catalysts supported on metal-organic frameworks: selective alcohol oxidation and structure-activity relationship, *J. Am. Chem. Soc.* 140 (2018) 8652–8656.
- [63] X. Liu, Y. Jiao, Y. Zheng, M. Jaroniec, S.-Z. Qiao, Synthesis of a nickel single-atom catalyst based on NiN $_4$ C $_x$ active sites for highly efficient CO $_2$ reduction utilizing a gas diffusion electrode, *ACS Appl. Energy Mater.* 3 (2020) 8739–8745.

- [64] X. Guo, S. Huang, Tuning nitrogen reduction reaction activity via controllable σ magnetic moment: A computational study of single Fe atom supported on defective graphene, *Electrochim. Acta* 284 (2018) 392–399.
- [65] C. Morell, A. Grand, A. Toro-Labbé, New dual descriptor for chemical reactivity, *J. Phys. Chem. A* 109 (2005) 205–212.
- [66] C. Morell, A. Grand, A. Toro-Labbé, Theoretical support for using the $\delta f(r)$ descriptor, *Chem. Phys. Lett.* 425 (2006) 342–346.
- [67] J. Padmanabhan, R. Parthasarathi, M. Elango, V. Subramanian, B.S. Krishnamoorthy, S. Gutierrez-Oliva, A. Toro-Labbé, D.R. Roy, P.K. Chattaraj, Multiphilic descriptor for chemical reactivity and selectivity, *J. Phys. Chem. A* 37 (2007) 9130–9138.
- [68] G. Kresse, J. Furthmüller, Efficiency of ab-initio total energy calculations for metals and semiconductors using a plane-wave basis set, *Comput. Mater. Sci.* 6 (1996) 15–50.
- [69] P.E. Blochl, Projector augmented-wave method, *Phys. Rev. B: Condens. Matter Mater. Phys.* 50 (1994) 17953–17979.
- [70] J.P. Perdew, K. Burke, M. Ernzerhof, Generalized gradient approximation made simple, *Phys. Rev. Lett.* 77 (1996) 3865–3868.
- [71] A.M. Koster, P. Calaminici, M.E. Casida, R.F. Moreno, G. Geudtner, A. Goursot, T. Heine, A. Ipatov, F. Janetzko, J.M. del Campo, et al., deMon 5.0 (2006) deMon Developers.
- [72] P. Calaminici, F. Janetzko, A.M. Koster, R. Mejia-Olvera, B. Zuniga-Gutierrez, Assessment of density functional theory optimized basis sets for gradient corrected functionals to transition metal systems: the case of small Ni_n ($n \leq 5$) clusters, *J. Chem. Phys.* 126 (2007) 1–10.
- [73] N. Godbout, D.R. Salahub, J. Andzelm, E. Wimmer, Optimization of gaussian-type basis sets for local spin density functional calculations. part i. boron through neon, optimization technique and validation, *Can. J. Phys.* 70 (1992) 560.
- [74] P. Calaminici, F. Janetzko, A.M. Köster, R. Mejia-Olvera, B. Zúñiga Gutiérrez, Density functional theory optimized basis sets for gradient corrected functionals: 3d transition metal systems, *J. Chem. Phys.* 126 (2007) 044108.
- [75] A.J.H. Wächters, Gaussian basis set for molecular wavefunctions containing third-row atoms, *J. Chem. Phys.* 52 (1970) 1033.
- [76] <http://www.theochem.uni-stuttgart.de>, 2020. Accessed: 2020-07-01.
- [77] K.L. Schuchardt, B.T. Didier, T. Elsethagen, L. Sun, V. Gurumoorthi, J. Chase, J. Li, T.L. Windus, Basis set exchange: a community database for computational sciences, *J. Chem. Inf. Model.* 47 (2007) 1045–1052.
- [78] D. Kumar, S. Krishnamurty, S. Pal, Dissociative adsorption of molecular hydrogen on bn-doped graphene-supported aluminum clusters, *J. Phys. Chem. C* 121 (2017) 26493–26498.
- [79] M.L. Cefon, T. Gomez, M. Calatayud, C. Cárdenas, Computing the fukui function in solid-state chemistry: application to alkaline earth oxides bulk and surfaces, *J. Phys. Chem. A* 124 (2020) 2826–2833.
- [80] W. Tang, E. Sanville, G. Henkelman, A grid-based bader analysis algorithm without lattice bias, *J. Phys.: Condens. Matter* 21 (2009) 084204.
- [81] R. Flores-Moreno, J.V. Melin, J. Ortiz, G. Merino, Efficient evaluation of analytic fukui functions, *J. Chem. Phys.* 129 (2008) 224105.
- [82] J.I. Martínez Araya, Why is the dual descriptor a more accurate local reactivity descriptor than fukui functions?, *J. Math. Chem.* 53 (2015) 451–465.
- [83] M.A. Nazrulla, S. Krishnamurty, K.L.N. Phani, Discerning site selectivity on graphene nanoflakes using conceptual density functional theory based reactivity descriptors, *J. Phys. Chem. C* 118 (2014) 23058–23069.
- [84] K. Momma, F. Izumi, Vesta 3 for three-dimensional visualization of crystal, volumetric and morphology data, *J. Appl. Crystallogr.* 44 (2011) 1272–1276.
- [85] P.K. Chattaraj, Chemical reactivity and selectivity: local HSAB principle versus frontier molecular orbital theory, *J. Phys. Chem. A* 105 (2001) 511–513.
- [86] B.B. Xiao, L. Yang, E.H. Song, Q. Jiang, The VN₃ embedded graphene with the improved selectivity for nitrogen fixation, *Appl. Surf. Sci.* 513 (2020) 145855.
- [87] C. Choi, S. Back, N.-Y. Kim, J. Lim, Y.-H. Kim, Y. Jung, Suppression of hydrogen evolution reaction in electrochemical N₂ reduction using single-atom catalysts: a computational guideline, *ACS Catal.* 8 (2018) 7517–7525.
- [88] W. Qiu, X.-Y. Xie, J. Qiu, W.-H. Fang, R. Liang, X. Ren, X. Ji, G. Cui, A.M. Asiri, G. Cui, B. Tang, X. Sun, High-performance artificial nitrogen fixation at ambient conditions using a metal-free electrocatalyst, *Nat. Commun.* 9 (2018) 3485.



Contents lists available at ScienceDirect

Applied Surface Science

journal homepage: www.elsevier.com/locate/apsusc

Corrigendum

Corrigendum to “Electrocatalytic nitrogen reduction on defective graphene modulated from single atom catalyst to aluminium clusters” [Appl. Surf. Sci. 623 (2023) 157024]

Ashakiran Maibam^{a,b,c}, Sailaja Krishnamurthy^{a,c,*}, Ravichandar Babarao^{b,d,*}^a Physical and Materials Division, CSIR-National Chemical Laboratory, Pune 411008, India^b School of Science, Centre for Advanced Materials and Industrial Chemistry (CAMIC), RMIT University, Melbourne 3001, Victoria, Australia^c Academy of Scientific and Innovative Research (AcSIR), Ghaziabad 201002, India^d CSIRO, Normanby Road, Clayton 3168, Victoria, Australia

The authors regret, that has an issue with the format in the affiliation of the institute that will grant PhD to the student. The correct format of

affiliation is updated as above.

The authors would like to apologise for any inconvenience caused.

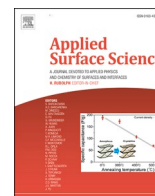
DOI of original article: <https://doi.org/10.1016/j.apsusc.2023.157024>.

* Corresponding authors at: Physical and Materials Division, CSIR-National Chemical Laboratory, Pune 411008, India (S. Krishnamurthy). School of Science, Centre for Advanced Materials and Industrial Chemistry (CAMIC), RMIT University, Melbourne 3001, Victoria, Australia (R. Babarao).

E-mail addresses: k.sailaja@ncl.res.in (S. Krishnamurthy), ravichandar.babarao@rmit.edu.au (R. Babarao).

<https://doi.org/10.1016/j.apsusc.2023.158482>

0169-4332/© 2023 The Author(s). Published by Elsevier B.V. All rights reserved.



Full Length Article

Electrocatalytic nitrogen reduction on defective graphene modulated from single atom catalyst to aluminium clusters

Ashakiran Maibam^{a,b,c}, Sailaja Krishnamurthy^{a,c,*}, Ravichandar Babarao^{b,d,*}

^a Physical and Materials Division, CSIR-National Chemical Laboratory, Pune 411 008, India

^b School of Science, Centre for Advanced Materials and Industrial Chemistry (CAMIC), RMIT University, Melbourne 3001, Victoria, Australia

^c Academy of Scientific and Innovative Research, CSIR-Human Resource Development Centre (CSIR-HRDC) Campus, Postal Staff College Area, Ghaziabad 201 002, Uttar Pradesh, India

^d CSIRO, Normanby Road, Clayton 3168, Victoria, Australia



ABSTRACT

Density Functional Theory (DFT) investigation on the most earth-abundant Al-based catalysts, has been conducted detailing its electronic properties and catalytic efficacy for nitrogen reduction at ambient condition. The Al-based catalysts have been modulated to perform as par a highly performing, but rare, Ru-single atom catalytic center by varying number of Al atoms, shape, and size. The coalesce of band-center, work function and electronic properties in metal atom catalysts along with N-N bond activation has been demonstrated to be responsible for an efficient nitrogen reduction reaction (NRR) with ΔG_{\max} of 0.78 eV in Al₅ supported on N-doped double vacancy graphene (Al₅@N₄-DVG) catalyst. Electron localization function analysis has shown a weak physisorption of N₂ in the Al-based catalysts. Projected Density of States (PDOS) illustrates the enhancement of aluminium electron density in Al₅@N₄-DVG led to enhanced orbital densities overlap of Al_p and N_p electrons. The Bader charge analysis and electronic analysis of the intermediates show efficient electron gain on the N atoms, leading to formation of NH₃ from the N_xH_y intermediates in Al₅@N₄-DVG catalyst.

1. Introduction:

With increasing demands for fuel and deteriorating fossil fuel reserves, the primary concern over the last five decades have been exploring sustainable fuels and revamping energy efficient technologies. However, the research to achieve ambient temperature reduction of nitrogen to ammonia is far from perceivable. The N₂ molecule being non-polarizable, highly inert and a strong triple bond, its dissociation energy of 940 kJ/mol is attainable only under high temperature and pressure [1]. This also lays forth the constant reliance on the highly energy intensive Haber-Bosch process of ammonia synthesis. Therefore, a scalable and viable synthetic route of N₂ reduction at ambient conditions is an absolute necessity. The electrocatalytic nitrogen reduction reaction (eNRR) is one green approach to replace Haber-Bosch process, as this process can be actuated from renewable sources of energy and ammonia synthesis can be regulated at ambient conditions [2]. However, electrochemical N₂ reduction is laced with two major challenges: a large NRR overpotential and low NH₃ faradaic efficiency (FE) caused by its competing hydrogen evolution reaction (HER) [3,4].

An extensive research in the recent years have been made to improve the Faradaic efficiency of NRR by implementing noble-earth metal

electrocatalysts (Pd, Au, Ru, etc.), transition metal electrocatalysts (Mo, Fe, Co, V, etc.), and metal-free electrocatalysts (B-doped graphene, black phosphorus, etc.) [5–12]. Efficient NRR performance at lower overpotentials have been reported mostly on metal based electrocatalysts; in particular, NRR with FE > 20% till date has been reported on Ru single atom catalysts anchored on N-doped porous carbon (21% FE) and active Mo/MoO₂ species anchored on carbon cloth (FE = 22.3% FE) [13,14]. A major advantage of such metal centers@porous carbon electrocatalyst is the synergistic utilization of buffer electrons from the two-dimensional (2D) substrates and the catalytic metal center. These metal centers route the delocalised electrons from the 2D surfaces into the antibonding orbitals of N₂ molecule leading to an activation of the N-N bond, which in turn is an essential determinant to the reduction of N₂. Consequently, this has prompted computationally driven studies on several noble and earth abundant transition metal centers@2D electrocatalysts for nitrogen reduction [15,16].

In this respect, the main group metals owing to their electronic arrangement show only specific oxidation number and restricted orbital states fail to exhibit purported N₂ reduction, except for Li and Al clusters. Li has been reported to be used directly as a catalyst for NRR or via a lithium-mediated route as metallic Li forms the only stable nitride, Li₃N

* Corresponding authors at: Physical and Materials Division, CSIR-National Chemical Laboratory, Pune 411 008, India (S. Krishnamurthy). School of Science, Centre for Advanced Materials and Industrial Chemistry (CAMIC), RMIT University, Melbourne 3001, Victoria, Australia (R. Babarao).

E-mail addresses: k.sailaja@ncl.res.in (S. Krishnamurthy), ravichandar.babarao@rmit.edu.au (R. Babarao).

<https://doi.org/10.1016/j.apsusc.2023.157024>

Received 30 November 2022; Received in revised form 13 February 2023; Accepted 12 March 2023

Available online 15 March 2023

0169-4332/© 2023 The Author(s). Published by Elsevier B.V. This is an open access article under the CC BY-NC-ND license (<http://creativecommons.org/licenses/by-nc-nd/4.0/>).

in ambient conditions. The Li-mediated NRR electrocatalysts are known to exhibit high NRR FE closely approaching 100% in a high-concentration imide-based lithium salt interface [17]. However, the implementation of Li for NRR becomes unsustainable due to its limited presence in the earth's crust which correspond to only 0.002–0.006 wt %. On the other hand, Al being the most abundant metal in earth's crust, has been less explored for ambient nitrogen reduction. Notable reports have been made on Al-based electrocatalyst for ammonia fixation include Li-aided Al doped graphene, aluminium (III) coordination complex, Al-Co₃O₄/NF, MoAlB single crystals, and Al-N₂ battery with an Al - ionic liquid electrolyte. Huang et al implemented Al metal as a dopant on graphene as a ligating center to the N_xH_y intermediates generated by Li + ion aided reduction of N₂ to ammonia at ambient conditions [18]. A substantial advancement in NRR performance of Al-electrocatalysts had been realized by Berben and co-workers when an aluminium (III) complex with 0.3 M Bu₄NPF₆ THF and DMAPH + electrolyte exhibited ammonia production at – 1.16 V (vs. SCE) with 21% FE in ambient condition [19]. However, Al as a catalytic metal center for nitrogen fixation has been reported in urchin like Al-doped Co₂O₃ nanospheres (Al-Co₃O₄/NF) with a FE of 6.25% at – 0.2 V vs RHE by Yuan et. al, and in a multicomponent boride, MoAlB wherein the layered electrocatalyst reported by Ma and co-workers showed ammonia production with a FE of 30.1% at –0.05 V vs RHE [20,21]. The highest FE of 51.2% at –0.1 V for Al-based electrocatalyst in ammonia production has been reported by Zhi and co-workers in a rechargeable Al-N₂ battery composed of a graphene-supported Pd (graphene/Pd) cathode and Al anode with an ionic liquid electrolyte (AlCl₄/1-butyl-3-methylimidazolium chloride) [22]. The study reveals a higher feasibility of AlN ($\Delta G = -287$ kJ/mol) formation as compared to Li₃N ($\Delta G = -154$ kJ/mol), thereby revealing a more spontaneous nitriding reaction in Al over Li. However, AlN is extremely susceptible to air unlike its lithium counterpart, and it gets easily oxidised, thereby the catalytic activity of Al gets thwarted.

Fundamentally, Al being an element of boron family possess similar electronic distribution and certain similarities in electronic properties can be expected. Boron has been reported in several metal-free electrocatalyst as a dopant or catalytic center that can hold N₂ and influence ammonia production via an electron “donor-acceptor” mechanism [23,24]. While the “donor-acceptor” mechanism is unlikely to occur in Al atom catalyst due to a lower electronegativity of Al (1.61) as compared to B (2.01), Al clusters have been reported to chemisorb N₂ and activate the N-N bond effectively. Aguado et al. reported the chemisorption of N₂ and N-N bond activation upto 1.65 Å on Al₄₄ nanoclusters with an energy barrier of 3.4 eV [25]. The N-N bond activation barrier becomes as low as 0.65 eV in smaller Al-clusters, in particular, Al₅ cluster on BN-graphene, as observed by Kumar and co-workers [26]. Henceforth, it is important to probe into these smaller Al clusters and explore the plausibility of implementing them as NRR electrocatalyst. Furthermore, the experimental realization of Al-based catalysts on graphene is not far-fetched research as synthesis of pristine Al-clusters with pulsed laser vaporization can be dated back to 2007 by Neal et. al. [27] With experimental improvements brought about by electron-beam irradiation, single atom substitution on graphene has been reported by Zagler and co-workers [28]. However, the evidence of graphene-Al clusters/nanoparticle composites is as well-known as other graphene-metal composites and the synthesis route follows the conventional chemical exfoliation or powder metallurgy technique [29–31]. In this work, we make a radical comparison of the electronic properties of NRR active Ru and Mo single atom to Al atom and Al-clusters (Al_n) supported on N-doped double vacancy graphene (N₄-DVG). The study focuses on modulating the electronic and catalytic properties of atomic Al catalysts by inducing changes in their shape and size.

2. Computational details:

All metal atoms and clusters supported N-doped double vacancy graphene (M@N₄-DVG) systems, as shown in Fig. 1 are optimized using Density Functional Theory (DFT) calculations with Vienna ab – initio Simulation Package (VASP.5.4.4) [32]. The ionic-electronic interactions on all systems are sampled with a $2 \times 2 \times 1$ Monkhorst-Pack kpoint grid and 520 eV energy cut-off with a generalized gradient approximation Perdew-Burke-Ernzerhof (PBE) functional [33]. All M@N₄-DVG systems have been relaxed with DFT-D3 corrections to incorporate long range forces till the atomic forces and energies converge to 0.005 eV/Å and 10⁻⁵ eV/atom, respectively [34]. Electronic property analysis has been carried out to evaluate the density of states and Bader charges of the M@N₄-DVG systems by considering a higher kpoint grid of ($9 \times 9 \times 1$) Monkhorst-Pack grid [35]. The thermal stability of the M@N₄-DVG systems analysed through Ab initio molecular dynamics (AIMD) simulations carried out in an NVT ensemble at 298 K described with a Nose-Hoover thermostat at 3 ps time step for 10 ps [36]. Furthermore, the feasibility of achieving chemically stable M@N₄-DVG systems is realized via the binding energies (E_b) of atomic metal catalysts and clusters on the N₄-DVG system computed using the equation,

$$E_b = (E_{M@N_4-DVG}) - (E_{N_4-DVG}) - E_M \quad (1)$$

where, $E_{M@N_4-DVG}$ is the total electronic energy of Ru, Mo, Al metal atom catalysts or Al_n (n = 2–7) clusters supported N₄-DVG systems, E_{N_4-DVG} is the total electronic energy of N₄-DVG systems and E_M is the electronic energy of Ru, Mo, Al single atom catalysts or Al_n clusters. Following this, the N₂ chemisorption efficacy on the M@N₄-DVG catalysts is investigated via the end-on and side-on modes of N₂ adsorption; and the adsorption energy, E_{ads} is computed using the equation,

$$E_{ads} = (E_{M@N_4-DVG-N_2}) - (E_{M@N_4-DVG}) - E_{N_2} \quad (2)$$

where, $E_{M@N_4-DVG-N_2}$ is the total electronic energy of M@N₄-DVG system after N₂ adsorption, $E_{M@N_4-DVG}$ and E_{N_2} are the total electronic energy of M@N₄-DVG systems and free N₂ molecule, respectively.

The free energy of the N_xH_y intermediates involved in the Nitrogen Reduction Reaction (NRR) is represented by the Gibbs free energy change, ΔG and the computational Standard Hydrogen Electrode model of Nørskov et al. has been implemented to calculate ΔG using the following equation [37].

$$\Delta G = \Delta E + \Delta ZPE - T \Delta S(3)$$

where, ΔE and ΔZPE is the change in electronic energy and zero-point energy respectively, ΔS is the change in entropy at room temperature, T is room temperature (298.15 K). The zero-point energy and entropy corrections are computed from the non-negative vibrational frequencies of the gas phase species in each intermediate. The potential rate-determining step (PDS) for the reaction is intermediate step with the highest free energy change (ΔG_{max}) and the limiting potential, U_L is equal to $-(\Delta G_{max})/e$. For an electrocatalyst under applied potential, the free energy is calculated as, $\Delta G_{NRR} = \Delta E + \Delta ZPE - T\Delta S + neU + \Delta G_{pH}$, where n is the number of electrons, U is the applied electrode potential equivalent to the limiting potential, U_L and ΔG_{pH} is the free energy correction to pH of the solvent. The pH correction to free energy is represented by $\Delta G_{pH} = 2.303 \times k_B T \times \text{pH}$, where k_B is the Boltzmann constant. The pH value is assumed to be zero as the overpotential of NRR is unaffected by the change in pH. [38–39].

3. Results and Discussions:

The electronic stability of the M@N₄-DVG systems as evaluated from the binding energy calculations show the metal single atoms (Ru, Mo and Al) to be positioned in the N tetra-coordinated vacancy in the graphene plane, while the Al_n clusters are anchored with one Al atom occupying the double vacant site in graphene plane (i.e., in-plane) and

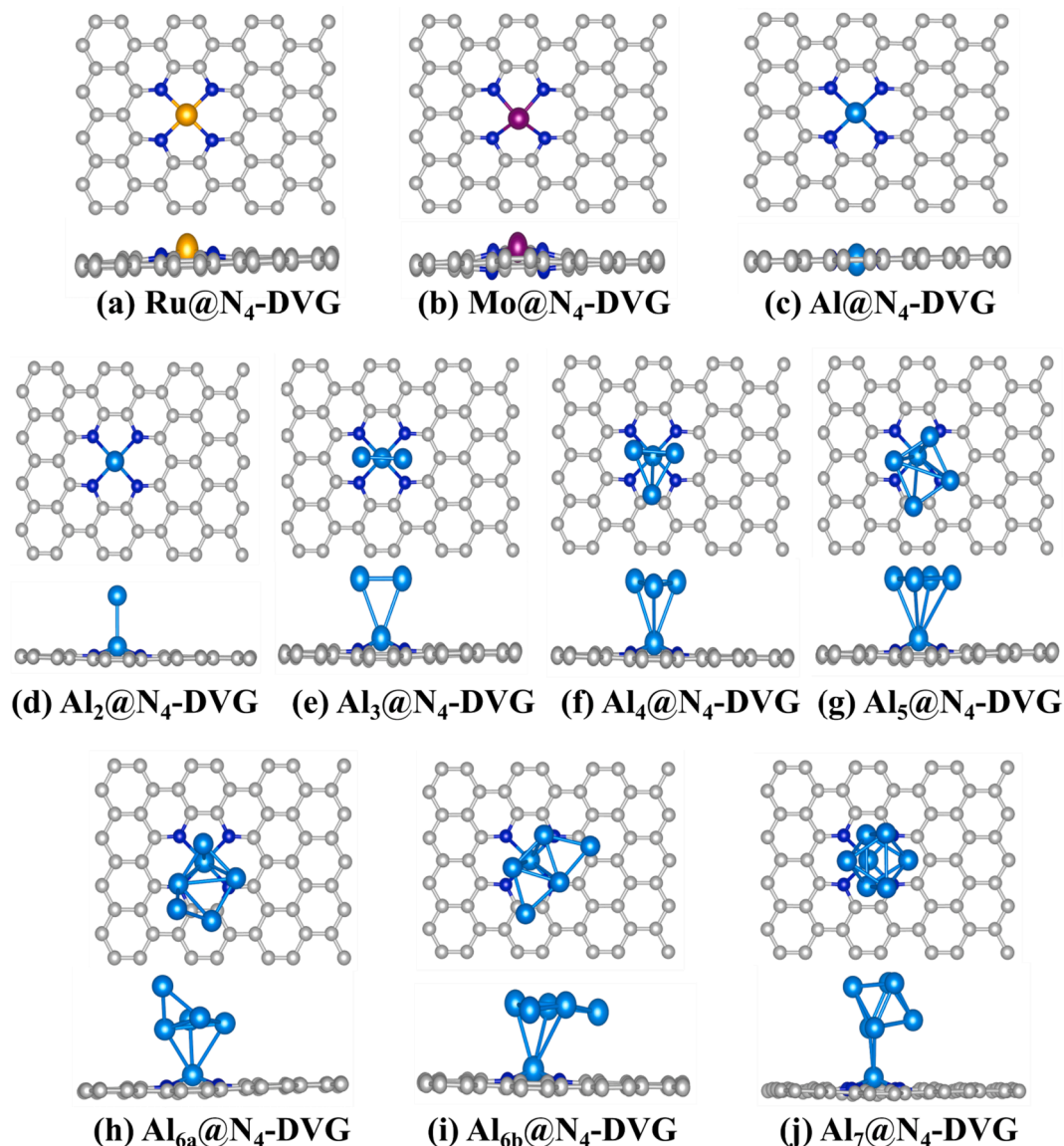


Fig. 1. Top and side views of Ru and Mo single atom supported on N-doped double vacancy graphene considered as reference to Al atom and Al-clusters (Al_n) supported N-doped double vacancy graphene ($M@N_4$ -DVG).

the remaining Al atoms bound to the in-plane Al-atom. Mo single atom ($Mo@N_4$ -DVG) has been found to possess the highest binding energy of -9.78 eV followed by $Ru@N_4$ -DVG with -8.19 eV and $Al@N_4$ -DVG with -7.81 eV. The Al_n clusters supported N_4 -DVG systems show a gradual decrease in their binding energies as the size of the clusters increase. The Al_n clusters with a planar geometry and higher coordination with the in-plane Al are more stable with binding energies ranging from -7.1 to -7.5 eV as provided in [Supporting Information, Table S1](#). On the other hand, $Al_7@N_4$ -DVG system with a nearly spherical structure and two coordinated Al atoms to the in-plane Al atom show the least binding energy of -5.82 eV. Larger clusters are thus, not considered in this study as they tend to form spherical and symmetric structures. For ambient nitrogen fixation, the thermal stability of all $M@N_4$ -DVG systems are further analysed through AIMD simulations at 298 K and small structural distortions are observed in $Al_4@N_4$ -DVG, $Al_5@N_4$ -DVG and $Al_7@N_4$ -DVG while both Al_6 clusters showed large distortions after 10 ps, see [Supporting Information Figure S1](#). Henceforth, all the $M@N_4$ -DVG systems, except $Al_{6a}@N_4$ -DVG and $Al_{6b}@N_4$ -DVG are eligible candidates to be implemented as stable catalysts at room temperature and further electrocatalytic studies will be carried out on the stable

catalysts.

The catalytic activity of a system, being an inflection of electronic properties and charge distribution or transfer efficiency, can be primitively assessed from its work function (Φ) and p-band center. While catalysts with a lower work-function will require a smaller energy to activate the N_2 molecule, a more positive p-band center will ascertain the p-orbitals of the active centers are closer to the Fermi level and possess higher carrier density. A comparative plot of work function and p-band centers of Ru, Mo, Al metal atoms and Al_n clusters in [Fig. 2\(a\)](#) shows the Ru single atom with most positive p-band center of -5.25 eV and work function of 4.29 eV. The p-band centers of Ru and Mo has been computed in place of d-band center to have a consistent comparison with Al which possess only p-orbitals. Ru, being the best performing metal single atom catalyst on N-doped graphene, is used as a reference for another active transition metal, Mo and our metal atom of interest Al and its clusters, Al_n . $Al@N_4$ -DVG system with Al single atom shows a much lower (i.e., negative) work function than the Ru or Mo counterparts, however its p-band center is relatively more negative (-5.74 eV) thereby inferring a lower charge carrier density. Although the work function gradually increases with the increase in size of Al_n clusters and

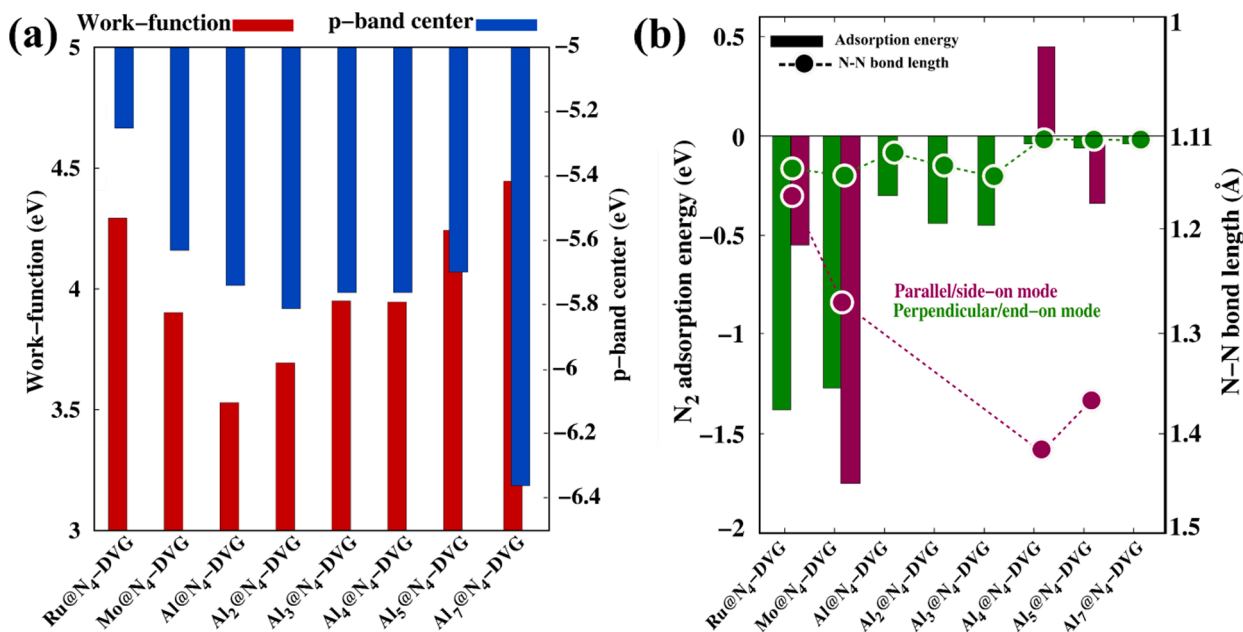


Fig. 2. (a) Comparative plot of work function and p-band center of all M@N₄-DVG systems, red and blue histograms represent the work function and p-band center respectively. (b) N₂ adsorption energies and N-N bond elongation on the M@N₄-DVG systems, the histograms represent N₂ adsorption energy while the points represent N-N bond length in Å. (For interpretation of the references to colour in this figure legend, the reader is referred to the web version of this article.)

a decrease in catalytic activity is expected, the p-band centers show an interesting trend with the Al₅@N₄-DVG system has its p-band center at -5.69 eV and more positive than Al@N₄-DVG. This primitive screening of catalytic activity is ratified through the N₂ adsorption strengths of the M@N₄-DVG catalysts. While the presence of d-orbitals in Ru and Mo single atom catalyst allow both parallel and perpendicular modes of N₂ adsorption on Ru@N₄-DVG and Mo@N₄-DVG, the most optimal adsorption mode and site of N₂ on the Al_n@N₄-DVG catalysts are found to vary with the change in shape and size of the Al cluster. The most exothermic adsorption of N₂ in perpendicular and parallel mode has been considered as N₂ adsorption sites on Al_n@N₄-DVG catalysts and are shown in Table S2 of Supporting Information. From Fig. 2(b), it is evident that lower (or positive) p-band center in Ru@N₄-DVG influences the exothermic adsorption of N₂, while a lower work function is responsible for the same in Mo@N₄-DVG. The higher activity and exothermic adsorption of N₂ on Al₅ cluster can also be ratified due to the shape and orientation of the Al atoms that are available for interaction with the incoming N₂ molecule. As the Al_n cluster size increases, one Al

atom lies in-plane to the N-doped graphene sheet while the remaining Al atoms orient themselves with 3 or 4 as its coordination number. While most Al_n clusters prefer to form 3-coordination leading to triangular facets, the stable Al₅@N₄-DVG catalyst prefer to form a rectangular facet with four Al-atoms exposed as catalytic sites from the ELF plots as shown in Table S3 of Supporting Information. Furthermore, the Bader charge analysis provided in Table S3 ensures these exposed Al atoms to be electron rich while the Al-atom ingrained to the graphene plane is positively charged or electron deficient. This further corroborates to the lower N-N activation of Al single atom as compared to electron rich Al-atoms lying above the graphene plane which can easily render electrons to N₂ molecule.

The N₂ adsorption energies on Al single atom and its clusters are relatively lower than the transition metal counterparts; however, a similar trend of work-function influencing adsorption can be observed in Al@N₄-DVG, Al₂@N₄-DVG and Al₃@N₄-DVG while the p-band center becomes accountable for Al₅@N₄-DVG. More interestingly, Al₅@N₄-DVG is the only Al_n based catalyst that shows exothermic side-on N₂

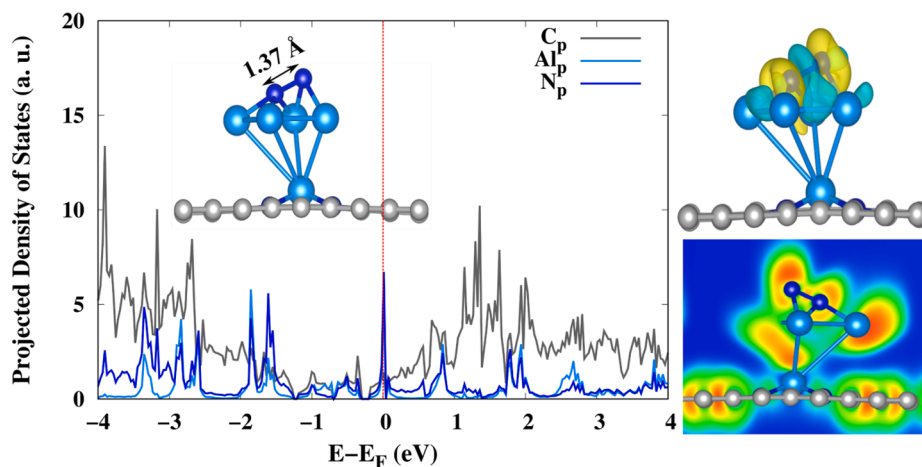


Fig. 3. Projected density of states (PDOS) with Charge density difference (CDD) and Electron location function (ELF) plots of side-on N₂ adsorbed on Al₅@N₄-DVG. The CDD and ELF plots were made using VESTA software.[40].

adsorption (-0.34 eV) and N-N bond activation (1.37 Å) brought about with the nitrogen atoms attached to different Al centers. Fig. 3 shows the overlap of Al p-orbitals ($\text{Al}_5@N_4\text{-DVG}$) and N p-orbitals (N_2) in the Fermi region of PDOS and electron localization function (ELF) plot with localized electrons on the N_2 . Besides $\text{Al}_5@N_4\text{-DVG}$, the systems of interest that show exothermic N_2 adsorption and N-N bond activation are $\text{Ru}@N_4\text{-DVG}$, $\text{Mo}@N_4\text{-DVG}$, $\text{Al}@N_4\text{-DVG}$, $\text{Al}_2@N_4\text{-DVG}$ and $\text{Al}_3@N_4\text{-DVG}$. The electron localization functions of adsorbed N_2 on the above-mentioned $M@N_4\text{-DVG}$ catalysts are provided in Supporting Information, Figure S2. ELF plots with higher electron density concentration on the atoms will correspond to ionic bonding while contribution from covalent bonding can be accounted when the electron density is concentrated on the respective bond between two atoms. A prominent electron localization on N_2 can be observed in $\text{Ru}@N_4\text{-DVG}$ and

$\text{Mo}@N_4\text{-DVG}$ systems inferring an ionic bonding or stronger binding which can be interpreted as chemisorption led by electron transfer, whereas a more covalent bonding between Al atoms and N_2 molecule can be observed in the Al-based catalysts inferring towards physisorption of N_2 . The presence of higher electron density in Al_n clusters as compared to Al single atom can be a major contributor in enhancing the catalytic activity of Al metal for NRR. This is supported by the PDOS plot of N_2 adsorbed $\text{Al}@N_4\text{-DVG}$ catalyst in Figure S3, Supporting Information shows minimal contribution from the Al p-orbitals. However, in aluminium cluster catalysts the contribution of Al p-orbitals is found to increase gradually along with a shift towards the Fermi level due to the conducting nature of Al. The distribution of electron density as seen from ELF plots and smaller orbital overlap between Al and N_2 can be inferred as N_2 physisorption on the Al-based catalysts and the N_2

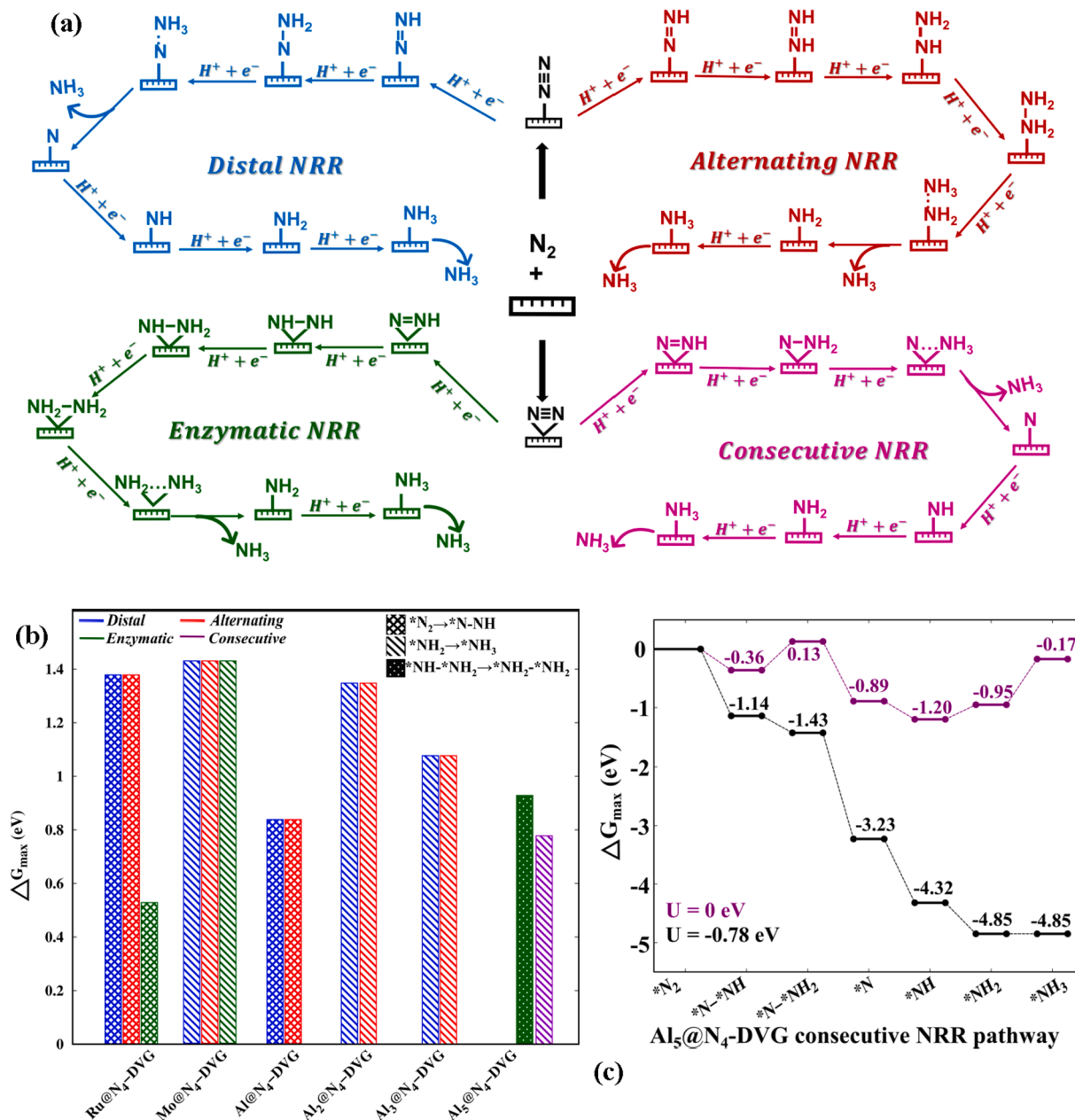


Fig. 4. (a) Possible mechanistic routes of nitrogen reduction reaction; distal and alternating route for N_2 adsorbed in end-on mode, while enzymatic and consecutive route is observed in side-on adsorbed N_2 . (b) ΔG_{\max} (in eV) with potential rate determining step on all active $M@N_4\text{-DVG}$ catalysts. (c) Consecutive route of nitrogen reduction on $\text{Al}_5@N_4\text{-DVG}$ catalyst computed under applied voltage of 0 V (dark-violet line) and -0.78 V (black line) respectively, the Gibbs free is calculated following the computational hydrogen electrode model of Nørskov. [37]. (For interpretation of the references to colour in this figure legend, the reader is referred to the web version of this article.)

adsorption energies corroborate to this finding.

Following this screening of N_2 activation, the mechanisms of nitrogen reduction reaction (NRR) on all possible routes, Fig. 4(a), are explored on the select $M@N_4$ -DVG catalysts that show exothermic N_2 adsorption. Nitrogen reduction on $Ru@N_4$ -DVG and $Mo@N_4$ -DVG catalysts with Ru and Mo single atom center have been investigated via the distal, alternating and enzymatic route. The consecutive route has been found unfeasible as the $*N-NH_2$ intermediate could not be realized on the single atoms. Computational calculations on $Al@N_4$ -DVG, $Al_2@N_4$ -DVG and $Al_3@N_4$ -DVG catalysts that show end-on N_2 adsorption have been restricted only for the distal and alternating route. Finally, $Al_5@N_4$ -DVG catalyst which showed exothermic side-on N_2 adsorption have been investigated for enzymatic and consecutive route of NRR, with multiple Al atoms being involved in N_2 adsorption, the consecutive route becomes feasible in this catalyst. The free energy diagrams of the above-mentioned routes of NRR reaction coordinates on stable $M@N_4$ -DVG catalysts are provided in Supporting Information, Figure S4-S9. The reduction of N_2 to NH_3 is a multistep reaction with six elementary protonation steps and release of two NH_3 molecules, the usual uphill reaction steps are the first ($*N_2 \rightarrow *N_2H$) and last protonation ($*NH_2 \rightarrow *NH_3$) steps in all routes along with the fourth protonation ($*N_2H_3 \rightarrow *N_2H_4$) step in alternating route. The uphill elementary step with the highest energy barrier becomes the potential rate determining step (PDS) of NRR and a summary of all possible routes and the PDS with ΔG_{max} values on all $M@N_4$ -DVG catalysts as shown in Fig. 4(b). The ΔG_{max} value on Ru single atom, reported as the best catalyst, has been found to be 0.53 eV in the first protonation step. However, Mo single atom which has been reported as an active NRR catalyst shows a relatively high energy barrier of 1.43 eV in the last protonation step. The ΔG_{max} values on the Al-based catalysts are 0.84 eV ($*N_2 \rightarrow *N_2H$), 1.35 eV ($*NH_2 \rightarrow *NH_3$) and 1.08 eV ($*NH_2 \rightarrow *NH_3$) in $Al@N_4$ -DVG, $Al_2@N_4$ -DVG and $Al_3@N_4$ -DVG respectively. While Al single atom and smaller Al-clusters show a relatively higher NRR performance than Mo single atom, the NRR performance improves to 0.78 eV in $Al_5@N_4$ -DVG catalyst that showed exothermic side-on N_2 adsorption. Furthermore, upon application of an external potential 0.78 eV as shown in Fig. 4(c), the elementary ($*NH_2 \rightarrow *NH_3$) protonation steps become exothermic, thereby inferring this catalyst can also be implemented as an electrocatalyst.

A detailed electronic analysis of the Bader charges as shown in Fig. 5 (a) of $Ru@N_4$ -DVG shows a correlation between the charge transfer from Ru to the N atoms. Most importantly, the PDS fourth protonation step, $*NH-NH_2 \rightarrow *NH_2-NH_2$ step has been found to show a large difference between Ru charge and N charges, thus signifying that the electronic barrier essential to bring about ammonia production. $Al@N_4$ -DVG catalyst that show a preference of the alternating route with better stabilized $*N_xH_y$ intermediates exhibit contrastingly higher Bader charge difference in the last protonation step although the PDS is the first protonation step, $*N_2 \rightarrow *N-NH$. This is in concordance to an uphill step of 0.81 eV observed in NH_3 formation as shown in the Supporting Information, Figure S6. Furthermore, in the ELF plot shown in Fig. 5(b) inset for NH_3 intermediate, a relatively higher electron density can be observed in the N atoms from the Al single atom along with Al-N covalent bond further stabilising the system. This possess a major challenge in the functionality and applicability of $Al@N_4$ -DVG catalyst, as the active Al metal site gets deactivated due to strong adsorption efficacy of NH_3 , which is -0.90 eV exergonic from N_2 adsorption. Interestingly, $Al_5@N_4$ -DVG catalyst behaves similar to $Ru@N_4$ -DVG catalyst and shows a large variation in Bader charge of Al and N only in its PDS step, i. e., $*NH_2 \rightarrow NH_3$ step, Fig. 5(c). Additionally, the dissemination of electron density in the constituting Al atoms in Al_5 center leads to efficient electron transfer to N atoms, leading to formation of NH_3 without the manifestation of any covalent bond between Al center and N atoms of N_xH_y intermediates. The corresponding NH_3 adsorption on $Al_5@N_4$ -DVG is exoergic by -0.41 eV as compared to N_2 adsorption and the possibility of catalytic center deactivation or poisoning can be reduced as 5-Al

metal centers are involved. Another similarity of the $Al_5@N_4$ -DVG catalyst to the $Ru@N_4$ -DVG catalyst is an exclusive NRR selectivity over the competing hydrogen evolution reaction (HER), Fig. 5(d). An interesting outlook can be accounted on the NRR performance of $Al_5@N_4$ -DVG catalyst in the presence of water solvent, details of implementing solvent model and calculations are discussed in Supplementary Information. N_2 molecule being non-polar, its adsorption energy in water should be endothermic as compared to its value in vacuum; while the protonated N_xH_y intermediates possess dipoles and water as a solvent enhances the formation of N_xH_y intermediates. Thereby, a lower adsorption energy of N_2 and higher free energies of N_xH_y intermediates on $Al_5@N_4$ -DVG system can be expected with solvent effects and the same has been compared with the energetics in vacuum for the consecutive route of NRR on $Al_5@N_4$ -DVG, as seen in Fig. 5(e). In the presence of water, the adsorption energy of N_2 on $Al_5@N_4$ -DVG system reduces from -0.06 eV to -0.05 eV in perpendicular mode and -0.37 eV to -0.27 eV in parallel mode. As anticipated, the following protonation steps leading to formation of N_xH_y intermediates are energetically favourable with more negative ΔG values when compared to vacuum state (Figure S10). The corresponding ΔG_{max} reduces from 0.78 eV to 0.70 eV for the consecutive route and PDS shift from the last protonation step, $*NH_2 \rightarrow NH_3$ in vacuum to fourth protonation step, $*N \rightarrow *NH$ in water solvent. This can be attributed to the solvation of the $*N$ intermediate with open coordination sites and the water pockets hindering the transport of H^+ to form the $*NH$ intermediate. Contrastingly, the protonation of $*NH_2$ intermediate to NH_3 intermediate which was less feasible in vacuum becomes more facile as water can enhance the transport of protons and formation of NH_3 . This also substantiates that $Al_5@N_4$ -DVG catalyst can be rendered for lab-scale experimentations in aqueous conditions.

A comparison of the NRR performance on the Al-based catalysts has been highlighted in Table S4 of Supplementary Information. The ΔG_{max} of NRR on $Al_5@N_4$ -DVG catalyst has been observed to be higher than several homoatomic or heteroatomic bimetallic transition metal catalysts, however in several cases of homoatomic catalysts, i.e., $Ru_2@PC_6$, $Cu_2@NG$, $Ni_4@Gr$ catalysts the NRR performance is on-par and higher in some cases. It can also be noted that Al_5 cluster anchored on BN-doped graphene showed the lowest barrier for N-N bond activation in the study carried out by Kumar et al. and our studies concur to their findings. [26] Aluminium clusters on N-doped double vacancy graphene, despite a less attractive NRR performance than transition metal single atoms, perform as par the Ru single atom catalyst with a high selectivity for NRR and a trade-off can be achieved when researchers aim for scalable and sustainable catalyst for ammonia production.

4. Conclusions

In this study, DFT investigation has been made to conform an earth-abundant metal Al to conform and exhibit similar catalytic properties to another rare earth transition metal, Ru for nitrogen reduction. Al-based catalysts have been modulated into a Ru-single atom like catalytic center by varying number of Al centers. A detailed study on the electronic and thermal stability of the model catalysts have been made via AIMD studies and the catalytic properties are primitively scoured through their inherent electronic properties. An analysis of the electron localization function and projected density of states plots shows a strong chemisorption in the transition metal, while a weak physisorption is observed in the Al-based catalysts. The change in shape and size of the atomic Al clusters reflects to a change in their corresponding catalytic properties, and Al_5 supported on N-doped double vacancy graphene (N_4 -DVG) conform to Ru-single atom like catalyst. Bader charge analysis of the NRR reaction intermediates show a similarity in the large charge transfer to N atoms from Ru single atom and Al_5 center, with respective ΔG_{max} of 0.53 eV and 0.78 eV in $Ru@N_4$ -DVG and $Al_5@N_4$ -DVG catalysts. Despite a higher free energy change in the potential rate determining step, the high NRR selectivity of $Al_5@N_4$ -DVG catalyst makes it a

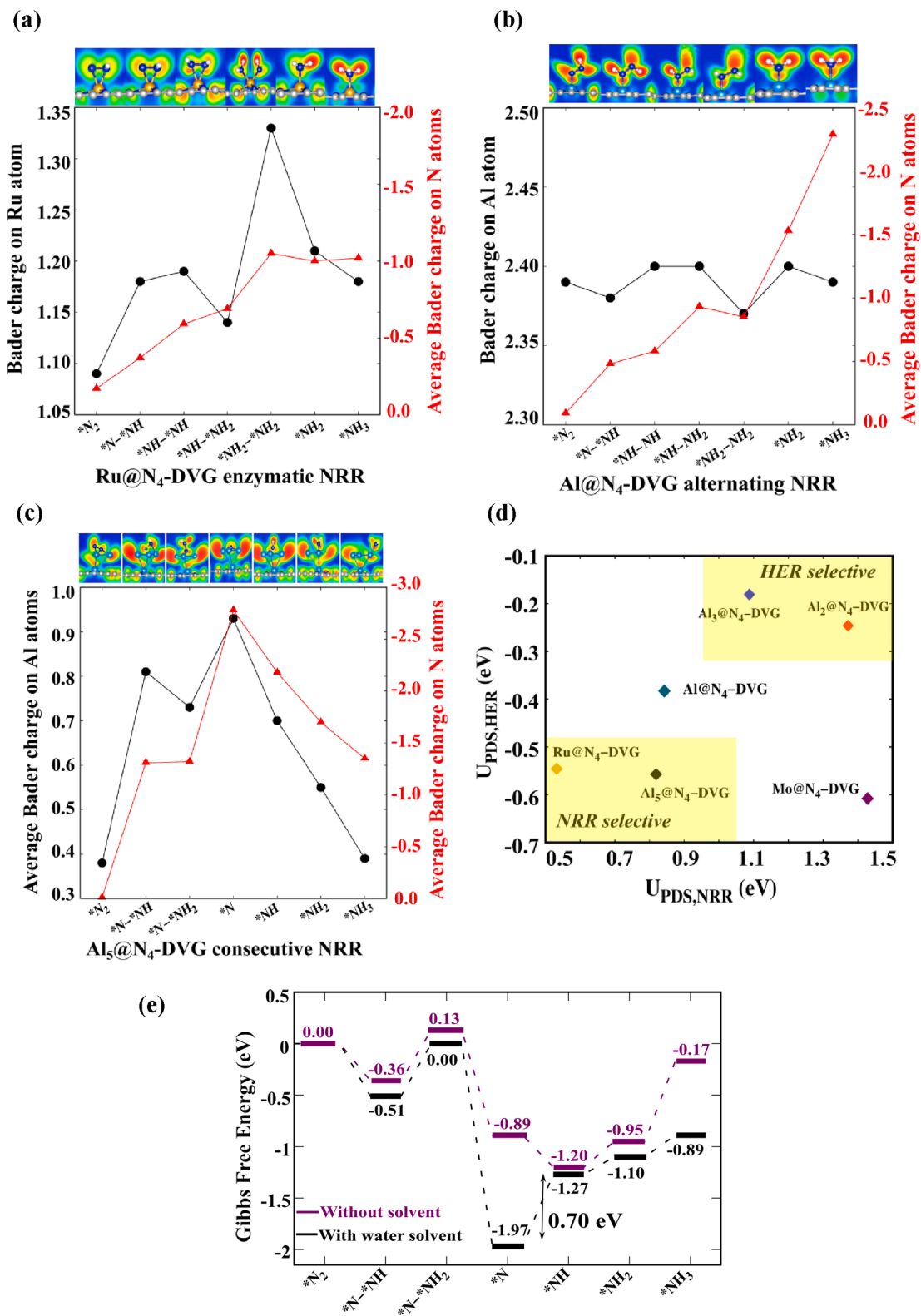


Fig. 5. Bader charge analysis on the metal centers and N atoms of the N_xH_y intermediates of enzymatic, alternating and consecutive NRR routes on (a) Ru@N₄-DVG, (b) Al@N₄-DVG, (c) Al₅@N₄-DVG, respectively (d) NRR vs HER selectivity plot of the active M@N₄-DVG catalysts, Ru@N₄-DVG and Al₅@N₄-DVG show exclusive NRR selectivity as compared to the rest of the Al-based catalysts; (e) Free energy diagram of consecutive NRR on Al₅@N₄-DVG without and with water solvent, and the corresponding ΔG_{max} reduces from 0.78 eV to 0.70 eV.

highly attractive catalyst for electrocatalytic ammonia production. The understanding from this work can be used to further the research on developing Al-based catalysts for nitrogen fixation and feasible ambient ammonia production with the most abundant metal, aluminium.

CRedit authorship contribution statement

Ashakiran Maibam: Conceptualization, Methodology, Formal analysis, Investigation, Data curation, Writing – original draft. **Sailaja Krishnamurthy:** Software, Validation, Supervision, Writing – original draft. **Ravichandar Babarao:** Conceptualization, Software, Validation, Supervision, Writing – original draft.

Declaration of Competing Interest

The authors declare that they have no known competing financial interests or personal relationships that could have appeared to influence the work reported in this paper.

Data availability

No data was used for the research described in the article.

Acknowledgement

A.M. acknowledges AcSIR-RMIT for hosting the Joint-PhD Program and RMIT University for research funding. The authors gratefully acknowledge National Computing Infrastructure (NCI), and Pawsey supercomputing centre, Australia for providing the computational resources.

Appendix A. Supplementary material

Supplementary data to this article can be found online at <https://doi.org/10.1016/j.apsusc.2023.157024>.

References

- N. Cherkasov, A.O. Ibadon, P. Fitzpatrick, A review of the existing and alternative methods for greener nitrogen fixation, *Chem. Eng. Process. Process Intensif.* 90 (2015) 24–33, <https://doi.org/10.1016/j.ccep.2015.02.004>.
- C.J.M. Van Der Ham, M.T.M. Koper, D.G.H. Heterscheid, Challenges in reduction of dinitrogen by proton and electron transfer, *Chem. Soc. Rev.* 43 (2014) 5183–5191, <https://doi.org/10.1039/c4cs00085d>.
- D. Liu, M. Chen, X. Du, H. Ai, K.H. Lo, S. Wang, S. Chen, G. Xing, X. Wang, H. Pan, Development of Electrocatalysts for Efficient Nitrogen Reduction Reaction under Ambient Condition, *Adv. Funct. Mater.* 31 (2021) 1–36, <https://doi.org/10.1002/adfm.202008983>.
- D. Chanda, R. Xing, T. Xu, Q. Liu, Y. Luo, S. Liu, R.A. Tufa, T.H. Dolla, T. Montini, X. Sun, Electrochemical nitrogen reduction: recent progress and prospects, *Chem. Commun.* 57 (2021) 7335–7349, <https://doi.org/10.1039/d1cc01451j>.
- J. Wang, L. Yu, L. Hu, G. Chen, H. Xin, X. Feng, Ambient ammonia synthesis via palladium-catalyzed electrohydrogenation of dinitrogen at low overpotential, *Nat. Commun.* 9 (2018), <https://doi.org/10.1038/s41467-018-04213-9>.
- M. Nazemi, M.A. El-Sayed, Electrochemical synthesis of ammonia from N₂ and H₂O under ambient conditions using pore-size-controlled hollow gold nanocatalysts with tunable plasmonic properties, *J. Phys. Chem. Lett.* 9 (2018) 5160–5166, <https://doi.org/10.1021/acs.jpclett.8b02188>.
- Z. Geng, Y. Liu, X. Kong, P. Li, K. Li, Z. Liu, J. Du, M. Shu, R. Si, J. Zeng, Achieving a record-high yield rate of 120.9 μg NH₃/mgcat⁻¹h⁻¹ for N₂ electrochemical reduction over Ru single-atom catalysts, *Adv. Mater.* 30 (2018) 2–7, <https://doi.org/10.1002/adma.201803498>.
- J. Han, X. Ji, X. Ren, G. Cui, L. Li, F. Xie, H. Wang, B. Li, X. Sun, MoO₃ nanosheets for efficient electrocatalytic N₂ fixation to NH₃, *J. Mater. Chem. A.* 6 (2018) 12974–12977, <https://doi.org/10.1039/c8ta03974g>.
- M. Wang, S. Liu, T. Qian, J. Liu, J. Zhou, H. Ji, J. Xiong, J. Zhong, C. Yan, Over 56.55% Faradaic efficiency of ambient ammonia synthesis enabled by positively shifting the reaction potential, *Nat. Commun.* 10 (2019) 1–8, <https://doi.org/10.1038/s41467-018-08120-x>.
- W. Guo, Z. Liang, J. Zhao, B. Zhu, K. Cai, R. Zou, Q. Xu, Hierarchical cobalt phosphide hollow nanocages toward electrocatalytic ammonia synthesis under ambient pressure and room temperature, *Small, Methods.* 2 (2018) 1–6, <https://doi.org/10.1002/smdt.201800204>.
- X. Yu, P. Han, Z. Wei, L. Huang, Z. Gu, S. Peng, J. Ma, G. Zheng, Boron-doped graphene for electrocatalytic N₂ Reduction, *Joule.* 2 (2018) 1610–1622, <https://doi.org/10.1016/j.joule.2018.06.007>.
- L. Zhang, L.X. Ding, G.F. Chen, X. Yang, H. Wang, Ammonia synthesis under ambient conditions: selective electroreduction of dinitrogen to ammonia on black phosphorus nanosheets, *Angew. Chemie - Int. Ed.* 58 (2019) 2612–2616, <https://doi.org/10.1002/anie.201813174>.
- H. Tao, C. Choi, L.X. Ding, Z. Jiang, Z. Han, M. Jia, Q. Fan, Y. Gao, H. Wang, A. W. Robertson, S. Hong, Y. Jung, S. Liu, Z. Sun, Nitrogen fixation by Ru single-atom electrocatalytic reduction, *Chem.* 5 (2019) 204–214, <https://doi.org/10.1016/j.chempr.2018.10.007>.
- J. Chen, H. Wang, Z. Wang, S. Mao, J. Yu, Y. Wang, Redisposition of Mo-based catalysts and the rational design of super small-sized metallic Mo species, *ACS Catal.* (2019) 5302–5307, <https://doi.org/10.1021/acscatal.8b04634>.
- A. Maibam, T. Govindaraja, K. Selvaraj, S. Krishnamurthy, Dinitrogen activation on graphene anchored single atom catalysts: Local site activity or surface phenomena, *J. Phys. Chem. C.* 123 (2019) 27492–27500, <https://doi.org/10.1021/acs.jpcc.9b06757>.
- A. Maibam, S. Krishnamurthy, Nitrogen activation to reduction on a recyclable V-SAC/BN-graphene heterocatalyst sifted through dual and multiphilic descriptors, *J. Colloid Interface Sci.* 600 (2021) 480–491, <https://doi.org/10.1016/j.jcis.2021.05.027>.
- H.-L. Du, M. Chatti, R.Y. Hodgetts, P.V. Cherepanov, C.K. Nguyen, K. Matuszek, D. R. MacFarlane, A.N. Simonov, Electroreduction of nitrogen at almost 100% current-to-ammonia efficiency, *Nature.* 609 (2022), <https://doi.org/10.1038/s41586-022-05108-y>.
- Y.H. Tian, S. Hu, X. Sheng, Y. Duan, J. Jakowski, B.G. Sumpter, J. Huang, Non-transition-metal catalytic system for N₂ reduction to NH₃: A Density Functional Theory study of Al-doped graphene, *J. Phys. Chem. Lett.* 9 (2018) 570–576, <https://doi.org/10.1021/acs.jpclett.7b03094>.
- T.J. Sherbow, E.J. Thompson, A. Arnold, R.L. Sayler, R.D. Britt, L.A. Berben, Electrochemical reduction of N₂ to NH₃ at low potential by a molecular aluminum complex, *Chem. - A Eur. J.* 25 (2019) 454–458, <https://doi.org/10.1002/chem.201804454>.
- X.W. Lv, Y. Liu, R. Hao, W. Tian, Z.Y. Yuan, Urchin-like Al-doped Co₃O₄ nanospheres rich in surface oxygen vacancies enable efficient ammonia electro-synthesis, *ACS Appl. Mater. Interfaces.* 12 (2020) 17502–17508, <https://doi.org/10.1021/acsami.0c00647>.
- Y. Fu, P. Richardson, K. Li, H. Yu, B. Yu, S. Donne, E. Kisi, T. Ma, Transition metal aluminum boride as a new candidate for ambient-condition electrochemical ammonia synthesis, *Nano-Micro Lett.* 12 (2020) 1–13, <https://doi.org/10.1007/s40820-020-0400-z>.
- Y. Guo, Q. Yang, D. Wang, H. Li, Z. Huang, X. Li, Y. Zhao, B. Dong, C. Zhi, A rechargeable Al-N₂ battery for energy storage and highly efficient N₂ fixation, *Energy Environ. Sci.* 13 (2020) 2888–2895, <https://doi.org/10.1039/d0ee01241f>.
- A. Maibam, S. Krishnamurthy, M. Ahmad Dar, Electrocatalytic nitrogen reduction directed through the p-band center of boron on B₅AC@Mo₂C, *Mater. Adv.* 3 (2022) 592–598, <https://doi.org/10.1039/d1ma00953b>.
- A. Maibam, R. Babarao, S. Krishnamurthy, Doped 2D VX₂ (X = S, Se, Te) monolayers as electrocatalysts for ammonia production: A DFT based study, *Appl. Surf. Sci.* 602 (2022), 154401, <https://doi.org/10.1016/j.apsusc.2022.154401>.
- B. Cao, A.K. Starace, O.H. Judd, I. Bhattacharyya, M.F. Jarrold, J.M. López, A. Aguado, Activation of dinitrogen by solid and liquid aluminum nanoclusters: A combined experimental and theoretical study, *J. Am. Chem. Soc.* 132 (2010) 12906–12918, <https://doi.org/10.1021/ja103356r>.
- D. Kumar, S. Pal, S. Krishnamurthy, N₂ activation on Al metal clusters: Catalytic role of BN-doped graphene support, *Phys. Chem. Chem. Phys.* 18 (2016) 27721–27727, <https://doi.org/10.1039/c6cp03342c>.
- C.M. Neal, G.A. Breaux, B. Cao, A.K. Starace, M.F. Jarrold, Improved signal stability from a laser vaporization source with a liquid metal target, *Rev. Sci. Instrum.* 78 (2007), <https://doi.org/10.1063/1.2751393>.
- G. Zagler, M. Stecher, A. Trentino, F. Kraft, C. Su, A. Postl, M. Längle, C. Pesenhofer, C. Mangler, E. Harriet Ahlgren, A. Markevich, A. Zettl, J. Kotakoski, T. Susi, K. Mustonen, Beam-driven dynamics of aluminium dopants in graphene 9 (2022), <https://doi.org/10.1088/2053-1583/ac6c30>.
- B. Somasekaran, A. Thirunarayananaswamy, I. Palaniavel, Synthesis of graphene and fabrication of aluminium-Grp nanocomposites: A review, *Mater. Today Proc.* 50 (2021) 2436–2442, <https://doi.org/10.1016/j.matpr.2021.10.262>.
- V. Khanna, V. Kumar, S.A. Bansal, Mechanical properties of aluminium-graphene/carbon nanotubes (CNTs) metal matrix composites: Advancement, opportunities and perspective, *Mater. Res. Bull.* 138 (2021), 111224, <https://doi.org/10.1016/j.materresbull.2021.111224>.
- I.G. Brodova, A.N. Petrova, I.G. Shirinkina, D.Y. Rasposienko, L.A. Yolshina, R. V. Muradyrov, S.V. Razorenov, E.V. Shorokhov, Mechanical properties of submicrocrystalline aluminium matrix composites reinforced by “in situ” graphene through severe plastic deformation processes, *J. Alloys Compd.* 859 (2021), 158387, <https://doi.org/10.1016/j.jallcom.2020.158387>.
- G. Kresse, J. Furthmüller, Efficiency of ab-initio total energy calculations for metals and semiconductors using a plane-wave basis set, *Comput. Mater. Sci.* 6 (1996) 15–50, [https://doi.org/10.1016/0927-0256\(96\)00008-0](https://doi.org/10.1016/0927-0256(96)00008-0).
- J.P. Perdew, K. Burke, M. Ernzerhof, Generalized gradient approximation made simple, *Phys. Rev. Lett.* 77 (1996) 3865–3868, <https://doi.org/10.1103/PhysRevLett.77.3865>.
- S. Grimme, J. Antony, S. Ehrlich, H. Krieg, A consistent and accurate ab initio parametrization of density functional dispersion correction (DFT-D) for the 94 elements H-Pu, *J. Chem. Phys.* 132 (2010), <https://doi.org/10.1063/1.3382344>.

- [35] W. Tang, E. Sanville, G. Henkelman, A grid-based Bader analysis algorithm without lattice bias, *J. Phys. Condens. Matter.* 21 (2009), <https://doi.org/10.1088/0953-8984/21/8/084204>.
- [36] S. Nosé, A unified formulation of the constant temperature molecular dynamics methods, *J. Chem. Phys.* 81 (1984) 511–519, <https://doi.org/10.1063/1.447334>.
- [37] J.K. Nørskov, J. Rossmeisl, A. Logadottir, L. Lindqvist, J.R. Kitchin, T. Bligaard, H. Jónsson, Origin of the overpotential for oxygen reduction at a fuel-cell cathode, *J. Phys. Chem. B.* 108 (2004) 17886–17892, <https://doi.org/10.1021/jp047349j>.
- [38] J. Zhao, Z. Chen, Single Mo atom supported on defective boron nitride monolayer as an efficient electrocatalyst for nitrogen fixation: a computational study, *J. Am. Chem. Soc.* 139 (2017) 12480–12487, <https://doi.org/10.1021/jacs.7b05213>.
- [39] C. Ling, X. Niu, Q. Li, A. Du, J. Wang, Metal-free single atom catalyst for N₂ fixation driven by visible light, *J. Am. Chem. Soc.* 140 (2018) 14161–14168, <https://doi.org/10.1021/jacs.8b07472>.
- [40] K. Momma, F. Izumi, VESTA: A three-dimensional visualization system for electronic and structural analysis, *J. Appl. Crystallogr.* 41 (2008) 653–658, <https://doi.org/10.1107/S0021889808012016>.



Cite this: DOI: 10.1039/d1ma00953b

Electrocatalytic nitrogen reduction directed through the p-band center of boron on $\text{B}_{\text{SAC}}@\text{Mo}_2\text{C}^\dagger$

Ashakiran Maibam,^{id} ^{ab} Sailaja Krishnamurty,^{id} ^{*ab} and Manzoor Ahmad Dar,^{id} ^{*c}

Greener modes of ammonia synthesis via the electrocatalytic route have been investigated on pristine and defective Mo_2C based monolayers anchored with metal-free boron atom catalysts. Boron single atom catalysts (SACs) on the defective Mo_2C monolayer has been found to activate N_2 strongly with an adsorption energy of -1.92 eV and reduce it to NH_3 efficiently with a significantly low overpotential of 0.41 eV. The exothermic adsorption of N_2 and low overpotential for the nitrogen reduction reaction (NRR) appertain to the p-band center of the boron atom catalyst and charge transfer between the adsorbed N_2 and the catalyst, respectively. This work brings forth the correlation between electron occupancy on the boron center and NRR catalytic efficiency on a metal-free $\text{SACs}@\text{Mo}_2\text{C}$ monolayer couple, thereby serving as a lead in designing metal free electrocatalysts for the NRR.

Received 13th October 2021,
Accepted 6th November 2021

DOI: 10.1039/d1ma00953b

rsc.li/materials-advances

1 Introduction

With the rise in global temperature and greenhouse gas emissions, most industrial processes aim to achieve carbon neutrality. However, one process with an extremely high carbon footprint accounting for 6% of global CO_2 emissions and the consumption of approximately 1–2% of global energy¹ is the Haber–Bosch² ammonia synthesis process. With ammonia being an irreplaceable precursor in agriculture, various industries and energy applications,^{3,4} there is an urgent need to develop greener techniques for NH_3 synthesis through photocatalytic, electrocatalytic or photo-electrocatalytic routes to meet the current demands.^{5,6} The optimal goal towards achieving ammonia economy is to develop a catalyst that reduces N_2 to NH_3 under ambient conditions like the nitrogenase enzyme. The electrocatalytic route of nitrogen fixation is an attractive alternative owing to its efficiency and environment-friendly nature.^{7,8} However, with N_2 being a highly stable molecule with a N–N triple bond energy of 940 kJ mol⁻¹, the kinetics associated with the electrocatalytic nitrogen reduction reaction (NRR) are sluggish and the faradaic efficiency is low.⁷ As a

result, the competing hydrogen evolution reaction (HER) is usually preferred over the sluggish NRR. Therefore, it is essential to design new and smart materials with high electrical conductivity that have the capability to subjugate the HER and enhance the NRR. Several scarce metals such as Ru,^{9,10} Au^{11,12} and Pd^{13,14} have been reported as highly efficient electrocatalysts for the NRR with faradaic efficiencies of up to 36.6%,¹³ their cost and availability are issues that cannot be overcome. Hence, identifying cost effective electrocatalysts based on earth abundant metals such as Mo, Fe, and Co, *etc.* as potential alternatives for the NRR is the need of the hour.¹⁵

Notably, Mo metal is present as an active centre in nitrogenase enzymes, and possesses the requisite electronic structure to capture N_2 molecules and has been extensively studied for the NRR.¹⁶ Several other Mo-based two-dimensional (2D) materials, nanoparticles and nanoclusters, single atom catalysts (SACs) and organometallic complexes have been reported as efficient catalysts for the NRR.^{17–26} While Mo-containing organic and inorganic complexes efficiently adsorb and form stable dinitrogen complexes, their application as electrocatalysts or electrodes are not warranted.¹⁸ Mo clusters and SACs, on the other hand, require a conducting/semi-conducting support for further usage as electrocatalysts.^{19,20,22,27} In this regard, Mo-based 2D materials such as MoS_2 ,^{24,28–31} MXenes (Mo_2C)^{32–34} and MBenes (Mo_2B_2)^{35,36} are appealing electrocatalysts owing to their high electrical conductivity and the presence of active Mo metal centres. These 2D materials not only show high hydrophilicity, stability and conductivity but are interesting from the catalytic aspect of nitrogen reduction as the Mo metal is accessible to the nitrogen molecule. Compared

^a Physical and Materials Division, CSIR-National Chemical Laboratory, Pune 411 008, India. E-mail: sailaja.raaj@gmail.com

^b Academy of Scientific and Innovative Research, CSIR-Human Resource Development Centre (CSIR-HRDC) Campus, Postal Staff College area, Gaziabad, 201 002, Uttar Pradesh, India

^c Department of Chemistry, Islamic University of Science and Technology, Awantipora, Jammu and Kashmir 192122, India. E-mail: manzoor.dar@islamicuniversity.edu.in

† Electronic supplementary information (ESI) available. See DOI: 10.1039/d1ma00953b



to MBenes, MXenes have been extensively investigated experimentally for the electrocatalytic NRR.^{32,37–39}

While computational studies on the electrochemical applications of Mo₂C based 2D materials have been extensively carried out, they have rarely been explored for the electrocatalytic NRR. One notable study on the electrocatalytic application of Mo₂C for the NRR was made recently by Zhang *et al.* wherein Mo₂C monolayers were investigated for the NRR through density functional theory (DFT) calculations.³⁴ It would be imperative to recollect that effective strategies to fine tune and improve the N₂ binding efficacy on a 2D monolayer are structural modifications and incorporating active atomic centers on it.⁴⁰ Thereby, pristine and defective Mo₂C monolayers coupled with a metal free single atom catalyst, in particular boron, are expected to enhance the N₂ adsorption and inherently improve the NRR process. Several experimental and computational studies have reported boron based metal free catalysts on 2D materials to remarkably augment the electrocatalytic NRR by promoting N₂ adsorption and inhibiting the HER.^{41–43} The boron center behaves as a Lewis acid with empty p-orbitals, thereby resulting in a strong π–π* interaction with N₂ and less energy demanding subsequent protonation steps for the NRR.^{44,45}

The correlation between charge transfer from the catalytic center and nitrogen reduction efficacy is one aspect of paramount importance that has not been explored to date. Thus, in the present work, we conducted a comprehensive investigation to provide a complete picture concerning the fundamental understanding of nitrogen activation and reduction on active boron atoms anchored on a pristine Mo₂C monolayer. Specifically, the coupling effect of boron single atom catalysts with defects on the Mo₂C monolayer and its influence on nitrogen activation and reduction was thoroughly investigated. The p-band center and electronic structure of 2D Mo₂C monolayers upon the anchoring of non-metallic boron atoms directly influences their NRR catalytic efficiency. Based on our results, we found that a single boron atom catalyst anchored on a defective Mo₂C monolayer can effectively produce NH₃ with a record low overpotential of 0.41 eV.

2 Computational details

All DFT calculations were carried out with the Vienna *ab initio* Simulation Package (VASP).⁴⁶ The generalized gradient approximation (GGA) and the Perdew–Burke–Ernzerhof (PBE)⁴⁷ functional has been employed with an energy cutoff of 532 eV to describe all electron core–interactions. A DFT-D3 correction method has been incorporated to account for the long-range van der Waals (vdW) interactions.⁴⁸ All the catalyst systems sampled with a (5 × 5 × 1) Monkhorst–Pack k-point grid and a vacuum space of 20 Å along the Z-direction are relaxed until the atomic energy and forces converge to 10^{−5} eV per atom and 0.005 eV Å^{−1}, respectively. For the density of states and electronic structure calculations, a higher (11 × 11 × 1) Monkhorst–Pack k-point grid has been employed.

The stability of atomic boron catalysts on Mo₂C and its analogues is evaluated in terms of binding energy, E_b which is calculated by using the equation,

$$E_b = (E_{B_{\text{cat}}@Mo_2C}) - (E_{Mo_2C}) - (E_{B_{\text{cat}}}) \quad (1)$$

where, $E_{B_{\text{cat}}@Mo_2C}$ and E_{Mo_2C} are the total electronic energies of the 2D Mo₂C monolayer with and without atomic boron catalysts and $E_{B_{\text{cat}}}$ is the electronic energy of atomic boron. The adsorption of N₂ on the 2D Mo₂C monolayer has been computed for the parallel and perpendicular modes and the efficiency of these materials to chemisorp N₂ molecule has been calculated in terms of the N₂ adsorption energy, (E_{ads}) as given below,

$$E_{\text{ads}} = (E_{B_{\text{cat}}@Mo_2C-N_2}) - (E_{B_{\text{cat}}@Mo_2C}) - (E_{N_2}) \quad (2)$$

where, $E_{B_{\text{cat}}@Mo_2C-N_2}$, $E_{B_{\text{cat}}@Mo_2C}$ and E_{N_2} are the total electronic energies of N₂ adsorbed systems, B_{cat}@Mo₂C and free N₂ molecules, respectively.

The Gibbs free energy change, ΔG in every protonation step of the NRR has been calculated by employing the computational SHE (standard hydrogen electrode) model proposed by Nørskov *et al.*⁴⁹ using the equation,

$$\Delta G = \Delta E + \Delta ZPE - T\Delta S \quad (3)$$

where, ΔE is the change in electronic energy, ΔZPE is the change in zero-point energy, T is the room temperature (298.15 K) and ΔS is the change in entropy. The zero-point energies and entropy contributions are calculated by considering the vibrational frequencies of the adsorbed gas phase species. Furthermore, the overpotential for the electrocatalytic NRR on the Mo₂C monolayer and its analogues has been calculated as $\eta = U_{\text{SHE}} - U_{\text{PDS}}$, where $U_{\text{SHE}} = -0.16$ eV, is the standard reduction potential of N₂ to NH₃ and $U_{\text{PDS}} = \Delta G_{\text{max}}/e$ for the NRR pathway.

3 Results and discussion

3.1 N₂ adsorption on B_{cat}Mo₂C

The stability of atomic boron catalysts on Mo₂C is one of the fundamental prerequisites for their implementation as electrocatalysts for the NRR. Boron has been anchored on conventional pristine 1T-Mo₂C as a single atom catalyst (SAC) or a diatom catalyst (DAC), respectively referred to as B_{SAC}@Mo₂C and B_{DAC}@Mo₂C from now onwards. The geometric structures of the B_{SAC}@Mo₂C and B_{DAC}@Mo₂C catalysts are presented in Fig. S2 (see the ESI†). Anchoring B_{DAC} on Mo₂C was found to be more feasible with a binding energy of −7.07 eV as compared to B_{SAC} (−6.90 eV). The 2D Mo₂C monolayer was then subjected to two major surface modifications: a Mo-vacancy and defective Mo₂C with non-metal dopants as shown in Fig. 1. Mo₂C with a vacant Mo-site is referred to as Mo₂C–Mo_{vac} and defective Mo₂C obtained by replacing one Mo atom from the surface with metal-free dopants is designated as Mo₂C–X_{def}, where X = B, C, N, P and S. On these Mo-vacant and defective analogues of Mo₂C, we next adsorbed B single atoms to create a metal-free



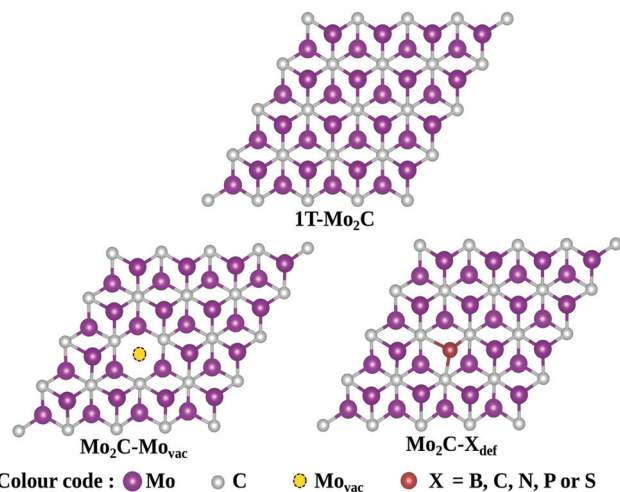


Fig. 1 The model 2D 1T-Mo₂C monolayer with surface modifications considered in this study.

catalyst couple for nitrogen activation and reduction. The binding energy of B_{SAC} ranges from -5.35 eV on the Mo₂C-Mo_{vac} catalyst to -6.25 eV, -5.37 eV, -7.92 eV, -5.81 eV and -4.77 eV respectively, on the Mo₂C-B_{def}, Mo₂C-C_{def}, Mo₂C-N_{def}, Mo₂C-P_{def} and Mo₂C-S_{def} catalysts. The exothermic binding energies of the boron atom catalysts on all Mo₂C analogues illustrates the stability of the boron SAC integrated on the defective Mo₂C monolayers.

We next investigated the N₂ adsorption efficacy and electronic properties of the B_{cat}@Mo₂C catalysts through the d-band centre of Mo, the p-band centre of B and the projected density of states (PDOS) with reference to pristine 1T-Mo₂C. Fig. 2 highlights the N₂ adsorption energies of the B_{cat}@Mo₂C catalysts with reference to 1T-Mo₂C and the correlation between N₂ adsorption with the d-band center of Mo and the p-band center of B. B_{SAC}@Mo₂C and B_{DAC}@Mo₂C exhibit a lower exothermic

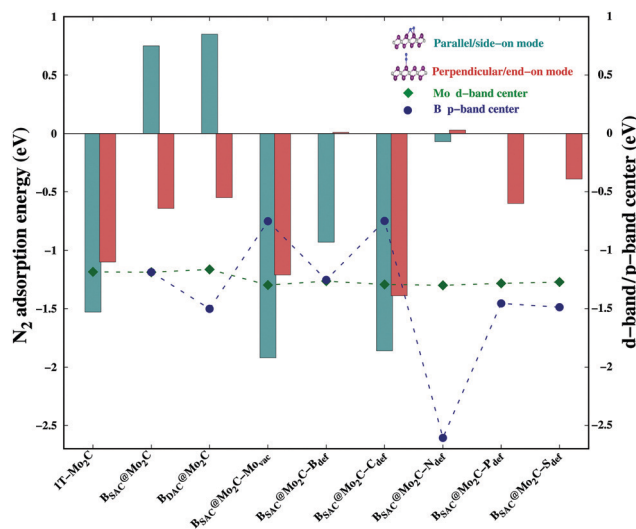


Fig. 2 N₂ adsorption energies in different modes, and the Mo d-band center and B p-band center on different B_{cat}@Mo₂C catalysts.

end-on mode of dinitrogen adsorption with E_{ads} values of -0.64 eV and -0.55 eV, respectively with respect to -1.10 eV on 1T-Mo₂C. It can also be noted that there are no significant changes in the Mo d-band center when B_{SAC} and B_{DAC} are anchored on Mo₂C, however the B p-center on B_{SAC}@Mo₂C is more positive than that of B_{DAC}@Mo₂C. A more positive B p-band center infers that the B p-orbitals are closer to the Fermi level ($E_F = 0$ eV), which in turn leads to the feasible adsorption of N₂. Generating a Mo-vacancy on the Mo₂C monolayer leads to a less positive Mo d-band center, but in contrast, the B p-band becomes more positive, which in turn leads to higher chemisorption (-1.92 eV) of N₂ on B_{SAC}@Mo₂C-Mo_{vac}. Moreover, on analysing the Bader charges on the B_{cat} centers, all the B_{cat} centers are found to be negatively charged, thereby implying that there is a charge transfer from the Mo₂C monolayer to B. The only exception being the B_{SAC}@Mo₂C-N_{def} and B_{SAC}@Mo₂C-S_{def} systems with positively charged or nearly neutral B_{cat} centers, respectively. Interestingly, these two systems possess a more negative B p-band center as compared to the rest of the systems, and thereby show lower exothermic N₂ adsorption. It is also important to note that a higher exothermic N₂ adsorption is not only influenced by the B p-band center but also by a more pronounced overlap between the π orbitals of the B and N atoms. The parallel/side-on mode of N₂ adsorption involves two B-N bonds, and results in two peaks in the PDOS plot (inset) with a greater electron density overlap (see Fig. 3(a)) compared to a single B-N bond for the perpendicular/end-on mode of N₂ adsorption (Fig. 3(b)) on B_{SAC}@Mo₂C-Mo_{vac}. The B_{SAC}@Mo₂C-X_{def} catalysts follow a similar pattern of N₂ adsorption. For instance, B_{SAC}@Mo₂C-C_{def} with a more positive B p-band center exhibits better chemisorption of N₂ when compared to B_{SAC}@Mo₂C-N_{def} with a highly negative p-band center of B. It can be established that the adsorption and activation of N₂ is influenced by the p-band center of B_{cat} on the B-anchored Mo₂C catalysts. Interestingly, it was noticed that the N₂ chemisorption efficacy of B_{SAC} with a Mo-vacancy is on a par with that of B_{SAC} with C-defective Mo₂C, while the rest of the non-metals, *i.e.* B, P, S and N show moderate to minimal adsorption of N₂. Apart from the B p-band center, the N₂ adsorption trends could also be rationalized in terms of electronic properties such as charge difference density (CDD) and the PDOS plots provided in Fig. S3 of the ESI.† The PDOS plots also show the very interesting phenomenon of a synergistic effect between the C from the Mo₂C and B_{cat} centers. The systems that show a higher exothermic N₂ adsorption, in turn show a more pronounced overlap between the C p-orbitals and B p-orbitals, thus the synergistic effect of C and B enhances the N₂ adsorption efficiency in the B_{cat}@Mo₂C catalysts.

3.2 N₂ reduction on B_{cat}@Mo₂C catalysts

Finally we explored the thermodynamics for the reduction of N₂ to NH₃ on the B_{cat}@Mo₂C catalysts that showed strong exothermic N₂ chemisorption. Also the NRR pathways on B_{SAC}@Mo₂C and B_{DAC}@Mo₂C were analysed to deduce whether the role of a second B atom enhances or inhibits the reduction process. Among the defective monolayers with surface modification,



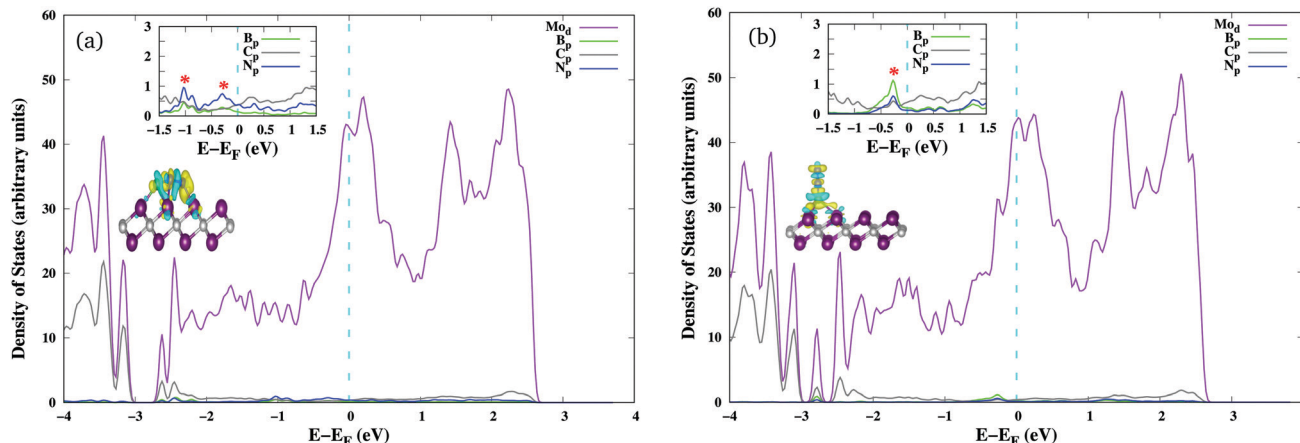
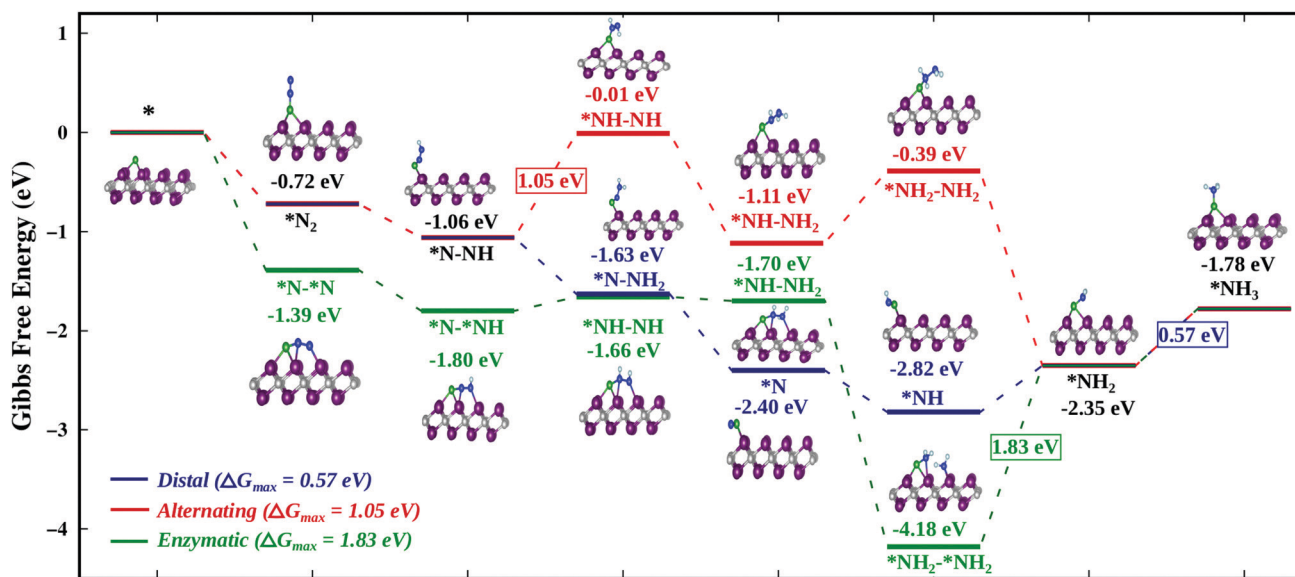


Fig. 3 PDOS of N_2 adsorbed on $B_{SAC}@Mo_2C-Mo_{vac}$ with the insets showing hybridisation of the N p-orbitals and B p-orbitals and the CDD plot generated isosurface density set to $0.003 e \text{ \AA}^{-3}$. (a) PDOS and CDD plots of N_2 adsorbed on $B_{SAC}@Mo_2C-Mo_{vac}$ via the parallel/side-on mode. (b) PDOS and CDD plots of N_2 adsorbed on $B_{SAC}@Mo_2C-Mo_{vac}$ via the perpendicular/end-on mode.

$B_{SAC}@Mo_2C-Mo_{vac}$ and $B_{SAC}@Mo_2C-C_{def}$ were considered as both showed highly exothermic chemisorption of dinitrogen in both the parallel as well as the perpendicular mode. Previous studies have revealed that the reduction of N_2 can proceed via three pathways, *viz.* distal or alternating and enzymatic, respectively, for N_2 adsorbed in the perpendicular and parallel modes. On the $B_{SAC}@Mo_2C$ and $B_{DAC}@Mo_2C$ catalysts with N_2 adsorbed preferentially in an end-on mode, the NRR pathway was explored through the distal and alternating routes as shown in Fig. S4 and S5 of the ESI.† The last protonation step, *i.e.* $*NH_2 \rightarrow *NH_3$ has been found to be the potential determining step (PDS) for nitrogen reduction on $B_{SAC}@Mo_2C$ and $B_{DAC}@Mo_2C$ for both the distal and alternating route with a ΔG_{max} of 1.10 eV and 0.90 eV, respectively. The corresponding

overpotentials, η for reducing nitrogen to ammonia on the two catalysts are therefore, 0.94 eV and 0.74 eV, respectively. It would be interesting to note that $B_{SAC}@Mo_2C$, which is more exergonic towards N_2 (-0.15 eV) as compared to $B_{SAC}@Mo_2C$ (-0.05 eV) follows a more uphill first protonation step (0.21 eV) and a complementary more uphill PDS. For the $B_{SAC}@Mo_2C-Mo_{vac}$ monolayer with one Mo-atom vacancy that shows exothermic N_2 adsorption in the side-on as well as end-on modes, the NRR mechanisms for all three possible routes were computed and are presented in Fig. 4. Although, the parallel mode of N_2 adsorption is more exergonic than the perpendicular mode, and we expect the enzymatic route to be favoured over the distal or alternating route, the limiting potential for the NRR on the $B_{SAC}@Mo_2C-Mo_{vac}$ catalyst was



Free Energy Diagram of NRR on $B_{SAC}@Mo_2C-Mo_{vac}$ substrate

Fig. 4 Free energy profile of the nitrogen reduction reaction via the distal, alternating and enzymatic routes on the $B_{SAC}@Mo_2C-Mo_{vac}$ catalyst.



found to be 0.57 eV ($^*\text{NH}_2 \rightarrow ^*\text{NH}_3$) for the distal, 1.05 eV ($^*\text{N-NH} \rightarrow ^*\text{NH-NH}$) for the alternating and 1.83 eV ($^*\text{NH}_2\text{-}^*\text{NH}_2 \rightarrow ^*\text{NH}_2$) for the enzymatic route. The distal route, which involves the protonation of only one nitrogen atom to form the first ammonia molecule, can be seen to show downhill reaction steps until the fourth protonation step. The preference for the distal mode could be accounted for by less steric hindrance caused by subsequent protonation on the nitrogen atoms. It is interesting to note that the $\text{B}_{\text{SAC}}@\text{Mo}_2\text{C-Mo}_{\text{vac}}$ catalyst shows a high affinity for capturing the $^*\text{NH}_2$ moiety as it can be found from the enzymatic route. The $^*\text{NH}_2\text{-}^*\text{NH}_2$ intermediate shows a highly exergonic adsorption with dissociation of the N-N bond and the adsorption of one $^*\text{NH}_2$ on the Mo atom of the monolayer. Dissociating the N-N bond would be the ultimate goal of the NRR, however, if the catalyst holds onto the ammonia molecule strongly, the effectiveness and applicability of the catalyst is restricted. As a result, the enzymatic route would be a highly unlikely and unfavoured route for reducing N_2 molecules. A similar case of the high exergonic adsorption of the $^*\text{NH}_2\text{-}^*\text{NH}_2$ intermediate can be seen for the $\text{B}_{\text{SAC}}@\text{Mo}_2\text{C-C}_{\text{def}}$ catalyst (Fig. S6, ESI[†]), wherein the limiting potentials for nitrogen reduction were found to be 1.42 eV for the distal and alternating routes ($^*\text{NH}_2 \rightarrow ^*\text{NH}_3$) and 2.26 eV for the enzymatic route ($^*\text{NH}_2\text{-}^*\text{NH}_2 \rightarrow ^*\text{NH}_2$). The limiting potentials and the corresponding potential determining steps on the above mentioned $\text{B}_{\text{cat}}@\text{Mo}_2\text{C}$ catalysts are summarised in Table 1.

While an exergonic adsorption of N_2 is essential for the feasible capture of N_2 , it is not the only deciding factor for successful nitrogen reduction. There have been no accounts correlating dinitrogen adsorption to the efficacy of nitrogen reduction and the corresponding limiting potential. The exergonic free energy of N_2 follows the order $\text{B}_{\text{SAC}}@\text{Mo}_2\text{C-Mo}_{\text{vac}} > \text{B}_{\text{SAC}}@\text{Mo}_2\text{C-C}_{\text{def}} > \text{B}_{\text{SAC}}@\text{Mo}_2\text{C} > \text{B}_{\text{DAC}}@\text{Mo}_2\text{C}$, however the limiting potential of nitrogen reduction follows the order $\text{B}_{\text{SAC}}@\text{Mo}_2\text{C-C}_{\text{def}} > \text{B}_{\text{SAC}}@\text{Mo}_2\text{C} > \text{B}_{\text{DAC}}@\text{Mo}_2\text{C} > \text{B}_{\text{SAC}}@\text{Mo}_2\text{C-Mo}_{\text{vac}}$. In order to correlate the N_2 adsorption and the limiting potential, we probe into the electronic properties of the adsorbed N_2 and N_xH_y species *via* the Bader charges on the B atom and N atoms for all the $\text{B}_{\text{cat}}@\text{Mo}_2\text{C}$ catalysts as shown in Fig. 5. The N-atoms are seen to be negatively charged on all the N_xH_y intermediates and tend to be more electron rich for subsequent reaction steps thereby making the protonation facile. While the differences in Bader charge on the N-atoms

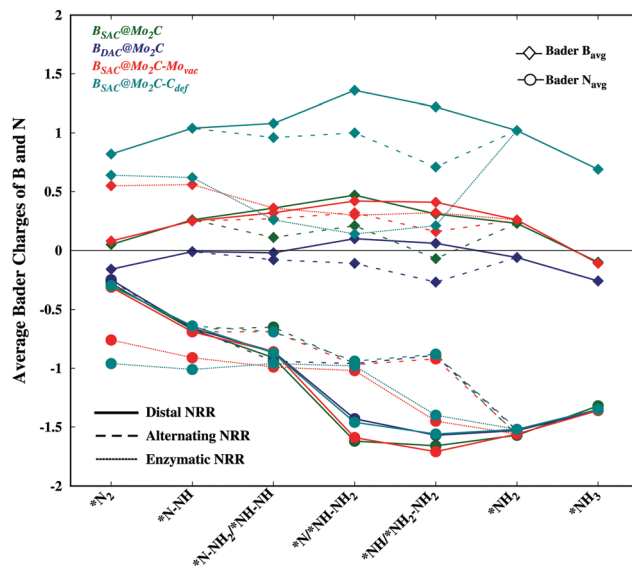


Fig. 5 Bader charges on N and B atom catalysts for N_xH_y intermediates involved in the free energy diagram for the NRR on all the $\text{B}_{\text{cat}}@\text{Mo}_2\text{C}$ catalysts.

are minute for different catalysts, the charges on the B-atoms are prominent with less positive B-atoms on the $\text{B}_{\text{DAC}}@\text{Mo}_2\text{C}$, $\text{B}_{\text{SAC}}@\text{Mo}_2\text{C-Mo}_{\text{vac}}$ and $\text{B}_{\text{SAC}}@\text{Mo}_2\text{C}$ catalysts, followed by the $\text{B}_{\text{SAC}}@\text{Mo}_2\text{C-C}_{\text{def}}$ catalyst. A highly positive B-atom on the corresponding N_xH_y intermediates would deplete the negative charge on the N-atom, thereby restricting the protonation steps as seen in the case of $\text{B}_{\text{SAC}}@\text{Mo}_2\text{C-C}_{\text{def}}$. Therefore, the $\text{B}_{\text{SAC}}@\text{Mo}_2\text{C-Mo}_{\text{vac}}$ catalyst with strong N_2 chemisorption captures the dinitrogen molecule effectively and the electron deficient B-atom aids the protonation steps in the NRR, thus making it an attractive electrocatalyst with a limiting potential of 0.57 eV and an overpotential of 0.41 eV. In contrast, the relatively high limiting potential of 1.10 eV for $\text{B}_{\text{SAC}}@\text{Mo}_2\text{C}$ in spite of the similar charges on the B-atoms can be accounted for by a less exergonic N_2 adsorption as compared to $\text{B}_{\text{SAC}}@\text{Mo}_2\text{C-Mo}_{\text{vac}}$. Additionally, $\text{B}_{\text{DAC}}@\text{Mo}_2\text{C}$ with electron rich B-atoms shows a relatively higher limiting potential of 0.90 eV owing to its less exergonic N_2 adsorption. We further correlate our analogy to the first protonation step of the NRR, which is usually considered a crucial step in the NRR. It has been reported that a

Table 1 Gibbs free energies, ΔG (eV) of N_2 adsorption, first protonation and rate determining step (ΔG_{max}) and overpotential, η for all routes of the NRR on the $\text{B}_{\text{cat}}@\text{Mo}_2\text{C}$ catalysts

$\text{B}_{\text{cat}}@\text{Mo}_2\text{C}$ catalysts	NRR route	ΔG_{N_2} (eV)	$\Delta G_{\text{N}_2} \rightarrow \Delta G_{\text{N}_2\text{H}}$ (eV)	Rate determining step	ΔG_{max} (eV)	η (eV)
$\text{B}_{\text{SAC}}@\text{Mo}_2\text{C}$	Distal	-0.15	0.21	$^*\text{NH}_2 \rightarrow ^*\text{NH}_3$	1.10	0.94
	Alternating	-0.15	0.21	$^*\text{NH}_2 \rightarrow ^*\text{NH}_3$	1.10	0.94
$\text{B}_{\text{DAC}}@\text{Mo}_2\text{C}$	Distal	-0.05	0.02	$^*\text{NH}_2 \rightarrow ^*\text{NH}_3$	0.90	0.74
	Alternating	-0.05	0.02	$^*\text{NH}_2 \rightarrow ^*\text{NH}_3$	0.90	0.74
$\text{B}_{\text{SAC}}@\text{Mo}_2\text{C-Mo}_{\text{vac}}$	Distal	-0.72	-0.34	$^*\text{NH}_2 \rightarrow ^*\text{NH}_3$	0.57	0.41
	Alternating	-0.72	-0.34	$^*\text{N-NH} \rightarrow ^*\text{NH-NH}$	1.05	0.89
	Enzymatic	-1.38	-0.42	$^*\text{NH}_2\text{-}^*\text{NH}_2 \rightarrow ^*\text{NH}_2$	1.83	1.67
$\text{B}_{\text{SAC}}@\text{Mo}_2\text{C-C}_{\text{def}}$	Distal	-0.88	0.30	$^*\text{NH}_2 \rightarrow ^*\text{NH}_3$	1.42	1.26
	Alternating	-0.88	0.30	$^*\text{NH}_2 \rightarrow ^*\text{NH}_3$	1.42	1.26
	Enzymatic	-1.23	-0.07	$^*\text{NH}_2\text{-}^*\text{NH}_2 \rightarrow ^*\text{NH}_2$	2.26	2.10



less endergonic or exergonic $*\text{N}_2 \rightarrow *\text{N}_2\text{H}$ step leads to a lower limiting potential for nitrogen reduction. Upon comparison of the free energies of the first protonation steps, the $\text{B}_{\text{cat}}@\text{Mo}_2\text{C}$ catalysts with less endergonic free energies, *i.e.*, $\text{B}_{\text{SAC}}@\text{Mo}_2\text{C}-\text{Mo}_{\text{vac}}$ (-0.34 eV) and $\text{B}_{\text{DAC}}@\text{Mo}_2\text{C}$ (0.02 eV) exhibit lower limiting potentials as compared to $\text{B}_{\text{SAC}}@\text{Mo}_2\text{C}$ and $\text{B}_{\text{SAC}}@\text{Mo}_2\text{C}-\text{C}_{\text{def}}$. This analogy holds true only for the distal and alternating routes wherein N_2 has been adsorbed in the end-on mode. Our previous argument correlating N_2 adsorption free energies and Bader charges is in agreement with the analogy of first protonation energies, and therefore can give insightful information on the mutual correlation between the free energies of the adsorption and electronic properties that directly govern the limiting potentials of the NRR on $\text{B}_{\text{cat}}@\text{Mo}_2\text{C}$ catalysts. Furthermore, the $\text{B}_{\text{SAC}}@\text{Mo}_2\text{C}-\text{Mo}_{\text{vac}}$ catalyst with one Mo-vacancy is found to efficiently capture and accentuate the catalytic activity of the boron SAC with a very low overpotential of 0.41 eV for the NRR. This study provides an in-depth analysis of the electronic factors crucial for efficient N_2 adsorption and reduction, and proposes the $\text{B}_{\text{SAC}}@\text{Mo}_2\text{C}-\text{Mo}_{\text{vac}}$ catalyst as a potential candidate for the NRR.

4 Conclusions

In summary, a detailed and systematic DFT investigation has been carried out to analyse the efficacy of N_2 adsorption and reduction on $\text{B}_{\text{cat}}@\text{Mo}_2\text{C}$ monolayers. Our study identifies a metal-free boron anchored defective Mo_2C monolayer with superior electrocatalytic activity for the NRR at 0.41 eV on account of a more positive p-band center and the negative charge of boron SACs that implicitly stabilizes the intermediates along the energy profile of the NRR. The insights gained from this work can be implemented for further research towards the design of efficient B-atom based electrocatalysts for the nitrogen reduction reaction.

Author contributions

Ashakiran Maibam: calculation, methodology, investigation and analysis. Sailaja Krishnamurthy and Manzoor Ahmad Dar: conceptualization and work design. All authors contributed equally to writing, reviewing and editing the manuscript.

Conflicts of interest

There are no conflicts of interest to declare.

Acknowledgements

A. M. acknowledges the CSIR for funding of the SRF (Senior Research Fellowship). M. A. D. acknowledges the Start-up research grant (SRG/2020/00654) from the SERB, India for financial support towards the completion of this work. The authors gratefully acknowledge the National Supercomputing Mission (NSM) for providing the computing resources of

'PARAM Brahma' at IISER Pune, which is implemented by C-DAC and supported by the Ministry of Electronics and Information Technology (MeitY) and the Department of Science and Technology (DST), Government of India.

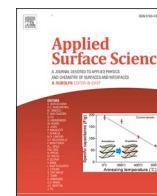
Notes and references

- 1 N. Cherkasov, O. Ibadon and P. Fitzpatrick, *Chem. Eng. Process.*, 2015, **90**, 24–33.
- 2 C. J. M. Ham, M. T. M. Koper and D. G. H. Hetterscheid, *Chem. Soc. Rev.*, 2014, **43**, 5183–5191.
- 3 J. W. Erisman, M. A. Sutton, J. Galloway, Z. Klimont and W. Winiwarter, *Nat. Geosci.*, 2008, **1**, 636–639.
- 4 A. Afif, N. Radenahmad, Q. Cheok, S. Shams, J. H. Kim and A. K. Azad, *Renewable Sustainable Energy Rev.*, 2016, **60**, 822–835.
- 5 G. Zheng, J. M. Yan and G. Yu, *Small Methods*, 2019, **3**, 1900070.
- 6 X. Xue, R. Chen, C. Yan, P. Zhao, Y. Hu, W. Zhang, S. Yang and Z. Jin, *Nano Res.*, 2019, **12**, 1229–1249.
- 7 C. Tang and S.-Z. Qiao, *Chem. Soc. Rev.*, 2019, **48**, 3166–3180.
- 8 G. Qing, R. Ghazfar, S. T. Jackowski, F. Habibzadeh, M. M. Ashtiani, C.-P. Chen, M. R. Smith III and T. W. Hamann, *Chem. Rev.*, 2020, **120**, 5437–5516.
- 9 H. Tao, C. Choi, L.-X. Ding, Z. Jiang, Z. Han, M. Jia, Q. Fan, Y. Gao, H. Wang, A. W. Robertson, S. Hong, Y. Jung, S. Liu and Z. Sun, *Chem*, 2019, **5**, 204–214.
- 10 Y. Yao, H. Wang, X.-Z. Yuan, H. Li and M. Shao, *ACS Energy Lett.*, 2019, **4**, 1336–1341.
- 11 Q. Qin, T. Heil, M. Antonietti and M. Oschatz, *Small Methods*, 2018, **2**, 1800202.
- 12 K. Zhang, R. Guo, F. Pang, J. He and W. Zhang, *ACS Sustainable Chem. Eng.*, 2019, **7**, 10214–10220.
- 13 H. Zhao, D. Zhang, H. Li, W. Qi, X. Wu, Y. Han, W. Cai, Z. Wang, J. Lai and L. Wang, *Adv. Energy Mater.*, 2020, **10**, 2002131.
- 14 G. Deng, T. Wang, A. A. Alshehri, K. A. Alzahrani, Y. Wang, H. Ye, Y. Luo and X. Sun, *J. Mater. Chem. A*, 2019, **7**, 21674–21677.
- 15 S. L. Foster, S. I. Perez Bakovic, R. D. Duda, S. Maheshwari, R. D. Milton, S. D. Minter, M. J. Janik, J. N. Renner and L. F. Greenlee, *Nat. Catal.*, 2018, 490–500.
- 16 B. M. Hoffman, D. Lukoyanov, Z.-Y. Yang, D. R. Dean and L. C. Seefeldt, *Chem. Rev.*, 2014, **114**, 4041–4062.
- 17 X. Guo, X. Wan and J. Shui, *Cell Rep. Phys. Sci.*, 2021, **2**, 100447.
- 18 K. C. MacLeod and P. L. Holland, *Nat. Chem.*, 2013, **5**, 559–565.
- 19 D. K. Yesudoss, G. Lee and S. Shanmugam, *Appl. Catal., B*, 2021, **287**, 119952.
- 20 L. Han, X. Liu, J. Chen, R. Lin, H. Liu, F. Lü, S. Bak, Z. Liang, S. Zhao, E. Stavitski, J. Luo, R. R. Adzic and H. L. Xin, *Angew. Chem., Int. Ed.*, 2019, **58**, 2321–2325.
- 21 Q. Li, S. Qiu, C. Liu, M. Liu, L. He, X. Zhang and C. Sun, *J. Phys. Chem. C*, 2019, **123**, 2347–2352.



- 22 A. Maibam, T. Govindaraja, K. Selvaraj and S. Krishnamurty, *J. Phys. Chem. C*, 2019, **123**, 27492–27500.
- 23 L. R. Johnson, S. Sridhar, L. Zhang, K. D. Fredrickson, A. S. Raman, J. Jang, C. Leach, A. Padmanabhan, C. C. Price, N. C. Frey, A. Raizada, V. Rajaraman, S. A. Saiprasad, X. Tang and A. Vojvodic, *ACS Catal.*, 2020, **10**, 253–264.
- 24 B. H. R. Suryanto, D. Wang, L. M. Azofra, M. Harb, L. Cavallo, R. Jalili, D. R. G. Mitchell, M. Chatti and D. R. MacFarlane, *ACS Energy Lett.*, 2019, **4**, 430–435.
- 25 B. Zhang, J. Zhou, S. R. Elliott and Z. Sun, *J. Mater. Chem. A*, 2020, **8**, 23947–23954.
- 26 Q. Li, L. He, C. Sun and X. Zhang, *J. Phys. Chem. C*, 2017, **121**, 27563–27568.
- 27 P. Ou, X. Zhou, F. Meng, C. Chen, Y. Chen and J. Song, *Nanoscale*, 2019, **11**, 13600–13611.
- 28 T. Yang, T. T. Song, J. Zhou, S. Wang, D. Chi, L. Shen, M. Yang and Y. P. Feng, *Nano Energy*, 2020, **68**, 104304.
- 29 L. Zhang, X. Ji, X. Ren, Y. Ma, X. Shi, Z. Tian, A. M. Asiri, L. Chen, B. Tang and X. Sun, *Adv. Mater.*, 2018, **30**, 1800191.
- 30 X. Zhai, L. Li, X. Liu, Y. Li, J. Yang, D. Yang, J. Zhang, H. Yan and G. Ge, *Nanoscale*, 2020, **12**, 10035–10043.
- 31 C. Ma, X. Yan, H. He, B. Liu and S. Yan, *Sustainable Energy Fuels*, 2021, **5**, 2415–2418.
- 32 K. Ba, G. Wang, T. Ye, X. Wang, Y. Sun, H. Liu, A. Hu, Z. Li and Z. Sun, *ACS Catal.*, 2020, **10**, 7864–7870.
- 33 K. P. Ramaiyan, S. Ozden, S. Maurya, D. Kelly, S. K. Babu, A. Benavidez, F. G. Garzon, Y. S. Kim, C. R. Kreller and R. Mukundan, *J. Electrochem. Soc.*, 2020, **167**, 044506.
- 34 B. Zhang, J. Zhou, S. R. Elliott and Z. Sun, *J. Mater. Chem. A*, 2020, **8**, 23947–23954.
- 35 S. Qi, Y. Fan, L. Zhao, W. Li and M. Zhao, *Appl. Surf. Sci.*, 2021, **536**, 147742.
- 36 X. Yang, C. Shang, S. Zhou and J. Zhao, *Nanoscale Horiz.*, 2020, **5**, 1106–1115.
- 37 Y. Liu, L. Gu, X. Zhu, Q. Zhang, T. Tang, Y. Zhang, Y. Li, J. Bao, Z. Dai and J.-S. Hu, *J. Mater. Chem. A*, 2020, **8**, 8920–8926.
- 38 X. Ren, J. Zhao, Q. Wei, Y. Ma, H. Guo, Q. Liu, Y. Wang, G. Cui, A. M. Asiri, B. Li, B. Tang and X. Sun, *ACS Cent. Sci.*, 2019, **5**, 116–121.
- 39 Y. Ma, T. Yang, H. Zou, W. Zang, Z. Kou, L. Mao, Y. Feng, L. Shen, S. J. Pennycook, L. Duan, X. Li and J. Wang, *Adv. Mater.*, 2020, **32**, 2002177.
- 40 A. Maibam and S. Krishnamurty, *J. Colloid Interface Sci.*, 2021, **600**, 480–491.
- 41 X. Liu, X. Jiao, Y. Zheng and S.-Z. Qiao, *ACS Catal.*, 2020, **10**, 1847–1854.
- 42 C. Liu, Q. Li, C. Wu, J. Zhang, Y. Jin, D. R. MacFarlane and C. Sun, *J. Am. Chem. Soc.*, 2019, **141**, 2884–2888.
- 43 S. Xiao, F. Luo, H. Hua and Z. Yang, *Chem. Commun.*, 2020, **56**, 446–449.
- 44 L. Shi, Q. Li, C. Ling, Y. Zhang, Y. Ouyang, X. Baia and J. Wang, *J. Mater. Chem. A*, 2019, **7**, 4865–4871.
- 45 C. Ling, X. Niu, Q. Li, A. Du and J. Wang, *J. Am. Chem. Soc.*, 2018, **140**, 14161–14168.
- 46 G. Kresse and J. Furthmuller, *Comput. Mater. Sci.*, 1996, **6**, 15–50.
- 47 J. P. Perdew, K. Burke and M. Ernzerhof, *Phys. Rev. Lett.*, 1996, **77**, 3865–3868.
- 48 S. Grimmea, J. Antony, S. Ehrlich and H. Krieg, *J. Chem. Phys.*, 2010, **132**, 154104.
- 49 J. K. Nørskov, J. Rossmeisl, A. Logadottir, L. Lindqvist, J. R. Kitchin, T. Bligaard and H. Jónsson, *J. Phys. Chem. B*, 2004, **108**, 17886–17892.





Full Length Article

Doped 2D VX₂ (X = S, Se, Te) monolayers as electrocatalysts for ammonia production: A DFT based studyAshakiran Maibam^{a,b,c}, Ravichandar Babarao^{b,d,*}, Sailaja Krishnamurty^{a,c,*}^a Physical and Materials Division, CSIR-National Chemical Laboratory, Pune 411 008, India^b School of Science, RMIT University, Melbourne 3001, Victoria, Australia^c Academy of Scientific and Innovative Research, CSIR-Human Resource Development Centre (CSIR-HRDC) Campus, Postal Staff College area, Ghaziabad 201 002, Uttar Pradesh, India^d CSIRO, Normanby Road, Clayton 3168, Victoria, Australia

ARTICLE INFO

Keywords:

Nitrogen Reduction Reaction
Vanadium dichalcogenides
Electrocatalysts
DFT
Non metal dopants
1T and 2H phases

ABSTRACT

Electrocatalytic nitrogen fixation under ambient conditions on vanadium dichalcogenides (VX₂) with non-metal dopants has been explored herein. Understanding the interface chemistry, inherent electronic and acute synergistic nature of non-metal dopants on two unique phases of VX₂ has been meticulously explored through a scrutiny of several non-metal atoms as catalytic centers. The efficacy of N₂ chemisorption and N—N bond activation has been implemented as crucial parameters to realize boron and carbon doped VX₂ monolayers to be electrocatalytically active for nitrogen reduction reaction (NRR). Detailed investigation on the NRR mechanism brings out the pivotal role of thermodynamic favourability for product formation obtained from Gibbs free energy differences. The charge transfer on N and π-π* orbital hybridization and electron “donor-acceptor” mechanism between the non-metal and N₂ has been found to modulate the electrocatalytic barrier for NRR on VX₂ monolayers. This study proposes boron doped VS₂ as an efficient chemically feasible, earth abundant sustainable electrocatalyst for NRR with an overpotential as low as 0.06 eV.

1. Introduction

With the average CO₂ concentration in the air hitting a maximum of 419 ppm in 2021, global warming and climate change are looming over the earth. To meet the 2030 sustainable goals, there is a need to halt the release of greenhouse gases in the atmosphere and curb processes that have a high carbon footprint.[1] One industrial process associated with 6 % of global CO₂ emissions is artificial nitrogen fixation via the Haber-Bosch process.[2,3] Ammonia is one of the most influential chemicals driving the economy of several countries and its latent energy density, when tapped properly will open up avenues for new generation fuels. Consequently, there is a need to develop carbon free technologies for artificial nitrogen fixation through electrocatalytic, photocatalytic, or photoelectrocatalytic routes to cater to the ever-increasing demand for ammonia.[4] The crux of achieving ammonia economy via an electrocatalytic route for artificial nitrogen fixation is one of the most sought after green modes of ammonia synthesis and several materials have been explored for efficient nitrogen fixation.[5,6] However, the major setback in the advancement of electrocatalytic nitrogen reduction

reaction (eNRR) is the slothful kinetics of N—N triple bond dissociation in addition to a low yield and Faradaic efficiency.[7] Henceforth, it is imperative to develop state-of-the-art highly conducting smart chemically affordable materials for prospective applications in eNRR.

A remarkably inexpensive material of high electrical conductivity and prospects for application as electrocatalysts is transition metal dichalcogenides (TMDs).[8,9] These two-dimensional (2D) materials possess exceptional properties as compared to their bulk counterparts and have piqued the interest of several researchers since the last decade.[10,11] Interestingly, TMDs have been reported to exhibit metallic or semiconducting properties upon varying the combination of chalcogens (S, Se, Te) with different transition metals. Most intriguingly, the change in crystal phases can also influence the electronic as well as magnetic properties. This ambidexterity in the electronic and magnetic properties of TMDs further makes them attractive candidates for novel applications. Notably, vanadium dichalcogenides, VX₂ (X = S, Se, Te) which shows intrinsic ferromagnetism is one such TMD with versatile attributes that exhibits different electronic and magnetic properties in different phases, i.e., 1 T and 2H phases or with different dichalcogens.

* Corresponding authors.

E-mail addresses: ravichandar.babarao@rmit.edu.au (R. Babarao), k.sailaja@ncl.res.in (S. Krishnamurty).<https://doi.org/10.1016/j.apsusc.2022.154401>

Received 8 April 2022; Received in revised form 26 July 2022; Accepted 26 July 2022

Available online 29 July 2022

0169-4332/© 2022 Elsevier B.V. All rights reserved.

[12–14] Recent studies on vanadium dichalcogenides have prompted the 1 T phase of VX_2 to be metallic, while the 2H phase is semimetallic in VS_2 and VSe_2 and metallic in VTe_2 monolayers. Several experimental and computational studies have also reported the 2H phase to show higher stability and magnetic moment than the 1 T phase for VS_2 monolayers, while most studies of VSe_2 and VTe_2 monolayers are focused on the metallic 1 T-phase. [15–20] Besides showing conformable properties, the presence of vanadium metal in nitrogenase enzyme, its high catalytic activity for nitrogen reduction along with natural abundance and durability is an added advantage of these vanadium based materials for application in eNRR. [21,22] Furthermore, the electronic, magnetic, and optical properties of the VX_2 monolayers can be altered either by inducing physical constraints like mechanical strain, modulating temperature, tuning the material width and thickness, or chemical influence such as metal or non-metal doping and charge doping. [23–28].

In this aspect, it would be imperative to look into introducing dopants on vanadium dichalcogenides as this approach has been pursued widely on several 2D materials as a non-destructive, chemically feasible method to activate the dormant basal planes and calibrate the electrocatalytic activity of VX_2 monolayers. The debate would then be to critically choose the dopants that will enhance the electrocatalytic properties of these monolayers for nitrogen fixation. While metal atom dopants and non-metals have been explored simultaneously, it is important that research on developing efficient electrocatalysts for nitrogen fixation also accounts for the sustainability of developing these novel materials and the dopants to be employed. Non-metal dopants offer an advantage of non-toxicity and abundance when compared to metals, and one such non-metal dopant that has been extensively employed as a dopant on several 2D materials for promoting nitrogen fixation is boron. [29–32].

In this work, we have investigated the role of several non-metals dopants for activating the electrocatalytic activity of vanadium dichalcogenides. It would be essential to probe for a non-metal dopant that would lead to synergistic activation of the different phases of vanadium dichalcogenide monolayers. This work delves into the criticality of considering the N–N bond elongation as another parameter to be considered alongside the Gibbs Free energy of N_2 adsorption and the first protonation step as we have discussed in our previous work. [33] Furthermore, we believe a linear relationship between Gibbs Free energy differences of the intermediate steps in NRR plays an integral role in determining the limiting potential of nitrogen reduction. From our results, we found boron and carbon atoms when doped on 2H and 1 T phases, respectively, of VS_2 monolayers to synergistically enhance their electrocatalytic properties and produce ammonia at limiting potentials as low as 0.22 eV and 0.42 eV, respectively.

2. Computational details

Spin-polarized DFT calculations to optimize all vanadium dichalcogenide monolayers were carried out with Vienna *ab-initio* Simulation Package (VASP.5.4). [34] An energy cut-off of 400 eV has been employed to describe all electron interactions in the framework of a generalized gradient approximation Perdew-Burke-Ernzerhof (PBE) functional. [35] The long-range van der Waals (vdW) interactions between TMD monolayers have been incorporated in the electronic calculations with a DFT-D3 correction. [36] All the VX_2 monolayer has been sampled with a vacuum space of 20 Å along the Z-direction and a $(5 \times 5 \times 1)$ Monkhorst-Pack kpoint grid. The vanadium dichalcogenide monolayer systems are allowed to relax till the atomic energy and forces reach a cut-off of 10^{-6} eV/atom and 0.001 eV/Å respectively. The electronic property analysis has been carried out by considering a higher kpoint grid of $(11 \times 11 \times 1)$ Monkhorst-Pack grid. *Ab initio* molecular dynamics simulations (AIMD) simulations have been performed with a Nosé–Hoover thermostat of 298 K in an NVT ensemble for 10 ps, with a time step of 3 fs to evaluate the thermodynamic stability of VX_2 systems.

[37–39] The feasibility of formation of 1 T and 2H monolayer phases of pristine and non-metal doped vanadium dichalcogenides has been computed in terms of formation energy per atom, E_{form} by using the equation,

$$E_{\text{form}} = \frac{1}{n} (E_{VX_2@Y_{\text{cat}}} - N_V E_V - N_X E_X - N_Y E_{Y_{\text{cat}}}) \quad (1)$$

where, n is the number of atoms in a TMD monolayer, $E_{VX_2@Y_{\text{cat}}}$ is the total electronic energy of the pristine or non-metal doped vanadium dichalcogenide monolayer, N_a and E_a are the number of atoms and corresponding electronic energies of each isolated atom respectively, X is the chalcogen (S, Se or Te) and Y is the non-metal dopant.

N_2 adsorption on the basal plane of pristine and non-metal doped VX_2 monolayers could proceed either through the end-on or side mode modes. The end-on or perpendicular mode of N_2 adsorption has been observed to be more prominent over the side-on or parallel mode on all VX_2 systems, thereby only the end-on mode of nitrogen adsorption will be presented in this study. The N_2 chemisorption efficacy of all pristine and doped VX_2 monolayers is.

calculated as adsorption energy, E_{ads} with the equation below,

$$E_{\text{ads}} = E_{VX_2@Y_{\text{cat}}-N_2} - E_{VX_2@Y_{\text{cat}}} - E_{N_2} \quad (2)$$

where, $E_{VX_2@Y_{\text{cat}}-N_2}$, $E_{VX_2@Y_{\text{cat}}}$ and E_{N_2} are the total electronic energies of N_2 adsorbed VX_2 systems, pristine and doped $VX_2@Y_{\text{cat}}$ and free N_2 molecule, respectively.

The energetics of each intermediate protonation step in the Nitrogen Reduction Reaction is represented by the Gibbs free energy change, ΔG . The computational Standard Hydrogen Electrode model of Nørskov et al. [40] has been implemented to calculate ΔG using the following equation,

$$\Delta G = \Delta E + \Delta ZPE - T\Delta S \quad (3)$$

where, ΔE and ΔZPE are the change in electronic energy and zero-point energy respectively,

ΔS is the change in entropy at room temperature, T is room temperature (298.15 K). All zero-point energy and entropy corrections are computed from the non-negative vibrational frequencies of the gas phase species in each intermediate. Finally, the overpotential for electrocatalytic NRR has been calculated as $\eta = U_{\text{SHE}} - U_{\text{PDS}}$, where $U_{\text{SHE}} = -0.16$ eV, is the standard reduction potential of N_2 to NH_3 and $U_{\text{PDS}} = \Delta G_{\text{max}}/e$ for the NRR pathway.

3. Results and discussions

3.1. Formation of $VX_2@Y_{\text{cat}}$ monolayers and N_2 chemisorption

The formation energies of pristine and non-metal doped vanadium dichalcogenide monolayers, $VX_2@Y_{\text{cat}}$ have been computed to be approximately -4.9 eV/atom, -4.4 eV/atom and -3.8 eV/atom respectively for the sulphides, selenides and tellurides systems. The highly negative formation energies confirm the experimental feasibility of synthesizing the vanadium dichalcogenide monolayers, and the vanadium disulphides to be more stable than the other dichalcogenides. Two different phases of vanadium dichalcogenides have been considered owing to earlier reports that 2H- VS_2 phase shows higher stability and magnetic moment over its 1 T phase. The 2H phase of pristine VS_2 shows a slightly higher formation energy (-4.94 eV/atom) and magnetic moment of $0.98 \mu_B$ as compared to $0.47 \mu_B$ of 1 T- VS_2 . Contrastingly, pristine VSe_2 showed higher formation energies (-4.44 eV/atom) in its metallic 1 T-phase with a higher magnetic moment of $0.90 \mu_B$ in the semimetallic 2H-phase. VTe_2 , on the other hand, demonstrated higher stability with a formation energy of -3.81 eV/atom and a magnetic moment of $0.15 \mu_B$ in its 1 T-phase exclusively.

The $VX_2@Y_{\text{cat}}$ systems are further modeled with a chalcogen vacancy ($VX_2@X_{\text{vac}}$) and substitutional doping of non-metals on the chalcogen

vacancy to generate $VX_2@Y_{\text{cat}}$ (Fig. 1). The formation energies of $VX_2@Y_{\text{cat}}$ systems are found to be higher than their corresponding pristine counterparts with a few exceptions in VS_2 and VSe_2 when the non-metal dopant is heavier than the parent chalcogen, e.g., $VS_2@Se$, $VS_2@Te$ and $VSe_2@Te$. The magnetic properties, on the other hand, show a gradual decrease as non-metal dopants are introduced in the $VX_2@Y_{\text{cat}}$ systems except for 2H- $VTe_2@B$ and 2H- $VTe_2@C$ systems. The highly exothermic formation energies of $VX_2@Y_{\text{cat}}$ systems demonstrate the stability of both 1 T and 2H phase of vanadium dichalcogenides and their magnetic moments further exemplifies the incidence of ferromagnetic nature of these systems. The corresponding values of formation energy, d-band centers and magnetic moments of all $VX_2@Y_{\text{cat}}$ systems are provided in Supplementary Table S1.

The N_2 chemisorption efficacy and the extent of N—N bond activation on 1 T and 2H phases of all $VX_2@Y_{\text{cat}}$ systems are then investigated to determine the synergistically favourable non-metal dopant for a family of VX_2 . The adsorption energies and N—N bond lengths of the dinitrogen molecule adsorbed in end-on or perpendicular mode on all $VX_2@Y_{\text{cat}}$ systems are shown in Fig. 2(a). It can be observed that pristine VX_2 systems show minimal to moderately exothermic N_2 adsorption without activating or elongating the N—N bond. Such systems would imperatively require a large potential when employed for nitrogen fixation as the nitrogen atoms remain strongly bonded. $VX_2@X_{\text{vac}}$ systems except 1 T- VS_2 and 1 T- VTe_2 , boron and carbon doped $VX_2@B$ and $VX_2@C$ systems show favourable N_2 adsorption as well as N—N bond activation up to 1.16 Å. Interestingly, for boron and carbon doped VS_2 and VSe_2 systems, the non-metals play a major role in tuning the catalytic property of the monolayer. Although both boron and carbon dopant showed higher N_2 adsorption on 1 T phases of VS_2 and VSe_2 ; boron induces a higher N—N bond activation on 2H phase while carbon doping leads to a more pronounced N—N bond elongation on 1 T phase. However, on VTe_2 systems, the impact of B or C doping is not very prominent as N_2 adsorption and N—N bond activation remain nearly similar in both 1 T and 2H phases. Eventually, it can be deduced that boron and carbon dopants synergistically enhance the catalytic

properties of 2H and 1 T phases respectively, of VS_2 and VSe_2 ; whilst VTe_2 monolayers prefer both boron and carbon dopants. The $VX_2@N$ systems show a unique aspect of high N—N bond activation under endothermic conditions, thereby excess energy is needed to ensure N_2 adsorption and this condition is the most unfavourable scenario for electrocatalysis. It would be imperative to recapitulate that the N_2 adsorption energies and activated N—N bond lengths of $VX_2@B$ and $VX_2@C$ systems are comparable to earlier reports made by Wu et. al on W-doped BP monolayer and Mo-doped Fe_3P monolayer. [41,42] It can also be noted that the N_2 adsorption energies of $VX_2@Si$ systems range from -0.02 eV to -0.14 eV and is comparable to those observed by Gholizadeh et. al on Si-doped graphene systems.[43] The rest of non-metal dopants: Si, P, S, Se and Te show weak N_2 chemisorption as well as bond elongation, thereby employing these heavier non-metal dopants will be unfavourable. A Bader charge[44] analysis of adsorbed N_2 molecule highlights an extensive charge gain mostly on the $VX_2@B$ and $VX_2@C$ systems followed by $VX_2@X_{\text{vac}}$ and 1 T-phases of $VX_2@N$. These systems with higher charge transfer on N_2 correspond to the systems showing N—N bond activation or elongation, thereby justifying our reasoning behind consideration of N—N bond length elongation as a crucial parameter. The plot of average Bader charge on N-atoms upon adsorption on $VX_2@Y_{\text{cat}}$ monolayers with respect to the d-band centers of the corresponding monolayers in Fig. 2(b) shows the charge transfer on the $VX_2@X_{\text{vac}}$, $VX_2@B$ and $VX_2@C$ systems are facilitated by a more positive d-band center, which in turn corroborates to higher exothermicity of N_2 adsorption. In particular, $VTe_2@B$ and $VTe_2@C$ systems with a more positive d-band center has been found to show higher charge transfer and N_2 chemisorption as compared to its VS_2 or VSe_2 counterparts. Taking the efficacy of N_2 chemisorption, N—N bond elongation, Bader charge on N-atoms and d-band center of the monolayers into account; the non-metal doped VX_2 systems of interest which show exothermic N_2 adsorption, N—N bond elongation and charge gain on N_2 are the $VX_2@B$ and $VX_2@C$ systems in both phases along with 1 T- $VS_2@N$, 2H-phases of $VX_2@X_{\text{vac}}$ and 1 T- $VSe_2@Se_{\text{vac}}$. Moving forward, we will focus on the energy profile and NRR

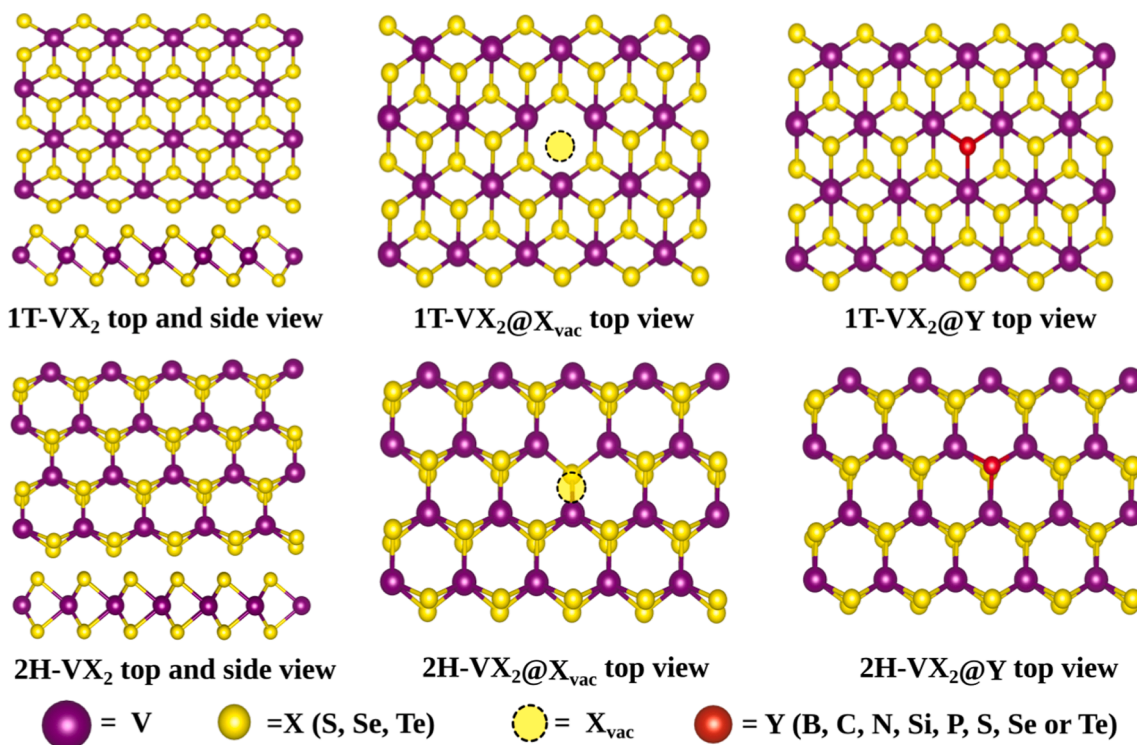


Fig. 1. Top and side views of 1 T and 2H phases of pristine vanadium dichalcogenides, top views of VX_2 monolayer with chalcogen vacancy ($VX_2@X_{\text{vac}}$) and non-metal dopant ($VX_2@Y$).

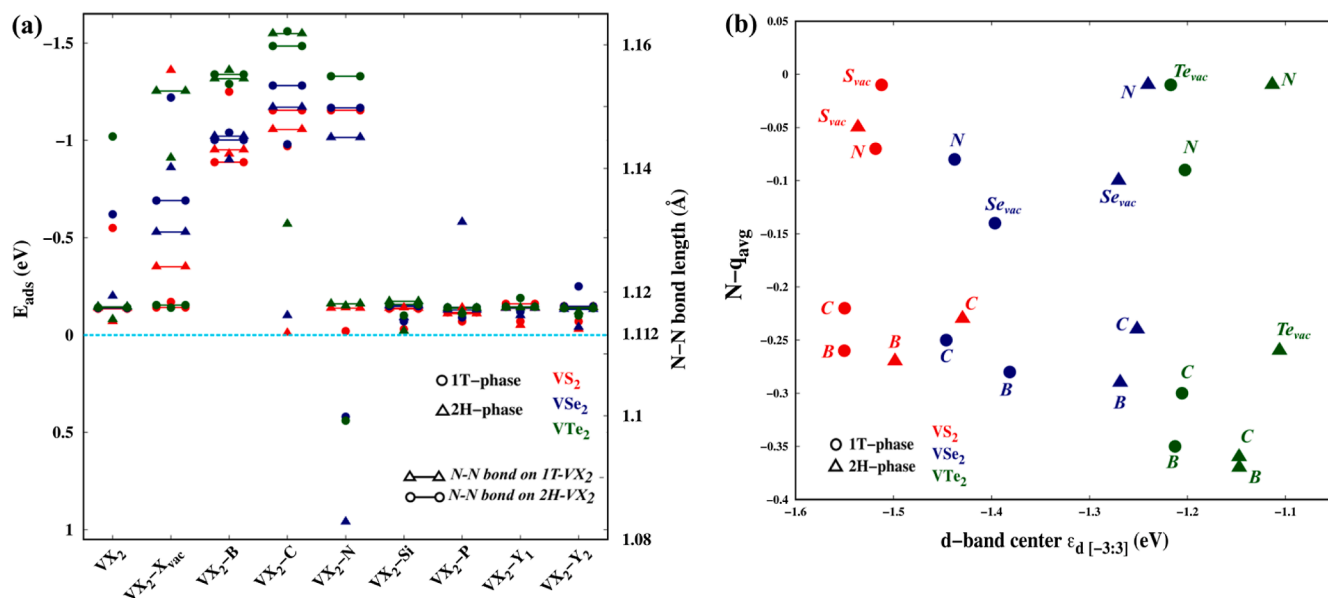


Fig. 2. (a) N_2 adsorption energies on all $VX_2@Y_{\text{cat}}$ systems with the corresponding N—N bond lengths (Å), cyan line corresponds to 0 eV of N_2 adsorption and N—N bond length in free dinitrogen molecule (1.112 Å). (b) Average Bader charge on N-atoms of N_2 upon adsorption on $VX_2@Y_{\text{cat}}$ monolayers plotted w.r.t the d-band centers of the corresponding monolayers.

mechanism of these active $VX_2@Y_{\text{cat}}$ monolayers to determine the limiting potential for NRR and decipher the critical factors that affect the limiting potential.

3.2. N_2 reduction on $VX_2@Y_{\text{cat}}$ monolayers

Following the chemisorption of N_2 and electronic analysis on catalytically active $VX_2@Y_{\text{cat}}$, $VX_2@B$ and $VX_2@C$ monolayers, we investigated the thermodynamics of ammonia synthesis from dinitrogen via the associative pathway. Taking into account that only the perpendicular or end-on mode of N_2 adsorption is more prominent, the two possible routes of associative NRR pathway are the distal and alternating routes. [45] The distal route involves protonation of end N to release NH_3 , followed by subsequent protonation of the next N; whereas the alternating route shows alternate protonation of N atoms to form ammonia.

The free energy profile of ammonia synthesis on all $VX_2@Y_{\text{cat}}$ systems is provided in Supplementary Information, Figures S2-S7. The most probable route of N_2 reduction has been deliberated by accounting the lowest energy barrier on the free energy profiles of each $VX_2@Y_{\text{cat}}$ system and plotted in Fig. 3(a).

The chemically modified vanadium disulphide, VS_2 monolayers are found to show equivalent preference of distal and alternating route with the first protonation step, $*N_2 \rightarrow *N-NH$ as the potential rate determining step (PDS), except on 1 T- $VS_2@C$ system with PDS in its last protonation step, i.e., $*NH_2 \rightarrow *NH_3$. Intriguingly, the lowest NRR limiting potential on the two different phases of VS_2 has been found to be 0.42 eV and 0.22 eV on 1 T- $VS_2@C$ and 2H- $VS_2@B$, respectively. It would be important to recollect that the synergistic doping of carbon and boron on 1 T- VS_2 and 2H- VS_2 also led to strong chemisorption of N_2 and N—N bond activation. Coming to $VSe_2@Y_{\text{cat}}$ monolayers,

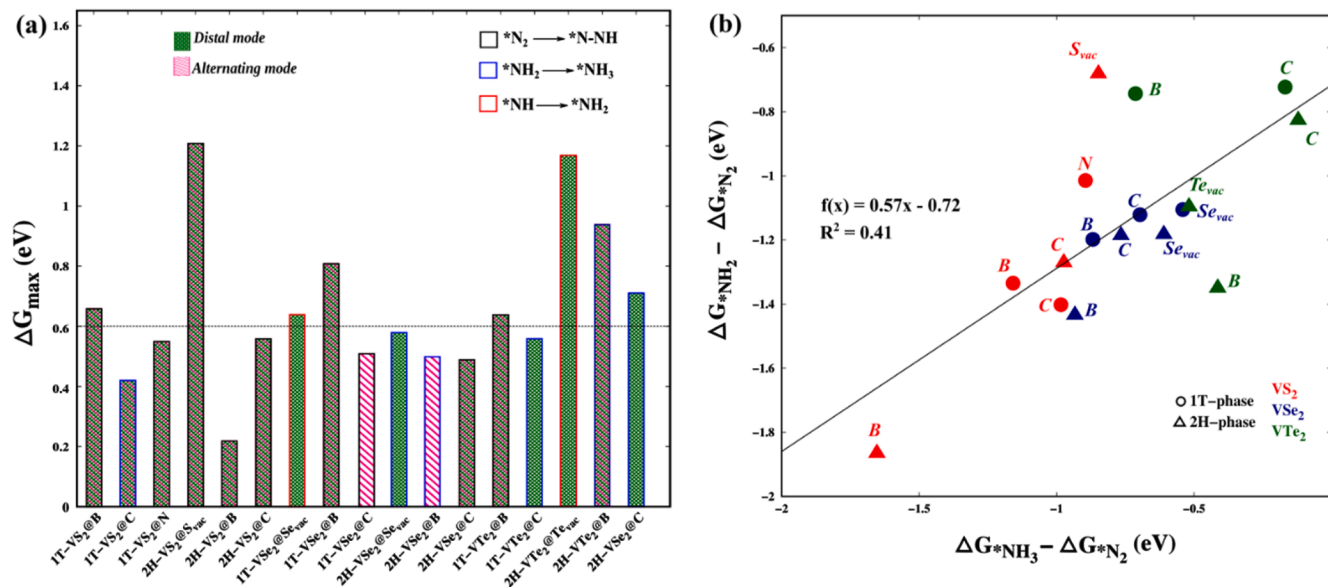


Fig. 3. (a) NRR limiting potentials (ΔG_{max}), captions indicate the potential rate determining step and preference of distal or alternating route, (b) Gibbs free energy difference plot between two crucial protonation steps and N_2 adsorption.

$VSe_2@Se_{vac}$ systems are found to show a preference for the distal route on both 1 T and 2H-phases, while 1 T- $VSe_2@C$ and 2H- $VSe_2@B$ systems advance through the alternating route with an equal prevalence of distal and alternating route of NRR on 1 T- $VSe_2@B$ and 2H- $VSe_2@C$ systems. Nonetheless, a lower barrier for nitrogen reduction on VSe_2 has been observed on 1 T- $VSe_2@C$, 2H- $VSe_2@B$ and 2H- $VSe_2@C$ with limiting potentials of 0.51 eV, 0.50 eV and 0.49 eV, respectively. In both phases of VTe_2 monolayers, the boron-doped systems show an identical affinity for distal or alternating route, while the remaining show a prevalence of the distal route over the alternating path with a lower energy barrier on 1 T- $VTe_2@C$ and 2H- $VTe_2@C$. In retrospect, the lowest energy barrier for 1 T as well as 2H phases of VTe_2 , which has been reported to be metallic, is observed on the carbon doped systems. Similarly, the prevalence of carbon doping can be found to lower the NRR limiting potential on the metallic 1 T phases of VS_2 and VSe_2 , while boron doping does the same on the semi-metallic 2H phases. The energetics of the active $VX_2@Y_{cat}$ monolayers are further investigated to elucidate the critical aspects of each intermediate step in factors that affect the limiting potential of NRR. Two crucial intermediate steps of NRR are the first ($*N_2 \rightarrow *N-NH$) and last ($*NH_2 \rightarrow \cdot NH_3$) protonation steps, with both processes being endergonic. As such, these two steps are the most prominent rate limiting steps in all of the systems we have considered, except for 1 T- $VSe_2@Se_{vac}$ and 2H- $VTe_2@Te_{vac}$ where the $*NH \rightarrow *NH_2$ is the energy uphill step. Also, conceptually for a multistep reaction, the $*NH_2$ and $\cdot NH_3$ intermediates can be considered as systems belonging to the product side wherein the reactant is the $*N_2$ intermediate, and the feasibility of such a reaction increases as the exoergicity between the product and reactant increases. This analogy can be implemented as a rationale for achieving a lower energy barrier in the NRR process by mapping a Gibbs Free energy difference plot. In Fig. 3 (b), a nearly linear relationship can be observed between the Gibbs free energy differences of products to reactant, i.e., $\cdot NH_3 - *N_2$ w.r.t. $*NH_2 - *N_2$. The 2H- $VS_2@B$ system with the lowest limiting potential of 0.22 eV is found to show a larger energy difference (~ 2.0 eV) between $*NH_2$ to $*N_2$ and $\cdot NH_3$ to $*N_2$, thereby emphasizing that systems with a higher potential to form the products, i.e., NH_3 or alike intermediates are prone to show a lower limiting potential for NRR. [46,47] The remaining $VX_2@B$ and $VX_2@C$ systems with energy barriers 0.49 eV to 0.58 eV show Gibbs free energy differences of 1.2 to 1.4 eV and a lower tenacity of product formation as compared to 2H- $VS_2@B$. Except for $VSe_2@Se_{vac}$ systems which show a lower limiting NRR potential, the $VS_2@S_{vac}$ and $VTe_2@Te_{vac}$ systems show a much lower energy difference or lower exoergicity of $\cdot NH_3$ intermediate and the energy differences are found to be around 0.5 eV to 1.0 eV. Amongst all the active $VX_2@Y_{cat}$ monolayers, the systems of significance will be systems with a lower NRR limiting potential wherein a lower electrode potential would be needed for implementing them as electrocatalysts for NRR. Therefore, 2H- $VS_2@B$ and 1 T- $VS_2@C$ systems with ΔG_{max} of 0.22 eV and 0.42 eV, respectively are of interest and their electronic properties are investigated further for their application as electrocatalysts for NRR.

3.3. NRR mechanism on 2H- $VS_2@B$ and 1 T- $VS_2@C$

A detailed electronic analysis through Projected Density of States (PDOS) and charge density plots of these systems reveal that the p-orbitals of non-metal dopants to hybridize with the empty π^* orbitals of N_2 , this orbital overlap coupled with charge transfer inherently leads to electron occupation in the antibonding π orbitals of N_2 leading to activation of the N–N bond. The PDOS, charge density difference plots and Electron Localization Function (ELF) contour plots of 1 T- $VS_2@C$ and 2H- $VS_2@B$ monolayers, as shown in Supplementary Figure S8, demonstrate the overlap of carbon and nitrogen p-orbitals to hybridize with the π^* orbitals on N_2 , respectively and the localization of electron density around the N_2 molecule, thereby affirming the electron transfer on the adsorbed N_2 . The electronic properties of each intermediate nitrogen reduction step on 2H- $VS_2@B$ systems has been further investigated to

root out the essential parameter behind the energy barrier for NRR. The segmented p-states of B and N alone for the $*N_xH_y$ intermediates observed via the distal route of NRR has been plotted in Fig. 4. The chemisorption of N_2 on 2H- $VS_2@B$ has been found to be associated with a $\pi-\pi^*$ hybridization between the B p-states and N p-states. These electronic orbitals hybridization or overlap gets more enhanced as the adsorbed N_2 gets reduced and the N p-states turn into electron rich states. Prior to the first ammonia desorption in the $*N-NH_2$ intermediate, a charge back-transfer from the filled N p-states to the empty p-states of B can be observed. The σ -back donation augments the activity of the boron center and assists in following protonation steps to form the second NH_3 molecule. Such electron back-donation could not be observed on our next best system, 1 T- $VS_2@C$ and we believe the thermodynamic favourability of NH_3 formation from N_2 along with the electron “donor–acceptor” mechanism between boron and nitrogen is responsible for high NRR performance.

In terms of electrocatalytic application for NRR, the distal and alternating routes of dinitrogen reduction on 1 T- $VS_2@C$ and 2H- $VS_2@B$ has been investigated at applied potentials of 0.42 V and 0.22 V respectively and is shown in Fig. 5. The Gibbs free energies of each intermediate protonation steps are computed through the computational hydrogen electrode (CHE) model proposed by Nørskov et al. [40],

$$\Delta G_{cNRR} = \Delta E + \Delta ZPE - T\Delta S - neU,$$

where ΔG is the free energy change of each intermediate step (as calculated in equation (3)), n is the number of electrons and U is the applied potential.

The endergonic intermediate steps in both systems are the first ($*N_2 \rightarrow *N_2H$) and last ($*NH_2 \rightarrow *NH_3$) protonation steps with the PDS being either of the two steps. The initially energy uphill step of $*N_2H$ formation in 1 T- $VS_2@C$ becomes exoergic under the application of an applied potential of 0.42 V. Similarly, the endoergic sixth protonation step to form 1 T- $VS_2@C-NH_3$ intermediate is also found to flip into an exergonic process as shown in Fig. 5(a). The analogous endoergic intermediate steps of 2H- $VS_2@B$ are also found to revert into energy downhill processes in Fig. 5(b) upon application of 0.22 V. It can be observed that with the application of an external potential equivalent to their respective limiting potentials in 1 T- $VS_2@C$ and 2H- $VS_2@B$, all the intermediate protonation steps of NRR become feasible and thereby employed for electrocatalytic nitrogen reduction. Furthermore, our analogy of synergic non-metal doping on vanadium dichalcogenides has shown that 1 T- $VS_2@C$ and 2H- $VS_2@B$ are the best electrocatalysts so far with NRR limiting potentials of 0.42 eV and 0.22 eV, respectively. The corresponding overpotentials, η of 0.26 eV and 0.06 eV respectively on boron or carbon doped VX_2 systems are the lowest reported so far on vanadium dichalcogenides. [48,49].

Consequently, the NRR selectivity of 1 T- $VS_2@C$ and 2H- $VS_2@B$ systems have also been investigated and it has been found that both systems can selectively suppress the competing hydrogen evolution reaction (HER). Although the adsorption of H is usually more negative than N_2 adsorption, former involves proton and electron transfer, thereby it is easily influenced by electrode potential. N_2 adsorption, on the other hand, does not involve proton transfer and the more appropriate step to be considered is the first protonation step of NRR, i.e., $*N_2H$ adsorption. Therefore, the selectivity of NRR over HER can be evaluated from the free energy difference of $*H$ and $*N_2H$ adsorption, $\Delta G(*H) - \Delta G(*N_2H)$. Fig. 6(a) shows the $\Delta G(*H) - \Delta G(*N_2H)$ vs NRR limiting potential plot of all active $VX_2@Y_{cat}$ systems and it can be seen that 2H- $VS_2@B$ shows a relatively higher selectivity as well as activity for NRR. With the exception of 1 T- $VS_2@B$ and 1T- $VS_2@N$, all the catalytically active $VX_2@Y_{cat}$ systems possess enhance NH_3 production as supported as exothermic- NH_3 formation on all $VX_2@Y_{cat}$ systems in Figures S2-S7. Finally, for the best catalyst 2H- $VS_2@B$, besides the chemical stability, the thermal stability has been investigated at room temperature, 298 K. It can be seen from Fig. 6(b) that the structure of

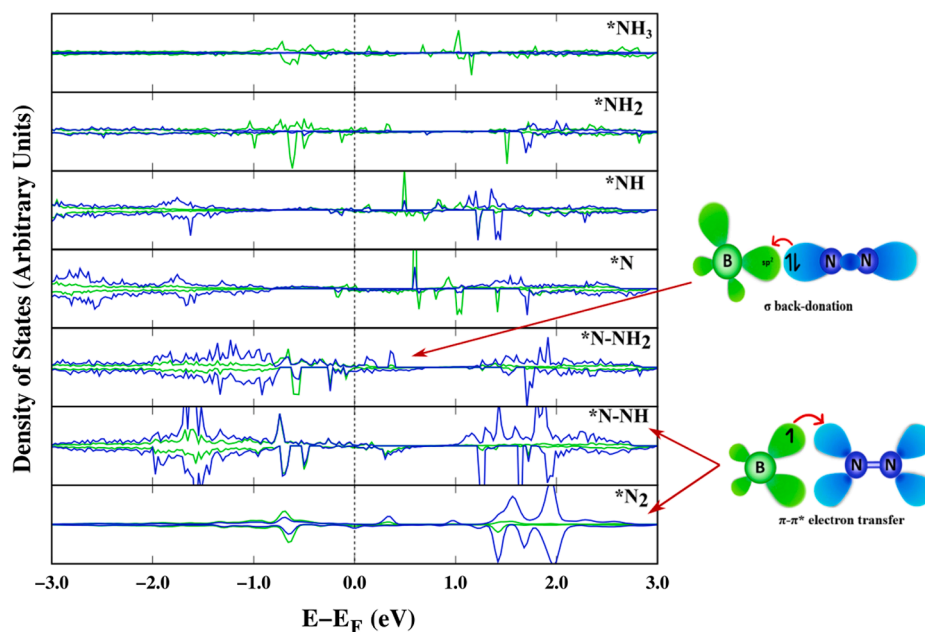


Fig. 4. Segmented Projected Density of States of B p-states (green line) and N p-states of all the N_xH_y intermediates from the distal route of NRR on 2H- $VS_2@B$ monolayer.

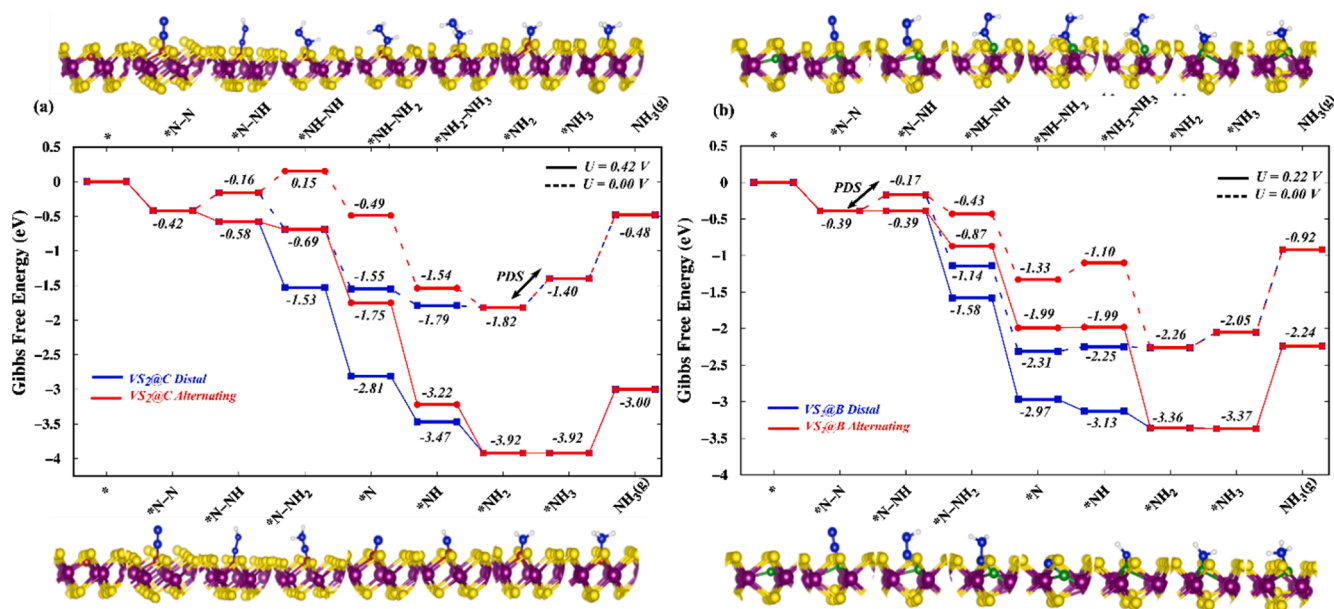


Fig. 5. Gibbs free energy diagrams of distal and alternating NRR at zero and applied potentials equivalent to their respective limiting potentials on (a) 1 T- $VS_2@C$ (0 V and 0.42 V), (b) 2H- $VS_2@B$ (0 V and 0.22 V).

2H- $VS_2@B$ is retained and there are no structural distortions after 10 ps, this is also supported by the total electronic energy of the systems which remains nearly constant throughout the simulation. This elucidates the possibility of experimental realization of B-doped vanadium disulphide in 2H-phase as a thermally stable, highly active and selective electrocatalyst for NRR at room temperature. This study presents a detailed analysis of synergistically introducing a non-metal dopant on vanadium dichalcogenides monolayer for developing efficient electrocatalysts for NRR and delves into energy difference and electronic factors as crucial parameters for N_2 adsorption, activation and reduction. We propose vanadium dichalcogenide monolayers with substitutionally doped boron as potential electrocatalyst for NRR.

4. Conclusions

In summary, a detailed study has been made on the synergistic doping of several non-metal dopants on vanadium dichalcogenide monolayers to enhance its electrocatalytic activity. An analysis of the electronic properties on $VX_2@Y_{cat}$ catalysts with high N_2 chemisorption efficacy demonstrates an overlap between the p-orbitals of non-metal dopants with the empty antibonding π^* orbitals of N_2 . This $\pi-\pi^*$ orbital hybridization coupled with high charge transfer on N_2 inherently leads to N–N activation and reduction of dinitrogen to ammonia. Further investigation on the energetics of the intermediate steps of NRR brings forth a correlation between the limiting potential and thermodynamic favourability of NH_3 (i.e., product) formation from N_2 (i.e.,

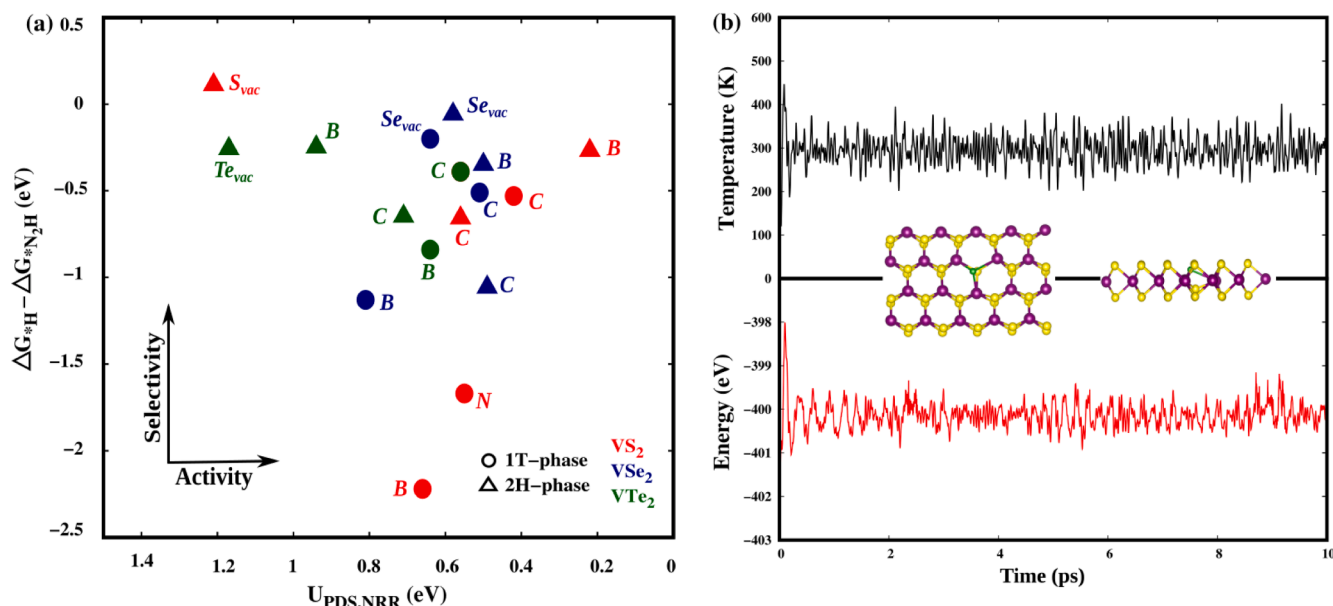


Fig. 6. (a) Selectivity of NRR over HER on select active $VX_2@Y_{cat}$ systems, the more positive the $\Delta G(^*H) - \Delta G(^*N_2H)$, the higher is the NRR selectivity, (b) Total energy and temperature of 2H- $VS_2@B$ as a function of time during the AIMD simulation for 10 ps at 298 K.

reactant) along with the electron “donor–acceptor” mechanism between boron and nitrogen. Our findings propose 1 T- $VS_2@C$ and 2H- $VS_2@B$ as efficient electrocatalysts with high NRR performance at overpotentials of 0.26 eV and 0.06 eV, respectively. The understanding from this work can be implemented for further research on introducing earth abundant, non-toxic non-metal doped transition metal dichalcogenides electrocatalysts for nitrogen reduction reaction.

CRediT authorship contribution statement

Ashakiran Maibam: Conceptualization, Methodology, Writing – original draft, Writing – review & editing. **Ravichandar Babarao:** Validation, Resources, Data curation, Writing – review & editing, Supervision. **Sailaja Krishnamurty:** Validation, Resources, Data curation, Writing – review & editing, Supervision.

Declaration of Competing Interest

The authors declare that they have no known competing financial interests or personal relationships that could have appeared to influence the work reported in this paper.

Data availability

Data will be made available on request.

Acknowledgement

A.M. acknowledges CSIR for SRF (Senior Research Fellowship) funding and AcSIR-RMIT for hosting the Joint PhD Program. The authors gratefully acknowledge National Computing Infrastructure (NCI), Australia and National Supercomputing Mission (NSM) for providing computing resources of ‘PARAM Brahma’ at IISER Pune, implemented by C-DAC and supported by the Ministry of Electronics and Information Technology (MeitY) and Department of Science and Technology (DST), Government of India.

Appendix A. Supplementary material

Supplementary data to this article can be found online at <https://doi.org/10.1016/j.apsusc.2022.154401>.

[org/10.1016/j.apsusc.2022.154401](https://doi.org/10.1016/j.apsusc.2022.154401).

References

- [1] United Nations, UN General Assembly, Transforming our world : the 2030 Agenda for Sustainable Development, 21 October 2015, A/RES/70/1, available at: <https://www.refworld.org/docid/57b6e3e44.html> [accessed 28 November 2019], 16301 (2015) 1–35.
- [2] N. Cherkasov, A.O. Ibhaddon, P. Fitzpatrick, A review of the existing and alternative methods for greener nitrogen fixation, *Chem. Eng. Process. Process Intensif.* 90 (2015) 24–33, <https://doi.org/10.1016/j.cep.2015.02.004>.
- [3] C.J.M. Van Der Ham, M.T.M. Koper, D.G.H. Hetterscheid, Challenges in reduction of dinitrogen by proton and electron transfer, *Chem. Soc. Rev.* 43 (2014) 5183–5191, <https://doi.org/10.1039/c4cs00085d>.
- [4] X. Xue, R. Chen, C. Yan, P. Zhao, Y. Hu, W. Zhang, S. Yang, Z. Jin, Review on photocatalytic and electrocatalytic artificial nitrogen fixation for ammonia synthesis at mild conditions: Advances, challenges and perspectives, *Nano Res.* 12 (2019) 1229–1249, <https://doi.org/10.1007/s12274-018-2268-5>.
- [5] H. Sun, H.-Q. Yin, W. Shi, L.-L. Yang, X.-W. Guo, H. Lin, J. Zhang, T.-B. Lu, Z.-M. Zhang, Porous β -FeOOH nanotube stabilizing Au single atom for high-efficiency nitrogen fixation, *Nano Res.* 15 (2022) 3026–3033, <https://doi.org/10.1007/s12274-021-3937-3>.
- [6] H. Yin, L. Yang, H. Sun, H. Wang, Y. Wang, M. Zhang, T. Lu, Z. Zhang, W/Mo-poloxometalate-derived electrocatalyst for high-efficiency nitrogen fixation, *Chin. Chem. Lett.* 17 (2022), <https://doi.org/10.1016/j.ccl.2022.03.060>.
- [7] C. Tang, S.Z. Qiao, How to explore ambient electrocatalytic nitrogen reduction reliably and insightfully, *Chem. Soc. Rev.* 48 (2019) 3166–3180, <https://doi.org/10.1039/c9cs00280d>.
- [8] P. Wang, Y. Huan, P. Yang, M. Cheng, J. Shi, Y. Zhang, Controlled syntheses and multifunctional applications of two-dimensional metallic transition metal dichalcogenides, *Accounts, Mater. Res.* 2 (2021) 751–763, <https://doi.org/10.1021/accounts.1c00092>.
- [9] B. Zhao, D. Shen, Z. Zhang, P. Lu, M. Hossain, J. Li, B. Li, X. Duan, 2D metallic transition-metal dichalcogenides: structures, synthesis, properties, and applications, *Adv. Funct. Mater.* 31 (2021) 1–36, <https://doi.org/10.1002/adfm.202105132>.
- [10] H. Pan, Electronic and magnetic properties of vanadium dichalcogenides monolayers tuned by hydrogenation, *J. Phys. Chem. C.* 118 (2014) 13248–13253, <https://doi.org/10.1021/jp503030b>.
- [11] M. Abdulsalam, D. Joubert, Structural, electronic and optical properties of TcX_2 ($X = S, Se, Te$) from first principles calculations, *Comput. Mater. Sci.* 115 (2016) 177–183, <https://doi.org/10.1016/j.commatsci.2015.12.053>.
- [12] H.R. Fuh, C.R. Chang, Y.K. Wang, R.F.L. Evans, R.W. Chantrell, H.T. Jeng, Newtype single-layer magnetic semiconductor in transition-metal dichalcogenides VX_2 ($X = S, Se$ and Te), *Sci. Rep.* 6 (2016) 1–11, <https://doi.org/10.1038/srep32625>.
- [13] N. Guo, X. Fan, Z. Chen, Z. Luo, Y. Hu, Y. An, D. Yang, S. Ma, Electronic and magnetic properties of group-V TMDs monolayers with defects: A first-principles study, *Comput. Mater. Sci.* 176 (2020), 109540, <https://doi.org/10.1016/j.commatsci.2020.109540>.
- [14] R. Samal, C.S. Rout, Recent developments on emerging properties, growth approaches, and advanced applications of metallic 2D layered vanadium

- dichalcogenides, *Adv. Mater. Interfaces*. 7 (2020) 1–24, <https://doi.org/10.1002/admi.201901682>.
- [15] A.H.M.A. Wasey, S. Chakrabarty, G.P. Das, Quantum size effects in layered VX₂ (X=S, Se) materials: Manifestation of metal to semimetal or semiconductor transition, *J. Appl. Phys.* 117 (2015), 064313, <https://doi.org/10.1063/1.4908114>.
- [16] F. Arnold, R.M. Stan, S.K. Mahatha, H.E. Lund, D. Curcio, M. Dendzik, H. Bana, E. Travaglia, L. Bignardi, P. Lacovig, D. Lizzit, Z. Li, M. Bianchi, J.A. Miwa, M. Bremholm, S. Lizzit, P. Hofmann, C.E. Sanders, Novel single-layer vanadium sulphide phases, *2D Mater.* 5 (2018) 0455009, <https://doi.org/10.1088/2053-1583/aad0c8>.
- [17] Z. Zhang, J. Niu, P. Yang, Y. Gong, Q. Ji, J. Shi, Q. Fang, S. Jiang, H. Li, X. Zhou, L. Gu, X. Wu, Y. Zhang, Van der Waals epitaxial growth of 2D metallic vanadium diselenide single crystals and their extra-high electrical conductivity, *Adv. Mater.* 29 (2017) 1–9, <https://doi.org/10.1002/adma.201702359>.
- [18] F. Li, K. Tu, Z. Chen, Versatile electronic properties of VSe₂ bulk, few-layers, monolayer, nanoribbons, and nanotubes: a computational exploration, *J. Phys. Chem. C* 118 (2014) 21264–21274, <https://doi.org/10.1021/jp507093t>.
- [19] P.K.J. Wong, W. Zhang, J. Zhou, F. Bussolotti, X. Yin, L. Zhang, A.T. N'Diaye, S. A. Morton, W. Chen, J. Goh, M.P. De Jong, Y.P. Feng, A.T.S. Wee, Metallic 1T Phase, 3d1 electronic configuration and charge density wave order in molecular beam epitaxy grown monolayer vanadium ditelluride, *ACS Nano* 13 (2019) 12894–12900, <https://doi.org/10.1021/acsnano.9b05349>.
- [20] K. Sugawara, Y. Nakata, K. Fujii, K. Nakayama, S. Souma, T. Takahashi, T. Sato, Monolayer VTe₂: incommensurate fermi surface nesting and suppression of charge density waves, *Phys. Rev. B* 99 (2019) 1–6, <https://doi.org/10.1103/PhysRevB.99.241404>.
- [21] D. Rehder, Vanadium nitrogenase, *J. Inorg. Biochem.* 80 (2000) 133–136, [https://doi.org/10.1016/S0162-0134\(00\)00049-0](https://doi.org/10.1016/S0162-0134(00)00049-0).
- [22] A. Maibam, S. Krishnamurthy, Nitrogen activation to reduction on a recyclable V-SAC/BN-graphene heterocatalyst sifted through dual and multiphilic descriptors, *J. Colloid Interface Sci.* 600 (2021) 480–491, <https://doi.org/10.1016/j.jcis.2021.05.027>.
- [23] G. Duvjir, B.K. Choi, I. Jang, S. Ulstrup, S. Kang, T. Thi Ly, S. Kim, Y.H. Choi, C. Jozwiak, A. Bostwick, E. Rotenberg, J.G. Park, R. Sankar, K.S. Kim, J. Kim, Y. J. Chang, Emergence of a metal-insulator transition and high-temperature charge-density waves in VSe₂ at the monolayer limit, *Nano Lett.* 18 (2018) 5432–5438, <https://doi.org/10.1021/acs.nanolett.8b01764>.
- [24] S. Memarzadeh, M.R. Roknabadi, M. Modarresi, A. Mogulkoc, A.N. Rudenko, Role of charge doping and strain in the stabilization of in-plane ferromagnetism in monolayer VSe₂ at room temperature, *2D Mater.* 8 (2021), 035022, <https://doi.org/10.1088/2053-1583/abf626>.
- [25] P.M. Coelho, K. Lasek, K. Nguyen Cong, J. Li, W. Niu, W. Liu, I.I. Oleynik, M. Batzill, Monolayer modification of VTe₂ and its charge density wave, *J. Phys. Chem. Lett.* 10 (2019) 4987–4993, <https://doi.org/10.1021/acs.jpclett.9b01949>.
- [26] T. Wang, Y. Li, C. Xia, X. Zhao, Y. An, X. Dai, Magnetic vanadium sulfide monolayers: transition from a semiconductor to a half metal by doping, *J. Mater. Chem. C* 4 (2016) 8111–8120, <https://doi.org/10.1039/c6tc01962e>.
- [27] N. Luo, C. Si, W. Duan, Structural and electronic phase transitions in ferromagnetic monolayer VS₂ induced by charge doping, *Phys. Rev. B* 95 (2017) 1–7, <https://doi.org/10.1103/PhysRevB.95.205432>.
- [28] Y. Cui, W. Fan, X. Liu, J. Ren, Y. Gao, Electronic conductivity of two-dimensional VS₂ monolayers: a first principles study, *Comput. Mater. Sci.* 200 (2021), 110767, <https://doi.org/10.1016/j.commatsci.2021.110767>.
- [29] X. Liu, Y. Jiao, Y. Zheng, S.Z. Qiao, Isolated boron sites for electroreduction of dinitrogen to ammonia, *ACS Catal.* 10 (2020) 1847–1854, <https://doi.org/10.1021/acscatal.9b04103>.
- [30] C. Liu, Q. Li, C. Wu, J. Zhang, Y. Jin, D.R. Macfarlane, C. Sun, Single-boron catalysts for nitrogen reduction reaction, *J. Am. Chem. Soc.* 141 (2019) 2884–2888, <https://doi.org/10.1021/jacs.8b13165>.
- [31] A. Maibam, T. Govindaraja, K. Selvaraj, S. Krishnamurthy, Dinitrogen activation on graphene anchored single atom catalysts: local site activity or surface phenomena, *J. Phys. Chem. C* 123 (2019) 27492–27500, <https://doi.org/10.1021/acs.jpcc.9b06757>.
- [32] J. Wu, Y.-X. Yu, Electric-field controllable metal-free materials as efficient electrocatalysts for nitrogen fixation, *J. Phys. Chem. C* 125 (2021) 23699–23708, <https://doi.org/10.1021/acs.jpcc.1c06464>.
- [33] A. Maibam, S. Krishnamurthy, M. Ahmad Dar, Electrocatalytic nitrogen reduction directed through the p-band center of boron on B_{SAC}@Mo₂C, *Mater. Adv.* 3 (2022) 592–598, <https://doi.org/10.1039/d1ma00953b>.
- [34] G. Kresse, J. Furthmüller, Efficiency of ab-initio total energy calculations for metals and semiconductors using a plane-wave basis set, *Comput. Mater. Sci.* 6 (1996) 15–50, [https://doi.org/10.1016/0927-0256\(96\)00008-0](https://doi.org/10.1016/0927-0256(96)00008-0).
- [35] J.P. Perdew, K. Burke, M. Ernzerhof, Generalized gradient approximation made simple, *Phys. Rev. Lett.* 77 (1996) 3865–3868, <https://doi.org/10.1103/PhysRevLett.77.3865>.
- [36] S. Grimme, J. Antony, S. Ehrlich, H. Krieg, A consistent and accurate ab initio parametrization of density functional dispersion correction (DFT-D) for the 94 elements H-Pu, *J. Chem. Phys.* 132 (15) (2010) 154104.
- [37] S. Nosé, A unified formulation of the constant temperature molecular dynamics methods, *J. Chem. Phys.* 81 (1) (1984) 511–519.
- [38] W.G. Hoover, Canonical dynamics: Equilibrium phase-space distributions, *Phys. Rev. A* 31 (3) (1985) 1695–1697.
- [39] G. Kresse, J. Hafner, Ab initio molecular dynamics for liquid metals, *Phys. Rev. B* 47 (1) (1993) 558–561.
- [40] J.K. Nørskov, J. Rossmeisl, A. Logadottir, L. Lindqvist, J.R. Kitchin, T. Bligaard, H. Jónsson, Origin of the overpotential for oxygen reduction at a fuel-cell cathode, *J. Phys. Chem. B* 108 (2004) 17886–17892, <https://doi.org/10.1021/jp047349j>.
- [41] J. Wu, J.-H. Li, Y.-X. Yu, Single Nb or W atom-embedded BP monolayers as highly selective and stable electrocatalysts for nitrogen fixation with low-onset potentials, *ACS Appl. Mater. Interfaces* 13 (2013) 10026–10036, <https://doi.org/10.1021/acsami.0c21429>.
- [42] J. Wu, J.-H. Li, Y.-X. Yu, Highly stable Mo-doped Fe₂P and Fe₃P monolayers as low-onset-potential electrocatalysts for nitrogen fixation, *Catal. Sci. Technol.* 11 (2021) 1419–1429, <https://doi.org/10.1039/D0CY02192J>.
- [43] R. Gholizadeh, Y.-X. Yu, N₂O + CO reaction over Si- and Se-doped graphenes: an ab initio DFT study, *Appl. Surf. Sci.* 357 (2015) 1187–1195, <https://doi.org/10.1016/j.apsusc.2015.09.163>.
- [44] W. Tang, E. Sanville, G. Henkelman, A grid-based Bader analysis algorithm without lattice bias, *J. Phys. Condens. Matter* 21 (8) (2009) 084204.
- [45] S.L. Foster, S.I.P. Bakovic, R.D. Duda, S. Maheshwari, R.D. Milton, S.D. Minteer, M. J. Janik, J.N. Renner, L.F. Greenlee, Catalysts for nitrogen reduction to ammonia, *Nat. Catal.* 1 (2018) 490–500, <https://doi.org/10.1038/s41929-018-0092-7>.
- [46] A. Bar-Even, A. Flamholz, E. Noor, R. Milo, Thermodynamic constraints shape the structure of carbon fixation pathways, *Biochimica et Biophysica Acta (BBA) - Bioenergetics* 1817 (9) (2012) 1646–1659.
- [47] P.J. Halling, Thermodynamic favorability of end products of anaerobic glucose metabolism, *ACS Omega* 5 (2020) 15843–15849, <https://doi.org/10.1021/acsomega.0c00790>.
- [48] Q. Li, Y. Guo, Y. Tian, W. Liu, K. Chu, Activating VS₂ basal planes for enhanced NRR electrocatalysis: the synergistic role of S-vacancies and B dopants, *J. Mater. Chem. A* 8 (2020) 16195–16202, <https://doi.org/10.1039/d0ta05282e>.
- [49] L. Zhang, Z. Hu, Point defects in VS₂ monolayer towards NH₃ synthesis, *Mater. Des.* 209 (2021), 110006, <https://doi.org/10.1016/j.matdes.2021.110006>.